
Electromagnetic Probes in Heavy-Ion Collisions

Habilitation

Hendrik van Hees
Johann-Wolfgang-Goethe-Universität Frankfurt
Institut für Theoretische Physik
Max-von-Laue-Straße 1
D-60438 Frankfurt am Main

April 20, 2017

vorgelegt beim Fachbereich Physik der Johann-Wolfgang-Goethe-Universität Frankfurt

Diese Habilitationsschrift wird per kumulativem Verfahren verfasst. Aus diesem Grund besteht sie aus zwei Teilen.

Teil I ist eine detaillierte Zusammenfassung der theoretischen Arbeiten, die in einem thematischen Zusammenhang mit dem Habilitationsthema

„Electromagnetic Probes in Heavy-Ion Collisions“

stehen. Sie ist in englischer Sprache verfasst.

Teil II enthält die Veröffentlichungen, die für das Thema der Habilitation relevant sind. Die Artikel wurden im Zeitraum 2000-2016 in internationalen Zeitschriften publiziert.

Aus Copyright-Gründen wurden in dieser on-line-Ausgabe der Habilitationsschrift statt der in Zeitschriften publizierten Artikel die arXiv-Preprints eingebunden.

Contents

Contents	3
I Summary	5
1 Introduction	7
2 QCD matter and electromagnetic probes	9
2.1 QCD and its local gauge symmetry	9
2.2 Approximate chiral symmetry and hadron phenomenology	11
2.3 The QCD phase diagram	16
2.4 Electromagnetic radiation from a transparent thermal source	17
2.5 Dileptons and chiral symmetry	19
2.6 Abelian vector-meson-dominance model	22
3 Electromagnetic probes in NN and AA collisions	29
3.1 Dilepton production in pp- and np-collisions at GSI-SIS energies	29
3.2 Models for electromagnetic probes in heavy-ion collisions	34
3.2.1 Electromagnetic radiation from the QGP	35
3.2.2 Electromagnetic radiation from a hot/dense hadron gas	37
3.2.3 Bulk-evolution models	46
3.3 Dilepton production in heavy-ion collisions	49
3.3.1 Dielectron production at GSI-SIS energies	50
3.3.2 Dimuon production at top CERN-SPS energy	51
3.3.3 Dileptons at FAIR and RHIC-BES energies	52
3.3.4 Dileptons at RHIC and LHC energies	54
3.4 Photon production in heavy-ion collisions	55
3.5 Outlook: dileptons and the QCD phase diagram	57
Summarized work	63
Bibliography	65

II Publications	79
H. van Hees, J. Knoll, Finite pion width effects on the rho-meson, Nucl. Phys. A 683 , 369 (2000)	81
H. van Hees, R. Rapp, Comprehensive Interpretation of Thermal Dileptons Measured at the CERN Super Proton Synchrotron, Phys. Rev. Lett. 97 , 102301 (2006)	97
H. van Hees, R. Rapp, Dilepton radiation at the CERN super-proton synchrotron, Nucl. Phys. A 806 , 339 (2008)	102
R. Rapp, J. Wambach, H. van Hees, The Chiral Restoration Transition of QCD and Low Mass Dileptons, Landolt-Börnstein I/23 , 4 (2009)	132
H. van Hees, C. Gale, R. Rapp, Thermal photons and collective flow at energies available at the BNL Relativistic Heavy-Ion Collider, Phys. Ref. C 84 , 054906 (2011)	180
J. Weil, H. van Hees, U. Mosel, Dilepton production in proton-induced reactions at SIS energies with the GiBUU transport model, Eur. Phys. J. A 48 , 111 (2012)	190
H. van Hees, M. He, R. Rapp, Pseudo-critical enhancement of thermal photons in relativistic heavy-ion collisions? Nucl. Phys. A 933 , 256 (2015)	208
R. Rapp, H. van Hees, Thermal dileptons as fireball thermometer and chronometer, Phys. Lett. B 753 , 586 (2016)	225
S. Endres, H. van Hees, J. Weil, M. Bleicher, Coarse-graining approach for dilepton production at energies available at the CERN Super Proton Synchrotron, Phys. Rev. C 91 , 054911 (2015)	229
S. Endres, H. van Hees, J. Weil, M. Bleicher, Dilepton production and reaction dynamics in heavy-ion collisions at SIS energies from coarse-grained transport simulations, Phys. Rev. C 92 , 014911 (2015)	244
G. Ramalho, M. T. Peña, J. Weil, H. van Hees, U. Mosel, Role of the pion electromagnetic form factor in the $\Delta(1232) \rightarrow \gamma^*N$ timelike transition, Phys. Rev. D 93 , 033004 (2016)	259
S. Endres, H. van Hees, M. Bleicher, Photon and dilepton production at the Facility for Antiproton and Ion Research and beam-energy scan at the Relativistic Heavy-Ion Collider using coarse-grained microscopic transport simulations, Phys. Rev. C 93 , 054901 (2016)	270
S. Endres, H. van Hees, M. Bleicher, Energy, centrality, and momentum dependence of dilepton production at collider energies in a coarse-grained transport approach, Phys. Rev. C 94 , 024912 (2016)	292

Part I

Summary

Chapter 1

Introduction

The following thesis summarizes papers related to my work on electromagnetic (em.) probes in heavy-ion collisions [1, 2, 3, 4, 5, 6, 7, 8, 9, 10, 11, 12, 13].

The main motivation to investigate the production of lepton-antilepton (e^-e^+ and $\mu^-\mu^+$) pairs (dileptons) and photons (electromagnetic probes) in heavy-ion collisions is that for these probes the created hot and dense medium, consisting of partonic and hadronic matter, is transparent, i.e., their mean free path is much larger than the extension of this fireball. Thus the measured spectra of dileptons and photons provide a space-time weighted average over the entire evolution of the medium with negligible distortions of the signal by final-state interactions.

The measured production spectra are thus directly related to the electromagnetic current-correlation function of the strongly interacting particles, and the precise measurement of the invariant-mass spectrum of dileptons provide insight into the in-medium spectral properties of partons and hadrons. This is particularly interesting, because in the low-mass region ($M_{\ell+\ell^-} \lesssim 1$ GeV) the electromagnetic current is dominated by the vector-isovector part with quantum numbers of the ρ meson and thus to the spontaneously broken approximate chiral symmetry of QCD in the light-quark sector.

In the vacuum and at low temperatures and densities the chiral symmetry is spontaneously broken due to the formation of a quark condensate, $\langle \bar{q}q \rangle \neq 0$, while at high temperatures and/or net-baryon densities one expects the chiral symmetry to be restored through the melting of the quark condensate. This implies that the hadronic mass spectrum becomes degenerate between the hadron multiplets forming chiral partners. In the sector of the vector mesons, particularly the isovector-vector $\rho(770)$ meson should become degenerate with its chiral partner, the isovector-axial-vector $a_1(1260)$.

Within the so-called vector-meson dominance (VMD) model, which assumes that the hadronic electromagnetic current is proportional to the neutral vector-meson fields, the measurement of dilepton-invariant-mass spectra in the medium thus sheds light on the microscopic mechanism behind the expected substantial changes of the vector-meson mass spectrum. Indeed, using effective hadronic models based on (extended) VMD, together with detailed simulations of the bulk-medium evolution can describe satisfactorily all known data about the production of dileptons and photons in heavy-ion collisions ranging from the lowest to the highest beam energies available at SIS 18 (GSI), the SPS (CERN), RHIC (BNL), and the LHC (CERN). The conclusion from these studies is that the masses of the light vector mesons, ρ , ω , and ϕ do not considerably change in the hot and dense medium while their spectral shape broadens tremendously, leading to a significant enhancement of the dilepton yield in the invariant-mass range below the ρ/ω peak. According to the hadronic models this broadening of the vector meson's spectral shape is mostly driven by interactions with baryon (and anti-baryon) resonances, particularly the low-mass tail down to the dilepton threshold.

1. Introduction

Although a direct measurement of the corresponding axial-vector chiral partner channels is not feasible, through the successful theoretical description of the dilepton data from partonic and hadronic sources, one can conclude indirectly that the restoration of chiral symmetry is driven by the melting of the resonance structure of hadrons towards a continuum. Particularly the dilepton and photon production rates extrapolated from the low-temperature/density region via hadronic and down from the high-temperature/density region from hard-thermal-loop improved QCD (or from first determinations of the electromagnetic-current correlation function from lattice-QCD (lQCD) calculations) merge smoothly into each other at temperatures close to the pseudo-critical phase-transition temperature for deconfinement and chiral-symmetry restoration, $T_c \simeq 155\text{-}160$ MeV as evaluated with lQCD.

Chapter 2

QCD matter and electromagnetic probes

The Standard Model of elementary particles describes the known matter to an astonishing accuracy. According to this quantum-field theoretical model all visible matter consists of quarks and leptons, spin-1/2 Dirac fermions which interact via the strong, weak and electromagnetic interactions, which are described within the paradigm of local gauge symmetry, i.e., via their interaction with gauge bosons introduced to extend global symmetries of field multiplets admitting a global semisimple compact Lie-symmetry group to the corresponding local symmetry. In this chapter we briefly summarize the Standard Model as far as it is needed to relate the observables concerning electromagnetic probes in heavy-ion collisions to its fundamental and “accidental” symmetries. Concerning the various sign conventions we follow [DGH92].

2.1 QCD and its local gauge symmetry

Quantum Chromodynamics describes the interactions of quarks, the fundamental building blocks of hadrons, based on a local SU(3) gauge symmetry. Each of the quarks transforms according to the fundamental representation of SU(3), i.e., they form triplets under the symmetry transformation. The corresponding charge-like quantum numbers are referred to as **color**. Further, there exist six quark flavors, up, down, strange, charm, bottom (or beauty) and top (or truth). In the following we collectively write q for the quark fields,

$$q = (u, d, s, c, b, t), \quad (2.1.1)$$

where each of the Dirac spinors $u, d, s, c, b,$ and t builds a color triplet.

The generators of the color-symmetry transformations are given in terms of the Gell-Mann matrices as

$$\tau^a = \frac{1}{2} \lambda^a, \quad a \in \{1, \dots, 8\} \quad (2.1.2)$$

and build a basis of the Lie algebra $\mathfrak{su}(3)$. The τ^a are chosen such that

$$\text{Tr}(\tau^a \tau^b) = \frac{1}{2} \delta^{ab}, \quad (2.1.3)$$

and the commutator relations

$$[\tau^a, \tau^b] = i f^{abc} \tau^c \quad (2.1.4)$$

define the totally antisymmetric real structure constants f^{abc} .

2. QCD matter and electromagnetic probes

The Lagrangian for the free quarks,

$$\mathcal{L} = \bar{q}(i\cancel{D} - \hat{m}_q)q, \quad (2.1.5)$$

where the diagonal real mass matrix $\hat{m}_q = \text{diag}(m_u, m_d, m_s, m_c, m_b, m_t)$ acts in flavor space, is invariant under global unitary transformations in color space,

$$q \rightarrow q' = \exp(-ig\chi^a\tau^a)q = U(\chi)q \quad (2.1.6)$$

with the real coupling constant g . To extend this global symmetry to a local gauge symmetry one introduces the gauge-boson (**gluon**) fields $A_\mu = \tau^a A_\mu^a$ and the gauge-covariant derivative

$$D_\mu = \partial_\mu + igA_\mu = \partial_\mu + ig\tau^a A_\mu^a. \quad (2.1.7)$$

Then, writing in (2.1.5) a covariant instead of a partial derivative,

$$\mathcal{L}_{\text{quarks}} = \bar{q}(i\cancel{D} - \hat{m}_q)q, \quad (2.1.8)$$

the Lagrangian becomes invariant under local gauge transformations, i.e., making $\chi^a = \chi^a(x)$ space-time dependent, when the gauge fields are defined to transform as

$$A'_\mu = U(\chi)A_\mu U^\dagger(\chi) - \frac{i}{g}U(\chi)\partial_\mu U^\dagger(\chi). \quad (2.1.9)$$

Indeed, the second term is again an $\text{su}(3)$ matrix (i.e., a hermitean and traceless $\mathbb{C}^{3 \times 3}$ matrix).

To construct a kinetic term for the gluon fields, we define the field-strength tensor

$$F_{\mu\nu} = \frac{1}{ig} [D_\mu, D_\nu] = \partial_\mu A_\nu - \partial_\nu A_\mu + ig [A_\mu, A_\nu], \quad (2.1.10)$$

which transforms under the local gauge transformations (2.1.6) with the adjoint representation of the color $\text{SU}(3)$,

$$F'_{\mu\nu} = UF_{\mu\nu}U^\dagger. \quad (2.1.11)$$

Thus we can define the kinetic term of the gluon fields as

$$\mathcal{L}_{\text{gluons}} = -\frac{1}{2}\text{Tr}(F_{\mu\nu}F^{\mu\nu}) = -\frac{1}{4}F_{\mu\nu}^a F^{a\mu\nu}, \quad (2.1.12)$$

which is not only a bilinear form of the derivatives of the gauge fields but also contains three-gluon and four-gluon interactions, as becomes clear when we write (2.1.10) in terms of the field components, using (2.1.4),

$$F_{\mu\nu}^a = \partial_\mu A_\nu^a - \partial_\nu A_\mu^a - gf^{abc}A_\mu^b A_\nu^c. \quad (2.1.13)$$

We do not give the details about how to quantize the now complete QCD Lagrangian (see, e.g., [BL86, Wei96, Sch14])

$$\mathcal{L}_{\text{QCD}} = -\frac{1}{4}F_{\mu\nu}^a F^{a\mu\nu} + \bar{q}(i\cancel{D} - \hat{m}_q)q. \quad (2.1.14)$$

We only mention that the perturbative renormalization-group analysis of QCD revealed that the running coupling constant decreases with increasing renormalization scales (**asymptotic freedom**), i.e., the strong interaction becomes perturbative only in the limit of large energy-momentum transfers in scattering processes [GW73, Pol73] (cf. Fig. 2.1).

2.2. Approximate chiral symmetry and hadron phenomenology

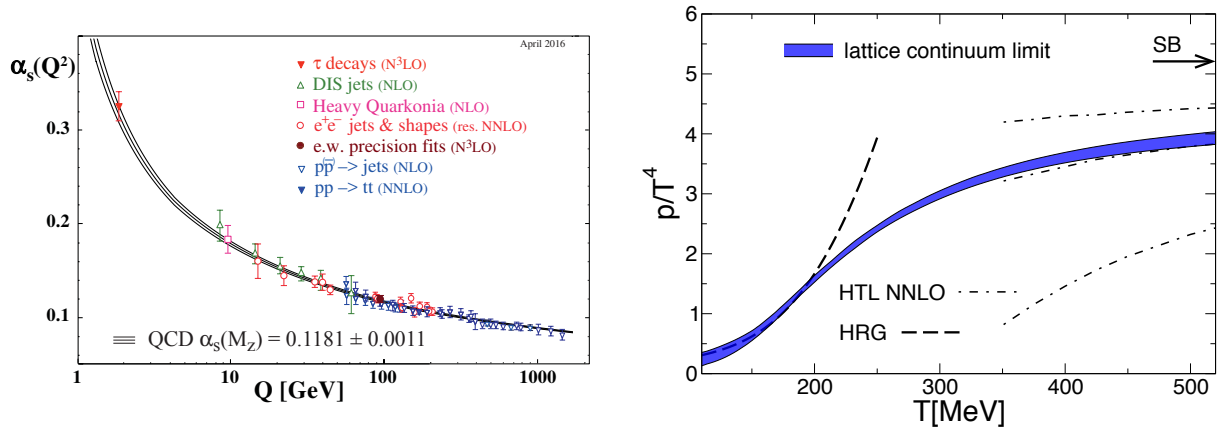


Figure 2.1: *Left panel: The running coupling α_s as a function of the energy scale Q . The respective degree of QCD perturbation theory used in the extraction of α_s is indicated in brackets (NLO: next-to-leading order; NNLO: next-to-next-to leading order; res. NNLO: NNLO matched with resummed next-to-leading logs; N³LO: next-to-NNLO). Figure taken from [P⁺ 16]. Right panel: Continuum-extrapolated results from a lattice calculation [BFH⁺ 14] of the QCD EoS at $\mu_B = 0$ in comparison to a hadron-resonance gas calculation at low temperatures (dashed black line) and NNLO hard-thermal loop pQCD results with three different renormalization scales $\mu = \pi T, 2\pi T, 4\pi T$ [ALSS11]. Figure taken from [BFH⁺ 14].*

A non-perturbative consequence of QCD is confinement, i.e., the empirical fact that all color charges are confined in color-less bound states. Phenomenologically these are the known hadrons, i.e., **baryons** consisting of three (constituent) quarks and mesons consisting of an anti-quark and a quark.

Asymptotic freedom implies that matter of strongly interacting particles should undergo a phase transition, where hadrons are the relevant effective degrees of freedom in the vacuum and at low temperatures and densities to a state, where quarks and gluons (or quark-gluon like quasiparticles) become the relevant degrees of freedom. Lattice-QCD calculations at finite temperature and $\mu_B = 0$ indeed show that the thermodynamic potentials (like energy density and pressure) show a strong raise at temperatures around $T_c \simeq 150$ -160 MeV [Kar02, LP03, Phi13]. The corresponding equations of state are well reproduced at low temperature $T \lesssim T_c$ by a hadron-resonance gas thermal model [KRT03a, KRT03b, ABMSW12, BFH⁺ 14] and for $T \gtrsim 2$ -3 T_c with hard-thermal-loop resummed pQCD [BIR01, BIR99], i.e., quasi-free quarks and gluons in the medium, which indeed indicates the change of effective degrees of freedom from hadrons at low and quarks and gluons at high temperatures (cf. Fig. 2.1).

2.2 Approximate chiral symmetry and hadron phenomenology

In the previous Section we have discussed the local color-gauge symmetry as the fundamental symmetry underlying the construction of the interactions between quarks and gluons as the fundamental building blocks of the hadrons (i.e., mesons and baryons). At low energies, however, phenomenologically only the color-neutral hadrons occur as effective degrees of freedom, and only these are observable as asymptotic free states in the usual sense of relativistic quantum field theory. The only known way to evaluate the properties of hadrons in “ab-initio QCD calculations” is lQCD, but this is restricted to low net-baryon densities (or small baryochemical potentials, μ_B) and is evaluated in Euclidean quantum field theory. Usually it is difficult to analytically continue to Minkowski space, which is particularly

2. QCD matter and electromagnetic probes

interesting for quantities like the em. current correlation function, which is important for a theoretical understanding of em. probes in heavy-ion collisions.

Thus in the low-energy region, effective models for hadrons are needed for a comprehensive analysis of em. probes. The most important guideline for building such effective models is the approximate chiral symmetry of the strong interactions, which has already been known before the discovery of QCD [NJL61a, NJL61b, DGH92, Koc97].

Since quarks are not observable as free particles, the determination of their masses relies on IQCD calculations of the hadron-mass spectrum, varying the corresponding bare quark masses, combined with perturbative methods to relate the bare quark masses determined from the lattice calculation to the renormalized masses, usually using the $\overline{\text{MS}}$ -renormalization scheme based on dimensional regularization (for a review, see the section on quark masses in [P⁺16]). It turns out that the light-quark masses (at a renormalization scale $\mu = 2 \text{ GeV}$) are $m_u = 2.3_{-0.5}^{+0.7} \text{ MeV}$, $m_d = 4.8_{-0.3}^{+0.5} \text{ MeV}$, and $m_s = (95 \pm 5) \text{ MeV}$. These masses are small compared to typical hadronic scales of about 1 GeV. Thus one can consider the limit $\hat{m}_q \rightarrow 0$.

For simplicity we only take into account the u and d quarks which form the isospin doublet $\psi = (u, d)$. For these two quarks the QCD Lagrangian in the chiral limit (i.e., setting $\hat{m}_{ud} = 0$) reads

$$\mathcal{L}_\chi = -\frac{1}{4}F_{\mu\nu}^a F^{a\mu\nu} + \bar{\psi}i\not{D}\psi. \quad (2.2.1)$$

Now we can decompose the Dirac spinors in their chirality eigenstates,

$$\psi_L = P_L \psi, \quad \psi_R = P_R \psi, \quad (2.2.2)$$

using the projection operators

$$P_L = \frac{1}{2}(\mathbb{1} - \gamma^5), \quad P_R = \frac{1}{2}(\mathbb{1} + \gamma^5), \quad (2.2.3)$$

with $\gamma^5 = i\gamma^0\gamma^1\gamma^2\gamma^3$, obeying

$$P_L^2 = P_L, \quad P_R^2 = P_R, \quad P_L P_R = P_R P_L = 0. \quad (2.2.4)$$

Since $\{\gamma^5, \gamma^\mu\} = 0$ and $\gamma^{5\dagger} = \gamma^5$ we have

$$\bar{\psi}_L = \psi_L^\dagger \gamma^0 = \bar{\psi} P_R, \quad \bar{\psi}_R = \psi_R^\dagger \gamma^0 = \bar{\psi} P_L. \quad (2.2.5)$$

Thus we find after some simple algebra

$$\bar{\psi} \gamma^\mu \psi = \bar{\psi}_L \gamma^\mu \psi_L + \bar{\psi}_R \gamma^\mu \psi_R, \quad (2.2.6)$$

$$\bar{\psi} \psi = \bar{\psi}_L \psi_R + \bar{\psi}_R \psi_L. \quad (2.2.7)$$

This implies that the Lagrangian in the chiral limit is invariant under a global symmetry group $\text{SU}(2)_L \times \text{SU}(2)_R \times \text{U}(1)_V \times \text{U}(1)_A$, because we can apply separate isospin rotations to the left- and right-handed parts of the quark doublet,

$$\psi_L \rightarrow g_L \psi_L = \exp(-i\vec{\alpha}_L \cdot \vec{t}) \psi_L, \quad \psi_R \rightarrow g_R \psi_R = \exp(-i\vec{\alpha}_R \cdot \vec{t}) \psi_R, \quad (2.2.8)$$

where $\vec{t} = \vec{\sigma}/2$ are the usual $\text{su}(2)$ matrices, defined to act in flavor space, i.e., mixing u and d in the flavor doublet (u, d) . Further, of course, also the multiplication of the left- and right-handed parts with

2.2. Approximate chiral symmetry and hadron phenomenology

different phase factors does not change the Lagrangian (2.2.1). However, for the following it is more convenient to write this independent U(1) symmetries as the vector- and axial-isoscalar transformations

$$\psi \rightarrow \exp(-i\alpha_V)\psi, \quad \psi \rightarrow \exp(-i\alpha_V\gamma^5)\psi. \quad (2.2.9)$$

On the classical level the corresponding Noether currents

$$j_{L,R}^{a\mu} = \bar{\psi}_{L,R} t^a \gamma^\mu \psi_{L,R}, \quad j_V^\mu = \bar{\psi} \gamma^\mu \psi, \quad j_A^\mu = \bar{\psi} \gamma^\mu \gamma^5 \psi \quad (2.2.10)$$

are conserved due to this chiral symmetry. For reasons, becoming clear in a moment, it is more common to consider the vector- and axial-isovector currents

$$j_V^{a\mu} = j_R^\mu + j_L^\mu = \bar{\psi} t^a \gamma^\mu \psi, \quad j_A^{a\mu} = j_R^\mu - j_L^\mu = \bar{\psi} t^a \gamma^\mu \gamma^5 \psi, \quad (2.2.11)$$

which are, of course, also conserved.

One should, however note that for QCD the U(1)_A symmetry is broken in the quantized theory by an anomaly [Adl69, BJ69, PS95, Wei96, Sch14], as reveals the perturbative evaluation of triangle diagrams involving, e.g., two vector-isoscalar and an axial-isoscalar current¹. The reason is that there exists no regularization scheme that keeps both the U(1)_V and U(1)_A symmetries. Thus one can choose, which of the corresponding two currents (or any linear combination of them) (2.2.9) survives the quantization of the model choosing corresponding renormalization conditions. However since the vector-isoscalar current is proportional to the electromagnetic current of the quarks, we must keep the U(1)_V symmetry intact, i.e., we have to renormalize the triangle diagram such that the vector-isoscalar current Ward-Takahashi identities hold in the usual form, because otherwise one would break the local gauge invariance of the electromagnetic interaction explicitly by the anomaly and invalidate QED for the quarks. One should note that there is no anomaly in the vector-isovector and axialvector-isovector symmetry, because the critical triangle diagram is $\propto \text{Tr } t^a \text{Tr } \tau^b \tau^c = 0$ (with the flavor su(2) and color su(3) matrices t^a and τ^b).

Further we note that the anomalous breaking of the U(1)_A symmetry due to the electromagnetic interaction² is welcome, because in context with the electromagnetic interaction of pions it makes the observed decay rates of the electromagnetic decay of the neutral pion $\pi^0 \rightarrow \gamma\gamma$ or the related Dalitz decay $\pi^0 \rightarrow \gamma e^+ e^-$ consistent with the now to be discussed PCAC (partial conservation of the axial (isovector) current) hypothesis (see, e.g., [DGH92, Wei96, Sch14]).

¹In the path-integral formalism the anomalous breaking is due to the non-invariance of the fermionic path-integral measure, and the form of the anomalous symmetry breaking holds at any order of perturbation theory [Fuj79, Fuj80]. In either way, the relevant trace from the triangle diagram of the involved color matrices is $\text{Tr } \tau^a \tau^b = N_{\text{flavor}} \delta^{ab}/2$, where we have taken into account also the trace over the number of flavors, which gives simply the factor N_{flavor} . The anomaly can be summarized in the formula

$$\partial_\mu j_A^\mu = -\frac{g^2 N_{\text{flavor}}}{32\pi^2} \epsilon^{\mu\nu\rho\sigma} F_{\mu\nu}^a F_{\rho\sigma}^a.$$

²In the triangle diagram with one axial-isovector and two electromagnetic vector currents, contrary to the case of QCD we the relevant trace of the flavor-degrees of freedom is $\text{Tr } t^a \hat{q}^2$, where \hat{q} is the charge matrix of the quarks also acting in flavor space. For our two-flavor case we have $\hat{q} = \text{diag}\{2/3, -1/3\}$ and thus one finds $\text{Tr } t^a \hat{q}^2 = N_{\text{color}} \delta^{a3}/6$. Since t^3 refers to the neutral pion, one has the anomaly

$$\partial_\mu j_A^{a\mu} = -\frac{N_{\text{color}} e^2 \delta^{a3}}{3 \cdot 32\pi^2} \epsilon^{\mu\nu\rho\sigma} F_{\mu\nu} F_{\rho\sigma},$$

where $F_{\mu\nu}$ is the electromagnetic field-strength tensor. The axial isovector current for $a = 3$ is associated with the neutral pion, and the evaluation of the anomaly results in an excellent agreement between the measured decay rate for $\pi^0 \rightarrow \gamma\gamma$ for $N_{\text{color}} = 3$, which was one of the first “measurements” of the number of colors.

2. QCD matter and electromagnetic probes

The mass term

$$\mathcal{L}_{\chi B} = -\bar{\psi} \hat{m}_{ud} \psi = -\bar{\psi}_L \hat{m}_{ud} \psi_R - \bar{\psi}_R \hat{m}_{ud} \psi_L, \quad \hat{m}_{ud} = \text{diag}(m_u, m_d) \quad (2.2.12)$$

breaks the chiral symmetry explicitly. If the light-quark masses were equal, the Lagrangian would still be symmetric under the vector-isovector transformations with $g_L = g_R$, i.e., there would still be the isospin symmetry left unbroken, i.e.,

$$\psi \rightarrow g_V \psi, \quad g_V = \exp(-i\vec{\alpha}_V \cdot \vec{t}) \quad (2.2.13)$$

would still be a symmetry transformation, while the axial-vector-isovector transformations

$$\psi \rightarrow g_A \psi, \quad g_A = \exp(-i\vec{\alpha}_A \cdot \vec{t} \gamma^5) \quad (2.2.14)$$

were no symmetry transformations anymore. Of course, the vector-isoscalar symmetry

$$\psi \rightarrow \exp(-i\alpha_V) \psi \quad (2.2.15)$$

is also left unbroken by the mass term.

Now, despite the fact that $m_u \neq m_d$ in the hadronic world isospin symmetry is only slightly broken. This is due to the fact that a large part of the mass of hadrons like the nucleons is dynamically generated by the strong interaction, and thus the observed isospin-symmetry breaking can be considered as a small perturbation which is due to the difference in the bare up- and down-quark masses (which, however, are small compared to the typical hadron-mass scale of around 1 GeV) and the electromagnetic interaction. Thus in the hadronic world the isospin symmetry is valid to a much higher accuracy than suggested by the large difference of the small up- and down-quark masses in the QCD Lagrangian.

Since the interaction part of QCD is chirally symmetric one would expect that the dynamically generated hadron masses should show a symmetry according to the full chiral symmetry group. In other words, with the full $SU(2)_L \times SU(2)_R$ symmetry, the hadron-mass spectrum should be degenerate, i.e., there should be hadrons with equal mass and opposite parity. E.g., in the meson sector the lowest lying scalar and pseudoscalar mesons are the pseudoscalar pions $m_\pi \simeq 140$ MeV and the scalar $f_0(500)$ or $\sigma(500)$ meson with a mass of around 400-550 MeV; for the vector mesons we have the $\rho(770)$ with a mass of 775 MeV and the $a_1(1260)$ with a mass of 1230 MeV. In the baryonic sector we find the nucleons with a mass of about 938 MeV and their chiral partner the $N(1535)$ with a mass of 1525-1545 MeV (all mass values are quoted from [O⁺14]).

This suggests that even in the chiral limit of vanishing quark masses the chiral symmetry is spontaneously broken, i.e., since the (approximate) isospin symmetry is observed in nature, this indicates that in the QCD ground state a non-vanishing quark condensate,

$$\langle \Omega | \bar{\psi} \psi | \Omega \rangle \neq 0, \quad (2.2.16)$$

forms due to the strong attractive interactions in the quark-antiquark channel. This implies that the ground state in the chiral limit is symmetric under the vector-isovector rotations g_V but not under the axialvector-isovector rotations g_A . According to the Noether theorem the generators of these symmetries are the corresponding charges of the Noether currents (2.2.11)

$$Q_V^a = \int_{\mathbb{R}^3} d^3 \vec{x} j_V^{a0}, \quad Q_A^a = \int_{\mathbb{R}^3} d^3 \vec{x} j_A^{a0}. \quad (2.2.17)$$

2.2. Approximate chiral symmetry and hadron phenomenology

Thus while $Q_V^a |\Omega\rangle = 0$

$$Q_A^a |\Omega\rangle \neq 0. \quad (2.2.18)$$

On the other hand due to the symmetry

$$[Q_A^a, H] = 0, \quad (2.2.19)$$

which implies that the QCD vacuum state is degenerate. Now we can define energy-momentum eigenstates

$$|\pi^a(\vec{p})\rangle = -\frac{2i}{f_\pi} \int_{\mathbb{R}^3} d^3\vec{x} \exp(i\vec{p} \cdot \vec{x}) j_A^{a0}(x) |\Omega\rangle. \quad (2.2.20)$$

Since for $\vec{p} = 0$, according to (2.2.17) the integral in this equation is just the Noether-charge operator Q_A^a , the energy for $\vec{p} = 0$ must be $E_{\vec{p}=0} = 0$, because $Q_A^a |\Omega\rangle$ has the same energy as the ground state. This implies that the state (2.2.20) describes a meson-like excitation with $m_\pi = 0$. This is the famous Goldstone theorem: If a continuous symmetry is spontaneously broken to a smaller subgroup (in our case $SU(2)_L \times SU(2)_R \rightarrow SU(2)_V$) there must be as many massless scalar or pseudoscalar bosons in the particle spectrum of the model as independent broken symmetries, the Nambu-Goldstone bosons. Here, these are the $\dim SU(2)_L \times SU(2)_R - \dim SU(2)_V = 3$ pions. Normalizing the momentum eigenstates as usual by the convention

$$\langle \pi^b(\vec{q}) | \pi^a(\vec{p}) \rangle = 2E_{\vec{p}} (2\pi)^3 \delta^{ab} \delta^{(3)}(\vec{p} - \vec{q}), \quad (2.2.21)$$

it follows that

$$\langle \pi^b(\vec{q}) | J_A^{a0}(x) \Omega \rangle = iE_{\vec{q}} f_\pi \delta^{ab} \exp(i\vec{q} \cdot \vec{x}) \quad (2.2.22)$$

or, in manifestly covariant form,

$$\langle \pi^b(\vec{q}) | J_A^{a\mu}(x) \Omega \rangle = i f_\pi q^\mu \delta^{ab} \exp(i\vec{q} \cdot \vec{x}). \quad (2.2.23)$$

Since (in the chiral limit) the axial current is conserved this again implies $q_\mu q^\mu = 0$, i.e., the masslessness of the particle described by the momentum eigenstates $|\pi^a(\vec{q})\rangle$. The constant $f_\pi \simeq 92$ MeV is determined from the semileptonic decay of the charged pions like $\pi^- \rightarrow \mu \bar{\nu}_\mu$ and thus called the pion-decay constant³.

Taking into account the explicit breaking of chiral symmetry by the quark-mass terms (and neglecting the anomalous breaking of the axial isovector symmetry by the electromagnetic interaction) one finds

$$\partial_\mu J_A^{a\mu} = i\bar{\psi} \{ \hat{m}_{ud}, t^a \} \psi. \quad (2.2.24)$$

Due to this explicit breaking of the chiral symmetry the pions acquire a small mass $m_\pi \simeq 139$ MeV. Using (2.2.24) together with (2.2.23), now using $q_\mu q^\mu = m_\pi^2$ leads to the Gell-Mann-Oakes-Renner (GMOR) relation

$$m_\pi^2 f_\pi^2 = V^3 (m_u + m_d), \quad V^3 = |\langle \Omega | \bar{u}u | \Omega \rangle| = |\langle \Omega | \bar{d}d | \Omega \rangle|. \quad (2.2.25)$$

Plugging in the above given values for the various quantities, we find $V \simeq 285$ MeV.

³Note that the value differs in the literature by factors $\sqrt{2}$ or 2 due to different definitions of the factors in (2.2.20) from the here chosen convention, which is taken from [PS95, Koc97, Sch14].

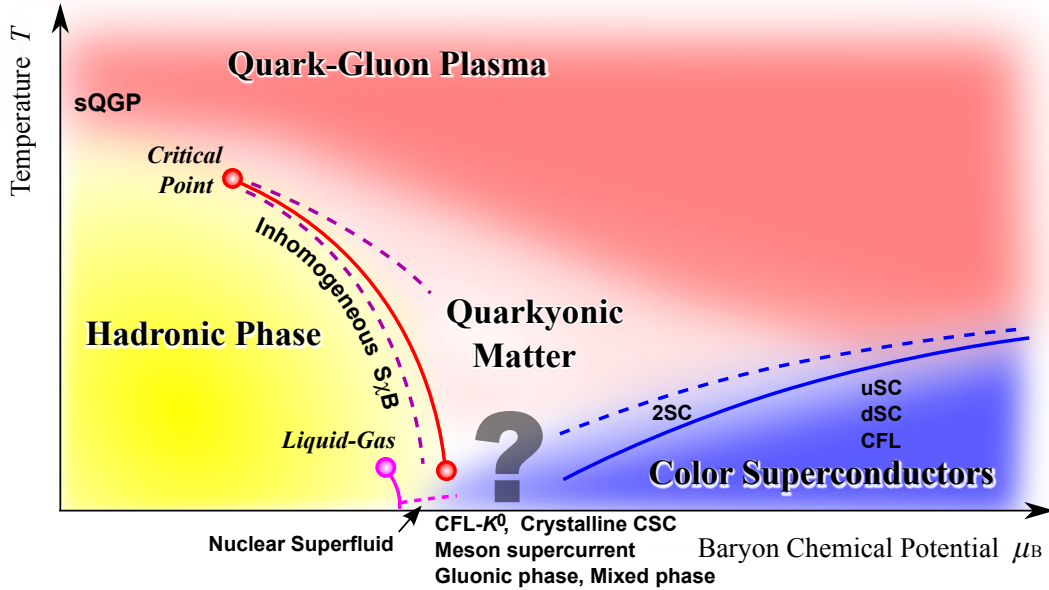


Figure 2.2: Schematic QCD phase diagram with possible phase boundaries based on chiral symmetry. Figure taken from [FH11].

2.3 The QCD phase diagram

Asymptotic freedom of QCD suggests that hadronic matter at high temperatures and densities undergoes a transition to a state, where quarks and gluons become the relevant microscopic degrees of freedom. Under such extreme conditions one also expects that the $\bar{q}q$ condensate melts and the above discussed (approximate) chiral symmetry is restored [FHK⁺11].

On a fundamental level this can only be investigated with lattice-QCD simulations at finite temperature and vanishing baryochemical potential $\mu_B = 0$. For physical masses of the light u-, d-, and s-quarks lQCD calculations show that the transition from a hot and dense hadronic medium to a partonic quark-gluon plasma (deconfinement-confinement transition) and the chiral transition are both of cross-over type and occur around the same (pseudo-)critical temperature $T_c \simeq 150\text{-}160$ MeV [Kar02, Phi13, BEF⁺11]. Here the chiral phase transition is characterized by the quark condensate as an order parameter. For the deconfinement-confinement transition one uses Polyakov loops as indicators for the transition, although they are order parameters only in “quenched QCD”, i.e., when dynamical quarks are neglected.

Although considerable progress has been made to overcome the problem to evaluate the QCD Equation of State (EoS) at $\mu_B \neq 0$ with lQCD methods, here effective hadronic or quark-meson models based on chiral symmetry have to be used to explore possible scenarios for phase transitions from hadronic to partonic matter. Many of these models indicate that the phase transition at $T = 0$ is a first-order transition, i.e., in the $T\text{-}\mu_B$ one expects that at lower temperatures and large net-baryon densities a first-order transition line should occur, which ends at a critical point, where the transition becomes of 2nd order. On the other hand some lQCD calculations indicate that such a critical point also might not exist [Phi13].

Recently, many effective theories, based on the approximate chiral symmetry of QCD in the light-quark sector have been investigated at finite temperature and baryochemical potential. For a realistic

2.4. Electromagnetic radiation from a transparent thermal source

description of the EoS also the gluonic degrees of freedom have to be considered to account for the confinement properties of QCD. For this purpose effective chiral models like the Nambu-Jona-Lasinio model [MO96, Pis00, Fuk04, MRS06, RTW06, GMMR06, SFR07, KKMY08] or quark-meson models (i.e., a linear σ model with quarks and mesons as elementary degrees of freedom) [KS07, SPW07, MJH10, GT10, HPS11, MS10] have been generalized by the inclusion of Polyakov-loop degrees of freedom (so-called Polyakov-loop extended Nambu-Jona-Lasinio (PNJL) or quark-meson (PQM) models, respectively). These models can well reproduce the findings in lQCD calculations at vanishing or small baryochemical potential, and thus one may hope that they may also be successfully extrapolated to higher net-baryon densities.

For a realistic description of the QCD-phase diagram, calculations going beyond a pure mean-field model (Ginzburg-Landau approximation) are necessary, as the functional renormalization group [JW96, SP99, Tet03, SW05, SW07, SW08, SFN⁺10, NSS⁺10, SSFR10, SFR11]. Here one needs the dependence of the deconfinement-transition temperature on quark-flavor number and density in the Polyakov-Loop potential, which are estimated with perturbative hard/dense-thermal-loop (HTL/DTL) techniques. E.g., within a PQM model [Sch12] such techniques lead to the location of the critical point at a quite large baryochemical potential, $\mu_{B,\text{crit}} \simeq 300$ MeV, and low temperature, $T_{\text{crit}} \simeq 20$ MeV. At the same time the region, where chiral symmetry is restored but matter is still (effectively) confined (“quarkyonic state” predicted based on the large- N_c limit of QCD [MP07, HMP08]) becomes quite small.

2.4 Electromagnetic radiation from a transparent thermal source

Starting from this Section, following [RW00a] and [4], we briefly discuss general ideas on the radiation of both dileptons (e^+e^- and $\mu^+\mu^-$ pairs) and photons from a thermal source of strongly interacting particles. As discussed in Chapter 3, the hot and dense fireballs created in heavy-ion collisions behave with good accuracy like a collectively expanding fluid close to local thermal equilibrium, i.e., as a strongly coupled many-body system as far as the strong interaction is concerned. On the other hand the medium is transparent for leptons and photons that interact with the medium only via the electromagnetic and weak interactions. As we shall derive in a moment, this implies that the radiation of electromagnetic probes can be expressed in terms of the equilibrium **electromagnetic current-current correlation function**, with the average taken in the fully interacting quantum field theory as far as the strong interaction is concerned and in leading order of the electromagnetic interaction, $\mathcal{O}(\alpha_{\text{em}})$ for photons and $\mathcal{O}(\alpha_{\text{em}}^2)$ for dileptons [Fei76, MT85, GK91].

We derive the corresponding McLerran-Toimela formula for dileptons, assuming a (locally) equilibrated medium with a fluid cell at rest. The aim is to calculate the dilepton-production rate,

$$\frac{dR_{\ell^+\ell^-}}{d^4k} = \frac{dN_{\ell^+\ell^-}}{d^4x d^4k}, \quad (2.4.1)$$

i.e., the number of $\ell^+\ell^-$ -pairs per time and volume and pair ℓ energy and momentum. To that end we work in an interaction picture with the “undisturbed Hamiltonian” fully including the strong interactions of quarks and gluons or hadrons and the “interaction Hamiltonian” given by the electromagnetic interaction

$$H_I = e \int_{\mathbb{R}^3} d^3\vec{x} J_{\text{em}}^\mu(t, \vec{x}) A_\mu(t, \vec{x}). \quad (2.4.2)$$

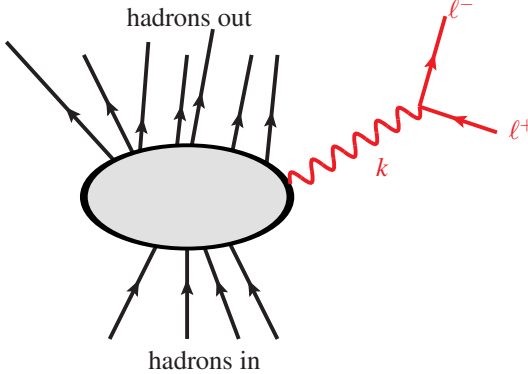
2. QCD matter and electromagnetic probes

On the fundamental level the electromagnetic current J_{em}^μ is given by

$$J_{\text{em}}^\mu = -(\bar{\psi}_e, \bar{\psi}_\mu, \bar{\psi}_\tau)\gamma^\mu \begin{pmatrix} \psi_e \\ \psi_\mu \\ \psi_\tau \end{pmatrix} + \frac{2}{3}(\bar{\psi}_u, \bar{\psi}_c, \bar{\psi}_t)\gamma^\mu \begin{pmatrix} \psi_u \\ \psi_c \\ \psi_t \end{pmatrix} - \frac{1}{3}(\bar{\psi}_d, \bar{\psi}_s, \bar{\psi}_b)\gamma^\mu \begin{pmatrix} \psi_d \\ \psi_s \\ \psi_b \end{pmatrix}. \quad (2.4.3)$$

Working in leading order of the electromagnetic interaction a schematic Feynman diagram for the transition-matrix element for the production of one $\ell^+\ell^-$ pair $|i\rangle \rightarrow |f'\rangle = |f, \ell^+\ell^-(k)\rangle$, where i and f are arbitrary hadronic initial and final states, is given by

$S_{f'i} =$



$(2.4.4)$

$$= e \left\langle f \left| \int d^4x J_{\text{em}}^\mu(x) \right| i \right\rangle D_\gamma^{\mu\nu}(x, x') \bar{u}_\ell(x) \gamma_\nu v_\ell(x').$$

Here u_ℓ and v_ℓ are the usual free Dirac spinors for the lepton and the antilepton in the final state, and $D_\gamma^{\mu\nu}$ is the photon propagator in an arbitrary gauge, e.g., in the Feynman gauge, where it reads in momentum representation

$$D_\gamma^{\mu\nu}(k) = -\frac{\eta^{\mu\nu}}{k^2 + i0^+}. \quad (2.4.5)$$

In the momentum representation the matrix element reads

$$S_{f'i} = iT_{f'i}(2\pi)^4 \delta^{(4)}(P_f + k - P_i) \quad (2.4.6)$$

and the dilepton-production rate according to ‘‘Fermi’s trick’’ [PS95]

$$\frac{dR}{d^4k} = (2\pi)^4 \left\langle \delta^{(4)}(P_f + k - P_i) | T_{f'i} |^2 \right\rangle \quad (2.4.7)$$

with the expectation value taken over all hadronic initial states with the (grand-canonical) equilibrium statistical operator, written in the local rest frame of the fluid cell,

$$\rho = \frac{1}{Z} \exp \left[-\frac{1}{T} (\mathbf{H}_{\text{QCD}} - \mu_B \mathbf{Q}_B) \right], \quad Z = \text{Tr} \exp \left[-\frac{1}{T} (\mathbf{H}_{\text{QCD}} - \mu_B \mathbf{Q}_B) \right]. \quad (2.4.8)$$

Here T is the fluid cell’s temperature and μ_B the baryochemical potential to take into account the conservation of the net-baryon number under the strong and electromagnetic interactions (i.e., the Noether charge of the $U(1)_V$ symmetry (2.2.15)). In (2.4.8) one also sums over all possible final hadronic states and the spin-degrees of freedom of the lepton and antilepton. Making use of the analytic properties of the retarded current-correlation function, the final result reads [GK91]

$$\frac{dR_{\ell^+\ell^-}}{d^4k} = -\frac{\alpha_{\text{em}}^2}{3\pi^3} \frac{k^2 + 2m_\ell^2}{(k^2)^2} \sqrt{1 - \frac{4m_\ell^2}{k^2}} \eta_{\mu\nu} \text{Im} \Pi_{\text{em,ret}}^{\mu\nu}(k) n_B(k^0). \quad (2.4.9)$$

2.5. Dileptons and chiral symmetry

Here

$$n_B(k^0) = \frac{1}{\exp(k^0/T) - 1} \quad (2.4.10)$$

denotes the Bose-Einstein distribution function, and

$$i\Pi_{\text{em,ret}}^{\mu\nu} = \int_{\mathbb{R}^4} d^4x \exp(ik \cdot x) \langle [J_{\text{em}}^\mu(x), J_{\text{em}}^\nu(0)] \rangle_{T, \mu_B} \Theta(x^0) \quad (2.4.11)$$

is the retarded electromagnetic current-current-correlation function evaluated in the grand-canonical equilibrium state (2.4.8) and to any order concerning the strong interaction. Thus, (2.4.9) implies that the measurement of the dilepton spectral function in heavy-ion collisions provides information about the em. current-current correlation function of strongly interacting matter in thermal equilibrium. According to the above derivation of (2.4.9) of course the measured dilepton spectra are only accessible as a space-time weighted average over the entire fireball evolution. This implies that modeling the dilepton production in heavy-ion collisions to interpret the corresponding data must include a comprehensive understanding of the relevant microscopic processes for dilepton production in the medium as well as a detailed description of the fireball evolution. This will be discussed in the next Chapter.

We note that a completely analogous analysis as for the dilepton rate above leads to the expression for the Lorentz-invariant photon rate,

$$q^0 \frac{dR_\gamma}{d^3\vec{q}} = -\eta_{\mu\nu} \text{Im} \Pi_{\text{em,ret}}^{\mu\nu}(q) n_B(q^0), \quad q^0 = |\vec{q}|, \quad (2.4.12)$$

i.e., photons probe the same em. current-current-correlation function at the photon point.

2.5 Dileptons and chiral symmetry

In this Section we discuss the relation of the electromagnetic current-correlation function in a strongly interacting medium to the approximate chiral $SU(2)_L \times SU(2)_R \times U(1)_V$ symmetry of QCD, as discussed in Sect. 2.2.

On the fundamental level of the Standard Model the key is the decomposition of the light (u- and d-) quarks' electromagnetic current

$$J_{\text{em,ud}} = \frac{2}{3} \bar{\psi}_u \gamma^\mu \psi_u - \frac{1}{3} \bar{\psi}_d \gamma^\mu \psi_d, \quad (2.5.1)$$

cf. (2.4.3), in an isovector and an isoscalar component. To that end we just have to remember that the electrically neutral component of the isovector current is given by

$$J_V^{3\mu} = \bar{\psi}_{ud} t^3 \gamma^\mu \psi_{ud} = \frac{1}{2} (\bar{\psi}_u \gamma^\mu \psi_u - \bar{\psi}_d \gamma^\mu \psi_d), \quad (2.5.2)$$

which carries the quantum numbers of the neutral $\rho(770)$ meson. The isoscalar current reads

$$j_V^\mu = \bar{\psi}_u \gamma^\mu \psi_u + \bar{\psi}_d \gamma^\mu \psi_d, \quad (2.5.3)$$

which carries the quantum numbers of the $\omega(770)$ meson. Now, as is immediately clear from (2.5.1-2.5.3) the electromagnetic current (2.5.1) can be written as

$$J_{\text{em,ud}}^\mu = J_V^{3\mu} + \frac{1}{6} j_V^\mu. \quad (2.5.4)$$

2. QCD matter and electromagnetic probes

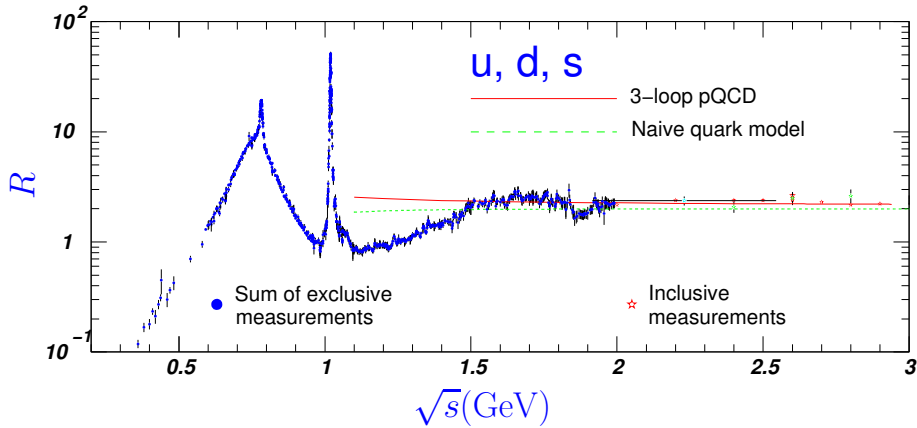


Figure 2.3: The ratio $\sigma_{e^+e^- \rightarrow \text{hadrons}}/\sigma_{e^+e^- \rightarrow \mu^+\mu^-}$ in the low- and intermediate-mass region. Figure taken from [Y⁺06].

To extend this pattern to also include the strange quark⁴ we only have to add $J_{\text{em},s}^\mu = -1/3 \bar{\psi}_s \gamma^\mu \psi_s$ to (2.5.1). Then we can write the electromagnetic current of the three light quarks in the form

$$J_{\text{em},\text{uds}} = \frac{1}{\sqrt{2}} \left[\frac{1}{\sqrt{2}} (\bar{\psi}_u \gamma^\mu \psi_u - \bar{\psi}_d \gamma^\mu \psi_d) + \frac{1}{3\sqrt{2}} (\bar{\psi}_u \gamma^\mu \psi_u + \bar{\psi}_d \gamma^\mu \psi_d) - \frac{\sqrt{2}}{3} \bar{\psi}_s \gamma^\mu \psi_s \right]. \quad (2.5.5)$$

It is suggestive to associate the three terms in the bracket with the corresponding light vector mesons ρ , ω , and ϕ . The relative weights in the electromagnetic current correlation function is thus 9:1:2. Empirically the partial decay widths of the light vector mesons to dielectrons are $\Gamma_{\rho \rightarrow e^+e^-}/\Gamma_{\omega \rightarrow e^+e^-} \simeq 10.5$ and $\Gamma_{\phi \rightarrow e^+e^-}/\Gamma_{\omega \rightarrow e^+e^-} \simeq 1.9$ [O⁺14], which is not too far from the naive parton argument based on (2.5.5).

In hadronic models the assumption that the hadronic electromagnetic current is proportional to the neutral vector-meson fields, the so-called **vector-meson dominance model (VMD)** [Sak60, GS68, KLZ67] leads to a quite successful description of hadronic electromagnetic transition form factors, particularly the electromagnetic form factor of the pion, as will be discussed in the Chpt. 3. Very accurate measurements of the hadronic em. current-current-correlation function are provided by the inclusive hadron production in the reaction $e^+ + e^- \rightarrow \text{hadrons}$, which is usually depicted in terms of the ratio

$$R = \frac{\sigma_{e^+e^- \rightarrow \text{hadrons}}}{\sigma_{e^+e^- \rightarrow \mu^+\mu^-}}, \quad (2.5.6)$$

as shown in Fig. 2.3 as a function of the invariant mass of the electron-positron pair $M = \sqrt{s}$. The low-mass region $2m_e \leq M \lesssim m_\phi$ is dominated by the three light vector mesons, ρ , ω , and ϕ , followed in the intermediate-mass region $m_\phi \lesssim M \lesssim M_{J/\psi}$ by a broader vector-meson resonance ρ' and a continuum that is well-described in the naive parton model, where the ratio is given by

$$R_{\text{parton model}} = N_c \sum_{f \in \{u,d,s\}} q_f^2 = 3 \left(\frac{4}{9} + 2 \cdot \frac{1}{9} \right) = 2. \quad (2.5.7)$$

⁴Since also the strange-quark mass is small compared to the typical hadronic scale of 1 GeV one can extend the approximate chiral $SU(2)_L \times SU(2)_R \times U(1)_V$ symmetry of the ud-quark sector of QCD to the uds-quark sector with the symmetry group $SU(3)_L \times SU(3)_R \times U(1)_V$. The symmetry is spontaneously broken to $SU(3)_V \times U(1)_V$ and of course also explicitly broken by the quark masses and the electroweak interactions. The pseudo-Goldstone bosons are grouped into the pseudoscalar $SU(3)$ octet, consisting of the 3 pions, 4 kaons, and one η^0 .

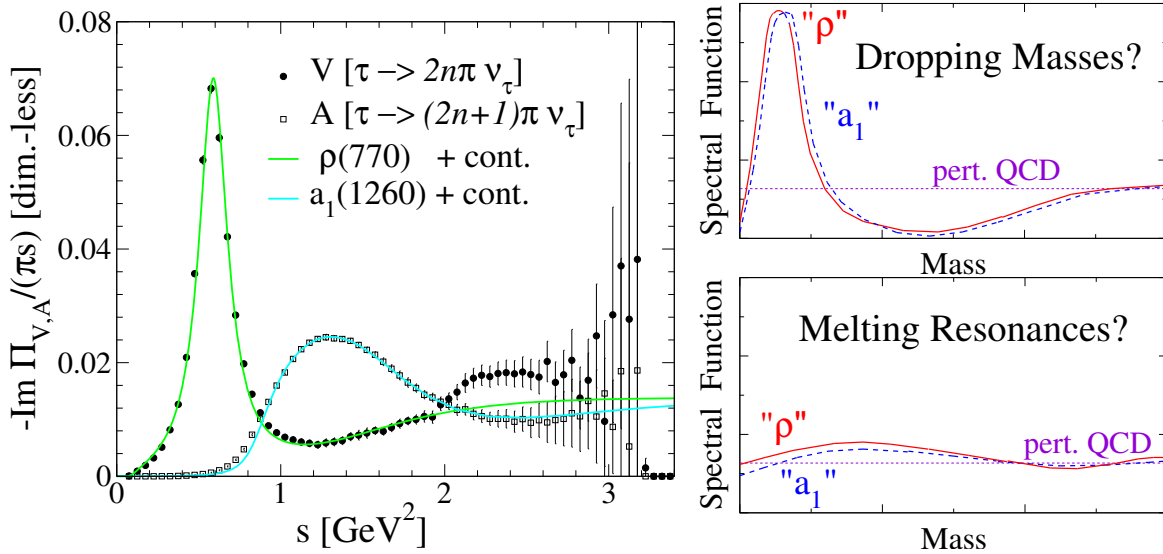


Figure 2.4: *Left panel: The isovector-vector and -axial-vector current correlation functions as a function of the total center-momentum energy of the pions ($s = E_{\text{cm}}^2$) as extracted from τ -lepton decay to an even and odd number of pions [B⁺ 98] together with model fits with vacuum ρ - and a_1 -meson spectral functions and a perturbative continuum [Rap03]. Right panel: Possible scenarios for the effect of chiral-symmetry restoration to the vector-axial-vector spectral functions in the hot and dense medium. Figure taken from [4].*

From the electroweak sector of the Standard Model it is known that the vector and axial-vector strong-isovector current-correlation functions are directly related to the charged electroweak current, which is of the clean “ $V - A$ structure” (see, e.g., [Nac90]). Taking into account parity conservation of the strong interaction it is clear that the semileptonic decay $\tau \rightarrow \nu_\tau + \text{pions}$ of τ -leptons together with the known weak coupling constant (or equivalently the Fermi constant in the effective four-fermion model) and the relevant CKM-matrix element $|V_{ud}|$ allows for an accurate quantitative separation of the current-correlation functions into the isovector- and axial-vector channel by exclusive measurements of the partial τ -lepton decay widths into an even or odd number of pions respectively. As shown in Fig. 2.4 these data can be seen as an accurate demonstration of the spontaneous breaking of the (approximate) chiral symmetry of QCD in the light-quark sector.

One of the fundamental questions addressed with the accurate measurement of dileptons in heavy-ion collisions is to learn about how this chiral symmetry of QCD is realized at low energies, i.e., in which way the dynamical generation of hadron masses by the strong interaction comes about, at least for the ρ meson, which dominates the electromagnetic current-current correlation function in the low-mass region as explained above. As the detailed analysis of effective hadronic models shows, chiral symmetry can be realized in (at least) two possible ways. E.g. in terms of “hidden-local-symmetry models”, which describe the massive vector (ρ) and in its generalized version also the axial-vector (a_1) meson with a “Higgsed” additional local chiral gauge symmetry (usually realized in a non-linear way) [BKU⁺85, BKY88, HY03]. It can be realized either by introducing only the ρ -meson as a gauge field, corresponding to the unbroken part $SU(2)_V$ of the $SU(2)_L \times SU(2)_R$ or both a ρ and an a_1 meson. In this kind of models chiral symmetry can be realized in the so-called vector manifestation, where the longitudinal part of the ρ meson becomes the chiral partner of the pions, which leads to a dropping mass towards the chiral phase transition. On the other hand, even in the same class of models, also the

usual realization of chiral symmetry is possible, where the chiral partners are ρ and a_1 , and the mass spectra of these two mesons become degenerate by a large broadening of their spectral functions in the medium [HS06, HSW08].

2.6 Abelian vector-meson-dominance model

As a simple but successful example for an effective theory to describe the electrodynamics of hadrons we briefly discuss the original vector-meson dominance (VMD) model by [Sak60, GS68, KLZ67], where it is assumed that the electromagnetic current of hadrons is proportional to the fields describing the light vector mesons ρ , ω , and ϕ [Sak60, GS68, KLZ67]. In the strict version of this model an electromagnetic transition of hadrons is always mediated through the formation of a light vector meson. Here, we shall summarize the model in the most basic form for the description of the electrodynamics of the charged pions and ρ mesons. One uses the Stueckelberg formalism to formulate an Abelian gauge symmetry with a massive gauge field. Contrary to the non-Abelian case this leads to a consistent renormalizable gauge theory without employing the Higgs mechanism [Col86].

To make the local gauge symmetry explicit, one introduces in addition a neutral scalar field θ , the “Stueckelberg ghost”

$$\mathcal{L}_\rho = -\frac{1}{4}V_{\mu\nu}V^{\mu\nu} + \frac{M^2}{2}V_\mu V^\mu + \frac{1}{2}(\partial_\mu\theta)(\partial^\mu\theta) + M\theta\partial_\mu V^\mu \quad (2.6.1)$$

with $V_{\mu\nu} = \partial_\mu V_\nu - \partial_\nu V_\mu$. As is easily shown, the model is invariant under the infinitesimal local gauge transformation

$$\delta V_\mu = \partial_\mu \delta\chi, \quad \delta\theta = M\delta\chi, \quad (2.6.2)$$

where $\delta\chi = \delta\chi(x)$ is an arbitrary infinitesimal scalar field. By direct calculation, one verifies that under this transformation the Lagrangian changes only by a complete four-divergence,

$$\delta\mathcal{L}_\rho = \partial_\mu(M^2V^\mu\delta\chi + M\theta\partial^\mu\delta\chi), \quad (2.6.3)$$

which means that indeed the action functional is gauge invariant.

The quantization is straight forward with the path-integral method à la Faddeev and Popov, using an R_ξ like 't Hooft gauge-fixing condition,

$$\partial_\mu V^\mu + m\xi\theta = 0, \quad (2.6.4)$$

which leads to the effective gauge-fixed Lagrangian

$$\begin{aligned} \mathcal{L}_{\text{gf},\rho} = & -\frac{1}{4}V_{\mu\nu}V^{\mu\nu} + \frac{M^2}{2}V_\mu V^\mu - \frac{1}{2\xi}(\partial_\mu V^\mu)^2 \\ & + \frac{1}{2}(\partial_\mu\theta)(\partial^\mu\theta) - \frac{\xi M^2}{2}\theta^2 + (\partial_\mu\eta^*)(\partial^\mu\eta) - \xi M^2\eta^*\eta. \end{aligned} \quad (2.6.5)$$

Here, ξ is an arbitrary real parameter and η and η^* Grassmann-valued Faddeev-Popov-ghost fields. Characteristically for an Abelian gauge model the Stueckelberg and Faddeev-Popov ghosts are non-interacting and thus can be neglected later on in loop calculations⁵.

⁵They are important, e.g., to obtain the correct partition sum for an ideal gas of massive vector bosons: The Lagrangian (2.6.5) has three vector-field components of mass M and one of mass $\sqrt{\xi}M$, one Stueckelberg-ghost-field component of mass $\sqrt{\xi}M$ and two Faddeev-Popov-ghost components of mass $\sqrt{\xi}M$. The unphysical time-like component of the gauge field is thus compensated by “adding” another unphysical Stueckelberg-ghost field, both of which are “subtracted” by the also unphysical Faddeev-Popov ghost field, leading to three physical degrees of freedom with mass M as it should be for a massive vector boson.

2.6. Abelian vector-meson-dominance model

The derivation of the free time-ordered vector-meson propagator in momentum space is now based on the Lagrangian (2.6.5), leading to

$$\Delta_V^{\mu\nu}(p) = -\frac{\eta^{\mu\nu}}{p^2 - M^2 + i0^+} + \frac{(1 - \xi)p^\mu p^\nu}{(p^2 - M^2 + i0^+)(p^2 - \xi M^2 + i0^+)}. \quad (2.6.6)$$

Here $(\eta^{\mu\nu}) = \text{diag}(1, -1, -1, -1)$ is the usual Minkowski metric. For any finite positive ξ this propagator indeed has the appropriate power-counting features for a meson propagator in a renormalizable model with only massive degrees of freedom. In the limit $\xi \rightarrow 0$ one obtains the ‘‘Landau gauge’’ with an explicitly transversal vector-meson propagator, and in the limit $\xi \rightarrow \infty$ one obtains the ‘‘unitary gauge’’, leading to the Proca description of the vector meson, resulting however in a not manifestly renormalizable theory⁶. In the following we shall use the ‘‘Feynman gauge’’ with $\xi = 1$, which is most convenient for practical calculations.

The introduction of the pions is now straight forward. Defining the covariant derivative of the complex pion field ϕ by

$$D_\mu \phi = (\partial_\mu + ig V_\mu) \phi, \quad (2.6.7)$$

the hadronic Lagrangian of our simple model for pions and ρ mesons reads

$$\mathcal{L}_{\text{had}} = \mathcal{L}_{\text{gf},\rho} + (D_\mu \phi)^* (D^\mu \phi) - m_\pi \phi^* \phi - \frac{\lambda}{8} (\phi^* \phi)^2. \quad (2.6.8)$$

The gauge transformation for the pion field is given by

$$\phi \rightarrow \exp(-ig \delta \chi) \phi \simeq (1 - ig \delta \chi) \phi. \quad (2.6.9)$$

Finally we also need to couple the hadrons to the photon field since we like to find a model for the electromagnetic form factor of the pion. The gauge-fixed photon-field Lagrangian reads

$$\mathcal{L}_{\text{gf},\gamma} = -\frac{1}{4} F_{\mu\nu} F^{\mu\nu} - \frac{1}{2\xi'} (\partial_\mu A^\mu)^2 + (\partial_\mu \tilde{\eta}^*) (\partial^\mu \tilde{\eta}), \quad F_{\mu\nu} = \partial_\mu A_\nu - \partial_\nu A_\mu. \quad (2.6.10)$$

The coupling of the pions to the photon field is achieved by substituting the covariant derivative in the hadronic Lagrangian (2.6.8) by

$$D_\mu \rightarrow \tilde{D}_\mu = D_\mu + ie A_\mu. \quad (2.6.11)$$

The ρ meson couples to the photon also via the gauge-invariant $\rho\gamma$ -mixing term (Kroll-Lee-Zumino coupling)

$$\mathcal{L}_{\rho\gamma} = -\frac{e}{2g'} V_{\mu\nu} F^{\mu\nu} \quad (2.6.12)$$

Finally we add the electrons that couple directly only to the photons in the usual way of spinor QED,

$$\mathcal{L}_{\text{el}} = \bar{\psi} (i\rlap{\not{D}} - m_e + e\rlap{\not{A}}) \psi. \quad (2.6.13)$$

Phenomenologically the ρ meson is not a stable particle but a broad resonance with a peak mass around 770 MeV and a width of around 150 MeV in the isovector-vector channel of elastic pion scattering. Thus, when evaluating the one-loop self-energy, we must give renormalization conditions based on *physical*, i.e., observable quantities. The most simple quantity is the electromagnetic form factor of

⁶Of course, the gauge-invariant S -matrix elements are renormalizable but not the off-shell proper vertex functions.

2. QCD matter and electromagnetic probes

pions that can be defined by the pion-annihilation process $\pi^+ + \pi^- \rightarrow e^+ + e^-$ (or equivalently the inverse process $e^+ + e^- \rightarrow \pi^+ + \pi^-$).

To find the appropriate renormalization conditions we thus start with the evaluation of the photon-polarization tensor. The photon's mass is protected to stay zero by the appropriate Ward-Takahashi identity and thus the photon-polarization tensor is transverse and only needs wave-function renormalizations.

Thus we have

$$\Pi_\gamma^{\mu\nu}(k) = s\Pi_\gamma(s)\Theta^{\mu\nu}(k), \quad s = k^2 \quad (2.6.14)$$

with the projection operator

$$\Theta^{\mu\nu}(k) = \eta^{\mu\nu} - \frac{k^\mu k^\nu}{k^2}. \quad (2.6.15)$$

The scalar quantity Π_γ is (at most) logarithmically divergent and is renormalized by a photon-wave-function renormalization counter term.

In the following we calculate the photon polarization to order $\alpha_{\text{em}} = e^2/(4\pi)$ but with the completely resummed one-loop correction for the ρ -meson propagator.

At tree level the renormalized photon polarization becomes

$$\Pi_{\gamma,0}(s) = \frac{e^2}{g'^2} \frac{s}{s - M^2}, \quad (2.6.16)$$

where the renormalization constant is determined by the fact that the photon propagator must have a pole at $s = k^2 = 0$ with residuum 1, leading to the renormalization condition

$$\Pi_\gamma(s=0) = 0. \quad (2.6.17)$$

Now we dress the ρ -meson propagator with the complete $\pi\pi$ - and e^+e^- -one-loop corrections to its self-energy. Similarly to the photon the Abelian local gauge invariance of the original Lagrangian ensures that the ρ -meson self-energy is transverse either and thus that again there is only a wave-function renormalization. This means we have

$$i\Pi_{\rho\pi\pi}^{\mu\nu}(p) = \begin{array}{c} \begin{array}{ccc} \begin{array}{c} \mu \\ \text{---} \end{array} & \begin{array}{c} \text{---} \\ l \end{array} & \begin{array}{c} \nu \\ \text{---} \end{array} \\ \begin{array}{c} \text{---} \\ l+p \end{array} & \begin{array}{c} \text{---} \\ l \end{array} & \begin{array}{c} \text{---} \\ l+p \end{array} \\ \begin{array}{c} \text{---} \\ p \end{array} & & \end{array} = is\Pi_{\rho\pi\pi}(s)\Theta^{\mu\nu}(p), \quad s = p^2. \quad (2.6.18) \end{array}$$

Since in physical quantities the (dressed) ρ -meson propagator appears usually in connection with photon mixing, a convenient renormalization condition is

$$\Pi_\rho(s=0) = 0, \quad (2.6.19)$$

which determines the wave-function counterterm and ensures that the photon propagator is correctly normalized at the photon point when dressed via the $\gamma\rho$ -mixing vertex.

The main contribution comes from the pion loops. Using dimensional regularization, it is easy to show that the regularized ρ -meson self-energy at the one-loop level,

$$\Pi_{\rho\pi\pi}^{\mu\nu}(p) = -ig^2\mu^{2\epsilon} \int \frac{d^{2\omega}l}{(2\pi)^{2\omega}} \left[\frac{(2l+p)^\mu(2l+p)^\nu}{(l^2 - m_\pi^2 + i0^+)[(l+p)^2 - m_\pi^2 + i0^+]} - \frac{2\eta^{\mu\nu}}{l^2 - m_\pi^2 + i0^+} \right], \quad (2.6.20)$$

2.6. Abelian vector-meson-dominance model

is indeed transverse and that the renormalized self-energy is determined by

$$\begin{aligned} \Pi_{\rho\pi\pi,\text{ren}}(s) = & \frac{g^2}{288\pi^2 s^2} \left\{ 16s(3m_\pi^2 - s) + 3(4m_\pi^2 - s)\sqrt{s(s - 4m_\pi^2)} \right. \\ & \left. \times \left[\ln\left(\frac{2m_\pi^2 - s + \sqrt{s(s - 4m_\pi^2)}}{m_\pi^2}\right) - \ln\left(\frac{2m_\pi^2 - s - \sqrt{s(s - 4m_\pi^2)}}{m_\pi^2}\right) \right] \right\}. \end{aligned} \quad (2.6.21)$$

For numerical evaluations, one has to set $s \rightarrow s + i0^+$ to obtain the correct branch of the square-root and logarithm function for real s .

The dressed ρ -propagator reads

$$G_\rho^{\mu\nu}(p) = -\frac{\Theta^{\mu\nu}(p)}{p^2 - M^2 - p^2 \Pi_{\rho\pi\pi}(p^2)} - \frac{\Lambda^{\mu\nu}(p)}{p^2 - M^2 + i0^+}, \quad (2.6.22)$$

where we have defined the longitudinal projector as $\Lambda^{\mu\nu}(p) = p^\mu p^\nu / p^2$. This explicitly shows that the unphysical longitudinal part of the ρ propagator is as for the free propagator, i.e., the longitudinal part of the vector field is non-interacting as it should be.

Now we can calculate the pion electromagnetic form factor to leading order in e but to arbitrary order in g by using the dressed ρ propagator and the one-loop correction to the $\rho\gamma$ mixing,

$$i\Gamma_{\gamma\pi\pi}^\mu = \text{[Tree-level diagram]} + \text{[One-loop pion loop on rho]} + \text{[One-loop pion loop on photon]}. \quad (2.6.23)$$

In the last diagram the pion loop has to be renormalized with the same condition as the corresponding ρ -polarization contribution, because the electromagnetic form factor of the pion, defined by

$$i\Gamma_{\gamma\pi\pi}^\mu = -ieF[(r - q)^2](q^\mu + r^\mu) \quad (2.6.24)$$

must fulfill the condition

$$F(0) = 1, \quad (2.6.25)$$

because by convention the electromagnetic coupling e ($\alpha_{\text{em}} = e^2/(4\pi) \simeq 1/137$) is determined at zero momentum transfer. After some algebra the properly renormalized form factor turns out to be

$$F_{\pi\pi}(s) = \frac{s(1 - g/g') - M^2}{s - M^2 - s\Pi_{\rho\pi\pi}(s)}. \quad (2.6.26)$$

Here, we have assumed the external pion legs to be on-shell, and thus only the transverse part of the ρ -meson propagator enters here as it should be for physical processes. The external photon line is taken off-shell.

For the special choice $g' = g$ the form factor becomes a pure ρ -meson pole, which means that in leading order in the electromagnetic coupling the hadronic electromagnetic current is strictly proportional to the ρ -meson field. This parameter choice thus realizes the so-called **strict vector-meson dominance (VMD) model**. For an arbitrary ρ - γ coupling g' we call it the **extended VMD model**.

A physical process to test the model in the time-like region against observables is the annihilation process $\pi^+ + \pi^- \rightarrow e^+ + e^-$. We are interested in the polarization averaged matrix element

$$\frac{dR}{d^4k} = \left| \overline{\sum_i \sum_f \mathcal{M}_{fi}} \right|_{p+q=k}^2. \quad (2.6.27)$$

2. QCD matter and electromagnetic probes

The matrix element is given by the diagram

$$i\mathcal{M}_{fi} = \quad (2.6.28)$$

The averaging over the initial and the summation over the final state can be done with help of the optical theorem. E.g., the summation over the electron states is equivalent to the evaluation of the one-loop photon-polarization diagram for the Schwinger-Keldysh real-time polarization $s\Pi_{\gamma ee}^{21}(s)$ ($s = (p + q)^2 = k^2$), where the indices 1 and 2 refer to the time-ordered and anti-time-ordered branch of the contour [Hee00]. In the here considered vacuum case the relation to the time-ordered polarization function is very simple,

$$i\Pi_{\gamma ee}^{21}(s) = -\text{Im}\Pi_{\gamma ee}^{11}(s) = -\text{Im}\Pi_{\gamma ee}(s). \quad (2.6.29)$$

The same holds for the summation over the pion-initial state. Here we need

$$i\Pi_{\rho\pi\pi}^{12}(s) = -\text{Im}\Pi_{\rho\pi\pi}^{11}(s). \quad (2.6.30)$$

Finally we obtain

$$\frac{dR}{d^4k} = e^2 |F_{\pi\pi}(s)|^2 \text{Im}\Pi_{\gamma ee}(s) \text{Im}\Pi_{\rho\pi\pi}(s). \quad (2.6.31)$$

The photon-polarization from the ρ loop is given by

$$\Pi_{\gamma ee}^{\mu\nu}(k) = s\Pi_{\gamma ee}(k^2)\Theta^{\mu\nu}(k), \quad \Pi_{\gamma ee}(0) = 1 \quad (2.6.32)$$

and can be evaluated with the standard formulae of dimensional regularization [Ram89]. The renormalized result is

$$\begin{aligned} \Pi_{\gamma ee}(s) = & -\frac{e^2}{72\pi^2 s^2} \left\{ 2s(12m_e^2 + 5s) + 3\sqrt{s(s - 4m_e^2)} \right. \\ & \times \left[\ln\left(\frac{2m_e^2 - s + \sqrt{s(s - 4m_e^2)}}{m_e^2}\right) - \ln\left(\frac{2m_e^2 - s - \sqrt{s(s - 4m_e^2)}}{m_e^2}\right) \right] \right\}. \end{aligned} \quad (2.6.33)$$

For completeness in the following we also include the order e^4 contribution to the ρ -polarization function defined by

$$i\Pi_{\rho ee}^{\mu\nu}(p) = \quad = is\Pi_{\rho ee}(s)\Theta^{\mu\nu}(p), \quad s = p^2 \quad (2.6.34)$$

leading to

$$\Pi_{\rho ee}(s) = \frac{e^2}{g'^2} \Pi_{\gamma ee}(s). \quad (2.6.35)$$

Of course, this contribution at order $\mathcal{O}(\alpha_{\text{em}}^2) = \mathcal{O}(e^4)$ to the ρ -polarization tensor is only significant below the two-pion threshold, where it provides the only spectral strength of the ρ meson.

2.6. Abelian vector-meson-dominance model

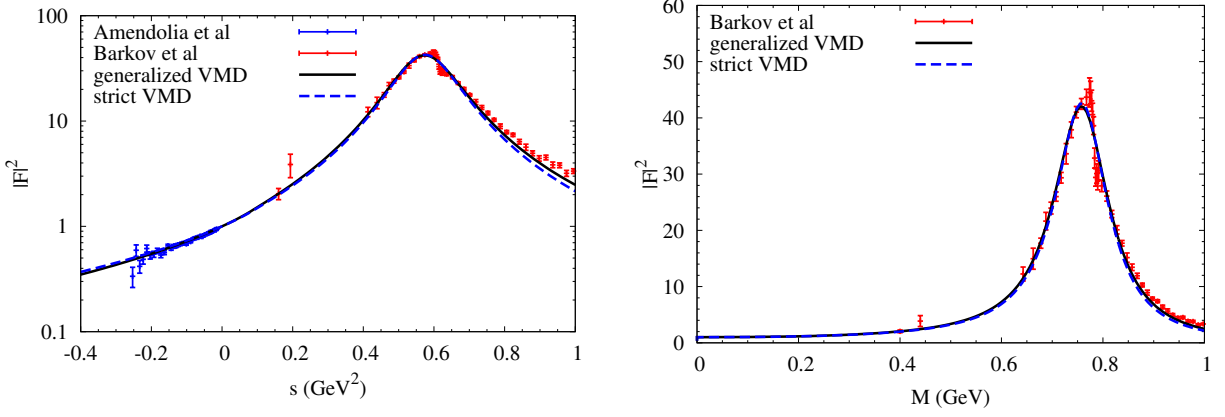


Figure 2.5: *Fit of the model to data on the pion electromagnetic form factor in both the spacelike [A⁺86] and timelike [BCE⁺85] region (left). Note that the form factor is plotted on a logarithmic scale as a function of s . The right panel shows the time-like part on a linear scale as a function of invariant mass $M = \sqrt{s}$ [Hee99].*

Including this correction, the ρ propagator reads

$$G_{\rho}^{\mu\nu}(p) = -\frac{\Theta^{\mu\nu}(p)}{p^2 - M^2 - p^2\Pi_{\rho\pi\pi}(p^2) - p^2\Pi_{\rho ee}(p^2)} - \frac{\Lambda^{\mu\nu}(p)}{p^2 - M^2 + i0^+}. \quad (2.6.36)$$

The electromagnetic pion form factor has been measured in both the timelike [BCE⁺85] as well as the spacelike [A⁺86] region and can be used to fit our model parameters. The former is assessed by the electron-positron annihilation process $e^+ + e^- \rightarrow \pi^+ + \pi^-$ discussed above and the latter by the elastic scattering of pions on electrons:

$$i\mathcal{M}_{fi} = \quad (2.6.37)$$

As can be seen from Fig. 2.5 the model allows an excellent fit for both the extended and the strict vector-meson dominance model. The resulting best-fit parameters are

$$\begin{aligned} \text{generalized vector-meson dominance: } & M = 763.1 \text{ MeV}, \quad g = 5.461, \quad g' = 5.233, \\ \text{strict vector-meson dominance: } & M = 763.1 \text{ MeV}, \quad g \stackrel{!}{=} g' = 5.328. \end{aligned} \quad (2.6.38)$$

The slight deviations of the model from the data around the peak region is due to the contribution of the isoscalar channel (ω meson) which is not considered here.

2. QCD matter and electromagnetic probes

Chapter 3

Electromagnetic probes in NN and AA collisions

In this Chapter, some of my works on electromagnetic probes in heavy-ion collisions [1, 2, 3, 4, 5, 6, 7, 8, 9, 10, 11, 12, 13] are summarized. For completeness also some details on the hadronic effective model for the in-medium spectral functions of the vector mesons used in these works is reviewed.

The summary is organized as follows: First I briefly review various effective hadronic models to describe the dilepton and photon production in heavy-ion collisions at lower beam energies and in the hadronic phase of the fireball evolution of the strongly interacting matter created at higher beam energies. The models have to be defined in the vacuum first (Sect. 3.1). Then, in Sect. 3.2 the evaluation of the models for dilepton and photon production from a medium in thermal equilibrium is discussed. This includes both the radiation from a partonic (QGP) (Sect. 3.2.1) and from a hot and/or dense hadron-resonance gas (Sect. 3.2.2).

In the following I describe the modeling of the bulk-medium evolution in heavy-ion collisions, which reach from simple blast-wave parameterizations over hydrodynamical calculations to the coarse-graining approach to make microscopic transport simulations applicable to dilepton and photon production utilizing the rates obtained from the thermal quantum-field theoretical calculations of the corresponding production rates (Sect. 3.2.3).

Finally, the models are applied and compared to data on dileptons (Sect. 3.3) and photons (Sect. 3.4) in heavy-ion collision experiments ranging from the lowest beam energies at the GSI SIS18 to the highest beam energies obtained at the CERN LHC heavy-ion experiments as well as predictions for future experiments at the future FAIR and NICA facilities. Finally first investigations on the QCD phase diagram in terms of a comprehensive analysis of electromagnetic probes at different beam energies (as is, e.g., addressed in the RHIC “beam-energy scan”) are summarized in Sect. 3.5.

3.1 Dilepton production in pp- and np-collisions at GSI-SIS energies

Before addressing the emission of dileptons and photons from a nearly equilibrated expanding fireball of strongly interacting matter it is important to first describe the electrodynamics of hadrons in effective hadronic models since an ab-initio treatment on the level of quarks and gluons is not feasible. In this section we thus briefly discuss the pertinent models used in the further description of electromagnetic probes in heavy-ion collisions.

In [6] we used the Gießen Boltzmann-Uehling-Uhlenbeck transport model (GiBUU) [BGG⁺12] to describe the dilepton production in nucleus-nucleus collisions at energies provided by the heavy-ion synchrotron (SIS) at the Gesellschaft für Schwerionenforschung (GSI) and measured by the HADES

3. Electromagnetic probes in NN and AA collisions

collaboration. It is incorporating a hadron-resonance model [TCE⁺97] using resonance parameters and branching ratios from the partial-wave analysis of Manley [MS92] with one important modification: Manley introduces the $\rho\Delta$ decay channels only to account for missing inelasticities which are not contained in the one- and two-pion final states. This implies that the Manley analysis is not really sensitive to the true strength of the $\rho\Delta$ final state. We thus replace the $\rho\Delta$ by $\sigma\Delta$ decays in order to avoid overestimating ρ production in accordance with the data. The partial widths of the resonances are parameterized according to

$$\Gamma(m) = \Gamma_0 \frac{m_0}{m} \left(\frac{q}{q_0} \right)^3 \frac{q_0^2 + \Lambda^2}{q^2 + \Lambda^2}, \quad (3.1.1)$$

where m_0 is the decaying resonance's pole mass, m the off-shell mass, Γ_0 the on-shell decay width, and q_0 and q are the final-state center-mass momenta for the masses m_0 and m , respectively; Λ is a cutoff parameter in the sense of a hadronic form factor. The Teis model [TCE⁺97] has been extended to cover the entire beam-energy range of the HADES experiment (up to $E_{\text{kin}} = 3.5$ GeV), taking into account the following nucleon-nucleon scattering channels:

1. $NN \rightarrow NN$
2. $NN \rightarrow N\Delta$,
3. $NN \rightarrow NN^*$, $N\Delta^*$,
4. $NN \rightarrow \Delta\Delta$,
5. $NN \rightarrow \Delta N^*$, $\Delta\Delta^*$,
6. $NN \rightarrow NN\pi$ (non-res. BG)
7. $NN \rightarrow NN\omega$, $NN\pi\omega$, $NN\phi$ (non-res.),
8. $NN \rightarrow BYK$ (with $B = N, \Delta$; $Y = \Lambda, \Sigma$).

The elastic cross sections, item 1, are parameterized according to Cugnon et al. [CVL96] (for beam momenta below $p_{\text{lab}} \approx 2.776$ GeV) and the PDG [M⁺94] (above); see also [BGG⁺12] for details. The single-resonance excitation channels (items 2 and 3) are taken from the Teis analysis. The $N\Delta$ channel employs the one-boson-exchange model by Dmitriev et al. [DSG86], and the higher resonances are produced in a pure phase-space approach with constant matrix elements,

$$\sigma_{NN \rightarrow NR} = \frac{C_I}{p_i s} \frac{|\mathcal{M}_{NR}|^2}{16\pi} \int d\mu \mathcal{A}_R(\mu) p_F(\mu), \quad (3.1.2)$$

where p_i and p_F are the center-mass momenta in the initial and final state, and the matrix elements have been fitted previously by Teis to exclusive meson production (π , 2π , η , and ρ). The spectral functions of the various resonances are parameterized as

$$\mathcal{A}_R(\mu) = \frac{1}{\pi} \frac{\mu \Gamma_R(\mu)}{(\mu^2 - M_R^2)^2 + \mu^2 \Gamma_R^2(\mu)}. \quad (3.1.3)$$

All production channels are treated isospin-symmetric with the corresponding Clebsch-Gordan coefficients, C_J . The only exception concerns the $S_{11}(1535)$ resonance, which is assumed to be the only

3.1. Dilepton production in pp- and np-collisions at GSI-SIS energies

channel for exclusive η production, which is known to be significantly larger in pn than in pp collisions [C⁺98], leading to

$$|\mathcal{M}_{\text{pn} \rightarrow \text{NN}^*(1535)}|^2 = 6.5 \cdot |\mathcal{M}_{\text{pp} \rightarrow \text{NN}^*(1535)}|^2. \quad (3.1.4)$$

Another isospin asymmetry is introduced for the $P_{11}(1440)$ state,

$$|\mathcal{M}_{\text{pn} \rightarrow \text{NN}^*(1440)}|^2 = 2 \cdot |\mathcal{M}_{\text{pp} \rightarrow \text{NN}^*(1440)}|^2. \quad (3.1.5)$$

New compared to the original Teis analysis is also the consideration of double-resonance production in order to extend the validity of the model to cover the beam-energy range up to the highest SIS energy ($\sqrt{s} \simeq 3.2$ GeV). Also these are treated in a phase-space approach assuming constant scattering-matrix elements,

$$\sigma_{\text{NN} \rightarrow \Delta R} = \frac{C_I}{p_i s} \frac{|\mathcal{M}_{\Delta R}|^2}{16\pi} \int d\mu_1 d\mu_2 \mathcal{A}_{\Delta}(\mu_1) \mathcal{A}_R(\mu_2) \mathcal{P}_F(\mu_1, \mu_2). \quad (3.1.6)$$

Also three new production channels have been added:

1. $\text{NN} \rightarrow \Delta S_{11}(1535) (\rightarrow \text{NN}\pi\eta)$,
2. $\text{NN} \rightarrow \Delta N^* (\rightarrow \text{NN}\pi\rho)$, $N^* = D_{13}(1520), S_{11}(1650), F_{15}(1680), P_{13}(1720)$,
3. $\text{NN} \rightarrow \Delta\Delta^* (\rightarrow \text{NN}\pi\rho)$, $\Delta^* = S_{31}(1620), D_{33}(1700), F_{35}(1905)$.

For lack of experimental data the pertinent matrix elements, $\mathcal{M}_1 = 60$ mb GeV², $\mathcal{M}_2 = 12$ mb GeV² and $\mathcal{M}_3 = 21$ mb GeV², are fixed by fitting the corresponding PYTHIA cross sections for $\pi\eta$ and $\pi\rho$ production. As can be seen in Fig. 3.1 this description leads to a successful description of the total inelastic pp and np cross section.

The production of ω and ϕ mesons are parameterized via [Sib96]

$$\sigma(\text{pp} \rightarrow \text{pp}V, \text{pp}\pi V) = a(1-x)^b x^c, \quad \text{with } x = s_0/s, \quad (3.1.7)$$

where $s_0 = (2m_N + m_V)^2$ is the threshold energy, and the parameters are given in Table 3.1 Finally, for

	$\sqrt{s_0}$ [GeV]	a [mb]	b	c	Ref.
ω	2.658	5.3	2.3	2.4	[AB ⁺ 07]
$\pi\omega$	2.796	1.0	1.5	1.1	-
ϕ	2.895	0.01	1.26	1.66	[Par09]

Table 3.1: *Parameters for vector-meson production. Table taken from [6]*

dilepton production, in GiBUU a strict vector-meson dominance framework is implemented,

$$\Gamma_{V \rightarrow e^+e^-}(\mu) = C_V \frac{m_V^4}{\mu^3}, \quad (3.1.8)$$

where μ is the off-shell mass of the vector meson and m_V is its pole mass. The constants C_V (for $V \rightarrow e^+e^-$) are adjusted to $C_\rho = 9.078 \cdot 10^{-6}$, $C_\omega = 7.666 \cdot 10^{-7}$, and $C_\phi = 1.246 \cdot 10^{-6}$ to fit the partial decay widths [N⁺10].

3. Electromagnetic probes in NN and AA collisions

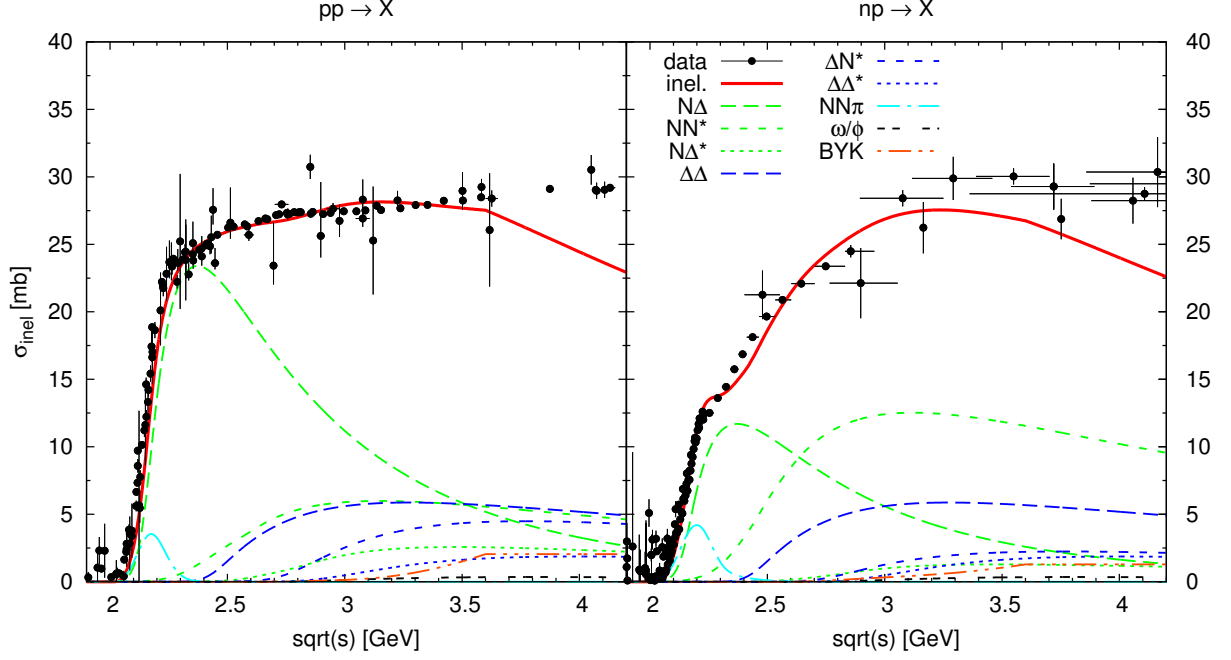


Figure 3.1: Inelastic pp and pn cross sections in the resonance model. The data points shown here have been obtained by subtracting the parameterized elastic cross section from the total cross section data [N⁺ 10]. Figure taken from [6].

For the Dalitz decays of the pseudo-scalar mesons the parameterization [Lan85],

$$\frac{d\Gamma_{P \rightarrow \gamma e^+ e^-}}{d\mu} = \frac{4\alpha_{\text{em}}}{3\pi} \frac{\Gamma_{P \rightarrow \gamma\gamma}}{\mu} \left(1 - \frac{\mu^2}{m_P^2}\right)^3 |F_P(\mu)|^2, \quad (3.1.9)$$

is used, with $\Gamma_{\pi^0 \rightarrow \gamma\gamma} = 7.8 \cdot 10^{-6}$ MeV, $\Gamma_{\eta \rightarrow \gamma\gamma} = 4.6 \cdot 10^{-4}$ MeV and the form factors,

$$F_{\pi^0}(\mu) = 1 + b_{\pi^0} \mu^2, \quad b_{\pi^0} = 5.5 \text{ GeV}^{-2}, \quad (3.1.10)$$

$$F_{\eta}(\mu) = \left(1 - \frac{\mu^2}{\Lambda_{\eta}^2}\right)^{-1}, \quad \Lambda_{\eta} = 0.676 \text{ GeV}. \quad (3.1.11)$$

These decays show an anisotropic angular distribution, according to

$$\frac{d\Gamma_{P \rightarrow \gamma e^+ e^-}}{d\cos\theta} \propto 1 + \cos^2(\theta), \quad (3.1.12)$$

where θ is the angle of the electron with respect to the momentum of the dilepton. All other decays are treated isotropically.

The ω -Dalitz decay is parameterized as in [BC97, Eff99],

$$\frac{d\Gamma_{\omega \rightarrow \pi^0 e^+ e^-}}{d\mu} = \frac{2\alpha_{\text{em}}}{3\pi} \frac{\Gamma_{\omega \rightarrow \pi^0 \gamma}}{\mu} \times \left[\left(1 + \frac{\mu^2}{\mu_{\omega}^2 - m_{\pi}^2}\right)^2 - \frac{4\mu_{\omega}^2 \mu^2}{(\mu_{\omega}^2 - m_{\pi}^2)^2} \right]^{3/2} \times |F_{\omega}(\mu)|^2, \quad (3.1.13)$$

$$|F_{\omega}(\mu)|^2 = \frac{\Lambda_{\omega}^4}{(\Lambda_{\omega}^2 - \mu^2)^2 + \Lambda_{\omega}^2 \Gamma_{\omega}^2}$$

3.1. Dilepton production in pp - and np -collisions at GSI-SIS energies

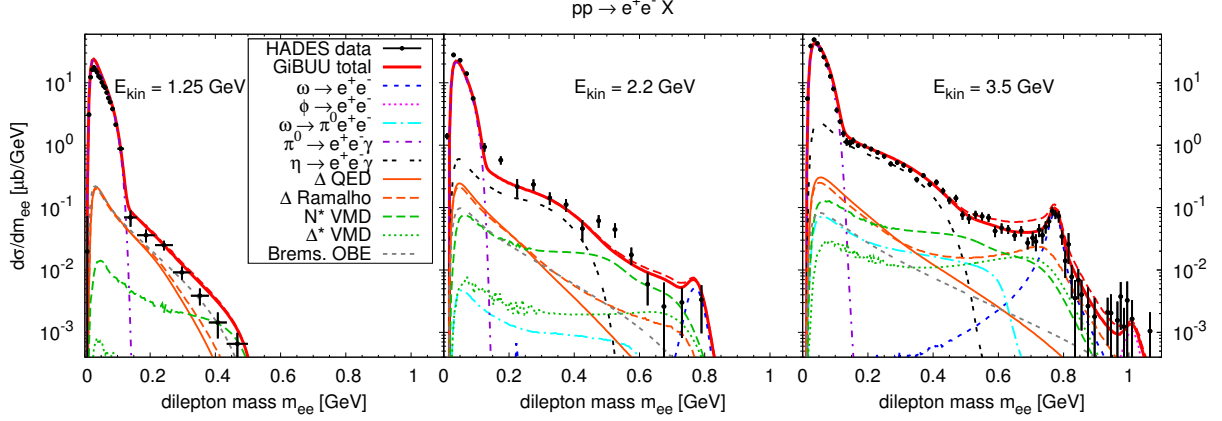


Figure 3.2: Transport-model calculations of dilepton mass spectra $d\sigma/dm_{ee}$ from proton-proton collisions ($pp \rightarrow e^+e^- X$) at three different beam energies, with and without a $\Delta \rightarrow \gamma^* N$ form factor, compared to experimental data measured with the HADES detector [$A^+ 10b$, $A^+ 12c$, $A^+ 12b$]. Figure taken from [11].

with $\Gamma_{\omega \rightarrow \pi^0 \gamma} = 0.703 \text{ MeV}$, $\Lambda_{\omega} = 0.65 \text{ GeV}$ and $\Gamma_{\omega} = 75 \text{ MeV}$. For the Δ -Dalitz decay the parameterization

$$\frac{d\Gamma_{\Delta \rightarrow N e^+ e^-}}{d\mu} = \frac{2\alpha_{em}\Gamma_{\Delta \rightarrow N \gamma^*}}{3\pi\mu}, \quad (3.1.14)$$

$$\Gamma_{\Delta \rightarrow N \gamma^*} = \frac{\alpha_{em}}{16} \frac{(m_{\Delta} + m_N)^2}{m_{\Delta}^3 m_N^2} [(m_{\Delta} + m_N)^2 - \mu^2]^{1/2} [(m_{\Delta} - m_N)^2 - \mu^2]^{3/2} |F_{\Delta}(\mu)|^2$$

from [KF02] is used. Theoretical models for the N - Δ transition form factor usually assume one or more VMD-inspired peaks in the time-like region [KMFF02, CPTW04, WI05]. However, the data in the space-like region does not provide sufficient constraints to fix the behavior in the time-like region. In order to demonstrate the uncertainty connected to this form factor, we will in the following use as an example the model of [WI05]. More recently we have also shown that the electromagnetic transition form factor of the Δ can be successfully described with the VMD approach [11].

In this way also all other Dalitz decays of baryon resonances are treated in the spirit of the VMD ansatz by employing the step-wise process $R \rightarrow N \rho \rightarrow N e^+ e^-$ within the transport simulation. Thereby it is important to implement the small width of the ρ meson below the two-pion threshold due to the dilepton decay. However, one should note that the smallness of the ρ -decay width in this low-mass region is compensated by the propagator of the virtual photon in Sect. 3.1.8.

In pn scattering also the pertinent bremsstrahlung contribution is considered in phase-space corrected soft-photon approximation [GK89, WBC⁺90],

$$\frac{d\sigma_{pn \rightarrow p n e^+ e^-}}{dM dE d\Omega} = \frac{\alpha_{em}^2}{6\pi^3} \frac{q}{ME^2} \bar{\sigma}(s) \frac{R_2(s_2)}{R_2(s)}, \quad (3.1.15)$$

$$\bar{\sigma}(s) = \frac{s - (m_1 + m_2)^2}{2m_1^2} \sigma_{el}^{pn}(s), \quad (3.1.16)$$

$$R_2(s) = \sqrt{1 - (m_1 + m_2)^2/s}, \quad (3.1.17)$$

$$s_2 = s + M^2 - 2E\sqrt{s}, \quad (3.1.18)$$

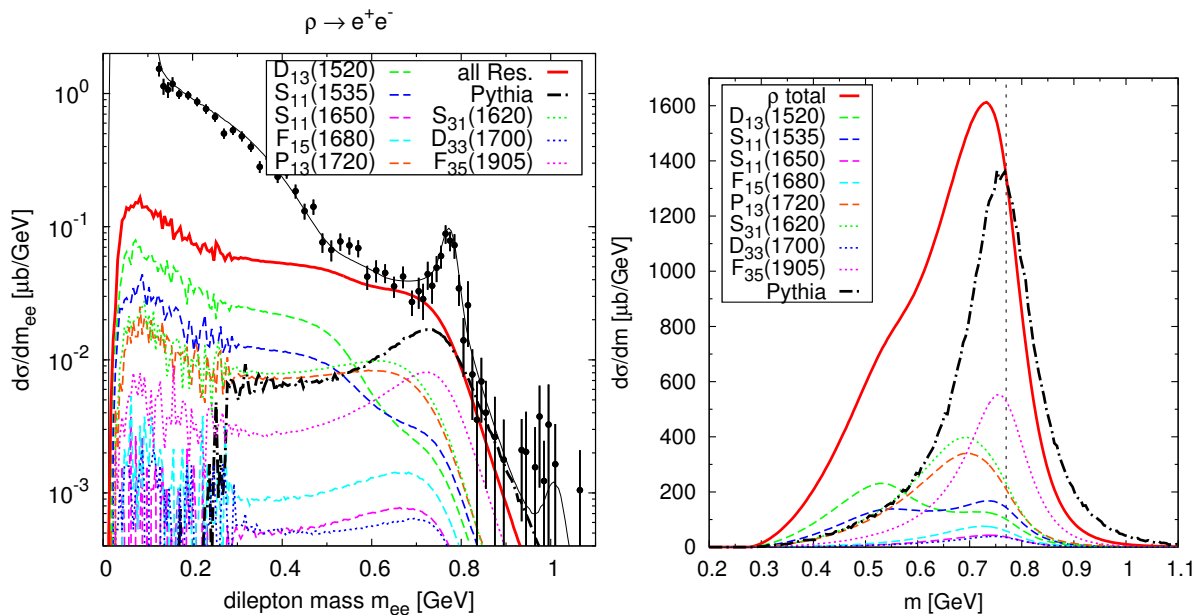


Figure 3.3: Left panel: Resonance contributions to the ρ channel in the dilepton mass spectrum. Right panel: Resonance contributions to the ρ mass distribution. The dashed line indicates the vacuum pole mass of the ρ meson. For comparison we also show the ρ meson contribution from earlier Pythia simulations [WGM11]. Figure taken from [6].

where M is the mass of the dilepton pair, q , E and Ω are its momentum, energy and solid angle in the pn center-of-mass frame and s is the Mandelstam's variable. Further, m_1 is the mass of the proton, m_2 is the mass of the neutron, and $\sigma_{\text{el}}^{\text{pn}}$ is the elastic pn cross section.

To demonstrate the excellent agreement of this framework with the corresponding data on dilepton production in pp and dp collisions from the HADES collaboration in Fig. 3.2 we show the e^+e^- -invariant-mass spectra at the three available beam energies. We close this summary of the GiBUU model to describe dilepton production in pp and pn collisions by noting that the ρ -spectral function appears to be already modified compared to the shape expected from the “definition” of the corresponding resonance in the review of particle physics [O⁺14]. As described in Sect. 2.6, there it is defined as the resonance of the process $e^+ + e^- \rightarrow \pi^+ + \pi^-$ in the isovector-vector channel. In our model, however the ρ meson is also produced via baryon-resonance Dalitz decays, which leads to a small downward mass shift of the corresponding resonance peak (which moves to about $M \simeq 730$ MeV and the development of a shoulder around $M \simeq 500$ MeV, mainly due to the low-mass resonances like the $D_{13}(1520)$ (see Fig. 3.3). For the dileptons these Dalitz-decay contributions lead to a significant contribution in the low-mass region, particularly below the two-pion threshold and a rather smooth shape of the dilepton-invariant-mass spectrum without a pronounced “ ρ peak”, which is due to the $1/m^3$ factor in the VMD description (3.1.8).

3.2 Models for electromagnetic probes in heavy-ion collisions

To address the production of dileptons and photons in heavy-ion collisions, the medium modifications of the electromagnetic current-current correlator entering the production rate as discussed in Sect. 2.4, cf. Eqs. (2.4.9) and (2.4.12) for dileptons and photons, respectively, have to be evaluated. At higher

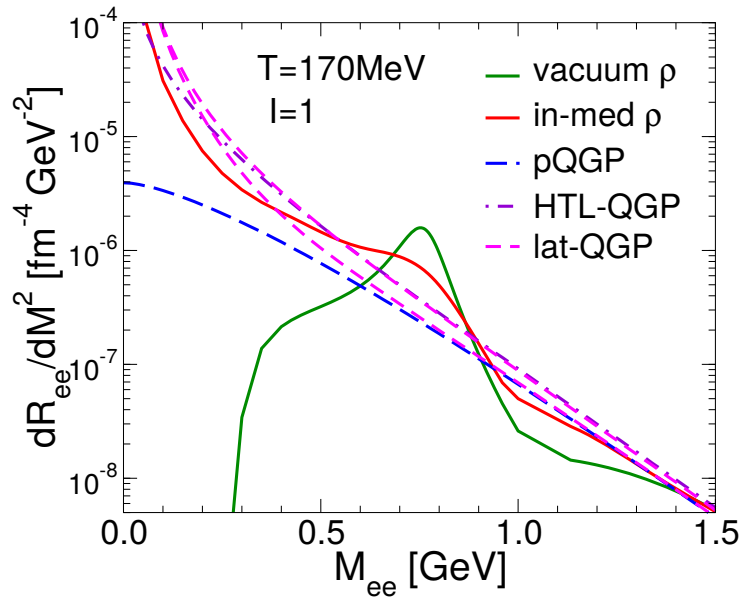


Figure 3.4: Dilepton-emission rate as a function of invariant mass at $T = 170$ MeV from $q\bar{q} \rightarrow \ell^+\ell^-$ annihilation in leading order perturbation theory (blue line), a leading-order hard-thermal loop calculation (violet line), and a lattice-QCD (red line) in comparison to the calculation from hadronic effective theory with and without medium effects. Fig. taken from [Rap13b].

collision energies the produced matter becomes hot and dense enough to enter the deconfined phase of a quark-gluon plasma and then evolves as an expanding and cooling fireball undergoing the transition to a hot and dense hadron-resonance gas that finally decouples to freely streaming hadrons observed in the detectors.

As a comparison of the found particle abundances and spectra with relativistic hydrodynamic simulations shows, the hot and dense fireball in this evolution is well described by a medium close to local thermal equilibrium. This allows the use of the equilibrium in-medium electromagnetic current-current correlation function in (2.4.9) and (2.4.12) to describe the dilepton and photon production in heavy-ion collisions. Since the electromagnetic probes are emitted during the entire evolution of the medium, both a detailed description of this collective dynamics of the medium as well as the production rates are necessary over a wide range of temperatures and baryochemical potentials. In the following we first briefly describe the quantum-field theoretical models for the in-medium production rates and then the bulk-evolution models used in this work.

3.2.1 Electromagnetic radiation from the QGP

At leading order (LO) in α_{em} , the basic process for dilepton production in the partonic phase is $q\bar{q}$ annihilation, $q + \bar{q} \rightarrow \ell^- + \ell^+$. In terms of the current-current correlation function, which in quantum-field theoretical view is just given by the photon polarization function (or photon self-energy), this refers to the one-loop diagram,

3. Electromagnetic probes in NN and AA collisions



Its evaluation leads to the dilepton production rate from the QGP at temperature T and quark-chemical potential $\mu_q = \mu_B/3$ [CFR87].

$$\begin{aligned} \text{Im}\Pi_{\text{em}}^{(\text{QGP})}(k) &= -\sum_f q_f^2 \frac{N_c}{12\pi} \frac{T k^2}{|\vec{k}|} \ln\left(\frac{\{x_- + \exp[-(k^0 + \mu)/T]\}[x_+ + \exp(-\mu/T)]}{\{x_+ + \exp[-(k^0 + \mu)/T]\}[x_- + \exp(-\mu/T)]}\right) \\ &= \frac{C_{\text{em}} N_c}{12\pi} M^2 \hat{f}_2(k_0, k; T) \end{aligned} \quad (3.2.1)$$

with

$$x_{\pm} = \exp\left(-\frac{E_{\pm}}{T}\right), \quad E_{\pm} = \frac{1}{2}(k^0 \pm |\vec{k}|). \quad (3.2.2)$$

However, at lower invariant dilepton masses the rate is tremendously enhanced by taking into account the leading-order α_s corrections employing the hard-thermal-loop (HTL) resummation techniques to dress the quark propagators [BPY90]: Although both quarks and gluons acquire a thermal mass $\sim gT$ bremsstrahlung contributions within the HTL resummation leads to an enhancement of the dilepton-production rates down to the two-lepton threshold (cf. Fig. 3.4).

More recently the dilepton-production rates have also been calculated in thermal lattice QCD [DFK⁺11, BFMW13, KLM⁺12]. Here the Euclidean-time vector-current correlation function,

$$\Pi_B(\tau, q; T) = \int_0^\infty \frac{dq_0}{2\pi} \rho_V(q_0, q, T) \frac{\cosh[q_0(\tau - 1/2T)]}{\sinh(q_0/2T)}, \quad (3.2.3)$$

is evaluated in quenched QCD for $T = 1.45T_c$ at $q = 0$. The spectral function is obtained from these numerical results by fitting the parameters Γ and χ in the ansatz

$$\rho_V(q_0) = S_{\text{BW}} \frac{q_0 \Gamma/2}{q_0^2 + \Gamma^2/4} + \frac{C_{\text{em}} N_c}{2\pi} (1 + \chi) q_0^2 \tanh(q_0/2T) \quad (3.2.4)$$

for the spectral function to the numerical results for (3.2.3).

To use the corresponding dilepton rates in calculations to describe heavy-ion collisions an extrapolation to finite three-momentum is needed. In [Rap13b] such an extrapolation is provided by using the transverse part of the electromagnetic spectral function from the leading-order pQCD photon rate for the three-momentum dependence of the spectral function (3.2.4), replacing the Breit-Wigner piece. This finally leads to the parameterization

$$\begin{aligned} \text{Im}\Pi_T &= -\frac{C_{\text{em}}}{12\pi} M^2 \left[\hat{f}_2(k_0, |\vec{k}|; T) + 2\pi\alpha_s \frac{T^2}{M^2} KF(M^2) \ln\left(1 + \frac{2.912k_0}{4\pi\alpha_s T}\right) \right] \\ &= \frac{C_{\text{em}} N_c}{12\pi} M^2 \left[\hat{f}_2(k_0, |\vec{k}|; T) + Q_{\text{lat}}^{(T)}(k_0, |\vec{k}|) \right]. \end{aligned} \quad (3.2.5)$$

Here $K = 2$ is introduced to account for the enhancement of the photon rate over the LO rate and to better reproduce the low-energy limit of the lattice-QCD spectral function. To accommodate the

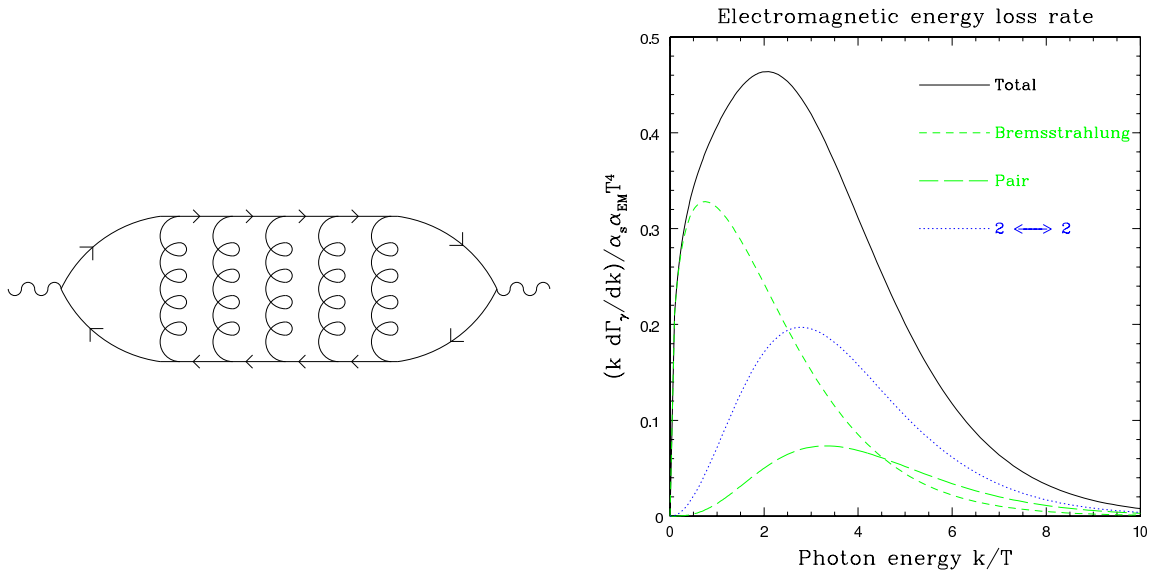


Figure 3.5: *Left panel: Typical ladder diagram for the leading-order contribution to the electromagnetic current-correlation function in a QGP. Resummed have to be ladders with arbitrary numbers of rungs. Right panel: Total energy distribution of photons. Figures taken from [AMY01].*

behavior at higher energies an additional form factor $F(M^2) = \Lambda^2/(\Lambda^2 + M^2)$ with $\Lambda = 2T$ has been used. In Fig. 3.4 the upper (lower) dashed line correspond to this parameterization with (without) this form factor. Finally one has to also reconstruct the longitudinal part of the current-correlation function. This is achieved by using the standard construction of gauge-invariant s-wave ρ -baryon interactions, $\Pi_L = (M^2/q_0^2)\Pi_T$ [RW00b].

To evaluate the em. current-correlation function for photons, due to infrared and collinear divergences of bremsstrahlung processes a resummation process [AMY01] for ladder diagrams of the type shown in Fig. 3.5 is necessary in addition to the naive leading α_s -order quasi-elastic gluo-Compton and $q + \bar{q} \rightarrow \gamma + g$ -annihilation processes. Cutting ladder diagrams with N rungs shows that this resummation adds coherently all processes for which the photon is emitted before and after N quark-antiquark collisions, which implies the proper implementation of the Landau-Pomeranchuk-Migdal effect [KV96].

3.2.2 Electromagnetic radiation from a hot/dense hadron gas

At lower temperatures and densities the low-mass dilepton spectrum is governed by the in-medium spectral functions of the light vector mesons, ρ , ω , and ϕ in the sense of the vector-meson dominance model. For the description of this contribution to the dilepton rate in heavy-ion collisions we use the ‘‘Rapp-Wambach Model’’ based on [RCW96, RCW97, UBRW98, RUBW98, RG99] as summarized in [RW99]. The evaluation of the spectral properties of the vector mesons in a dense and hot hadronic medium consists in the determination of their self-energies in thermal and chemical equilibrium. Here we concentrate on the ρ meson. Microscopically the corresponding in-medium contributions consist of (i) modification of the pion loop in the $\rho\pi\pi$ loop as in (2.6.18) and (ii) direct couplings of the ρ meson to both mesons and baryons. As will become clear, particularly the baryon contributions play a crucial role in describing the dilepton spectra in heavy-ion collisions at all energies. Although at the highest available collision energies at RHIC and LHC the net-baryon density is low ($\mu_B \simeq 0$), the total baryon density $n_B + n_{\bar{B}}$ is high, and thus leads to significant modifications of the ρ -meson spectral

3. Electromagnetic probes in NN and AA collisions

function, contributing particularly in the low-mass tail of the dilepton invariant-mass spectrum.

The $\rho\pi\pi$ interaction is based on the interaction Lagrangian [RCW96, RCW97]

$$\mathcal{L}_{\rho\pi\pi} = g_{\rho\pi\pi}(\vec{\pi} \times \partial^\mu \vec{\pi}) \cdot \vec{\rho}_\mu \quad (3.2.6)$$

with $\vec{\pi}$ and $\vec{\rho}_\mu$ the isovector pion and isovector ρ -meson fields, respectively. To account for medium modifications of the pion, the pion self-energy Σ_π is evaluated employing particle-hole excitations [EW88, RW94], where the pions interact with nucleons and Δ resonances through excitations of the type NN^{-1} , ΔN^{-1} , $N\Delta^{-1}$, and $\Delta\Delta^{-1}$. In order to guarantee the transversality of the ρ self-energy the corresponding vertex corrections to restore the pertinent Ward-Takahashi identities have to be taken into account [UBRW98]. The needed ρN and $\rho\pi N$ couplings are obtained from the pionic Lagrangian by minimal coupling to the πN couplings,

$$\begin{aligned} \mathcal{L}_{\rho N} &= -\frac{g}{2} \bar{\psi} \not{\rho} \tau_3 \psi, \\ \mathcal{L}_{\rho\pi N} &= ig \frac{f_N}{m_\pi} \bar{\psi} \gamma^5 \not{\rho} \vec{\tau} \psi \cdot T_3 \vec{\pi}, \end{aligned} \quad (3.2.7)$$

and the $\pi\Delta$ couplings,

$$\begin{aligned} \mathcal{L}_{\rho\Delta} &= g \bar{\psi}_\mu \not{\rho} T_3^{(3/2)} \psi^\mu - \frac{g}{3} \bar{\psi}_\mu (\gamma^\mu \rho_\nu + \gamma_\nu \rho^\mu) T_3^{(3/2)} \psi^\nu + \frac{g}{3} \bar{\psi}_\mu \gamma^\mu \not{\rho} T_3^{(3/2)} \gamma_\nu \psi^\nu, \\ \mathcal{L}_{\rho\pi N\Delta} &= -ig \frac{f_\Delta}{m_\pi} \bar{\psi} T^\dagger \psi_\mu \rho^\mu \cdot T_3 \vec{\phi} + \text{h.c.} \end{aligned} \quad (3.2.8)$$

One way to fix the various parameters in the model is to aim at a description of data on photon absorption on nucleons and nuclei. For that purpose the direct coupling of the ρ meson to various baryon resonances has to be addressed [RUBW98]. The corresponding interaction Lagrangians are given by p-wave couplings of positive parity states and s-wave couplings of negative-parity states to the ρN system, which read in the here employed non-relativistic limit

$$\begin{aligned} \mathcal{L}_{\rho BN}^{(\text{p-wave})} &= \frac{f_{\rho BN}}{m_\rho} \Psi_B^\dagger(\vec{s} \times \vec{q}) \cdot \vec{\rho}_a t_a \Psi_N + \text{h.c.}, \\ \mathcal{L}_{\rho BN}^{(\text{s-wave})} &= \frac{f_{\rho BN}}{m_\rho} \Psi_B^\dagger(q_0 \vec{s} \cdot \vec{\rho}_a - \rho_a^0 \vec{s} \cdot \vec{q}) t_a \Psi_N + \text{h.c.} \end{aligned} \quad (3.2.9)$$

Here, \vec{s} denote spin (transition) operators for $J = 1/2$ and $J = 3/2$ and t the isospin (transition) operators for $I = 1/2$ and $I = 3/2$, depending on the quantum numbers of the baryon $B = N(939)$, $\Delta(1232)$, $N(1720)$ (positive parity) as well as $B = N(1520)$, $\Delta(1620)$, $\Delta(1700)$ (negative parity). For the spin-5/2 $\Delta(1905)$ a tensor coupling of the type $(R_{ij} q_i \rho_{j,a} T_a)$ is employed.

The in-medium self-energies from the resulting baryon nucleon-hole loop diagrams are of the form

$$\Sigma_{\rho\alpha}^{(0),T}(q_0, q) = - \left(\frac{f_{\rho\alpha} F_{\rho\alpha}(q)}{m_\rho} \right) SI(\rho\alpha) Q^2 \phi_{\rho\alpha}(q_0, q), \quad (3.2.10)$$

where $Q^2 = q^2, q_0^2$ for p- and s-wave couplings. Also a monopole form factor $F_{\rho\alpha}(q) = \Lambda_\rho^2 / (\Lambda_\rho^2 + q^2)$ has been introduced, and $SI(\rho\alpha)$ denotes the spin-isospin factor; $\phi_{\rho\alpha}(q_0, q)$ is the Lindhard function corresponding to the one-loop self-energy diagram. The photoabsorption cross section within the strict

3.2. Models for electromagnetic probes in heavy-ion collisions

B	$l_{\rho N}$	$SI(\rho BN^{-1})$	$\Gamma_{\rho N}^0$ (MeV)	$\left(\frac{f_{\rho BN}^2}{4\pi}\right)_{\text{est}}$	$\left(\frac{f_{\rho BN}^2}{4\pi}\right)_{\text{fit}}$	Γ^{med} [MeV]
N(939)	p	4	–	4.68	5.8	0
$\Delta(1232)$	p	16/9	–	18.72	23.2	15
N(1520)	s	8/3	24	6.95	5.5	250
$\Delta(1620)$	s	8/3	22.5	1.01	0.7	50
$\Delta(1700)$	s	16/9	45	1.2	1.2	50
N(1720)	p	8/3	105	8.99	9.2	50
$\Delta(1905)$	p	4/5	210	17.6	18.5	50

Table 3.2: Properties of the ρBN vertices as derived from the interaction Lagrangians (3.2.9); columns from left to right: baryon resonance, relative angular momentum in the ρN decay, spin-isospin factor, partial decay width into ρN as extracted from [EHTM97, PPL⁺98], coupling constant as estimated from $\Gamma_{\rho N}^0$ (for N(939) and $\Delta(1232)$ we have indicated the values from the BONN potential [MHE87] which uses somewhat harder form factors), coupling constant as in the fit to photoabsorption data, in-medium correction to the total decay width (cf. Fig. 3.6). Table taken from [RUBW98].

vector-meson dominance model reads

$$\frac{\sigma_{\gamma A}^{\text{abs}}}{A} = -\frac{4\pi\alpha_{\text{em}}}{q_0} \frac{(m_{\rho}^{(0)})^4}{g^2} \frac{1}{\rho_N} \text{Im} D_{\rho}^T(q_0, \vec{q}; \rho_N). \quad (3.2.11)$$

On the other hand it is known that this strict realization of the vector-meson dominance ansatz tends to overestimate the $B \rightarrow N\gamma$ branching fractions with the hadronic couplings determined from the corresponding $B \rightarrow \rho N$ decay widths. This can, however, be corrected by using the extended realization of VMD in [KLZ67], which allows to adjust the $BN\gamma$ coupling at the photon point independently [FP97]. As shown in Fig. 3.6, making use of this freedom a satisfactory fit of the data on photoabsorption on protons as well as nuclei can be achieved, resulting in the values of the various coupling constants given in Table 3.2. We note that this model leads to very similar in-medium modifications of the ρ -meson spectral function as the model discussed in Sect. 3.1 (cf. [4]).

Finally the in-medium modifications of the ρ meson due to direct interactions with various mesons has to be taken into account [RG99]. At temperatures relevant for the hadron-gas phase of the medium created in heavy-ion collisions the most abundant hadrons are the pseudoscalar pseudo-Goldstone mesons $P = \pi, K$. So the heavier mesons can be treated as “ ρP states”, i.e., vector (V) and axial-vector mesons (A). The corresponding interaction Lagrangians, obeying chiral symmetry and (via the VMD conjecture) electromagnetic gauge invariance read

$$\begin{aligned} \mathcal{L}_{\rho PA} &= G_{\rho PA} A_{\mu} (\eta^{\mu\nu} q_{\alpha} p^{\alpha} - q^{m\mu} p^{\nu}) \rho_{\nu} P, \\ \mathcal{L}_{\rho PV} &= G_{\rho PV} \epsilon_{\mu\nu\rho\sigma} k^{\mu} V^{\nu} q^{\rho} \rho^{\sigma} P, \end{aligned} \quad (3.2.12)$$

with the four-momenta p^{μ} , q^{μ} , and k^{μ} of the pseudoscalar, ρ , and vector or axial-vector meson, respectively. The ρP scattering through a vector-meson resonance is due to the Wess-Zumino anomaly.

Further the ρP scattering can also be mediated by a pseudoscalar resonance, $\rho\pi \rightarrow \pi'(1300)$ with the interaction Lagrangian

$$\mathcal{L}_{\rho PP'} = G_{\rho PP'} P'(k \cdot q p_{\mu} - p \cdot q k_{\mu}) \rho^{\mu} P. \quad (3.2.13)$$

3. Electromagnetic probes in NN and AA collisions

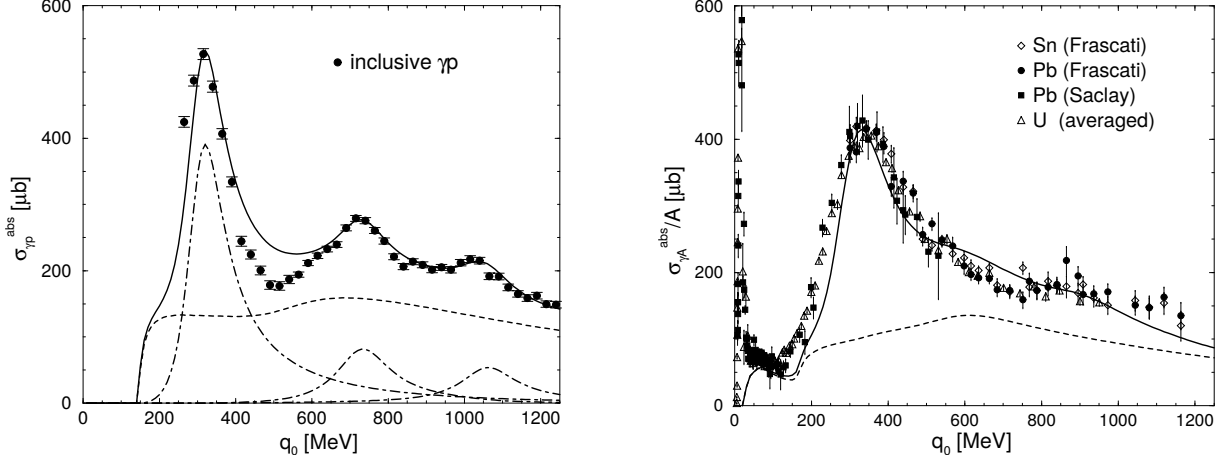


Figure 3.6: *Left panel: Total photoabsorption cross section on the proton. The solid line represents the full result of the fit of the model; the dashed lines show the $\pi\pi$ non-resonant background and the three dominant ρN resonances $\Delta(1232)$, $N(1520)$, and $N(1720)$. The data are from [A⁺72]. Right panel: Total photoabsorption cross section on various nuclei. The solid line represents the full result of the in-medium model calculation and the short-dashed line the $\pi\pi$ background, both calculated at a nuclear density $\bar{\rho}_N = 0.8\rho_0$. The long-dashed line corresponds to a linear-density approximation, reflecting the line shape of the left figure. The data are taken from [LBB⁺78, A⁺84, Ahr85, FSH⁺92, B⁺93, B⁺96]. The figures are taken from [RUBW98].*

R	$I^G J^P$	Γ_{tot} (MeV)	ρh Decay	$\Gamma_{\rho h}^0$ (MeV)	$\Gamma_{\gamma h}^0$ (MeV)
$\omega(782)$	$0^- 1^-$	8.43	$\rho\pi$	~ 5	0.72
$h_1(1170)$	$0^- 1^+$	~ 360	$\rho\pi$	seen	?
$a_1(1260)$	$1^- 1^+$	~ 400	$\rho\pi$	dominant	0.64
$K_1(1270)$	$\frac{1}{2} 1^+$	~ 90	ρK	~ 60	?
$f_1(1285)$	$0^+ 1^+$	25	$\rho\rho$	≤ 8	1.65
$\pi'(1300)$	$1^- 0^-$	~ 400	$\rho\pi$	seen	?

Table 3.3: *Mesonic Resonances R with masses $m_R \leq 1300$ MeV and substantial branching ratios into final states involving direct ρ 's (hadronic) or ρ -like photons (radiative). Table taken from [RG99].*

Finally, there are ρVA vertices related to anomaly terms,

$$\mathcal{L}_{\rho VA} = G_{\rho VA} \epsilon_{\mu\nu\rho\sigma} p^\mu V^\nu \rho^{\rho\alpha} k_\alpha A^\sigma - \frac{\lambda}{2} (k_\beta A^\beta)^2, \quad (3.2.14)$$

with the field-strength tensor $\rho_{\mu\nu} = q_\mu \rho_\nu - q_\nu \rho_\mu$. The second term on the right-hand side is a gauge-fixing term for the axial-vector field, and the Feynman gauge is chosen by setting $\lambda = 1$.

The considered vector and axial-vector mesons as well as the heavy pseudoscalar $\pi'(1300)$ with their corresponding decay properties to ρh and γh partial decay widths are summarized in Table 3.3. These widths are calculated with the above defined interaction vertices, taking into account the finite width of the ρ meson. Additionally hadronic dipole-form factors,

$$F_{\rho PR}(q_{\text{cm}}) = \left(\frac{2\Lambda_{\rho P}^2 + m_R^2}{2\Lambda_{\rho P}^2 + [\omega_\rho(q_{\text{cm}}) + \omega_P(q_{\text{cm}})]^2} \right)^2, \quad (3.2.15)$$

3.2. Models for electromagnetic probes in heavy-ion collisions

R	$IF(\rho h R)$	$G_{\rho h R}$ (GeV $^{-1}$)	$\Lambda_{\rho h R}$ (MeV)	$\Gamma_{\rho h}^0$ (MeV)	$\Gamma_{\gamma h}^0$ (MeV)
$\omega(782)$	1	25.8	1000	3.5	0.72
$h_1(1170)$	1	11.37	1000	300	0.60
$a_1(1260)$	2	13.27	1000	400	0.66
$K_1(1270)$	2	9.42	1000	60	0.32
$f_1(1285)$	1	35.7	800	3	1.67
$\pi'(1300)$	2	9.67	1000	300	0

Table 3.4: Results of the fit to the decay properties of ρ - h induced mesonic resonances R with masses $m_R \leq 1300$ MeV (the $f_1(1285)$ and $\pi'(1300)$ coupling constants are in units of GeV $^{-2}$). $IF(\rho h R)$ denotes the isospin factor in the decay-matrix element. Table taken from [RG99].

are introduced.

The medium modifications of the ρ -meson self-energy and the corresponding spectral function is then evaluated with these model parameters. As is nicely demonstrated in Fig. 3.7, any process adds to the imaginary part of the self-energy, i.e., the ρ -meson width, while the contribution to the real part around the vacuum mass can be positive or negative, depending on whether the effective interaction due to the involved meson resonances is repulsive or attractive, respectively. The net result is a considerable broadening of the ρ -meson's spectral shape with only moderate mass shifts. The same qualitative feature is also seen when taking all the in-medium effects on the ρ -meson self-energy into account, i.e., the modification of the pion cloud in the $\rho\pi\pi$ loop as well as the just discussed direct interactions of the ρ with mesonic and baryonic resonances, one finds a tremendous broadening of the spectral function with only small mass shifts [RW99]. It is important to note that the baryons provide a lot of spectral strength in the low-mass tail, which within the VMD model leads to a considerable enhancement of the dilepton-production rate down to the $\ell^+\ell^-$ threshold. As already shown in Fig. 3.4 the full in-medium dilepton-production rates close to the pseudo-critical temperature for the chiral phase transition, obtained by extrapolating the pertinent partonic rates down and the hadronic rates up to temperatures around $T_c \simeq 160$ MeV become very similar, hinting at a restoration of chiral symmetry through “melting of the vector-meson resonances” merging smoothly into the corresponding QCD continuum.

In the intermediate-mass region, $m_\phi \lesssim M_{\ell^+\ell^-} \lesssim m_{J/\psi}$, medium modifications can be addressed approximately using a low-temperature/density expansion, leading to a mixing of the vector and axial-vector current-correlation functions via the presence of thermal pions [DEI90],

$$\begin{aligned}\Pi_V(q) &= (1 - \epsilon)\Pi_V^{\text{vac}}(q) + \epsilon\Pi_A^{\text{vac}}(q), \\ \Pi_A(q) &= \epsilon\Pi_V^{\text{vac}}(q) + (1 - \epsilon)\Pi_A^{\text{vac}}(q).\end{aligned}\tag{3.2.16}$$

The mixing coefficient ϵ is given by pion tadpole diagrams via a thermal loop integral,

$$\epsilon = \frac{2}{f_\pi^2} \int \frac{d^3\vec{k}}{(2\pi)^3 \omega_k^\pi} f_\pi(\omega_k^\pi; T),\tag{3.2.17}$$

where $\omega_k^\pi = \sqrt{m_\pi^2 + k^2}$ is the on-shell energy of the pion and $f_\pi = 93$ MeV the pion-decay constant. For $\epsilon \rightarrow 1/2$ this leads to a full restoration of chiral symmetry around $T = T_c \simeq 160$ MeV, i.e., degeneracy in the vector and axial-vector correlation function. In the intermediate mass region this leads to a smooth distribution resembling the QCD continuum.

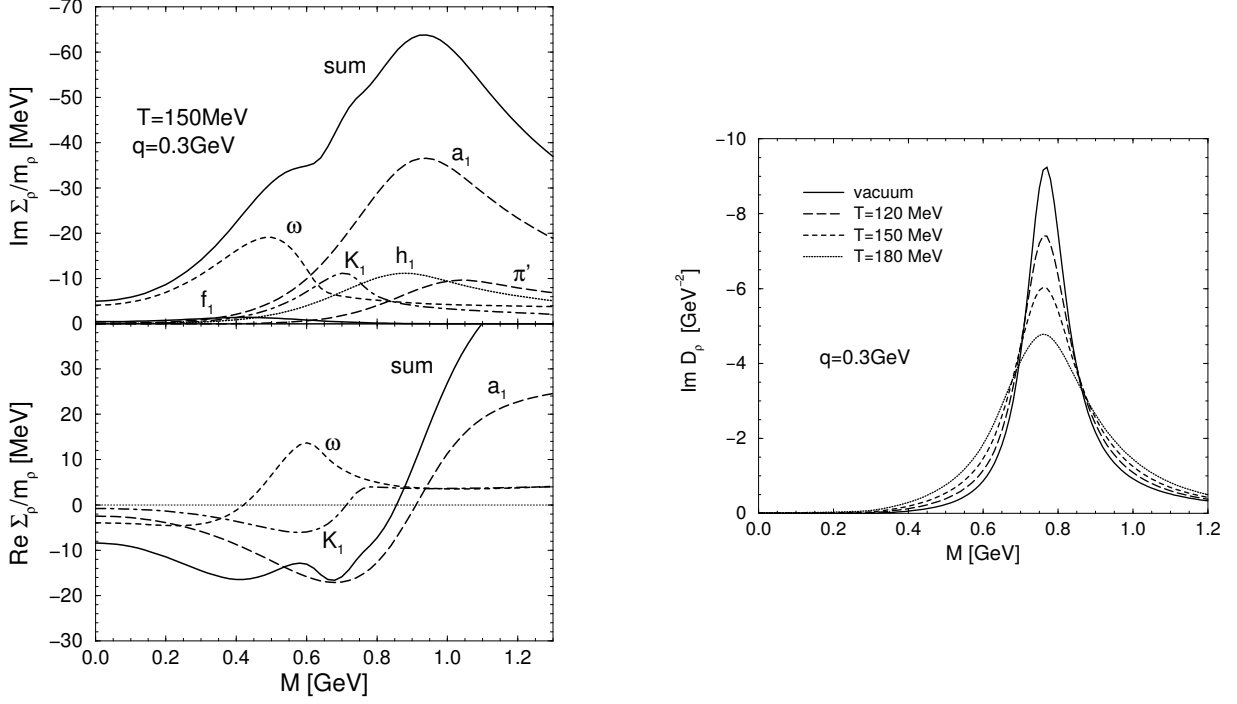


Figure 3.7: The polarization-averaged in-medium ρ -meson self-energy (left) and spectral function (right). Figures taken from [RG99].

In [2, 3] this chiral-mixing effect is implemented taking into account the presence of an effective pion chemical potential, which ensures the conservation of the pion number after chemical freezeout (in Boltzmann approximation), using (3.2.16) with a mixing parameter $\hat{\epsilon} = \frac{1}{2}\epsilon(T, \mu_\pi)/\epsilon(T_c, 0)$ and with a fugacity factor $z_\pi = \exp(\mu_\pi/T)$ in (3.2.17). Here it is important to avoid double counting with the above described in-medium evaluations of the ρ self-energy due to interactions with vector and axial-vector mesons, i.e., the two-pion piece and the part corresponding to the $a_1 \rightarrow \rho\pi$ decay have to be omitted. A detailed analysis, based on the chiral-reduction formalism [SYZ96, SYZ97], finally leads to

$$\Pi_V = (1 - \hat{\epsilon})z_\pi^4 \Pi_{V,4\pi}^{\text{vac}} + \frac{\hat{\epsilon}}{2}z_\pi^3 \Pi_{A,3\pi}^{\text{vac}} + \frac{\hat{\epsilon}}{2}(z_\pi^4 + z_\pi^5) \Pi_{A,5\pi}^{\text{vac}}. \quad (3.2.18)$$

As a further source of dileptons from a hot and dense hadronic medium, relevant at higher three-momenta, in [3] also contributions from the annihilation of a ρ meson through ω -meson t -channel exchange has been taken into account (cf. Fig. 3.8). The ρ - γ mixing vertex has been implemented by the Lagrangian $\mathcal{L}_{\rho\gamma} = -C m_\rho^2 A_\mu \rho^\mu$, using the strict VMD value $C = e/g_{\rho\pi\pi} = 0.052$ [RG99]. For the intermediate ρ -meson line in Fig. 3.8 the full in-medium propagator of the ρ meson has been used, and for the incoming ρ -meson line a weight $(-2m_\rho/\pi) \text{Im } D_\rho(m_\rho)$. The coupling $g_{\rho\omega\pi} = 25.8 \text{ GeV}^{-1}$ is fixed in [RG99] by a simultaneous fit to the hadronic and radiative ω decays, taking into account a hadronic dipole-form factor,

$$F(t) = \left(\frac{2\Lambda^2}{2\Lambda^2 - t} \right)^2 \quad (3.2.19)$$

with $\Lambda = 1 \text{ GeV}$. To ensure gauge invariance, the form factor is taken out of the integral, introducing

3.2. Models for electromagnetic probes in heavy-ion collisions

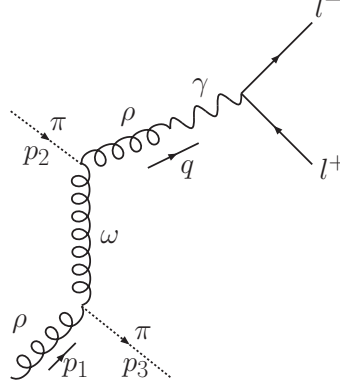


Figure 3.8: Feynman diagram describing the annihilation of a ρ meson, $\rho\pi \rightarrow \pi\ell^+\ell^-$ via the t -channel exchange of an ω meson. Figure taken from [3].

an average momentum transfer \bar{t} via [TRG04]

$$\frac{F^4(\bar{t})}{(m_\omega^2 - \bar{t})^2} = \frac{1}{2} \int_{-1}^1 dx \frac{F^4[t(x)]}{[m_\omega^2 - t(x)]^2}, \quad (3.2.20)$$

$$t(x) = M^2 + m_\pi^2 - 2(M^2 + q^2 - 2p \cdot qx).$$

Finally, to avoid double counting with the s -channel ω -exchange contribution, which is already included in the evaluation of the in-medium ρ self-energy, in evaluating the corresponding dilepton-emission rate from standard kinetic theory the integral has been restricted to the kinematic region $t < 0$ (for details, see [3]).

For a realistic description of the dilepton production in heavy-ion collisions one has to take into account also non-thermal sources: ρ decay after thermal freeze-out as well as decay of high-momentum ρ mesons and Drell-Yan pairs produced in primordial hard collisions.

For the decay of ρ mesons after thermal freezeout the usual Cooper-Frye description [3],

$$dN = q_\mu d\sigma^\mu \frac{d^3\vec{q}}{(2\pi)^3 q^0} f_B\left(\frac{q_\mu u^\mu}{T}\right), \quad (3.2.21)$$

is used, where q_μ is the four-momentum of the particle, $d\sigma^\mu$ a freezeout-surface element, and u^μ the local four-velocity of the fluid cell under consideration. To take into account the finite width of the ρ meson one uses the substitution

$$\frac{d^3\vec{q}}{q^0} = d^4q 2\Theta(q^0)\delta(q_\mu q^\mu - m^2) \rightarrow d^4q \frac{A_\rho}{\pi}, \quad A_\rho = -\frac{2}{3} \text{Im}(D_\rho)_\mu^\mu. \quad (3.2.22)$$

Within the VMD model the corresponding dilepton rate is given by the matrix element for the process $\rho \rightarrow \gamma^* \rightarrow \ell^+\ell^-$,

$$\frac{dN_{\ell\ell}}{d^3\vec{x}d^4q} = \frac{\alpha_{\text{em}}^2 m_\rho^4}{g_\rho^2 M^2} \frac{A_\rho}{2\pi^3} L(M) f_B\left(\frac{q \cdot u}{T}\right) \frac{q^0}{M\Gamma_\rho^{(\text{fo})}}, \quad (3.2.23)$$

where

$$L(M) = \left(1 + \frac{2m_\ell^2}{M^2}\right) \sqrt{1 - \frac{4m_\ell^2}{M^2}} \quad (3.2.24)$$

3. Electromagnetic probes in NN and AA collisions

is the dilepton phase-space factor. One should note that compared to the emission from a thermal source the spectral shape is modified by the life-time dilation factor $\gamma = q^0/M = \sqrt{\vec{q}^2 + M^2}/M$.

To estimate the contribution to the dilepton rate from ρ mesons produced in hard initial collisions, which do not fully equilibrate with the bulk medium, one starts from a phenomenological q_T spectrum in pp collisions,

$$\frac{1}{q_T} \frac{dN_{\text{prim}}}{dq_T} = \frac{A}{(1 + Bq_T^2)^a} \quad (3.2.25)$$

with $B = 0.525 \text{ GeV}^{-2}$ and $a = 5.5$ from fitting pp-scattering data [AB⁺91] (for 400 GeV pp collisions). The total number of primordial ρ mesons in AA collisions is estimated from the empirical freeze-out systematics of light-hadron production [3]. To take cold-nuclear matter effects into account the Cronin effect is implemented by a ‘‘Gaussian smearing’’ of the spectrum (3.2.25),

$$\frac{dN_{\text{prim}}^{\text{cron}}}{d^2q_T} = \int \frac{d^2q_T}{\pi\Delta k_T^2} \frac{dN_{\text{prim}}}{d^2k_T} \exp\left[-\frac{(q_T - k_T)^2}{\Delta k_T^2}\right], \quad (3.2.26)$$

with $\Delta k_T^2 = 0.2 \text{ GeV}^2$ based on direct-photon spectra in pA collisions [TRG04]. Finally the absorption of primordial ρ mesons through traversing the medium (‘‘jet quenching’’) is evaluated by estimating the escape probability

$$P = \exp\left[-\int dt \sigma_{\rho}^{\text{abs}}(t) \varrho(t)\right], \quad (3.2.27)$$

where

$$\sigma_{\rho}^{\text{abs}} = \begin{cases} \sigma_{\text{ph}} = 0.4 \text{ mb} & \text{for } t < q_0/m_{\rho}\tau_f, \\ \sigma_{\text{had}} = 5 \text{ mb} & \text{for } t > q_0/m_{\rho}\tau_f, \end{cases} \quad (3.2.28)$$

with the ρ -meson formation time $\tau_f = 1 \text{ fm}$; σ_{ph} and σ_{had} are the absorption cross sections for pre-hadrons and hadrons, respectively, and $\varrho(t)$ denotes the partonic or hadronic particle density of the medium.

Finally, the contribution to the dilepton yield from the Drell-Yan (DY) process, i.e., the quark-antiquark annihilation in hard initial collisions, is estimated using

$$\left. \frac{dN_{\text{DY}}^{\text{AA}}}{dM dy} \right|_{b=0} = \frac{3}{4\pi R_0^2} A^{4/3} \frac{d\sigma_{\text{DY}}^{\text{NN}}}{dM dy} \quad (3.2.29)$$

for central AA collisions with the root-mean squared radius $R_0 \simeq 1.05 \text{ fm}$ originating from folding over a Gaussian thickness function. The DY cross section in nucleon-nucleon collisions is given in leading order $\mathcal{O}(\alpha_s^0 \alpha_{\text{em}}^2)$ by

$$\frac{d\sigma_{\text{DY}}^{\text{NN}}}{dM dy} = K \frac{8\pi\alpha_{\text{em}}}{9sM} \sum_{q=u,d,s} e_q^2 [q(x_1)\bar{q}(x_2) + \bar{q}(x_1)q(x_2)]. \quad (3.2.30)$$

where $q(x_{1,2})$ and $\bar{q}(x_{1,2})$ denote the GRV94LO parton-distribution functions for quarks and anti-quarks [GRV95]. The K factor takes into account higher-order corrections in α_s with $K \simeq 1.5$ as inferred from data on DY production in pA collisions [SGH⁺98]. Higher-order effects also lead to a non-zero dilepton- q_T , which is adopted from the procedure by the NA50 Collaboration [A⁺99, A⁺00],

3.2. Models for electromagnetic probes in heavy-ion collisions

according to which in both pA and AA collisions the q_T dependence of the DY dileptons can be described by a Gaussian distribution,

$$\frac{dN_{\text{DY}}}{dM dy dq_T^2} = \frac{dN_{\text{DY}}}{dM dy} \frac{\exp(-q_T^2/2\sigma_{q_T}^2)}{2\sigma_{q_T}^2} \quad (3.2.31)$$

with $\sigma_{q_T} \simeq 0.8\text{-}1$ GeV.

The DY contribution in the region of low invariant mass and momentum, $M, q \lesssim 1.5$ GeV is problematic. In AA collisions it is small compared to the emission from thermal sources, but becomes significant at higher $q_T \gtrsim 1$ GeV. There the additional constraint by the photon point $M \rightarrow 0$ allows an extrapolation of the DY spectrum to lower mass [3]: Comparing the emission rate for dileptons from a thermal source (2.4.9) with that of photons (2.4.12) we see that for $q \gg M$

$$q_0 \frac{dN_{\ell\ell}}{dM d^3\vec{q}} = q_0 \frac{dN_\gamma}{d^3\vec{q}} \frac{2\alpha_{\text{em}}}{3\pi M}. \quad (3.2.32)$$

Thus we evaluate the DY- q_T spectrum at a mass $M_{\text{cut}} = 0.8\text{-}1$ GeV and extrapolate it down in mass by M_{cut}/M .

Finally, for photon production in addition to the already discussed hadronic model for the in-medium electromagnetic current correlator, some additional meson-exchange reactions (π , K , ρ , K^* , and a_1) in a meson gas become relevant at photon momenta $q \gtrsim 1$ GeV [TRG04]. Here a massive-Yang-Mills model based on a nonlinear $U_L(3) \times U_R(3)$ - σ model has been employed:

$$\begin{aligned} \mathcal{L} = & \frac{1}{8} F_\pi^2 \text{Tr} D_\mu U D^\mu U^\dagger + \frac{1}{8} F_\pi^2 \text{Tr} M (U + U^\dagger - 2) \\ & - \frac{1}{2} \text{Tr} (F_{\mu\nu}^L F^{L\mu\nu} + F_{\mu\nu}^R F^{R\mu\nu}) + m_0^2 \text{Tr} (A_\mu^L A^{L\mu} + A_\mu^R A^{R\mu}) + \gamma \text{Tr} F_{\mu\nu}^L U F^{R\mu\nu} U^\dagger \\ & - i\xi \text{Tr} (D_\mu U D_\nu U^\dagger F^{L\mu\nu} + D_\mu U^\dagger D_\nu U F^{R\mu\nu}). \end{aligned} \quad (3.2.33)$$

Here

$$\begin{aligned} U &= \exp\left(\frac{2i}{F_\pi} \sum_i \frac{\phi_i \lambda_i}{\sqrt{2}}\right) = \exp\left(\frac{2i}{F_\pi} \phi\right), \\ A_\mu^L &= \frac{1}{2}(V_\mu + A_\mu), \\ A_\mu^R &= \frac{1}{2}(V_\mu - A_\mu), \\ F_{\mu\nu}^{L,R} &= \partial_\mu A_\nu^{L,R} - \partial_\nu A_\mu^{L,R} - i g_0 [A_\mu^{L,R}, A_\nu^{L,R}], \\ D_\mu U &= \partial_\mu U - i g_0 A_\mu^L U + i g_0 U A_\mu^R, \\ M &= \frac{2}{3} \left[m_K^2 + \frac{1}{2} m_\pi^2 \right] - \frac{2}{\sqrt{3}} (m_K^2 - m_\pi^2) \lambda_8 \end{aligned} \quad (3.2.34)$$

with $F_\pi = 135$ MeV and the Gell-Mann matrices λ_i ; ϕ , V_μ , and A_μ are the pseudoscalar, vector and axial-vector meson matrices, respectively.

In the non-strange sector, including pions, ρ , and a_1 mesons, in [Son93] two parameter sets for the four free parameters have been fitted to the masses and widths of the ρ and a_1 mesons,

$$\begin{aligned} I: & \quad \tilde{g} = 10.3063, \quad \gamma = 0.3405, \quad \xi = 0.4473, \quad m_0 = 0.6253 \text{ GeV}, \\ II: & \quad \tilde{g} = 6.4483, \quad \gamma = -0.2913, \quad \xi = 0.0585, \quad m_0 = 0.875 \text{ GeV}. \end{aligned} \quad (3.2.35)$$

In [GG98] the D- and S-wave content in the $a_1 \rightarrow \rho\pi$ decay has been found to be $D/S = 0.36$ and $D/S = -0.099$ for parameter sets I and II, respectively. Given the experimental finding of $D/S = -0.107 \pm 0.016$, in the following parameter set II has been used, employing the kinetic-theory expression for a photon-production process, $1 + 2 \rightarrow 3 + \gamma$,

$$q_0 \frac{dR_\gamma}{d^3\vec{q}} = \int \frac{d^3\vec{p}_1}{2(2\pi)^3 E_1} \frac{d^3\vec{p}_2}{2(2\pi)^3 E_2} \frac{d^3\vec{p}_3}{2(2\pi)^3 E_3} (2\pi)^4 \delta^{(4)}(p_1 + p_2 \rightarrow p_3 + q) \times |\mathcal{M}|^2 \frac{f(E_1)f(E_2)[1 \pm f(E_3)]}{2(2\pi)^3}. \quad (3.2.36)$$

For the matrix elements, Born graphs in all possible s -, t -, and u -channels for reactions of the type $X + Y \rightarrow Z + \gamma$, $\rho \rightarrow Y + Z + \gamma$, and $K^* \rightarrow Y + Z + \gamma$, where for X , Y , and Z all combinations of ρ , π , K , and K^* mesons allowed by the conservation of charge, isospin, strangeness, and G parity have been considered. In addition also the same model for ω - t -channel exchange has been used for photons as for dileptons (analogous to Fig. 3.8 with a real photon instead of a dilepton, $\ell^+\ell^-$ in the final state). At all vertices hadronic dipole form factors (3.2.19) have been employed, ensuring gauge invariance by the averaging procedure defined in (3.2.20).

3.2.3 Bulk-evolution models

To evaluate the dilepton spectra in relativistic heavy-ion collisions in addition to the above discussed models for the various dilepton sources a reliable description of the evolution of the hot and dense medium created in such collisions is necessary. In the here discussed work simple **thermal-fireball parameterizations** (“blast-wave” models) as well as **coarse-grained transport simulations** have been employed.

The thermal-fireball parameterizations are motivated by the observation that at the higher collision energies the bulk evolution of the medium is well-described by hydrodynamical expansion of a hot medium. In its simplest form the fireball volume is taken as an expanding cylinder with volume [RW99]

$$V_{\text{FB}}(t) = \pi \left(r_{\perp,0} + \frac{1}{2} a_{\perp} t^2 \right)^2 \left(z_0 + v_{z,0} t + \frac{1}{2} a_z t^2 \right). \quad (3.2.37)$$

The initial transverse radius $r_{\perp,0}$ is determined by the centrality of the collision. The initial longitudinal size z_0 reflects the formation time $\tau_0 = 1 \text{ fm}/c$ of the thermal medium, which translates into $z_0 \simeq \tau_0 \Delta y = 1.8 \text{ fm}$, where $\Delta y = 1.8$ is the rapidity width of a thermal fireball. The values for the transverse acceleration are determined together with the fireball lifetime by the transverse-momentum spectra of hadrons, which are affected by the “Doppler blueshift” due to the radial flow. In accordance with hydrodynamical calculations the radial flow-velocity is assumed to grow linearly with r_{\perp} ,

$$v_{\perp}(t, r_{\perp}) = \frac{r_{\perp}}{r_{\perp,0} + a_{\perp} t^2 / 2} a_{\perp} t. \quad (3.2.38)$$

With given expansion parameters, the fireball life-time is determined by the condition for thermal freeze-out which can also be determined from measurements of the hadronic spectra (see, e.g., for SPS energies [B⁺97, A⁺98, A⁺01, A⁺07b, A⁺03a]). The time evolution of the temperature is determined by the simplifying assumption that the temperature is constant throughout the fireball volume (i.e., taken as an average temperature) and that the expansion is isentropic in accordance with ideal hydrodynamics, using an EoS. For $T > T_c$ an ideal partonic EoS and a hadron-resonance-gas (HRG) EoS for $T < T_c$ has

3.2. Models for electromagnetic probes in heavy-ion collisions

been used. In [2, 3] a first-order transition has been assumed, connecting the QGP and HRG phases with a mixed phase at $T = T_c = \text{const}$ with the hadron-gas fraction,

$$f_{\text{HG}}(t) = \frac{s_c^{\text{QGP}} - s(t)}{s_c^{\text{QGP}} - s_c^{\text{HG}}}. \quad (3.2.39)$$

Of course, also other EoS with a cross-over transition, which is more adequate at higher beam energies, like latPHG [HFR12] can be easily implemented. After chemical freeze-out the system falls off chemical equilibrium, and besides the usual baryochemical potential, μ_B , chemical potentials like μ_π and μ_K are introduced to keep the particle abundances fixed. The chemical potential of resonances is then determined through their (finally stable) decay products; e.g., for the Δ resonance, decaying mostly into πN , $\mu_\Delta = \mu_B + \mu_\pi$ or for the ρ meson $\mu_\rho = 2\mu_\pi$, etc.

To also take into account the elliptic flow of hadrons in order to address the resulting elliptic flow of photons, in [5, 7] an elliptic blast-wave description has been developed. Also the parameterization of the radial flow of the fireball boundary in (3.2.37) has been substituted by the corresponding relativistic motion of constant proper acceleration, i.e., the velocities and lengths of the major axes of the ellipse follow the time evolution

$$\begin{aligned} v_a(t) &= \frac{a_a t}{\sqrt{1 + (a_a t)^2}}, & v_b(t) &= \frac{a_b t}{\sqrt{1 + (a_b t)^2}}, \\ a(t) &= a_0 + \frac{\sqrt{1 + (a_a t)^2} - 1}{a_a}, & b(t) &= b_0 + \frac{\sqrt{1 + (a_b t)^2} - 1}{a_b}. \end{aligned} \quad (3.2.40)$$

To define the flow field, confocal elliptic coordinates,

$$\vec{x}_\perp = r_0(\sinh u \cos v, \cosh u \sin v) \quad (3.2.41)$$

are introduced to parameterize the ellipse at each time, t , and the radial-flow velocity field is parameterized as

$$\vec{v}_\perp = \frac{r}{r_{\text{max}}}(v_b \cos v, v_a \sin v). \quad (3.2.42)$$

The accelerations a_a and a_b are chosen differently in the QGP and hadronic phases and determined such that the transverse-momentum spectra and elliptic flow of hadrons (in the low- p_T range) are well described. It is assumed that multi-strange hadrons (like, e.g., the ϕ meson) freeze out kinetically already at the phase transition, while the light hadrons freeze out at the nominal kinetic freezeout (see Fig. 3.9).

For smaller beam energies the description of the bulk evolution of the medium created in heavy-ion collisions becomes questionable, and transport simulations become more reliable. On the other hand, a fully self-consistent off-equilibrium treatment of the in-medium properties of hadrons, which is necessary for a successful description of dilepton and photon production in heavy-ion collisions, is very challenging. In [9, 12, 10, 13] a **coarse-grained transport approach** has been developed. Here, the bulk evolution is simulated using the established transport simulation Ultrarelativistic Quantum Molecular Dynamics (UrQMD) [BBB⁺98, BZS⁺99, PBBS08]. Averaging over several runs, the phase-space distribution is mapped to a local equilibrium description within a space-time grid, using an appropriate EoS. In this way the thermal quantum-field theoretical results for the in-medium dilepton and photon production rates described above become applicable.

3. Electromagnetic probes in NN and AA collisions

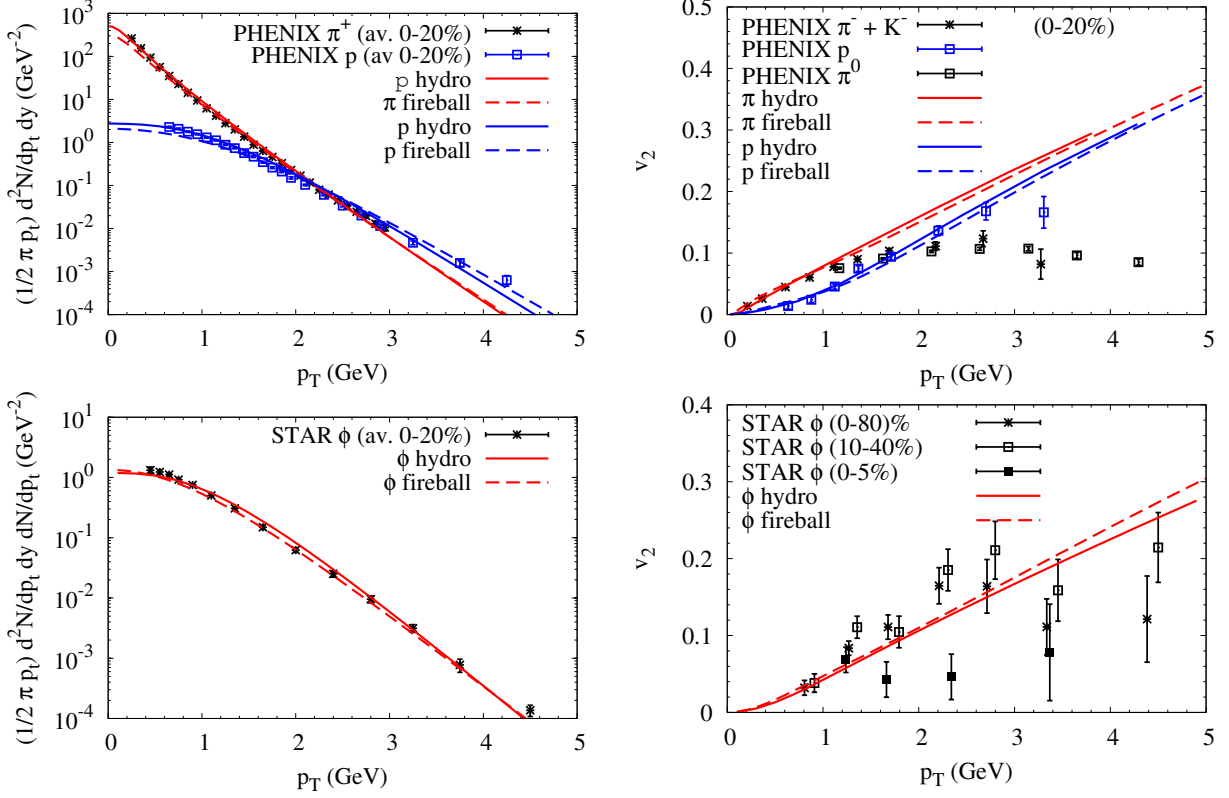


Figure 3.9: Fits to the spectra and elliptic flow of light hadrons ($T_{fo} \simeq 110$ MeV, upper two panels) and ϕ mesons ($T_{fo} = 160$ MeV, lower two panels) in Au-Au($\sqrt{s} = 200$ AGeV) collisions, using *EoS latPHG* [HFR12] within either the fireball (dashed lines) or ideal hydrodynamic model (solid lines). The data are taken from Refs. [A⁺07a, A⁺03b, A⁺04b, A⁺04a]. Figure taken from [7].

The grid of space-time cells is defined by $\Delta x = \Delta y = \Delta z = 0.7-0.8$ fm and $\Delta t = 0.2-0.6$ fm/c, and the energy-momentum tensor $T_{\mu\nu}$ and net-baryon four-flow j_{μ}^B in each cell are evaluated via

$$T^{\mu\nu} = \int d^3p \frac{p^{\mu} p^{\nu}}{p^0} f(\vec{x}, \vec{p}, t) = \frac{1}{\Delta V} \left\langle \sum_{i=1}^{N_b \in \Delta V} \frac{p_i^{\mu} \cdot p_i^{\nu}}{p_i^0} \right\rangle, \quad (3.2.43)$$

$$j_{\mu}^B = \int d^3p \frac{p^{\mu}}{p^0} f_B(\vec{x}, \vec{p}, t) = \frac{1}{\Delta V} \left\langle \sum_{i=1}^{N_{B/\bar{B}} \in \Delta V} \pm \frac{p_i^{\mu}}{p_i^0} \right\rangle,$$

where the averaging is understood as averaging over several UrQMD events. The four-velocity of the fluid cell is defined using the Eckart definition, i.e., according to the flow of the net-baryon number,

$$u^{\mu} = \frac{j_{\mu}^B}{\sqrt{j_{\mu}^B \cdot j_{\mu}^B}} = (\gamma, \gamma \vec{v}). \quad (3.2.44)$$

The transport simulations show that the assumption of isotropic thermal equilibrium in the fluid cells is not justified in the early stages of the collision. This kinetic off-equilibrium situation leads to the ansatz for the energy-momentum stress tensor within the anisotropic hydrodynamics approach [FR11, FMRS13, MNR16],

$$T^{\mu\nu} = (\varepsilon + P_{\perp}) u^{\mu} u^{\nu} - P_{\perp} \eta^{\mu\nu} - (P_{\perp} - P_{\parallel}) v^{\mu} v^{\nu}, \quad (3.2.45)$$

3.3. Dilepton production in heavy-ion collisions

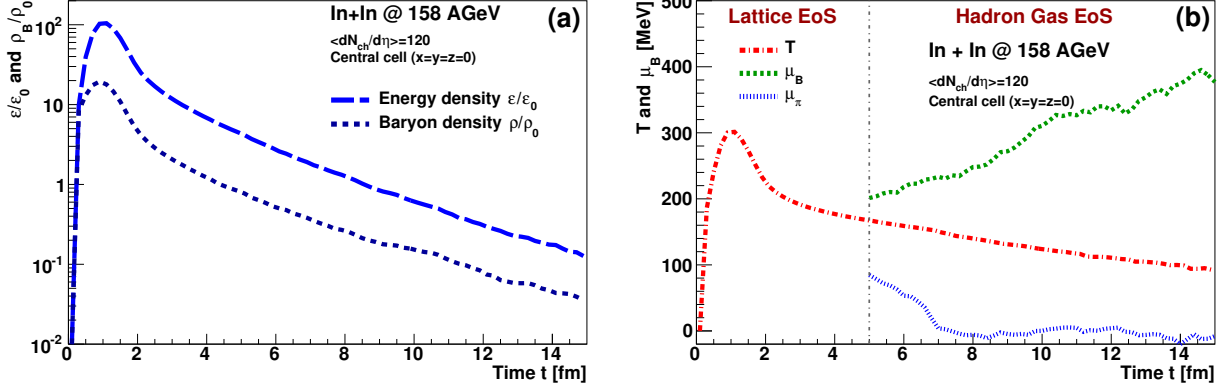


Figure 3.10: *Left panel: Time evolution of the baryon density ρ_B (short dashed) and energy density ε (long dashed) for the cell at the center of the coarse-graining grid ($x = y = z = 0$). The results are given in units of the ground-state densities ε_0 and ρ_0 . Right panel: Time evolution of the temperature T (red dash-dotted), baryon chemical potential μ_B (green short dashed) and the pion chemical potential μ_π (blue dotted) in the central cell. The thin grey line indicates the transition from the Lattice EoS to the Hadron Gas EoS at the transition temperature of $T = 170$ MeV. Figure taken from [9].*

where ε is the energy density, P_\perp and P_\parallel the pressures perpendicular and parallel to the beam direction; u^μ is the four-velocity of the fluid cell, and v^μ the four-vector of the beam direction. Then an effective energy density is obtained by the generalized EoS of a Boltzmann-like system via

$$\varepsilon_{\text{eff}} = \frac{\varepsilon}{r(x)} \quad (3.2.46)$$

with the relaxation function

$$r(x) = \begin{cases} \frac{x^{-1/3}}{2} \left(1 + \frac{x \operatorname{artanh} \sqrt{1-x}}{\sqrt{1-x}} \right) & \text{for } x \leq 1 \\ \frac{x^{-1/3}}{2} \left(1 + \frac{x \arctan \sqrt{x-1}}{\sqrt{x-1}} \right) & \text{for } x \geq 1 \end{cases}, \quad x = \left(\frac{P_\parallel}{P_\perp} \right)^{3/4}. \quad (3.2.47)$$

It turns out that ε_{eff} deviates from the nominal energy density,

$$\varepsilon = u_\mu u_\nu T^{\mu\nu}, \quad (3.2.48)$$

only in the first 1-2 fm/c of the time evolution, where the pressure anisotropy is large. The effective energy density and net-baryon density are used to determine the temperature and baryochemical potential as well as the pion and kaon chemical potentials to take into account chemical off-equilibrium, matching the EoS in the QGP phase based on lattice calculations [HFR12] with a hadron-resonance-gas EoS including the hadronic degrees of freedom implemented in UrQMD [ZSSB⁺02, PSB⁺08] based on a hadronic chiral model [PZS⁺99, ZZS07]. As an example Fig. 3.10 shows the time evolution of the net-baryon density, temperature, μ_B , and μ_π for the central cell of the medium created in 158 AGeV In-In collisions at the CERN SPS, as investigated in the NA60 experiment.

3.3 Dilepton production in heavy-ion collisions

In this Section the results of simulations for heavy-ion collisions at various beam energies is summarized. All calculations are based on the microscopic models for dilepton production described in Sects.

3. Electromagnetic probes in NN and AA collisions

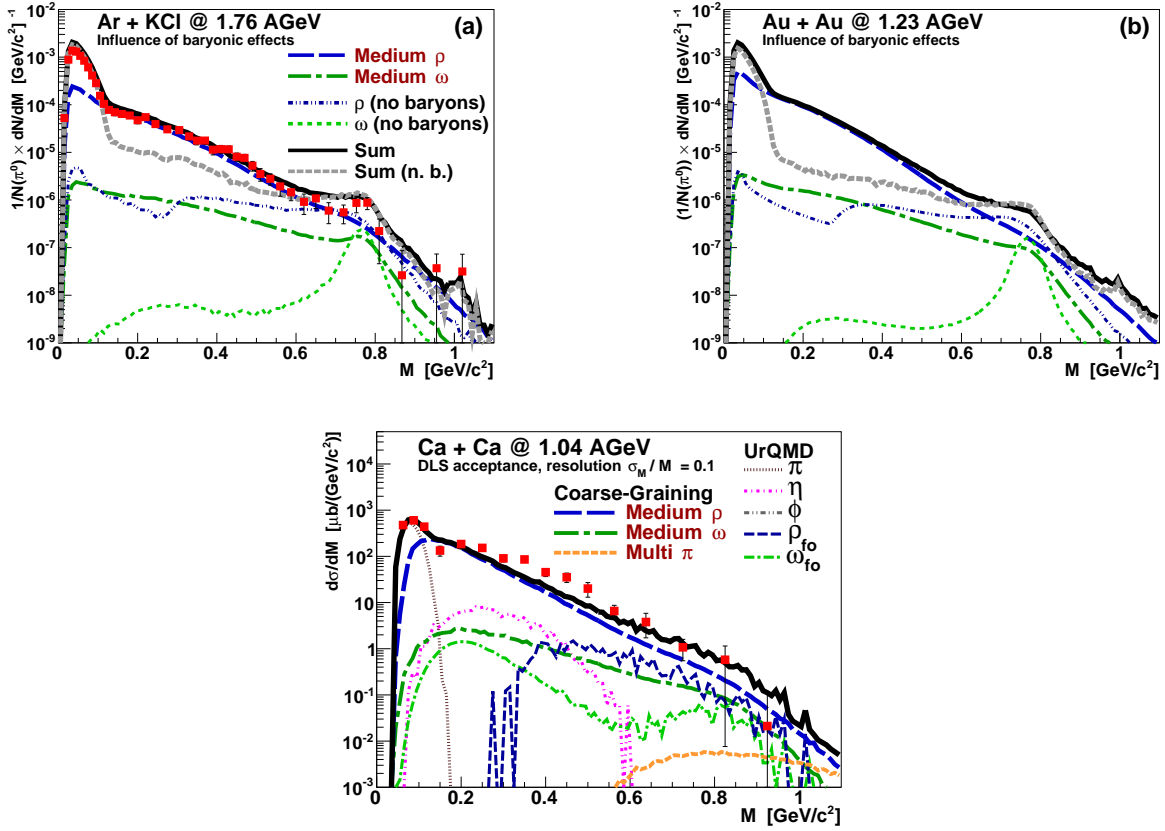


Figure 3.11: Upper panels: Comparison of invariant mass spectra with the full spectral function and for the case of no baryonic effects (i.e., for $\rho_{\text{eff}} = 0$). The dielectron yields for Ar+KCl collisions at $E_{\text{lab}} = 1.76$ AGeV (a) and for Au+Au at $E_{\text{lab}} = 1.23$ AGeV (b) are shown within HADES acceptance and normalized to the average number of produced π^0 . Note that the UrQMD contributions are included in the sum, but the different single yields are not shown explicitly for reasons of lucidity. Lower panel: Invariant-mass spectrum of the dielectron yield for Ca+Ca collisions at $E_{\text{lab}} = 1.04$ AGeV within the experimental acceptance. The result is compared to the data from the DLS Collaboration [P⁺ 97]. Figures taken from [10].

3.2.1 and 3.2.2 for the emission from a QGP and a hot and dense hadron gas in the deconfined and confined phases of the evolution of the medium using the models discussed in Sect. 3.2.3.

3.3.1 Dielectron production at GSI-SIS energies

In [10] the production of dielectrons in heavy-ion collisions at GSI-SIS energies as measured by the HADES collaboration has been simulated using the coarse-grained transport approach as described in Sect. 3.2.3. An ensemble of 1000 UrQMD events has been used to obtain sufficient statistics, particularly for the contributions from non-thermal ρ and ω mesons. The impact-parameter distribution has been adapted to the HADES trigger conditions for Ar+KCl reactions at a beam energy of 1.76 AGeV [A⁺11] and Au+Au collisions at 1.23 AGeV [Gal14a, Gal14b], using a Woods-Saxon-type fit, which in both cases approximately corresponds to a selection of the 0-40% most central collisions. For the Ar+KCl case, the number of neutral pions per event, used for the normalization of the spec-

3.3. Dilepton production in heavy-ion collisions

tra $N_{\pi_0}^{\text{sim}} \simeq 3.9$ agrees well with the experimental finding, $N_{\pi_0}^{\text{exp}} \simeq 3.5$. For the Au+Au collisions the simulation predicts $N_{\pi_0}^{\text{sim}} \simeq 8.0$. In the simulation the overall normalization of the dilepton yield uses the simulated π_0 yields. To compare the simulated spectra with the experimental result the HADES acceptance filter [HAD] as well as the appropriate momentum cuts have been employed. To also confront the model with the data from the DLS collaboration on Ca+Ca collisions at a beam energy of 1.04 AGeV the DLS acceptance filter (version 4.1) [DLS] is used as well as an RMS smearing of 10% to account for the detector resolution. In this case a minimum-bias simulation has been employed since for DLS no impact-parameter distributions are available. The final invariant-mass spectrum is normalized to the total cross section of a Ca+Ca reaction.

In Fig. 3.11 the results for dielectron production in Ar+KCl collisions are compared to the data from the HADES collaboration and predictions for Au+Au collisions within the HADES acceptance are made. The observed enhancement of dileptons over the “hadronic cocktail” is well explained by the medium modifications of the ρ and ω meson. To underline the importance of the baryonic medium the calculation has also been performed neglecting ρ - and ω -baryon interactions. In addition also contributions from the decays of ρ - and ω -mesons in “non-thermal cells” (i.e., for cells of the space-time grid, for which a temperature $T < 50$ MeV results from the coarse-graining procedure) are included. Here the microscopic transport-theoretical cross sections as implemented in UrQMD are used (for details, see [10]).

3.3.2 Dimuon production at top CERN-SPS energy

In [2, 3] and [9] the dimuon production in 158 AGeV In-In collisions as measured by the NA60 collaboration [A⁺06, A⁺08, D⁺07, A⁺09a, A⁺09b, Spe10] at the CERN SPS have been calculated. To describe the medium evolution both blast-wave parameterizations and the coarse-grained transport approach have been applied.

As shown in Fig. 3.12 both descriptions of the fireball evolution lead to an excellent description of the data. It is important to note that here the hadronic cocktail has been subtracted from the data by the NA60 collaboration, i.e., a fully acceptance corrected *excess* spectrum is shown. Also the contribution from decays of correlated D and \bar{D} mesons and, for invariant masses $M_{\mu^+\mu^-} > 1.2$ GeV, Drell-Yan processes is subtracted. In the low-mass region $2m_\mu < M_{\mu^+\mu^-} \lesssim 1$ GeV the dominant contribution to the excess yield is from the decay of the tremendously broadened ρ mesons from the “thermal” medium, while at higher masses the contribution from the QGP is the leading contribution. Again the importance of the medium modifications becomes evident by comparing the full result to the case, where the baryon contributions to the ρ -meson self-energy are neglected. Particularly the enhancement in the very-low-mass region towards the two-muon threshold is mostly due to the interactions of the ρ meson with baryons (and anti-baryons), i.e., due to Dalitz decays of baryon resonances, which are included in the thermal quantum-field theoretical evaluation of the in-medium ρ -self-energy. As shown in [9] the model also successfully describes the q_t dependence as well as the mass spectra in various q_t bins. It should also be noted that in the invariant-mass region $m_\phi \lesssim M_{\mu^+\mu^-} \lesssim M_{J/\psi}$ after the above mentioned subtraction of contributions from decays of correlated D- \bar{D} pairs and the Drell-Yan process, a basically purely thermal contribution from the resonance-free region of the dilepton emission allows a direct determination of the space-time weighted average of the temperature. In this intermediate-mass region ($T \ll M_{\mu^+\mu^-}$) the emission from the earlier hot stages of the fireball evolution dominates, as is also reflected in the model calculation which identifies the thermal emission from the QGP as the main source. Indeed, a fit of the experimental data leads to a temperature $T = 205 \pm 12$ MeV [Spe10], in accordance with the model.

3. Electromagnetic probes in NN and AA collisions

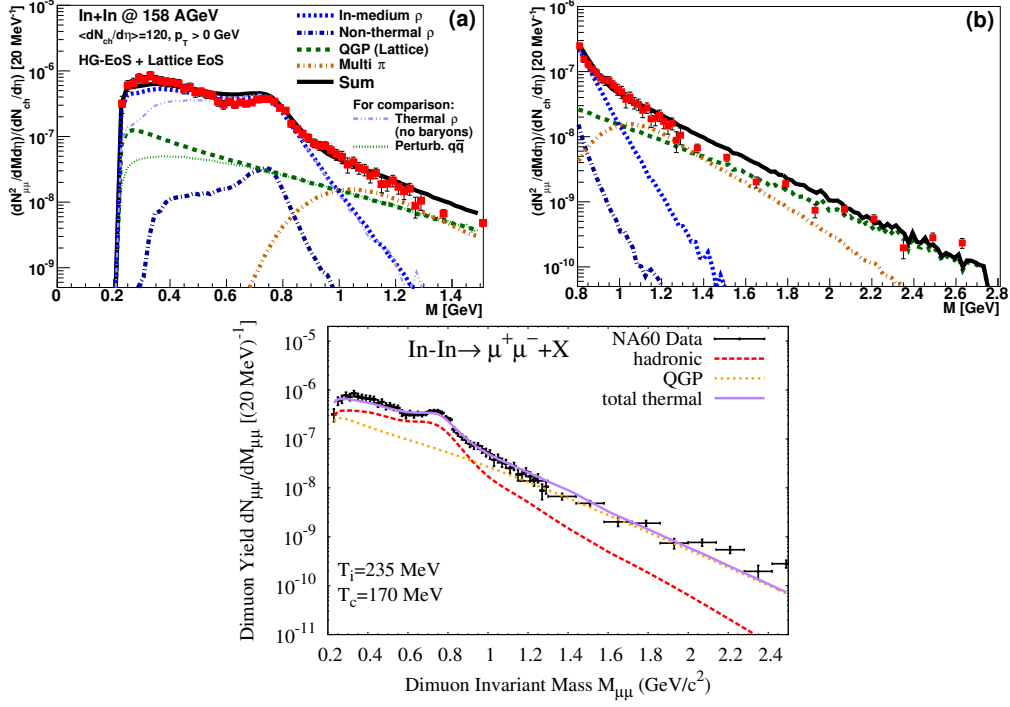


Figure 3.12: *Upper panels: Invariant mass spectra of the dimuon excess yield in In+In collisions at a beam energy of 158 AGeV, for the low-mass region up to 1.5 GeV (a) and the intermediate-mass regime up to 2.8 GeV (b) using the coarse-grained transport description of the medium. We show the contributions of the in-medium ρ emission (blue short dashed), the contribution from the Quark-Gluon Plasma, i.e., $q\bar{q}$ -annihilation, according to lattice rates [DFK⁺ 11, Rap13b] (green dashed) and the emission from multi-pion reactions (orange dash-dotted). Additionally a non-thermal transport contribution for the ρ is included in the yield (dark blue dash-dotted). Only left plot: For comparison the thermal ρ without any baryonic effects, i.e. for $\rho_{\text{eff}} = 0$, is shown (violet dash-double-dotted) together with the yield from pure perturbative $q\bar{q}$ -annihilation rates (green dotted). The results are compared to the experimental data from the NA60 Collaboration [A⁺09a, Spe10, A⁺09b]. Figures taken from [9]. Lower panel: The same model for the dimuon-production rates, using the blast-wave-fireball parameterization for the medium evolution. Figures taken from [8]).*

3.3.3 Dileptons at FAIR and RHIC-BES energies

With the motivation to find possible signatures of the various phase transitions in the phase diagram of strongly interacting matter a beam-energy scan (BES) program is ongoing at RHIC and is also planned by the Compressed Baryonic Matter (CBM) experiment at the upcoming Facility for Antiproton and Ion Research (FAIR). In [12] we have thus evaluated the invariant-mass spectra for the four beam energies, $E_{\text{lab}} = 2, 8, 15$ and 35 AGeV within the coarse-grained transport approach.

Since particularly at the lower beam energies the pion-chemical potential becomes quite large in the coarse-graining approach, we study its influence on the dilepton yield by using lower and upper boundaries with the following arguments: The lower bound is simply given by assuming $\mu_{\pi} = 0$. For the upper bound it should be noted that μ_{π} is an effective description for the off-chemical equilibrium nature of the medium, and thus in the here used Boltzmann approximation, its influence on the dilepton-

3.3. Dilepton production in heavy-ion collisions

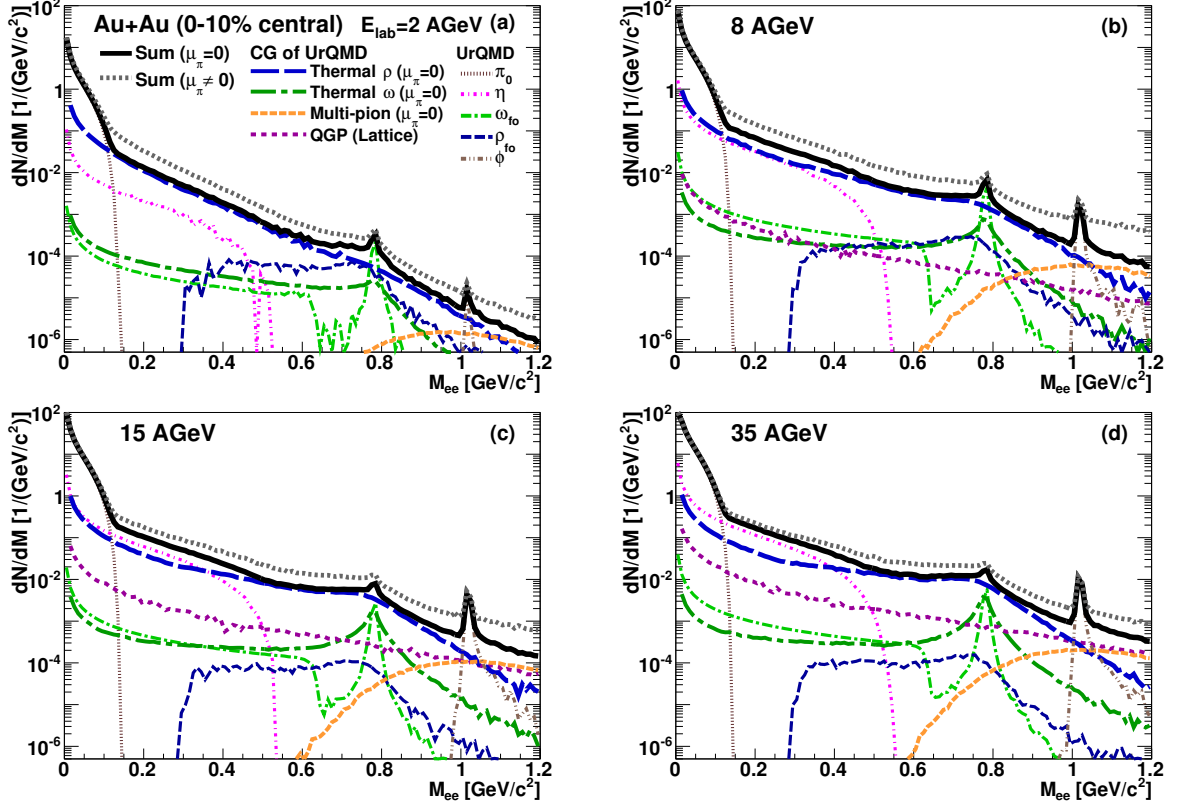


Figure 3.13: Dilepton invariant mass spectra for Au+Au reactions at different energies $E_{lab} = 2-35$ AGeV within the centrality class of 0-10% most central collisions. The resulting spectra include thermal contributions from the coarse-graining of the microscopic simulations (CG of UrQMD) and the non-thermal contributions directly extracted from the transport calculations (UrQMD). The hadronic thermal contributions are only shown for vanishing pion chemical potential, while the total yield is plotted for both cases, $\mu_\pi = 0$ and $\mu_\pi \neq 0$. Figure taken from [12]

production rate is given by a fugacity factor

$$z_\pi^n = \exp\left(\frac{n\mu_\pi}{T}\right), \quad (3.3.1)$$

where n is the difference in the number of pions in the initial and final state of the corresponding reaction process. For processes involving the ρ meson, particularly dilepton production in the here employed VMD model, not only two-pion production $\pi\pi \rightarrow \rho$ is relevant but, particularly at lower beam energies, baryonic channels like $\pi N \rightarrow N^*/\Delta \rightarrow \rho$ become important, for which $n < 2$. Thus, to estimate an upper limit of the influence of the pion chemical potential on the dilepton yield, we use $n = 2$ in our calculations.

As can be seen in Fig. 3.13, at all beam energies in the very-low-mass region, $M_{e^+e^-} < 0.15$ GeV, the dilepton yield is dominated by the Dalitz decays of neutral pions, $\pi^0 \rightarrow \gamma e^+e^-$, while beyond that region up to the vacuum-pole mass of the ρ meson of 770 MeV the main contribution is radiation from thermal sources with medium-modified ρ - and ω -meson spectral functions. Although the absolute yield of the thermal component increases with E_{lab} , its relative weight compared to the non-thermal η -Dalitz component and thus the enhancement above the hadronic cocktail contribution decreases.

3. Electromagnetic probes in NN and AA collisions

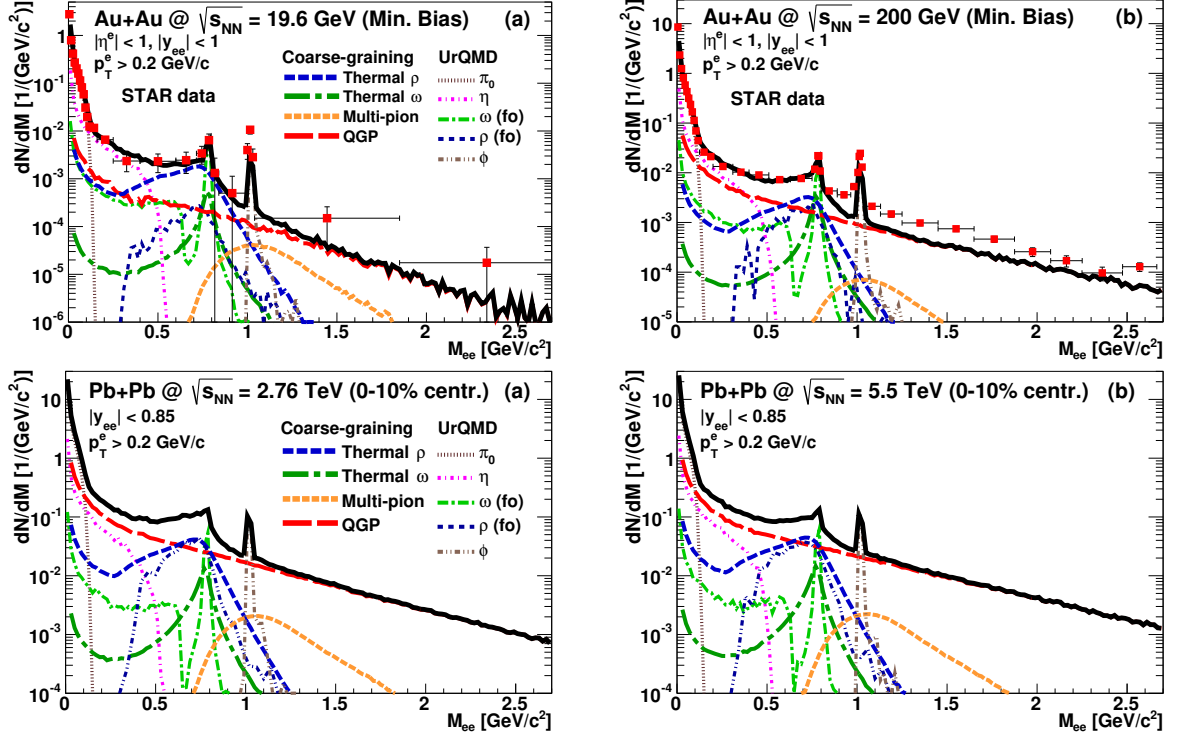


Figure 3.14: *Upper panel:* Dielectron invariant-mass spectra for minimum bias (i.e., 0-80% most central) Au+Au collisions at $\sqrt{s_{NN}} = 19.6$ GeV (a) and 200 GeV (b). The sum includes the thermal hadronic and partonic emission obtained with the coarse-graining procedure, and also the hadronic π -, η - and ϕ -decay contributions from UrQMD as well as the “freeze-out” contributions (from cold cells) of the ρ and ω mesons. The model results are compared to experimental data obtained by the STAR Collaboration [A⁺ 15]. *Lower panel:* Dielectron invariant-mass spectra for 0-10% most central Pb+Pb collisions at $\sqrt{s_{NN}} = 2.76$ TeV (a) and 5.5 TeV (b). The sum includes the thermal hadronic and partonic emission obtained with the coarse-graining approach, and also the hadronic π -, η , and ϕ decay contributions from UrQMD as well as the “freeze-out” contributions (from cold cells) of the ρ and ω mesons. Figures taken from [13]

Concerning the onset of deconfinement the calculations show that temperatures $T \simeq 170$ GeV are reached in the region of $E_{lab} = 6-8$ AGeV.

Note that here we use the same cross-over-transition EoS for the coarse-graining procedure as for the higher beam energies. A possible deviation of the dilepton spectra from these predictions might thus indicate a possible change in the nature of the confinement-deconfinement and/or chiral phase transition (see also Sect. 3.5).

3.3.4 Dileptons at RHIC and LHC energies

In [13] we have employed the coarse-grained transport approach to the evaluation of dilepton spectra at RHIC and LHC energies. In Fig. 3.14 the result is shown in comparison to experimental data on Au-Au collisions at the two beam energies $\sqrt{s_{NN}} = 19.6$ GeV and 200 GeV [A⁺ 15]. The calculation takes into account the single-electron rapidity, the dielectron pseudorapidity, and transverse-momentum electron

3.4. Photon production in heavy-ion collisions

cuts ($\eta_e < 1$, $\gamma_e < 1$, $p_t^e > 0.2$ GeV) to account for the STAR acceptance. For the low-mass region, $M_{e^+e^-} < 1$ GeV the data are well described within the model. In the region 0.3 GeV $< M_{e^+e^-} < 0.7$ GeV an excess above the hadronic cocktail has been observed, and within our model at the lower beam energy this region is dominated by thermal contributions from medium-modified ρ mesons, while at top RHIC energy the emission from the QGP prevails. In both cases the spectral function of the in-medium ρ meson shows more similarities with its vacuum shape than at the lower beam energies discussed in the previous sections. This is understandable by the fact that here the baryon-chemical potential μ_B is smaller than at lower beam energies, and a great part of the broadening in the peak region as well as the low-mass tail is mainly due to the baryon interactions of the ρ meson, as already emphasized before. At intermediate masses $M_{e^+e^-} > 1$ GeV our calculation underestimates the measured yield, which can be explained by the fact that here the contributions from Drell-Yan processes as well as decays of correlated $D\bar{D}$ mesons have been neglected. For further details on the comparison of the model on the data, see [13].

Also in Fig. 3.14 we present our predictions for Pb-Pb collisions at center-mass energies, available at the LHC, $\sqrt{s_{NN}} = 2.76$ TeV and 5.5 TeV. As to be expected also here the thermal ρ contribution in the low-mass region shows the vacuum-like peak structure as already seen at the lower RHIC energies; again this is due to the even smaller baryochemical potential at the higher beam energies. Compared to RHIC energies the fireball at LHC energies starts with considerable higher temperatures, leading to larger lifetimes for both the partonic and hadronic phase of the fireball evolution, resulting in larger contributions from both the QGP and the thermal vector mesons in the low-mass region.

3.4 Photon production in heavy-ion collisions

In [5, 7] the photon rates as described in Sect. 3.2 have been used with the elliptic thermal-fireball parametrization of the bulk evolution (Sect. 3.2.3) to evaluate the transverse-momentum spectra and elliptic flow, v_2 , of direct photons as measured at RHIC and LHC. In [5] first we have shown that the measured photon- q_t spectra favor a pretty large radial flow (Fig. 3.15).

To address the elliptic flow measured by the PHENIX collaboration in $\sqrt{s_{NN}} = 200$ GeV Au-Au collisions at RHIC [A⁺12a], the full elliptic fireball model (cf. Sect. 3.2.3) has been applied. Given the expectation that the photon emission is dominated by the early hot stages of the fireball evolution the surprisingly large elliptic flow of the direct photons indicate an early buildup of the elliptic flow of the bulk medium, which is compatible with the assumption that multi-strange hadrons freeze out around the deconfinement-confinement transition of the fireball. As can be seen in Fig. 3.15, however, the yield is dominated by emission from hadronic sources, as compared to radiation from the QGP phase of the fireball evolution. Nevertheless the model cannot fully account for the observed large elliptic flow, reaching just the lower end of the experimental error band (dominated by systematic uncertainties).

We also evaluated the effective-slope parameter, T_{eff} , of the calculated photon spectra to compare to the measured value of $T_{\text{eff}} = 221 \pm 19^{\text{stat}} \pm 19^{\text{sys}}$ MeV. While the temperature of the fireball only reaches values of that order, the effective slope of the photons is affected by the Doppler blueshift due to the radial flow of the emitting source, which can be estimated by the usual Doppler-shift formula for a massless particle,

$$T_{\text{eff}} \simeq T \sqrt{\frac{1 + \langle \beta \rangle}{1 - \langle \beta \rangle}}. \quad (3.4.1)$$

This shifts the overlap of the slope parameters as extracted from the calculation and the range indicated by experiment into the region of radiation from hadronic sources with fireball temperatures around

3. Electromagnetic probes in NN and AA collisions

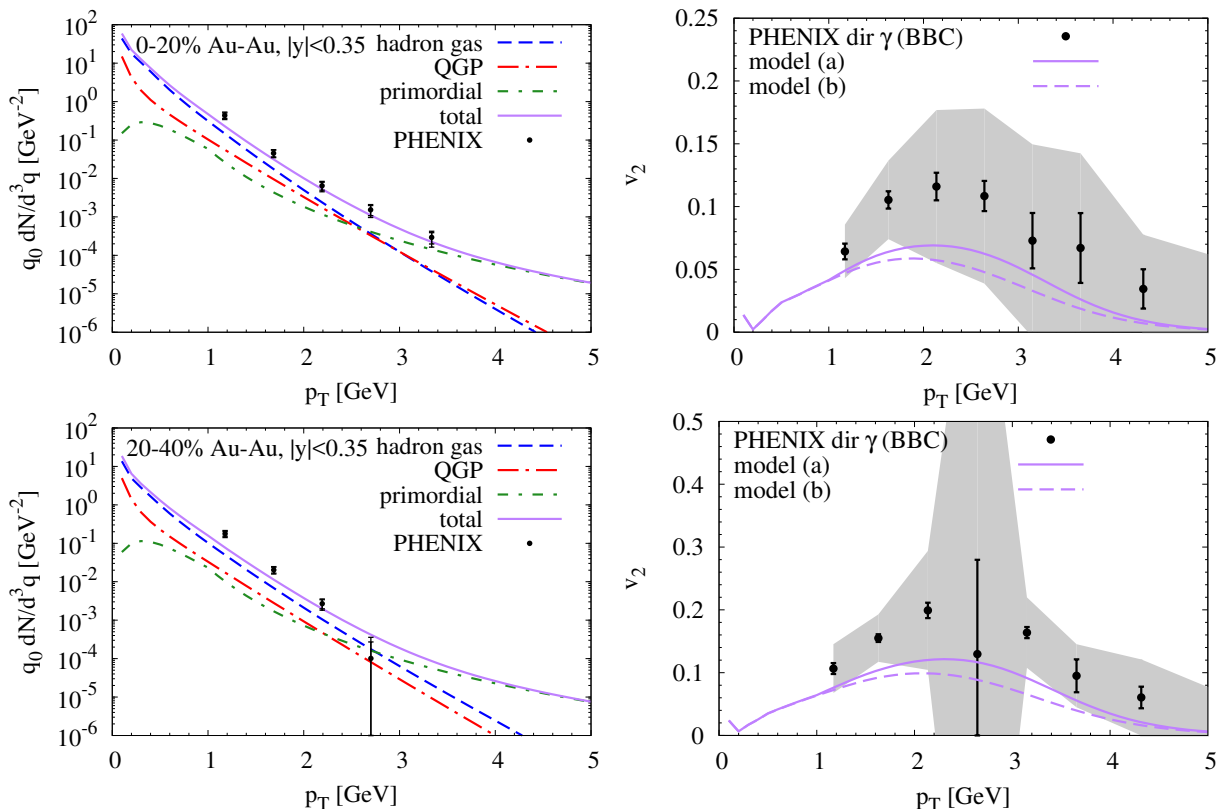


Figure 3.15: Comparison of our calculated direct-photon spectra (left panels) and their elliptic-flow coefficient (right panels) from an elliptically expanding fireball model with QGP and hadronic radiation, supplemented with primordial emission, to PHENIX data [$A^+ 10a$, $A^+ 12a$] in 0-20% (upper panels) and 20-40% (lower panels) central Au-Au ($\sqrt{s} = 200$ AGeV) collisions. The error bars indicate the statistical and the gray band the systematical errors. Models (a) and (b) in the right panels refer to the use of the p QCD parameterization and the PHENIX fit for primordial production, respectively (in the left panels, only model (a) is displayed). Figure taken from [5].

$T \simeq 100$ -150 MeV.

While in [5] a 1st-order EoS has been used, it has been updated to a cross-over transition in [7] as described in Sect. 3.2.3. Since in the present model the partonic and hadronic emission rates for temperatures around $T_c \simeq 160$ MeV are very similar (as also found for the dilepton-production rates, cf. Fig. 3.4), the photon spectra and v_2 do not change significantly. In addition to the comparison with the RHIC data the model has also been confronted with measurements by the ALICE collaboration on Pb-Pb collisions at $\sqrt{s_{NN}} = 2.76$ TeV at the LHC [Wil13, Loh13]. Also in this case the model underestimates both the yield and the v_2 of direct photons, as compared to the measurements (Fig. 3.16).

We also have compared the thermal-fireball model for the bulk evolution with a full ideal-hydrodynamics simulation with initial conditions tuned such as to lead to a similar early buildup of flow as the fireball model (particularly by assuming initial flow), which turn out to be quite consistent (see Fig. 3.17).

We have also discussed possible explanations for mechanisms that may lead to a better description of

3.5. Outlook: dileptons and the QCD phase diagram

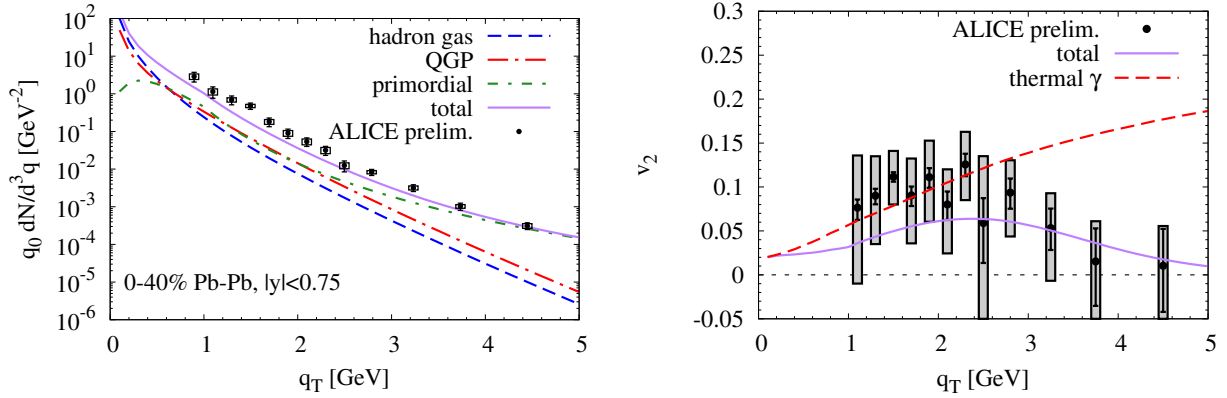


Figure 3.16: Direct photon spectra (left panel) and elliptic flow (right panel) from the expanding fireball in 0-40% Pb+Pb ($\sqrt{s} = 2.76$ ATeV) collisions using latPHG EoS, compared to preliminary ALICE data [Wil13, Loh13]. In the left panel, red, blue, green and purple lines represent QGP, hadronic and primordial contributions, as well as the total, respectively. In the right panel we show the combined thermal v_2 (red dashed line) and the total v_2 (purple solid line). Figure taken from [7].

the measured direct-photon data. To increase the yield from thermal radiation, one could use lower QGP-formation times, τ_0 , i.e., start with the thermal evolution earlier. However, although this of course leads to an increase in the photon yield above $q_t > 1$ GeV with a harder slope, the elliptic flow decreases, which is not favored by the data. In [SHPG14, Rap13a] it has been conjectured that in the pseudo-critical region of the fireball the photon rates may be enhanced over the here used AMY rates, which are based on pQCD parton-scattering rates, which tend to underestimate the interaction strength from the point of view of phenomenology as well as evaluations of η/s in lattice QCD, or the heavy-quark diffusion coefficient [ST09, RH09]. Around hadronization one expects confinement to play an important role, as, e.g., seen in lQCD calculations of the heavy-quark free energy [KZ05]. A stronger coupling in partonic scattering should also lead to a larger photon-emission rate [GSZ13]. Finally, also on the hadronic side, important mechanisms might be missing from the present model. In [7] we have shown that by enhancing the so far used model rates by a factor of 2 and then further amplified up to a factor of 3 at $T_c = 170$ MeV, linearly ramped up and down between temperatures $T = 140$ MeV and 200 MeV, one can indeed come closer to the experimental data.

3.5 Outlook: dileptons and the QCD phase diagram

One of the most challenging aims of contemporary heavy-ion-collision research is the identification of observables indicating changes in the nature of the confinement-deconfinement or the chiral phase transitions, e.g., the cross-over transition at low baryochemical potential to a first-order transition at higher net-baryon densities with a critical point at the end of the corresponding phase-transition line in the QCD phase diagram. This is the motivation for a concise “beam-energy scan”, already ongoing and RHIC and in the future at FAIR and NICA.

Since electromagnetic probes are emitted during all stages of the fireball evolution, leaving the hot and dense medium nearly unaffected by final-state interactions, they provide information not only about the in-medium properties of the electromagnetic current-current correlation function but also about the space-time evolution of the medium. Together with future high-precision measurements of dilepton production in heavy-ion collisions at various beam energies and for different system sizes, theoretical

3. Electromagnetic probes in NN and AA collisions

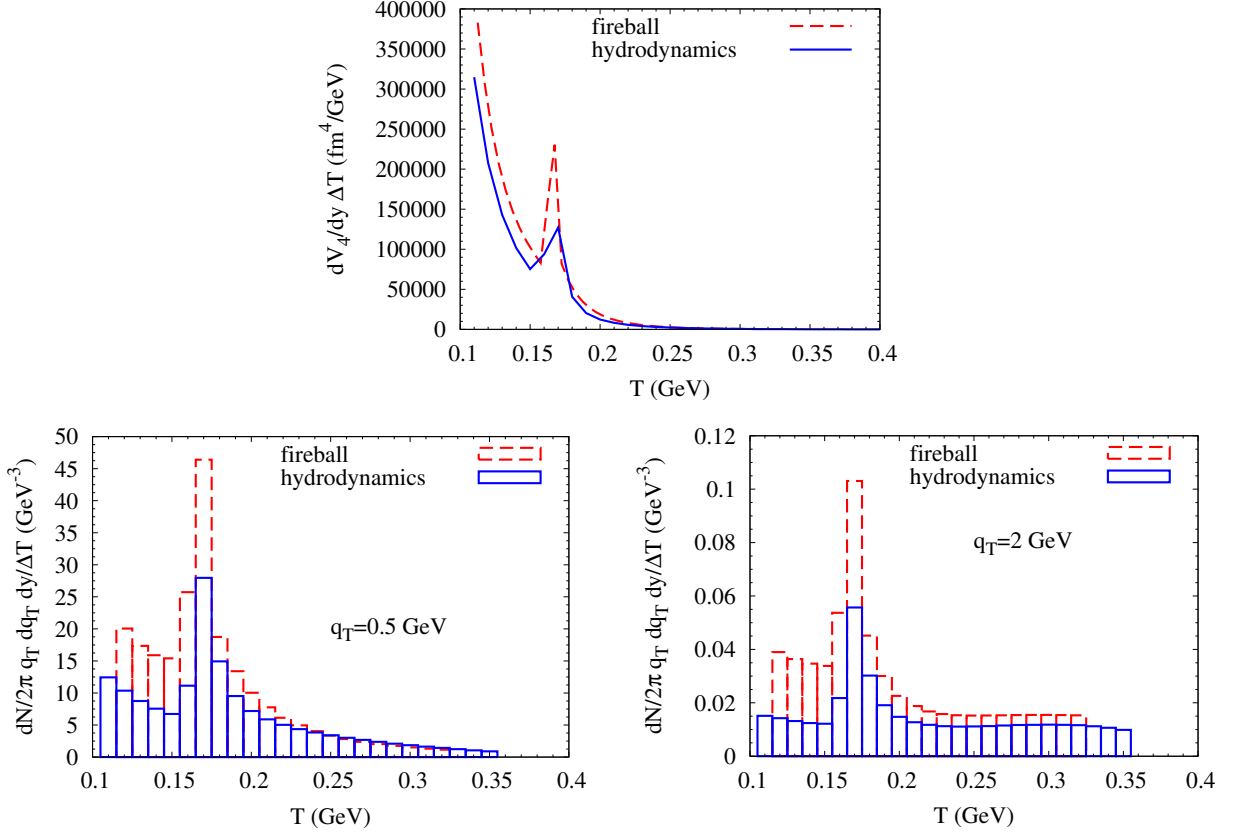


Figure 3.17: *Upper panel: Temperature evolution of the differential emission four-volume. Lower panel: double-differential photon emission rate (QGP for $T > T_{\text{pc}}$ and hadronic for $T < T_{\text{pc}}$) for two transverse momenta ($q_T = 0.5$ GeV and $q_T = 2$ GeV), in the expanding fireball (dashed lines) and hydrodynamic evolution (solid lines). Figure taken from [7].*

studies may also shed light on the phase structure of strongly interacting matter. E.g., the slope of the invariant-mass spectrum in the mass region $m_\phi < M_{\ell+\ell-} < m_{J/\psi}$ leads to a space-time weighted average of the invariant temperature of the medium (i.e., without blue shifts from radial flow as for slopes of q_t spectra, cf. the discussion in [3]), provided the hadronic cocktail, the contribution from decays of correlated $D\bar{D}$ decay, and Drell-Yan pairs can be subtracted from the experimental data with sufficient precision.

In [8] we have explored the possibilities for such studies within the above discussed theoretical model for dilepton production using the thermal-fireball parameterization of the medium, assuming the cross-over EoS (combining a hadron-resonance gas with a lQCD EoS as discussed in Sect. 3.2.3) for beam energies corresponding to center-mass energies in the range $\sqrt{s_{NN}} = 6.3$ GeV-200 GeV. We have determined the average temperature from the slopes of the invariant-mass spectrum of dileptons by fitting the dilepton spectrum in the range $M_{\ell+\ell-} = 1.5$ -2.5 GeV to

$$\frac{dR_{\ell+\ell-}}{dM_{\ell+\ell-}} \propto (MT)^{3/2} \exp\left(-\frac{M_{\ell+\ell-}}{T}\right). \quad (3.5.1)$$

Since in this mass range $M_{\ell+\ell-} \ll T$ the average is weighted towards the hot and early phases of the fireball evolution. As can be seen in the left panel of Fig. 3.18 the resulting ‘‘slope temperatures’’ are

3.5. Outlook: dileptons and the QCD phase diagram

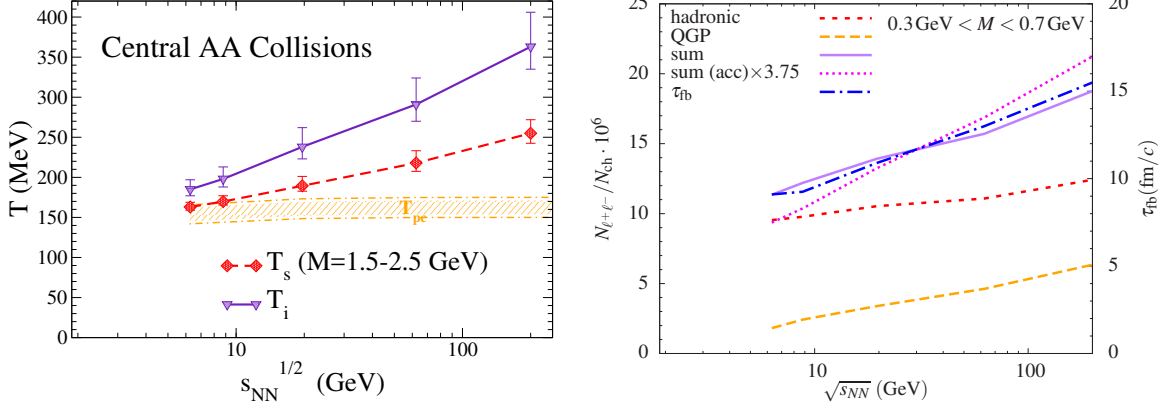


Figure 3.18: *Left panel:* Excitation function of the inverse-slope parameter, T_s , from intermediate-mass dilepton spectra ($M = 1.5$ - 2.5 GeV, diamonds connected with a dashed line) and initial temperature T_i (triangles connected with a solid line) in central heavy-ion collisions ($A \simeq 200$). The error bars on T_s and T_i correspond to a variation in the initial longitudinal fireball size, z_0 , by $\pm 30\%$ around the central values. The hatched area schematically indicates the pseudo-critical temperature regime at vanishing (and small) baryochemical potential as extracted from various quantities computed in l QCD [BFH⁺ 10]. *Right panel:* Excitation function of low-mass thermal dilepton radiation (“excess spectra”) in 0-10% central AA collisions ($A \simeq 200$), integrated over the mass range $M = 0.3$ GeV- 0.7 GeV, for QGP (dashed line) and in-medium hadronic (short-dashed line) emission and their sum (solid line). The underlying fireball lifetime (dot-dashed line) is given by the right vertical scale. Figures taken from [8]

smoothly increasing with beam energy and ranging from $T_s \simeq 160$ MeV at $\sqrt{s_{NN}} = 6$ GeV to 260 MeV at $\sqrt{s_{NN}} = 200$ GeV. The values at the higher beam energies are clearly above the pseudo-critical temperature of $T_c \simeq 160$ MeV but considerably lower than the initial fireball temperatures. This difference becomes smaller at the lower beam energies which is due to the (pseudo-)latent heat in the transition. This indicates that the beam-energy range around 10 GeV is promising to map out the phase-transition region, maybe indicating the onset of a first-order transition by developing a plateau of the slope curve, resembling a “caloric curve”.

Further, for a given model for the dilepton-production rates, together with the determination of the fireball parameters from the hadronic observables (cf. Sect. 3.2.3) the total yield of dileptons is a quite precise measure for the fireball lifetime. This is shown in Fig. 3.18: The yield is determined by integrating the invariant-mass spectra over the range $M_{\ell+\ell^-} = 0.3$ - 0.7 GeV, which is just below the ρ - and ω vacuum mass, so that it consists of contributions from both partonic and hadronic sources and is quite representative for the dilepton enhancement due to medium effects, dominated by interactions of the vector mesons with baryons. As can be seen, the yield follows closely the proper lifetime τ_{fb} of the fireball. It is important to note that this correlation is disturbed by either changing the invariant-mass range or by using yields within the typical single-electron cuts describing the detector acceptance (e.g., $p_t > 0.2$ GeV, $\gamma < 0.9$ for the STAR detector). Thus for such studies the availability of fully acceptance-corrected dilepton excess spectra is mandatory.

In [10] we have made similar studies concerning the system-size dependence of the bulk-medium dynamics at GSI-SIS energy, $E_{lab} = 1.76$ AGeV, within the coarse-grained transport approach (cf. Sect. 3.3.1). At these low energies one expects that the lifetime of the medium is defined by the time the colliding nuclei overlap, forming a highly excited hadronic medium dominated by baryons. This can be confirmed by investigating the bulk properties and associated with dilepton observables within the

3. Electromagnetic probes in NN and AA collisions

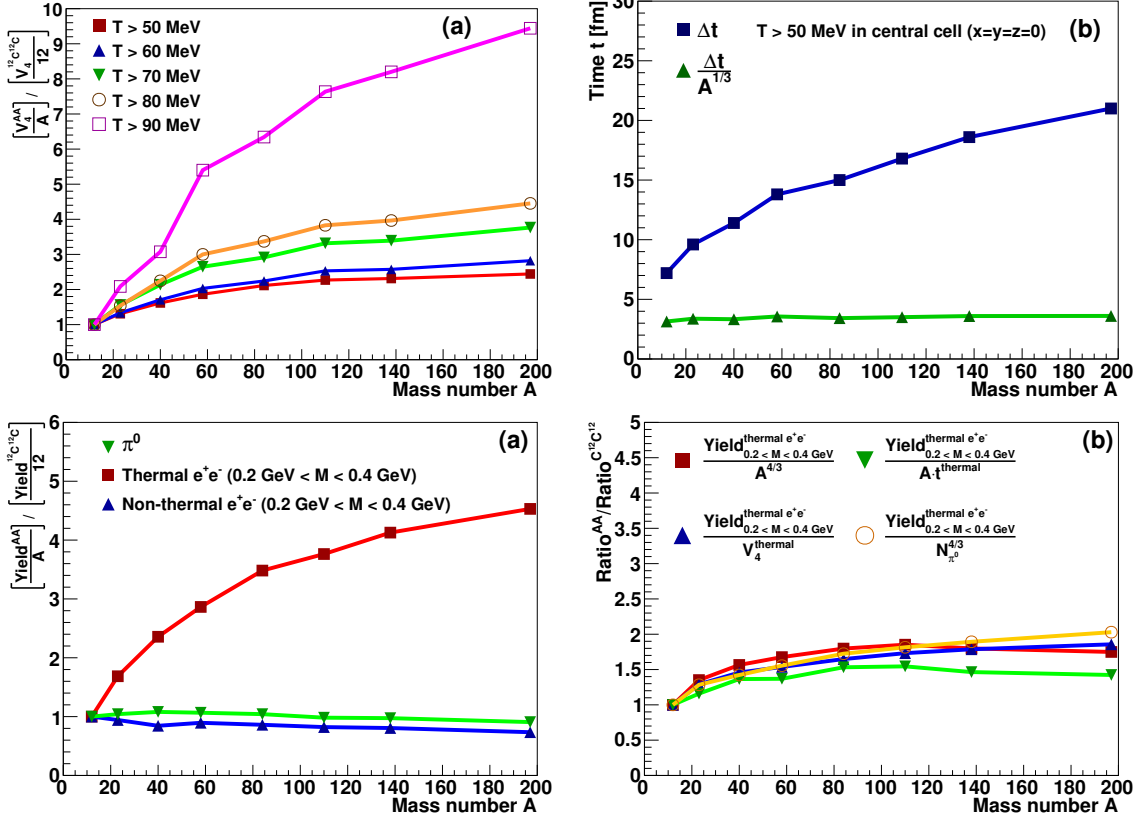


Figure 3.19: *Upper panels:* (a) Ratio of the thermal four-volume V_4 for different temperatures to the mass number A of the colliding nuclei. (b) Time duration over which the central cell of the coarse-graining grid (for $x = y = z = 0$) emits thermal dileptons. **Lower panels:** (a) Ratio of the thermal (red squares) and non-thermal dilepton yield (blue triangles) in the invariant-mass range from 0.2 to 0.4 GeV/ c^2 to the mass number A of the colliding nuclei, and the number of π^0 (green triangles). The results are normalized to the ratio obtained with $^{12}\text{C} + ^{12}\text{C}$ collisions. (b) Ratio of the thermal dilepton yield in the invariant mass range from 0.2 to 0.4 GeV/ c^2 scaled by various quantities. All four plots show the results for central collisions and a collision energy $E_{\text{lab}} = 1.76 A \text{ GeV}$. Figures taken from [10]

coarse-grained transport approach. In the upper panels of Fig. 3.19 the “thermal four-volume” is plotted, i.e., the sum of all spacetime cells $\Delta V \Delta t$ for which the temperature, obtained from the coarse-graining procedure (as described in Sect. 3.2.3), is above various given values as indicated in plot (a). Since the total volume of each of the nuclei is $V_{\text{nucl}} \propto A$ and the lifetime of the thermal medium is expected to be determined by the time the nuclei overlap during the collision one concludes that $\Delta t \propto r_{\text{Nucl}} \propto A^{1/3}$, and this is indeed confirmed in plot (b) by the fact that $\Delta t / A^{1/3} \simeq \text{const}$.

Also in Fig. 3.2.3 the system-size dependence of the e^+e^- yields (in the mass window $M_{e^+e^-} = 0.2 \text{ GeV} - 0.4 \text{ GeV}$) for emission from the medium (“thermal dileptons”) and from ρ decays after thermal freeze-out (“non-thermal dileptons”) as well as of neutral pions is shown. Since the “thermal dileptons” are emitted during the entire fireball evolution, one expects a scaling with the four-volume. On the other hand, the “non-thermal dilepton” as well as the pion yield is determined by the situation at thermal freezeout and thus scales with the three-volume of the corresponding cells (“freeze-out hypersurface”) with coarse-graining temperatures below 50 MeV. This is approximately confirmed by plot (b): Scaling the yield with $A^{4/3}$, $A \cdot t^{\text{thermal}}$, V_4^{thermal} , or $N_{\pi_0}^{4/3}$ leads to a roughly flat system-size dependence.

3.5. Outlook: dileptons and the QCD phase diagram

As we have demonstrated in all these studies, dilepton and photon production in heavy-ion collisions can be well described with partonic and effective hadronic models for the in-medium em. current-current correlation function. Thus, together with adequate descriptions of the bulk-medium evolution, these techniques provide a promising tool to understand probable signals of the details of the QCD phase diagram as soon as high-precision data on dileptons and photons in heavy-ion collisions at various beam energies become available in the future. Particularly, when deviations from the here provided results are observed, sensitivity for Equations of State with different phase-transition properties may be reached.

From the theoretical side, e.g., the exploitation of functional-renormalization-group methods that allow a consistent description of both the EoS and the in-medium spectral functions of the light vector mesons, can be a promising way for such further studies [TSW17, JRT⁺17].

3. Electromagnetic probes in NN and AA collisions

Summarized work

- [1] H. van Hees and J. Knoll, Finite pion width effects on the rho meson, Nucl. Phys. A **683**, 369 (2000), [http://dx.doi.org/10.1016/S0375-9474\(00\)00462-0](http://dx.doi.org/10.1016/S0375-9474(00)00462-0).
- [2] H. v. Hees and R. Rapp, Comprehensive interpretation of thermal dileptons at the SPS, Phys. Rev. Lett. **97**, 102301 (2006), <http://link.aps.org/abstract/PRL/V97/E102301>.
- [3] H. v. Hees and R. Rapp, Dilepton Radiation at the CERN Super Proton Synchrotron, Nucl. Phys. A **806**, 339 (2008), <http://dx.doi.org/10.1016/j.nuclphysa.2008.03.009>.
- [4] R. Rapp, J. Wambach, and H. van Hees, The Chiral Restoration Transition of QCD and Low Mass Dileptons, Landolt-Börnstein **23**, 134 (2010), http://dx.doi.org/10.1007/978-3-642-01539-7_6.
- [5] H. van Hees, C. Gale, and R. Rapp, Thermal Photons and Collective Flow at the Relativistic Heavy-Ion Collider, Phys. Rev. C **84**, 054906 (2011), <http://dx.doi.org/10.1103/PhysRevC.84.054906>.
- [6] J. Weil, H. van Hees, and U. Mosel, Dilepton production in proton-induced reactions at SIS energies with the GiBUU transport model, Eur. Phys. J. A **48**, 111 (2012), <http://dx.doi.org/10.1140/epja/i2012-12111-9>.
- [7] H. van Hees, M. He, and R. Rapp, Pseudo-Critical Enhancement of Thermal Photons in Relativistic Heavy-Ion Collisions, Nucl. Phys. A **933**, 256 (2015), <http://dx.doi.org/10.1016/j.nuclphysa.2014.09.009>.
- [8] R. Rapp and H. van Hees, Thermal Dileptons as Fireball Thermometer and Chronometer, Phys. Lett. B **753**, 586 (2016), <http://dx.doi.org/10.1016/j.physletb.2015.12.065>.
- [9] S. Endres, H. van Hees, J. Weil, and M. Bleicher, Coarse-graining approach for dilepton production at energies available at the CERN Super Proton Synchrotron, Phys. Rev. C **91**, 054911 (2015), <http://dx.doi.org/10.1103/PhysRevC.91.054911>.
- [10] S. Endres, H. van Hees, J. Weil, and M. Bleicher, Dilepton production and reaction dynamics in heavy-ion collisions at SIS energies from coarse-grained transport simulations, Phys. Rev. C **92**, 014911 (2015), <http://dx.doi.org/10.1103/PhysRevC.92.014911>.
- [11] G. Ramalho, M. T. Peña, J. Weil, H. van Hees, and U. Mosel, Role of the pion electromagnetic form factor in the $\Delta(1232) \rightarrow \gamma^* N$ timelike transition, Phys. Rev. D **93**, 033004 (2016), <http://dx.doi.org/10.1103/PhysRevD.93.033004>.

Summarized work

- [12] S. Endres, H. van Hees, and M. Bleicher, Photon and dilepton production at the Facility for Proton and Anti-Proton Research and beam-energy scan at the Relativistic Heavy-Ion Collider using coarse-grained microscopic transport simulations, *Phys. Rev. C* **93**, 054901 (2016), <http://dx.doi.org/10.1103/PhysRevC.93.054901>.
- [13] S. Endres, H. van Hees, and M. Bleicher, Energy, centrality and momentum dependence of dielectron production at collider energies in a coarse-grained transport approach, *Phys. Rev. C* **94**, 024912 (2016), <http://dx.doi.org/10.1103/PhysRevC.94.024912>.

Bibliography

- [A⁺72] T. A. Armstrong et al., Total hadronic cross-section of gamma rays in hydrogen in the energy range 0.265 GeV to 4.215 GeV, *Phys. Rev. D* **5**, 1640 (1972),
<https://doi.org/10.1103/PhysRevD.5.1640>.
- [A⁺84] J. Ahrens et al., Measurement of the Total Cross-section for ²³⁵U and ²³⁸U Photofission in the Δ Resonance Region, *Phys. Lett. B* **146**, 303 (1984),
[https://doi.org/10.1016/0370-2693\(84\)91701-5](https://doi.org/10.1016/0370-2693(84)91701-5).
- [A⁺86] S. Amendolia et al. (NA7 Collaboration), A Measurement of the Space-Like Pion Electromagnetic Form-Factor, *Nucl. Phys. B* **277**, 168 (1986),
[https://doi.org/10.1016/0550-3213\(86\)90437-2](https://doi.org/10.1016/0550-3213(86)90437-2).
- [A⁺98] H. Appelshäuser et al. (NA49), Hadronic expansion dynamics in central Pb + Pb collisions at 158 GeV per nucleon, *Eur. Phys. J. C* **2**, 661 (1998),
<https://doi.org/10.1007/s100520050168>.
- [A⁺99] M. C. Abreu et al. (NA38/NA50), Dimuon enhancement in nucleus nucleus ultrarelativistic interactions, *Nucl. Phys. A* **661**, 538 (1999),
[https://doi.org/10.1016/S0375-9474\(99\)85084-2](https://doi.org/10.1016/S0375-9474(99)85084-2).
- [A⁺00] M. C. Abreu et al. (NA38 and NA50), Dimuon and charm production in nucleus nucleus collisions at the CERN-SPS, *Eur. Phys. J. C* **14**, 443 (2000),
<https://doi.org/10.1007/s100520000373>.
- [A⁺01] F. Antinori et al. (WA97), Centrality dependence of the expansion dynamics in Pb Pb collisions at 158A GeV/c, *J. Phys. G* **27**, 2325 (2001),
<https://doi.org/10.1088/0954-3899/27/11/311>.
- [A⁺03a] D. Adamova et al. (CERES), Beam energy and centrality dependence of two pion Bose-Einstein correlations at SPS energies, *Nucl. Phys. A* **714**, 124 (2003),
[https://doi.org/10.1016/S0375-9474\(02\)01369-6](https://doi.org/10.1016/S0375-9474(02)01369-6).
- [A⁺03b] S. S. Adler et al. (PHENIX), Elliptic flow of identified hadrons in Au + Au collisions at $\sqrt{s_{NN}} = 200$ GeV, *Phys. Rev. Lett.* **91**, 182301 (2003),
<https://doi.org/10.1103/PhysRevLett.91.182301>.
- [A⁺04a] J. Adams et al. (STAR), Identified particle distributions in pp and Au+Au collisions at $\sqrt{s_{NN}} = 200$ GeV, *Phys. Rev. Lett.* **92**, 112301 (2004),
<https://doi.org/10.1103/PhysRevLett.92.112301>.

Bibliography

- [A⁺04b] S. S. Adler et al., Identified charged particle spectra and yields in Au + Au collisions at $\sqrt{s_{NN}} = 200$ GeV, Phys. Rev. C **69**, 034909 (2004), <https://doi.org/10.1103/PhysRevC.69.034909>.
- [A⁺06] R. Arnaldi et al. (NA60 Collaboration), First measurement of the ρ spectral function in high-energy nuclear collisions, Phys. Rev. Lett. **96**, 162302 (2006), <https://doi.org/10.1103/PhysRevLett.96.162302>.
- [A⁺07a] B. I. Abelev et al. (STAR), Partonic flow and phi-meson production in Au + Au collisions at $\sqrt{s_{NN}} = 200$ GeV, Phys. Rev. Lett. **99**, 112301 (2007), <https://doi.org/10.1103/PhysRevLett.99.112301>.
- [A⁺07b] F. Antinori et al. (NA57), Expansion dynamics of Pb-Pb collisions at 40A GeV/c viewed by negatively charged hadrons, J. Phys. G **33**, 403 (2007), <https://doi.org/10.1088/0954-3899/34/3/001>.
- [A⁺08] R. Arnaldi et al. (NA60 Collaboration), Evidence for radial flow of thermal dileptons in high-energy nuclear collisions, Phys. Rev. Lett. **100**, 022302 (2008), <https://doi.org/10.1103/PhysRevLett.100.022302>.
- [A⁺09a] R. Arnaldi et al. (NA60 Collaboration), Evidence for the production of thermal-like muon pairs with masses above 1 GeV/c² in 158 A GeV Indium-Indium Collisions, Eur. Phys. J. C **59**, 607 (2009), <https://doi.org/10.1140/epjc/s10052-008-0857-2>.
- [A⁺09b] R. Arnaldi et al. (NA60 Collaboration), NA60 results on thermal dimuons, Eur. Phys. J. C **61**, 711 (2009), <https://doi.org/10.1140/epjc/s10052-009-0878-5>.
- [A⁺10a] A. Adare et al. (PHENIX Collaboration), Enhanced production of direct photons in Au+Au collisions at $\sqrt{s_{NN}} = 200$ GeV and implications for the initial temperature, Phys. Rev. Lett. **104**, 132301 (2010), <https://doi.org/10.1103/PhysRevLett.104.132301>.
- [A⁺10b] G. Agakishiev et al. (HADES), Origin of the low-mass electron pair excess in light nucleus-nucleus collisions, Phys. Lett. B **690**, 118 (2010), <https://doi.org/10.1016/j.physletb.2010.05.010>.
- [A⁺11] G. Agakishiev et al. (HADES), Hyperon production in Ar+KCl collisions at 1.76A GeV, Eur. Phys. J. A **47**, 21 (2011), <https://doi.org/10.1140/epja/i2011-11021-8>.
- [A⁺12a] A. Adare et al. (PHENIX Collaboration), Observation of direct-photon collective flow in $\sqrt{s_{NN}} = 200$ GeV Au+Au collisions, Phys. Rev. Lett. **109**, 122302 (2012), <https://doi.org/10.1103/PhysRevLett.109.122302>.
- [A⁺12b] G. Agakishiev et al. (HADES), Inclusive dielectron production in proton-proton collisions at 2.2 GeV beam energy, Phys. Rev. C **85**, 054005 (2012), <https://doi.org/10.1103/PhysRevC.85.054005>.
- [A⁺12c] G. Agakishiev et al. (HADES), Inclusive dielectron spectra in p+p collisions at 3.5 GeV, Eur. Phys. J. A **48**, 64 (2012), <https://doi.org/10.1140/epja/i2012-12064-y>.

- [A⁺15] L. Adamczyk et al. (STAR), Measurements of Dielectron Production in Au+Au Collisions at $\sqrt{s_{NN}} = 200\text{GeV}$ from the STAR Experiment, *Phys. Rev. C* **92**, 024912 (2015), <https://doi.org/10.1103/PhysRevC.92.024912>.
- [AB⁺91] M. Aguilar-Benitez et al., Inclusive particle production in 400 GeV/c p p interactions, *Z. Phys. C* **50**, 405 (1991), <https://doi.org/10.1007/BF01551452>.
- [AB⁺07] M. Abdel-Bary et al. (COSY-TOF), Comparison of isoscalar vector meson production cross-sections in proton-proton collisions, *Phys. Lett. B* **647**, 351 (2007), <https://doi.org/10.1016/j.physletb.2007.02.046>.
- [ABMSW12] A. Andronic, P. Braun-Munzinger, J. Stachel and M. Winn, Interacting hadron resonance gas meets lattice QCD, *Phys. Lett. B* **718**, 80 (2012), <https://doi.org/10.1016/j.physletb.2012.10.001>.
- [Adl69] S. L. Adler, Axial vector vertex in spinor electrodynamics, *Phys. Rev.* **177**, 2426 (1969), <https://doi.org/10.1103/PhysRev.177.2426>.
- [Ahr85] J. Ahrens, The Total Absorption of Photons by Nuclei, *Nucl. Phys. A* **446**, 229C (1985), [https://doi.org/10.1016/0375-9474\(85\)90591-3](https://doi.org/10.1016/0375-9474(85)90591-3).
- [ALSS11] J. O. Andersen, L. E. Leganger, M. Strickland and N. Su, Three-loop HTL QCD thermodynamics, *JHEP* **08**, 053 (2011), [https://doi.org/10.1007/JHEP08\(2011\)053](https://doi.org/10.1007/JHEP08(2011)053).
- [AMY01] P. B. Arnold, G. D. Moore and L. G. Yaffe, Photon emission from quark gluon plasma: Complete leading order results, *JHEP* **12**, 009 (2001), <https://doi.org/10.1088/1126-6708/2001/12/009>.
- [B⁺93] N. Bianchi et al., Measurement of the total cross-section for ^{238}U photofission in the nucleon resonance region, *Phys. Lett. B* **299**, 219 (1993), [https://doi.org/10.1016/0370-2693\(93\)90251-C](https://doi.org/10.1016/0370-2693(93)90251-C).
- [B⁺96] N. Bianchi et al., Total hadronic photoabsorption cross-section on nuclei in the nucleon resonance region, *Phys. Rev. C* **54**, 1688 (1996), <https://doi.org/10.1103/PhysRevC.54.1688>.
- [B⁺97] I. G. Bearden et al. (NA44), Collective expansion in high-energy heavy ion collisions, *Phys. Rev. Lett.* **78**, 2080 (1997), <https://doi.org/10.1103/PhysRevLett.78.2080>.
- [B⁺98] R. Barate et al. (ALEPH Collaboration), Measurement of the spectral functions of axial-vector hadronic τ decays and determination of $\alpha_s(M_\tau^2)$, *Eur. Phys. J. C* **4**, 409 (1998), <https://publish.edpsciences.org/abstract/EPJC/V4/P409>.
- [BBB⁺98] S. Bass, M. Belkacem, M. Bleicher et al., Microscopic models for ultrarelativistic heavy ion collisions, *Prog. Part. Nucl. Phys.* **41**, 255 (1998), [https://doi.org/10.1016/S0146-6410\(98\)00058-1](https://doi.org/10.1016/S0146-6410(98)00058-1).
- [BC97] E. L. Bratkovskaya and W. Cassing, Dilepton production from AGS to SPS energies within a relativistic transport approach, *Nucl. Phys. A* **619**, 413 (1997), [https://doi.org/10.1016/S0375-9474\(97\)00140-1](https://doi.org/10.1016/S0375-9474(97)00140-1).

Bibliography

- [BCE⁺85] L. Barkov, A. Chilingarov, S. Eidelman et al., Electromagnetic Pion Form-Factor in the Timelike Region, *Nucl. Phys. B* **256**, 365 (1985), [https://doi.org/10.1016/0550-3213\(85\)90399-2](https://doi.org/10.1016/0550-3213(85)90399-2).
- [BEF⁺11] S. Borsanyi, G. Endrodi, Z. Fodor et al., Transition temperature and the equation of state from lattice QCD, Wuppertal-Budapest results, *J. Phys. G* **38**, 124101 (2011), <https://doi.org/10.1088/0954-3899/38/12/124101>.
- [BFH⁺10] S. Borsanyi, Z. Fodor, C. Hoelbling et al. (Wuppertal-Budapest), Is there still any T_c mystery in lattice QCD? Results with physical masses in the continuum limit III, *JHEP* **09**, 073 (2010), [https://doi.org/10.1007/JHEP09\(2010\)073](https://doi.org/10.1007/JHEP09(2010)073).
- [BFH⁺14] S. Borsanyi, Z. Fodor, C. Hoelbling et al., Full result for the QCD equation of state with 2+1 flavors, *Phys. Lett. B* **730**, 99 (2014), <https://doi.org/10.1016/j.physletb.2014.01.007>.
- [BFMW13] B. B. Brandt, A. Francis, H. B. Meyer and H. Wittig, Thermal Correlators in the ρ channel of two-flavor QCD, *JHEP* **1303**, 100 (2013), [https://doi.org/10.1007/JHEP03\(2013\)100](https://doi.org/10.1007/JHEP03(2013)100).
- [BGG⁺12] O. Buss, T. Gaitanos, K. Gallmeister et al., Transport-theoretical Description of Nuclear Reactions, *Phys. Rept.* **512**, 1 (2012), <https://doi.org/10.1016/j.physrep.2011.12.001>.
- [BIR99] J. P. Blaizot, E. Iancu and A. Rebhan, Selfconsistent hard thermal loop thermodynamics for the quark gluon plasma, *Phys. Lett. B* **470**, 181 (1999), [https://doi.org/10.1016/S0370-2693\(99\)01306-4](https://doi.org/10.1016/S0370-2693(99)01306-4).
- [BIR01] J. P. Blaizot, E. Iancu and A. Rebhan, Approximately selfconsistent resummations for the thermodynamics of the quark gluon plasma. 1. Entropy and density, *Phys. Rev. D* **63**, 065003 (2001), <https://doi.org/10.1103/PhysRevD.63.065003>.
- [BJ69] J. S. Bell and R. Jackiw, A PCAC puzzle: $\pi^0 \rightarrow \gamma\gamma$ in the sigma model, *Nuovo Cim. A* **60**, 47 (1969), <https://doi.org/10.1007/BF02823296>.
- [BKU⁺85] M. Bando, T. Kugo, S. Uehara, K. Yamawaki and T. Yanagida, Is the ρ Meson a Dynamical Gauge Boson of Hidden Local Symmetry?, *Phys. Rev. Lett.* **54**, 1215 (1985), <https://doi.org/10.1103/PhysRevLett.54.1215>.
- [BKY88] M. Bando, T. Kugo and K. Yamawaki, Nonlinear Realization and Hidden Local Symmetries, *Phys. Rept.* **164**, 217 (1988), [https://doi.org/10.1016/0370-1573\(88\)90019-1](https://doi.org/10.1016/0370-1573(88)90019-1).
- [BL86] D. Bailin and A. Love, *Introduction to Gauge Field Theory*, Adam Hilger, Bristol and Boston (1986).
- [BPY90] E. Braaten, R. D. Pisarski and T.-C. Yuan, Production of soft dileptons in the quark-gluon plasma, *Phys. Rev. Lett.* **64**, 2242 (1990), <https://link.aps.org/abstract/PRL/v64/p2242>.
- [BZS⁺99] M. Bleicher, E. Zabrodin, C. Spieles et al., Relativistic hadron hadron collisions in the ultrarelativistic quantum molecular dynamics model, *J. Phys. G* **25**, 1859 (1999), <https://doi.org/10.1088/0954-3899/25/9/308>.

- [C⁺98] H. Calen et al., Measurement of the quasifree $p + n \rightarrow p + n + \eta$ reaction near threshold, *Phys. Rev. C* **58**, 2667 (1998), <https://doi.org/10.1103/PhysRevC.58.2667>.
- [CFR87] J. Cleymans, J. Fingberg and K. Redlich, Transverse Momentum Distribution of Dileptons in Different Scenarios for the QCD Phase Transition, *Phys. Rev. D* **35**, 2153 (1987), <https://doi.org/10.1103/PhysRevD.35.2153>.
- [Col86] J. C. Collins, *Renormalization*, Cambridge University Press, Cambridge, New York, Melbourne (1986).
- [CPTW04] G. L. Caia, V. Pascalutsa, J. A. Tjon and L. E. Wright, $\gamma^*N\Delta$ form-factors from a relativistic dynamical model of pion electroproduction, *Phys. Rev. C* **70**, 032201 (2004), <https://doi.org/10.1103/PhysRevC.70.032201>.
- [CVL96] J. Cugnon, J. Vandermeulen and D. L'Hote, Simple parametrization of cross-sections for nuclear transport studies up to the GeV range, *Nucl. Instrum. Meth. B* **111**, 215 (1996), [https://doi.org/10.1016/0168-583X\(95\)01384-9](https://doi.org/10.1016/0168-583X(95)01384-9).
- [D⁺07] S. Damjanovic et al. (NA60), NA60 results on the rho spectral function in In In collisions, *Nucl. Phys. A* **783**, 327 (2007), <https://doi.org/10.1016/j.nuclphysa.2006.11.015>.
- [DEI90] M. Dey, V. L. Eletsky and B. L. Ioffe, Mixing of vector and axial mesons at finite temperature: an Indication towards chiral symmetry restoration, *Phys. Lett. B* **252**, 620 (1990), [https://doi.org/10.1016/0370-2693\(90\)90138-V](https://doi.org/10.1016/0370-2693(90)90138-V).
- [DFK⁺11] H.-T. Ding, A. Francis, O. Kaczmarek et al., Thermal dilepton rate and electrical conductivity: An analysis of vector current correlation functions in quenched lattice QCD, *Phys. Rev. D* **83**, 034504 (2011), <https://doi.org/10.1103/PhysRevD.83.034504>.
- [DGH92] J. F. Donoghue, E. Golowich and B. R. Holstein, *Dynamics of the Standard Model*, Cambridge University press (1992).
- [DLS] https://macdls.lbl.gov/DLS_WWW_Files/Filter_4.1/.
- [DSG86] V. Dmitriev, O. Sushkov and C. Gaarde, Δ Formation in the $^1\text{H} (^3\text{He}, ^3\text{H}) \Delta^{++}$ Reaction at Intermediate-energies, *Nucl. Phys. A* **459**, 503 (1986), [https://doi.org/10.1016/0375-9474\(86\)90158-2](https://doi.org/10.1016/0375-9474(86)90158-2).
- [Eff99] M. Effenberger, *Eigenschaften von Hadronen in Kernmaterie in einem vereinheitlichten Transportmodell*, Ph.D. thesis, Justus-Liebig-Universität Gießen (1999), <https://bibd.uni-giessen.de/gdoc/1999/uni/d990047.ps.gz>.
- [EHTM97] M. Effenberger, A. Hombach, S. Teis and U. Mosel, Photoabsorption on nuclei, *Nucl. Phys. A* **613**, 353 (1997), [https://doi.org/10.1016/S0375-9474\(96\)00408-3](https://doi.org/10.1016/S0375-9474(96)00408-3).
- [EW88] T. Ericson and W. Weise, *Pions and Nuclei*, Clarendon Press, Oxford (1988).
- [Fei76] E. Feinberg, Direct Production of Photons and Dileptons in Thermodynamical Models of Multiple Hadron Production, *Nuovo Cim. A* **34**, 391 (1976), <https://link.springer.com/article/10.1007%2F02783618?LI=true>.

Bibliography

- [FH11] K. Fukushima and T. Hatsuda, The phase diagram of dense QCD, Rept. Prog. Phys. **74**, 014001 (2011), <https://doi.org/10.1088/0034-4885/74/1/014001>.
- [FHK⁺11] B. Friman, C. Hohne, J. Knoll et al., The CBM physics book: Compressed baryonic matter in laboratory experiments, Lect.Notes Phys. **814**, pp. 980 (2011), <https://doi.org/10.1007/978-3-642-13293-3>.
- [FMRS13] W. Florkowski, M. Martinez, R. Ryblewski and M. Strickland, Anisotropic hydrodynamics, Nucl. Phys. A **904-905**, 803c (2013), <https://doi.org/10.1016/j.nuclphysa.2013.02.138>.
- [FP97] B. Friman and H. J. Pirner, P-wave polarization of the rho meson and the dilepton spectrum in dense matter, Nucl. Phys. A **617**, 496 (1997), <https://arxiv.org/abs/nucl-th/9701016>.
- [FR11] W. Florkowski and R. Ryblewski, Highly-anisotropic and strongly-dissipative hydrodynamics for early stages of relativistic heavy-ion collisions, Phys. Rev. C **83**, 034907 (2011), <https://doi.org/10.1103/PhysRevC.83.034907>.
- [FSH⁺92] T. Frommhold, F. Steiper, W. Henkel et al., Total photofission cross-section for ²³⁸U as a substitute for the photon absorption cross-section in the energy range of the first baryon resonances, Phys. Lett. B **295**, 28 (1992), [https://doi.org/10.1016/0370-2693\(92\)90084-H](https://doi.org/10.1016/0370-2693(92)90084-H).
- [Fuj79] K. Fujikawa, Path-Integral Measure for Gauge-Invariant Fermion Theories, Phys. Rev. Lett. **42**, 1195 (1979), <https://doi.org/10.1103/PhysRevLett.42.1195>.
- [Fuj80] K. Fujikawa, Path Integral for Gauge Theories with Fermions, Phys. Rev. D **21**, 2848 (1980), [Erratum: Phys. Rev.D **22**,1499(1980)], <https://doi.org/10.1103/PhysRevD.21.2848>, [10.1103/PhysRevD.22.1499](https://doi.org/10.1103/PhysRevD.22.1499).
- [Fuk04] K. Fukushima, Chiral effective model with the Polyakov loop, Phys. Lett. B **591**, 277 (2004), <https://doi.org/10.1016/j.physletb.2004.04.027>.
- [Gal14a] T. Galatyuk (2014), private communication.
- [Gal14b] T. Galatyuk (HADES), HADES overview, Nucl. Phys. A **931**, 41 (2014), <https://doi.org/10.1016/j.nuclphysa.2014.10.044>.
- [GG98] S. Gao and C. Gale, Off-shell effects in dilepton production from hot interacting mesons, Phys. Rev. C **57**, 254 (1998), <https://doi.org/10.1103/PhysRevC.57.254>.
- [GK89] C. Gale and J. I. Kapusta, Dilepton Radiation From Nucleon-nucleon Collisions, Phys. Rev. C **40**, 2397 (1989), <https://doi.org/10.1103/PhysRevC.40.2397>.
- [GK91] C. Gale and J. I. Kapusta, Vector dominance model at finite temperature, Nucl. Phys. B **357**, 65 (1991), [https://doi.org/10.1016/0550-3213\(91\)90459-B](https://doi.org/10.1016/0550-3213(91)90459-B).
- [GMMR06] S. K. Ghosh, T. K. Mukherjee, M. G. Mustafa and R. Ray, Susceptibilities and speed of sound from PNJL model, Phys. Rev. D **73**, 114007 (2006), <https://doi.org/10.1103/PhysRevD.73.114007>.

- [GRV95] M. Glück, E. Reya and A. Vogt, Dynamical parton distributions of the proton and small x physics, *Z. Phys. C* **67**, 433 (1995), <https://doi.org/10.1007/BF01624586>.
- [GS68] G. J. Gounaris and J. J. Sakurai, Finite-Width Corrections to the Vector-Meson-Dominance Prediction for $\rho \rightarrow e^+e^-$, *Phys. Rev. Lett.* **21**, 244 (1968), <https://link.aps.org/doi/10.1103/PhysRevLett.21.244>.
- [GSZ13] V. V. Goloviznin, A. M. Snigirev and G. M. Zinovjev, Towards azimuthal anisotropy of direct photons, *JETP Lett.* **98**, 61 (2013), <https://doi.org/10.1134/S0021364013150071>.
- [GT10] U. S. Gupta and V. K. Tiwari, Meson masses and mixing angles in the 2+1 flavor Polyakov quark meson sigma model and symmetry restoration effects, *Phys. Rev. D* **81**, 054019 (2010), <https://doi.org/10.1103/PhysRevD.81.054019>.
- [GW73] D. Gross and F. Wilczek, Ultraviolet Behavior of Nonabelian Gauge Theories, *Phys. Rev. Lett.* **30**, 1343 (1973), <https://doi.org/10.1103/PhysRevLett.30.1343>.
- [HAD] <https://www-hades.gsi.de/>.
- [Hee99] H. van Hees (1999), unpublished.
- [Hee00] H. van Hees, *Renormierung selbstkonsistenter Näherungen in der Quantenfeldtheorie bei endlichen Temperaturen*, Ph.D. thesis, TU Darmstadt (2000), <https://itp.uni-frankfurt.de/~hees/publ/doc.pdf>.
- [HFR12] M. He, R. J. Fries and R. Rapp, Ideal Hydrodynamics for Bulk and Multistrange Hadrons in $\sqrt{s_{NN}}=200$ AGeV Au-Au Collisions, *Phys. Rev. C* **85**, 044911 (2012), <https://doi.org/10.1103/PhysRevC.85.044911>.
- [HMP08] Y. Hidaka, L. D. McLerran and R. D. Pisarski, Baryons and the phase diagram for a large number of colors and flavors, *Nucl. Phys. A* **808**, 117 (2008), <https://doi.org/10.1016/j.nuclphysa.2008.05.009>.
- [HPS11] T. K. Herbst, J. M. Pawłowski and B.-J. Schaefer, The phase structure of the Polyakov-quark-meson model beyond mean field, *Phys. Lett. B* **696**, 58 (2011), <https://doi.org/10.1016/j.physletb.2010.12.003>.
- [HS06] M. Harada and C. Sasaki, Dropping ρ and A_1 meson masses at chiral phase transition in the generalized hidden local symmetry, *Phys. Rev. D* **73**, 036001 (2006), <https://doi.org/10.1103/PhysRevD.73.036001>.
- [HSW08] M. Harada, C. Sasaki and W. Weise, Vector-axialvector mixing from a chiral effective field theory at finite temperature, *Phys. Rev. D* **78**, 114003 (2008), <https://doi.org/10.1103/PhysRevD.78.114003>.
- [HY03] M. Harada and K. Yamawaki, Hidden local symmetry at loop: A new perspective of composite gauge boson and chiral phase transition, *Phys. Rept.* **381**, 1 (2003), [https://doi.org/10.1016/S0370-1573\(03\)00139-X](https://doi.org/10.1016/S0370-1573(03)00139-X).

Bibliography

- [JRT⁺17] C. Jung, F. Rennecke, R.-A. Tripolt, L. von Smekal and J. Wambach, In-Medium Spectral Functions of Vector- and Axial-Vector Mesons from the Functional Renormalization Group, *Phys. Rev. D* **95**, 036020 (2017), <https://doi.org/10.1103/PhysRevD.95.036020>.
- [JW96] D. Jungnickel and C. Wetterich, Effective action for the chiral quark-meson model, *Phys. Rev. D* **53**, 5142 (1996), <https://doi.org/10.1103/PhysRevD.53.5142>.
- [Kar02] F. Karsch, Lattice QCD at high temperature and density, *Lect. Notes Phys.* **583**, 209 (2002), https://doi.org/10.1007/3-540-45792-5_6.
- [KF02] M. I. Krivoruchenko and A. Faessler, Comment on delta radiative and Dalitz decays, *Phys. Rev. D* **65**, 017502 (2002), <https://doi.org/10.1103/PhysRevD.65.017502>.
- [KKMY08] K. Kashiwa, H. Kouno, M. Matsuzaki and M. Yahiro, Critical endpoint in the Polyakov-loop extended NJL model, *Phys. Lett. B* **662**, 26 (2008), <https://doi.org/10.1016/j.physletb.2008.01.075>.
- [KLM⁺12] O. Kaczmarek, E. Laermann, M. Müller et al., Thermal dilepton rates from quenched lattice QCD, *PoS Confinement X*, 185 (2012), https://pos.sissa.it/archive/conferences/171/185/Confinement%20X_185.pdf.
- [KLZ67] N. M. Kroll, T. D. Lee and B. Zumino, Neutral Vector Mesons and the Hadronic Electromagnetic Current, *Phys. Rev.* **157**, 1376 (1967), <https://link.aps.org/abstract/PR/v157/i5/p1376>.
- [KMFF02] M. I. Krivoruchenko, B. V. Martemyanov, A. Faessler and C. Fuchs, Electromagnetic transition form-factors and dilepton decay rates of nucleon resonances, *Annals Phys.* **296**, 299 (2002), <https://doi.org/10.1006/aphy.2002.6223>.
- [Koc97] V. Koch, Aspects of chiral symmetry, *Int. J. Mod. Phys. E* **6**, 203 (1997), <https://doi.org/10.1142/S0218301397000147>.
- [KRT03a] F. Karsch, K. Redlich and A. Tawfik, Hadron resonance mass spectrum and lattice QCD thermodynamics, *Eur. Phys. J. C* **29**, 549 (2003), <https://doi.org/10.1140/epjc/s2003-01228-y>.
- [KRT03b] F. Karsch, K. Redlich and A. Tawfik, Thermodynamics at nonzero baryon number density: A Comparison of lattice and hadron resonance gas model calculations, *Phys. Lett. B* **571**, 67 (2003), <https://doi.org/10.1016/j.physletb.2003.08.001>.
- [KS07] P. Kovacs and Z. Szep, The critical surface of the $SU(3)_L \times SU(3)_R$ chiral quark model at non-zero baryon density, *Phys. Rev. D* **75**, 025015 (2007), <https://doi.org/10.1103/PhysRevD.75.025015>.
- [KV96] J. Knoll and D. Voskresensky, Classical and Quantum Many-Body Description of Bremsstrahlung in Dense Matter (Landau-Pomeranchuk-Migdal Effect), *Ann. Phys. (NY)* **249**, 532 (1996), <https://doi.org/10.1006/aphy.1996.0082>.
- [KZ05] O. Kaczmarek and F. Zantow, Static quark anti-quark interactions in zero and finite temperature QCD. I. Heavy quark free energies, running coupling and quarkonium binding, *Phys. Rev. D* **71**, 114510 (2005), <https://doi.org/10.1103/PhysRevD.71.114510>.

- [Lan85] L. Landsberg, Electromagnetic Decays of Light Mesons, *Phys. Rept.* **128**, 301 (1985), [https://doi.org/10.1016/0370-1573\(85\)90129-2](https://doi.org/10.1016/0370-1573(85)90129-2).
- [LBB⁺78] A. Lepretre, H. Beil, R. Bergere et al., Total Photonuclear Absorption Cross-Section of Pb Measured with Quasimonochromatic Photons Between 25 MeV and 106 MeV, *Phys. Lett. B* **79**, 43 (1978), [https://doi.org/10.1016/0370-2693\(78\)90431-8](https://doi.org/10.1016/0370-2693(78)90431-8).
- [Loh13] D. Lohner (ALICE Collaboration), Measurement of Direct-Photon Elliptic Flow in Pb-Pb Collisions at $\sqrt{s_{NN}} = 2.76$ TeV, *J. Phys. Conf. Ser.* **446**, 012028 (2013), <https://doi.org/10.1088/1742-6596/446/1/012028>.
- [LP03] E. Laermann and O. Philipsen, The Status of lattice QCD at finite temperature, *Ann. Rev. Nucl. Part. Sci.* **53**, 163 (2003), [hep-ph/0303042](https://doi.org/10.1146/annurev.nucl.53.041002.110609), <https://doi.org/10.1146/annurev.nucl.53.041002.110609>.
- [M⁺94] L. Montanet et al. (Particle Data Group), Review of particle properties., *Phys. Rev. D* **50**, 1173 (1994), <https://doi.org/10.1103/PhysRevD.50.1173>.
- [MHE87] R. Machleidt, K. Holinde and C. Elster, The Bonn Meson Exchange Model for the Nucleon Nucleon Interaction, *Phys. Rept.* **149**, 1 (1987), [https://doi.org/10.1016/S0370-1573\(87\)80002-9](https://doi.org/10.1016/S0370-1573(87)80002-9).
- [MJH10] H. Mao, J. Jin and M. Huang, Phase diagram and thermodynamics of the Polyakov linear sigma model with three quark flavors, *J. Phys. G* **37**, 035001 (2010), <https://doi.org/10.1088/0954-3899/37/3/035001>.
- [MNR16] E. Molnár, H. Niemi and D. H. Rischke, Closing the equations of motion of anisotropic fluid dynamics by a judicious choice of a moment of the Boltzmann equation, *Phys. Rev. D* **94**, 125003 (2016), <https://doi.org/10.1103/PhysRevD.94.125003>.
- [MO96] P. N. Meisinger and M. C. Ogilvie, Chiral symmetry restoration and $Z(N)$ symmetry, *Phys. Lett. B* **379**, 163 (1996), [https://doi.org/10.1016/0370-2693\(96\)00447-9](https://doi.org/10.1016/0370-2693(96)00447-9).
- [MP07] L. McLerran and R. D. Pisarski, Phases of cold, dense quarks at large N_c , *Nucl. Phys. A* **796**, 83 (2007), <https://doi.org/10.1016/j.nuclphysa.2007.08.013>.
- [MRS06] E. Megias, E. Ruiz Arriola and L. Salcedo, Polyakov loop in chiral quark models at finite temperature, *Phys. Rev. D* **74**, 065005 (2006), <https://doi.org/10.1103/PhysRevD.74.065005>.
- [MS92] D. Manley and E. Saleski, Multichannel resonance parametrization of πN scattering amplitudes, *Phys. Rev. D* **45**, 4002 (1992), <https://doi.org/10.1103/PhysRevD.45.4002>.
- [MS10] G. Marko and Z. Szep, Influence of the Polyakov loop on the chiral phase transition in the two flavor chiral quark model, *Phys. Rev. D* **82**, 065021 (2010), <https://doi.org/10.1103/PhysRevD.82.065021>.
- [MT85] L. D. McLerran and T. Toimela, Photon and Dilepton Emission from the Quark-Gluon Plasma: Some General Considerations, *Phys. Rev. D* **31**, 545 (1985), <https://doi.org/10.1103/PhysRevD.31.545>.

Bibliography

- [N⁺10] K. Nakamura et al. (Particle Data Group), Review of particle physics, *J. Phys. G* **37**, 075021 (2010), <https://doi.org/10.1088/0954-3899/37/7A/075021>.
- [Nac90] O. Nachtmann, *Elementary Particle Physics - Concepts and Phenomenology*, Springer-Verlag, Berlin, Heidelberg, New York, London, Paris, Tokyo (1990).
- [N_{JL}61a] Y. Nambu and G. Jona-Lasinio, Dynamical Model of Elementary Particles Based on an Analogy with Superconductivity. I, *Phys. Rev.* **122**, 345 (1961), <https://doi.org/10.1103/PhysRev.122.345>.
- [N_{JL}61b] Y. Nambu and G. Jona-Lasinio, Dynamical Model of Elementary Particles Based on an Analogy with Superconductivity. II, *Phys. Rev.* **124**, 246 (1961), <https://doi.org/10.1103/PhysRev.124.246>.
- [N_{SS}⁺10] E. Nakano, B.-J. Schaefer, B. Stokic, B. Friman and K. Redlich, Fluctuations and isentropes near the chiral critical endpoint, *Phys. Lett. B* **682**, 401 (2010), <https://doi.org/10.1016/j.physletb.2009.11.027>.
- [O⁺14] K. Olive et al. (Particle Data Group), Review of Particle Physics, *Chin. Phys. C* **38**, 090001 (2014), <https://doi.org/10.1088/1674-1137/38/9/090001>.
- [P⁺97] R. J. Porter et al. (DLS), Dielectron cross-section measurements in nucleus-nucleus reactions at 1 AGeV, *Phys. Rev. Lett.* **79**, 1229 (1997), <https://doi.org/10.1103/PhysRevLett.79.1229>.
- [P⁺16] C. Patrignani et al. (Particle Data Group), Review of Particle Physics, *Chin. Phys. C* **40**, 100001 (2016), <https://doi.org/10.1088/1674-1137/40/10/100001>.
- [Par09] E. Ya. Paryev, Near-threshold ϕ meson production in proton-nucleus reactions and ϕ width in finite nuclei, *J. Phys. G* **36**, 015103 (2009), <https://doi.org/10.1088/0954-3899/36/1/015103>.
- [PBBS08] H. Petersen, M. Bleicher, S. A. Bass and H. Stöcker, UrQMD v2.3: Changes and Comparisons (2008), arXiv:0805.0567 [hep-ph], <https://arxiv.org/abs/0805.0567>.
- [Phi13] O. Philipsen, The QCD equation of state from the lattice, *Prog. Part. Nucl. Phys.* **70**, 55 (2013), <https://doi.org/10.1016/j.pnpnp.2012.09.003>.
- [Pis00] R. D. Pisarski, Quark gluon plasma as a condensate of SU(3) Wilson lines, *Phys. Rev. D* **62**, 111501 (2000), <https://doi.org/10.1103/PhysRevD.62.111501>.
- [Pol73] H. D. Politzer, Reliable Perturbative Results for Strong Interactions?, *Phys. Rev. Lett.* **30**, 1346 (1973), <https://doi.org/10.1103/PhysRevLett.30.1346>.
- [PPL⁺98] W. Peters, M. Post, H. Lenske, S. Leupold and U. Mosel, The Spectral function of the rho meson in nuclear matter, *Nucl. Phys. A* **632**, 109 (1998), [https://doi.org/10.1016/S0375-9474\(98\)00803-3](https://doi.org/10.1016/S0375-9474(98)00803-3).
- [PS95] M. Peskin and D. V. Schroeder, *An Introduction to Quantum Field Theory*, Addison-Wesley Publ. Comp., Reading, Massachusetts (1995).

- [PSB⁺08] H. Petersen, J. Steinheimer, G. Burau, M. Bleicher and H. Stöcker, A Fully Integrated Transport Approach to Heavy Ion Reactions with an Intermediate Hydrodynamic Stage, *Phys. Rev. C* **78**, 044901 (2008), <https://doi.org/10.1103/PhysRevC.78.044901>.
- [PZS⁺99] P. Papazoglou, D. Zschesche, S. Schramm et al., Nuclei in a chiral SU(3) model, *Phys. Rev. C* **59**, 411 (1999), <https://doi.org/10.1103/PhysRevC.59.411>.
- [Ram89] P. Ramond, *Field Theory: A Modern Primer*, Addison-Wesley, Redwood City, Calif., 2 edn. (1989).
- [Rap03] R. Rapp, Dileptons in high-energy heavy-ion collisions, *Pramana* **60**, 675 (2003), <https://doi.org/10.1007/BF02705167>.
- [Rap13a] R. Rapp, Dilepton Production in Heavy-Ion Collisions, *PoS CPOD2013*, 008 (2013), <https://pos.sissa.it/cgi-bin/reader/contribution.cgi?id=185/008>.
- [Rap13b] R. Rapp, Dilepton Spectroscopy of QCD Matter at Collider Energies, *Adv. High Energy Phys.* **2013**, 148253 (2013), <https://doi.org/10.1155/2013/148253>.
- [RCW96] R. Rapp, G. Chanfray and J. Wambach, Medium modifications of the rho meson at CERN SPS energies, *Phys. Rev. Lett.* **76**, 368 (1996), <https://doi.org/10.1103/PhysRevLett.76.368>.
- [RCW97] R. Rapp, G. Chanfray and J. Wambach, Rho meson propagation and dilepton enhancement in hot hadronic matter, *Nucl. Phys. A* **617**, 472 (1997), [https://doi.org/10.1016/S0375-9474\(97\)00137-1](https://doi.org/10.1016/S0375-9474(97)00137-1).
- [RG99] R. Rapp and C. Gale, ρ properties in a hot meson gas, *Phys. Rev. C* **60**, 024903 (1999), <https://doi.org/10.1103/PhysRevC.60.024903>.
- [RH09] R. Rapp and H. van Hees, Heavy Quarks in the Quark-Gluon Plasma (2009), published in R. C. Hwa, X.-N. Wang (Ed.), *Quark Gluon Plasma 4*, World Scientific, p. 111, <https://arxiv.org/abs/0903.1096>.
- [RTW06] C. Ratti, M. A. Thaler and W. Weise, Phases of QCD: Lattice thermodynamics and a field theoretical model, *Phys. Rev. D* **73**, 014019 (2006), <https://doi.org/10.1103/PhysRevD.73.014019>.
- [RUBW98] R. Rapp, M. Urban, M. Buballa and J. Wambach, A microscopic calculation of photoabsorption cross sections on protons and nuclei, *Phys. Lett. B* **417**, 1 (1998), [https://doi.org/10.1016/S0370-2693\(97\)01360-9](https://doi.org/10.1016/S0370-2693(97)01360-9).
- [RW94] R. Rapp and J. Wambach, Pion properties in a hot pi N Delta gas, *Nucl. Phys. A* **573**, 626 (1994), [https://doi.org/10.1016/0375-9474\(94\)90233-X](https://doi.org/10.1016/0375-9474(94)90233-X).
- [RW99] R. Rapp and J. Wambach, Low mass dileptons at the CERN SPS: Evidence for chiral restoration?, *Eur. Phys. J. A* **6**, 415 (1999), <https://doi.org/10.1007/s100500050364>.
- [RW00a] R. Rapp and J. Wambach, Chiral symmetry restoration and dileptons in relativistic heavy-ion collisions, *Adv. Nucl. Phys.* **25**, 1 (2000), <https://arxiv.org/abs/hep-ph/9909229>.

Bibliography

- [RW00b] R. Rapp and J. Wambach, Chiral symmetry restoration and dileptons in relativistic heavy ion collisions, *Adv. Nucl. Phys.* **25**, 1 (2000), https://doi.org/10.1007/0-306-47101-9_1.
- [Sak60] J. J. Sakurai, Theory of strong interactions, *Ann. Phys. (NY)* **11**, 1 (1960), [https://doi.org/10.1016/0003-4916\(60\)90126-3](https://doi.org/10.1016/0003-4916(60)90126-3).
- [Sch12] B.-J. Schaefer, Fluctuations and the QCD Phase Diagram, *Phys. Atom. Nucl.* **75**, 741 (2012), <https://doi.org/10.1134/S1063778812060270>.
- [Sch14] M. D. Schwartz, *Quantum field theory and the Standard Model*, Cambridge University Press, Cambridge, New York (2014).
- [SFN⁺10] V. Skokov, B. Friman, E. Nakano, K. Redlich and B.-J. Schaefer, Vacuum fluctuations and the thermodynamics of chiral models, *Phys. Rev. D* **82**, 034029 (2010), <https://doi.org/10.1103/PhysRevD.82.034029>.
- [SFR07] C. Sasaki, B. Friman and K. Redlich, Susceptibilities and the Phase Structure of a Chiral Model with Polyakov Loops, *Phys. Rev. D* **75**, 074013 (2007), <https://doi.org/10.1103/PhysRevD.75.074013>.
- [SFR11] V. Skokov, B. Friman and K. Redlich, Quark number fluctuations in the Polyakov loop-extended quark-meson model at finite baryon density, *Phys. Rev. C* **83**, 054904 (2011), <https://doi.org/10.1103/PhysRevC.83.054904>.
- [SGH⁺98] C. Spieles, L. Gerland, N. Hammon et al., A Microscopic calculation of secondary Drell-Yan production in heavy ion collisions, *Eur. Phys. J. C* **5**, 349 (1998), <https://doi.org/10.1007/s100520050279>.
- [SHPG14] C. Shen, U. W. Heinz, J.-F. Paquet and C. Gale, Thermal photons as a quark-gluon plasma thermometer reexamined, *Phys. Rev. C* **89**, 044910 (2014), <https://doi.org/10.1103/PhysRevC.89.044910>.
- [Sib96] A. A. Sibirtsev, Heavy meson production cross-sections from proton proton collisions, *Nucl. Phys. A* **604**, 455 (1996), [https://doi.org/10.1016/0375-9474\(96\)00102-9](https://doi.org/10.1016/0375-9474(96)00102-9).
- [Son93] C. Song, Photon emission from hot hadronic matter described by an effective chiral Lagrangian, *Phys. Rev. C* **47**, 2861 (1993), <https://doi.org/10.1103/PhysRevC.47.2861>.
- [SP99] B.-J. Schaefer and H.-J. Pirner, Renormalization group flow and equation of state of quarks and mesons, *Nucl. Phys. A* **660**, 439 (1999), [https://doi.org/10.1016/S0375-9474\(99\)00409-1](https://doi.org/10.1016/S0375-9474(99)00409-1).
- [Spe10] H. J. Specht (NA60 Collaboration), Thermal Dileptons from Hot and Dense Strongly Interacting Matter, *AIP Conf. Proc.* **1322**, 1 (2010), <https://doi.org/10.1063/1.3541982>.
- [SPW07] B.-J. Schäfer, J. M. Pawłowski and J. Wambach, The Phase Structure of the Polyakov-Quark-Meson Model, *Phys. Rev. D* **76**, 074023 (2007), <https://doi.org/10.1103/PhysRevD.76.074023>.

- [SSFR10] V. Skokov, B. Stokic, B. Friman and K. Redlich, Meson fluctuations and thermodynamics of the Polyakov loop extended quark-meson model, *Phys. Rev. C* **82**, 015206 (2010), <https://doi.org/10.1103/PhysRevC.82.015206>.
- [ST09] T. Schäfer and D. Teaney, Nearly Perfect Fluidity: From Cold Atomic Gases to Hot Quark Gluon Plasmas, *Rept. Prog. Phys.* **72**, 126001 (2009), <https://doi.org/10.1088/0034-4885/72/12/126001>.
- [SW05] B.-J. Schaefer and J. Wambach, The Phase diagram of the quark meson model, *Nucl. Phys. A* **757**, 479 (2005), <https://doi.org/10.1016/j.nuclphysa.2005.04.012>.
- [SW07] B.-J. Schaefer and J. Wambach, Susceptibilities near the QCD (tri)critical point, *Phys. Rev. D* **75**, 085015 (2007), <https://doi.org/10.1103/PhysRevD.75.085015>.
- [SW08] B.-J. Schaefer and J. Wambach, Renormalization group approach towards the QCD phase diagram, *Phys. Part. Nucl.* **39**, 1025 (2008), <https://doi.org/10.1134/S1063779608070083>.
- [SYZ96] J. V. Steele, H. Yamagishi and I. Zahed, Dilepton and Photon Emission Rates from a Hadronic Gas, *Phys. Lett. B* **384**, 255 (1996), [https://doi.org/10.1016/0370-2693\(96\)00802-7](https://doi.org/10.1016/0370-2693(96)00802-7).
- [SYZ97] J. V. Steele, H. Yamagishi and I. Zahed, Dilepton and photon emission rates from a hadronic gas. II, *Phys. Rev. D* **56**, 5605 (1997), <https://link.aps.org/abstract/PRD/V56/P05605>.
- [TCE⁺97] S. Teis, W. Cassing, M. Effenberger et al., Pion production in heavy ion collisions at SIS energies, *Z. Phys. A* **356**, 421 (1997), <https://doi.org/10.1007/s002180050198>.
- [Tet03] N. Tetradis, The Quark meson model and the phase diagram of two flavor QCD, *Nucl. Phys. A* **726**, 93 (2003), [https://doi.org/10.1016/S0375-9474\(03\)01624-5](https://doi.org/10.1016/S0375-9474(03)01624-5).
- [TRG04] S. Turbide, R. Rapp and C. Gale, Hadronic production of thermal photons, *Phys. Rev. C* **69**, 014903 (2004), <https://doi.org/10.1103/PhysRevC.69.014903>.
- [TSW17] R.-A. Tripolt, L. von Smekal and J. Wambach, Spectral functions and in-medium properties of hadrons, *Int. J. Mod. Phys. E* **26**, 1740028 (2017), <https://doi.org/10.1142/S0218301317400286>.
- [UBRW98] M. Urban, M. Buballa, R. Rapp and J. Wambach, Momentum dependence of the pion cloud for ρ mesons in nuclear matter, *Nucl. Phys. A* **641**, 433 (1998), [https://doi.org/10.1016/S0375-9474\(98\)00476-X](https://doi.org/10.1016/S0375-9474(98)00476-X).
- [WBC⁺90] G. Wolf, G. Batko, W. Cassing et al., Dilepton production in heavy ion collisions, *Nucl. Phys. A* **517**, 615 (1990), [https://doi.org/10.1016/0375-9474\(90\)90222-8](https://doi.org/10.1016/0375-9474(90)90222-8).
- [Wei96] S. Weinberg, *The Quantum Theory of Fields*, vol. 2, Cambridge University Press (1996).
- [WGM11] J. Weil, K. Gallmeister and U. Mosel, In-Medium Properties of Vector Mesons in a Transport Approach, *PoS BORMIO2011*, 053 (2011), <https://arxiv.org/abs/1105.0314>.

Bibliography

- [WI05] Q. Wan and F. Iachello, A unified description of baryon electromagnetic form factors, *Int. J. Mod. Phys. A* **20**, 1846 (2005), <https://doi.org/10.1142/S0217751X05023463>.
- [Wil13] M. Wilde (ALICE), Measurement of Direct Photons in pp and Pb-Pb Collisions with ALICE, *Nucl. Phys. A* **904-905**, 573c (2013), <https://doi.org/10.1016/j.nuclphysa.2013.02.079>.
- [Y⁺06] W. M. Yao et al. (Particle Data Group), Review of particle physics, *J. Phys. G* **33**, 1 (2006), <https://pdg.lbl.gov>.
- [ZSSB⁺02] D. Zschesche, S. Schramm, J. Schaffner-Bielich, H. Stöcker and W. Greiner, Particle ratios at RHIC: Effective hadron masses and chemical freezeout, *Phys. Lett. B* **547**, 7 (2002), [https://doi.org/10.1016/S0370-2693\(02\)02736-3](https://doi.org/10.1016/S0370-2693(02)02736-3).
- [ZZS07] D. Zschesche, G. Zeeb and S. Schramm, Phase structure in a hadronic chiral model, *J. Phys. G* **34**, 1665 (2007), <https://doi.org/10.1088/0954-3899/34/7/007>.

Part II

Publications

Finite pion width effects on the rho-meson

Hendrik van Hees¹ and Jörn Knoll²

*Gesellschaft für Schwerionenforschung
Planckstr. 1
64291 Darmstadt*

Abstract

We study the influence of the finite damping width of pions on the in-medium properties of the ρ -meson in an interacting meson gas model at finite temperature. Using vector dominance also implications on the resulting dilepton spectra from the decay of the ρ -meson are presented. A set of coupled Dyson equations with self-energies up to the sunset diagram level is solved self consistently. Following a Φ -derivable scheme the self-energies are dynamically determined by the self-consistent propagators. Some problems concerning the self-consistent treatment of vector or gauge bosons on the propagator level, in particular, if coupled to currents arising from particles with a sizable damping width, are discussed.

Key words:

Rho-meson, Medium modifications, Dilepton production, Self-consistent approximation schemes.

PACS: 14.40.-n

1 Introduction and summary

The question how a dense hadronic medium changes the properties of vector mesons compared to their free space characteristics has attracted much attention in recent times. Experimentally this question is studied in measurements of the dilepton production rates in heavy ion collisions. Recent experiments by the CERES and DLS collaborations [1–3] show that the low lepton pair mass spectrum is significantly enhanced in the range between 300 MeV and 600 MeV compared to the yield that one expects from the corresponding rates in pp-collisions.

¹ e-mail:h.vanhees@gsi.de

² e-mail:j.knoll@gsi.de

From the theoretical side various mechanisms are proposed to explain these influences of a hadronic matter surrounding on the spectral properties of vector mesons[4–11]. With the upgrade of CERES and the new dilepton project HADES at GSI a more precise view on the spectral information of vector mesons is expected. Still in most of theoretical investigations the damping width gained by stable particles due to collisions in dense matter is either ignored or treated within an extended perturbation theory picture[12]. In this contribution we study the in-medium properties of the ρ -meson due to the damping width of pions in a dense meson gas within a self-consistent scheme.

The field theoretical model, which is inspired from vector meson dominance theories[13], is discussed in section 2. Thereby the finite pion width is modelled with a four-pion self-interaction in order to keep the investigation as simple as possible. The coupling strength is adjusted as to produce a pion damping-width of reasonable strength, such as to simulate the width a pion would obtain in a baryon rich environment due to the strong coupling to baryonic resonance channels, like the Δ -resonance. The self-consistent equations of motion are derived from Baym's Φ -functional[14–16] and the problem of renormalisation is left aside by taking into account only the imaginary parts of the self-energies but keeping the normalisation of the spectral function fixed.

This self-consistent treatment described in section 3 respects the conservation laws for the expectation values of conserved currents and at the same time ensures the dynamical as well as the thermodynamical consistency of the scheme. Especially the effects of bremsstrahlung and annihilation processes are taken into account consistently.

Finally in section 4 we discuss the principal problems with the treatment of vector mesons in such a scheme which are mainly due to the fact that within the Φ -functional formalism the vertex corrections necessary to ensure the Ward-Takahashi identities for the propagator are ignored. In our model calculations we work around this problem by projecting onto the transverse part of the propagators such that the errors of this shortcoming can be expected to be small. In the appendix we elaborate on some details of this projection method.

2 The model

In order to isolate the pion width effects we consider a purely mesonic model system consisting of charged pions, neutral ρ -mesons, and also the chiral part-

ner of the ρ^- , the a_1 -meson, with the interaction Lagrangian

$$\mathcal{L}^{\text{int}} = g_{\rho\pi\pi}\rho_\mu\pi^*\overleftrightarrow{\partial}^\mu\pi + g_{\pi\rho a_1}\pi\rho_\mu a_1^\mu + \frac{g_{\pi^4}}{8}(\pi^*\pi)^2 + cc. \quad (1)$$

We do not explicitly write down the free Lagrangian, but we like to mention that we consider the ρ -meson as a gauge particle. The first two coupling constants are adjusted to provide the corresponding vacuum widths of the ρ^- and a_1 -meson at the nominal masses of 770 MeV and 1200 MeV and widths of $\Gamma_\rho = 150$ MeV and $\Gamma_{a_1} = 400$ MeV, respectively. The four- π interaction is used as a tool to furnish additional collisions among the pions. The idea of this term is to provide pion damping widths of about 50 MeV or more as they would occur due to the strong coupling to the NN^{-1} and ΔN^{-1} channels in an environment at finite baryon density.

The Φ -functional method originally invented by Baym[15] provides a self-consistent scheme applicable even in the case of broad resonances. It is based on a resummation for the partition sum [14,16]. Its two particle irreducible part $\Phi\{G\}$ generates the irreducible self-energy $\Sigma(x, y)$ via a functional variation with respect to the propagator $G(y, x)$, i.e.

$$-i\Sigma(x, y) = \frac{\delta i\Phi}{\delta iG(y, x)}. \quad (2)$$

Thereby Φ , constructed from two-particle irreducible closed diagrams of the Lagrangian (1) solely depends on fully resummed, i.e. self-consistently generated propagators $G(x, y)$. In graphical terms, the variation (2) with respect to G is realized by opening a propagator line in all diagrams of Φ . Further details and the extension to include classical fields or condensates into the scheme are given in ref. [17].

Truncating Φ to a limited subset of diagrams, while preserving the variational relation (2) between $\Phi^{(\text{appr.})}$ and $\Sigma^{(\text{appr.})}(x, y)$ defines an approximation with built-in consistency. Baym[15] showed that such a Dyson resummation scheme is conserving at the expectation value level of conserved currents related to global symmetries, realised as a linear representation of the corresponding group, of the original theory, that its physical processes fulfil detailed balance and unitarity and that at the same time the scheme is thermodynamically consistent. However symmetries and conservation laws may no longer be maintained on the correlator level, a draw-back that will lead to problems for the self-consistent treatment of vector and gauge particles on the propagator level, as discussed in sect. 3.

Interested in the effects arising from the damping width of the particles we discard all changes in the real part of the self energies, keeping however the sum-rule of the spectral functions normalised. In this way we avoid renormalisation problems which require a temperature independent subtraction scheme.

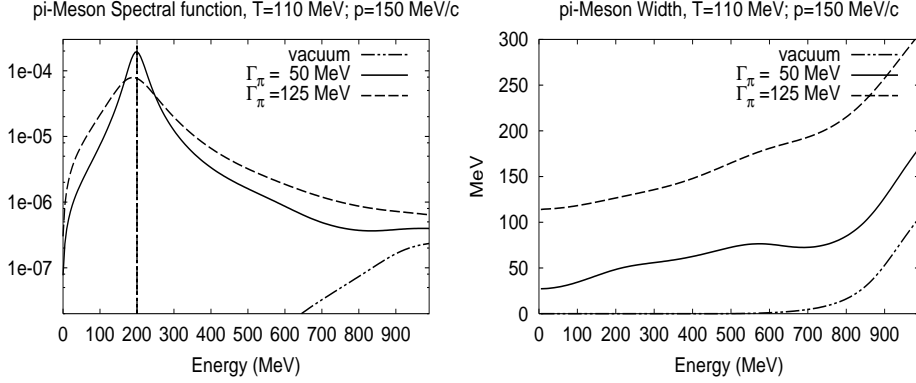


Fig. 1. Spectral function (left) and decay width (right) of the pion as a function of the pion energy at a pion momentum of 150 MeV/c in the vacuum and for two self-consistent cases discussed in the text.

The latter will be discussed in detail in a forthcoming paper [18]. Neglecting changes in real parts of the self-energies also entitles to drop tadpole contributions. The treatment of the tensor structure of the ρ - and a_1 -polarisation tensors is discussed in sect. 3. Here we first discuss the results of the self-consistent calculations.

For our model Lagrangian (1) and neglecting tadpole contributions one obtains the following diagrams for Φ at the two-point level which generate the subsequently given three self energies Π_ρ , Π_{a_1} and Σ_π

$$\begin{aligned}
 \Phi &= \frac{1}{2} \text{Diagram 1} + \frac{1}{2} \text{Diagram 2} + \frac{1}{2} \text{Diagram 3} \\
 \Pi_\rho &= \text{Diagram 4} + \text{Diagram 5} \\
 \Pi_{a_1} &= \text{Diagram 6} \\
 \Sigma_\pi &= \text{Diagram 7} + \text{Diagram 8} + \text{Diagram 9}
 \end{aligned}
 \tag{3}$$

They are the driving terms for the corresponding three Dyson equations, which form a coupled scheme which has to be solved self-consistently. The Φ -derivable scheme pictorially illustrates the concept of Newton's principle of *actio = reactio* and detailed balance. If the self-energy of one particle is modified due to the coupling to other species, these other species also obtain

a corresponding term in their self-energy. In the vacuum the ρ - and a_1 -meson self-energies have the standard thresholds at $\sqrt{s} = 2m_\pi$ and at $3m_\pi$ respectively. For the pion as the only stable particle in the vacuum with a pole at m_π the threshold opens at $\sqrt{s} = 3m_\pi$ due to the first and last diagram of Σ_π . Correspondingly the vacuum spectral function of the pion shows already spectral strength for $\sqrt{s} > 3m_\pi$, c.f. fig. 1 (left).

Self-consistent equilibrium calculations are performed keeping the full dependence of all two-point functions on three momentum \vec{p} and energy p_0 , and treating all propagators with their dynamically determined self-energies.

The examples shown refer to a temperature of $T = 110$ MeV appropriate for the CERES data. We discuss three different settings. First the ρ -meson polarisation tensor is calculated simply by the perturbative pion loop, i.e. with vacuum pion propagators and thermal Bose-Einstein weights (no self-consistent treatment). The two other cases refer to self-consistent solutions of the coupled Dyson scheme, where the four- π interaction is tuned such that the sun-set diagram provides a moderate pion damping width of about 50 MeV and a strong one of 125 MeV around the peak of the pion spectral function, c.f. fig. 1. Since in the thermal case any excitation energy is available, though with corresponding thermal weights, all thresholds disappear and the spectral functions show strength at *all* energies³! The pion functions shown in Fig. 1 at a fixed momentum of 150 MeV are plotted against energy in order to illustrate that there is significant strength also in the space-like region (below the light cone at 150 MeV) resulting from π - π scattering processes.

As an illustration we display a 3-d plot of the ρ -meson spectral function as a function of p_0 and $|\vec{p}|$ in Fig. 2, top left. The right part shows the transverse spectral function as a function of invariant mass at fixed three-momentum of 150 MeV/c in vacuum and for the two self-consistent cases. The minor changes at the low mass side of the ρ -meson spectral function become significant in the dilepton yields given in the left bottom panel. The reason lies in the statistical weights together with additional kinematical factors $\propto m^{-3}$ from the dilepton-decay mechanism described by the vector meson dominance principle[13]. For the moderate damping case ($\Gamma_\pi = 50$ MeV) we have decomposed the dilepton rate into partial contributions associated with π - π bremsstrahlung, π - π annihilation and the contribution from the a_1 -meson, which can be interpreted as the a_1 Dalitz decay.

The low mass part is completely dominated by pion bremsstrahlung contributions (like-charge states in the pion loop). This contribution, which vanishes

³ In mathematical terms: all branch-cuts in the complex energy plane reach from $-\infty$ to $+\infty$, and the physical sheets of the retarded functions are completely separated from the physical sheets of the corresponding advanced functions by these cuts.

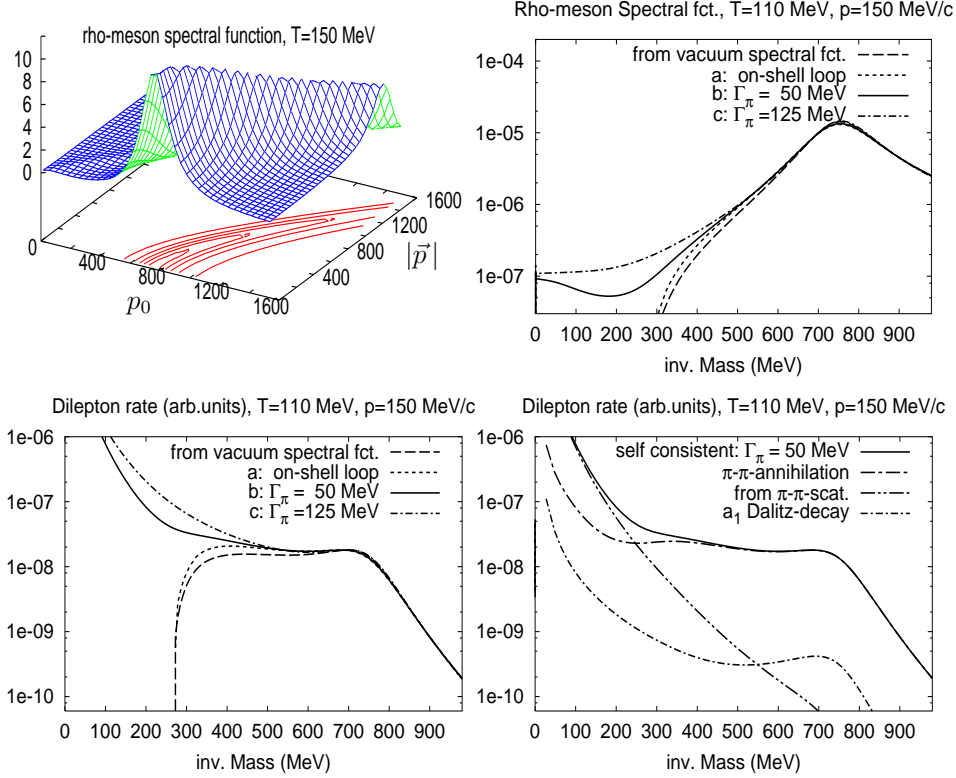


Fig. 2. top: ρ -meson spectral function, bottom: thermal dilepton rate.

in lowest order perturbation theory, is *finite* for pions with finite width. It has to be interpreted as bremsstrahlung, since the finite width results from collisions with other particles present in the heat bath. Compared to the standard treatment, where the bremsstrahlung is calculated independently of the π - π annihilation process, this self-consistent treatment has a few advantages. The bremsstrahlung contribution is calculated consistently with the annihilation process, it appropriately accounts for the Landau-Pomeranchuk suppression at low invariant masses [19] and at the same time includes the in-medium pion electromagnetic form-factor for the bremsstrahlung part. As a result the finite pion width adds significant strength to the mass region below 500 MeV compared to the trivial treatment with the vacuum spectral function. Therefore the resulting dilepton spectrum essentially shows no drop any more in this low mass region already for a moderate pion width of 50 MeV. The a_1 Dalitz decay contribution can be read off from the partial ρ -meson width due to the π - a_1 loop in Π_ρ . This component is seen to be unimportant at all energies in the present calculations where medium modifications of the masses of the mesons are discarded. The latter can be included through renormalised dispersion relations within such a consistent scheme.

3 Longitudinal and transverse components

While scalar particles and couplings can be treated self-consistently with no principle problems at any truncation level, considerable difficulties and undesired features arise in the case of vector particles. The origin lies in the fact that, though in Φ -derivable Dyson resummations symmetries and conservation laws are fulfilled at the expectation value level, they are generally no longer guaranteed at the correlator level. Considering the ρ -meson as a gauge particle one has to care about local gauge symmetries, where the situation is even worse, because the symmetry of the quantised theory is not the original one but the non-linear BRST symmetry [20,21]. Contrary to perturbation theory, where the loop expansion corresponds to a strict power expansion in \hbar and symmetries are maintained order by order, partial resummations mix different orders and thus are violating the corresponding symmetries. It is obvious that the scheme discussed above indeed violates the Ward identities on the correlator level and thus the vector-meson polarisation tensor is no longer 4-dimensionally transverse. This means that unphysical states are propagated within the internal lines of the Φ -derivable approximation scheme which leads to a number of conceptual difficulties and to explicit difficulties in the numerical treatment of the problem. In the above calculations we have worked around this problem in the following way.

For the exact polarisation tensor we know that for $\vec{p} = 0$ the temporal components exactly vanish $\Pi^{00}(q) = \Pi^{0i}(q) = \Pi^{i0}(q) = 0$ for $q_0 \neq 0$, while this is not the case for the self-consistently constructed tensor [19]. Indeed these components are tied to the conservation of charge and therefore involve a relaxation time for a conserved quantity which is of course infinite while the self-consistent result always reflects the damping time of the propagators in the loop. This behaviour is studied in detail in ref. [19], both on the classical and quantum many body Green's function level within the real time formalism. There it has been shown that current conservation can only be restored through a resummation of all the scattering processes in a transport picture which amounts to a Bethe-Salpeter ladder resummation in the corresponding quantum field theory description. This will be discussed to some extent in sect. 4. At this level it is important to realise that the spatial components generally suffer less corrections from this resummation in case that the relaxation time for the transverse current-current correlator is comparable to the damping time of the propagators in the loop. The time components, however, suffer significant corrections. Thus our strategy for the self-consistent loop calculation is the following: from the loop calculation of the polarisation tensors Π (of the ρ -meson) we evaluate only the information obtained for the spatial components Π^{ik} . Taking the following two spatial traces (details are given in the appendix A)

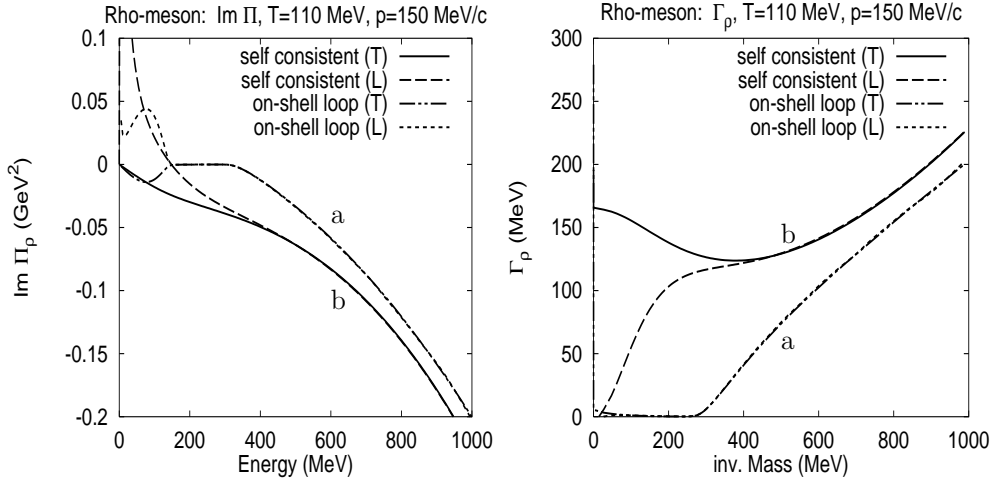


Fig. 3. *Left: Imaginary part of the Longitudinal (L) and transverse (T) ρ -meson polarisation tensor at $T = 110$ MeV. case (a): finite temperature on-shell-loop calculation; case (b): self-consistent calculation for the case where $\Gamma_\pi = 125$ MeV. Right: the same for the corresponding widths $\Gamma_\rho = -\text{Im } \Pi_\rho/p^0$.*

$$\left. \begin{aligned} 3\Pi_3 &= -g_{ik}\Pi^{ik} = 2\Pi_T + \frac{(q^0)^2}{q^2}\Pi_L \\ \Pi_1 &= \frac{p_i p_k}{\vec{q}^2}\Pi^{ik} = \frac{(q^0)^2}{q^2}\Pi_L \end{aligned} \right\} \Leftrightarrow \partial_\mu \Pi^{\mu\nu} = 0 \quad (4)$$

permits to deduce the 3-dim. longitudinal and transverse tensor components Π_L and Π_T under the condition that the polarisation tensor is exactly 4-dim. transversal. This construction thus fulfils current conservation on the correlator level.

The result of this procedure is shown in fig. 3 for the components of the ρ -meson polarisation tensor for a finite spatial momentum of $\vec{p} = 150$ MeV. The plots show $\text{Im } \Pi_L$ and $\text{Im } \Pi_T$ first for the on-shell loop result, i.e. with vacuum pion spectral functions and thermal occupations. For this on-shell loop case to very good approximation one finds $\Pi_L = \Pi_T$ for time like momenta, while as expected they deviate in sign for space-like momenta. The longitudinal component exactly vanishes on the light cone and changes sign there. Thus the tensor is entirely transverse on the light cone as it should! Switching to the self-consistent results the threshold gap between $\sqrt{s} \in [0, 2m_\pi]$ is completely filled. At non-zero momenta \vec{p} the longitudinal and transverse component deviate from one another towards low invariant masses, i.e. $\sqrt{s} < 400$ MeV in this case, while they are identical for large \sqrt{s} as they should. As both components Π_L and Π_T are constructed from different moments of the numerically given Π^{ik} , the agreement of the two components at large \sqrt{s} shows the numerical precision of the employed loop integration method. The resulting behaviour is further clarified in the right part of fig. 3, which shows the resulting damp-

ing width of the ρ -meson $\Gamma_\rho(p) = -\text{Im}\Pi_\rho(p)/p^0$. One sees that the typical threshold behaviour of the on-shell loop is completely changed in the self-consistent result. The transverse width is with $\Gamma_T \approx 150\text{MeV}$ almost constant over the displayed invariant mass range! For the longitudinal component one has to consider the kinematical factor entering in specific tensor components, e.g. $\Pi^{00} = \Pi_L \bar{q}^2/q^2$, such that also Γ^{00} is about constant.

While current conservation has been restored on the correlator level by the procedure above, the Ward–Takahashi identities are certainly not fulfilled. Thus the whole procedure will not be gauge covariant. Still from the experience discussed in ref. [19] we expect that this method provides a good approximation to the in-medium polarisation tensor at finite temperature. In particular for the light pions which at $T = 150\text{MeV}$ have already quite relativistic energies we expect that the mutual scattering leads to fairly isotropic distributions after each scattering such that the memory on some initial fluctuation of the pion current is already lost after the first collision, c.f. the discussions in ref. [19] and in the next section.

4 Symmetries and gauge invariance

In view of the difficulties to provide a gauge-invariant scheme one may raise the question: *is there a self-consistent truncation scheme beyond the mean field level for the gauge fields, which preserves gauge invariance?* In particular we are interested that the internal dynamics, i.e. the dynamical quantities like classical fields and propagators which enter the self-consistent set of equations remain gauge covariant.

At the mean field level the gauge fields couple to the expectation values of the vector currents and gauge covariance is fully maintained. This level is explored in all hard thermal loop (HTL) approaches [22–25]. For the π - ρ -meson system the mean field approximation is given by the following Φ -derivable scheme (again omitting the tadpole term for the pion self-energy)


$$\Phi\{G_\pi, \rho\} = \cancel{\text{tadpole}} + \text{loop} \quad (5)$$

$$\Sigma_\pi = \cancel{\text{tadpole}} + \text{loop} \quad (6)$$

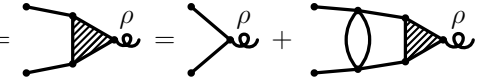
$$(\partial^\nu \partial_\nu - m^2) \rho^\mu = j^\mu = \text{tadpole} \quad (7)$$

Here full lines represent the self-consistent pion propagators and curly lines with a cross represent the classical ρ -meson field, governed by the classical field equations of motion (7). Since Φ is invariant with respect to gauge transformations of the classical vector field ρ^μ , the resulting equations of motion are gauge covariant.


The step to construct symmetry preserving correlation functions is provided by considering the linear response of the system on fluctuations in the background field [26,15], see also [27] in the context of gauge and Goldstone bosons. Thereby gauge covariance also holds for fluctuations $\rho^\mu + \delta\rho^\mu$ around mean field solution of (6 - 7). Thus, one can then define a gauge covariant *external* polarisation tensor via variations with respect to the background field $\delta\rho^\mu$

$$\Pi_{\mu\nu}^{\text{ext}}(x_1, x_2) = \frac{\delta}{\delta\rho^\mu(x_2)} \frac{\delta\Phi[G_\pi, \rho]}{\delta\rho^\nu(x_1)} \Big|_{G_\pi[\rho]} = \text{Diagram} \quad (8)$$


as a linear response to fluctuations around the mean field. This tensor can be accessed through a corresponding three-point-vertex equation

$$\frac{\delta G_\pi}{\delta\rho^\mu} = \text{Diagram 1} = \text{Diagram 2} + \text{Diagram 3} \quad (9)$$


In order to maintain all symmetries and invariances, the four-point Bethe-Salpeter Kernel in this equation has to be chosen consistently with the Φ -functional (5) [15,26], i.e. as a second functional variation of Φ with respect to the propagators

$$K_{1234} = \frac{\delta^2\Phi}{\delta G_{12}\delta G_{34}} = \text{Diagram} \quad (10)$$


Thereby the pion propagator entering the ladder resummation (9) is determined by the self-consistent solution of Eq. (6) at vanishing classical ρ -field. In particular this ladder resummation accounts for real physical scattering processes, a phenomenon already discussed in [19] for the description of Bremsstrahlung within a classical transport scheme (Landau-Pomeranchuk-Migdal effect). From this point of view one clearly sees that the pure Φ -functional formalism without the vertex corrections (9) just describes the “decay of states” due to collision broadening. Thus in the Φ -Dyson scheme (3) all components of the *internal* ρ -meson polarisation tensor have a *time-decaying* behaviour with a decay constant given by the pion damping rate Γ_π . However, the exact tensor has at least two decay times, one for the transverse components and a second one which involves the conserved charge and which naturally is infinite. The Dyson resummation fails to cope with this, since there also the 00-component approximately behaves like

$$\Pi_\rho^{00}(\tau, \vec{p} = 0) \propto e^{-\Gamma_\pi\tau} \quad (11)$$

in a mixed time–momentum representation. This clearly violates charge conservation, since $\partial_0 \Pi_\rho^{00}(\tau, \vec{p})|_{\vec{p}=0}$ does not vanish! Yet, accounting coherently for the multiple scattering of the particles through the vertex resummation (9) keeps track of the “charge flow” into other states and thus restores charge conservation. Within classical considerations the ladder resummation (9) indeed yields

$$\Pi_\rho^{00}(\tau, \vec{p} = 0) \propto \sum_n \frac{(\Gamma\tau)^n}{n!} e^{-\Gamma\tau} = 1 \quad (12)$$

confirming charge conservation. For further details c.f. ref. [19]. From the physics discussions above it is clear that these conclusions hold also for constant self–energies with a constant imaginary part. This is opposed to the vacuum case where a constant self–energy would not require any vertex correction! The formal origin of this difference lies in the fact that in the real time formulation of the field theory all relations become matrix relations from the contour time ordering. In particular the three point functions then have three independent retarded components⁴ (c.f. [28,29]) and the corresponding Ward–Takahashi identities involve both retarded and advanced self energy terms which differ in the sign of their imaginary parts. Thus even for constant self–energies the terms related to the width do no longer cancel out in these identities in the true real time case at finite T .

5 Comments and prospects

We presented self–consistent calculations of the vector meson production in a pion gas environment, where the width of the pion was generated by a pion four–vertex interaction. The novel part is that through the damping width standard thresholds known from vacuum calculations disappear and that contributions arising from pion bremsstrahlung and from π – π –annihilation are treated within the same scheme, and are therefore consistent with one another. With reasonable damping width for the pions the calculations show significant contributions to the dilepton spectrum in the mass range below 400 MeV. In the second part we discussed the particular features related to the self–consistent treatment of vector or gauge bosons.

Vertex corrections of various types were already considered in the literature in the context of the ρ –meson. They dealt with the case, where the pion couples to the nuclear sector, and vertex corrections related to the p –wave coupling of the π – N – Δ –vertex were included on phenomenological grounds using

⁴ In the Matsubara formalism this corresponds to the fact that the different energy arguments of three point functions can be placed on different half planes.

Landau–Migdal parameterisations for the Δ - N interaction [30,31]. There the employed quasi-particle loops are straightforward and the “bubble” resummation (algebraic) also. More involved vertex corrections were considered in refs. [6] and by many others later, e.g. [12]. However in none of those papers the vertex corrections were done self-consistently, nor were they proven to restore gauge invariance, nor has there the question been addressed which vertex corrections are required, once the propagators in the self-energy loop of the gauge particles have a significant damping width. The latter question was addressed in ref. [19] in the context of photon production and put on formal grounds here. Using the background field scheme we explained above the steps to come to a consistent vertex equation (9-10). It is neither some vertex equation nor the exact vertex equation: it is precisely *the* vertex equation which pertains to the self-consistent pion self-energy given by (6) at vanishing background field. The consistency comes about by the fact that both, the pion self energy (6) and the Bethe–Salpeter kernel (10), are generated from the same Φ -functional (5). The method is general and applies to any kind of Φ -functional supplemented by terms coupling to background gauge fields.

Two problems are to be mentioned in this context, a practical and a principle one. The practical problem concerns the fact that there is no feasible algorithm to calculate the external polarisation tensor (8). Already for our most simple example one has to solve the ladder re-summation in the Bethe–Salpeter equation with *full off-shell momentum dependence* for the three-point vertex given by (9). Even if one restricts oneself to the simplifying case of vanishing ρ -meson three-momentum for this vertex the numerical effort increases by about two orders of magnitude (for the full momentum dependence a factor 10^5) compared to the presented numerical solution of self-consistent self-energies and is thus out of reach in practice.

However there is yet a principle problem. What one constructs by the vertex equation is the *external* polarisation tensor of the vector meson. It has all desired features. However, the corresponding vector-meson propagator does not take part in the self-consistent scheme. This so constructed external propagator is fine in all cases, where the vector meson couples perturbatively to a source, e.g. like the photon to the electromagnetic current of a source system. For the case of the ρ -meson recoupling effects may already be of some importance, and for sure for gluons in an interacting quark-gluon plasma such recoupling effects are important, and the vector meson is a sensible component in the self-consistent scheme. In such cases, however, one sees that in self-consistent truncation schemes there is generally a difference between the self-consistent internal propagator and the external propagator constructed from the Bethe–Salpeter ladder resummation. While the first violates Ward–Takahashi identities, the latter fulfils them.

Therefore presently we see no obvious self-consistent scheme where vector

particles are treated dynamically beyond mean field, i.e. with dynamical propagators, and which at the same time complies with gauge invariance also for the *internal* propagation, unless one solves the exact theory. The work around presented in sect. 3 at least guarantees that the polarisation tensor remains four-dimensional transverse and thus no unphysical modes are appearing in the scheme. The problem of renormalisation omitted here is investigated separately using subtracted dispersion relations [18]. Thus for vector particles a fully self-consistent scheme with all the features of the Φ -functional, especially to ensure the consistency of dynamical and thermodynamical properties of the calculated propagators together with the conservation laws on both the expectation value and the correlator level remains an open problem.

The self-consistent equilibrium calculations presented here also serve the goal to gain experience about particles with broad damping width aiming towards a transport scheme for particles beyond the quasi-particle limit [32], see also [33–35].

Acknowledgements

We like to thank G. Baym, B. Friman, Y. Ivanov, E. Kolomeitsev, and D. Voskresensky for helpful discussions. Part of the formal considerations concerning gauge invariance were developed during our stay at the workshop “Non-Equilibrium Non-Equilibrium Dynamics in Quantum Field Theory” at the National Institute of Nuclear Theory at the University of Washington, especially in discussions with E. Mottola.

A Decomposition of the polarisation tensor

In spherically symmetric systems the polarisation tensor Π can be decomposed into three components (4-longitudinal (l) and the two 4-transverse components, the longitudinal (L) and transverse (T) one)

$$\Pi^{\mu\nu} = \Pi_l^{\mu\nu} + \Pi_L^{\mu\nu} + \Pi_T^{\mu\nu} \quad (\text{A.1})$$

$$\Pi_l^{\mu\nu} = -\frac{q^\mu q^\nu}{q^2} \Pi_l \quad (\text{A.2})$$

$$\Pi_L^{\mu\nu} = \left(-g^{\mu\nu} - \delta^{\mu\nu} + \frac{q^\mu q^\nu}{q^2} + \frac{\vec{q}^\mu \vec{q}^\nu}{\vec{q}^2} \right) \Pi_L \quad (\text{A.3})$$

$$\Pi_T^{\mu\nu} = \left(\delta^{\mu\nu} - \frac{\vec{q}^\mu \vec{q}^\nu}{\vec{q}^2} \right) \Pi_T. \quad (\text{A.4})$$

Here $\delta^{\mu\nu}$ and \vec{q}^{μ} are defined such that the time-components vanish. The spatial part and the 00-component become

$$\Pi^{ik} = \left(\delta^{ik} - \frac{\vec{q}^i \vec{q}^k}{\vec{q}^2} \right) \Pi_T + \frac{(q^0)^2}{q^2} \frac{q^i q^k}{\vec{q}^2} \Pi_L - \frac{q^i q^k}{q^2} \Pi_l \quad (\text{A.5})$$

$$\Pi^{00} = \left(-g^{00} + \frac{(q^0)^2}{q^2} \right) \Pi_L - \frac{(q^0)^2}{q^2} \Pi_l. \quad (\text{A.6})$$

In terms of the 4- and 3-traces we define

$$\begin{aligned} 4\Pi_4 &= -\text{Tr}_4\{\Pi^{\mu\nu}\} = -g_{\mu\nu}\Pi^{\mu\nu} = -\Pi^{00} + \text{Tr}_3\{\Pi^{ik}\} \\ &= \Pi_l + \Pi_L + 2\Pi_T \end{aligned} \quad (\text{A.7})$$

$$3\Pi_3 = \text{Tr}_3\{\Pi^{ik}\} = -g_{ik}\Pi^{ik} = 2\Pi_T + \frac{(q^0)^2}{q^2} \Pi_L - \frac{\vec{q}^2}{q^2} \Pi_l. \quad (\text{A.8})$$

One further can use

$$\Pi_1 = \frac{p_i p_k}{\vec{q}^2} \Pi^{ik} = \frac{(q^0)^2}{q^2} \Pi_L - \frac{\vec{q}^2}{q^2} \Pi_l. \quad (\text{A.9})$$

Taking into account the information contained in the two traces Π_1 and Π_3 , and the condition for 4-dim. transversality, $\Pi_l = 0$, a conserved polarisation tensor can be constructed.

References

- [1] G. Agakishiev, et al., Enhanced Production of Low-Mass Electron Pairs in 200 GeV/Nucleon S-Au Collisions at the CERN Super Proton Synchrotron, Phys. Rev. Lett. 75 (1995) 1272.
- [2] P. Wurm, et al., New Results from NA45/CERES, Nucl. Phys. A590 (1995) 103c–116c.
- [3] R. J. Porter, et al., Dielectron Cross Section Measurements in Nucleus-Nucleus Reactions at 1.0 A GeV, Phys. Rev. Lett. 79 (1997) 1229–1232.
- [4] C. Gale, J. I. Kapusta, Vector Dominance Model at Finite Temperature, Nuclear Physics B357 (1991) 65.
- [5] R. Rapp, J. Wambach, Chiral symmetry restoration and dileptons in relativistic heavy-ion collisions, preprint: hep-ph/9909229 (1999).
- [6] M. Herrmann, B. L. Friman, W. Nörenberg, Properties of rho mesons in nuclear matter, Nucl. Phys. A560 (1993) 411–436.

- [7] R. Rapp, G. Chanfray, J. Wambach, Rho meson propagation and dilepton enhancement in hot hadronic matter, Nucl. Phys. A617 (1997) 472–495.
- [8] R. Rapp, J. Wambach, Low mass dileptons at the cern-sps: Evidence for chiral restoration?, Eur. Phys. J. A6 (1999) 415–420.
- [9] M. Urban, M. Buballa, R. Rapp, J. Wambach, Momentum dependence of the pion cloud for rho mesons in nuclear matter, Nucl. Phys. A641 (1998) 433.
- [10] R. Rapp, M. Urban, M. Buballa, R. Rapp, J. Wambach, A microscopic calculation of photoabsorption cross sections on protons and nuclei, Phys. Lett. B417 (1998) 1.
- [11] R. Rapp, C. Gale, ρ properties in a hot meson gas, Phys. Rev. C60 (1999) 024903.
- [12] M. Urban, M. Buballa, R. Rapp, J. Wambach, Modifications of the rho meson from the virtual pion cloud in hot and dense matter, Nucl. Phys. A673 (2000) 357.
- [13] N. M. Kroll, T. D. Lee, B. Zumino, Neutral Vector Mesons and the Hadronic Electromagnetic Current, Phys. Rev. 157 (1967) 1376.
- [14] J. Luttinger, J. Ward, Ground-State Energy of a Many-Fermion System II, Phys. Rev. 118 (1960) 1417.
- [15] G. Baym, Self-Consistent Approximations in Many-Body Systems, Phys. Rev. 127 (1962) 1391.
- [16] M. Cornwall, R. Jackiw, E. Tomboulis, Effective Action for Composite Operators, Phys. Rev. D10 (1974) 2428.
- [17] Y. B. Ivanov, J. Knoll, D. N. Voskresensky, Self-Consistent Approximations to Non-equilibrium Many-Body Theory, Nucl. Phys. A657 (1999) 413.
- [18] H. van Hees, J. Knoll, Renormalization of self-consistent approximations, in preparation (2000).
- [19] J. Knoll, D. Voskresensky, Classical and Quantum Many-Body Description of Bremsstrahlung in Dense Matter (Landau-Pomeranchuk-Migdal Effect), Annals of Physics 249 (1996) 532.
- [20] C. Becchi, A. Rouet, R. Stora, Renormalization of Gauge Theories, Annals of Physics 98 (1976) 287.
- [21] I. V. Tyutin, E. S. Fradkin, Sov. Journ. Phys. 16 (1972) 835.
- [22] E. Braaten, Diagnosis and treatment of the plasmon problem of hot QCD, Nucl. Phys. Proc. Suppl. 23A (1991) 351–361.
- [23] R. D. Pisarski, Resummation and the gluon damping rate in hot QCD, Nucl. Phys. A525 (1991) 175–188.
- [24] J.-P. Blaizot, E. Iancu, Kinetic theory and quantum electrodynamics at high temperature, Nucl. Phys. B390 (1993) 589–620.

- [25] R. Jackiw, V. P. Nair, High temperature response functions and the nonabelian Kubo formula, *Phys. Rev. D*48 (1993) 4991–4998.
- [26] G. Baym, L. Kadanoff, Conservation Laws and Correlation Functions, *Phys. Rev.* 124 (1961) 287.
- [27] A. Denner, S. Dittmaier, Dyson summation without violating ward identities and the goldstone-boson equivalence theorem, *Phys. Rev. D*54 (1996) 4499–4514.
- [28] D. Hou, E. Wang, U. Heinz, N-point functions at finite temperature, *J. Phys. G*24 (1998) 1861.
- [29] E. Wang, U. Heinz, Nonperturbative calculation of the shear viscosity in hot ϕ^4 theory in real time, *Phys. Lett. B*471 (1999) 208.
- [30] C. L. Korpa, P. J. Siemens, L. Xiong, C. M. Ko, Dilepton production from pion-pion annihilation in a nuclear medium, *Phys. Lett. B*246 (1990) 333.
- [31] M. Asakawa, C. M. Ko, P. Levai, X. J. Qiu, Rho meson in dense hadronic matter, *Phys. Rev. C*46 (1992) 1159.
- [32] Y. B. Ivanov, J. Knoll, D. N. Voskresensky, Resonance transport and kinetic entropy, *Nucl. Phys. A*672 (2000) 313.
- [33] M. Effenberger, U. Mosel, Off-shell effects on particle production, *Phys. Rev. C*60 (1999) 051901.
- [34] S. Leupold, Towards a test particle description of transport processes for states with continuous mass spectra, *Nucl. Phys. A*672 (2000) 475.
- [35] W. Cassing, S. Juchem, Semiclassical transport of hadrons with dynamical spectral functions in A + A collisions at SIS/AGS energies, *Nucl. Phys. A*672 (2000) 417.

Comprehensive Interpretation of Thermal Dileptons at the SPS

Hendrik van Hees and Ralf Rapp

Cyclotron Institute and Physics Department, Texas A&M University, College Station, Texas 77843-3366, USA

(Dated: February 2, 2008)

Employing thermal dilepton rates based on medium-modified electromagnetic correlation functions we show that recent dimuon spectra of the NA60 collaboration in central In-In collisions at the CERN-SPS can be understood in terms of radiation from a hot and dense hadronic medium. Earlier calculated ρ -meson spectral functions, as following from hadronic many-body theory, provide an accurate description of the data up to dimuon invariant masses of about $M \simeq 0.9$ GeV, with good sensitivity to details of the predicted ρ -meson line shape. This, in particular, identifies baryon-induced effects as the prevalent ones. We show that a reliable description of the ρ contribution opens the possibility to study further medium effects: at higher masses ($M \simeq 0.9$ -1.5 GeV) 4-pion type annihilation is required to account for the experimentally observed excess (possibly augmented by effects of “chiral mixing”), while predictions for thermal emission from modified ω and ϕ line shapes may be tested in the future.

PACS numbers:

Introduction. Electromagnetic probes occupy a special role in the study of strongly interacting matter produced in energetic collisions of heavy nuclei: once produced, photons and dileptons leave the reaction zone essentially undistorted, carrying direct information from the hot and dense medium to the detectors. While the ultimate goal in analyzing pertinent experiments is to infer signatures of QCD phase transitions (chiral symmetry restoration and/or deconfinement), the more imminent (and relatively easier) objective is to extract medium modifications of the electromagnetic (e.m.) spectral function [1, 2]. Recent data from the NA60 collaboration [3] on dimuon invariant-mass spectra in In-In collisions at the CERN Super-Proton-Synchrotron (SPS) have raised the experimental precision to an unprecedented level, posing serious challenges to theoretical models. After subtraction of late hadronic decay sources (“cocktail”), the excess dimuon radiation exhibits features of a (broadened) peak around the free ρ -mass ($m_\rho \simeq 0.77$ GeV) with a substantial enhancement at both lower and higher invariant masses. Theoretical predictions [4, 5] based on an expanding fireball have confirmed that a broadened ρ -meson, as following from hadronic many-body theory, is in line with the NA60 dimuons, while a dropping ρ -mass [6, 7], characterized by a spectrum centered around a mass of 0.4-0.5 GeV, is inconsistent with the data¹. Both scenarios were consistent with earlier dilepton data by the CERES collaboration [9].

The objective of the present letter is twofold: First, we improve on earlier (shape-based) comparisons of our

predictions to data based on in-medium ρ spectral functions. With a slight modification of the expanding fireball model, we quantitatively reproduce (shape and absolute magnitude of) the low-mass NA60 data in central In-In collisions. The spectral shape turns out to be sensitive to properties of the ρ in some detail. Second, having determined in this way the contributions of the 2π piece to the in-medium e.m. correlator, we investigate remaining enhancements in the $\mu^+\mu^-$ spectrum. Above $M_{\mu\mu} \simeq 0.9$ GeV, using empirical fits to the isovector-vector (V) and -axialvector (A) spectra in vacuum, a calculation with the free emission rate underestimates the data. When including medium effects due to chiral V - A mixing [10], with an assumed critical temperature of $T_c = 175$ MeV (consistent with the fireball), the description improves. While more precise conclusions have to await more accurate data and calculations, our estimates indicate that dilepton radiation from heavy-ion collisions at the SPS emanates from matter close to the expected QCD phase boundary. Finally, we address medium effects on the narrow vector mesons ω and ϕ .

Thermal Dileptons and Medium Effects. The differential rate for thermal lepton-pair production per unit 4-volume and 4-momentum can be expressed as [11, 12, 13]

$$\frac{dN_{ll}}{d^4x d^4q} = -\frac{\alpha^2}{3\pi^3} \frac{L(M^2)}{M^2} \text{Im}\Pi_{\text{em},\mu}^\mu(M, q) f^B(q_0; T) \quad (1)$$

in terms of the retarded e.m. current-current correlator

$$\Pi_{\text{em}}^{\mu\nu}(q) = i \int d^4x e^{iq \cdot x} \Theta(x^0) \langle [\mathbf{J}_{\text{em}}^\mu(x), \mathbf{J}_{\text{em}}^\nu(0)] \rangle, \quad (2)$$

a final-state lepton phase-space factor, $L(M)$, and the thermal Bose function, $f^B(q_0; T)$. $\alpha = e^2/(4\pi) = 1/137$ denotes the fine structure constant and $M^2 = q_0^2 - q^2$ the dilepton invariant mass with energy q_0 and 3-momentum

¹ A reinterpretation of the dropping-mass scenario [2] within a Hidden Local Symmetry approach for vector mesons [8] has not been confronted with dilepton data yet. However, any dropping-mass scenario will face the challenge of accounting for the large portion of strength seen in the NA60 data around the free ρ -mass.

q . The central objective in the following is the evaluation of medium modifications of the e.m. spectral function.

In the low-mass region (LMR, $M \leq 1$ GeV), the free e.m. correlator is saturated by the light vector mesons ρ , ω and ϕ . Our main focus is on the ρ -meson (which dominates the dilepton yield in the LMR), but we also investigate radiation from (and medium effects on) the ω and ϕ . Although their contribution is suppressed relative to the ρ , it is an inevitable consequence of our assumption of the formation of a thermalized medium.

Medium modifications of the ρ -meson are implemented using hadronic many-body theory [4], accounting for interactions in hot hadronic matter via (i) a dressing of its pion cloud with baryon-hole excitations and thermal Bose factors, (ii) direct resonances on surrounding mesons (π , K , ρ) and baryons (nucleons, Δ 's, hyperons, etc.). The effective interaction vertices (coupling constants and form factors) have been carefully constrained by a combination of hadronic and radiative decay branchings, by photoabsorption on nucleons and nuclei, and by $\pi N \rightarrow \rho N$ scattering. The resulting ρ spectral functions in cold nuclear matter comply with constraints from QCD sum rules [14]; they have successfully been employed to dilepton spectra at full SPS energy [9], and to predict an even larger enhancement at lower SPS energies [15, 16]. When averaged over a typical space-time evolution, the in-medium ρ width at SPS amounts to $\Gamma_\rho^{\text{med}} \simeq 350$ MeV, almost 3 times the vacuum value. Close to the expected QCD phase the ρ -resonance has melted, $\Gamma_\rho(T_c) \simeq m_\rho$. ‘‘Rhosobar’’ excitations ($\rho \rightarrow BN^{-1}$) lead to low-mass strength in the ρ spectral function that cannot be represented in Breit-Wigner form.

Medium effects on the ω and ϕ have thus far received less attention, especially in the context of ultrarelativistic heavy-ion collisions (URHICs). For the ω we will employ the same approach as for the ρ [17]. The predicted average ω width in the hadronic phase of URHICs is $\Gamma_\omega^{\text{med}} \simeq 100$ MeV [16]. For the ϕ , collision rates in a meson gas amount to a broadening by ~ 20 MeV at $T=150$ MeV [18]. The dressing of the kaon cloud is presumably the main effect for ϕ modifications in nuclear matter, increasing its width by ~ 25 MeV at saturation density $\varrho_0=0.16$ fm $^{-3}$ [19]. Recent data on ϕ absorption in nuclear photoproduction suggest even larger values [20]. Since a comprehensive treatment of the ϕ in hot and dense matter is not available at present, we will consider the ϕ width as a parameter.

Another important ingredient in our analysis are dilepton production channels beyond the ρ , ω and ϕ . For the free emission rate these can be inferred from the inverse process of e^+e^- annihilation, or hadronic τ decays as measured in Z^0 decays [21], enabling a decomposition of the (isovector part of) e.m. spectral function into 2- and 4-pion pieces. While the former are saturated by the ρ -meson, we fit the latter by an appropriate (onset

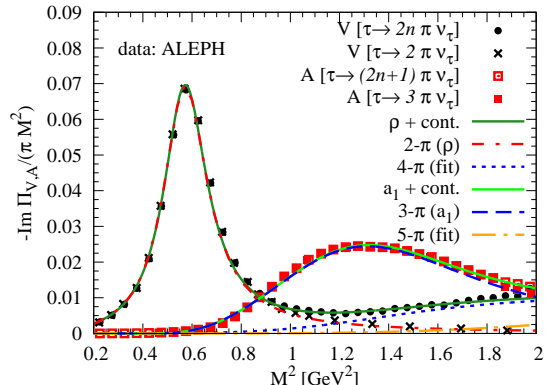


FIG. 1: Free isovector-vector and -axialvector spectral functions as measured in hadronic τ -decays [21], compared to fits to 3- and 4- π contributions (the 2- π piece follows from the ρ).

of a) continuum [22], cf. Fig. 1. Rather than evaluating medium effects in the intermediate-mass region (IMR; $1 \text{ GeV} \leq M \leq 3 \text{ GeV}$) in a phenomenological approach [23], we here employ model-independent predictions based on chiral symmetry. To leading order in temperature one finds a mixing of the free V and A correlators [10],

$$\Pi_{V,A}(q) = (1 - \varepsilon) \Pi_{V,A}^{\text{vac}}(q) + \varepsilon \Pi_{A,V}^{\text{vac}}(q), \quad (3)$$

where $\varepsilon = 2I(T)/f_\pi^2$ ($f_\pi = 93$ MeV: pion decay constant) is determined by the pion tadpole diagram with a loop integral $I(T) = \int (d^3k/(2\pi)^3) f^\pi(\omega_k; T)/\omega_k$ (ω_k : pion energy). For $\varepsilon = 1/2$ (at $T_c^{\text{mix}} \simeq 160$ MeV) V and A correlators degenerate signaling chiral symmetry restoration. Eq. (3) holds in the soft pion limit, i.e., when neglecting the pion 4-momentum in $\Pi_{V,A}$. A more elaborate treatment [24, 25] will broaden and reduce the enhancement around $M \simeq 1.1$ GeV. To estimate the mixing effect on the 4- π contribution to dilepton emission, we evaluate the vector correlator, Eq. (3), with a mixing parameter $\varepsilon = I(T, \mu_\pi)/2I(T_c, 0)$, where critical temperature, $T_c = 175$ MeV, and pion chemical potentials ($\mu_\pi > 0$) are in accord with the thermal fireball evolution discussed below ($m_\pi = 139.6$ MeV). The 2-pion piece has been removed as it is included via the ρ .

Finally, we account for emission from the QGP, even though its contribution at SPS energies is small. We employ the hard-thermal-loop improved emission rate for $q\bar{q}$ annihilation [26], which has the conceptually attractive feature that it closely coincides with the rate in hadronic matter when both are extrapolated to the expected phase transition region. This is suggestive for a kind of quark-hadron duality [4] and has the additional benefit that the emission from the expanding fireball becomes rather insensitive to details of how the phase transition is implemented (such as critical temperature or ‘‘latent heat’’).

Thermal Fireball Model. To calculate dilepton spectra

we need to specify a space-time evolution of A-A collisions. Based on evidence from hadronic spectra and abundances that the produced medium at SPS energies reaches equilibrium [27], we adopt a thermal fireball model focusing on central In-In with collective expansion and hadrochemistry as estimated from data in heavier systems. We use a cylindrical volume expansion [4],

$$V_{\text{FB}}(t) = (z_0 + v_z t) \pi (r_{\perp} + 0.5a_{\perp} t^2)^2, \quad (4)$$

with transverse acceleration $a_{\perp} = 0.08c^2/\text{fm}$, longitudinal velocity $v_z = c$, formation time $\tau_0 = 1\text{fm}/c$ and initial transverse radius $r_{\perp} = 5.15\text{fm}$. With hadrochemical freeze-out at $(\mu_N^{\text{chem}}, T^{\text{chem}}) = (232, 175)\text{ MeV}$ and a total fireball entropy of $S = 2630$ (using a hadron-resonance gas equation of state), we have $dN_{\text{ch}}/dy \simeq 195 \simeq N_{\text{part}}$. Isentropic expansion allows to convert the entropy density, $s(t) = S/V(t)$, into temperature and baryon density. The evolution starts in the QGP ($T(\tau_0) = 197\text{ MeV}$), passes through a mixed phase at $T^{\text{chem}} = T_c$ and terminates at thermal freezeout ($T_{\text{fo}} \simeq 120\text{ MeV}$). In the hadronic phase, meson chemical potentials $(\mu_{\pi, K, \eta})$ are introduced to preserve the observed hadron ratios [4]. When applied to dilepton production, the largest uncertainty resides in the fireball lifetime (being proportional to the dilepton yields), controlled by a_{\perp} and T_{fo} , which can be better constrained once hadronic data for In-In are available. We emphasize, however, that all contributions to the dilepton spectrum (QGP, ρ , ω , ϕ and 4π) are tied to the *same* evolution thus fixing their relative weights.

Systematic Comparison to NA60 Data. Thermal $\mu^+\mu^-$ spectra for central In-In are computed by convoluting the emission rate, Eq. (1), over the fireball evolution,

$$\frac{dN_{ll}}{dM} = \int_0^{t_{\text{fo}}} dt V_{\text{FB}}(t) \int \frac{d^3q}{q_0} \frac{dN_{ll}}{d^4x d^4q} z_{\pi}^n \frac{M}{\Delta y} A(M, q_t, y), \quad (5)$$

where A denotes the detector acceptance which has been carefully tuned to NA60 simulations [28]. The fugacity factor, $z_{\pi}^n = e^{n\mu_{\pi}/T}$, accounts for chemical off-equilibrium in the hadronic phase with $n=2, 3, 4$ for the ρ , ω and 4π contributions, respectively (for the mixing term in Eq. (3) we adopt $\varepsilon \Pi_A^{\text{vac}} \propto z_{\pi}^4$ [25]).

Earlier comparisons [3] of NA60 data to theoretical predictions [5] have focused on the contribution from the ρ -meson which dominates in the LMR. While the shape of the in-medium ρ spectral function describes the experimental spectra well, the absolute yields were overestimated by $\sim 20\%$. This discrepancy can be resolved by an increase of the transverse fireball expansion (a_{\perp}) which, on the one hand, reduces the fireball lifetime by 30% (from 10 to 7 fm/c) and, on the other hand, generates harder transverse-momentum (q_t) spectra, which is also welcome by preliminary data [3]. Consequently, the ρ contribution is reduced, and once QGP emission and correlated charm-decays ($D, \bar{D} \rightarrow \mu^+, \mu^- X$) are added,

the spectra in the LMR are very well described, cf. Fig. 2. Despite the strong ρ broadening, the ρ +QGP+charm

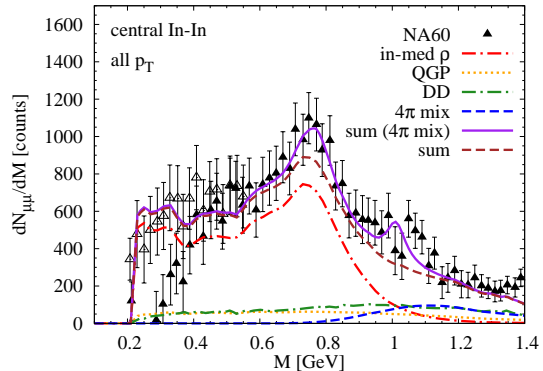


FIG. 2: NA60 excess dimuons [3] in central In-In collisions at SPS compared to thermal dimuon radiation using in-medium e.m. rates. The individual contributions arise from in-medium ρ -mesons [4] (dash-dotted red line), 4π annihilation with chiral $V-A$ mixing (dashed blue line), QGP (dotted orange line) and correlated open charm (dash-dotted green line); the upper dashed line is the sum of the above, while the solid purple line additionally includes in-medium ω and ϕ decays [17].

sources are insufficient to account for the enhancement at $M \geq 0.9\text{ GeV}$. This is not surprising, as 4π contributions are expected to take over (augmented by a pion fugacity factor, $e^{4\mu_{\pi}/T}$). Adding the 4π piece with chiral mixing, Eq. (3), nicely accounts for the missing yield in the IMR, leading to a satisfactory overall description (upper dashed line in Fig. 2). Going one step further still, we argue that in-medium decays of the narrow vector mesons, ω and ϕ , should be included. Whereas their decays after freezeout are subtracted as part of the “cocktail” assuming a vacuum line shape, contributions whose width goes beyond the experimental mass resolution will survive in the excess spectrum. With the predicted in-medium ω spectral function [17] the agreement between theory and data for $M = 0.7\text{--}0.8\text{ GeV}$ seems to improve. The ϕ contribution is implemented with a two-kaon fugacity, $e^{2\mu_K/T}$, and a strangeness suppression factor γ_s^2 ($\gamma_s \simeq 0.75$ at SPS [29]). The ϕ yield following from the fireball model is not incompatible with data, but conclusions on the spectral shape cannot be drawn at present.

To better appreciate the relevance of the in-medium effects, Fig. 3 shows two scenarios where (i) baryon-induced interactions are neglected, and (ii) the vacuum e.m. rate is employed. The latter is ruled out; the meson-gas scenario, which differs from the full result in Fig. 2 by factors of 1.5-2 in the LMR, is not favored by experiment either. Definite conclusions on the in-medium ρ , especially on the baryon-driven enhancement close to the dimuon threshold, require a reduction in systematic uncertainty, indicated by the open and filled data points. Finally, Fig. 4 illustrates the signature of chiral $V-A$ mix-

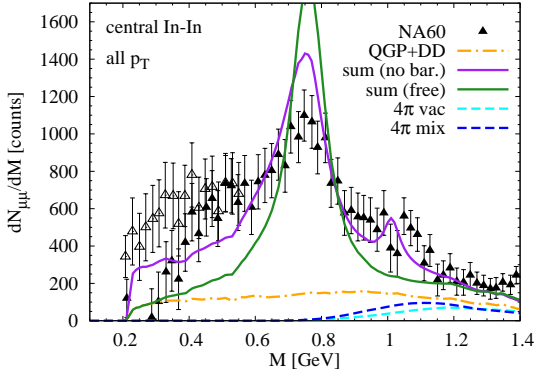


FIG. 3: NA60 data [3] compared to thermal dimuon spectra using (i) in-medium ρ , ω - and ϕ -mesons without baryon effects (+QGP+charm+in-med.-4 π ; solid purple line), and (ii) free ρ (+QGP+charm+free 4 π ; solid green line).

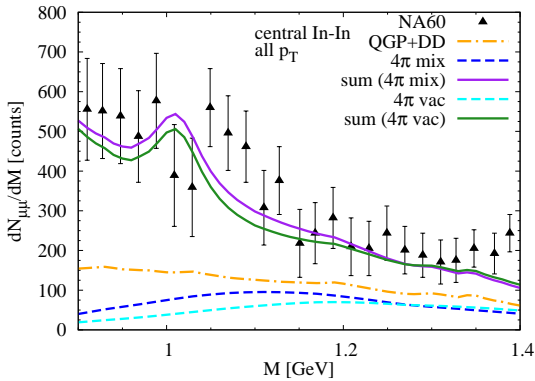


FIG. 4: NA60 data [3] in the IMR compared to thermal dimuon spectra with different implementations of the 4- π contribution, using either its vacuum form (lower dashed line) or including chiral mixing (upper dashed line), and corresponding total spectra (lower and upper solid line, respectively).

ing in the IMR, where the full result of Fig. 2 is compared to a calculation with the 4- π piece in the e.m. rate replaced by its vacuum form (Eq. (3) with $\varepsilon=0$). While the latter is not incompatible with the data, an identification of medium effects requires better precision than currently available (both from theory and experiment).

Conclusion. We have conducted a quantitative investigation of the dimuon excess measured by NA60 in In(158A GeV)-In. Focusing on central collisions, where the notion of thermal radiation is most adequate, we have shown that a medium modified e.m. spectral function properly accounts for absolute yields and spectral shape of the data. While the overall normalization of the spectrum is subject to uncertainties in the underlying fireball model (especially its lifetime), the relative strength of the different components in the spectrum (ρ , ω and ϕ decays,

4- π type annihilation) is fixed. Our results confirm the prevalent role of a strongly broadened ρ -meson in the LMR, but also suggest substantial medium effects on the line shapes of ω and ϕ . In addition, the IMR might bear footprints of chiral V - A mixing, which would support the notion that the matter produced in A-A collisions at the SPS is close to chiral restoration. A more quantitative connection to chiral order parameters, e.g., by evaluating in-medium chiral sum rules [22], should be pursued with high priority.

Acknowledgments. We are grateful to S. Damjanovic and H.J. Specht for discussion and information on the NA60 acceptance. HvH thanks the A. v. Humboldt foundation for support via a Feodor Lynen fellowship. This work was supported in part by a U.S. National Science Foundation CAREER award under grant PHY-0449489.

- [1] R. Rapp, J. Wambach, Adv. Nucl. Phys. **25**, 1 (2000).
- [2] G. E. Brown, M. Rho, Phys. Rept. **396**, 1 (2004).
- [3] S. Damjanovic et al. [NA60 Collaboration] (2005), nucl-ex/0510044; Phys. Rev. Lett. **96**, 162302 (2006).
- [4] R. Rapp, J. Wambach, Eur. Phys. J. A **6**, 415 (1999).
- [5] R. Rapp, J. Phys. G **31**, S217 (2005).
- [6] W. Cassing, W. Ehehalt, C.M. Ko, Phys. Lett. B **363**, 35 (1995).
- [7] G.-Q. Li, C.M. Ko, G. E. Brown, Nucl. Phys. **A606**, 568 (1996).
- [8] M. Harada, K. Yamawaki, Phys. Rept. **381**, 1 (2003).
- [9] G. Agakichiev et al. [CERES Collaboration], Eur. Phys. J. C **41**, 475 (2005).
- [10] M. Dey, V.L. Eletsky, B.L. Ioffe, Phys. Lett. B **252**, 620 (1990).
- [11] L.D. McLerran, T. Toimela, Phys. Rev. D **31**, 545 (1985).
- [12] H.A. Weldon, Phys. Rev. D **42**, 2384 (1990).
- [13] C. Gale, J.I. Kapusta, Nucl. Phys. **B357**, 65 (1991).
- [14] S. Leupold, W. Peters, U. Mosel, Nucl. Phys. **A628**, 311 (1998).
- [15] D. Adamova et al. [CERES Collaboration], Phys. Rev. Lett. **91**, 042301 (2003).
- [16] R. Rapp (2002), nucl-th/0204003.
- [17] R. Rapp, Phys. Rev. C **63**, 054907 (2001).
- [18] L. Alvarez-Ruso, V. Koch, Phys. Rev. C **65**, 054901 (2002).
- [19] D. Cabrera et al., Nucl. Phys. **A733**, 130 (2004).
- [20] J.K. Ahn et al., Phys. Lett. B **608**, 215 (2005).
- [21] R. Barate et al. [ALEPH Collaboration], Eur. Phys. J. **C4**, 409 (1998).
- [22] J. I. Kapusta, E. V. Shuryak, Phys. Rev. **D49**, 4694 (1994).
- [23] G.Q. Li and C. Gale, Phys. Rev. C **58**, 2914 (1998).
- [24] J. V. Steele, H. Yamagishi, I. Zahed, Phys. Rev. D **56**, 5605 (1997).
- [25] M. Urban, M. Buballa and J. Wambach, Phys. Rev. Lett. **88**, 042002 (2002).
- [26] E. Braaten, R. D. Pisarski, T.-C. Yuan, Phys. Rev. Lett. **64**, 2242 (1990).

- [27] P. Braun-Munzinger, K. Redlich, J. Stachel (2003),
nucl-th/0304013.
- [28] S. Damjanovic, private communication (2006).
- [29] F. Becattini, et al., Phys. Rev. **C69**, 024905 (2004).

Dilepton Radiation at the CERN Super Proton Synchrotron

Hendrik van Hees and Ralf Rapp

Cyclotron Institute and Physics Department, Texas A&M University, College Station, Texas 77843-3366, USA
(Dated: February 11, 2013)

A quantitative evaluation of dilepton sources in heavy-ion reactions is performed taking into account both thermal and non-thermal production mechanisms. The hadronic thermal emission rate is based on an electromagnetic current-correlation function with a low-mass region (LMR, $M \lesssim 1$ GeV) dominated by vector mesons (ρ , ω , ϕ) and an intermediate-mass region (IMR, $1 \text{ GeV} \leq M \leq 3 \text{ GeV}$) characterized by (the onset of) a multi-meson continuum. A convolution of the emission rates over a thermal fireball expansion results in good agreement with experiment in the low-mass spectra, confirming the predicted broadening of the ρ meson in hadronic matter in connection with the prevalence of baryon-induced medium effects. The absolute magnitude of the LMR excess is mostly controlled by the fireball lifetime, which in turn leads to a consistent explanation of the dilepton excess in the IMR in terms of thermal radiation. The analysis of experimental transverse-momentum (q_T) spectra reveals discrepancies with thermal emission for $q_T \gtrsim 1$ GeV in noncentral In-In collisions, which we address by extending our calculations by: (i) a refined treatment of ρ decays at thermal freezeout, (ii) primordially produced ρ 's subject to energy-loss, (iii) Drell-Yan annihilation, and (iv) thermal radiation from t -channel meson exchange processes. We investigate the sensitivity of dilepton spectra to the critical temperature and hadro-chemical freezeout of the fireball. The ρ broadening in the LMR turns out to be robust, while in the IMR Quark-Gluon Plasma radiation is moderate unless the critical temperature is rather low.

PACS numbers:

I. INTRODUCTION

Dilepton invariant-mass spectra provide the unique opportunity to directly probe the electromagnetic (e.m.) spectral function of the hot and dense medium created in energetic collisions of heavy nuclei [1, 2, 3]. In the low-mass region (LMR, $M \leq 1$ GeV), this enables the study of modifications of the light vector mesons ($V=\rho$, ω , ϕ) caused by their interactions with the surrounding matter particles and/or changes in the underlying condensate structure. In the intermediate-mass region (IMR, $1 \text{ GeV} \leq M \leq 3 \text{ GeV}$), electromagnetic emission is expected to become continuum-like with rather well-defined strength rendering it a suitable tool to infer temperatures of the excited system (well) before interactions cease (“thermal freezeout”).

Dilepton measurements in heavy-ion collisions at the CERN-SPS (at center-of-mass energies of $\sqrt{s}=17.3$ and 8.8 AGeV) have proven the presence of substantial excess radiation beyond e.m. final-state decays of produced hadrons in both the LMR [4, 5] and IMR [6, 7, 8]. This, in particular, corroborated the presence of interacting *matter* over a duration of ~ 10 - 15 fm/c in central Pb-Au collisions. Moreover, the spectral shape of the excess in the LMR could only be accounted for if major medium modifications of the vacuum ρ -meson line shape were incorporated [1, 2, 3]. Both the implementation of a dropping mass or a strong broadening of its width as following from hadronic many-body approaches, were compatible with the large enhancement observed at masses below the free ρ mass. In addition, with the same underlying fireball model (lifetime and temperature evolution), reasonable agreement with the enhancement mea-

sured in the IMR [7, 8] has been established [9] (as well as with direct photon spectra [10, 11]). The excess for $M \geq 1.5$ GeV was largely attributed to four-pion type annihilations in the hadronic phase, with a strength determined by the vacuum e.m. spectral function, while the calculated Quark-Gluon Plasma (QGP) contribution to the thermal yield amounted to $\sim 30\%$ (~ 10 - 20% in the LMR [12]).

A recent, substantial, improvement in statistics and mass resolution in low-mass dimuon spectra in In-In collisions [13] shows good agreement with predictions for thermal radiation with in-medium ρ -meson broadening as following from hadronic many-body calculations [12, 14]. The shape of the excess radiation is well described from threshold ($M = 2m_\mu$) to $M \simeq 0.9$ GeV, while the absolute yield is overpredicted by about 30%. The latter can be accommodated by a minor adjustment in the thermal fireball evolution (amounting to a 30% lower fireball lifetime), and after inclusion of in-medium ω and ϕ decays (whose contribution is mostly localized around their free mass), as well as four-pion type annihilation (which sets in at masses $M \gtrsim 0.9$ GeV), a quantitative description of the NA60 invariant-mass spectra from threshold to ~ 1.4 GeV in central In-In collisions emerges [15] (see also Refs. [16, 17]). While the inclusive mass spectra are well described, the comparison of the calculations with newly released transverse pair-momentum (q_T) spectra [18] reveals some discrepancies at $q_T > 1$ GeV in semicentral In-In.

In the present article we reiterate the main points of our previous study of dilepton invariant-mass spectra at the SPS, and extend the analysis to q_T spectra. In particular, we conduct a detailed analysis of sources at high

q_T , in terms of (i) an improved treatment of ρ decays at thermal freezeout (which are subject to maximal blue shift due to transverse flow), (ii) a component of primordial (hard-produced) ρ mesons subject to energy loss when traversing the medium (using high- p_T pion spectra as a guideline), (iii) Drell-Yan (DY) annihilation in primordial N - N collisions which we extrapolate to small mass by imposing constraints from real photon production, and (iv) meson t -channel exchange contributions to the thermal production rate which are not included in the many-body vector-meson spectral functions (but which have been found to be a significant source at high q_T in real photon production [11])¹. Another interesting issue which has received little attention thus far is how uncertainties in the critical temperature and hadrochemical evolution of the fireball affect dilepton spectra. For hadro-chemical freezeout we investigate the sensitivity to temperatures in the range $T_{\text{ch}} \simeq 160$ -175 MeV, representative for top SPS energy according to recent thermal model analyses [21, 22]. In connection with updates of lattice-QCD results indicating a critical temperature up to $T_c \simeq 190$ -200 MeV [23], this, in particular, opens the possibility of a chemically equilibrated hot and dense hadronic phase for, say, $T = 160$ -190 MeV, which we also consider. We furthermore conduct a quantitative study of effective slope parameters of the NA60 q_T spectra, where the investigations of the fireball chemistry are supplemented with variations of the transverse flow velocity. Finally, we revisit the consequences of our fireball refinements on our previous evaluations [24] of dielectron spectra as measured by CERES/NA45 in semicentral Pb-Au collisions [4], as well as recent data in central Pb-Au [25].

Our article is organized as follows: in Sec. II we recall the main ingredients of our approach to calculate thermal emission rates, based on the e.m. spectral function in the vacuum (Sec. II A), followed by discussing medium effects on hadronic emission at low mass (due to in-medium ρ , ω and ϕ spectral functions; Sec. II B) and at intermediate mass (due to finite- T chiral mixing; Sec. II C); a new element not included in previous spectral-function calculations are t -channel meson-exchange reactions which therefore are elaborated in more detail in Sec. II D, while we will be brief on partonic emission from a Quark-Gluon Plasma (Sec. II E). In Sec. III we evaluate nonthermal dilepton sources: ρ -meson decays at thermal freezeout (whose decay kinematics differ from thermal radiation; Sec. III A), an estimate of primordial ρ 's at large q_T (which do not thermalize; Sec. III B), and Drell-Yan an-

nihilation (with an extrapolation to low mass; Sec. III C). In Sec. IV we recollect the ingredients to our thermal fireball model for the space-time evolution of the medium in heavy-ion collisions, including variations in hadrochemical freezeout and critical temperature. In Sec. V we implement all dilepton sources into the fireball to compute dimuon invariant-mass (Sec. V A) and transverse-momentum spectra (Sec. V B) in comparison to NA60 data; the effect of hadrochemistry and T_c on NA60 spectra is worked out in Sec. V C, followed by a slope analysis of q_T spectra (Sec. V D) in the context of which we also investigate different radial flow scenarios; the improvements in the fireball and dilepton source description as deduced from the NA60 data are confronted with previous and new CERES/NA45 data in Sec. V E. Sec. VI contains a summary and conclusions.

II. THERMAL DILEPTON RADIATION

A. Emission Rate and Electromagnetic Spectral Function

In thermal equilibrium the rate of dilepton emission per four-volume and four-momentum can be related to the hadronic e.m. spectral function as [26]

$$\frac{dN_{ll}}{d^4x d^4q} = - \frac{\alpha^2}{3\pi^3} \frac{L(M^2)}{M^2} \text{Im} \Pi_{\text{em},\mu}^\mu(M, q; \mu_B, T) \times f^B(q_0; T), \quad (1)$$

which in this article we will refer to as thermal dileptons (or thermal radiation). The retarded e.m. current-current correlator is given by

$$\Pi_{\text{em}}^{\mu\nu}(q) = i \int d^4x e^{iq \cdot x} \Theta(x^0) \langle [\mathbf{J}_{\text{em}}^\mu(x), \mathbf{J}_{\text{em}}^\nu(0)] \rangle, \quad (2)$$

where $\alpha = e^2/(4\pi) = 1/137$ denotes the fine structure constant, $M^2 = q_0^2 - q^2$ the dilepton invariant mass squared with energy q_0 and three-momentum q , and $f^B(q_0; T)$ the thermal Bose distribution function (T : temperature, μ_B : baryon chemical potential). The final-state lepton phase space factor,

$$L(M) = \left(1 + \frac{2m_l^2}{M^2}\right) \sqrt{1 - \frac{4m_l^2}{M^2}}, \quad (3)$$

depends on the lepton mass, $m_l = 0.511(105.6)$ MeV for electrons (muons; $l = e, \mu$), but quickly approaches one above threshold, $M = 2m_l$ (e.g., $L(M = 0.3 \text{ GeV}) = 0.89$ for dimuons).

In the vacuum, the e.m. spectral function, $\text{Im} \Pi_{\text{em}}(M)$, is well known from e^+e^- annihilation into hadrons. It is characterized by the light vector resonances $\rho(770)$, $\omega(782)$ and $\phi(1020)$ at low mass (vector dominance model (VDM)) and a perturbative quark-antiquark continuum

¹ Note that contributions (ii)-(iv) have little bearing on the inclusive invariant-mass spectra which are predominantly populated by low-momentum sources with $q_T \lesssim 1$ GeV. Therefore, the inclusion of these contributions does not upset our earlier description of inclusive M spectra in terms of thermal radiation and freezeout ρ 's. Initial results of these studies have been reported in Refs. [19, 20].

at higher mass,

$$\text{Im } \Pi_{\text{em}} = \begin{cases} \sum_{V=\rho,\omega,\phi} \left(\frac{m_V^2}{g_V}\right)^2 \text{Im } D_V, & M \lesssim M_{\text{dual}} \\ -\frac{N_c M^2}{12\pi} \left(1 + \frac{\alpha_s}{\pi} + \dots\right) \sum_i (e_i)^2, & M \gtrsim M_{\text{dual}} \end{cases} \quad (4)$$

($N_c = 3$: number of colors, α_s : strong coupling constant, e_i : the electric quark charge in units of the electron charge, and i is running over up, down and strange quark flavors for $M < 3$ GeV). $M_{\text{dual}} \simeq 1.5$ GeV signifies a “duality” scale above which the total cross section for $e^+e^- \rightarrow$ hadrons (and thus the strength of $\text{Im } \Pi_{\text{em}}$) essentially behaves perturbatively with little impact from subsequent hadronization. Since the hadronic final state in e^+e^- annihilation approximately resembles a thermal medium (except for strangeness), time-reversal invariance of strong and electromagnetic interactions implies that, to leading order in temperature, the equilibrium dilepton emission rate of hadronic matter is determined by the free e.m. correlator, $\Pi_{\text{em}}^{\text{vac}}$, cf. also Refs. [9, 27].

In the hadronic basis, the e.m. spectral function is dominated by the isovector (ρ) channel while the isoscalar channels are suppressed. The SU(3)-flavor quark model, *e.g.*, predicts a weighting of 9:1:2 for the e.m. couplings of ρ , ω and ϕ , respectively. These values are roughly in line with the electromagnetic decay widths $\Gamma_{V \rightarrow ee} = \frac{4\pi\alpha^2}{3} m_V / g_V^2 = 7.0, 0.60$ and 1.27 keV for ρ , ω and ϕ , respectively (the empirical values of the ϕ width should be corrected for phase space by the ratio $m_\omega/m_\phi=0.77$).

The vector-isovector channel furthermore provides the most direct link to chiral symmetry: under chiral rotations, the ρ channel transforms into the axialvector-isovector (a_1) one. Thus, the a_1 is commonly identified as the chiral partner of the ρ .² The pertinent spectral functions in free space have been accurately measured in hadronic τ decays [29, 30], cf. Fig. 1, and evaluated in terms of chiral order parameters (f_π , four-quark condensates) using Weinberg sum rules [31, 32]. To leading order in temperature (*i.e.*, for a hot pion gas), the mutual in-medium modifications of vector and axialvector channels can be inferred from chiral symmetry alone, as will be discussed in Sec. II C below.

The main objective for the remainder of this Section is a realistic evaluation of the in-medium e.m. spectral function. In the LMR, we assume that vector dominance remains valid in the medium. Our calculations of the V -meson spectral functions, $A_V = -2 \text{Im } D_V$, utilize effective hadronic Lagrangians, where the interaction vertices and coupling constants are constrained

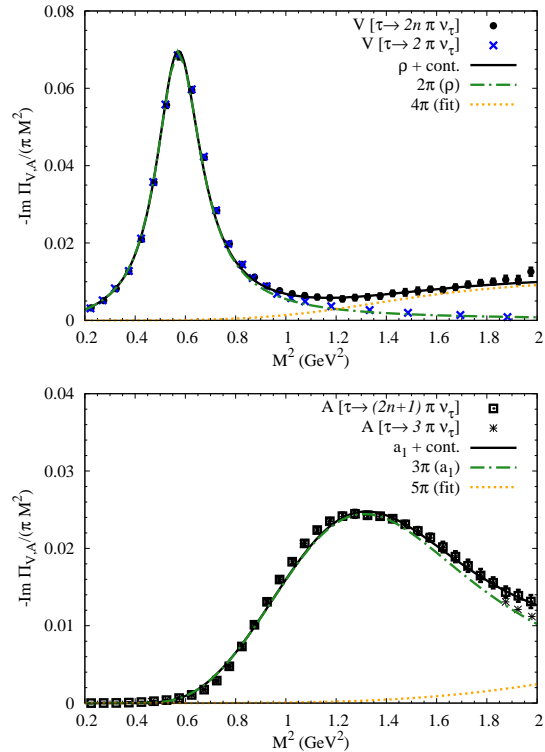


FIG. 1: (Color online) Free isovector-vector (upper panel) and -axialvector (lower panel) spectral functions as measured in hadronic τ -decays [29], compared to fits with three- and four-pion contributions (the two-pion piece follows from the previously calculated ρ propagator [33]).

by gauge and chiral symmetry, as well as empirical decay and scattering data. Medium effects are calculated within hadronic many-body theory *without* introducing explicit medium dependencies of the bare parameters in the Lagrangian (which require information beyond the effective hadronic theory). A careful comparison of our predictions for dilepton spectra in heavy-ion collisions with experiment can then serve as a basis for identifying medium effects that go beyond the hadronic many-body framework.

B. Hadronic Emission at Low Mass: In-Medium Vector Mesons

Since the prevalent role in the LMR of the e.m. correlator is played by the ρ meson, the latter has been the main focus for studying in-medium effects in thermal dilepton production. However, with the current precision of the NA60 dilepton data on the 10-20% level, thermal emission from ω and ϕ decays becomes relevant. Their contributions are an inevitable consequence of the formation of a thermal medium, and we therefore incorporate

² An alternative has recently been suggested in Ref. [28] in terms of the “Vector Manifestation” (VM) of chiral symmetry, where the chiral partner of the (longitudinal) ρ is identified with the pion.

them along with pertinent medium modifications.

Within the VDM the in-medium e.m. correlator in the LMR remains directly proportional to the vector-meson spectral functions as in Eq. (4). The key objective is then to calculate the vector-meson selfenergies at finite temperature and baryon density (ϱ_B), Σ_V , figuring into the propagator as

$$D_V = \frac{1}{M^2 - (m_V^{(0)})^2 - \Sigma_{VP} - \Sigma_{VM} - \Sigma_{VB}}. \quad (5)$$

Here, $m_V^{(0)}$ denotes the bare mass, and the selfenergy contributions are classified into three types: (i) medium modifications of the pseudoscalar meson cloud, Σ_{VP} ($P = \pi\pi, 3\pi$ or $K\bar{K}$ for $V = \rho, \omega$ or ϕ , respectively), and direct interactions of V with (ii) mesons and (iii) baryons from the surrounding heat bath, Σ_{VM} and Σ_{VB} . One should also note that without the implementation of a phase transition into a realistic hadronic model (which has not been achieved thus far), many-body calculations are to be considered as an extrapolation beyond a certain temperature and/or density. We estimate that, under SPS conditions, our approach should be reliable up to temperatures of about $T \simeq 150$ MeV, where the total hadron density amounts to about $\varrho_h \simeq 2\varrho_0$ (with a net-baryon density of about $0.7\varrho_0$), while it has increased to about $5\varrho_0$ at the expected phase boundary at $T_c \simeq 175$ MeV. In the following we briefly recall the construction of, and constraints on, the underlying effective Lagrangians.

1. ρ Meson

The first step in the calculation of a realistic ρ propagator is a proper description of its coupling to the pion cloud in vacuum (giving rise to its two-pion decay width, $\Gamma_{\rho\pi\pi}(m_\rho) \simeq 150$ MeV). A suitable chiral effective Lagrangian can be obtained by, *e.g.*, introducing the vector fields as local gauge fields into the chiral pion Lagrangians and implementing the photon field via vector dominance [34, 35],

$$\begin{aligned} \mathcal{L}_{\pi\rho\gamma} = & g_\rho \vec{\rho}_\mu \cdot (\vec{\pi} \times \partial^\mu \vec{\pi}) \\ & - \frac{1}{2} g_\rho^2 [\vec{\rho}_\mu \cdot \vec{\rho}^\mu \vec{\pi}^2 - \vec{\rho}^\mu \cdot \vec{\pi} \vec{\rho}_\mu \cdot \vec{\pi}] \\ & + \frac{em_\rho^2}{g_\rho} A_\mu \rho_3^\mu. \end{aligned} \quad (6)$$

The pertinent two-pion and one-pion-tadpole diagrams specify the ρ 's pion cloud in the vacuum with a transverse selfenergy (using a proper regularization procedure). The coupling constant, g_ρ , a cutoff parameter, Λ_ρ (to render the pion loops finite), and the bare ρ -mass, $m_\rho^{(0)}$, can be readily adjusted to reproduce P -wave $\pi\pi$ scattering phase shifts and the pion e.m. formfactor in free

space [33]. This model also predicts the two-pion part of the τ -decay data well, cf. Fig. 1.

Based on the above model in the vacuum, we adopt the in-medium ρ propagator from the hadronic many-body approach developed in Refs. [24, 33, 36], to which we refer the reader for more details. Modifications of the pion cloud are induced by an in-medium π propagator which is dressed with standard NN^{-1} and ΔN^{-1} excitations in nuclear matter, supplemented with appropriate vertex corrections to maintain a conserved vector current. While the calculations of nuclear pion-cloud modifications are often restricted to the case of vanishing ρ three-momentum ("back-to-back" kinematics), we here employ the extension to finite three-momentum worked out in Ref. [33]. This is particularly important in that it enables (i) to constrain the corresponding medium effects by nuclear photo-absorption data [37] and $\pi N \rightarrow \rho N$ scattering, and (ii) a meaningful application to dilepton transverse momentum spectra. At finite temperature, where a (large) fraction of nucleons is thermally excited into baryons, only the nucleon density should be employed. To account for (i) $\pi B N^{-1}$ excitations into higher resonances and (ii) $\pi B_2 B_1^{-1}$ excitations ($B_1 \neq N$), an "effective" nucleon density $\varrho_N^{\text{eff}} \equiv \varrho_N + 0.5\varrho_B$ ($B \neq N$) has been used in the pion propagators [24] (we estimate the uncertainty implied by this prescription to be about $\pm 10\%$). In addition, effects of antibaryons are added by multiplying ϱ_N^{eff} with a factor $(1 + \bar{p}/p)$ where \bar{p}/p denotes the measured antiproton-to-proton ratio (this is a small correction at SPS energies but becomes essential at RHIC [38]). The modifications of the pion cloud induced by a pion gas have been found to be rather small in various analyses [39, 40, 41, 42, 43]. A large part of the pion-gas effect is already provided by the Bose enhancement factor, $[1 + f^\pi(\omega_1) + f^\pi(\omega_2)]$ [41], while low-energy $\pi\pi$ interactions are suppressed by chiral symmetry. The former is included in the present calculations, but the latter are neglected (being much weaker than baryon-induced effects).

Direct interactions of the (bare) ρ with baryons and mesons have been approximated by resonance interactions (pion-exchange interactions, including spacelike pions, are implicit in the nuclear modifications of the pion-cloud part). For $\rho + N \rightarrow B$ (*i.e.*, $\rho B N^{-1}$ excitations), this includes both S -wave scattering into negative-parity baryons and P -wave scattering into positive-parity baryons, with $B = N(1520), \Delta(1620), \Delta(1700)$ and $N, \Delta(1232), N(1440), N(1720), \Delta(1905), N(2000)$, respectively. An estimate of the involved couplings and cutoff parameters can be obtained by reproducing the empirical $B \rightarrow \rho N, \gamma N$ decay widths, but more reliable constraints follow from comprehensive scattering data. For the present model, in addition to hadronic decay branchings, cold nuclear matter effects induced in both the pion cloud and via resonant ρN interactions have been checked against total photoabsorption cross sections on the nucleon and nuclei [37], as well as $\pi N \rightarrow \rho N$ scattering data [1, 44]. Whereas γN and ρN scattering

relates to the low-density limit of the ρ -spectral function, γA data constrain $\text{Im} D_\rho(M \rightarrow 0, q)$ close to nuclear saturation density, $\varrho_0 = 0.16 \text{ fm}^{-3}$. For the finite-temperature case, excitations on hyperons of the type $\rho Y_2 Y_1^{-1}$ are incorporated for $Y_1 = \Lambda(1115), \Sigma(1192)$ and Y_2 resonances with quantum numbers equivalent to the nonstrange sector and appreciable empirical decay widths into ρ 's and/or photons. $\rho B_2 B_1^{-1}$ excitations on thermally excited nonstrange baryons (*e.g.*, $\Delta(1930)\Delta^{-1}$) are included but turned out to be small.

In the meson gas, direct ρ - M interactions on thermal mesons ($M = \pi, K, \rho$) have been scrutinized in Ref. [45], again based on s -channel resonance dominance, $\rho M \rightarrow R$, and with pertinent Lagrangians satisfying basic requirements of vector-current conservation and chiral symmetry. As in the case of excited baryons, the couplings and cutoffs have been estimated from combined hadronic and radiative decay widths. The most important contributions to the ρ propagator arise from axialvector mesons, $R = a_1(1260)$ (chiral partner of the ρ), $h_1(1170)$ and $K_1(1270)$, as well as the $\omega(782)$.

Another valuable consistency check for the in-medium properties of hadrons are QCD sum rules. The latter relate a dispersion integral over a spectral function to an operator product expansion (OPE) for the correlation function at spacelike four-momenta, $q_\mu q^\mu < 0$. The nonperturbative coefficients of the OPE involve quark and gluon condensates whose in-medium modifications reflect upon (an energy integral over) the spectral function. Generically, a reduction of the condensates leads to a softening of the spectral function, *i.e.*, a shift of strength to lower mass. However, as has been elaborated in Ref. [46] for the case of cold nuclear matter, the additional low-mass strength in the in-medium ρ spectral function can be due to both a reduced mass or a broadening of the width, or a combination thereof. The pertinent “allowed band” for width and mass values at normal nuclear matter density has been quantified in Ref. [46]. For the ρ spectral function employed here [24], one finds a mass and width of $(m_\rho, \Gamma_\rho)|_{\varrho_0} \simeq (820, 450) \text{ MeV}$ at nuclear saturation density and vanishing three-momentum. These values turn out to be consistent with the band derived in Ref. [46] (*cf.* middle panel of Fig. 2 in there), but more extensive (*i.e.*, different densities and temperatures) and quantitative comparisons are certainly desirable (*e.g.*, the low-mass strength (shoulder) in the ρ spectral function which is induced by “Pisobar” ($\pi\Delta N^{-1}$) and “Rhosobar” ($\rho B N^{-1}$) excitations, cannot be represented in Breit-Wigner form as underlying Ref. [46]). However, at this point, there is no indication for changes in the bare parameters in the Lagrangian, *i.e.*, at nuclear saturation density hadronic many-body effects saturate the reduction of quark and gluon condensates as required by QCD sum rules.

The ρ -spectral functions under fireball conditions representing the evolution of the hadronic phase at full SPS energy ($\sqrt{s} = 17.3 \text{ AGeV}$) are displayed in the upper panel of Fig. 2. The resonance strongly broadens with lit-

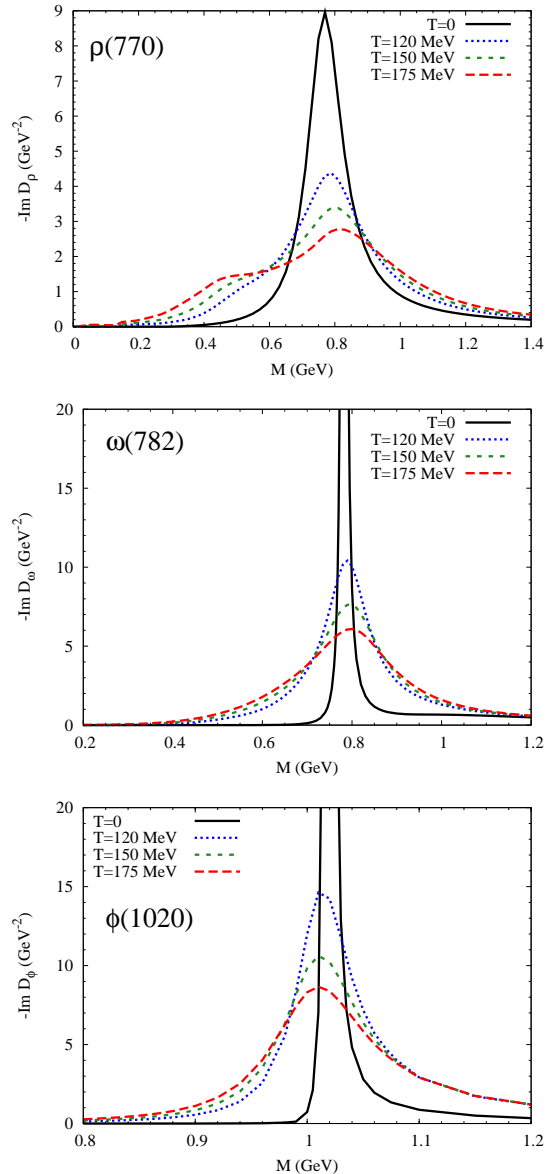


FIG. 2: (Color online) In-medium spectral functions of ρ (upper panel), ω (middle panel) and ϕ (lower panel) under conditions representative for the time evolution of heavy-ion collisions at full SPS energy: $(\mu_N, \mu_\pi, \mu_K, T) [\text{MeV}] = (232, 0, 0, 175), (331, 39, 62, 150), (449, 79, 136, 120)$ and vacuum for the dotted, short-dashed, long-dashed and solid lines, respectively.

tle, if any, mass shift, essentially leading to its “melting” close to the expected phase boundary. These features are a rather generic consequence of a multilevel excitation spectrum in which real parts occur with altering signs while imaginary parts are negative definite and strictly

add up. Also note the development of a pronounced low-energy strength around $M = 0.4$ GeV which leads to a very large enhancement over the vacuum spectral function (and will be augmented by thermal Bose factors in the dilepton rate). At lower temperatures, the presence of meson-chemical potentials (for π , K , η) implies higher meson and baryon densities than in chemical equilibrium at a given temperature, entailing stronger medium effects. The build-up of the chemical potentials (necessary to preserve the experimentally observed hadron ratios throughout the hadronic cooling) therefore facilitates the observation of in-medium effects in the dilepton spectra. A strong broadening of the ρ in hot and dense matter has also been reported in other calculations at finite T and ϱ_B [47, 48].

The in-medium ρ -spectral function has been rather extensively employed to calculate dilepton spectra in heavy-ion collisions. At full SPS energy it has been implemented into fireball models [24, 36], transport simulations [49] and hydrodynamic evolutions [50], with fair success (and consistency) in describing CERES/NA45 data in central and semicentral Pb-Au collisions [4]. When averaged over a typical space-time evolution, the in-medium ρ width at SPS amounts to $\Gamma_\rho^{\text{med}} \simeq 350\text{--}400$ MeV, almost three times its vacuum value, implying $\Gamma_\rho(T_c) \simeq m_\rho$ when extrapolated to the expected QCD-phase boundary. Despite an experimental pion-to-baryon ratio of $\sim 5 : 1$, medium effects induced by baryons have been identified as essential at SPS energies early on [36]. This has led to the prediction of an even larger excess at lower beam energies, which was tentatively confirmed in a 40 AGeV Pb+Au run of CERES/NA45 [5] (albeit with rather large errors). The lightlike limit of the ρ -spectral function has been applied to calculate thermal photon spectra [11], supplemented with meson-exchange reactions which are not included in $\text{Im} D_\rho$ (these become significant at momenta above 1 GeV and will be discussed in Sec. II D below). After convolution over the same fireball model as used for dileptons, the direct-photon excess observed by WA98 in central Pb-Pb reactions at SPS [10], as well as by PHENIX in central Au-Au collisions at RHIC [51], can be reasonably well accounted for (with additional primordial and QGP photon sources, the latter being subdominant at SPS). The in-medium ρ -spectral function following from hadronic many-body theory [24] has thus passed a rather wide range of both theoretical and phenomenological tests, in both cold nuclear as well as hot hadronic matter.

2. ω Meson

Medium effects on the ω have received less attention so far, especially in the context of ultrarelativistic heavy-ion collisions (URHICs) where its dilepton decays are dominated by free decays after thermal freezeout (commonly referred to as a ‘‘cocktail’’ contribution). We here adopt the same approach as for the ρ , following Ref. [38]. In

the vacuum, the hadronic ω width, $\Gamma_{\omega \rightarrow 3\pi}$, is composed to approximately equal parts of a direct $\omega \rightarrow 3\pi$ and a $\omega \rightarrow \rho\pi$ coupling, represented by anomalous terms in the interaction Lagrangian,

$$\mathcal{L}_{\omega\rho\pi} = G_{\omega\rho\pi} \epsilon_{\mu\nu\sigma\tau} \omega^\mu \partial^\nu \bar{\rho}^\sigma \cdot \partial^\tau \bar{\pi}, \quad (7)$$

$$\mathcal{L}_{\omega 3\pi} = G_{\omega 3\pi} \epsilon_{\mu\nu\sigma\tau} \omega^\mu (\partial^\nu \bar{\pi} \times \partial^\sigma \bar{\pi}) \cdot \partial^\tau \bar{\pi}. \quad (8)$$

With a hadronic formfactor cutoff-parameter, $\Lambda_{\omega\rho\pi} = 1$ GeV, and using the VDM [45], one finds for the radiative decay width $\Gamma_{\omega \rightarrow \pi\gamma} = 0.72$ MeV which approximately agrees with the updated experimental value of 0.76 ± 0.03 MeV [52].

In cold nuclear matter, the renormalization of the π - ρ cloud has been found to be rather sensitive to the medium effects on the ρ [38, 48, 53, 54], which is due to the fact that the $\omega \rightarrow \pi\rho(\rightarrow \pi\pi\pi)$ decay proceeds via the low-mass tail of the ρ -spectral function below its nominal mass of 770 MeV. In Ref. [53] 80% of the estimated in-medium broadening at nuclear saturation density is attributed to the in-medium ρ spectral function (taken from Ref. [33]), resulting in $\Gamma_{\omega P}(\varrho_0) \simeq 60$ MeV. Likewise, a large contribution to second order in the nuclear density, $\mathcal{O}(\varrho_N^2)$, to $\Gamma_{\omega P}(\varrho_N)$ arises due to the simultaneous dressing of both π and ρ [54]. Following Ref. [38], we restrict ourselves to the impact of the in-medium ρ by folding the phase space in the $\omega \rightarrow \pi\rho$ -decay width over the spectral function evaluated in the previous section,

$$\Gamma_{\omega \rightarrow \rho\pi}(s) = \frac{2G_{\omega\rho\pi}^2}{8\pi} \int_0^{M_{\text{max}}} \frac{M dM}{\pi} A_\rho(M) 2q_{\text{cm}}^3 \times [1 + f^\pi(\omega_\pi) + f^\rho(E_\rho)] F_{\omega\rho\pi}(q_{\text{cm}})^2, \quad (9)$$

where $M_{\text{max}} = \sqrt{s} - m_\pi$, $\omega_\pi^2 = m_\pi^2 + q_{\text{cm}}^2$, $E_\rho^2 = M^2 + q_{\text{cm}}^2$, and q_{cm} is the three-momentum of π and ρ in the rest frame of the ω . In addition we account for cold-nuclear matter effects due to the two most important direct ω - N excitations, $\omega N(1520)N^{-1}$ and $\omega N(1650)N^{-1}$, as identified in Ref. [55] in a coupled-channel analysis of empirical vector-meson nucleon scattering amplitudes. Recent measurements of $\pi^0\gamma$ -invariant mass spectra in photon-induced production off hydrogen and Nb targets have revealed a low-mass shoulder [56] that has been interpreted as reduced ω mass in nuclear matter. However, this interpretation is not free of controversy and may also be explained by a large increase of the ω width to about 90 MeV [57]. The latter is compatible with the ω propagator employed in the present paper.

Finite-temperature effects on the ω propagator include Bose-enhancement factors in the π - ρ cloud, the in-medium ρ propagator in Eq. (9), a schematic estimate of the inelastic $\pi\omega \rightarrow \pi\pi$ width based on Ref. [58], and a full calculation of the thermal $\omega + \pi \rightarrow b_1(1235)$ loop [38].

The predicted average ω width in the hadronic phase of URHICs is $\Gamma_\omega^{\text{med}} \simeq 100$ MeV [12], cf. middle panel of Fig. 2, quite consistent with the results of Ref. [59]. This has the interesting consequence [38] that if dilepton spectra

in HICs show a structure of ~ 100 MeV width in the ρ -/ ω mass region, it would be an unambiguous signature of the in-medium ω spectral function since it is narrower than the lower limit given by a free ρ contribution, $\Gamma_\omega^{\text{med}} < \Gamma_\rho^{\text{vac}} \simeq 150$ MeV.

3. ϕ Meson

For the ϕ , collision rates in a meson gas have been estimated to amount to a broadening by ~ 20 MeV at $T = 150$ MeV [60]. The dressing of the kaon cloud is presumably the main effect for ϕ modifications in nuclear matter, increasing its width by ~ 25 MeV at saturation density [61]. Recent data on ϕ absorption in nuclear photoproduction suggest substantially larger values [62]. Since a quantitative, empirically constrained treatment of the ϕ in hot and dense matter is not available at present, we will consider the ϕ width as a parameter. Following Ref. [15] we augment the microscopic calculations of Ref. [38] by a factor of 4 to roughly agree with the phenomenological values extracted from nuclear photoproduction [62]. The corresponding ϕ spectral functions under SPS conditions are displayed in the lower panel of Fig. 2. The average width over the fireball evolution amounts to $\Gamma_\phi^{\text{med}} \simeq 80$ MeV.

C. Hadronic Emission at Intermediate Mass: Multi-Pion Annihilation

Above the ϕ mass, the hadronic structure of the (vacuum) e.m. correlator becomes more involved being characterized by overlapping broad resonances which combine into continuum-like multi-meson states (most notably isovector four-pion states), recall Fig. 1. To estimate medium effects in this regime, we take recourse to model-independent predictions following from a low-temperature expansion evaluated using chiral-reduction techniques for the corresponding matrix elements involving thermal pions. This method has been first worked out in Ref. [63] in the chiral limit ($m_\pi = 0$) and leads to the chiral mixing formula for the isovector part of vector and axialvector correlators,

$$\begin{aligned} \Pi_V(q) &= (1 - \varepsilon) \Pi_V^{\text{vac}}(q) + \varepsilon \Pi_A^{\text{vac}}(q), \\ \Pi_A(q) &= \varepsilon \Pi_V^{\text{vac}}(q) + (1 - \varepsilon) \Pi_A^{\text{vac}}(q). \end{aligned} \quad (10)$$

The mixing coefficient ε is determined by pion tadpole diagrams via a loop integral

$$\varepsilon = \frac{2}{f_\pi^2} \int \frac{d^3k}{(2\pi)^3 \omega_k^\pi} f^\pi(\omega_k^\pi, T) \quad (11)$$

(ω_k^π : on-shell pion energy, $f_\pi = 93$ MeV: pion decay constant). For $\varepsilon \rightarrow 1/2$, V and A correlators degenerate signaling chiral-symmetry restoration (at $T_c^{\text{mix}} \simeq 160$ MeV). Note that the admixture of the axialvector part in the

$M = 1$ -1.5 GeV region (which corresponds to the a_1 resonance) fills in the ‘‘dip’’ structure of the vector correlator (recall Fig. 1); for $\varepsilon \rightarrow 1/2$ both spectral functions merge into the perturbative-QCD continuum for $M \geq 1$ GeV which has been interpreted [1] as a lowering of the quark-hadron duality scale, M_{dual} , cf. Eq. (4). The simple form of Eq. (10) only holds in the soft-pion limit, *i.e.*, when neglecting the pion four-momenta in $\Pi_{V,A}$. More elaborate treatments [64, 65] will broaden and somewhat reduce the enhancement in the $M \simeq 1$ -1.5 GeV region [66]. We here implement the mixing effect on the (isovector) four-pion part utilizing Eq. (10) with a mixing parameter $\hat{\varepsilon} = \frac{1}{2} \varepsilon(T, \mu_\pi) / \varepsilon(T_c, 0)$ with finite pion mass ($m_\pi = 139.6$ MeV), critical temperature, T_c , and pion chemical potentials ($\mu_\pi > 0$) implemented as an overall fugacity factor, $z_\pi = e^{\mu_\pi/T}$, in Boltzmann approximation (μ_π varies according to the thermal fireball evolution discussed in Sec. IV below). The two-pion piece, as well as the three-pion piece corresponding to a_1 decay, $a_1 \rightarrow \pi + \rho$, have been removed as they are included via the ρ -spectral function as discussed above. A detailed analysis of the derivation of Eq. (10) in the presence of a finite pion-chemical potential leads to the following expression for the mixing effect on the vector-isovector current correlation function:

$$\Pi_V(q) = (1 - \hat{\varepsilon}) z_\pi^4 \Pi_{V,4\pi}^{\text{vac}} + \frac{\hat{\varepsilon}}{2} z_\pi^3 \Pi_{A,3\pi}^{\text{vac}} + \frac{\hat{\varepsilon}}{2} (z_\pi^4 + z_\pi^5) \Pi_{A,5\pi}^{\text{vac}}. \quad (12)$$

D. Hadronic Emission at High Momentum: Meson t -Channel Exchange

As discussed in the Introduction, a current discrepancy in the theoretical description of the NA60 data concerns the dilepton yield at high transverse pair-momentum, $q_T > 1$ GeV, for masses $M \leq 1$ GeV. It is therefore important to scrutinize the vector-meson spectral function calculations for high momentum sources. The latter are typically associated with t -channel meson exchanges, rather than s -channel resonances whose decay products are suppressed at momenta far off the resonance. In the spectral-function approach, t -channel exchange processes are encoded in medium modifications of the pseudoscalar meson cloud. As elaborated in Sec. II B 1, the pion-cloud modifications of the ρ explicitly include interactions with baryons, but not with thermal mesons. Consequently, t -channel meson exchanges are present for ρB interactions, but not for $\rho\pi$. E.g., the experimental $\pi N \rightarrow \rho N$ cross section is properly reproduced at large \sqrt{s} where t -channel π exchange dominates. Indeed, it has been found in Ref. [11] in the context of thermal photon production that t -channel exchanges in $\rho + \pi \rightarrow \pi + \gamma$ outshine the contributions from the ρ -spectral function at momenta above ~ 1 GeV for $T = 200$ MeV (at smaller temperatures the importance of t -channel exchanges is reduced). Most notably, ω exchange emerged as the single most important hadronic high- q_T thermal photon source.

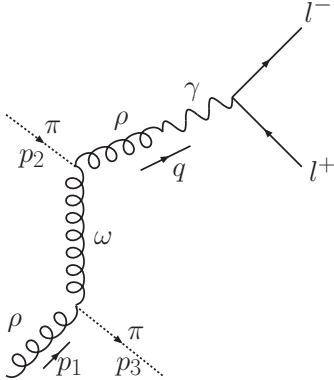


FIG. 3: The Feynman diagram corresponding to the annihilation of a ρ meson via ω -meson exchange in the t channel.

To estimate the relevance of t -channel exchanges in $\pi\rho$ scattering for thermal dileptons, we adopt the same sim-

plified treatment as in Ref. [11], properly extended to a finite invariant mass of the virtual photon (lepton pair): rather than implementing the pertinent diagram into the ρ selfenergy, we employ the standard kinetic theory expression for the thermal production rate

$$\begin{aligned} \frac{dN_{\pi\rho\rightarrow\pi ll}^{(t\text{-ch})}}{d^4x d^4q} &= \int \frac{d^3p_1}{2\omega_{p_1}^\rho (2\pi)^3} \int \frac{d^3p_2}{2\omega_{p_2}^\pi (2\pi)^3} \int \frac{d^3p_3}{2\omega_{p_3}^\pi (2\pi)^3} \\ &\times (2\pi)^4 \delta^{(4)}(p_1 + p_2 - p_3 - q) \sum |\mathcal{M}_{\pi\rho\rightarrow\pi ll}|^2 \\ &\times [1 + z_\pi f^B(\omega_{p_3}^\pi; T)] \frac{z_\pi^3 f^B(\omega_{p_1}^\rho; T) f^B(\omega_{p_2}^\pi; T)}{4(2\pi)^6}, \end{aligned} \quad (13)$$

which allows to calculate the contribution for $\pi + \rho \rightarrow \pi + l^+ + l^-$ in terms of the corresponding matrix element, $\mathcal{M}_{\pi\rho\rightarrow\pi ll}$, in Born approximation. The latter substantially facilitates the task of maintaining gauge invariance. For the $\rho\omega\pi$ vertex, the anomalous-coupling Lagrangian, Eq. (7), is used to calculate the matrix element,

$$\begin{aligned} \sum |\mathcal{M}_{\omega t}|^2 &= \frac{4\pi^2 \alpha g_{\rho\omega\pi}^4 C^2}{M^2} (m_\rho^{(0)})^4 |D_\rho(M)|^2 \frac{1}{|t - m_\omega^2|^2} L(M) \Theta(M - 2m_l) \\ &\times \{ (M^2 - m_\pi^2)^2 (m_\pi^2 - m_\rho^2)^2 - 2t [m_\pi^2 (M^2 - m_\rho^2)^2 + (M^2 - m_\pi^2)(m_\rho^2 - m_\pi^2)s] \\ &+ t^2 [(M^2 + 2m_\pi^2 + m_\rho^2)^2 - 2(M^2 + 2m_\pi^2 + m_\rho^2)s + 2s^2] - 2t^3 (M^2 + 2m_\pi^2 + m_\rho^2 - s) + t^4 \}, \end{aligned} \quad (14)$$

corresponding to the Feynman diagram depicted in Fig. 3; M denotes the invariant mass of the lepton pair; $s = (p_1 + p_2)^\mu (p_1 + p_2)_\mu$ and $t = k^\mu k_\mu$ are the usual Mandelstam variables with $k^\mu = (p_3 - p_1)^\mu$ the exchanged four-momentum. The $\rho\gamma$ vertex has been written in the form [45]

$$\mathcal{L}_{\rho\gamma} = -C m_\rho^2 A_\mu \rho^\mu \quad (15)$$

where $C = e/g_\rho = 0.052$. Medium effects on the ρ meson are implemented by using the full in-medium propagator, $D_\rho(M)$, for the intermediate ρ meson which couples to the photon (upper ρ line in Fig. 3, with $M^2 = q^2$) and by folding Eq. (14) over the in-medium spectral function for the incoming ρ (lower ρ line in Fig. 3, with $m_\rho^2 = p_1^2$ and a weight $-2m_\rho/\pi \text{Im} D_\rho(m_\rho)$). To avoid double counting with the ω s -channel graph already included in the in-medium ρ -selfenergy, the integral in Eq. (13) is restricted to spacelike ω -exchange momenta, *i.e.*, $t < 0$. The coupling constant, $g_{\rho\omega\pi} = 25.8 \text{ GeV}^{-1}$, has been fixed in [45] by a simultaneous fit to the hadronic and radiative ω decays including a hadronic dipole-form factor,

$$F(t) = \left(\frac{2\Lambda^2}{2\Lambda^2 - t} \right)^2, \quad (16)$$

with $\Lambda = 1 \text{ GeV}$. To maintain gauge invariance in a sim-

plified way as in Ref. [11], we pull the formfactor outside the integral and introduce an average momentum transfer, \bar{t} (adapted to the finite mass of the virtual photon), according to

$$\frac{F^4(\bar{t})}{(m_\omega^2 - \bar{t})^2} = \frac{1}{2} \int_{-1}^1 dx \frac{F^4[t(x)]}{[m_\omega^2 - t(x)]^2}, \quad (17)$$

$$t(x) = M^2 + m_\pi^2 - 2(M^2 + q^2 - qp_x). \quad (18)$$

The amplitude, Eq. (14), is then multiplied by $F^4(\bar{t})$. Eq. (13) furthermore accounts for pion fugacity factors, z_π due to finite pion chemical potentials, implemented in Boltzmann approximation (*e.g.*, for the incoming π and ρ this amounts to a total fugacity of z_π^3). In Fig. 4 we summarize our results for the ω t -channel emission rate, integrated over three-momentum, for conditions along our default trajectory for In(158 AGeV)+In collisions at SPS (including finite μ_π). The upper panel illustrates that the implementation of the in-medium ρ propagator (which was not done in Ref. [11]) leads to a notable reduction in the emission rate, which is mostly due to the reduction in the intermediate ρ propagator, $|D_\rho(M)|^2$. We have verified that medium effects on the ω propagator are negligible (in the spacelike regime finite-width effects are insignificant as long as $\Gamma_\omega \ll m_\omega$). In the middle panel,

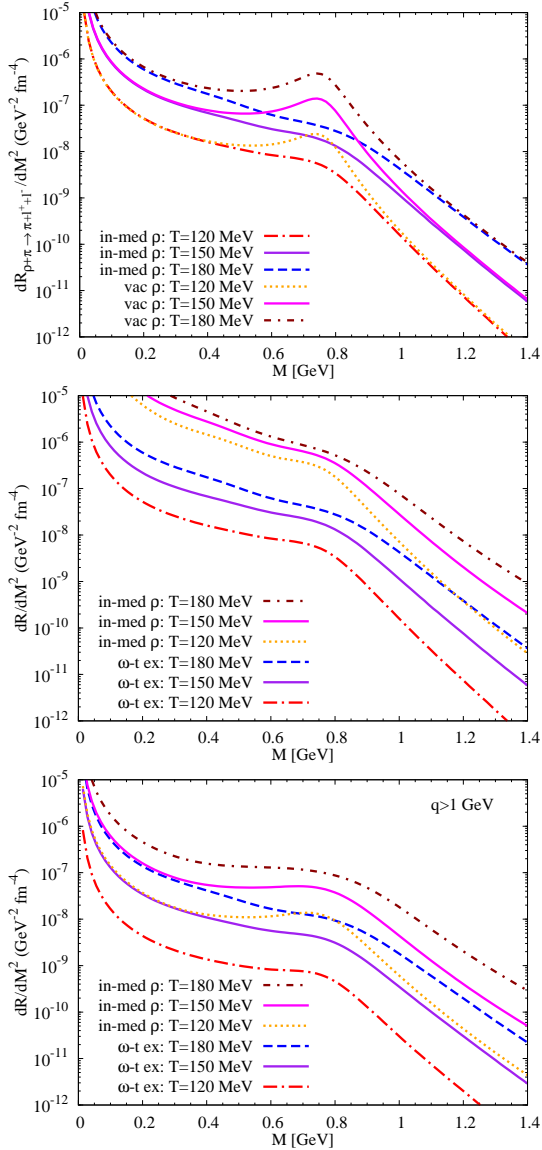


FIG. 4: Three-momentum integrated thermal emission rates from ω t -channel exchange in the $\pi\rho \rightarrow \pi e^+e^-$ reaction. Upper panel: comparison of the rates when using either the free or the in-medium ρ propagators in both the matrix element and the incoming ρ -mass distribution. Middle panel: comparison of the in-medium ω t -channel rates with thermal rates from the full in-medium ρ spectral function. Lower panel: same as middle panel, but restricting the momentum integration to $q > 1$ GeV. All curves for $T=150$ MeV and 120 MeV include pertinent pion fugacities at $\mu_\pi = 39$ MeV and 79 MeV, respectively.

the comparison of the in-medium ω t -channel rates to the ones from the full in-medium ρ spectral function [24],

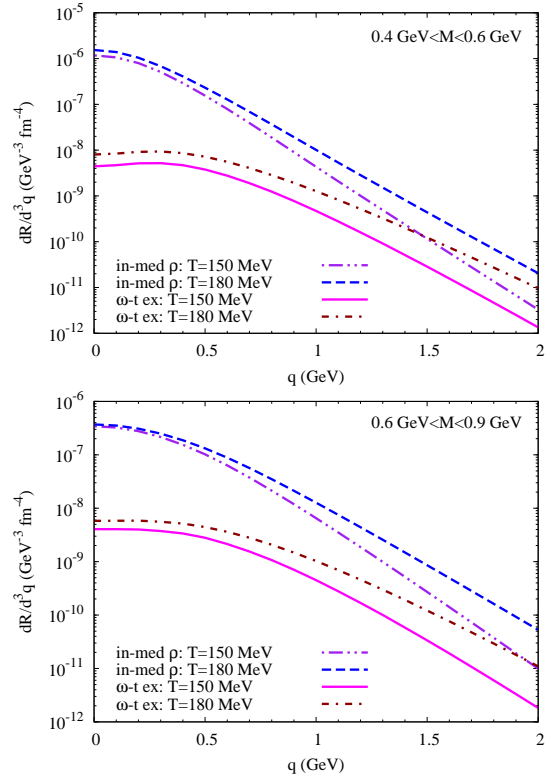


FIG. 5: Mass-integrated dilepton rates as a function of three-momentum for ω t -channel exchange in $\pi\rho \rightarrow \pi e^+e^-$ (computed with in-medium ρ propagators) and the leading contribution from the full in-medium- ρ spectral function. As in Fig. 4, the results for $T=150$ MeV include pion fugacity factors.

based on Eq. (1), confirms that the former contribution is indeed small in magnitude. However, if one applies a three-momentum cut of $q > 1$ GeV (lower panel), the relative magnitude of the t -channel contribution increases, as anticipated at the beginning of this section. But even in this case the relative strength of the ω t -channel exchange is rather moderate. The increasing contribution at higher momentum can be more directly seen when integrating the rate, Eq. (13), over invariant mass bins and plotting it versus q , cf. Fig. 5.

As indicated above, in our calculations of dilepton spectra in Sec. V, we will implement the ω t -channel emission rate, Eq. (13), by an incoherent addition to the main contribution, Eq. (1). This neglects interference terms in the pertinent selfenergy contribution in the (denominator of the) ρ spectral function, which is justified due to the relative smallness of the ω t -channel part. To simulate the presence of other t -channel processes (*e.g.*, π and a_1 exchange), guided by the photon rate calculations of Ref. [11], we will multiply the ω t -channel contribution by a factor of 2 in our calculation of dilepton spectra

below.

E. Partonic Emission: Quark-Antiquark Annihilation

Emission from the QGP is calculated using the hard-thermal-loop improved rate for $q\bar{q}$ annihilation [67], including an extrapolation to finite three-momentum. It turns out [68] that this rate has the conceptually attractive feature that it closely coincides with the rate in hadronic matter when both are extrapolated to the expected phase-transition region. This is suggestive for a kind of quark-hadron duality [24] and has the additional benefit that the emission from the expanding fireball can be anticipated to become rather insensitive to details of how the phase transition is implemented (*e.g.*, to the values for the critical temperature or “latent heat”). This point will be studied explicitly in Sec. V C below.

Recent (experimental and theoretical) developments suggest that the QGP features significant nonperturbative effects for temperatures up to $\sim 1.5-2T_c$, *e.g.*, the survival of (hadronic) resonances and/or bound states, even in the light-quark sector. Possible consequences for the dilepton emission rate have been estimated in Ref. [69]. Depending on the width of these states, a maximal enhancement of up to a factor of ~ 2 over the perturbative QGP emission rate at intermediate masses (*i.e.*, in the mass range of 1.5-2 GeV) is conceivable. We will not further pursue this possibility in the present paper.

III. DILEPTON SOURCES OTHER THAN THERMAL RADIATION

In this section we address dilepton sources other than radiation from a thermal source as given by Eq. (1), *i.e.*, ρ decays after thermal freezeout, decays of primordially produced ρ mesons which escape the fireball, and primordial Drell-Yan annihilation. For simplicity, we generically refer to these sources as “non-thermal”, even though the freezeout decays, *e.g.*, are represented by thermal “blast-wave” spectra commonly used to characterize light hadron spectra in heavy-ion collisions.

A. ρ Mesons at Thermal Freezeout

Dilepton decays of long-lived hadrons (most notably Dalitz decays of η and ω , as well as exclusive l^+l^- decays of ω and ϕ) can be rather well separated from the freezeout of the interacting fireball in heavy-ion collisions, which has given rise to the notion of the “hadronic decay cocktail” contribution to dilepton spectra, computed using the free spectral shape of the decaying mesons. For the ρ meson, due to its short lifetime, such a separation is not well defined. Therefore, when adding thermal radiation to the cocktail, the ρ is commonly removed from

the latter and implemented into the thermal yield. In previous works [15, 24, 36] this was done by running the fireball an extra ~ 1 fm/c using the in-medium ρ spectral function. It turns out [19, 20], however, that this description of ρ decays at thermal freezeout carries an extra factor of $1/\gamma$ relative to a standard blast-wave spectrum of hadrons at thermal freezeout, where $\gamma = q_0/M$ is the usual Lorentz factor. Roughly speaking, the in-medium radiation given by Eq. (1) is proportional to the electromagnetic decay width times the fireball lifetime, $(\Gamma_U/\gamma)\tau_{\text{FB}}$, while decays after freezeout are proportional to the branching ratio of electromagnetic to total lifetime, $\Gamma_U/\Gamma_\rho^{\text{fo}}$, where the γ factor cancels (as usual, we define Γ_X as the partial decay width in the rest system of the particle). The remainder of this section will give a more detailed discussion of this.

To account for the correct time dilation effects in the calculation of dilepton decays of ρ -mesons after thermal freezeout, we use the standard Cooper-Frye description [70],

$$dN = q_\mu d\sigma^\mu \frac{d^3q}{(2\pi)^3 q^0} f_B \left(\frac{q_\nu u^\nu}{T} \right), \quad (19)$$

for the phase-space distribution of an on-shell particle ($q_\mu q^\mu = m^2$) at thermal freezeout; T and $u^\nu = \gamma(1, \beta_\perp)$ denote the local temperature and four velocity (flow) of the fluid cells of the medium, and $d\sigma^\mu$ is the hypersurface normal vector defined by an appropriate freezeout condition. In accordance with the homogeneous fireball model described in Sec. IV, thermal freezeout at a constant time $t = x^0$ in the laboratory frame is assumed, *i.e.*, $(d\sigma^\mu) \equiv (d^3x, 0, 0, 0)$. The in-medium ρ spectral function at freezeout is introduced via the substitution

$$\frac{d^3q}{q_0} \rightarrow d^4q \, 2\delta^+(q_\mu q^\mu - m^2) \rightarrow d^4q \frac{A_\rho}{\pi}, \quad (20)$$

where $A_\rho = -2/3 \text{Im}(D_\rho)_\mu^\mu$ (as before) includes the average over the three polarizations via the Lorentz trace which runs over the physical (*i.e.*, four-momentum transverse) components of the propagator. To properly treat the low-mass tails of the spectral function, one would have to resolve the individual resonance decays figuring into the ρ selfenergy. To simplify our task, we circumvent this problem by employing the vacuum form of the ρ selfenergy augmented with a width corresponding to the full-width-half-maximum of the in-medium spectral function at thermal freezeout ($\Gamma_\rho^{\text{fo}} \simeq 260$ MeV). The distribution of ρ mesons at thermal freezeout then reads

$$\frac{dN_\rho^{\text{fo}}}{d^3x d^4p} = p_0 \frac{3A_\rho}{8\pi^4} f_B \left(\frac{p_\nu u^\nu}{T} \right). \quad (21)$$

In accordance with the averaging procedure over the freezeout duration, we evaluate the transverse four-velocity for the freezeout ρ at a time $\Delta\tau_\rho^{\text{fo}}/2 \simeq 0.5$ fm/c after the thermal emission, Eq.(1), has shut off. The dilepton rate follows by folding with the appropriate partial decay width. Within our vector-meson dominance

model this is given by the matrix element for the process $\rho \rightarrow \gamma^* \rightarrow l^+ + l^-$, and after integration over $t \in (t_{fo}, \infty)$ this results in

$$\begin{aligned} \frac{dN_{ll}^{(fo)}}{d^3x d^4q} &= \frac{q^0}{M} \frac{\alpha^2 m_\rho^4}{g_\rho^2 M^2} \frac{A_\rho}{2\pi^3} L(M) f^B \left(\frac{p_\nu u^\nu}{T} \right) \frac{1}{\Gamma_\rho^{fo}} \\ &= \frac{q_0}{M} \frac{1}{\Gamma_\rho^{fo}} \left(\frac{dN_{ll}}{d^4x d^4q} \right)_{t=t_{fo}}, \end{aligned} \quad (22)$$

where L is the dilepton-phase space factor (3). The second line of Eq. (22) shows that the momentum dependence of the dilepton distribution from ρ decays after thermal freeze-out deviates from the rate from a thermal source (1) by a Lorentz factor $\gamma \equiv q_0/M = \sqrt{M^2 + q^2}/M$. The physical origin of this difference is the time dilation of the total lifetime of a freeze-out ρ meson with three-momentum q which is absent in the formula for radiation from a thermal source, because its ρ -meson abundance at each instant of time is fixed by the temperature and pion-chemical potential of the medium (as required by detailed balance of ρ formation and decay), and thus the total number of thermal dileptons is determined by the lifetime of the fireball. Note, however, that the thermal rate is proportional to Γ_{ll} with an associated time dilation factor $1/\gamma$. The freezeout- ρ dilepton spectra are thus equivalent to standard blast-wave descriptions of stable hadrons [85].

Our default assumption for the radial profile of the flow field is a linear dependence on the radius according to

$$\beta_\perp(r, t) = \beta_\perp^s \frac{r}{R(t)}, \quad (23)$$

where $R(t) = r_0 + a_\perp t^2/2$ is the radius of the fire-cylinder, $\beta_\perp^s = a_\perp t$ its surface speed, and $r \leq R(t)$ the radial coordinate of the fluid cell related to the volume element $d^3x = 2\pi r dr dz$ (since we neither address azimuthal asymmetries nor peripheral collisions in this work, we approximate the cross sectional area of the fire cylinder as a circle).

B. Primordial ρ Mesons

Another source of non-thermal dileptons is the decay of ρ mesons which originate from primordial hard-scattering processes and traverse the interaction zone without equilibrating. We evaluate this contribution within a schematic jet-quenching model [20], as follows.

First, we construct the q_T spectrum of primordial ρ mesons assuming a power law,

$$\frac{1}{q_T} \frac{dN_{\text{prim}}}{dq_T} = \frac{A}{(1 + Bq_T^2)^a}, \quad (24)$$

with parameters estimated from p - p scattering data [71], $B = 0.525 \text{ GeV}^{-2}$ and $a = 5.5$. The total number of primordial ρ 's in A - A collision is determined based on the

empirical freezeout systematics of light hadron production, *i.e.*, we calculate the expected total number of ρ mesons in In-In at $T_c = 175$ MeV and match the norm of the primordial spectrum, Eq. (24), to it. At the same time, we have to take care of the correct scaling properties of the spectrum at high momentum: while the (total) yield at low q_T is proportional to the number of participant nucleons, the high- q_T yield should scale with the number of primordial N - N collisions. We implement this transition by a continuous linear switching between the two regimes over the range $1 \text{ GeV} < q_T < 3 \text{ GeV}$.

Second, we implement a Cronin effect for A - A collisions by a ‘‘Gaussian smearing’’ of Eq. (24),

$$\frac{dN_{\text{prim}}^{\text{cron}}}{d^2q_T} = \int \frac{d^2k_T}{\pi \Delta k_T^2} \frac{dN_{\text{prim}}}{d^2k_T} \exp \left[-\frac{(q_T - k_T)^2}{\Delta k_T^2} \right], \quad (25)$$

with a conservative estimate of $\Delta k_T^2 = 0.2 \text{ GeV}^2$ as extracted in Ref. [11] based on direct photon spectra in p - A reactions.

Third, we calculate a suppression factor representing the probability for primordial ρ mesons to escape the medium without rescattering, using Monte Carlo techniques. In line with our fireball model, we start from a spatially homogeneous distribution in the transverse plane at the QGP formation time. The escape probability for a ρ with momentum q is then calculated as

$$P = \exp \left(- \int dt \sigma_\rho^{\text{abs}}(t) \varrho(t) \right), \quad (26)$$

where the absorption cross section

$$\sigma_\rho^{\text{abs}}(t) = \begin{cases} \sigma_{\text{ph}} = 0.4 \text{ mb} & \text{for } t < q_0/m_\rho \tau_{\text{f}} \\ \sigma_{\text{had}} = 5 \text{ mb} & \text{for } t > q_0/m_\rho \tau_{\text{f}} \end{cases} \quad (27)$$

depends on the ρ -meson formation time in its rest frame, which is assumed to be $\tau_{\text{f}} = 1$ fm, augmented by Lorentz time dilation in the fireball frame; σ_{ph} and σ_{had} denote the pre-hadronic and hadronic absorption cross sections of the ρ , respectively, and $\varrho(t)$ the corresponding particle density of the fireball medium (partonic or hadronic; if the ρ meson has not formed by the time the system has hadronized, we use constituent quark scaling to infer the partonic density as $\varrho_{\text{p}} = 3\varrho_{\text{had}}$, and vice versa).

A rough check of our construction may be obtained by comparing the ρ spectra to measured pion spectra in A - A collisions at the SPS. Since pion spectra contain both a hard (primordial) and a soft (thermal + flow) component, a comparison with our ρ spectra should contain both the primordial part constructed in this section and the thermal freezeout contribution described in the previous section, III A. We do this comparison in terms of the nuclear modification factor, R_{AA} , defined as the ratio of the spectrum in A - A collisions over the collision-number scaled spectrum in p - p . The upper panel of Fig. 6 shows that the jet-quenching + freezeout- ρ model results in fair agreement with a recent compilation of R_{AA} for pions in S-Au and Pb-Pb systems from various experiments at full SPS

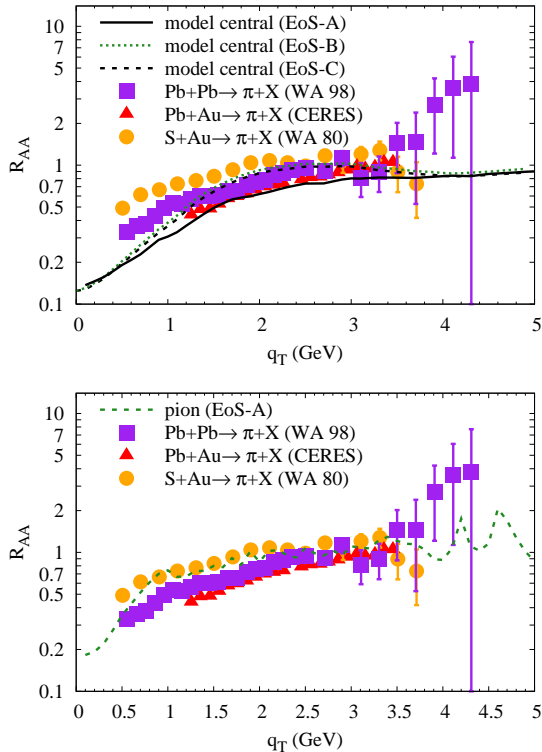


FIG. 6: (Color online) Nuclear modification factor for transverse momentum spectra of ρ (upper panel) and π mesons (lower panel) from primordial (hard) production plus thermal freezeout, compared to a compilation of data for R_{AA} of pions at full SPS energy [72] for central collisions with the standard equation of state (EoS-A, full line) and an EoS with $T_{ch} = 160$ MeV (EoS-B+C as discussed in Sec. IV, dashed line). The primordial ρ spectra include effects of initial Cronin smearing and jet-quenching in the expanding fireball, while the thermal freezeout ρ 's are taken from Sec. III A (same for the pions, but without finite-width effects).

energy [72]. As a check of this procedure, as well as of the fireball model, we plot in the lower panel of Fig. 6 the calculated pion R_{AA} for central In-In at SPS (as a sum of the jet-quenching plus thermal-freezeout components) for central In-In at SPS; the agreement with data is reasonable (note that resonance decays are not included, which are mostly concentrated at low q_T).

C. Drell-Yan Annihilation and Correlated Charm Decays

In the high-mass region (HMR, $M > 3$ GeV), dilepton spectra in nuclear collisions are expected to be dominated by the Drell-Yan (DY) process, *i.e.*, primordial annihilation of quarks and antiquarks within the incoming nucleons. To leading order, this process does not

depend on the strong coupling constant (it is purely electromagnetic, $\mathcal{O}(\alpha_s^0 \alpha_{em}^2)$) and can therefore be rather reliably evaluated, provided one has a good knowledge of the parton-distribution functions (PDFs) within the nucleon. In a central collision ($b = 0$) of two equal nuclei with mass number A , the invariant-mass spectrum of Drell-Yan pairs per unit rapidity is given by

$$\left. \frac{dN_{DY}^{AA}}{dM dy} \right|_{b=0} = \frac{3}{4\pi R_0^2} A^{4/3} \frac{d\sigma_{DY}^{NN}}{dM dy} \quad (28)$$

in terms of the standard DY cross section in an elementary nucleon-nucleon (N - N) collision,

$$\frac{d\sigma_{DY}^{NN}}{dM dy} = K \frac{8\pi\alpha}{9sM} \sum_{q=u,d,s} e_q^2 [q(x_1)\bar{q}(x_2) + \bar{q}(x_1)q(x_2)] \quad (29)$$

Here, $q(x_{1,2})$ and $\bar{q}(x_{1,2})$ denote the (collinear) quark and anti-quark distribution functions, respectively (neglecting nuclear effects). Their arguments are related to the center-of-mass (cms) rapidity, y , and the invariant mass of the lepton pair as $x_{1,2} = xe^{\pm y}$ with $x = M/\sqrt{s}$, where \sqrt{s} is the cms energy of the N - N collision. The root-mean-squared radius parameter in Eq. (28), $R_0 \simeq 1.05$ fm, arises from a folding over a Gaussian thickness function; for simplicity, we will adopt Eq. (28) also for non-central collisions with an accordingly reduced number of participants, A . For the parton distribution functions we employ the leading-order parameterization from Ref. [73] (GRV94LO), which incorporate isospin asymmetries in the sea-quark distributions which significantly reduce the need for additional isospin corrections for nuclei with $N \neq Z$ (*e.g.*, less than 5% for Pb-Pb collisions), which will be neglected here [74]. In Eq. (29) higher-order corrections in α_s are encoded in an empirical K factor, which turns out to be $K \simeq 1.5$ to reproduce DY production in p - A collisions [74].

In addition to generating a K factor, higher-order effects manifest themselves in a nonzero pair- q_T of the DY dileptons. To obtain a realistic q_T spectrum, we follow the procedure adopted by the NA50 collaboration [7, 8]: based on a comprehensive analysis of p - A and A - A collisions at the SPS it has been found that the IMR and HMR dilepton spectra can be fairly well described by assuming a Gaussian shape for the DY spectrum,

$$\frac{dN_{DY}}{dM dy dq_T^2} = \frac{dN_{DY}}{dM dy} \frac{\exp(-q_T^2/2\sigma_{q_T}^2)}{2\sigma_{q_T}^2} \quad (30)$$

with $\sigma_{q_T} \simeq 0.8 - 1$ GeV. In Ref. [9], a value of $\sigma_{q_T} \simeq 0.8$ GeV has resulted in reasonable agreement with the NA50 q_T spectra for IMR dimuons in central Pb-Pb; for $\sigma_{q_T} \simeq 0.9$ GeV, which increases the spectrum at $q_T = 2$ GeV by 50%, the agreement with NA50 would still be acceptable. Here, we adopt $\sigma_{q_T} \simeq 0.8$ GeV providing a conservative estimate of the DY contribution.

The extrapolation of the DY spectrum to the regions where both mass and momentum are small (say, below

$M, q_T \simeq 1.5$ GeV) is problematic, but fortunately its contribution in this regime is small compared to, *e.g.*, thermal emission in A - A collisions. There is, however, an additional constraint provided by the photon point ($M \rightarrow 0$) which allows to extrapolate the DY spectra to low mass, at least for reasonably large momenta, $q_T > 1$ GeV (which is the regime where the DY yield is noticeable). Formally, the photon-production rate follows from the dilepton one by taking the limit $M \rightarrow 0$. More specifically, this is encoded in the relation

$$q_0 \frac{dR_\gamma}{d^3q} = -\frac{\alpha}{2\pi^2} \text{Im} \Pi_{\text{em},\mu}^\mu(M=0, q) f^B(q_0; T) \quad (31)$$

with the same e.m. current-current correlation function, $\Pi_{\text{em}}^{\mu\nu}$ of Eq. (2), as in the dilepton rate, Eq. (1). For $q \gg M$, the M -dependence of Π_{em}^μ is weak, and the difference between $q_0 \frac{dN_\mu}{dM d^3q}$ and $q_0 \frac{dR_\gamma}{d^3q}$ amounts to a factor of $\frac{2\alpha}{3\pi M}$. Thus we can evaluate the DY q_T spectrum at a mass M_{cut} and extrapolate it down in mass to the photon point using the factor M_{cut}/M . For $M_{\text{cut}}=0.8$ - 1 GeV, in connection with $\sigma_{q_T} \simeq 0.8$ GeV, reasonable agreement with the primordial photon spectrum of Ref. [11] is found.

In addition, there could be “pre-equilibrium” contributions from secondary Drell-Yan processes [74] (*e.g.*, $\pi N \rightarrow \mu\mu X$ involving primordially produced pions), which turn out to be rather sensitive to the pion formation time. *E.g.*, for $\tau_{\text{form}}^\pi = 1$ fm/ c , the enhancement over primordial Drell-Yan annihilation in central S-U was found to be $\sim 10\%$ at $M = 2$ GeV. In a thermal emission description, which we employ here after a rather early thermalization time of $\tau_0 = 1$ fm/ c , it is difficult to separate pre-equilibrium radiation from thermal emission (*e.g.*, secondary Drell-Yan in π - N interactions might overlap with thermal q - \bar{q} annihilation). A rough estimate of pre-equilibrium effects may be obtained by varying the thermalization time; decreasing, *e.g.*, τ_0 to 0.8 fm/ c (which is close to the overlap time of the 2 colliding nuclei at SPS energies) increases the QGP contribution at $q_T = 2$ GeV by $\sim 50\%$, which is less than 10% of the Drell-Yan contribution at all masses considered.

For the dilepton contribution from correlated decays of D and \bar{D} mesons we use the experimental result from p - p collisions extrapolated to In-In, as provided by the NA60 collaboration [13]. As a note of caution, we remark that recent measurements at the Relativistic Heavy-Ion Collider (RHIC) report substantial modifications of heavy-quark spectra in Au-Au collisions, relative to p - p (as inferred from a suppression and elliptic flow of “non-photonic” single-electron spectra associated with semileptonic decays of open-charm (and -bottom) hadrons) [75, 76]. Such (possibly nonperturbative [77]) medium modifications of the charm momentum spectra presumably translate into a softening of the invariant-mass spectra of l^+l^- pairs as well. At the SPS, the shorter QGP lifetime is likely to lead to smaller effects, but an explicit measurement of the (delayed) charm decays has been presented recently [78].

IV. THERMAL FIREBALL EVOLUTION

Our description of the space-time evolution of central and semicentral A - A collisions is approximated by an expanding thermal fireball characterized by a time dependent cylindrical volume as [24],

$$V_{\text{FB}}(t) = \pi \left(r_{\perp,0} + \frac{1}{2} a_{\perp} t^2 \right)^2 \left(z_0 + v_{z,0} t + \frac{1}{2} a_z t^2 \right), \quad (32)$$

where we neglect effects due to a finite ellipticity. The initial transverse radius $r_{\perp,0}$ is determined by the centrality of the collision (*e.g.*, $r_{\perp,0} = 5.15(4.6)$ fm for central (semicentral) In-In collisions). The initial longitudinal size, z_0 , is equivalent to the formation time, τ_0 , of the thermal medium, which we fix at the standard value of $\tau_0 = 1$ fm/ c (translating into $z_0 \simeq \tau_0 \Delta y = 1.8$ fm, where $\Delta y = 1.8$ represents the rapidity width of a thermal fireball). For the longitudinal expansion we employ a moderate acceleration, $a_z = 0.045c^2/\text{fm}$, together with an initial velocity of $v_{z,0} = 0.6c$ (reminiscent to Ref. [24]), but the dilepton invariant-mass spectra are essentially unaffected if we use $(v_{z,0}, a_z) = (c, 0)$ as in Ref. [15]. The most important parameter is the transverse acceleration. More recent applications of the fireball model, both in the dilepton [15] and charm diffusion [77] context, have used larger values than in previous work [24, 38], in the range $a_{\perp} = 0.08 - 0.1c^2/\text{fm}$. Here, we employ $a_{\perp} = 0.085c^2/\text{fm}$ as in Ref. [20].

The time evolution of the temperature is determined assuming entropy conservation. At a given collision energy, the hadro-chemistry of the fireball is characterized by thermal-model fits to the observed hadron ratios. In our default scenario we assume the chemical freezeout temperature to coincide with the critical temperature for QGP formation, at $T_{\text{ch}} = T_c = 175$ MeV. For central and semicentral In(158A GeV)+In collisions we fix the entropy per (net) baryon at $s/\rho_B^{\text{net}} = 27$, which, using a hadronic resonance gas (HG) equation of state (EoS), translates into an associated baryon chemical potential of $\mu_B^{\text{ch}} = 232$ MeV, well within the uncertainties of recent thermal model fits at SPS [21, 22] (all other chemical potentials being zero). The subsequent hadronic trajectory in the phase diagram is then constructed at fixed $s/\rho_B^{\text{net}} = 27$ (isentropic expansion) with the additional constraints of pion, kaon, η and antibaryon number conservation, requiring the build-up of corresponding chemical potentials. For a given number of nucleon participants (*i.e.*, collision centrality), the fireball entropy amounts to $S = 2630(1890)$ for central (semicentral) In-In collisions, translating into a charged particle multiplicity of $dN_{\text{ch}}/dy \simeq 195(140) \simeq N_{\text{part}}$ (for a chemical freezeout temperature of $T_{\text{ch}} = 160$ MeV, as considered below, the multiplicities increase by less than 5%). Using the relation between the total entropy and volume, $S = s(t) \cdot V(t)$, the entropy density, $s(t)$, can be used to determine the time evolution of temperature and baryon density (along the hadronic trajectory) using the HG

EoS, and similarly for the QGP phase using a quasiparticle EoS. The volume partition in the HG-QGP mixed phase is calculated from the standard mixed-phase construction, where the fraction of matter in the hadronic phase is given by

$$f_{\text{HG}}(t) = \frac{s_c^{\text{QGP}} - s(t)}{s_c^{\text{QGP}} - s_c^{\text{HG}}}, \quad (33)$$

where $s_c^{\text{HG,QGP}}$ denote the critical entropy densities at T_c . With a formation time of $\tau_0 = 1 \text{ fm}/c$, the evolution for central (semicentral) In-In starts in the QGP at $T_0 = 197(190) \text{ MeV}$, passes through a mixed phase at $T^{\text{ch}} = T_c = 175 \text{ MeV}$, and terminates at thermal freezeout at around $T_{\text{fo}} \simeq 120\text{-}135 \text{ MeV}$.

The main uncertainties associated with the fireball evolution are the transverse acceleration as well as the overall lifetime (which is somewhat correlated to the longitudinal expansion). It turns out that the latter is rather sensitive to the absolute magnitude of the experimentally observed dilepton excess radiation, resulting in $\tau_{\text{fo}} \simeq 6 \text{ fm}/c$ for central In-In collisions. The remaining uncertainty consists of the interplay between longitudinal and transverse expansion. As mentioned above, the variations considered in our previous works [15, 20], $a_{\perp} = 0.08\text{-}0.085 c^2/\text{fm}$ and $(v_z^0, a_z) = (c, 0)\text{-}(0.6c, 0.045 c^2/\text{fm})$, have negligible impact on the invariant mass spectra, while the longitudinal-acceleration scenario, which we will focus on here, allows for a slightly larger transverse expansion which appears to be favored by the rather hard q_T spectra. In principle, more accurate information on the final state of the expansion can be obtained once hadronic spectra for In-In are available (our pion spectra are actually in reasonable agreement with S-Au data, recall lower panel of Fig. 6). For central Pb-Pb collisions at SPS energies, the typical results for transverse surface velocity and thermal freezeout temperature are $(\beta_{\perp}^s/c, T_{\text{fo}}[\text{MeV}]) = (0.65 \pm 0.1, 120 \pm 10)$ [79, 80, 81, 82], which is quite comparable to the values used here for In-In. We emphasize that all contributions to the dilepton spectrum (QGP, ρ , ω , ϕ , and four-pion) are tied to the *same* evolution, thus fixing their relative weights.

Finally, to illustrate the uncertainties associated with the underlying equation of state we will investigate three combinations of critical and chemical freezeout temperatures roughly covering the current theoretical and experimental ranges:

- (A) Our default scenario, employed in most of our calculations thus far, consisting of identical T_c and T_{ch} at an ‘‘intermediate’’ value of 175 MeV ; thermal freezeout is fixed at $(\mu_{\pi}^{\text{fo}}, T_{\text{fo}}) = (79, 120) \text{ MeV}$ (semicentral In-In).
- (B) A scenario with a relatively small and identical critical and chemical freezeout temperature at $(\mu_B^{\text{ch}}, T_{\text{ch}}) = (240, 160) \text{ MeV}$, compatible with recent thermal model fits in Refs. [21, 22]. For dilepton spectra the most important consequences

of this scenario are a significantly extended QGP phase which will increase its thermal emission contribution and reduce the hadronic one, in particular at intermediate masses. In addition, due to smaller pion chemical potentials in the subsequent hadronic phase, the freezeout temperature (at fixed fireball lifetime) will be larger than with EoS-A, at $(\mu_{\pi}^{\text{fo}}, T_{\text{fo}}) = (37, 136) \text{ MeV}$.

- (C) A scenario with a large critical temperature $T_c = 190 \text{ MeV}$ (as suggested by recent lattice QCD computations [23], which maximizes (minimizes) the space-time volume occupied by the hadronic (QGP) phase. Since chemical freezeout at such a temperature is questionable, we allow for a chemically equilibrated hadronic phase until chemical-freeze out sets in under the same conditions as in EOS-B, at $(\mu_B^{\text{ch}}, T_{\text{ch}}) = (240, 160) \text{ MeV}$.

V. COMPARISON TO DILEPTON SPECTRA AT SPS

We now turn to a systematic analysis of experimental dilepton spectra as measured at the SPS by the NA60 and CERES/NA45 collaborations in In-In and Pb-Au collisions, respectively. Based on the various ingredients developed in the previous sections, we first address the NA60 invariant-mass and transverse-momentum spectra, followed by a consistency check with earlier and updated CERES data.

A. Invariant Mass Spectra

Thermal $\mu^+\mu^-$ invariant-mass spectra for A - A collisions are computed by integrating the emission rate, Eq. (1), over the fireball evolution (as well as three-momentum),

$$\frac{dN_{ll}}{dM} = \frac{M}{\Delta y} \int_0^{t_{\text{fo}}} dt V_{\text{FB}}(t) \int \frac{d^3q}{q_0} \frac{dN_{ll}}{d^4x d^4q} z_P^n \text{Acc}(M, q_T, y), \quad (34)$$

where Acc denotes the detector acceptance which has been carefully tuned to NA60 simulations [83]. The fugacity factor, $z_P^n = e^{n\mu_P/T}$, arises due to chemical off-equilibrium in the hadronic phase for $T < T_{\text{ch}}$; it depends on the thermal emission source under consideration, cf. Eq. (4): for the ρ , ω and four-pion contributions one has z_P^n with $n = 2, 3, 4$, respectively, while for the ϕ one has $z_K^2 \cdot \gamma_s^2$, where $\gamma_s \simeq 0.75$ accounts for strangeness undersaturation for medium-size nuclear collision systems at the SPS [84]. In addition, appropriate fugacities figure into the various in-medium selfenergy contributions.

Initial comparisons [13] of NA60 data to theoretical predictions [14] have focused on the contribution from

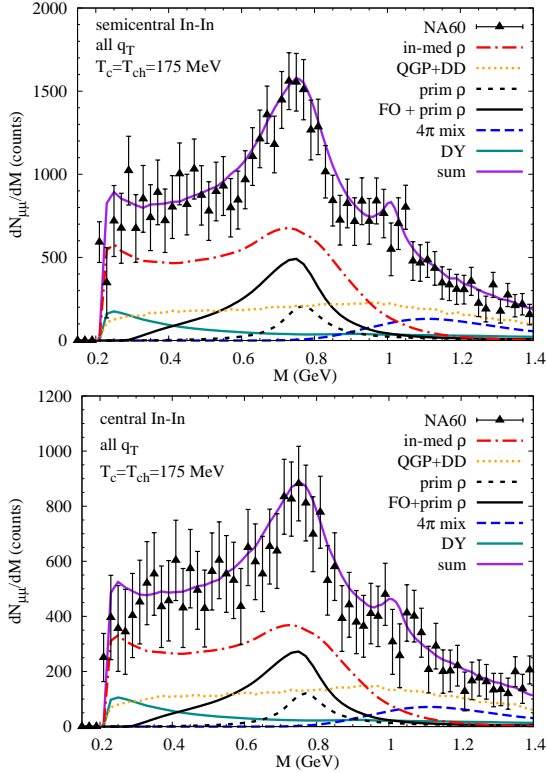


FIG. 7: (Color online) NA60 excess dimuon spectra [13] in semicentral (upper panel) and central (lower panel) In-In collisions at SPS compared to theoretical calculations using an in-medium e.m. spectral function. The individual contributions arise from in-medium ρ -mesons [24] (dash-dotted red line), 4π annihilation with chiral $V-A$ mixing (dashed blue line), QGP plus correlated open charm decays (dotted orange line) and Drell-Yan annihilation (solid turquoise line); the upper dashed brown line is the sum of the above, while the solid purple line additionally includes in-medium ω and ϕ decays as well as freezeout plus primordial ρ s (solid black line). In the semi-central data, the uncertainty due to the η cocktail subtraction is indicated by the open and filled data points (the former are based on an estimated η yield at high q_T while the latter represent an upper limit on the η by subtracting the dimuon spectrum to zero at threshold).

the ρ meson which dominates in the LMR. The shape of the in-medium ρ -spectral function describes the experimental spectra well, but the absolute yields have been overestimated by $\sim 30\%$. This discrepancy has been resolved [15] by increasing the transverse fireball expansion (a_\perp), reducing the fireball lifetime to about 6-7 fm/ c , cf. Sec. IV above. In addition, the larger transverse expansion leads to harder emission spectra in q_T , which will be helpful in understanding the q_T spectra, as discussed in the following sections.

Fig. 7 summarizes our results for the mass spectra in semicentral and central In(158 AGeV)-In collisions, com-

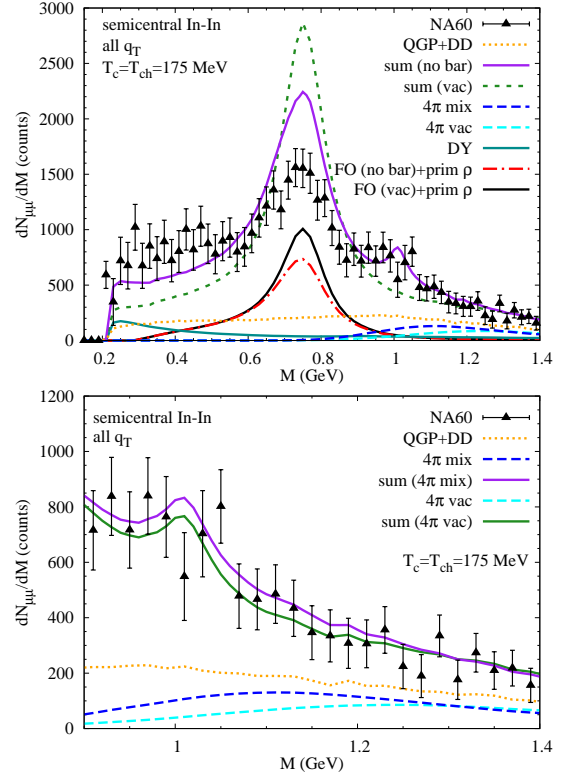


FIG. 8: (Color online) Upper panel: NA60 data [13] compared to thermal dimuon spectra using (i) in-medium ρ -, ω - and ϕ -mesons without baryon effects (+QGP+charm+in-medium four-pion; solid purple line), and (ii) free ρ (+QGP+charm+free four-pion; dashed green line). Lower panel: NA60 data [13] in the IMR compared to thermal dimuon spectra with different implementations of the four-pion contribution, using either its vacuum form (lower dashed line) or including chiral mixing (upper dashed line), and corresponding total spectra (lower and upper solid line, respectively).

puted for the EoS-A scenario ($T_c = T_{ch} = 175$ MeV). The modifications relative to our previous work [15] are: (i) the freezeout ρ has been separated from the in-medium ρ contribution, (ii) primordial ρ and (iii) Drell-Yan contributions have been added. As a result of the separation (i), the thermal emission lifetime is now slightly smaller, 6.5(6.2) fm/ c for central (semicentral) collisions. The inclusive mass spectra (and pertinent conclusions) are essentially identical to those in Ref. [15], *i.e.*, the predicted in-medium effects on ρ spectral function lead to good agreement with the data in the LMR, while the same fireball evolution also reproduces the observed excess in the IMR well. The largest source here is four-pion annihilation, together with smaller contributions from open-charm decays and QGP emission. In-medium ϕ decays are noticeable but not very significant relative to the un-

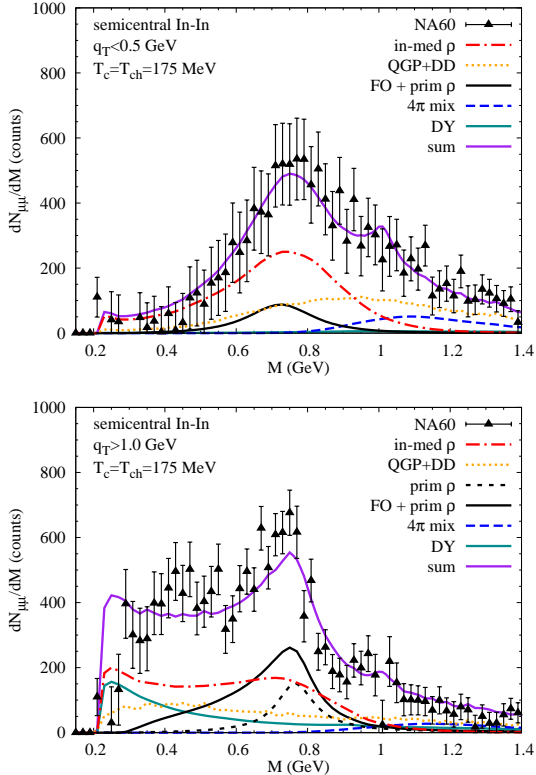


FIG. 9: (Color online) Dimuon invariant mass spectra in two different bins of transverse pair momentum, q_T [13]. Upper panel: $q_T \leq 0.5$ GeV; lower panel: $q_T \geq 1.0$ GeV.

certainty in the data.

The sensitivity to the medium effects in the e.m. correlator is further illustrated in Fig. 8. The upper panel demonstrates that a free ρ spectral function is ruled out, but also one which only includes modifications due to a meson gas clearly does not reproduce the data, due to both a too narrow peak and a lack of enhancement below the free ρ mass, especially when approaching the dimuon threshold. In the lower panel one sees that the effect of chiral mixing on the 4π contribution amounts to up to a factor of ~ 2 enhancement in the a_1 resonance region, but the effect on the total is rather moderate. Thus, no strong case on the chiral mixing can be made at present. The prevalence of the four-pion contribution in the IMR is reminiscent to the hydrodynamic calculations in Ref. [16] where hadronic rates calculated in the chiral reduction formalism have been employed. On the contrary, in the fireball calculations of Ref. [17] QGP emission dominates in the IMR. We elucidate on this discrepancy in Sec. VC below.

In Figs. 9 and 10 we compare our theoretical calculations to NA60 M -spectra binned into regions of low ($q_T < 0.5$ GeV) and high ($q_T > 1.0$ GeV) transverse pair

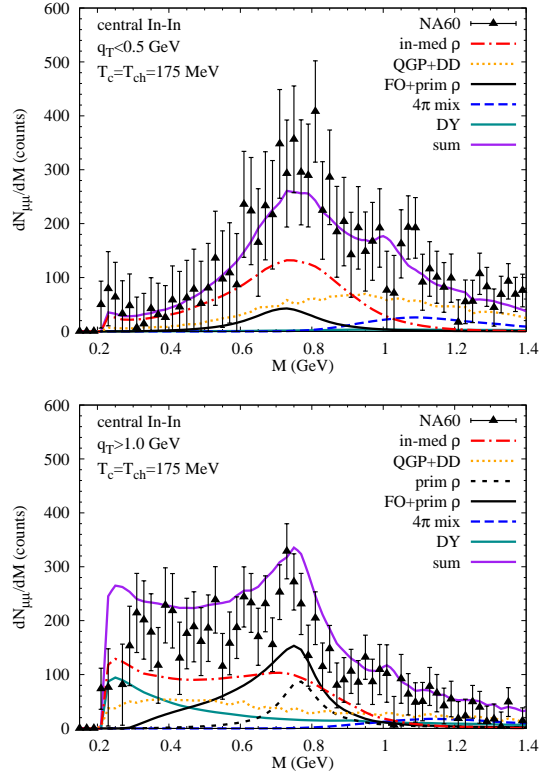


FIG. 10: (Color online) The same as Fig. 9 but for central collisions.

momentum, for both semicentral and central collisions. Also in this representation the agreement is fair. There is possibly an indication of a slight over- (under-) estimate in the high- q_T bin for (semi-) central collisions. To further scrutinize this issue we now turn to q_T spectra, binned in invariant mass.

B. Transverse Momentum Spectra

In analogy to Eq. (34) for M spectra, q_T spectra are computed by integrating the dilepton rate, Eq. (1), over the space-time evolution of the fireball and a suitable interval in invariant mass, $[M_{\min}, M_{\max}]$. However, since the available experimental spectra have been corrected for the detector acceptance, the Monte-Carlo simulation of the acceptance function (with radial and angular dependencies due to directed (radial flow) and random (thermal) motion of the virtual photon) is now replaced by explicit integrations over the radial coordinate, r , of the fireball, the azimuthal angle, ϕ_q , of the virtual photon

momentum and its rapidity, y ,

$$\frac{dN_{ll}}{q_T dq_T} = \int_0^{t_{fo}} dt \int_0^{R(t)} dr \int_{M_{\min}}^{M_{\max}} dM \int_0^{2\pi} d\phi_q \int_{y<}^{y>} dy 2\pi r z(t) \times M z_P^n \frac{dN_{ll}}{d^4x d^4q}. \quad (35)$$

As before, $R(t)$ denotes the radius of the expanding fire-cylinder (corresponding to the first parenthesis in Eq. (32)), $z(t)$ its longitudinal length (second parenthesis in Eq. (32)). Note that the rate, Eq. (1), is calculated in the thermal rest frame while the integrations in Eq. (35) are in the laboratory frame. The relation between the four-momentum, q^μ , in the laboratory frame and the one in the local rest frame of the fluid cells, \bar{q}^μ , is determined by a boost with the radial flow velocity, Eq. (23). Due to rotational invariance the thermal rate, Eq. (1), depends only on the magnitude of the three-momentum in the thermal rest frame and therefore one of the integrations over the spatial and momentum azimuthal angles in Eq. (35) becomes trivial yielding a factor of 2π . To gain qualitative insights into the behavior of dilepton q_T spectra from thermal sources, let us assume that the three-momentum dependence of the hadronic e.m. current correlator is weak (it would be absent in the absence of medium effects), so that for not too large invariant-mass intervals, the integrand in Eq. (35) can be considered constant except for the Bose distribution. For $M \gg T$, it is possible to approximate the qualitative behavior of the q_T spectra in analytic form [85, 86]. For a linear flow profile, Eq. (23), and in Boltzmann approximation one has

$$\frac{dN_{ll}}{q_T dq_T dM dt} = C \int_0^{R(t)} dr \int_0^{2\pi} d\phi \int_{-\infty}^{\infty} dy \times r \exp\left(-\frac{q_0 - |\beta_\perp| q_T \cos\phi}{T\sqrt{1-\beta_\perp^2}}\right), \quad (36)$$

with C weakly q_T dependent. Substituting $q_0 = m_\perp \cosh y$ ($m_T = \sqrt{M^2 + q_T^2}$) the integrals over y and ϕ are given by modified Bessel functions. For the y -integral we can use their asymptotic form for $m_T/T \geq M/T \gg 1$:

$$\frac{dN_{ll}}{q_T dq_T dM dt} = C \int_0^{R(t)} dr r \sqrt{\frac{2\pi T \sqrt{1-\beta_\perp^2}}{m_T}} \times \exp\left(-\frac{m_T}{T\sqrt{1-\beta_\perp^2}}\right) I_0\left(\frac{|q_T||\beta_\perp|}{T\sqrt{1-\beta_\perp^2}}\right). \quad (37)$$

In the non-relativistic limit, $q_T \ll M$, we use the asymptotic form $I_0(x) \simeq_{x \rightarrow 0} 1 + x^2/4 \simeq \exp(x^2/4)$ to obtain

$$\frac{dN_{ll}}{q_T dq_T dM dt} \simeq_{q_T \ll M} C \int_0^{R(t)} dr r \sqrt{\frac{2\pi T \sqrt{1-\beta_\perp^2}}{m_T}} \times \exp\left(-\frac{m_T}{T\sqrt{1-\beta_\perp^2}} + \frac{q_T^2 \beta_\perp^2}{4T^2(1-\beta_\perp^2)}\right). \quad (38)$$

We have numerically verified that this expression can be further simplified by the following approximate treatment of the r integral: In the pre-factor of the exponential substitute β_\perp by its average over r ,

$$\langle \beta_\perp \rangle = \frac{2}{R^2} \int_0^R dr r \beta_\perp^s \frac{r}{R} = \frac{2}{3} \beta_\perp^s; \quad (39)$$

use the r average of the argument in the exponential, which, together with the non-relativistic approximation $q_T \simeq_{q_T \ll M} \sqrt{2M(m_T - M)}$, results in

$$\frac{dN_{ll}}{q_T dq_T dM dt} \simeq_{q_T \ll M} C \sqrt{2\pi T \sqrt{1-\langle \beta_\perp \rangle_r^2}} \times \exp\left(-\frac{M^2 \langle \beta_\perp \rangle_r^2}{2T^2}\right) \times \sqrt{\frac{1}{m_T}} \exp\left(-\frac{m_T}{T_{\text{eff}}}\right) \quad (40)$$

where

$$T_{\text{eff}} = \frac{T}{1 - (M - T)(\beta_\perp^s)^2 / (4T)} \simeq_{\beta_\perp^s \rightarrow 0} T + \frac{M}{2} \langle \beta_\perp^2 \rangle_r, \quad (41)$$

and $\langle \beta_\perp^2 \rangle_r = (\beta_\perp^s)^2 / 2$. The form for $\beta_\perp^s \ll 1$ is the known ‘‘pocket formula’’ for the parametric dependence of the effective slopes of hadronic q_T spectra on the fireball temperature, the particle mass and the surface-flow velocity [86]. We recall that in the ultrarelativistic limit, $q_T \gg M$, the dependence of the effective temperature on the radial velocity is given by the Doppler blue-shift expression for a thermalized gas of massless particles,

$$T_{\text{eff}}(\beta_\perp) = T \sqrt{\frac{1+\beta_\perp}{1-\beta_\perp}}, \quad (42)$$

which follows from the large- q_T limit of I_0 in Eq. (37) [86] which also provides an additional factor $1/\sqrt{q_T}$. For our r -dependent flow profile the effective temperature is given by the blue-shift value for an average value $\langle \beta_\perp \rangle_r = \xi \beta_\perp^s$ where $\xi \in (0, 1)$ is not easily determined by simple approximations of the radial integral. Numerical studies show that in the case of a linear radial-flow profile, Eq. (23), and typical parameters in the region of the ρ peak ($M = 0.75$ GeV, $\beta_\perp^s \simeq 0.5$), $\xi \simeq 0.8-0.85$ leads to a good estimate for T_{eff} at high q_T .

It is important to note that for vector-meson decays after thermal freezeout, cf. Sec. III A), the q_T spectra are harder by an additional factor m_T/M , *i.e.*, applying the same approximations to Eq. (22) as used to derive Eq. (40), one obtains

$$\begin{aligned} \frac{dN_u^{(fo)}}{q_T dq_T dM} \Big|_{q_T \ll M} &\cong C \sqrt{2\pi T} \sqrt{1 - \langle \beta_{\perp} \rangle_r^2} \\ &\times \exp\left(-\frac{M^2(\beta_{\perp}^s)^2}{2T^2}\right) \\ &\times \frac{\sqrt{m_T}}{M} \exp\left(-\frac{m_T}{T_{\text{eff}}}\right) \frac{1}{\Gamma_{\rho}^{(fo)}} \end{aligned} \quad (43)$$

with T_{eff} again given by Eq. (41).

The additional factor m_T/M in (43) compared to (40) originates from the additional factor q^0/M in the Cooper-Frye (CF) formula (22) compared to the McLerran-Toimela (MT) emission formula (1), as discussed in detail in Sec. III A.

The above discussion of effective slopes in thermal emission spectra obviously does not apply to non-thermal dilepton sources, *i.e.*, decays of “primordial ρ mesons” (Sec. III B) and Drell-Yan annihilation (Sec. III C). Both are characterized by a power-law behavior at high q_T , where their contribution becomes potentially important. Toward lower q_T , the primordial ρ contribution is much suppressed due to ρ absorption (“jet quenching”), while the Drell-Yan process is no longer well-defined. However, the Drell-Yan dileptons carry the hardest slope of all sources considered, which renders even a naive extrapolation of their spectra to low q_T very small (no more than a few percent for $q_T \leq 1$ GeV in all mass bins below $M = 1.4$ GeV). At $q_T \simeq 2$ GeV, in turn, the Drell-Yan contribution is quite appreciable.

Figs. 11 and 12 summarize our calculations for semicentral and central In-In collisions, respectively, in three different mass bins in comparison to the NA60 data [18]. Open-charm decays have been removed from the experimental spectra and are consequently not included in the theory curves either. The parameters of our fireball evolution are as described in Sec. IV within our default EoS-A scenario ($T_c = T_{\text{ch}} = 175$ MeV). Since the overall normalization of the experimental spectra is not known at present, we have fixed it in each mass bin using the invariant mass spectra in the low- q_T bin ($0 \leq q_T \leq 0.5$ GeV). This easily translates into a 10-20% uncertainty in the absolute normalization. For the central collisions the agreement between theory and data is quite satisfactory in all mass bins. In the high-mass bin $1 \text{ GeV} \leq M \leq 1.4$ GeV, lower panel in Fig. 12), this procedure appears to overestimate somewhat the q_T spectra at $q_T \geq 1$ GeV, which, however, seems not to be reflected in the corresponding q_T bin in the mass spectra (lower panel in Fig. 10). This could very well be due to the uncertainty in the underlying normalization procedure. Note again that the compared to Ref. [15] additionally implemented hard components (primordial ρ 's and Drell-Yan) are insignificant at $q_T \leq 1$ GeV, *i.e.*, for the total

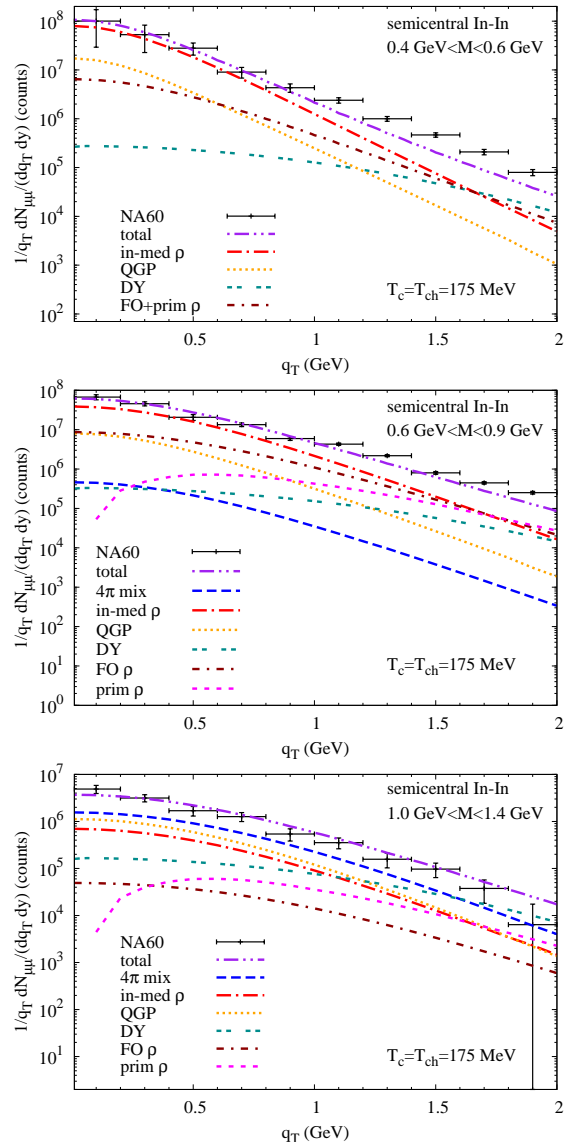


FIG. 11: (Color online) Dimuon transverse pair-momentum spectra in semicentral In(158 AGeV)-In collisions for three bins of invariant mass [18]. Upper panel: $0.4 \text{ GeV} \leq M \leq 0.6 \text{ GeV}$; middle panel: $0.6 \text{ GeV} \leq M \leq 0.9 \text{ GeV}$; lower panel: $1.0 \text{ GeV} \leq M \leq 1.4 \text{ GeV}$.

yield and the understanding of the spectral shape of the inclusive M -spectra. On the other hand, at higher q_T , these contributions are essential (even dominant) for a proper description of the spectra. In fact, in semicentral collisions, the experimental transverse momentum spectra in the two mass bins below ($0.4 \text{ GeV} \leq q_T \leq 0.6 \text{ GeV}$) and around ($0.6 \text{ GeV} \leq q_T \leq 0.9 \text{ GeV}$) the free ρ -meson mass turn out to be underestimated (and too soft) for

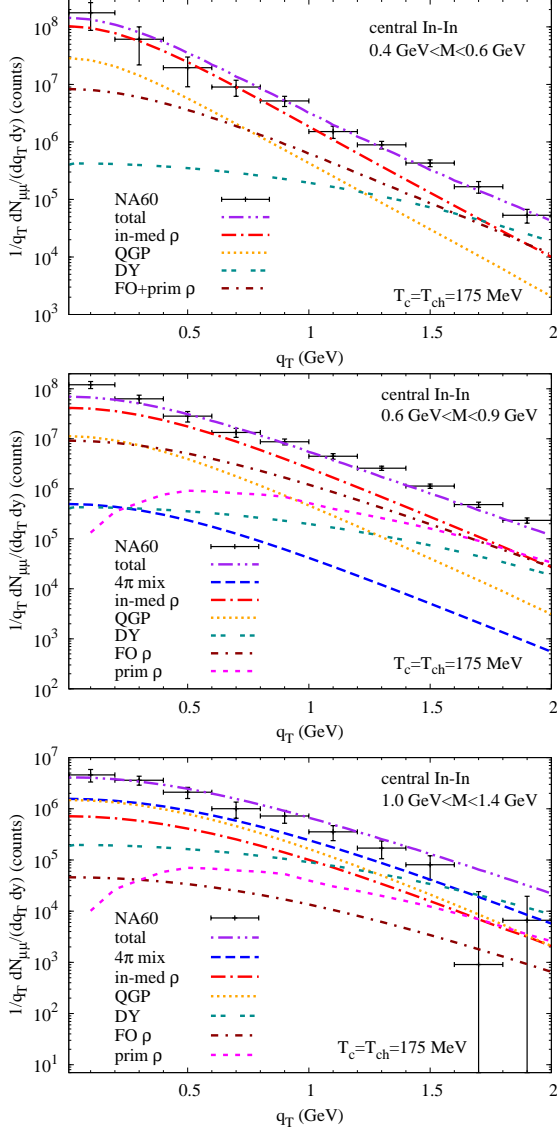


FIG. 12: (Color online) Same as Fig. 11, but for central In(158 AGeV)-In.

$q_T \gtrsim 1$ GeV. Especially in the low-mass bin, the discrepancy again appears to be larger than one could anticipate from the mass spectrum in the 0.4-0.6 GeV regime in the $q_T \geq 1$ GeV bin (lower panel in Fig. 9). The fact remains, however, that the theoretical q_T spectra in the low and intermediate mass bin are somewhat too soft. Even though the final transverse flow velocity of the fireball model is about 7% smaller for semicentral relative to central In-In collisions, this difference would not be able to account for the discrepancy (it amounts to a change in slope by about 10 MeV for the freeze-out ρ , and even

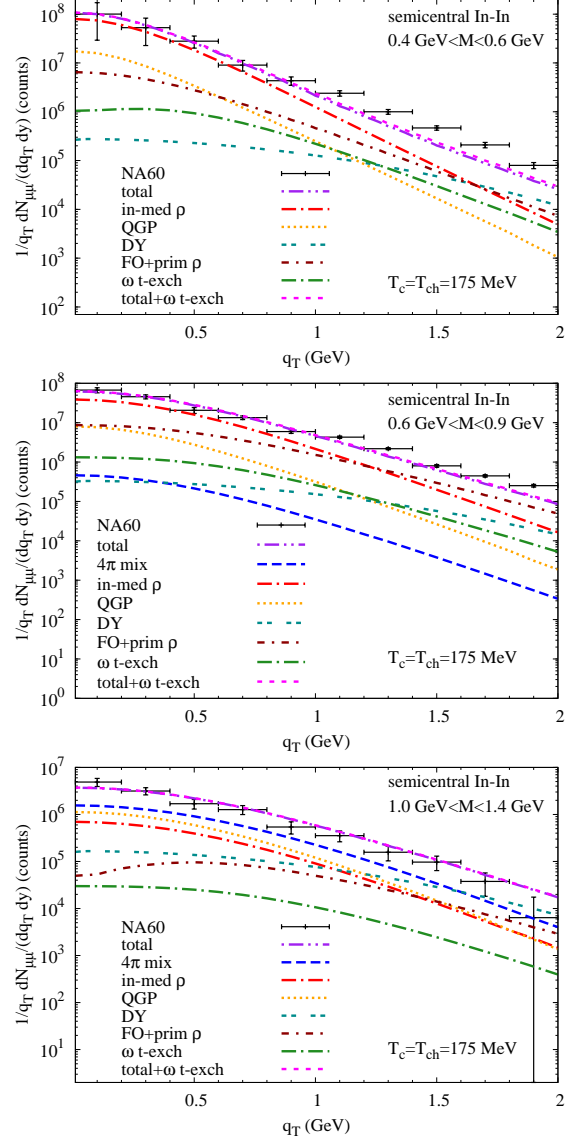


FIG. 13: (Color online) Same as Fig. 11, but additionally including (factor 2 augmented) contributions from ω t -channel exchange in $\pi\rho \rightarrow \pi\mu\mu$.

less for thermal radiation). The nuclear suppression factor, $R_{AA}(q_T)$, in Fig. 6 (solid line) suggests that there might be room for a 30% increase of the primordial plus freezeout ρ contribution (possibly more if one could compare to the R_{AA} of ρ mesons; due to their larger mass a more pronounced flow effect could enhance their R_{AA}). Whether this would suffice in the low-mass bin, is questionable.

Another possibility consists of meson t -channel exchange in elastic scattering of ρ mesons off pions in

the heat bath (with subsequent conversion into a lepton pair). These processes have been calculated previously for real photon production [11] (which are given by the same diagrams except that the final-state photon is on-shell), where ω exchange has been found to be the most important process at high q_T ; however, contributions from other exchange processes (*e.g.*, π and a_1 exchange in $\pi\rho \rightarrow \pi\gamma$, or reactions involving strange mesons [11]) are also appreciable. To roughly account for the latter, we augment the rates computed in Sec. IID by a factor of two (in addition, we recall that $\pi\rho$ initial states in the hadronic fireball emission carry a pion fugacity factor to the third power, z_π^3). The convolution of these rates over the fireball evolution leads to a contribution to dilepton- q_T spectra as shown by the lower dash-dotted line in each of the panels in Fig. 13; it indeed provides the hardest spectrum among all thermal sources (QGP, in-medium vector mesons and four-pion annihilation), in line with the rates displayed in Fig. 5. Consequently, the relative importance of the t -channel processes grows with q_T but remains rather moderate even at $q_T \simeq 2$ GeV, up to 15% and 5% of the total theoretical yield in the $M = 0.4$ - 0.6 GeV and 0.6 - 0.9 GeV mass bins, respectively (negligible for $M > 1$ GeV). Note that the slopes of the t -channel emission spectra resemble the data quite well, but our present estimate of their strength is insufficient to resolve the discrepancies at high q_T . However, their impact on the slope of the total spectra is not insignificant, as we will see in Sec. VD below.

C. Hadro-Chemical Freezeout and Critical Temperature

In all our calculations of thermal dilepton spectra thus far, the medium evolution was based on the notion that the critical (T_c) and chemical freezeout (T_{ch}) temperature coincide, at $T_c = T_{\text{ch}} = 175$ MeV. More recent theoretical (lattice QCD) and phenomenological (thermal model fits to hadron ratios) studies, however, allow for the possibilities that T_c could be significantly larger (190-200 MeV) and T_{ch} significantly smaller (150-160 MeV). While a smaller $T_c \simeq 160$ MeV is still viable, a larger T_{ch} appears unlikely since in a high-density hadronic phase number-changing reactions affecting the chemistry are to be expected (in addition, thermal model fits start to become unstable at temperatures above ~ 180 MeV due to uncertainties in the high-lying, high degeneracy hadron resonance spectrum). Therefore, in this section we study the sensitivity of the invariant-mass and q_T spectra to the hadro-chemistry of the fireball, keeping its geometry and flow parameterization as well as the total lifetime the same as before (including all normalizations, where applicable). As quoted in Sec IV, in addition to our standard equation of state (EoS-A: $T_c = T_{\text{ch}} = 175$ MeV), we investigate two alternative scenarios: EoS-B with $T_c = T_{\text{ch}} = 160$ MeV and EoS-C with $T_c = 190$ MeV, $T_{\text{ch}} = 160$ MeV. In general, a lower

chemical freezeout temperature (where all meson chemical potentials are by definition zero) entails a larger volume at chemical freezeout, and thus also smaller baryon chemical potentials (*i.e.*, smaller baryon densities), as well as smaller meson chemical potentials in the subsequent evolution. This furthermore implies that, to obtain roughly the same overall dilepton yield, thermal freezeout occurs at a *larger* temperature (and smaller $\mu_{\pi,K}$), which, in principle, leads to (somewhat) harder q_T spectra, both at thermal freezeout and for thermal emission throughout the hadronic evolution. In the remainder of this Section, we focus on semicentral collisions.

We start our investigation within the ‘‘EoS-B’’ scenario, *i.e.*, $T_c = T_{\text{ch}} = 160$ MeV. The resulting M - and q_T -spectra are compiled in Figs. 14 and 15, respectively. The smaller T_c implies a longer duration of both the QGP and mixed phase (the latent heat for EoS-B is larger than for EoS-A since entropy density for the QGP EoS drops slower with T than for the HG EoS), while the duration of the hadronic phase is accordingly reduced. As noted above, the thermal-freezeout temperature has increased to $T_{\text{fo}} = 136$ MeV (compared to $T_{\text{fo}} = 120$ MeV for EoS-A). As an immediate consequence, QGP radiation is significantly enhanced, while the hadronic yield is slightly reduced (both for in-medium ρ in the LMR and four-pion in the IMR). The overall quality in the description of the invariant-mass spectra is quite comparable to the EoS-A scenario. The somewhat harder spectra implied by the larger hadronic temperatures for EoS-B (most notably for the freezeout ρ) lead to a slight increase of the dilepton yield in the ρ mass region in the $q_T \geq 1$ GeV momentum bin (compare lower panels in Figs. 9 and 14). However, in the low- ($0.4 \text{ GeV} \leq M \leq 0.6 \text{ GeV}$) and intermediate-mass ($0.6 \text{ GeV} \leq M \leq 0.9 \text{ GeV}$) bins of the q_T spectra, the improvement at high q_T is rather marginal, while in the higher mass ($1.0 \text{ GeV} \leq M \leq 1.4 \text{ GeV}$) there is essentially no change compared to the EoS-A calculation (recall Fig. 11), despite the fact that the QGP contribution is now larger than the four-pion one.

Turning to the EoS-C scenario (summarized in Figs. 16 and 17), the large value of $T_c = 190$ MeV leads to a QGP and mixed phase which is shorter than for EoS-A, but there is now a ‘‘high-density’’ (chemically equilibrated) hadronic phase down to $T_{\text{ch}} = 160$ MeV, followed by a subsequent chemical off-equilibrium evolution which is identical to EoS-B. Obviously, the QGP emission yield is the smallest of all three scenarios, while the hadronic yield (both in-medium ρ 's and four-pion annihilation) is the largest, possibly implying a slight overestimate in the ρ -mass region of the inclusive mass spectra (13% larger than for EoS-A, which could be readjusted by a slightly reduced lifetime). The high-density hadronic phase helps in the q_T spectra in the low- and intermediate-mass bin, for which, at high q_T , the discrepancy is the smallest for the three scenarios. In the highest mass bin, even the rather large ratio of four-pion annihilation over QGP emission does not upset the agreement with the q_T spectra, indicating that a large part of the four-pion emission

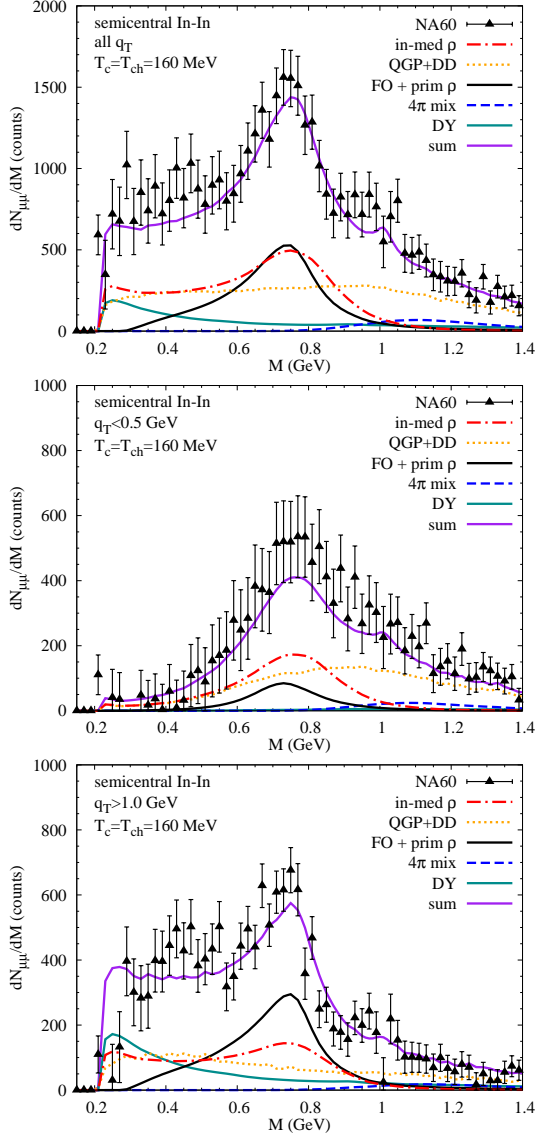


FIG. 14: (Color online) The same as Fig. 9, but for a fireball with a critical temperature $T_c = 160$ MeV and a chemical-freezeout temperature $T_{ch} = 160$ MeV (EoS-B).

emanates from the high-density hadronic phase.

Since the question of four-pion vs. QGP emission in the IMR has drawn considerable attention in the recent literature [87], we take a closer look at their interplay in our three scenarios in Fig. 18. The plot illustrates again that with EoS-B ($T_c = T_{ch} = 160$ MeV) the QGP contribution exceeds the in-medium four-pion annihilation over the entire IMR considered (note that the tails of the ρ spectral function are not included). The opposite trend applies to our default EoS-A scenario, and

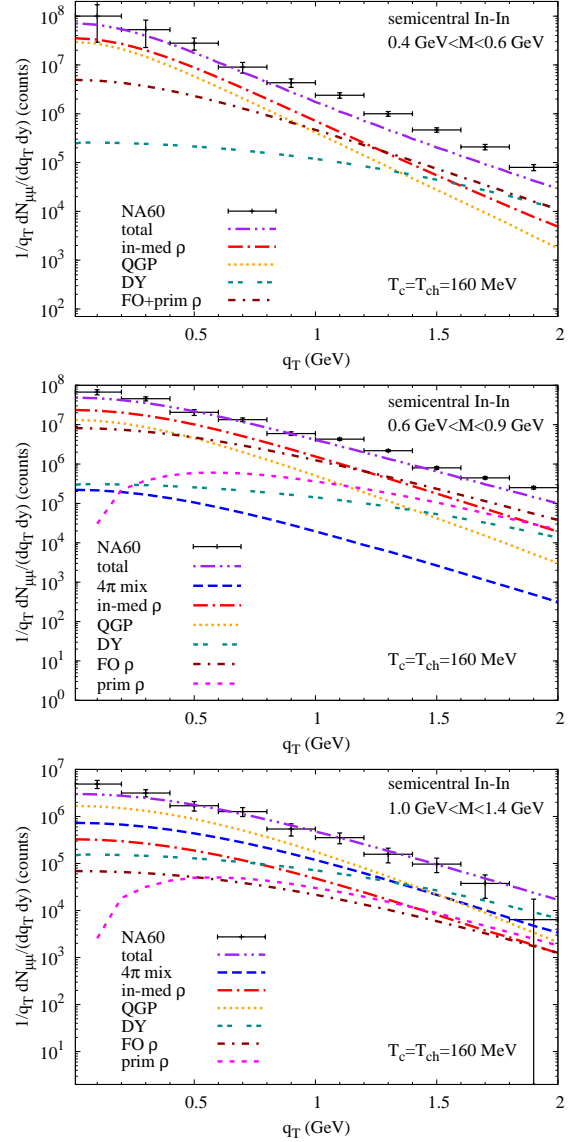


FIG. 15: (Color online) The same as Fig. 11, but for a fireball with a critical temperature $T_c = 160$ MeV and a chemical-freezeout temperature $T_{ch} = 160$ MeV (EoS-B).

even more so for EoS-C. Especially the large difference between EoS-B and EoS-C clearly demonstrates that the major portion of the four-pion emission emanates from the high-density hadronic phase (EoS-B and EoS-C have an identical hadronic evolution below $T_{ch} = 160$ MeV); a similar argument applies to EoS-A, *i.e.*, four-pion emission does not primarily arise in the late stages (with large flow) despite an enhancement through large pion-fugacity factors. The basic reason for this can be understood by inspecting the temperature-mass differential emission

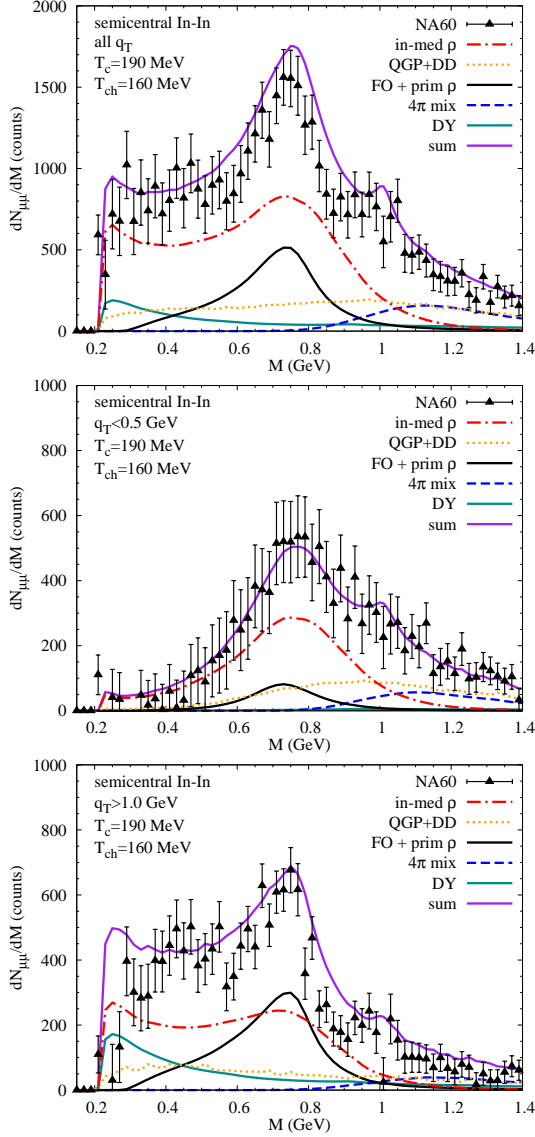


FIG. 16: (Color online) The same as Fig. 9, but for a fireball with a critical temperature $T_c = 190$ MeV and a chemical-freezeout temperature $T_{ch} = 160$ MeV (EoS-C).

yield which is roughly given by [14]

$$\frac{dN_{ll}}{dM dT} \propto \text{Im} \Pi_{\text{em}}(M, T) e^{-M/T} T^{-5.5}, \quad (44)$$

characterized by the standard thermal exponential factor and a power in temperature resulting from the three-momentum integral over the Boltzmann factor and, most importantly, the volume expansion. Assuming a weak temperature dependence of the e.m. spectral function (medium effects bias the emission toward higher T), a

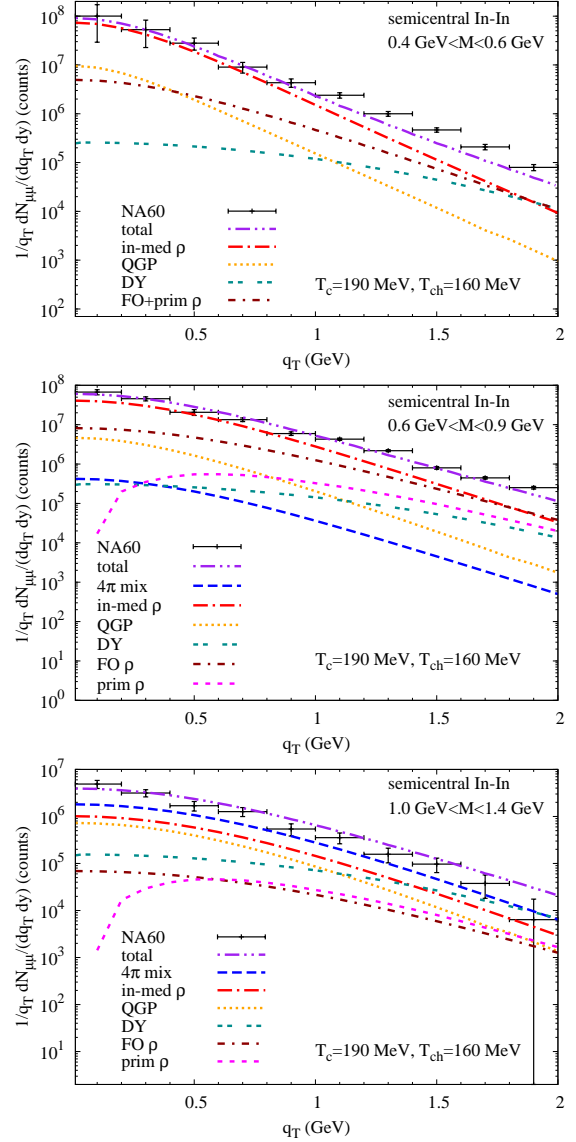


FIG. 17: (Color online) The same as Fig. 11, but for a fireball with a critical temperature $T_c = 190$ MeV and a chemical-freezeout temperature $T_{ch} = 160$ MeV (EoS-C).

differentiation over T identifies the temperature of maximum emission as $T_{\text{max}} \simeq M/5.5$. In the IMR of interest here, this means a T_{max} right around T_c (note that, at T_c , the hadronic phase has an extra “advantage” of a roughly twice larger volume compared to the QGP due to the latent heat), consistent with our fireball emission pattern.

We conclude this section by noting that “reasonable” variations in hadro-chemical freezeout and critical temperature have a very moderate impact on the invariant-

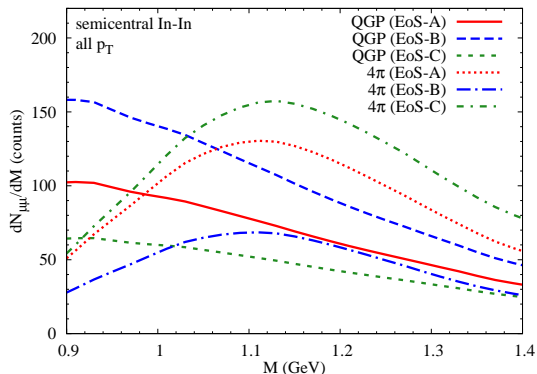


FIG. 18: (Color online) Comparison of the QGP and four-pion contributions to the dilepton yield in the intermediate mass region for the three equations of state, as discussed in the text. The 2-pion part, which is significant up to $M \simeq 1.1$ GeV, is not shown.

mass spectra as seen by NA60. On the one hand, this implies little sensitivity to the concrete values of T_c and T_{ch} . On the other hand, it means that our results are very robust with respect to uncertainties in these quantities. The main reason for this robustness is the “quark-hadron duality” of the underlying (medium-modified) emission rates from the hadronic and QGP phase in the relevant temperature regime, $T = 160$ - 190 MeV, in both LMR (ρ melting) and IMR (including chiral mixing). As such, it provides additional support to the medium modifications in the employed rates. In the IMR, this “duality” does not allow for a (maybe even academic) distinction between a high-density hadronic or partonic source. Partitions with either component dominant are viable in both mass and transverse momentum spectra. Concerning the high- q_T region of the lower two mass bins, our calculations indicate a slight preference for EOS-B and EOS-C, due to their smaller T_{ch} , implying larger temperatures in the hadronic evolution.

D. Slope analysis

To complete our analysis of the q_T spectra we perform in this section a quantitative analysis of effective slope parameters following the procedure adopted by the NA60 collaboration for the experimental data [18, 87, 88]. The q_T spectra have been divided into several invariant-mass bins, in each of which the data have been fitted to the function

$$\frac{1}{q_T} \frac{dN}{dq_T} = \frac{1}{m_T} \frac{dN}{dm_T} = C \exp\left(-\frac{m_T}{T_{eff}}\right), \quad (45)$$

where the fit range is typically taken as $0.4 \text{ GeV} < q_T < 1.8 \text{ GeV}$, but the extracted slopes are rather insensitive to variations as long as the lower limit is above 0.4 GeV .

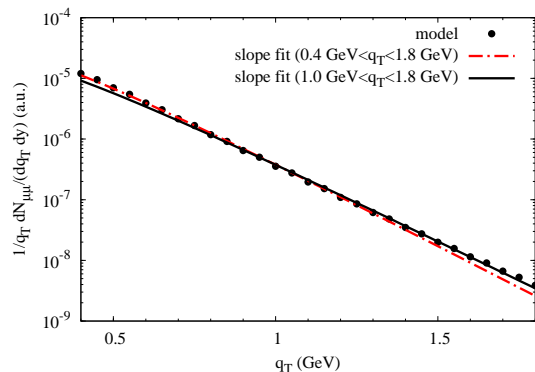


FIG. 19: (Color online) Dependence of the effective-slope fits, Eq. (45), to our theoretical q_T spectra without the Drell-Yan contribution (dots) on the fit range in q_T (as indicated in the legends) for the mass bin $0.3 \text{ GeV} \leq M \leq 0.4 \text{ GeV}$.

In addition, the experimental q_T spectra exhibit little dependence on centrality (except for peripheral collisions), and therefore the slope analysis has been performed for inclusive q_T spectra with $dN_{ch}/dy > 30$. In our theoretical analyses we focus on semicentral collisions.

We have tried to follow the same procedure (see also Ref. [89]), but as illustrated by the dash-dotted line in Fig. 19, a fit to our theoretical spectra (represented by the dots) in the above range ($0.4 \text{ GeV} < q_T < 1.8 \text{ GeV}$) slightly underestimates the effective slopes toward higher q_T , especially in the lower mass bins. Part of the problem is the bias of the fit toward low q_T where the yield is the largest and thus dominates the total χ^2 . To better reproduce the theoretical spectral shape with the above function we have therefore chosen to (i) restrict the fit range to $1 \text{ GeV} < q_T < 1.8 \text{ GeV}$, and (ii) minimize the χ^2 for the logarithm of the spectra. The resulting fit (solid line in Fig. 19) indeed agrees better with the theoretical spectra. This effect becomes more pronounced when the Drell-Yan component is included (which, in fact, might indicate that our extrapolation overestimates the DY yield at low mass).

Based on the slightly revised procedure, our slope analysis is carried out for the total sum of all calculated q_T spectra components in twelve $\Delta M = 0.1 \text{ GeV}$ mass bins in the range $0.2 \text{ GeV} < M < 1.4 \text{ GeV}$ (corresponding to the experimental ones) for semicentral In-In; by default, the Drell-Yan and meson t -channel contributions are not included, but studied in separate fits by adding them to the totals. As in the experimental analysis, correlated open-charm decays are removed altogether. Our systematic study addresses variations in the EoS as well as the possibility of another $\sim 15\%$ increase in the transverse acceleration of the fireball expansion, *i.e.*, $a_{\perp} = 0.1c^2/\text{fm}$ (which is, in fact, the value we have used in our calculations for heavy-flavor observables at RHIC [77], as extracted from the hydrodynamic model of Ref. [95]). Specifically, we evaluate the following scenarios, as sum-

marized in the six panels of Fig. 20:

- (a) the default fireball expansion with EoS-A ($T_c = T_{\text{ch}} = 175$ MeV), characterized by a thermal freezeout with temperature and radial flow surface velocity of $(T_{\text{fo}}, \beta_{\perp, \text{fo}}^s) = (120 \text{ MeV}, 0.57c)$;
- (b) the default fireball expansion with EoS-B ($T_c = T_{\text{ch}} = 160$ MeV) and $(T_{\text{fo}}, \beta_{\perp, \text{fo}}^s) = (136 \text{ MeV}, 0.57c)$;
- (c) the default fireball expansion with EoS-C ($T_c = 190$ MeV, $T_{\text{ch}} = 160$ MeV) and $(T_{\text{fo}}, \beta_{\perp, \text{fo}}^s) = (136 \text{ MeV}, 0.57c)$;
- (b⁺) the same as in (b), but with a transverse fireball acceleration $a_{\perp} = 0.1 c^2/\text{fm}$ yielding $(T_{\text{fo}}, \beta_{\perp, \text{fo}}^s) = (135 \text{ MeV}, 0.65c)$;
- (c⁺) the same as in (c), but with a transverse fireball acceleration $a_{\perp} = 0.1 c^2/\text{fm}$ yielding $(T_{\text{fo}}, \beta_{\perp, \text{fo}}^s) = (135 \text{ MeV}, 0.65c)$;
- (c₁⁺⁺) the same as in (c⁺), but additionally including the contribution from meson- t -channel exchange with in-medium ρ propagator (cf. Sec. IID);
- (c₂⁺⁺) the same as in (c₁⁺⁺), but using the vacuum ρ propagator in the meson- t -channel exchange contribution.

The upper two panels of Fig. 20 compare the impact of the three different EoS using our baseline acceleration of $a_{\perp} = 0.085c^2/\text{fm}$. The default scenario EoS-A (a) falls short of the empirical slopes by a significant margin of up to 50-60 MeV in the LMR, while reaching the lower end of the data in the IMR. The higher hadronic temperatures of scenarios EoS-B (b) and EoS-C (c) improve the situation by about 15-20 MeV in the LMR, approximately reflecting the increase in the hadronic fireball temperatures (e.g., $T_{\text{fo}} = 136$ MeV compared to $T_{\text{fo}} = 120$ MeV at thermal freezeout). Scenario EoS-B (b) additionally improves around the ρ peak due to a larger weight of the relatively hard components from decays of freezeout and primordial ρ , since the overall thermal hadronic emission is smaller than for EoS-A and EoS-C (compare Fig. 15 to Figs. 7 and 16). However, for both EoS-B and EoS-C the slopes in the LMR are still below the data, even though the shape is not too bad.

In an attempt to improve on the slopes, we investigate a further increase of the transverse acceleration to values representative for RHIC energies [77, 95], from $0.085 c^2/\text{fm}$ to $0.1 c^2/\text{fm}$ for EoS-B and EoS-C (scenarios (b⁺) and (c⁺), shown in the middle panels of Fig. 20). While this increases the effective slopes at all emission stages, it is more efficient for the later hadronic sources (in accordance with the blue-shift pocket formulae given in Sec. VB). Consequently, the LMR exhibits further improvement, and, importantly, the consistency with the data in the IMR is not spoiled due to the fact that the

main contributions there arise from earlier stages with higher temperatures and less flow (dominated either by the contributions from the QGP phase for EoS-B or four-pion annihilation in the high-density hadronic phase for EoS-C, cf. Fig. 18). At this point, EoS-B provides somewhat better agreement and one might be tempted to take this as evidence for a prevalently partonic emission source, as suggested in Refs. [87, 88]. However, remaining uncertainties preclude an unambiguous interpretation, as we will now show.

In the two bottom panels of Fig. 20 we focus on the EoS-C scenario with $a_{\perp} = 0.1c^2/\text{fm}$. The left panel illustrates the sensitivity of the slopes to the additional inclusion of t -channel meson exchange processes. As discussed in the previous section, their spectra alone carry a slope very similar to the data; not surprisingly, their inclusion increases the slopes in the LMR with no impact on the IMR slopes. When implementing the t -channel meson exchanges with the vacuum ρ propagator, the effect on the slopes is somewhat larger compared to using the in-medium D_{ρ} , especially in the free ρ mass region. A single $\pi\rho$ scattering with unmodified ρ mesons would most closely represent interactions of ρ mesons in a kinetic regime (rescattering without thermalization), and thus provide a missing link between the two extremes of thermal radiation and primordial ρ 's surviving jet quenching (no reinteraction) in our baseline calculations (note that there is no contribution from “quenched” ρ 's). The overall level of agreement with the data is now very similar to EoS-B. Also recall that $T_c = 190$ MeV maximizes the ratio of hadronic to QGP emission; for $T_c = 175$ MeV four-pion emission still outshines the QGP in the IMR, while the slope parameters are closer to the EoS-B scenario. The effect of the Drell-Yan contribution on the slopes is shown in the bottom-right panel of Fig. 20. In the IMR the change in slope is consistent with the experimental results (full vs. open squares), while in the lowest mass bins the uncertainties in the extrapolation of the DY are large. We emphasize again that more stringent constraints can be enforced once an accurate knowledge of the absolute normalization in the experimental mass and momentum spectra becomes available.

There are uncertainties in the experimental extraction of the slope parameters beyond the statistical error bars shown in the figures. In Ref. [88] a systematic error of ~ 7 MeV is estimated due to the subtraction of background and decay (cocktail) sources. For the LMR, it has been estimated that the subtraction of a potential Drell-Yan contribution could lower the effective slopes by 5-10 MeV. One should also be aware of that the applicability of hydrodynamic (or thermal fireball) descriptions is limited in transverse momentum, typically to $p_T \leq 2$ GeV for pion spectra at the SPS (consistent with where the spectra reach the collision-scaling regime in Fig. 6), and to significantly smaller p_T for elliptic flow. Fireball models might compensate for this to some extent by implementing a larger acceleration, which may be (part of) the reason that the dilepton slopes prefer

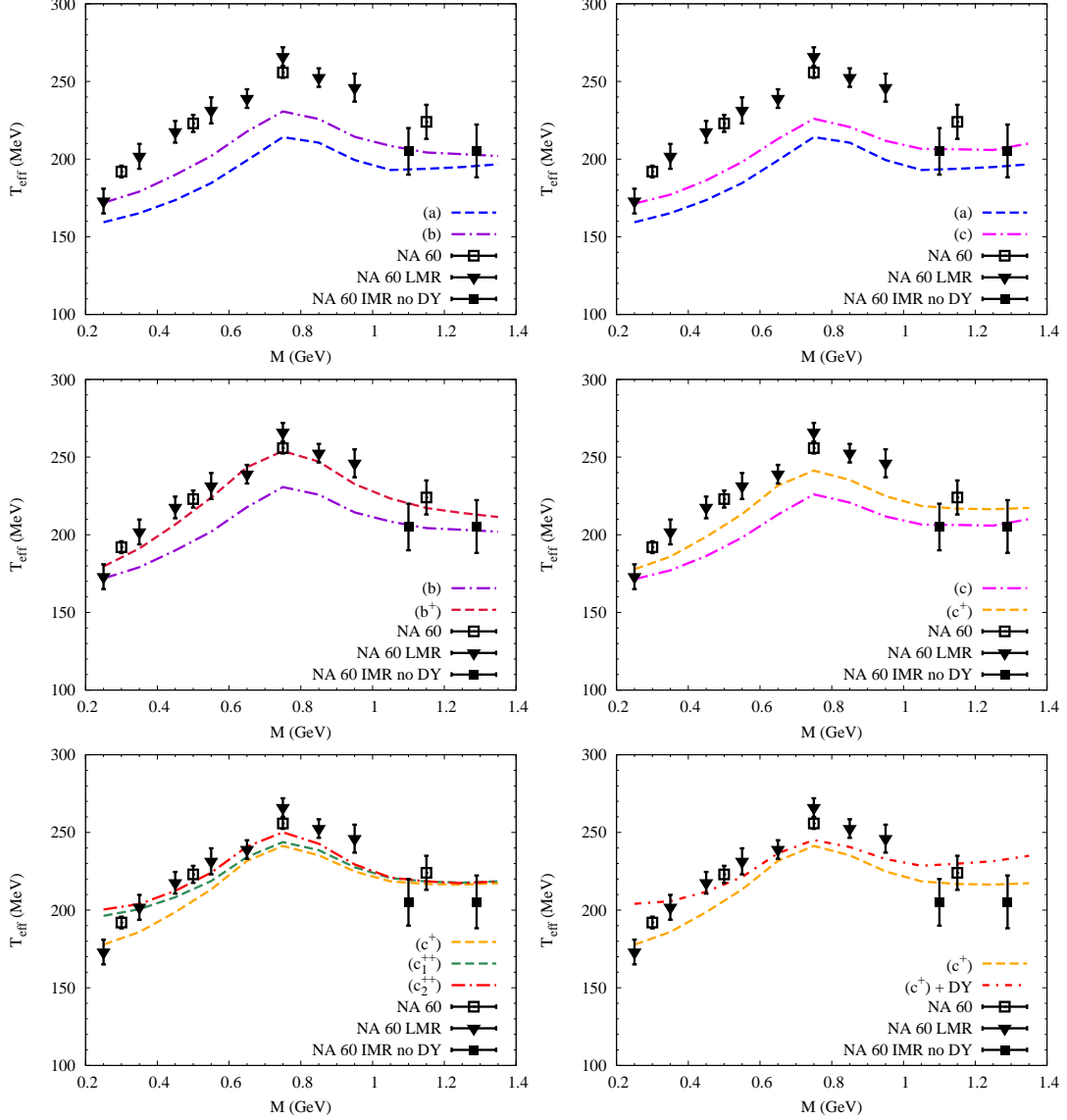


FIG. 20: (Color online) Effective slope parameters fitted to the theoretical q_T spectra using Eq. (45) for the following scenarios (by default, DY and t -channel meson exchange reactions are not included): top left: EoS-A (dashed line) vs. EoS-B (dash-dotted line), both with $a_{\perp} = 0.085c^2/\text{fm}$; top right: EoS-A (dashed line) vs. EoS-C (dash-dotted line), both with $a_{\perp} = 0.085c^2/\text{fm}$; middle left: EoS-B with either $a_{\perp} = 0.085c^2/\text{fm}$ (dash-dotted line) or $a_{\perp} = 0.1c^2/\text{fm}$ (dashed line); middle right: EoS-C with either $a_{\perp} = 0.085c^2/\text{fm}$ (dash-dotted line) or $a_{\perp} = 0.1c^2/\text{fm}$ (dashed line); bottom left: EOS-C with $a_{\perp} = 0.1c^2/\text{fm}$ (lower dashed line), additionally including meson t -channel contributions with free (dash-dotted line) or in-medium (middle dashed line) ρ propagator; bottom right: EOS-C with $a_{\perp} = 0.1c^2/\text{fm}$ (dashed line), additionally including Drell-Yan annihilation (dash-dotted line).

$a_{\perp} = 0.1c^2/\text{fm}$. To further scrutinize the q_T spectra, it would be very illuminating to reiterate earlier implementations of the dilepton rates from hadronic many-body theory into hydrodynamic [50] (with a more realistic hadro-chemistry) or transport [49] simulations. In

this context, a measurement of dilepton elliptic flow could provide further insights in the detailed emission history of the medium at SPS energies [90].

E. Update of Comparison to CERES/NA45 Data

After the refinements in our theoretical approach for SPS dilepton spectra in the context of the NA60 data, we revisit in this section the consequences for the comparison with CERES/NA45 in semicentral and central Pb-Au collisions, which showed good agreement in our earlier works [24, 36, 68]. In the following, we constrain ourselves to the above default scenario for the fireball evolution with a transverse acceleration of $a_{\perp} = 0.085 c^2/\text{fm}$. As in the In-In case, the increased expansion rate entails shorter fireball lifetimes; we choose the latter as to obtain the same thermal freezeout temperature for central ($T_{f_0} \simeq 106$ MeV) and semicentral ($T_{f_0} \simeq 112$ MeV) Pb-Au collisions as in our previous work [9, 24], implying a reduction by 2 fm/c for both centralities (13.5 \rightarrow 11.5 fm/c and 12 \rightarrow 10 fm/c, respectively). Also, since for the larger system sizes (*i.e.*, lifetimes) the freezeout- and cocktail- ρ contributions [4] are significantly suppressed relative to thermal radiation, and since we are not interested in (high-) q_t spectra here, we adopt the (old) simplified treatment for the freezeout ρ by running the fireball an additional duration of 1 fm/c [24]. The larger lifetimes relative to In-In collisions furthermore imply that the nonrelativistic formula for the surface expansion velocity, $v_{\perp}^s = a_{\perp} t$, approaches values uncomfortably close to c in the late stages of the collision. To implement a relativistically covariant acceleration in a simple way, we model the acceleration of the fireball in analogy to the relativistic motion for a charged particle in a homogeneous electric field. The radial surface velocity and fireball radius then take the form

$$\beta_{\perp}^s = \frac{a_{\perp} t/c}{\sqrt{1 + a_{\perp}^2 t^2/c^2}}, \quad (46)$$

$$r = r_0 + \frac{c^2}{a_{\perp}} \left(\sqrt{1 + a_{\perp}^2 t^2/c^2} - 1 \right),$$

which tames the acceleration at late times and matches the non-relativistic case for early times.

In the upper panel of Fig. 21 the updated calculations for dielectron spectra in semicentral Pb-Au collisions are compared to our previous results (using the same hadrochemistry and ρ spectral function), including experimental acceptance cuts as defined by CERES/NA45. For masses $M \gtrsim 0.6$ GeV, the ρ spectral function yield is reduced by 15-20%, directly reflecting the reduction in the lifetime of the hadronic phase in the fireball. At lower masses, however, the difference is smaller and eventually disappears for $M \lesssim 0.35$ GeV. The reason for this is the interplay of the single-electron cuts and the increase in transverse flow, where the latter gives larger momentum to both electrons which in turn have a larger probability to make it into the acceptance. For the QGP contribution, the difference is smaller (less than 10%) and weakly dependent on mass, since the increased transverse flow plays little role in the early phases (we recall that, for the canonical choice of the formation time, $\tau_0 = 1$ fm/c,

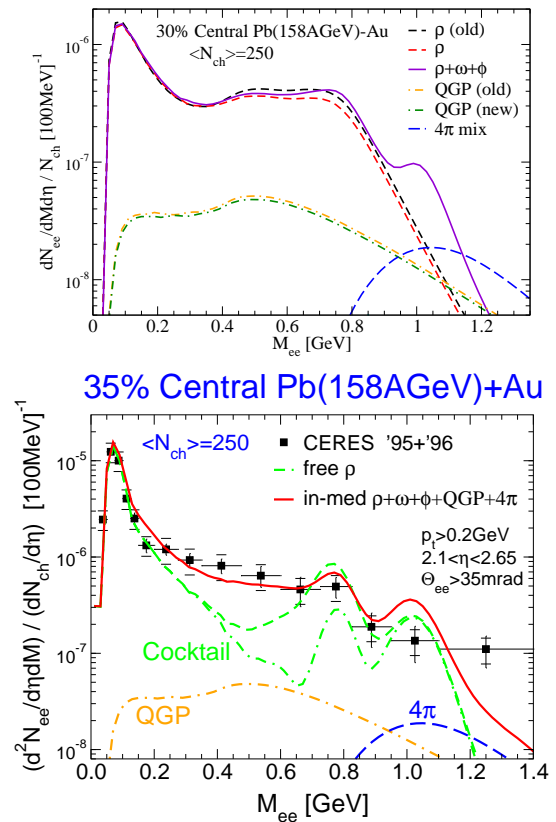


FIG. 21: (Color online) Upper panel: comparison of thermal dilepton spectra in semicentral Pb-Au collisions (including experimental acceptance) for ρ (short-dashed lines) and QGP emission (dash-dotted lines) using our previous (labeled “old”) and updated fireball evolution. The solid line is the sum of in-medium ρ , ω and ϕ contributions, while the long-dashed line results from four-pion annihilation including chiral mixing as described in Sec. II C. The Drell-Yan contribution is below the displayed range; correlated charm decays are neglected. Lower panel: The solid line is the total in-medium thermal emission + hadronic cocktail (dash-dotted line, adopted from the experimental evaluation [4]), compared to combined 1995/1996 CERES/NA45 data [4]. The short-dashed line is the sum of thermal emission with a vacuum ρ spectral function and the cocktail.

the initial temperature for 30% central Pb-Au amounts to $T_0 = 203$ MeV, and 210 MeV for 7% central). The addition of in-medium ω and ϕ decays affects the total yield mostly around the respective free masses, more significantly in the ϕ region. The in-medium four-pion contribution becomes relevant for masses $M \gtrsim 1$ GeV, with a relative strength compared to the other sources that closely resembles the In-In case. The Drell-Yan contribution does not show up on the scale of Fig. 21 (and has been restricted to masses above ~ 1 GeV). Correlated charm decays are not accounted for. The lower panel of

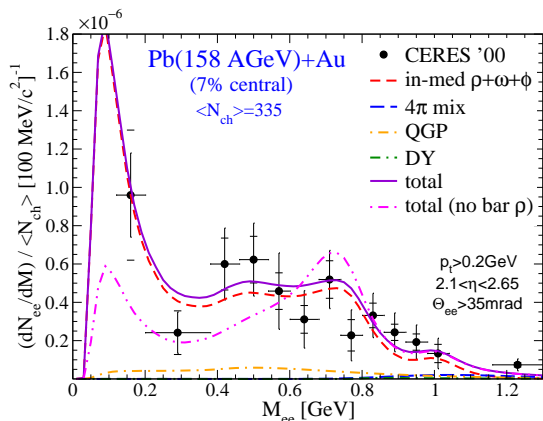


FIG. 22: (Color online) Comparison of theoretical calculations of dilepton excess spectra in central Pb-Au collision, compared to CERES/NA45 data [25]; for the line labeled “total (no bar ρ)” the full in-medium ρ spectral function has been replaced by the one which only includes medium effects in a meson gas.

Fig. 21 summarizes the comparison of the theoretical calculations with the combined 1996/1996 CERES/NA45 data [4], including the hadron decay cocktail. The level of agreement is very similar to the one with our earlier results [24, 68].

Finally, we turn to the most recent CERES data for central Pb(158 AGeV)-Au collisions [25], which are shown in Fig. 22 in a form similar to the NA60 data in the previous sections, *i.e.*, on a linear scale and with the cocktail subtracted. Again, our calculations employing the updated fireball describe these data fairly well. Variations of $\pm 20\%$ in the fireball lifetime (affecting the total dilepton yields at the same level with little change in the spectral shape), would still lead to reasonable agreement. The importance of baryon-induced medium modifications at SPS energies is reiterated by the dash-double-dotted curve where only meson-gas effects are included in the ρ spectral function; this scenario does not properly reproduce the experimental spectra. When comparing to the NA60 dimuon mass spectra, the four-pion and QGP contributions in the IMR appear smaller relative to the signal in the mass region below the free ρ mass. This is essentially due to the experimental acceptance, which for CERES/NA45 is significantly larger in the low-mass region than for NA60, especially for low-momentum lepton pairs.

A particularly striking feature of the theoretical predictions is the large enhancement below the two-pion threshold, which is closely connected with the approach to (and constraints from) the photon point. The very-low-mass excess is rather sensitive to the baryon-induced medium effects as well, as illustrated by the curve where the latter are switched off. Experimentally, this regime is only accessible with dielectrons (and after subtraction of the

π^0 Dalitz decay), and the first hint from data is consistent with the theoretical yield. Clearly, it would be very worthwhile to further explore this region.

VI. SUMMARY AND CONCLUSIONS

In the present paper, we have conducted a quantitative study of dilepton spectra in semi-/central heavy-ion collisions at full SPS energy ($\sqrt{s} = 17.3$ GeV). We have supplemented our earlier calculations of thermal radiation (which reproduce available mass spectra) with sources of non-thermal origin (expected to become relevant at high transverse momentum and for small systems), and we have scrutinized the results with respect to hadrochemical and flow properties of the underlying thermal fireball expansion.

The key quantity to describe thermal dilepton rates is the (imaginary part of the) electromagnetic current correlator. In hadronic matter, we have evaluated its medium modifications in terms of many-body spectral functions for the light vector mesons at low mass, and chiral vector-axialvector mixing for the continuum part at intermediate mass. Partonic emission above T_c has been approximated by perturbative quark-antiquark annihilation. An appealing feature of this description is a smooth merging of the hadronic rates with the partonic ones at temperatures around the expected phase transition, $T_c = 160$ -190 MeV. As a new ingredient we have computed thermal dilepton rates induced by t -channel meson exchange in $\pi\rho \rightarrow \pi l^+ l^-$ reactions, which we found to become relevant at momenta above ~ 1.5 GeV. We have augmented our approach by non-thermal sources, *i.e.*, Drell-Yan annihilation, as well as decays of ρ mesons from primordial production (subject to jet quenching) and from decoupling at thermal freezeout. We have emphasized that these ρ decays carry an extra kinematic Lorentz- γ factor relative to thermal radiation, resulting in harder dilepton- q_T spectra.

All sources have been implemented into a space-time evolution for A - A collisions at SPS, for which we employed an isentropic fireball model with QGP, mixed and hadron-gas phases and updated expansion parameters to better match the absolute dilepton yields measured by NA60. Hadrochemical freezeout and subsequent evolution are constructed in line with measured hadron multiplicities. The calculated dimuon invariant-mass spectra agree well with NA60 data in central and semicentral In-In collisions, including q_T bins below 0.5 GeV and above 1.0 GeV, thus confirming our earlier results for thermal emission and validating the predicted in-medium vector spectral functions (dominated, but not exhausted, by the ρ). When comparing to q_T spectra, the new sources contribute to provide good agreement for central collisions, while discrepancies persist with semicentral data at $q_T > 1$ GeV for masses around and below the free ρ mass. In particular, effective slope parameters for $q_T \geq 1$ GeV amount to $T_{\text{eff}} \simeq 160$ -210 MeV, $\sim 25\%$ short of the em-

pirically extracted values in the LMR.

We have investigated the sensitivity of our results to variations in the critical and chemical-freezeout temperature of the fireball. The spectral shape of the invariant-mass spectra turned out to be insensitive for the range $T_c = 160 - 190$ MeV. The reason is the “duality” of the thermal emission rates around T_c , rendering the “melting” of the ρ meson a robust signal. A low value of $T_c = 160$ MeV entails that QGP radiation dominates over hadronic emission in the IMR. A low value of $T_{\text{ch}} = 160$ MeV implies smaller pion chemical potentials (and thus higher temperatures) in the hadronic evolution, increasing the effective slope parameters by about 15-20 MeV, still ~ 30 MeV short of the data in the LMR.

In an attempt to resolve this discrepancy, we have implemented a $\sim 15\%$ increase in the transverse fireball acceleration as previously employed for central Au-Au collisions at RHIC energy. This elevates the slope to ~ 250 MeV around the free ρ mass (and properly reproduces the increase below), while still being consistent with the (upper) experimental value of 205 ± 20 MeV in the IMR where the blue shift effect is less pronounced due to the prevalently early emission. In particular, we have demonstrated that, within the current theoretical and experimental uncertainties, *both* scenarios for a predominant emission source in the IMR – hadronic (four-pion) or partonic – are viable. In either case, the radiation mostly emanates from matter at temperatures around $T_c \simeq 160 - 190$ MeV. An unambiguous distinction between a partonic and hadronic source in the IMR therefore appears difficult at SPS energies. The larger transverse flow developed in the partonic stage at RHIC energies could facilitate this task [91], although additional complications arise due to the much larger open-charm contribution and its in-medium modifications.

Finally we have checked that our refined assessment of dilepton sources, together with the improvements in the fireball expansion, preserves our previously found agreement with the CERES/NA45 dielectron spectra in Pb-Au collisions. The larger system size leads to an appreciable increase in thermal radiation, thus reducing the un-

certainties associated with the modeling of the break-up stage. In addition, dielectrons allow access to the mass region below the two-pion threshold, where the medium effects on the ρ -spectral function, augmented by the thermal Bose factor (and photon propagator), predict a large thermal dilepton signal. First data in this region support this signal, and further corroborate the importance of baryonic interactions for the in-medium ρ spectral function.

Future efforts should be pursued along several directions: first and foremost, the theoretically calculated vector spectral functions must be extended to their chiral partners (most notably the axialvector (a_1) channel as the partner of the ρ), to establish direct connections to chiral symmetry restoration. The evaluation of in-medium Weinberg sum rules [92], in connection with constraints from lattice QCD, will play an important role in this enterprise [93, 94]. Second, from the phenomenological side, the implementation of emission rates into both hydrodynamic and transport simulations should be reiterated, to compute q_T spectra and check whether the rather large acceleration of the fireball model can be justified for the In-In system at SPS. The study of dilepton elliptic flow [90] could shed further light on the time profile of the radiation. At RHIC energies, partonic collectivity increases significantly; an unexpectedly large dilepton excess in the LMR recently observed by PHENIX needs to be understood [96]. Work in several of these directions is in progress.

Acknowledgments

We are grateful to S. Damjanovic and H. J. Specht for discussion and information on the NA60 acceptance, and to A. Marin for providing us with the new CERES data. This work was supported in part by a U.S. National Science Foundation CAREER award under grant no. PHY-0449489.

-
- [1] R. Rapp and J. Wambach, *Adv. Nucl. Phys.* **25**, 1 (2000).
 - [2] J. Alam, S. Sarkar, P. Roy, T. Hatsuda, and B. Sinha, *Annals Phys.* **286**, 159 (2001).
 - [3] C. Gale and K. L. Haglin (2003), hep-ph/0306098.
 - [4] G. Agakichiev et al. (CERES Collaboration), *Eur. Phys. J. C* **41**, 475 (2005).
 - [5] D. Adamova et al. (CERES/NA45 Collaborations), *Phys. Rev. Lett.* **91**, 042301 (2003).
 - [6] A. L. S. Angelis et al. (HELIOS-3 Collaboration), *Eur. Phys. J. C* **13**, 433 (2000).
 - [7] M. C. Abreu et al. (NA38/NA50 Collaborations), *Nucl. Phys.* **A661**, 538 (1999).
 - [8] M. C. Abreu et al. (NA38 Collaboration), *Eur. Phys. J. C* **14**, 443 (2000).
 - [9] R. Rapp and E. V. Shuryak, *Phys. Lett. B* **473**, 13 (2000).
 - [10] M. M. Aggarwal et al. (WA98 Collaboration), *Phys. Rev. Lett.* **85**, 3595 (2000).
 - [11] S. Turbide, R. Rapp, and C. Gale, *Phys. Rev. C* **69**, 014903 (2004).
 - [12] R. Rapp (2002), nucl-th/0204003.
 - [13] R. Arnaldi et al. (NA60 Collaboration), *Phys. Rev. Lett.* **96**, 162302 (2006).
 - [14] R. Rapp, *J. Phys. G* **31**, S217 (2005).
 - [15] H. van Hees and R. Rapp, *Phys. Rev. Lett.* **97**, 102301 (2006).
 - [16] K. Dusling, D. Teaney, and I. Zahed, *Phys. Rev. C* **75**, 024908 (2007).
 - [17] J. Ruppert, C. Gale, T. Renk, P. Lichard, and J. I. Ka-

- pusta (2007), arXiv:0706.1934 [hep-ph].
- [18] S. Damjanovic et al. (NA60 Collaboration), Nucl. Phys. A **783**, 327 (2007).
- [19] R. Rapp, H. van Hees, and T. Strong, Braz. J. Phys. **37**, 779 (2007).
- [20] H. van Hees and R. Rapp, J. Phys. G **34**, S1051 (2007).
- [21] A. Andronic, P. Braun-Munzinger, and J. Stachel, Nucl. Phys. A **772**, 167 (2006).
- [22] F. Becattini, J. Manninen, and M. Gazdzicki, Phys. Rev. C **73**, 044905 (2006).
- [23] F. Karsch, J. Phys. G **34**, S627 (2007).
- [24] R. Rapp and J. Wambach, Eur. Phys. J. A **6**, 415 (1999).
- [25] D. Adamova et al. (CERES Collaboration) (2006), nucl-ex/0611022.
- [26] L. D. McLerran and T. Toimela, Phys. Rev. D **31**, 545 (1985).
- [27] G.-Q. Li and C. Gale, Phys. Rev. C **58**, 2914 (1998).
- [28] M. Harada and K. Yamawaki, Phys. Rept. **381**, 1 (2003).
- [29] R. Barate et al. (ALEPH Collaboration), Eur. Phys. J. C **4**, 409 (1998).
- [30] K. Ackerstaff et al. (OPAL Collaboration), Eur. Phys. J. C **7**, 571 (1999).
- [31] S. Weinberg, Phys. Rev. Lett. **18**, 507 (1967).
- [32] T. Das, V. S. Mathur, and S. Okubo, Phys. Rev. Lett. **19**, 859 (1967).
- [33] M. Urban, M. Buballa, R. Rapp, and J. Wambach, Nucl. Phys. A **641**, 433 (1998).
- [34] N. M. Kroll, T. D. Lee, and B. Zumino, Phys. Rev. **157**, 1376 (1967).
- [35] J. J. Sakurai, *Currents and Mesons* (University of Chicago Press, Chicago, 1969).
- [36] R. Rapp, G. Chanfray, and J. Wambach, Nucl. Phys. A **617**, 472 (1997).
- [37] R. Rapp, M. Urban, M. Buballa, and J. Wambach, Phys. Lett. B **417**, 1 (1998).
- [38] R. Rapp, Phys. Rev. C **63**, 054907 (2001).
- [39] A. Schenk, Nucl. Phys. B **363**, 97 (1991).
- [40] E. V. Shuryak, Nucl. Phys. A **533**, 761 (1991).
- [41] R. Rapp and J. Wambach, Phys. Lett. B **351**, 50 (1995).
- [42] H. van Hees and J. Knoll, Nucl. Phys. A **683**, 369 (2000).
- [43] A. Gomez Nicola, F. J. Llanes-Estrada, and J. R. Pelaez, Phys. Lett. B **606**, 351 (2005).
- [44] B. Friman (1998), nucl-th/9801053.
- [45] R. Rapp and C. Gale, Phys. Rev. C **60**, 024903 (1999).
- [46] S. Leupold, W. Peters, and U. Mosel, Nucl. Phys. A **628**, 311 (1998).
- [47] V. L. Eletsky, M. Belkacem, P. J. Ellis, and J. I. Kapusta, Phys. Rev. C **64**, 035202 (2001).
- [48] F. Riek and J. Knoll, Nucl. Phys. A **740**, 287 (2004).
- [49] W. Cassing, E. L. Bratkovskaya, R. Rapp, and J. Wambach, Phys. Rev. C **57**, 916 (1998).
- [50] P. Huovinen and M. Prakash, Phys. Lett. B **450**, 15 (1999).
- [51] K. Reygers (PHENIX Collaboration), AIP Conf. Proc. **870**, 736 (2006), nucl-ex/0608043.
- [52] W. M. Yao et al. (Particle Data Group), J. Phys. G **33**, 1 (2006).
- [53] M. Wachs, Ph.D. thesis, Technische Universität Darmstadt (2000), URL <http://elib.tu-darmstadt.de/diis/000050/>.
- [54] D. Cabrera and R. Rapp (2007), work in progress.
- [55] M. F. M. Lutz, G. Wolf, and B. Friman, Nucl. Phys. A **706**, 431 (2002).
- [56] D. Trnka et al. (CBELSA/TAPS Collaboration), Phys. Rev. Lett. **94**, 192303 (2005).
- [57] M. Kaskulov, E. Hernandez, and E. Oset, Eur. Phys. J. A **31**, 245 (2007).
- [58] K. Haglin, Nucl. Phys. A **584**, 719 (1995).
- [59] A. T. Martell and P. J. Ellis, Phys. Rev. C **69**, 065206 (2004).
- [60] L. Alvarez-Ruso and V. Koch, Phys. Rev. C **65**, 054901 (2002).
- [61] D. Cabrera, L. Roca, E. Oset, H. Toki, and M. J. Vicente Vacas, Nucl. Phys. A **733**, 130 (2004).
- [62] T. Ishikawa et al., Phys. Lett. B **608**, 215 (2005).
- [63] M. Dey, V.L. Eletsky, and B.L. Ioffe, Phys. Lett. B **252**, 620 (1990).
- [64] J. V. Steele, H. Yamagishi, and I. Zahed, Phys. Rev. D **56**, 5605 (1997).
- [65] M. Urban, M. Buballa, and J. Wambach, Phys. Rev. Lett. **88**, 042002 (2002).
- [66] H. van Hees and R. Rapp, Procs. of the 22nd Winter Workshop on Nuclear Dynamics 91 (2006), hep-ph/0604269.
- [67] E. Braaten, R. D. Pisarski, and T.-C. Yuan, Phys. Rev. Lett. **64**, 2242 (1990).
- [68] R. Rapp, Pramana **60**, 675 (2003).
- [69] J. Casalderrey-Solana and E. V. Shuryak (2004), hep-ph/0408178.
- [70] F. Cooper and G. Frye, Phys. Rev. D **10**, 186 (1974).
- [71] M. Aguilar-Benitez et al., Z. Phys. C **50**, 405 (1991).
- [72] D. d'Enterria, Eur. Phys. J. C **43**, 295 (2005).
- [73] M. Glück, E. Reya, and A. Vogt, Z. Phys. C **67**, 433 (1995).
- [74] C. Spieles et al., Eur. Phys. J. C **5**, 349 (1998).
- [75] A. Adare et al. (PHENIX Collaboration), Phys. Rev. Lett. **98**, 172301 (2007).
- [76] B. I. Abelev et al. (STAR Collaboration), Phys. Rev. Lett. **98**, 192301 (2007).
- [77] H. van Hees, V. Greco, and R. Rapp, Phys. Rev. C **73**, 034913 (2006).
- [78] R. Shahoyan [NA60 Collaboration], J. Phys. G **34**, S1029 (2007).
- [79] I. G. Bearden et al. (NA44 Collaboration), Phys. Rev. Lett. **78**, 2080 (1997).
- [80] H. Appelshäuser et al. (NA49 Collaboration), Eur. Phys. J. C **2**, 661 (1998).
- [81] F. Antinori et al. (WA97 Collaboration), J. Phys. G **27**, 2325 (2001); J. Phys. G **33**, 403 (2007).
- [82] D. Adamova et al. (CERES Collaboration), Nucl. Phys. A **714**, 124 (2003).
- [83] S. Damjanovic (2006), private communication.
- [84] F. Becattini, M. Gazdzicki, A. Keranen, J. Manninen, and R. Stock, Phys. Rev. C **69**, 024905 (2004).
- [85] E. Schnedermann, J. Sollfrank, and U. W. Heinz, Phys. Rev. C **48**, 2462 (1993).
- [86] M. I. Gorenstein, K. A. Bugaev, and M. Gazdzicki, Phys. Rev. Lett. **88**, 132301 (2002).
- [87] H. Specht (2007), arXiv:0710.5433v1 [nucl-ex].
- [88] R. Arnaldi et al. (NA60 Collaboration) (2007), arXiv:0711.1816 [nucl-ex].
- [89] T. Renk and J. Ruppert, arXiv:hep-ph/0612113.
- [90] U. W. Heinz, R. Chatterjee, E. S. Frodermann, C. Gale, and D. K. Srivastava, Nucl. Phys. A **783**, 379 (2007).
- [91] N. Xu, private communication (2007).
- [92] J. I. Kapusta and E. V. Shuryak, Phys. Rev. D **49**, 4694 (1994).
- [93] G. David, R. Rapp, and Z. Xu (2006), nucl-ex/0611009.

- [94] R. Rapp, J. Phys. G **34**, S405 (2007).
[95] P.F. Kolb, J. Sollfrank and U.W. Heinz, Phys. Rev. C **62**, 054909 (2000).
[96] S. Afanasiev et al. (PHENIX Collaboration) (2007), arXiv:0706.3034 [nucl-ex].

The Chiral Restoration Transition of QCD and Low Mass Dileptons

R. Rapp¹, J. Wambach² and H. van Hees³

¹Cyclotron Institute and Physics Department, Texas A&M University,
College Station, TX 77843-3366, U.S.A.

²TU Darmstadt, Schloßgartentr. 9, D-64289 Darmstadt, Germany

³Institut für Theoretische Physik, Justus-Liebig-Universität Giessen,
Heinrich-Buff-Ring 16, D-35392 Giessen, Germany

January 21, 2009

Abstract

Recent developments in the evaluation of vector-meson spectral functions in hot and dense matter are discussed with emphasis on connections to the chiral phase transition in QCD. Model independent approaches including chiral low-density expansions, lattice QCD, chiral and QCD sum rules are put into context with model predictions for in-medium vector-spectral function utilizing effective Lagrangians. Hadronic many-body calculations predict a strong broadening (and little mass shift) of the ρ spectral function which rapidly increases close to the expected phase boundary of hadronic and quark-gluon matter. Pertinent dilepton rates appear to degenerate with perturbative quark-antiquark annihilation in the Quark-Gluon Plasma, suggestive for chiral symmetry restoration. Applications to low-mass dilepton spectra in heavy-ion collisions result in quantitative agreement with recent high-quality data at the CERN-SPS. Thermal radiation from temperatures around T_c consistently reproduces the experimental dilepton excess observed at masses above 1 GeV as well. The interpretation of dilepton sources at high transverse momentum appears to be more involved.

Published in: Landolt-Brnstein **23**, 134 (2010),

DOI: 10.1007/978-3-642-01539-7_6

Preprint: arXiv:0901.3289v1 [hep-ph]

Contents

1	Introduction	3
1.1	QCD Vacuum and Chiral Restoration	3
1.2	Ultrarelativistic Heavy-Ion Collisions	4
1.3	Dilepton Spectroscopy	6
1.4	Outline	8
2	Chiral Symmetry, Condensates and Chiral Restoration	9
2.1	Condensates and Hadron Spectrum in Vacuum	9
2.2	Phase Diagram and Chiral Restoration	11
3	Vector Mesons in Medium	14
3.1	Dileptons and Electromagnetic Correlation Function	14
3.2	Medium Effects I: Model Independent	16
3.2.1	Chiral Reduction and Mixing	17
3.2.2	Lattice QCD and Susceptibilities	17
3.3	Sum Rules and Order Parameters	19
3.3.1	Chiral Sum Rules	19
3.3.2	QCD Sum Rules	20
3.4	Medium Effects II: Chiral Effective Models	22
3.4.1	Hidden Local Symmetry and Vector Manifestation	22
3.4.2	Massive Yang-Mills and Hadronic Many-Body Theory	23
3.5	Thermal Dilepton and Photon Rates	27
4	Interpretation of Dilepton Spectra	28
4.1	Medium Effects in Nuclei	29
4.2	Heavy-Ion Collisions	30
4.2.1	Thermal Evolution and Dilepton Sources	30
4.2.2	CERN-SPS I: NA60	33
4.2.3	CERN-SPS II: CERES/NA45 and WA98	37
4.2.4	Future Dilepton Measurements	39
4.3	Critical Appraisal	40
5	Conclusions	42

1 Introduction

The quest for the elementary entities of matter has always been a central objective in physics. Of no less interest is the emergence of the structure (or phases) of matter built from its basic constituents and their interactions. The exploration of matter governed by the strong force is at the forefront of contemporary research in nuclear physics. The most common form of strongly interacting matter in the present-day universe is contained in atomic nuclei, which are bound states of nucleons, i.e., protons and neutrons. Nuclear matter as found in the center of heavy nuclei is characterized by a nucleon (energy) density of about $\varrho_0 = 0.16 \text{ fm}^{-3}$ ($\varepsilon_0 = 0.15 \text{ GeV}/\text{fm}^3$), rendering one table spoon of this material a mass of about one million kilotons (10^{12} kg). The binding of nucleons is strong enough to cause a reduction of nuclear masses by about 1% compared to the sum of the rest mass of the individual nucleons, $m_N \simeq 940 \text{ MeV}/c^2$. But how does the mass of a nucleon arise? In the late 1960's it was discovered that the nucleon itself is a composite object, built of three “valence” quarks of *up* (*u*) and *down* (*d*) “flavor”. The bare masses of *u* and *d* quarks are only about 5-10 MeV/c^2 , and believed to be generated by a condensate of (yet to be discovered) Higgs bosons in the electroweak (EW) sector of the Standard Model of Elementary Particles. That is, about 98% of the nucleon's mass is generated dynamically by the strong interaction. Moreover, no individual quarks have been observed in nature thus far: they are “confined” into hadrons, either baryons or mesons (conglomerates of three valence quarks or of a quark and antiquark, respectively). In the 1970's, the quantum field theory underlying the strong force has been developed, Quantum Chromodynamics (QCD), based on quarks and gluons as fundamental degrees of freedom. This theory has been quantitatively confirmed in high-energy scattering experiments, where the strong coupling constant, $\alpha_s \simeq 0.1$, is relatively small and perturbation theory can be reliably utilized to obtain quantitative results for observables. However, at low momentum transfers, α_s becomes large, perturbation theory ceases to be applicable and nonperturbative mechanisms take over. It is in this regime where quark confinement and mass generation occur, posing formidable challenges for their theoretical understanding [1].

1.1 QCD Vacuum and Chiral Restoration

It turns out that confinement and mass generation are intimately connected with the phase structure of strongly interacting matter (see, e.g., Ref. [2]). In fact, even the structure of the QCD vacuum is far from trivial: similar to the EW sector, it is believed to be filled with condensates, which are closely related to the origin of hadronic masses. There are, however, important differences: the QCD condensates are made of (scalar) composites of quarks and gluons (rather than elementary fields like the Higgs boson), and they do not induce a breaking of the gauge symmetry. In what follows, the so-called “chiral” quark-antiquark condensate, $\langle 0|\bar{q}q|0\rangle \simeq (-250 \text{ MeV})^3$, will be of particular importance. It breaks the (approximate) chiral symmetry of QCD, which corresponds to the conservation of left and right “handedness” of massless quarks (applicable for the light *u* and *d* quarks, whose masses are parametrically small, $m_{u,d} \ll |\langle 0|\bar{q}q|0\rangle|^{1/3}$). While the quark condensate cannot be directly observed, its consequences are apparent in the excitations of the condensed ground state, i.e., in the hadron spectrum. Since chiral symmetry is a global symmetry (rather than a local one depending on space-time position), its spontaneous breaking must be accompanied by (almost) massless Goldstone bosons. For two quark flavors the latter are identified with the three charge states of the pion, whose mass, $m_\pi \simeq 140 \text{ MeV}$, is

“abnormally” small compared to that of all the other hadrons (e.g., $m_N \simeq 940$ MeV). The observed hadron spectrum encodes further evidences for the spontaneous breaking of chiral symmetry (SB χ S): chiral multiplets (e.g., $\rho(770)$ - $a_1(1260)$ or $N(940)$ - $N^*(1535)$), which would be degenerate if the ground state were chirally symmetric, exhibit a large mass splitting of typically $\Delta M \simeq 500$ MeV. The effects of SB χ S seem to (gradually) cease as one goes up in mass in the hadronic spectrum [3]. This is one of the indications that SB χ S is a low-energy, strong-coupling phenomenon which is no longer operative at high momentum transfers where perturbation theory becomes applicable.

When heating the QCD vacuum its condensate structure is expected to change. Loosely speaking, thermally excited hadrons “evaporate” condensed $\bar{q}q$ pairs which eventually leads to the restoration of the spontaneously broken chiral symmetry. Numerical computations of the lattice-discretized path integral for QCD at finite temperature predict chiral symmetry restoration (χ SR) to occur at a (pseudo-) critical temperature of $T_c \simeq 160$ - 190 MeV [4, 5], corresponding to an energy density of about $\varepsilon_c \simeq 1$ GeV/fm³. The chiral transition is characterized by a rapid decrease of the $\bar{q}q$ condensate, which, in fact, serves as an order parameter of strongly interacting matter. In the limit of vanishing light quark masses and for three quark flavors, this transition is of first order, while for realistic quark masses as realized in nature (two light quarks u and d and a more heavy strange quark, $m_s \simeq 120$ MeV), it is more likely a rapid cross-over. Key manifestations of chiral symmetry restoration are its (observable) consequences for the hadron spectrum. Chiral partners must degenerate implying massive medium modifications of hadronic spectral functions as the transition is approached. This notion is a quite general concept found, e.g., in solid state physics where phase transitions are routinely diagnosed utilizing “soft-mode spectroscopy”. This applies in particular to a second order phase transition where the mode associated with an order parameter becomes massless (soft). But even for bulk matter properties, rapid changes in the thermodynamic state variables are directly related to changes in the relevant degrees of freedom at the typical thermal scale (temperature or Fermi momentum). Interestingly, the chiral transition is accompanied by the dissolution of hadrons into quarks, i.e., the deconfinement transition, at the same temperature (at least for vanishing net baryon density). The reason for the apparent coincidence of the two transitions is not understood. The deconfined and chirally restored strongly interacting matter is commonly referred to as the Quark-Gluon Plasma (QGP). The experimental verification and theoretical understanding of the mechanisms leading to the QGP are central objectives in modern nuclear research.

1.2 Ultrarelativistic Heavy-Ion Collisions

The only way to produce and study hot and dense strongly interacting matter in the laboratory is by colliding atomic nuclei at high energies. Several large-scale experiments at ultrarelativistic bombarding energies, $E_{\text{lab}} \gg m_N$, have been conducted over the past ~ 20 years, most recently at the SPS at CERN (at center-of-mass energies up to $\sqrt{s} = 17.3$ AGeV) and at the Relativistic Heavy-Ion Collider (RHIC) at Brookhaven (up to $\sqrt{s} = 200$ AGeV) [6, 7] with the heaviest available nuclei at $A \simeq 200$ (Pb and Au).

The first question that needs to be answered is whether these reactions produce *equilibrated matter*, i.e., do the produced particles undergo sufficient rescattering to justify the notion of an interacting medium characterized by bulk thermodynamic variables? Extensive and systematic measurements of hadronic observables have lead to a positive answer. This is extremely exciting as it puts within grasp the possibility to recreate, at least for a

short moment, the matter which the early universe was made of just a few microseconds after the Big Bang! While hadronic measurements are discussed and interpreted in depth in other contributions of this volume, let us sketch some of their main features: transverse-momentum (p_T) spectra of different hadron species (pions, kaons, protons, etc.), which characterize the hadronic fireball just before break-up at its “thermal freeze-out”, exhibit a collective explosion reaching an average speed of about half the speed of light at a final temperature of $T_{fo}^{th} \simeq 100$ MeV. The ratios of the observed hadron species point at a significantly higher temperature of $T_{fo}^{ch} \simeq 160$ MeV [8, 9], i.e., the chemistry of the fireball (driven by inelastic scattering processes) appears to freeze out significantly earlier than kinetic equilibrium (maintained by elastic interactions). This is consistent with the large difference of empirical elastic (e.g., $\pi\pi \rightarrow \rho \rightarrow \pi\pi$ or $\pi N \rightarrow \Delta \rightarrow \pi N$) and inelastic (e.g., $\pi\pi \rightarrow K\bar{K}$) hadronic cross sections, with typical values of ~ 100 mb vs. ~ 1 mb, respectively. Since the cross sections determine the relaxation times according to $\tau \simeq (\varrho_h \sigma v_{rel})^{-1}$ (ϱ_h : hadron density, v_{rel} : relative velocity of the colliding hadrons), one obtains a clear hierarchy in the underlying relaxation times, $\tau_{th} \ll \tau_{ch}$. The interacting hadronic phase between chemical and thermal freeze-out will play an important role in the remainder of this article. More differential analyses of the flow patterns of the measured hadrons allow to trace back the matter properties to earlier times in the evolution of the fireball. In particular, the magnitude of the “elliptic flow” measured at RHIC indicates that the medium thermalizes on a rather short time scale, $\tau \leq 1$ -2 fm/c after initial impact, translating into (energy-) densities of a factor 10 or more above the critical one¹. A thermal (hydrodynamic) description [10, 11, 12, 13] of the fireball in semi-/central collisions of heavy nuclei at RHIC appears to be valid for hadrons up to momenta of $p_T \simeq 2$ -3 GeV, comprising approximately 95% of all produced particles. At high transverse momenta, $p_T > 5$ GeV, hadron production is dominated by hard scattering, i.e., a primordial parton-parton collision at high momentum transfer within the incoming nucleons, followed by fragmentation into (a spray of) hadrons (jets). In central Au-Au collisions at RHIC, a factor of ~ 5 suppression of high- p_T hadron production has been observed (“jet quenching”)². While these hadrons (or their parent quarks) do not thermalize, their suppression indicates a substantial coupling to the created medium, associated with an energy loss of a fast parton propagating through the fireball. The (energy-) density of the medium required to account for this effect is roughly consistent with the estimate inferred from a hydrodynamic description of the elliptic flow of low- p_T hadrons.

A second level of questions concerns the relevant degrees of freedom of the produced matter, i.e., whether there is explicit evidence that individual partons leave a distinctive footprint in observables. It turns out that the elliptic flow is again revealing interesting features in this context: it has been found [14, 15] that the elliptic-flow coefficient, $v_2^h(K_T)$, of all measured hadrons, $h=\pi, K, p, \Lambda, \Sigma, \phi, \dots$, exhibits a remarkable universality as a function of transverse kinetic energy, $K_T=m_T-m_h$ ($m_T=(p_T^2+m_h^2)^{1/2}$): when scaled with

¹Elliptic flow characterizes the azimuthal asymmetry in the p_T -spectra of particles (in the plane transverse to the beam axis). In a non-central heavy-ion collision, the initial nuclear overlap (interaction) zone is “almond-shaped”. If the system thermalizes before this spatial anisotropy is smeared out (e.g., due to free streaming), a larger pressure gradient builds up along the “short” compared to the “long” axis of the initial almond. This thermal pressure drives a collective expansion of the “almond” which is stronger along the short axis and thus results in particle momenta with a preference to be aligned with this axis. The magnitude of the elliptic flow is thus sensitive to how fast thermalization is established.

²Jet quenching is probably also present at the SPS but it is quantitatively smaller than at RHIC (about a factor of 2 suppression) and masked by a large initial p_T broadening in the interpenetrating nuclei prior to the hard scattering, known as “Cronin effect”.

the constituent-quark number content, n_q , of hadron h , all measured hadron- v_2 data appear to collapse on a single curve, $v_2^g(K_t \equiv K_T/n_q) = v_2^h(K_T)/n_q$. This has been interpreted as evidence for a collectively expanding partonic source hadronizing via quark coalescence. A fully consistent theoretical description of this phenomenon has not been achieved yet.

A third level of investigations has to address signals of the deconfinement and/or chiral restoration transitions. In a rigorous sense, this requires the assessment of order parameters associated with these transitions. However, changes in order parameters are not always easily observable. This is particularly true in the present context and we are led back to the idea of “mode spectroscopy”, to be conducted in the environment of a short-lived, rapidly expanding fireball of a heavy-ion collision. Individual (stable) hadrons emanating from the collision zone have all long recovered their free (vacuum) masses by the time they are measured in the detectors. A better observable are invariant-mass spectra of short-lived resonance decays, $h \rightarrow h_1 h_2$, with a lifetime, τ_h , comparable to, or smaller than, the lifetime of the interacting fireball, $\tau_{\text{FB}} \simeq 10 \text{ fm}/c$. Such a resonance (e.g., $\Delta \rightarrow \pi N$ or $\rho \rightarrow \pi\pi$) has a large probability to decay inside the medium so that its decay products can carry the information on its invariant-mass, $m_h^2 = (p_1 + p_2)^2$, at the point of decay to the detector. In principle, this would allow to determine the invariant-mass distribution (or spectral function) of the resonance h in the medium. The problem is that the decays products, h_1 and h_2 , are likely to undergo further rescattering in the fireball which destroys the desired invariant-mass information. The latter will thus be largely restricted to the dilute (break-up) stages of the medium in a heavy-ion collision.

1.3 Dilepton Spectroscopy

The decisive step to obtain access to hadronic spectral functions in the hot and dense regions of the medium is provided by electromagnetic (EM) probes, i.e., photons (γ) and dileptons (arising from virtual (timelike) photons, $\gamma^* \rightarrow l^+ l^-$ with $l=e$ or μ) [16, 17, 18]. These are not subject to the strong force and thus suffer negligible final-state interactions, with a mean free path which is much larger than the typical size of the fireball, $R_{\text{FB}} \simeq 10 \text{ fm}$. The natural candidates for in-medium spectroscopy are the vector mesons (V), which carry the quantum numbers of the photon (spin-parity $J^P=1^-$) and thus directly couple to exclusive dilepton final states, $V \rightarrow l^+ l^-$. In the low-mass region ($M \leq 1 \text{ GeV}$), which is the region of interest to study chiral restoration, the prominent vector mesons are $\rho(770)$, $\omega(782)$ and $\phi(1020)$. In fact, the famous vector dominance model (VDM) [19] asserts that the coupling of a (real or virtual) photon to *any* EM hadronic current exclusively proceeds via an intermediate vector meson (which is excellently satisfied in the mesonic sector but subject to corrections in the baryonic sector). Thus, if VDM holds in hadronic matter, dilepton emission is indeed equivalent to in-medium vector-meson spectroscopy. In thermal equilibrium, the contribution from the (isovector) ρ meson dominates over the ω by a factor of ~ 10 (factor ~ 5 over the ϕ , which, however, is thermally suppressed due to its larger mass). Furthermore, it can be shown [20] that, in the context of a heavy-ion collision, low-mass dilepton radiation from the hadronic phase dominates over the emission from a putative QGP phase, even at collider energies (RHIC and LHC)³. The excitement (and theoretical activity) in the field was further spurred by the suggestion of Brown and Rho [21] that the ρ -meson mass should drop to (almost) zero

³This is due to the much larger three-volume in the hadronic phase; at larger dilepton masses, $M > 1 \text{ GeV}$, the thermal Boltzmann factor, $e^{-q_0/T}$, augments the sensitivity to higher temperatures which increases the QGP contribution relative to the hadronic one in the inclusive dilepton spectrum.

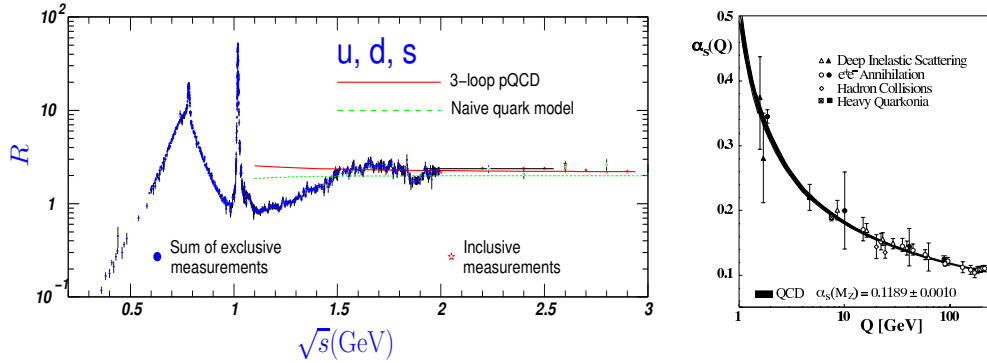


Figure 1: *Left panel:* ratio of cross sections, $R = \sigma_{ee \rightarrow \text{hadrons}} / \sigma_{ee \rightarrow \mu\mu}$, for electron-positron annihilation into hadrons relative to muon-antimuons, as a function of center-of-mass energy, \sqrt{s} . The experimental data exhibit a nonperturbative resonance regime up to $\sqrt{s} \simeq 1.1$ GeV, exhausted by the light vector mesons ρ , ω and ϕ , followed by a transition to an almost structureless perturbative regime at $\sqrt{s} \gtrsim 1.5$ GeV. The latter is well described by perturbative QCD (pQCD), especially for $\sqrt{s} \geq 2$ GeV, where residual “oscillations” (due to excited vector resonances) have essentially ceased. The naive quark-model prediction (leading-order pQCD, $\mathcal{O}(\alpha_s^0)$) is given by $R_{QM} = N_c \sum_{q=u,d,s} e_q^2 = 2$. *Right panel:* strong coupling constant as a function of momentum transfer [33]; note the increase of α_s toward small Q suggestive for the emergence of nonperturbative phenomena.

as a consequence of χ SR. Early dilepton measurements in S(200 AGeV)-Au collisions at the CERN-SPS by the CERES collaboration [22] found a large enhancement of the spectrum at invariant masses below the nominal ρ mass, i.e., for $M \simeq 0.2\text{--}0.7$ GeV. These data could be well described by a dropping-mass scenario implemented into relativistic transport models within a mean-field description [23, 24]. Subsequently, more “conventional” medium modifications of the ρ meson were investigated based on its rescattering on constituents of a hadronic medium, see, e.g., Refs. [25, 26, 27, 28] for reviews. The generic finding of these hadronic many-body calculations was a strong broadening of the ρ spectral function, which, when extrapolated to the putative phase transition temperature, $T_c \simeq 175$ MeV, leads to a complete “melting” of the resonance structure [29]. The broadening effect could account for a large part of the low-mass dilepton excess observed in S-Au collisions. The agreement was even better [30] with improved CERES/NA45 measurements carried out in the heavier Pb(158 AGeV)-Au system [31, 32]. The connection of the ρ melting to χ SR appeared to be less direct than in dropping-mass scenarios. However, in Refs. [34, 30] it was found that the hadronic dilepton rates following from the “melted” ρ close to T_c rather closely resemble the rates computed in a partonic description, i.e., perturbative quark-antiquark annihilation. In the vacuum, such a phenomenon is well known from the e^+e^- annihilation into hadrons: for $M \geq 1.5$ GeV the total cross section is well described within perturbative QCD using quark-antiquark final states, known as “parton-hadron duality”, cf. Fig. 1. It was therefore suggested that the conceptual implication of the ρ melting is a reduction of the “duality threshold” [34, 30], from $M_{\text{dual}} = 1.5$ GeV in the vacuum to essentially zero around T_c . Note that a “perturbative” dilepton rate automatically implies chiral restoration (i.e., degeneracy of vector and axialvector channels).

The accuracy in the 1995/1996 CERES/NA45 dielectron data [31, 32] did not allow for a decisive experimental discrimination of the dropping-mass and melting-resonance

scenarios. An important step forward was realized with the NA60 dimuon spectra [35] in In(158 AGeV)-In collisions at the SPS. Excellent mass resolution and superior statistics enabled, for the first time, an isolation of the “excess radiation” (by subtraction of final-state hadron decays). The shape of the excess spectrum clearly favors a broadened ρ spectral function over scenarios involving dropping masses. The original predictions of hadronic many-body theory [30, 20] are, in fact, in quantitative agreement [36] with the inclusive mass spectra in semi-/central In-In collisions. In the last round of CERES/NA45 data [37] excess spectra have also been extracted in Pb-Au collisions (by subtraction of final-state hadron decays using a statistical model [8]). While the overall data quality does not reach the level of NA60, the larger collision system and the access to very small dilepton masses in the dielectron channel (dimuons have a threshold of $2m_\mu=210$ MeV) can provide additional insights.

The dilepton program at the CERN-SPS has thus far reached the highest level of maturity in the heavy-ion context. It also included a CERES/NA45 measurement in a low-energy Pb(40 AGeV)-Au run [38], which produced tantalizing hints for an even larger excess than at 158 AGeV, but was unfortunately hampered by low statistics. At much lower, relativistic bombarding energies (1-2 AGeV), the DLS collaboration at the BEVALAC reported a very large dilepton excess [39], which has recently been confirmed by the HADES collaboration at SIS [40, 41]. On the other hand, the dilepton measurements at RHIC are still in their infancy (first data indicate substantial excess radiation [42]), but it will become a central component in future runs [43]. Very interesting results are also emerging from vector-meson spectroscopy in cold nuclei using elementary projectiles, i.e., photons [44, 45] or protons [46]. It turns out that all of these observables are closely related, and their broad understanding is essential for the determination of the in-medium vector-meson spectral functions. Of particular importance is the consistency of theoretical descriptions beyond phenomenological applications and the interrelations between different approaches (including effective hadronic and quark models, lattice QCD and constraints from sum rules), which will ultimately reveal the mechanisms of chiral restoration. In this article, we give an up-to-date account of these efforts with special emphasis on a broader picture in the context of χ SR.

1.4 Outline

Our article is organized as follows. In Sec. 2, we start by recollecting basic features of spontaneous chiral symmetry breaking in the QCD vacuum with emphasis on condensate structures and consequences for the hadronic excitation spectrum (sub-Sec. 2.1), followed by a discussion of in-medium condensates within the landscape of the QCD phase diagram (sub-Sec. 2.2). In Sec. 3, we scrutinize the links of the chain with which one hopes to connect thermal dilepton rates and (partial) χ SR. We first introduce the EM correlation function which is the basic quantity figuring into the thermal dilepton rate (sub-Sec. 3.1). Model-independent evaluations of medium effects can be obtained in the low-density limit from current algebra, in the high-temperature limit from perturbative QCD and, for vanishing baryon-chemical potential from lattice QCD (sub-Sec. 3.2). A valuable source of model-independent constraints is provided by chiral and QCD sum rules (sub-Sec. 3.3) which are energy moments of spectral functions that directly relate to order parameters of QCD and are generally not restricted in temperature and density. For practical applications, effective hadronic models are an indispensable tool (sub-Sec. 3.4); their reliability, based on the choice of interaction vertices and associated parameters, crucially hinges

on a thorough procedure of theoretical and phenomenological constraints; an important question will also be the fate of the vector dominance model in the medium. In Sec. 4 the theoretical developments are tested in recent dilepton production experiments, starting with elementary reactions off nuclei representative for medium effects in cold nuclear matter (sub-Sec. 4.1). The main part of Sec. 4 is devoted to an analysis of dilepton spectra in ultrarelativistic heavy-ion reactions (sub-Sec. 4.2), focusing on recent results obtained at the CERN-SPS by the NA60 and CERES/NA45 collaborations. The spectral analysis is completed by a critical assessment of the combined theoretical and experimental status to date (sub-Sec. 4.3). We finish with concluding remarks in Sec. 5.

2 Chiral Symmetry, Condensates and Chiral Restoration

It is generally accepted that strong interactions are described by Quantum Chromodynamics (QCD), introduced in 1973 [47, 48, 49], with a Lagrangian density given by

$$\mathcal{L}_{QCD} = \bar{q}(i\gamma^\mu D_\mu - \mathcal{M}_q)q - \frac{1}{4}G_{\mu\nu}^a G_a^{\mu\nu} \quad , \quad D_\mu = \partial_\mu + ig_s \frac{\lambda_a}{2} A_\mu^a \quad , \quad (1)$$

formulated in terms of elementary quark (q) and gluon (A_μ^a) fields (γ^μ and λ^a : Dirac and Gell-Mann matrices, respectively, $\mathcal{M}_q = \text{diag}(m_u, m_d, \dots)$: current-quark mass matrix). In addition to the local $SU(3)$ color gauge symmetry, \mathcal{L}_{QCD} possesses several global symmetries. The most relevant one in the present context is Chiral Symmetry, which can be exhibited by rewriting \mathcal{L}_{QCD} in terms of left- and right-handed quark fields, $q_{L,R} = \frac{1}{2}(1 \mp \gamma_5)q$:

$$\mathcal{L}_{QCD} = \bar{q}_L i\gamma^\mu D_\mu q_L + \bar{q}_R i\gamma^\mu D_\mu q_R - (\bar{q}_L \mathcal{M}_q q_R + \bar{q}_R \mathcal{M}_q q_L) - \frac{1}{4}G_{\mu\nu}^a G_a^{\mu\nu} \quad . \quad (2)$$

For small quark masses, i.e., u and d quarks, \mathcal{L}_{QCD} is approximately invariant under rotations $q_{L,R} \rightarrow e^{-i\vec{\alpha}_{L,R} \cdot \vec{\tau}/2} q_{L,R}$, where $\vec{\alpha}_{L,R}$ are 3 real angles and τ operates in (u - d) isospin space. Chiral invariance of the QCD Lagrangian thus refers to the conservation of quark handedness and isospin. Alternatively, one can rewrite the chiral rotations as $q \rightarrow e^{-i\vec{\alpha}_V \cdot \vec{\tau}/2} q$ and $q \rightarrow e^{-i\gamma_5 \vec{\alpha}_A \cdot \vec{\tau}/2} q$, giving rise to conserved isovector-vector and -axialvector currents,

$$\vec{j}_V^\mu = \bar{q}\gamma^\mu \vec{\tau} q \quad , \quad \vec{j}_A^\mu = \bar{q}\gamma^\mu \gamma_5 \vec{\tau} q \quad . \quad (3)$$

2.1 Condensates and Hadron Spectrum in Vacuum

As emphasized in the Introduction, the nonperturbative structure of the QCD vacuum is characterized by its condensates. A special role is played by the quark-antiquark ($q\bar{q}$) and gluon (G^2) condensates. Apart from being the condensates involving the minimal number of quark- and gluon-fields, the former is a main order parameter of SB χ S while the latter dominantly figures into the energy-momentum tensor of the theory. The vacuum expectation value of the latter's trace is given by

$$\langle T_\mu^\mu \rangle = \epsilon - 3P = -\langle G^2 \rangle + m_q \langle \bar{q}q \rangle \quad (4)$$

where $G^2 = -(\beta(g_s)/2g_s) G_a^{\mu\nu} G_{\mu\nu}^a$ involves the gluon-field strength tensor and the renormalization-group beta function, $\beta(g_s)$. The latter appears because the nonvanishing vacuum

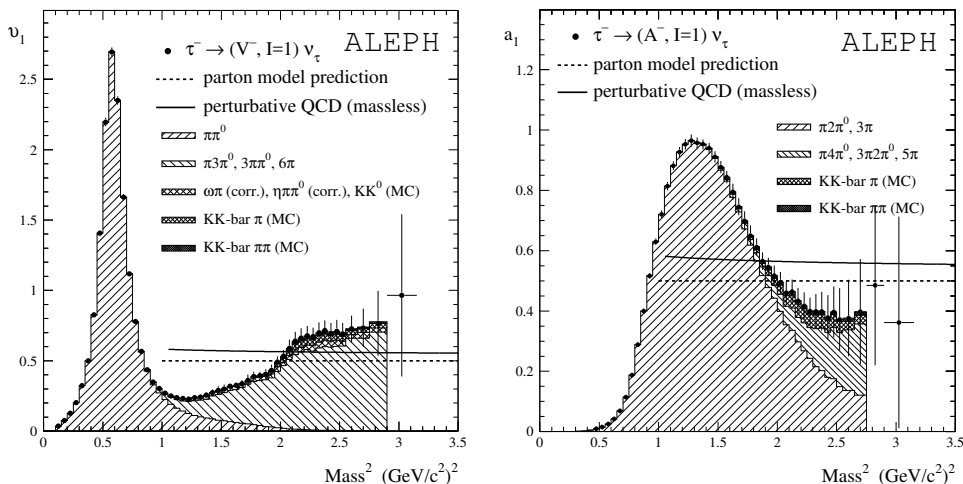


Figure 2: *Experimental data [50] of the isovector-vector ($IJ^P=11^-$, left panel) and isovector-axialvector ($IJ^P=11^+$, right panel) spectral functions from hadronic decays of τ leptons (produced in $\sqrt{s}=91$ GeV e^+e^- annihilation at LEP) into even and odd numbers of pions/kaons, respectively. The lines indicate theoretical calculations using pQCD.*

value of T_μ^μ breaks the scale invariance of the classical QCD Lagrangian, induced by quantum loop corrections. The small current light-quark masses, $m_q \simeq 5$ MeV, render the contribution of the quark condensate to T_μ^μ small. The absolute value of the gluon condensate is not precisely known, but presumably rather large, around $1.5 \text{ GeV}/\text{fm}^3 \simeq (330 \text{ MeV})^4$. In fact, the magnitude of the quark condensate is not small either, $\langle \bar{q}q \rangle \simeq (-250 \text{ MeV})^3$ per light-quark flavor, and about 50% of that for strange quarks. This implies that the vacuum is filled with ~ 5 quark-antiquark pairs per fm^3 ! Also note that the quark condensate maximally violates chiral symmetry by mixing right- and left-handed quarks, $\langle \bar{q}q \rangle = \langle \bar{q}_L q_R + \bar{q}_R q_L \rangle$, implying that a quark propagating through the vacuum can flip its chirality by coupling to the condensate. The intimate relation between chiral symmetry breaking and the associated Goldstone-boson nature of the pion is highlighted by the Gell-Mann-Oakes Renner (GOR) relation,

$$m_\pi^2 f_\pi^2 = -2m_q \langle \bar{q}q \rangle, \quad (5)$$

which combines the effects of explicit chiral symmetry breaking, $m_\pi^2 \propto m_q$, and SB χ S with the pion decay constant as order parameter.

One of the best direct empirical evidences for the spontaneous breaking of chiral symmetry is found in the vector channel, more specifically the isovector-vector channel ($IJ^P=11^+$) and its chiral partner, the isovector-axialvector one ($IJ^P=11^-$), precisely the Noether currents in Eqs. (3). The pertinent spectral functions have been measured with excellent precision (and a detailed decomposition of the hadronic final states) at the Large Electron-Positron collider (LEP) in hadronic τ decays by the ALEPH [50] and OPAL [51] collaborations, cf. Fig. 2. In the low-mass region, the strength of each of the two spectral functions is largely concentrated in a prominent resonance, i.e., the $\rho(770)$ and $a_1(1260)$. This very fact indicates that the low-mass regime is dominated by nonperturbative effects, while the (large) difference in mass and width of these resonances signals chiral

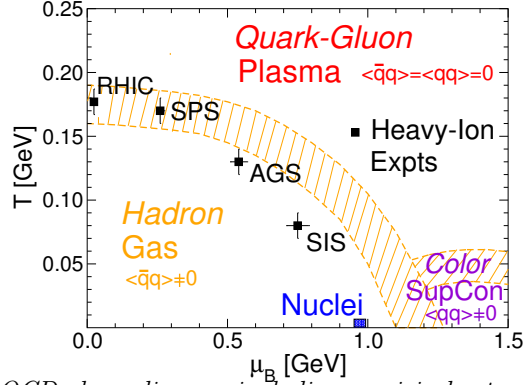


Figure 3: Schematic QCD phase diagram including empirical extractions of (μ_B, T) -values from observed hadron production ratios in heavy-ion experiments at different beam energies [8]; the bands indicate lattice-QCD and model estimates of the transition regions between HM, QGP and CSC; with the HM-QGP transition (along the finite T , $\mu_B=0$ axis) presumably a cross-over, and the HM-CSC one (along the finite μ_B , $T=0$ axis) possibly first order, there is presumably a second order endpoint, e.g., around $(\mu_B, T) \approx (400, 160)$ MeV.

symmetry breaking. This connection can be quantified by chiral sum rules developed by Weinberg [52] and others [53] in the late 1960's based on current algebra of chiral symmetry. These sum rules relate moments of the difference between vector and axialvector spectral functions to chiral order parameters. In the chiral limit ($m_\pi=0$) one has

$$f_n = - \int_0^\infty \frac{ds}{\pi} s^n [\text{Im} \Pi_V(s) - \text{Im} \Pi_A(s)] , \quad (6)$$

$$f_{-2} = f_\pi^2 \frac{\langle r_\pi^2 \rangle}{3} - F_A , \quad f_{-1} = f_\pi^2 , \quad f_0 = 0 , \quad f_1 = -2\pi\alpha_s \langle \mathcal{O} \rangle \quad (7)$$

(r_π : pion charge radius, F_A : coupling constant for the radiative pion decay, $\pi^\pm \rightarrow \mu^\pm \nu_\mu \gamma$, $\langle \mathcal{O} \rangle$: four-quark condensate).

2.2 Phase Diagram and Chiral Restoration

A schematic view of the QCD phase diagram is displayed in Fig. 3. It is roughly characterized by three major regimes (all of which most likely exhibit rich substructures): hadronic matter (HM) at small and moderate temperature (T) and baryon chemical potential (μ_B), Quark-Gluon Plasma (QGP) at high T and Color Super-Conductors (CSCs) at high μ_B but low T . The latter may occur in the core of neutron stars, but are unlikely to be produced in heavy-ion collisions and will not be further discussed here.

A key issue toward understanding the phase structure of QCD matter is the temperature and density dependence of its condensates. Various condensates serve as order parameters of broken symmetries and govern the (hadronic) excitation spectrum. The latter provides the connections to observables. A first estimate of the medium modifications of the condensates can be obtained in the low-density limit [55, 56], by approximating the thermal medium by non-interacting light hadrons, i.e., pions at finite T and nucleons at

finite ϱ_N . For the quark condensate, this leads to a linear density expansion of the type

$$\frac{\langle\langle\bar{q}q\rangle\rangle(T, \mu_B)}{\langle\bar{q}q\rangle} = 1 - \sum_h \frac{\varrho_h^s \Sigma_h}{m_\pi^2 f_\pi^2} \simeq 1 - \frac{T^2}{8f_\pi^2} - \frac{1}{3} \frac{\varrho_N}{\varrho_0} - \dots, \quad (8)$$

where ρ_h^s denotes the scalar density of hadron h , and Σ_h denotes its “ σ ”-term (Σ_h/m_q may be interpreted as the number of $\bar{q}q$ pairs inside hadron h which diminish the (negative) $\bar{q}q$ density of the condensate). In obtaining Eq. (8), the GOR relation (5) has been used. Alternatively, one can directly use the definition of the quark condensate in terms of the quark-mass derivative of the thermodynamic potential,

$$\langle\langle\bar{q}q\rangle\rangle = \frac{\partial\Omega}{\partial m_q}, \quad (9)$$

and evaluate the temperature and density-dependent part, $\bar{\Omega}(\mu_B, T) \equiv \Omega(\mu_B, T) - \Omega_{\text{vac}}$, in the free gas approximation. A similar strategy can be adopted for the gluon condensate, by utilizing its relation, Eq. (4), to the trace anomaly,

$$\langle\langle G^2 \rangle\rangle = -(\epsilon - 3P) + m_q \langle\langle\bar{q}q\rangle\rangle, \quad (10)$$

and estimating the ϱ_B - and T -dependent parts of pressure and energy density in suitable expansions. At finite temperature, for a massless pion gas, one has $\epsilon=3P$ and thus no correction to order T^4 (the system is scale invariant). It turns out that the lowest-order interaction contribution from (soft) $\pi\pi$ scattering does not contribute either so that the leading temperature dependence of the gluon condensate arises at order T^8 [54]. With the leading nuclear-density dependence as worked out in Refs. [55, 56], one has

$$\langle\langle G^2 \rangle\rangle = -\langle G^2 \rangle - (m_N - \Sigma_N)\varrho_N - \frac{\pi^2}{270} \frac{T^8}{f_\pi^4} \left(\ln \frac{\Lambda_p}{T} - \frac{1}{4} \right) \quad (11)$$

($\Lambda_p \simeq 275$ MeV is a renormalization scale). The above relations allow for some interesting insights. As already noted in Ref. [56], the linear-density expansions suggest that the gluon condensate is much less affected than the quark condensate, cf. also the upper panels in Fig. 4. It is not obvious whether recent finite- T lattice computations in QCD with 2+1 flavors support this picture (see the lower panels of Fig. 4), especially when approaching the critical temperature: both $\langle\langle\bar{q}q\rangle\rangle$ and $\langle\langle G^2 \rangle\rangle$ drop significantly around T_c and reach approximately zero at roughly $1.5 T_c$ (the perturbative interaction contribution to $\epsilon - 3P$ renders the gluon condensate negative at high T). The low-density expansion of the quark condensate seems to suggest that temperature effects are weaker than density effects (upper left panel in Fig. 4). This is, in fact, not the case: as a function of (pion-) *density*, the leading reduction of $\langle\langle\bar{q}q\rangle\rangle$ in a heat bath is quite comparable to cold nuclear matter, as determined by the coefficient in Eq. (8) which is in essence given by the respective σ terms, $\Sigma_\pi \simeq 70$ MeV compared to $\Sigma_N = 45 \pm 15$ MeV.

Another interesting observation can be made when taking the expectation value of the trace of the energy momentum tensor over a single nucleon state,

$$\langle N | T_\mu^\mu | N \rangle = -m_N = \langle N | G^2 | N \rangle + m_q \langle N | \bar{q}q | N \rangle. \quad (12)$$

Since the second term (related to the σ term) is small (or zero in the chiral limit), this relation seems to suggest that the major part of the nucleon mass is generated by the gluon condensate. This is to be contrasted with effective quark models (e.g., Nambu

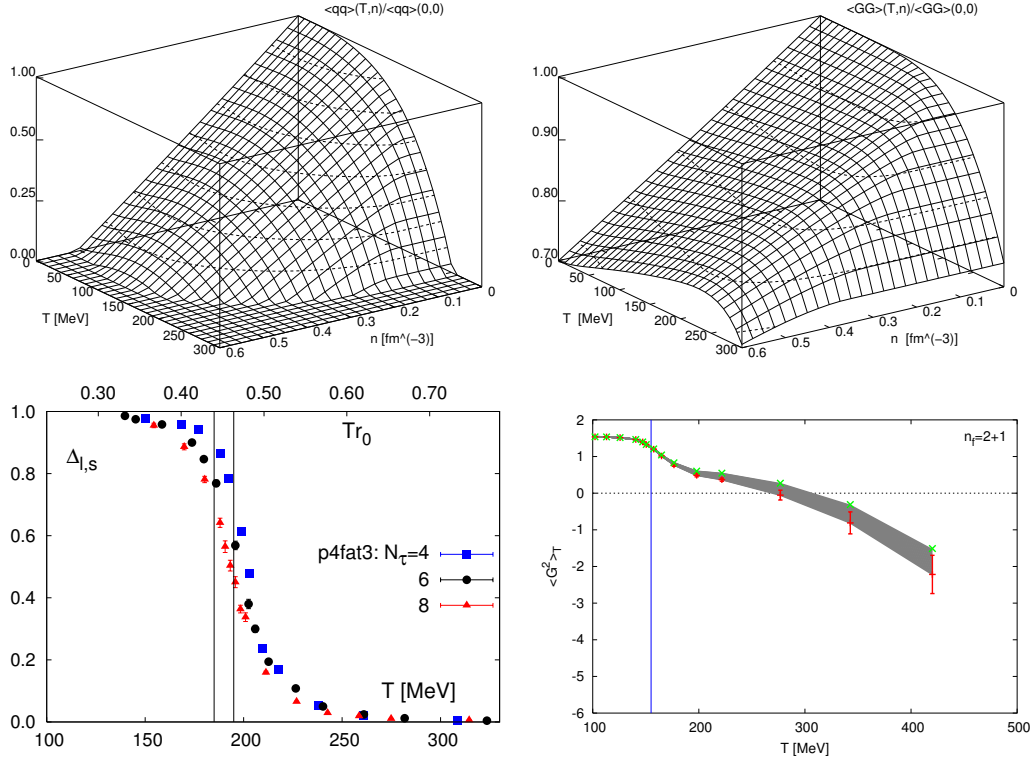


Figure 4: Upper panels: density and temperature dependence of the chiral (left) and the gluon condensate (right), normalized to their vacuum values [57], obtained in a low- T and $-q_N$ expansions. Lower panels: T dependence at $\mu_q=0$ of the (subtracted and renormalized) chiral condensate (left) [58] and of the gluon condensate (right) [59] as obtained from $N_f=2+1$ lattice QCD computations.

Jona-Lasinio) which, in mean field approximation, attribute the constituent quark mass entirely to the quark condensate, $m_q^* = G_{\text{eff}} \langle \bar{q}q \rangle$. One should also note that, at least in the QGP phase, the vanishing of the quark or gluon condensate does not necessarily imply quark “masses” to vanish. E.g., in perturbative QCD, partons in the QGP acquire a thermal mass $m_{q,g}^{\text{th}} \sim gT$. This mass term does not break chiral symmetry (its Dirac structure includes a γ_0 matrix) and presumably persists until close to T_c , thus supplanting the constituent quark mass, m_q^* , well before the latter vanishes. This has, of course, important consequences for the masses of hadronic states in the vicinity of T_c . In addition, large binding-energy effects can be present, e.g., for the pion: if the chiral transition is continuous, the pion’s Goldstone-boson nature could very well imply that it survives as a bound state at temperatures above T_c [60, 61, 62].

As emphasized above, the only known direct way to extract observable consequences of changes in the QCD condensate structure is to probe medium modifications in its excitation spectrum. This applies in particular for the quark condensate which has a rather small impact on the bulk properties of QCD matter being suppressed by m_q (the relation of the gluon condensate to the equation of state could, in principle, be tested via hydrodynamic or transport properties, but this turned out to be difficult in the context

of heavy-ion collisions [10]). The generic model-independent consequence of χ SR for the in-medium hadronic spectrum is the degeneracy of the spectral functions within chiral multiplets (i.e., for chiral partners), e.g., π -“ σ ”, N - $N^*(1535)$ and $\rho(770)$ - $a_1(1260)$. In the “ σ ” channel (which asymptotically corresponds to a scalar-isoscalar pion pair), interesting medium effects have been observed in pion- and photon-induced production of S -wave pion pairs off nuclei [63, 64, 65]. An accumulation of strength close to the two-pion threshold (which is not observed in the isotensor π - π channel) has been associated with an in-medium reduction of the “ σ ”-meson mass as a precursor effect of χ SR [66] (note that the leading-density approximation, Eq. (8), predicts a reduction of the quark condensate by $\sim 30\%$ already at normal nuclear matter density). However, nuclear many-body effects [67, 68], in particular the renormalization of the pion propagator in the nuclear medium, can essentially explain the experimental findings⁴. This raises an important question: to what extent do “conventional” in-medium effects encode mechanisms of χ SR? From the point of view of the “ σ ” spectral function alone, it is not possible to distinguish whether a softening is caused by many-body effects or genuine mass changes figuring via medium modifications of the mass parameter in the underlying effective Lagrangian. Thus, a distinction of medium effects into “conventional” ones and those associated with an apparent “direct” connection to χ SR is meaningless. Rather, a careful and exhaustive treatment of hadronic many-body effects is an inevitable ingredient for evaluating mechanisms of χ SR. As already alluded to in the Introduction, a practical problem of using the $\pi\pi$ decay channel for studying medium effects are the strong final-state interactions of the individual pions when exiting the nuclear medium [69]. The same applies to the heavy-ion collision environment, implying that the $\pi\pi$ channel can only probe the dilute stages of the produced medium. This problem is overcome by dilepton final states, on which we will focus in the following.

3 Vector Mesons in Medium

3.1 Dileptons and Electromagnetic Correlation Function

For a strongly interacting medium in thermal equilibrium the production rate of dileptons can be cast into the form [16, 18],

$$\frac{dN_{ll}}{d^4x d^4q} = -\frac{\alpha_{\text{em}}^2}{\pi^3 M^2} f^B(q_0; T) \frac{1}{3} g_{\mu\nu} \text{Im} \Pi_{\text{em}}^{\mu\nu}(M, q; \mu_B, T). \quad (13)$$

This expression is to leading order in the electromagnetic (EM) coupling constant, α_{em} , but exact in the strong interaction. The latter is encoded in the EM spectral function, defined via the retarded correlator of the hadronic EM current, $j_{\text{em}}^\mu(x)$,

$$\Pi_{\text{em}}^{\mu\nu}(q_0, q) = -i \int d^4x e^{iq \cdot x} \Theta(x_0) \langle\langle [j_{\text{em}}^\mu(x), j_{\text{em}}^\nu(0)] \rangle\rangle. \quad (14)$$

In the vacuum, the spectral strength is directly accessible via the total cross section for e^+e^- annihilation,

$$\sigma(e^+e^- \rightarrow \text{hadrons}) = \frac{4\pi\alpha_{\text{em}}^2}{s} \frac{(-12\pi)}{s} \text{Im} \Pi_{\text{em}}^{\text{vac}}(s), \quad (15)$$

recall Fig. 1 (the first factor is simply $\sigma(e^+e^- \rightarrow \mu^+\mu^-) = 4\pi\alpha_{\text{em}}^2/s$). As a function of invariant dilepton mass, $M^2 = q_0^2 - \vec{q}^2$, the spectrum basically decomposes into two regimes. In

⁴Similar results are obtained from a transport treatment of pion reinteractions in the medium [69].

the low-mass region (LMR, $M \leq 1$ GeV), the strength is absorbed in the three vector mesons $\rho(770)$, $\omega(782)$ and $\phi(1020)$ representing the lowest resonances in the two-pion, three-pion and kaon-antikaon channels, respectively. Thus, the EM current is well described within the vector dominance model (VDM) [19] as given by the field current identity,

$$j_{\text{em}}^\mu(M \leq 1 \text{ GeV}) = \frac{m_\rho^2}{g_\rho} \rho^\mu + \frac{m_\omega^2}{g_\omega} \omega^\mu + \frac{m_\phi^2}{g_\phi} \phi^\mu. \quad (16)$$

In the intermediate mass region (IMR, $1 \text{ GeV} < M \leq 3 \text{ GeV}$), the strength is reasonably well accounted for by a partonic description,

$$j_{\text{em}}^\mu(M > 1.5 \text{ GeV}) = \sum_{q=u,d,s} e_q \bar{q} \gamma^\mu q, \quad (17)$$

where e_q denotes the electric quark charge in units of the electron charge, e . The connection between the two representations can be exhibited by rearranging the charge-flavor content of the quark basis into hadronic isospin quantum numbers,

$$j_{\text{em}}^\mu = \frac{1}{\sqrt{2}} \left[\frac{\bar{u} \gamma^\mu u - \bar{d} \gamma^\mu d}{\sqrt{2}} + \frac{1}{3} \frac{\bar{u} \gamma^\mu u + \bar{d} \gamma^\mu d}{\sqrt{2}} - \frac{\sqrt{2}}{3} \bar{s} \gamma^\mu s \right], \quad (18)$$

reflecting the quark content of the (normalized) ρ (isospin $I=1$), ω ($I=0$) and ϕ ($I=0$) wave functions, respectively. Converting the isospin coefficients into numerical weights in the EM spectral function, one obtains

$$\text{Im } \Pi_{\text{em}} \sim \left[\text{Im } D_\rho + \frac{1}{9} \text{Im } D_\omega + \frac{2}{9} \text{Im } D_\phi \right], \quad (19)$$

which identifies the isovector (ρ) channel as the dominant source (experimentally it is even larger as given by the electromagnetic decay widths, $\Gamma_{\rho \rightarrow ee} / \Gamma_{\omega \rightarrow ee} \simeq 11$). Explicitly evaluating the EM correlators using the currents (16) and (17) yields

$$\text{Im } \Pi_{\text{em}}^{\text{vac}}(M) = \begin{cases} \sum_{V=\rho,\omega,\phi} \left(\frac{m_V^2}{g_V} \right)^2 \text{Im } D_V^{\text{vac}}(M) & , M < M_{\text{dual}}^{\text{vac}}, \\ -\frac{M^2}{12\pi} \left(1 + \frac{\alpha_s(M)}{\pi} + \dots \right) N_c \sum_{q=u,d,s} (e_q)^2 & , M > M_{\text{dual}}^{\text{vac}} \end{cases} \quad (20)$$

($M_{\text{dual}}^{\text{vac}} \simeq 1.5$ GeV, $N_c=3$: number of quark colors, $D_V = 1/[M^2 - m_V^2 - \Sigma_V]$: vector-meson propagators). The associated processes in the thermal dilepton *production* rates are, of course, the inverse of e^+e^- annihilation, i.e., two-pion, three-pion and $K\bar{K}$ annihilation (channeled through the ρ , ω and ϕ) in a hadronic phase⁵ and $q\bar{q}$ annihilation in a QGP. But what about hadronic emission in the IMR and QGP emission in the LMR? The former follows from time-reversal invariance of strong interactions: to the extent that the hadronic final state in e^+e^- annihilation can be represented by a statistical (thermal) distribution (which is empirically approximately satisfied), hadron-gas emission in the IMR corresponds to multi-hadron annihilation ($4\pi, 6\pi \rightarrow e^+e^-$, etc., which may be built from $2\rho, \pi a_1, \pi\omega$, etc.), with a total strength given by the partonic continuum. QGP emission in the LMR is, of course, closely related to a central question of this review: How

⁵Note that the dominance of the isovector channel is naturally associated with the annihilation of the two lightest constituents in a hadronic medium.

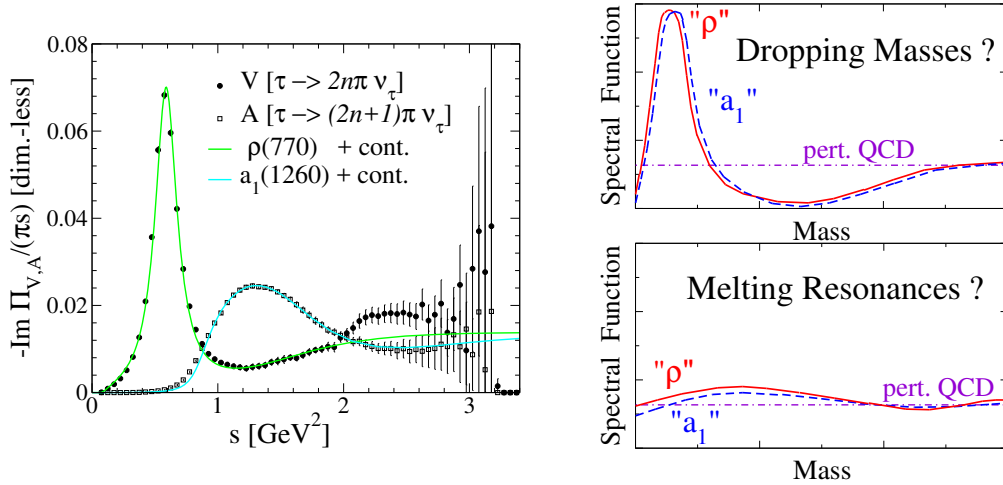


Figure 5: *Left panel: vector and axialvector spectral functions as measured in hadronic τ decays [50] with model fits using vacuum ρ and a_1 strength functions supplemented by perturbative continua [70]; right panel: scenarios for the effects of chiral symmetry restoration on the in-medium vector- and axial-vector spectral functions.*

does the dilute hadronic resonance gas rate evolve into the chirally restored, deconfined QGP rate? At sufficiently low temperatures and/or baryon densities virial expansions in a hadronic basis can provide initial insights. With increasing T and ϱ_B resummations become necessary for which many-body approaches are a suitable tool. It is currently an open question how far up in ϱ_B and T these calculations are reliable. Selfconsistent schemes are, in principle, capable of describing phase-transition dynamics, which, ideally, could be constrained by unquenched lattice-QCD calculations of the dilepton rate below T_c (energy sum rules turn out to be particularly useful to connect spectral functions to order parameters). Eventually, in the high-temperature limit, the LMR rate should recover perturbative $q\bar{q}$ annihilation, where a systematic evaluation of corrections becomes feasible again. The remainder of this section is devoted to a discussion of these approaches. With hindsight to Sec. 4, we will focus on models for which quantitative applications to dilepton observables have been made, with the isovector (ρ) channel playing the leading role. In the following, for brevity, we refer to the $IJ^P=11^\pm$ chiral partner channels as vector (V) and axialvector (A) ones. In the vacuum, both can be well represented by a low-lying resonance pole (ρ and a_1) and a continuum above, see left panel of Fig. 5. Two schematic scenarios for the degeneration of vector and axialvector channels at chiral restoration (“dropping mass” and “resonance melting”) are sketched in the right panel of Fig. 5.

3.2 Medium Effects I: Model Independent

In principle, model-independent assessments of medium effects do not involve free parameters. These can be realized by virial expansion schemes based on experimental input for vacuum spectral functions (valid for dilute hadronic matter), perturbative QCD calculations (valid in the high- T limit) or first-principle lattice QCD computations.

3.2.1 Chiral Reduction and Mixing

The leading temperature dependence of vector and axialvector correlators, $\Pi_{V,A}^{\mu\nu}$, i.e., their modification in a dilute pion gas, can be inferred from chiral reduction and current algebra. They allow to simplify 1-pion matrix elements of any operator according to

$$\langle 0|\mathcal{O}|\pi^a\rangle = -\frac{i}{f_\pi}\langle 0|[Q_A^a, \mathcal{O}]|0\rangle \quad , \quad [Q_A^a, j_{V,A}^{\mu,b}] = i\epsilon^{abc}j_{A,V}^{\mu,c} \quad , \quad (21)$$

where $\{a, b, c\}$ are isospin indices. Evaluating the Fourier transforms of the thermal expectation values in the chiral and soft pion limit (i.e., $m_\pi=0$ and neglecting any momentum transfer k from thermal pions in the heat bath), one obtains the ‘‘mixing’’ theorem [71]

$$\Pi_{V,A}(q) = (1 - \varepsilon) \Pi_{V,A}^0(q) + \varepsilon \Pi_{A,V}^0(q) \quad (22)$$

with the mixing parameter $\varepsilon=T^2/6f_\pi^2$ (the Lorentz structure remains as in the vacuum). The leading- T effect on the V and A correlators is a mere admixture of the chiral partner with a corresponding reduction of its original strength, via processes of the type $\pi+V \leftrightarrow A$ and $\pi+A \leftrightarrow V$; width and mass of the vacuum correlators are unaffected. For dilepton production, this implies a reduced ρ pole strength as well as an enhancement of the ‘‘dip’’ region, $M \simeq 1-1.5$ GeV, where the a_1 resonance provides a ‘‘maximal feeding’’.

When naively extrapolating the mixing expression, Eq. (22), to chiral restoration ($\varepsilon=1/2$), one finds $T_c=\sqrt{3}f_\pi=160$ MeV. This is, however, misleading for several reasons. First, this estimate does not coincide with a similar extrapolation for the vanishing of the chiral condensate, cf. Eq. (8). Second, even a moderate amendment in terms of a finite pion mass in the scalar density shifts the estimate to $T_c \simeq 225$ MeV. Both facts underline the inadequacy of the extrapolation of a lowest-order result. Third, the chiral and soft-pion limits are kinematically not a good approximation (e.g., at $T=150$ MeV, thermal pions typically bring in an energy of $\sim 300-400$ MeV). In cold nuclear matter, a similar mixing is operative via the coupling of the pion cloud of ρ and a_1 to the nuclear medium [72, 73].

A much more elaborate treatment of the chiral reduction formalism has been conducted in Refs. [74, 75, 76]. These calculations are based on realistic fits to vacuum correlators, do not invoke kinematic approximations (chiral or soft-pion limits) and include both pion and nucleon ensembles. The leading-density part has been subjected to constraints from nuclear photo-absorption including the first and second resonance region via $\Delta(1232)$ and $N(1520)$ excitations. This allows for meaningful applications to dilepton spectra which have been carried out and will be discussed in Sec. 4. Note that these calculations do not explicitly invoke the notion of VDM, but the fact that the vacuum correlators are constructed with ρ and a_1 pole dominance, which is not upset in the linear density scheme, implies that VDM is still present upon inclusion of medium effects.

3.2.2 Lattice QCD and Susceptibilities

First-principle computations of light-hadron correlation functions in medium are based on a lattice discretized form of the finite- T QCD partition function. Besides a finite lattice spacing, additional approximations currently involve the restriction to finite volumes as well as the use of unphysically large up- and down-quark masses in the simulations. Furthermore, the implementation of chiral symmetry is not trivial in the lattice formulation. The numerical evaluation of the QCD path integral, is facilitated by transforming the action to imaginary (Euclidean) time, which converts the oscillatory behavior of the

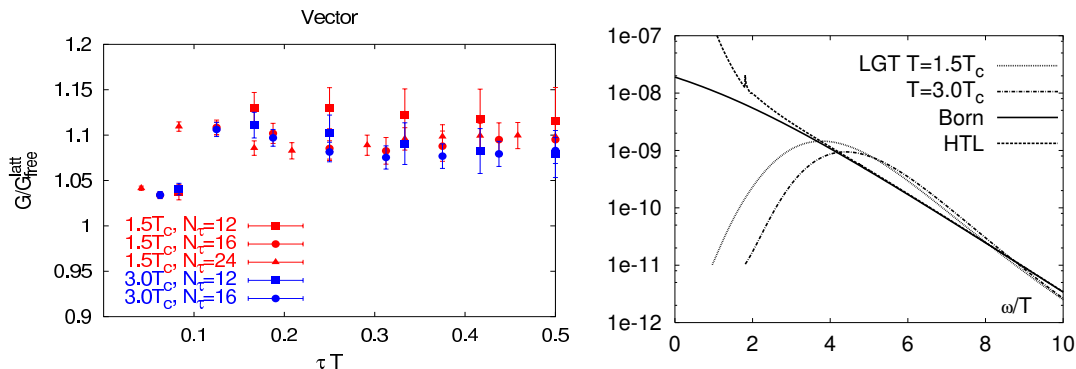


Figure 6: *Left panel: vector correlation function as a function of Euclidean time as evaluated in quenched lattice QCD for a gluon plasma at temperatures above T_c [77]. The in-medium correlators are normalized to the free one using the integration Kernel at the same temperature (the so-called “reconstructed” correlator). Right panel: thermal dilepton rates, $dN/(d^4q d^4x)$, in quenched lattice QCD as extracted from the correlation functions shown in the left panel using the maximum entropy method. The lattice results are compared to calculations in perturbation theory, either to leading order ($\mathcal{O}(\alpha_s^0)$) $q\bar{q}$ annihilation (solid line) or within the hard-thermal-loop (HTL) framework [78] (dashed line). All rates are calculated at a total pair 3-momentum of $q=0$, i.e., the dilepton energy, $\omega=q_0$, equals its invariant mass, M .*

integrand in the partition function into an exponential damping. The pertinent Euclidean correlation function, $\Pi(\tau)$, is related to the physical spectral function, $\rho = -2 \text{Im } \Pi$, via

$$\Pi(\tau, q; T) = \int_0^\infty \frac{dq_0}{2\pi} \rho(q_0, q; T) \frac{\cosh[(q_0(\tau - 1/2T))]}{\sinh[q_0/2T]}. \quad (23)$$

The resulting Euclidean vector correlators in “quenched” QCD⁶ above T_c shows a moderate enhancement over the free correlator, cf. left panel of Fig. 6 [77]. The extraction of the spectral function requires an inverse integral transform over a finite number of τ points⁷ which can only be achieved with a probabilistic treatment based on the “Maximum Entropy Method” [79]. The resulting strength function has been inserted into the dilepton rate and is compared to perturbative QCD (pQCD) rates in the right panel of Fig. 6. The leading-order pQCD corresponds to the $q\bar{q}$ strength distribution in Eq. (20), lower line, while the hard-thermal-loop (HTL) improved rate is from Ref. [78]. The latter shows the expected divergence for $M \rightarrow 0$ which is caused by the Bose factor and photon propagator which overcome the $\rho \propto q_0$ dependence of a retarded correlation function (cf. also Ref. [80]). This feature is not shared by the lattice result which might be an artifact of, e.g., the finite-volume restriction (it would also suggest a small or even vanishing photon production rate). On the other hand, the enhancement in the Euclidean correlator translates into an enhanced dilepton rate at energies of a few times the temperature. Whether this reflects a broad resonance structure is not clear at present.

⁶In the “quenched” approximation the fermionic part of the QCD action is neglected in the evaluation of the Euclidean path integral. This amounts to neglecting fermion loops.

⁷The (anti-) periodicity of the boson (fermion) fields at finite T restricts the Euclidean time direction to the interval $[0, \beta]$ where $\beta = 1/T$.

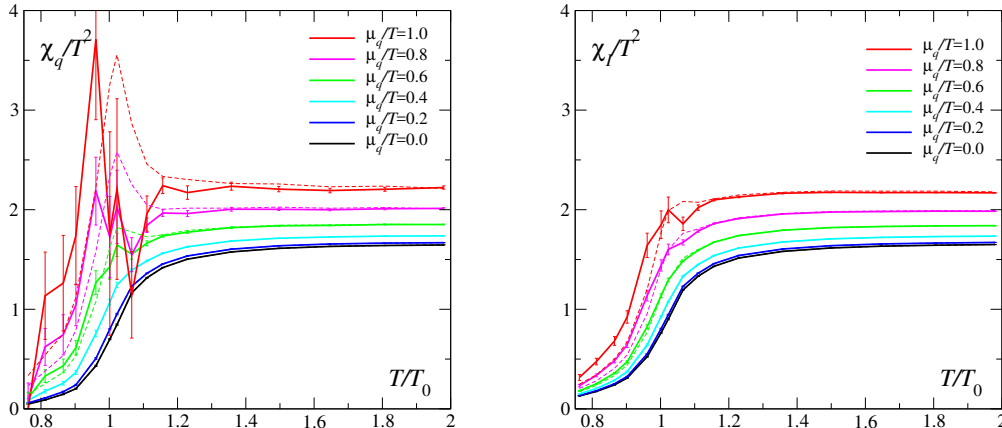


Figure 7: Isoscalar (left) and isovector (right) quark-number susceptibility for various quark chemical potentials, $\mu_q = \mu_B/3$, as computed in unquenched lattice QCD [81].

Additional constraints from lattice QCD are provided by susceptibilities which are defined as second-order derivatives of the thermodynamic potential. In our context, the quark-number susceptibilities are of special interest,

$$\chi_\alpha \sim \frac{\partial^2 \Omega}{\partial \mu_\alpha^2} \sim \Pi_\alpha(q_0 = 0, q \rightarrow 0), \quad (24)$$

which can be decomposed in isoscalar ($\mu_q = (\mu_u + \mu_d)/2$) and isovector ($\mu_I = (\mu_u - \mu_d)/2$) channels carrying the quantum numbers of the ω and ρ , respectively. The spacelike limits of the correlators basically represent the screening masses in the respective channels. Lattice QCD computations of the quark-number susceptibilities indicate that both ρ and ω channels behave smoothly with temperature for small chemical potentials, see Fig. 7. However, as μ_q increases, χ_q develops a peak whereas χ_I remains smooth. The former indicates an increase in the (local) baryon-number fluctuations and may be a precursor of the baryon-number discontinuity between hadronic and QGP phase as one is approaching a first-order line. Remarkably, this is not seen for the isospin fluctuations.

3.3 Sum Rules and Order Parameters

Sum rules are currently the most promising tool to connect the nonperturbative physics encoded in spectral functions to the condensate structure of the QCD vacuum. In particular, the Weinberg sum rules directly relate order parameters of χ SR to the axial-/vector spectral functions, which, in the medium, have not been exploited much to date.

3.3.1 Chiral Sum Rules

The Weinberg and DMO sum rules [52, 53], Eqs. (6), directly relate moments of the “vector minus axialvector” spectral functions to chiral order parameters. This is a rather fortunate situation in view of the dominant role that the isovector-vector (ρ) channel plays in dilepton production, recall Eq. (19). For $N_f=2$, the ω is a chiral singlet, while in the strangeness sector (ϕ), i.e., for $N_f=3$, chiral symmetry becomes much less accurate (e.g., $\langle\langle \bar{s}s \rangle\rangle$ persists much farther into the QGP).

As has been shown in Ref. [82], the Weinberg sum rules remain valid at finite temperature, albeit with two important modifications induced by the breaking of Lorentz invariance caused by the heat bath which defines a preferred rest frame: (i) each energy sum rule applies for a fixed three-momentum, and (ii) at finite three-momentum, the vector and axialvector spectral functions split into longitudinal and transverse modes,

$$\Pi_V^{\mu\nu} = \Pi_{V,A}^T P_T^{\mu\nu} + \Pi_{V,A}^L P_L^{\mu\nu}, \quad (25)$$

with individual sum rules for each of them. The explicit form is as follows:

$$-\int_0^\infty \frac{dq_0^2}{\pi(q_0^2 - q^2)} [\text{Im} \Pi_V^L(q_0, q) - \text{Im} \Pi_A^L(q_0, q)] = 0, \quad (26)$$

$$-\int_0^\infty \frac{dq_0^2}{\pi} [\text{Im} \Pi_V^{L,T}(q_0, q) - \text{Im} \Pi_A^{L,T}(q_0, q)] = 0, \quad (27)$$

$$-\int_0^\infty q_0^2 \frac{dq_0^2}{\pi} [\text{Im} \Pi_V^{L,T}(q_0, q) - \text{Im} \Pi_A^{L,T}(q_0, q)] = -2\pi\alpha_s \langle \langle \mathcal{O}_4 \rangle \rangle. \quad (28)$$

In writing Eqs. (26)-(28) the pionic piece of the (longitudinal) axialvector correlator has been absorbed into the definition of the in-medium spectral function, $\text{Im} \Pi_A^L(q_0, q)$; in the vacuum and in the chiral limit it is represented by a sharp state, $\text{Im} \Pi_\pi^{\mu\nu} = f_\pi^2 M^2 \delta(M^2) P_L^{\mu\nu}$. In this form it only contributes to the first sum rule, Eq. (26). However, in matter (and for $m_\pi > 0$) this is no longer true since the pion is expected to undergo substantial medium effects.

The in-medium chiral sum rules constitute a rich source of constraints on both energy and three-momentum dependence of in-medium spectral functions. The energy moments demonstrate that chiral restoration requires degeneracy of the entire spectral functions. Combining lQCD computations of order parameters with effective model calculations thus provides a promising synergy for deducing chiral restoration from experiment [43].

3.3.2 QCD Sum Rules

QCD sum rules are based on a (subtracted) dispersion relation for a correlation function in a given hadronic channel α , formulated for spacelike momenta $q^2 = -Q^2 < 0$ [83],

$$\Pi_\alpha(Q^2) = \Pi_\alpha(0) + \Pi'_\alpha(0) Q^2 + Q^4 \int \frac{ds}{\pi s^2} \frac{\text{Im} \Pi_\alpha(s)}{s + Q^2}. \quad (29)$$

The right-hand-side (*rhs*) contains the spectral function which is usually related to observables or evaluated in model calculations. On the left-hand-side (*lhs*), the correlation function is expanded into a power series of $1/Q^2$ (operator-product expansion = OPE) where the (Wilson) coefficients contain perturbative contributions as well as vacuum-expectation values of quark and gluon operators (the nonperturbative condensates; for practical purposes the convergence of the OPE is improved by means of a so-called Borel transformation which we do not discuss here). The explicit form of the OPE for vector and axialvector correlators reads (truncating higher order terms in m_q , α_s , etc.)

$$\frac{\Pi_V^{\text{vac}}}{Q^2} = -\frac{1 + \frac{\alpha_s}{\pi}}{8\pi^2} \ln \frac{Q^2}{\mu^2} + \frac{m_q \langle \bar{q}q \rangle}{Q^4} + \frac{1}{24Q^4} \langle \frac{\alpha_s}{\pi} G_{\mu\nu}^a{}^2 \rangle - \frac{112\pi\alpha_s}{81Q^6} \kappa \langle \bar{q}q \rangle^2 + \dots \quad (30)$$

$$\frac{\Pi_A^{\text{vac}}}{Q^2} = -\frac{1 + \frac{\alpha_s}{\pi}}{8\pi^2} \ln \frac{Q^2}{\mu^2} - \frac{m_q \langle \bar{q}q \rangle}{Q^4} + \frac{1}{24Q^4} \langle \frac{\alpha_s}{\pi} G_{\mu\nu}^a{}^2 \rangle + \frac{176\pi\alpha_s}{81Q^6} \tilde{\kappa} \langle \bar{q}q \rangle^2 + \dots \quad (31)$$

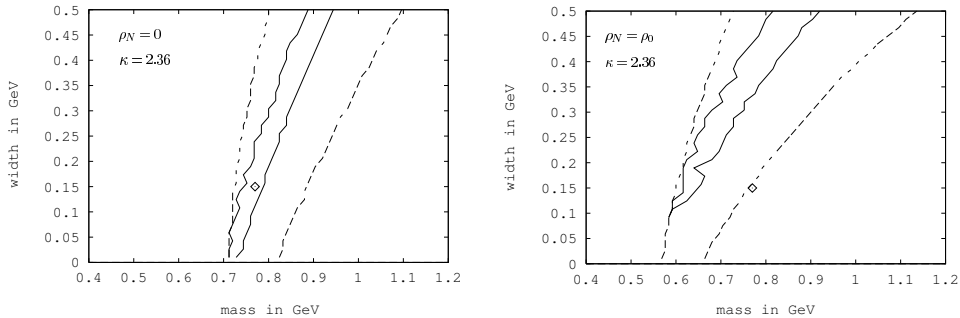


Figure 8: *QCD sum rule constraints on ρ meson mass and width as inferred from Breit-Wigner parameterizations of its spectral function [87] (left panel: vacuum, right panel: cold nuclear matter at saturation density). “Allowed” regions of mass and width are indicated by the bands between solid and dashed curves, corresponding to maximal deviations between the l.h.s and r.h.s. of the SR of 0.2% and 1%, respectively. The diamond depicts the corresponding vacuum parameters.*

where the four-quark condensates have been approximated by factorizing them into the squared two-quark condensate with parameters κ , $\tilde{\kappa}$ which simulate intermediate states other than the ground state (the scale μ is typically chosen around 1 GeV). Note that $\text{SB}\chi\text{S}$ is nicely reflected by the opposite signs of the quark-condensate terms in Π_V and Π_A , while the “flavor-blind” gluon condensate enters with the same sign. Qualitatively, the (positive) gluon condensate actually induces a softening of the spectral function (i.e., a larger weight at small s in the dispersion integral) [84]. On the other hand, for the vector channel, the negative contributions from the quark condensates on the *lhs* of the sum rule push spectral-function strength to larger s , relative to the axialvector channel (this may seem surprising in view of the masses of the pertinent resonances, $m_\rho=0.77$ GeV vs. $m_{a_1}=1.23$ GeV; recall, however, that the (longitudinal) axialvector channel contains a contribution from the axialvector current of the pion). Inserting numerical values, $\alpha_s=0.35$, $m_q=0.005$ GeV, $\langle\bar{q}q\rangle=(-0.25\text{ GeV})^3$ and $\langle\frac{\alpha_s}{\pi}G_{\mu\nu}^a{}^2\rangle=0.012\text{ GeV}^4$, leads to

$$\frac{\Pi_V^{\text{vac}}}{Q^2} = \frac{1}{8\pi^2} \left(-1.11 \ln \frac{Q^2}{\mu^2} - \frac{0.0062\text{ GeV}^4}{Q^4} + \frac{0.039\text{ GeV}^4}{Q^4} - \frac{0.029\text{ GeV}^6 \kappa}{Q^6} \right), \quad (32)$$

illustrating that the leading contributions arise from the gluon and four-quark condensates (especially for typical values of $\kappa \simeq 2.5$), while the impact of the quark condensate is rather moderate. For the vector channel, and in vacuum, there is a large cancellation between the gluon and 4-quark condensate terms. However, in the medium this is presumably lifted, especially at low T and ρ_B where quark and gluon condensates change rather differently. The stronger reduction of the “repulsive” 4-quark condensate relative to the “attractive” gluon condensate induces a softening of the spectral function in the dispersion integral. The softening can be satisfied by both broadening and/or a downward mass shift [85, 86, 87, 88, 89]. Quantitative studies (which also include effects of non-scalar condensates induced by hadron structure of the heat-bath particles) based on Breit-Wigner model spectral functions are displayed in Fig. 8. For the axialvector channel, the reduction in both condensates suggests a substantial loss of soft-mode strength which points at the dissolution of the pion mode (whose polestrength is given by f_π) as a consequence of (the approach toward) χSR .

Finally, it is instructive to compare ω and ρ mesons: while their OPE side is rather similar (governed by 4-quark condensates), the subtraction constant, $\Pi_V(0) = \varrho_N/4M_N$ to leading order in ϱ_N , makes a difference. It is given by the Thompson limit of the VN scattering amplitude and turns out to be identical in the ρ and ω sum rule. However, since $\text{Im } \Pi_\rho$ is larger than $\text{Im } \Pi_\omega$ by an isospin factor of $(g_\omega/g_\rho)^2 \simeq 9$ (recall Eq. (19)), the finite- ϱ_N subtraction actually stabilizes the ω sum rule, implying stronger medium effects (softening) on the ρ than on the ω (it amounts to a “repulsive” contribution on the OPE side counterbalancing the reduction in the 4-quark condensate).

3.4 Medium Effects II: Chiral Effective Models

Model-independent and/or low-density approaches as discussed above provide valuable constraints on the vector and axialvector correlators and their connections to QCD vacuum structure. However, quantitative calculations suitable for comparison with experiment require the construction of effective models. As indicated in the Introduction, in the low-mass region most of the thermal dilepton yield in heavy-ion collisions is expected to emanate from the hot/dense hadronic phase (even at collider energies), especially from the ρ channel. Hadronic chiral Lagrangians are therefore a suitable starting point, extended by the implementation of the low-lying vector mesons. This is usually done by a local gauging procedure of the chiral pion Lagrangian, thus realizing the gauge principle at the composite (hadronic) level. The most common approaches are based on non-linear realizations of chiral symmetry (i.e., without explicit σ meson) within the Hidden Local Symmetry (HLS) [90] or Massive Yang Mills (MYM) [91] schemes. Rather than reviewing these in a comprehensive form, we here focus on recent developments with relevance for dilepton production, i.e., the “vector manifestation” (VM) scenario of SB χ S within HLS [92] (Sec. 3.4.1), as well as hadronic many-body theory within MYM (Sec. 3.4.2).

3.4.1 Hidden Local Symmetry and Vector Manifestation

Within the HLS framework, an alternative realization of chiral symmetry in the meson spectrum has been suggested in Ref. [92], by identifying the chiral partner of the pion with the (longitudinal) ρ (rather than with the σ). This “vector manifestation” of chiral symmetry has been shown to give a satisfactory phenomenology of hadronic and EM decay branchings in the vacuum. When applied within a finite- T loop expansion, the ρ -meson mass was found to be affected at order T^4 (consistent with chiral symmetry), showing a slightly repulsive shift. However, when matching the hadronic axial-/vector correlators to pQCD in the spacelike regime (using an OPE), a reduction of the bare ρ mass has been inferred, consistent with “Brown-Rho” scaling [21]. In addition, vector dominance was found to be violated in the medium, leading to a gradual decoupling of the ρ from the EM current toward the critical temperature. However, the finite- T EM formfactor, which determines the dilepton production rate, clearly shows the downward moving ρ peak [93], see Fig. 9. An interesting question is how these features develop in the presence of finite baryon density.

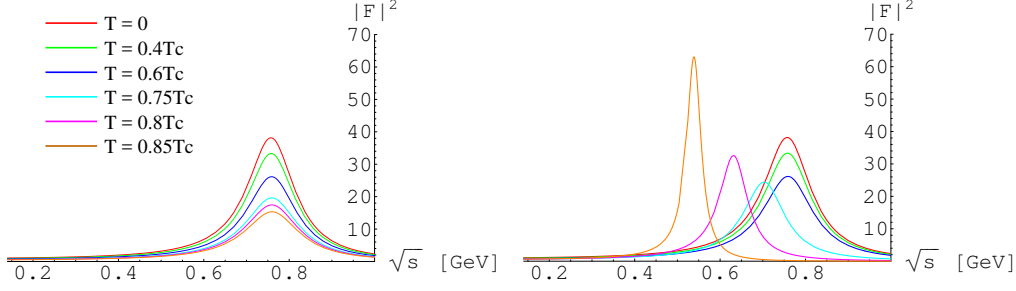


Figure 9: Pion EM formfactor at finite temperature in the HLS vector manifestation framework [93]; left panel: with finite- T loop effects; right panel: additionally including a T -dependence of the bare ρ mass above $T=0.7T_c$.

3.4.2 Massive Yang-Mills and Hadronic Many-Body Theory

As in HLS, the basic building block of the MYM Lagrangian is the chiral pion Lagrangian based on the unitary pion field,

$$U = \exp(i\sqrt{2}\phi/f_\pi), \quad \phi \equiv \phi_a \frac{\tau_a}{\sqrt{2}}. \quad (33)$$

Hadronic gauge fields, $A_{L,R}^\mu$ are introduced via the covariant derivative,

$$D^\mu U = \partial^\mu - ig(A_L^\mu U - U A_R^\mu) \quad (34)$$

and supplemented with kinetic and mass terms (with bare mass m_0). One has

$$\begin{aligned} \mathcal{L}_{\text{mym}} = & \frac{1}{4} f_\pi^2 \text{tr} [D_\mu U D^\mu U^\dagger] - \frac{1}{2} \text{tr} [(F_L^{\mu\nu})^2 + (F_R^{\mu\nu})^2] + m_0^2 \text{tr} [(A_L^\mu)^2 + (A_R^\mu)^2] \\ & - i\xi \text{tr} [D_\mu U D^\mu U^\dagger F_L^{\mu\nu} + D_\mu U D^\mu U^\dagger F_R^{\mu\nu}] + \sigma \text{tr} [F_L^{\mu\nu} U F_{R\mu\nu} U^\dagger], \end{aligned} \quad (35)$$

where the last two (non-minimal) terms are necessary to achieve a satisfactory phenomenology in the vacuum. After the identifications $\rho^\mu \equiv V^\mu = A_R^\mu + A_L^\mu$, $A^\mu = A_R^\mu - A_L^\mu$ (and a field redefinition of the axialvector field to remove a $\partial^\mu \vec{\pi} A^\mu$ term), the leading terms of the MYM Lagrangian take the form

$$\begin{aligned} \mathcal{L}_{\text{mym}} = & \frac{1}{2} m_\rho^2 \vec{\rho}_\mu^2 + \frac{1}{2} [m_\rho^2 + g^2 f_\pi^2] a_{1\mu}^2 + g^2 f_\pi \vec{\pi} \times \vec{\rho}^\mu \cdot \vec{a}_{1\mu} + \\ & g_{\rho\pi\pi}^2 [\vec{\rho}_\mu^2 \vec{\pi}^2 - \vec{\rho}^\mu \cdot \vec{\pi} \vec{\rho}_\mu \cdot \vec{\pi}] + g_{\rho\pi\pi} \vec{\rho}_\mu \cdot (\vec{\pi} \times \partial^\mu \vec{\pi}) + \dots \end{aligned} \quad (36)$$

($g_{\rho\pi\pi}^2 = \frac{1}{2} g^2$). Note that the Higgs mechanism induces the *splitting* of ρ and a_1 masses,

$$m_{a_1}^2 = m_\rho^2 + g^2 f_\pi^2, \quad m_\rho^2 = m_0^2, \quad (37)$$

which is entirely due to SB χ S (via f_π). The bare ρ mass itself is an *external* parameter, which is different from the HLS scheme discussed in the previous section. Electromagnetism is readily included into the MYM Lagrangian by adding the vector dominance coupling [91]

$$\mathcal{L}_{\rho\gamma} = \frac{em_\rho^2}{g_{\rho\pi\pi}} B_\mu \rho_3^\mu, \quad (38)$$

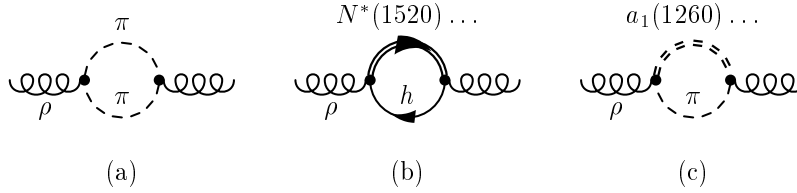


Figure 10: Graphical representation of self-energy diagrams characterizing the interactions of the ρ meson in hot and dense hadronic matter: (a) renormalization of its pion cloud due to modified pion propagators, and direct interactions of the ρ meson with (b) baryons and (c) mesons, typically approximated by baryon- and meson-resonance excitations [94, 30].

where B_μ denotes the photon field. In this scheme, VDM remains valid in the medium, and the task of computing the low-mass isovector axial/-vector correlators amounts to assessing the medium modifications of ρ and a_1 mesons.

The ρ -meson propagator in hot and dense hadronic matter can be written as

$$D_\rho^{L,T}(q_0, q; \mu_B, T) = \frac{1}{M^2 - m_V^2 - \Sigma_{\rho\pi\pi}^{L,T} - \Sigma_{\rho M}^{L,T} - \Sigma_{\rho B}^{L,T}}, \quad (39)$$

with transverse and longitudinal modes as defined in Eq. (25). The key quantities are the in-medium selfenergies, $\Sigma_\rho^{L,T}$, which may be classified as follows (cf. Fig. 10): $\Sigma_{\rho\pi\pi}$ accounts for the pion cloud of the ρ , which in the vacuum gives rise to its finite width via $\rho \rightarrow \pi\pi$. Direct interactions of the ρ with mesons ($M=\pi, K, \rho, \dots$) and baryons ($B=N, \Lambda, \Delta, \dots$) from the heat bath are represented by $\Sigma_{\rho M}$ and $\Sigma_{\rho B}$, respectively; they vanish in the vacuum. In terms of underlying scattering processes, the latter are typically resonance excitations (e.g., $\rho\pi \rightarrow a_1$ or $\rho N \rightarrow N(1520)$) while medium modifications of pions (e.g., $\pi N \rightarrow \Delta$) in $\Sigma_{\rho\pi\pi}$ correspond to, e.g., t -channel π exchange processes ($\rho N \rightarrow \pi\Delta$). When evaluating interactions which are not directly constrained by chiral (or gauge) symmetry (especially those involving higher resonances), phenomenological information is essential for a reliable determination of the coupling constants (and cutoff parameters in the hadronic formfactors to account for the finite size of the hadrons). The simplest form of such constraints are hadronic decay widths of resonances (e.g., $a_1 \rightarrow \rho\pi$), supplemented by radiative decays (e.g., $a_1 \rightarrow \gamma\pi$). However, especially for “subthreshold” states (e.g., $\omega \rightarrow \rho\pi$ or $N(1520) \rightarrow \rho N$), where the coupling is realized via the low-energy ($\pi\pi$ decay) tail of the ρ spectral function, empirical information can be rather uncertain. In this case, comprehensive constraints inferred from scattering data become invaluable. Unfortunately, in practice this is only possible for ρN interactions (e.g., via $\pi N \rightarrow \rho N$ or γN scattering), but, as it turns out, the modifications of the ρ due to interactions with nucleons are generally stronger than with pions. In addition, by using nuclear targets, one has the possibility to constrain (or test) the modifications in nuclear *matter*, rather than on a single nucleon (which corresponds to the leading-order density effect).

Let us start by discussing finite- T effects. Calculations of the ρ propagator in a hot pion gas based on the MYM scheme [95] have shown small medium effects. An extended analysis [96] of the ρ in hot meson matter, including resonance excitations ($\rho\pi \rightarrow a_1, \omega, h_1, \pi', a_2(1320)$, $\rho K \rightarrow K^*, K_1$, $\rho\rho \rightarrow f_1(1285)$) and pion Bose enhancement in $\Sigma_{\rho\pi\pi}$, leads to total broadening of ~ 80 MeV at $T=150$ MeV (corresponding to a pion density $\varrho_\pi=0.12 \text{ fm}^{-3} \simeq 0.75 \varrho_0$), with little mass shift. Approximately ~ 20 MeV of

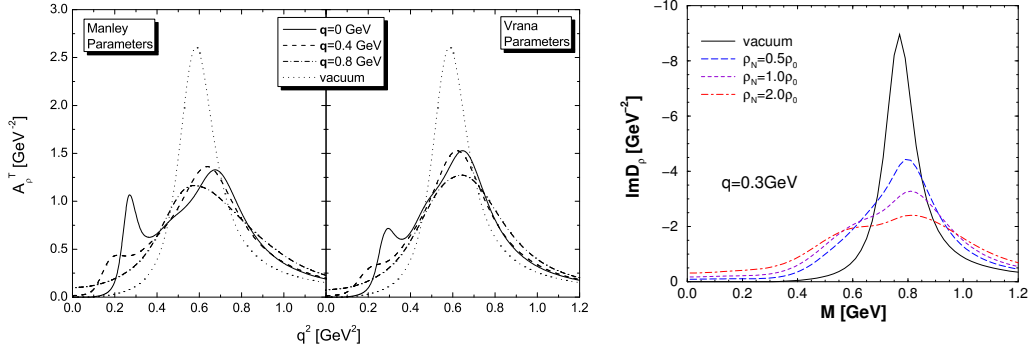


Figure 11: Comparison of ρ -meson spectral functions in cold nuclear matter within the hadronic many-body approaches of Refs. [100] (left panels, based on two different phase shift analysis of πN scattering [101, 102]) and [94, 30] (right panel).

the broadening is due to the $\pi\pi$ Bose factor (cf. also Ref. [97]) and ~ 50 - 60 MeV due to meson resonances. The latter is comparable to Refs. [98, 99] which are directly based on $\rho\pi$ and ρK scattering amplitudes.

Next, we turn to modifications in cold nuclear matter. Fig. 11 shows two calculations in which the underlying ρ self-energies have been rather thoroughly constrained. In Ref. [100] (left panels), a ρN resonance model (corresponding to $\Sigma_{\rho N}$) has been constructed utilizing a detailed analysis of empirical $\pi N \rightarrow \rho N$ phase shifts and inelasticities [101, 102]. The resulting ρ spectral functions are displayed at normal nuclear density (taken as $\rho_N = 0.15 \text{ fm}^{-3}$) for various three-momenta and two distinct data sets for constraints. A substantial broadening of close to ~ 200 MeV is found, with a slight upward peak shift of a few tens of MeV; the three-momentum dependence is relatively weak. In Refs. [94, 30], $\Sigma_{\rho N}$ and an in-medium pion cloud, $\Sigma_{\rho\pi\pi}$ (incorporating P -wave “pisobar” nucleon- and Δ -hole excitations and associated vertex corrections), have been calculated

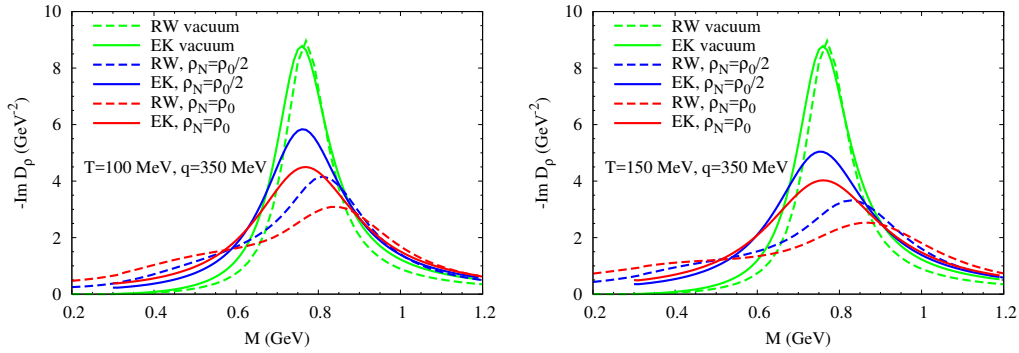


Figure 12: Comparison of ρ -meson spectral functions in hot and dense hadronic matter from Refs. [30] (dashed lines) and [99] (solid lines) at temperatures of $T=100$ MeV (left panel) and $T=150$ MeV (right panel) for nucleon densities of $\rho_N = 0.5, 1.0 \rho_0$ (the corresponding nucleon chemical potentials are $\mu_N = 673, 745$ MeV for $T=100$ MeV and $\mu_N = 436, 542$ MeV for $T=150$ MeV, respectively).

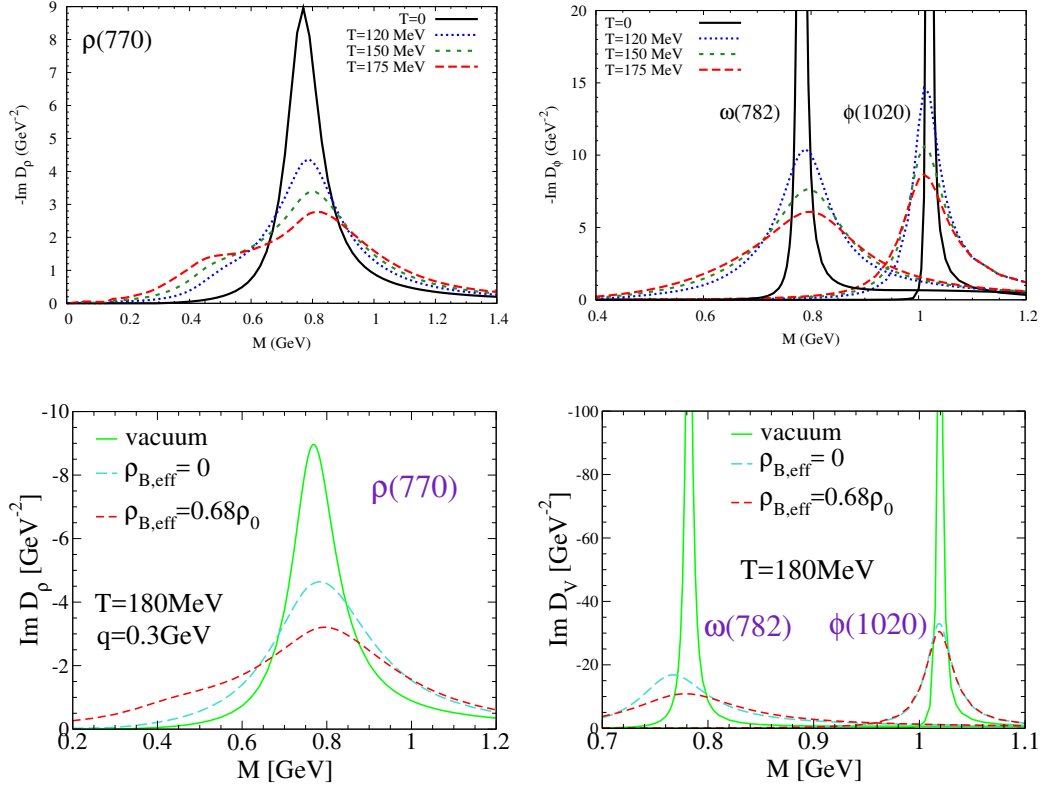


Figure 13: *In-medium spectral functions of light vector mesons in hot and dense hadronic matter based on the hadronic many-body approach of Refs. [103, 30, 105]; upper panel: under conditions resembling heavy-ion collisions at SPS (i.e., along an isentropic trajectory in the phase diagram which preserves the measured hadron ratios determined at $(\mu_B^{\text{chem}}, T_{\text{chem}}) \simeq (230, 175)$ MeV [106]; lower panels: at $(\mu_B, T) \simeq (25, 180)$ MeV (resembling chemical freeze-out at RHIC) with (short-dashed lines) and without (long-dashed lines) medium effects induced by anti-/baryons [20].*

and constrained by total photoabsorption data on the nucleon and nuclei [103], as well as total $\pi N \rightarrow \rho N$ cross sections. The resulting spectral functions are quite similar to the ones of Ref. [100], with a somewhat stronger broadening of ~ 300 MeV at $\rho_N = 0.16 \text{ fm}^{-3}$ and a comparable mass shift of ~ 40 MeV. It is quite remarkable that the predicted in-medium mass and width of $\sim (810, 450)$ MeV are in good agreement with the QCD sum rule constraints derived in Ref. [87], cf. right panel in Fig. 8. Both broadening and mass shift decrease at higher three-momentum, e.g., $(\Delta m_\rho, \Delta \Gamma_\rho) \simeq (30, 150)$ MeV at $q = 1$ GeV. Both calculations [100, 94] include a rather strong coupling to $\rho N(1520)N^{-1}$ excitations (appearing as a low-mass peak or shoulder in the ρ spectral function). This has been questioned in Ref. [104] based on a coupled channel analysis of S -wave ρN and ωN scattering, where all nucleon resonances but the $\Delta(1232)$ are generated dynamically via four-point interactions. The (generated) $N(1520)$ is deduced to primarily couple to ωN rather than ρN , entailing an in-medium ρ with significantly less broadening.

Finally, we turn to a hot and dense hadronic medium as expected to be formed in high-

energy heavy-ion collisions. In Fig. 12 the ρ spectral functions of the hadronic many-body calculations [94, 30] are compared to those obtained in the scattering-amplitude approach of Ref. [99]. The latter exhibit less broadening and a small (if any) downward mass shift of the ρ peak, compared to the upward shift in the many-body approach (mostly induced by baryonic effects). Consequently, in terms of spectral strength, the discrepancies between the two calculations are largest for masses around $M \simeq 0.7$ GeV, as well as for very low mass, $M \leq 0.4$ GeV, by up to a factor of ~ 2 . This mass region is much magnified in thermal dilepton production rates due to the Boltzmann factor and a photon propagator $\propto 1/M^2$. However, the amplitude approach only accounts for interactions with pions and nucleons, while the many-body calculations include estimates of ρ interactions with strange baryons and resonances [30]. This difference may account for some of the discrepancy.

In preparation for applications to dilepton spectra in URHICs, we summarize in Fig. 13 in-medium V -meson spectral functions in the many-body approach under conditions relevant for SPS (upper panels) [30, 106] and RHIC (lower panels) [105]. The ρ meson (left panels) “melts” when extrapolated to temperatures close to the expected phase boundary. Baryons play an essential role in the melting, even at RHIC (where the net baryon density is small), since the relevant quantity is the *sum* of baryon and antibaryon densities. The effects due to baryons and antibaryons are most prominent as an enhancement in the mass region below $M \simeq 0.5$ GeV. The ω and especially ϕ spectral functions (right panels) appear to be more robust. One should also point out that at $T=120,150$ MeV in the upper panels appreciable pion and kaon chemical potentials are present which sustain larger hadron densities and thus support stronger medium effects than in chemical equilibrium.

3.5 Thermal Dilepton and Photon Rates

The in-medium vector-meson propagators discussed in the preceding section are converted to thermal dilepton rates via Eqs. (20) (upper line) and (13). This is based on the assumption that VDM for the EM correlator remains valid in the medium⁸. The resulting three-momentum integrated thermal dilepton rates are summarized in Fig. 14. The left panel, which displays the isovector channel, reiterates that the ρ resonance signal disappears from the mass spectrum as one approaches the putative phase boundary. The hadronic rates also include an estimate of the leading- T chiral mixing effect, Eq. (22), in the mass region $M=1-1.5$ GeV. The comparison to perturbative $q\bar{q}$ annihilation reveals that the top-down extrapolated QGP rate closely coincide with the bottom-up extrapolated in-medium hadronic one, especially in case of the HTL-improved $q\bar{q}$ rate. This feature suggests that the hadronic rate has indeed approached χ SR (since the QGP rates are chirally symmetric at any finite order in perturbation theory) [34, 30]. The “matching” of QGP and hadronic rates occurs directly in the timelike regime without the need for in-medium changes of the bare parameters in the effective Lagrangian. Medium effects due to baryons play an important role in this mechanism; the situation is similar for small μ_B and close to T_c where the sum of baryon and antibaryon densities is appreciable, see right panel of Fig. 14. ω and especially ϕ mesons appear to be more robust, possibly surviving above T_c . The dilepton rates in the vector manifestation of HLS [93] look rather different; based on the pertinent pion EM formfactor, Fig. 9, a distinct ρ peak survives in the rate up to temperatures of at least $T=0.85 T_c \simeq 155$ MeV (assuming $T_c \simeq 180$ MeV).

⁸Strictly speaking, the EM correlator of Refs. [94, 30] includes corrections to VDM in the baryon sector as determined via photoabsorption spectra on the nucleon and nuclei [103]; the assumption is that this modified version of VDM is not affected at higher densities and at finite temperature.

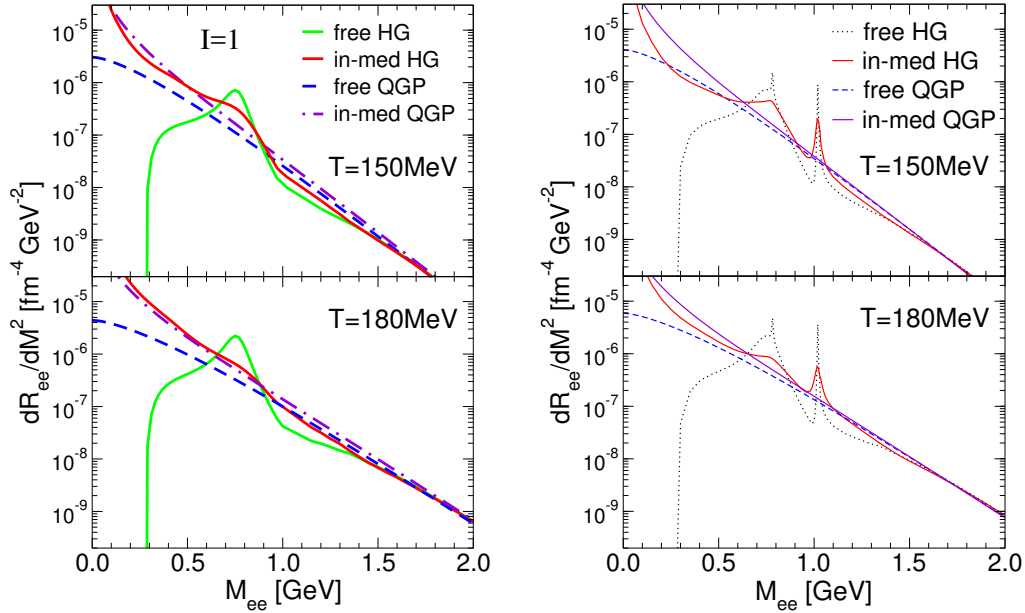


Figure 14: Three-momentum integrated thermal dilepton rates at fixed temperature [70, 107] for the vacuum ρ (dotted lines), the hadronic many-body approach of Refs. [103, 30] (solid lines) and for the QGP using either free $q\bar{q}$ annihilation (dashed line) or hard-thermal loop improved rates [78] (dash-dotted line). The left panel refers to the isovector (ρ) channel, under conditions resembling heavy-ion collisions at the SPS (fixed $\mu_B=270$ MeV). The right panel additionally includes isoscalar (ω and ϕ) channels and corresponds to small $\mu_B \simeq 25$ MeV appropriate for the conditions at collider energies.

Emission rates of dileptons are closely related to those of real photons which are determined by the lightlike limit ($q_0 = |\vec{q}|$) of the EM spectral function,

$$q_0 \frac{dN_\gamma}{d^4x d^3q} = -\frac{\alpha_{em}}{\pi^2} f^B(q_0; T) \text{Im} \Pi_{em}(M=0, q; \mu_B, T). \quad (40)$$

In Ref. [108] the in-medium ρ of Refs. [103, 30] has been found to constitute the dominant hadronic source of thermal photons for momenta up to $q \simeq 1$ GeV; above, t -channel meson exchange reactions not included in the spectral function (most notably π and ω exchange in $\pi\rho \rightarrow \pi\gamma$) take over, cf. left panel of Fig. 15. Similar to the dilepton case, at temperatures of 150-200 MeV, the strength of the combined thermal rate for hadronic photon production turns out to be very comparable to perturbative QGP emission, especially for the complete leading-order result [110].

4 Interpretation of Dilepton Spectra

In this section we will scrutinize experimental results for dilepton spectra in light of the theoretical developments elaborated above. A brief discussion of production experiments off nuclei, representing cold nuclear matter up to saturation density, will be followed by

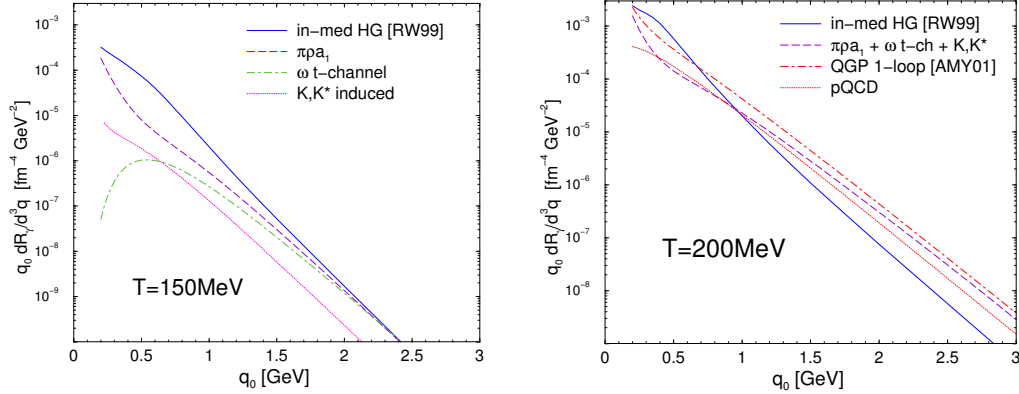


Figure 15: Thermal photon production rates in hot hadronic matter [108] (left panel), and compared to 1-loop [109] and full leading-order [110] QGP emission (right panel).

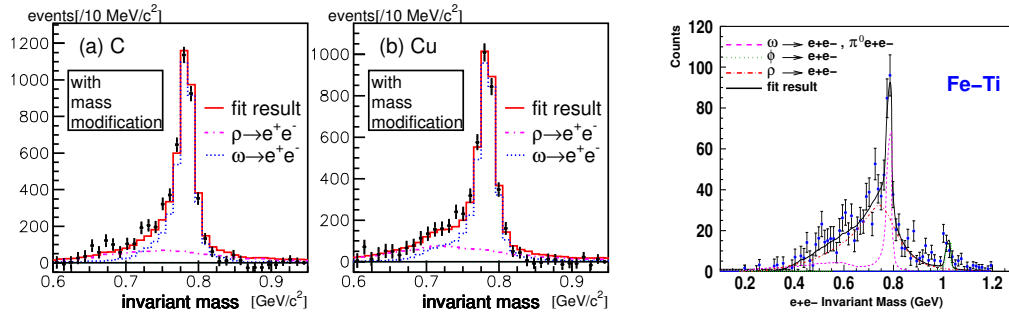


Figure 16: Invariant-mass spectra of e^+e^- in proton- (left) [46] and photon-induced (right) [45] reactions off nuclear targets.

a more extensive study of invariant-mass and momentum spectra in heavy-ion reactions involving hot and dense matter possibly probing the transition regime to the QGP.

4.1 Medium Effects in Nuclei

Dilepton production experiments off nuclei have the advantage over heavy-ion collisions that the medium is well-defined. Medium- to heavy ground-state nuclei resemble in their interior infinitely extended nuclear matter at vanishing temperature. Therefore the experiments probe to a large extent the properties of “cold nuclear matter”. However, a good knowledge of the production process is required, and medium effects are typically rather moderate, further reduced by surface effects and decays outside the nucleus especially at large three-momenta (which, in turn, are needed in the production process).

The E325 experiment at KEK [46] used 12 GeV proton projectiles and found significant differences in the spectra between C and Cu targets, see left panel of Fig. 16. After subtraction of combinatorial background as well as η and ω Dalitz decays, the best fit to the excess spectra using ω and ρ Breit-Wigner distributions was obtained with a mass shift of ca. 9% at nuclear matter density, and a ρ/ω ratio of about ~ 0.45 .

The CLAS experiment [45] used a photon beam at Jefferson Lab with incident energies $E_\gamma=0.6\text{-}3.8\text{GeV}$, directed on various nuclear targets. After subtraction of the

combinatorial background, determined with absolute normalization, the invariant-mass spectra are best reproduced with a ρ spectral distribution with a mass and width of $(m_\rho, \Gamma_\rho) = (775 \pm 5, 220 \pm 15)$ MeV, cf. right panel of Fig. 16. These values are well reproduced by Boltzmann transport calculations [111], and are consistent with the predictions of Refs. [94, 30] at $\varrho_N = 0.5 \varrho_0$ and $q = 1$ GeV, where $(\Delta m_\rho, \Delta \Gamma_\rho) \simeq (15, 75)$ MeV, see Ref. [112] for a recent calculation. An apparent difference between the E325 and CLAS spectra is that the background subtraction in the former removes any excess for $M \simeq 0.85$ -1 GeV; this suppresses (and possibly shifts down) the ρ contribution in the E325 fit.

Photoproduction experiments ($E_\gamma = 0.8$ -1.12 GeV) of P -wave $\pi^+\pi^-$ pairs off ${}^2\text{H}$, ${}^3\text{He}$ and ${}^{12}\text{C}$ were conducted by the TAGX collaboration [113]. The spectra for the ${}^{12}\text{C}$ target support medium effects in line with hadronic many-body ρ spectral functions [94, 30].

4.2 Heavy-Ion Collisions

In contrast to production experiments off nuclei, the (energy-) density of the medium created in heavy-ion collisions undergoes a rapid evolution after initial nuclear impact until break-up. Even under the simplifying assumption of local thermal equilibrium, a good knowledge of the temperature and baryon-density evolution is necessary to convert the dilepton rates discussed above into a space-time integrated spectrum. In addition, sources other than thermal radiation have to be considered, especially toward higher mass or q_t where the assumption of equilibrium becomes increasingly questionable. These issues are addressed in Sec. 4.2.1. Phenomenological analyses of dilepton spectra focus on recent SPS data from NA60 and CERES/NA45 in Secs. 4.2.2 and 4.2.3, respectively, with a short digression to direct photons (W98) and a brief outlook to future experiments in Sec. 4.2.4.

4.2.1 Thermal Evolution and Dilepton Sources

As discussed in Sec. 1.2, hadronic observables in URHICs point at a reasonable degree of thermalization of the bulk medium produced in these reactions. Therefore, we here focus on hydrodynamic and expanding fireball approaches utilizing the assumption of local thermal equilibrium.⁹

Thermal emission spectra follow from the convolution of the production rate, Eq. (13), over the space-time evolution of the medium,

$$\frac{dN_{ll}}{dM dy} = \frac{M}{\Delta y} \int_0^{\tau_{fo}} d\tau \int_{V_{FB}} d^3x \int \frac{d^3q}{q_0} \frac{dN_{ll}}{d^4x d^4q}(M, q; T, \mu_N, \mu_s, \mu_i) \text{Acc}(M, q_t, y), \quad (41)$$

where $\text{Acc}(M, q_t, y)$ accounts for the detector acceptance and Δy denotes the corresponding rapidity interval. The temperature and chemical potentials in general depend on space-time, (τ, \vec{x}) . Note that while μ_N and μ_s correspond to exact conservation of baryon number and strangeness, effective chemical potentials $\mu_i = \mu_{\pi, K, \eta, \dots}$ are needed to preserve the experimentally observed hadron ratios in the evolution of the hadronic phase between chemical ($T_{\text{ch}} = 155$ -175 MeV) and kinetic freezeout ($T_{\text{fo}} = 100$ -140 MeV).

An overview of several key input parameters of three thermal approaches [36, 106, 117, 118, 119, 120], which have been used to compute dimuon spectra in comparison

⁹Comparisons of dilepton spectra computed in hydrodynamic/fireball and transport calculations (based on similar in-medium spectral functions) have shown rather good agreement, see e.g. Refs. [114, 30], Ref. [115], or Refs. [106, 116].

	DZ	RR	HR
T_0	220 MeV (peak)	250 MeV (peak)	190 MeV (average)
T_c	170 MeV	170 MeV	175(160/190) MeV
T_{fo}	130 MeV	130 MeV	120(135) MeV
spatial	Glauber (initial)	Woods-Saxon	isotropic
v_{fo}^s	$\sim 0.5-0.55$	0.57	0.53
$v(r)$	approx. linear	$\rho_t \propto \sqrt{r}$	$v_t \propto r$
τ_{FB}	$\sim 8-9$ fm/c	~ 7.5 fm/c	~ 6.5 fm/c
QGP-EoS	massless ($N_f=3$)	quasi-particle model	massless ($N_f=2.3$)
HG-EoS	lowest SU(3) multipl.	$m_{B,M} \leq 2, 1.5$ GeV	$m_{B,M} \leq 2, 1.7$ GeV
s/ρ_B	42	26(?)	27
μ_π^{fo}	0	? ($\neq 0$)	80(35) MeV
EM rates	chiral virial	empirical scatt. ampl.	hadronic many-body

Table 1: *Fireball parameters employed in the calculations of dilepton spectra in In(158 AGeV)-In collisions in Refs. [117, 118] (DZ), [119, 120] (RR) and [36, 106] (HR).*

to NA60 data, is compiled in Tab. 1 (see also Ref. [125]). The overall range of the underlying parameters and assumptions is rather similar. This is not a coincidence but a consequence of constraints from measured hadron spectra at SPS energies [121, 122, 123, 124] which all of the three models have been subjected to. There are, however, noticeable differences. E.g., all approaches operate with a for SPS energies “canonical” formation time of $\tau_0=1$ fm/c, but the initial peak temperature in Ref. [120] is about 15% larger than in Ref. [117] (e.g., due to differences in the underlying QGP EoS). Averaging over the initial spatial density profile typically leads to a 15% smaller *average* temperature [126]; thus, $\bar{T}_0 \simeq 190$ MeV in Ref. [36] is quite consistent with $T_0^{\max} \simeq 220$ MeV in Ref. [117]. The slightly larger expansion velocity in Ref. [120] (surface velocity $v_{fo}^s=0.57$ at thermal freezeout), together with its square-root radial profile, imply larger boost factors in the q_t spectra which becomes significant at high momenta. In this approach preliminary NA60 pion spectra in semicentral In-In are saturated by thermal emission over the entire measured range up to $p_T \simeq 3$ GeV. Alternatively, in Ref. [106], based on an analysis of pion spectra in Pb-Au and S-Au collisions at SPS, the thermal component was found to account for the pion yields only up to $p_T \simeq 1$ GeV, requiring the introduction of a “primordial” component associated with initial hard scattering of the incoming nucleons. This interpretation is supported by the observation that the pion spectra for $p_T \geq 2$ GeV essentially scale with the number of binary $N-N$ collisions (N_{coll}), indicating that the hard component dominates the spectra at these momenta. The preliminary NA60 pion spectra are also well predicted in this approach, with a crossing of thermal and hard components at $p_T \simeq 1.2$ GeV. As discussed in Sec. 1.2, a valuable indicator of the degree of thermalization is the elliptic flow, $v_2(p_T)$. At SPS energies, ideal hydrodynamics overpredicts this quantity even at low p_T by about 30-50% (possibly due to neglecting effects of finite viscosity, in connection with initial temperatures in the vicinity of T_c where the EoS is presumably rather soft). Moreover, the experimental $v_2(p_T)$ in semicentral Pb-Au levels off at $p_T=1.5-2$ GeV [127, 128], indicative for a transition to a kinetic regime, while hydrodynamic results keep rising, overpredicting $v_2(p_T=2$ GeV) by about a factor of ~ 2 .

Concerning effective chemical potentials for pions (and other stable particles) between

chemical and thermal freezeout, their main effect is a faster cooling in the evolution of $T(\tau)$ (the equation of state, $P(\epsilon)$, is largely unaffected) [129, 130]. E.g., for $\mu_\pi=80$ MeV at $T=120$ MeV [36], the pion density, $\varrho_\pi(T, \mu_\pi)$, is enhanced by a factor of $\sim e^{80/120} \sim 2$ relative to $\mu_\pi=0$, and as large as $\varrho_\pi(T=150 \text{ MeV}, 0)$. Therefore, thermal freezeout at $(T_{\text{fo}}, \mu_\pi^{\text{fo}})=(130, 0)$ MeV [117] corresponds to a smaller pion density (and thus larger volume) than at $(T_{\text{fo}}, \mu_\pi^{\text{fo}})=(120, 80)$ MeV [36], consistent with the longer lifetime in Ref. [117].

Implications of varying critical and chemical-freezeout temperatures for dilepton spectra have been studied in Ref. [106]. The value of T_c affects the *relative* partition of QGP and hadronic emission, especially at masses $M \geq 1$ GeV where the Boltzmann factor augments the sensitivity to earlier phases and the hadronic rates are not enhanced by resonances. However, if hadronic and QGP rates are “dual” around T_c , this distinction is largely academic. Smaller T_{ch} ’s lead to smaller μ_i ’s in the subsequent hadronic evolution, and thus higher kinetic freezeout temperatures, e.g., $(T_{\text{fo}}, \mu_\pi^{\text{fo}})=(135, 35)$ MeV for $T_{\text{ch}}=160$ MeV.

Experimentally measured dilepton spectra contain sources other than thermal radiation represented by Eq. (41). A systematic evaluation of these sources has recently been conducted in Ref. [106], in terms of (i) final-state decays and (ii) primordial sources.

Dilepton decays of long-lived hadrons (mostly η , η' , ω and ϕ mesons) after thermal freezeout, commonly referred to as “hadron decay cocktail”, are usually based on chemical freezeout for their abundance and thermal freezeout for their p_T spectra. The situation is more involved for the ρ -meson, since its continuous regeneration implies relative chemical equilibrium with pions until thermal freezeout (to a certain extent this may also apply to ω and ϕ). In addition, its short lifetime is not well separated from the typical duration of the freezeout process. In Ref. [30], the final generation of ρ decays has been approximated by an extra 1 fm/ c of fireball lifetime. However, as has been clarified in Refs. [131, 106], when treating the final generation of ρ ’s as a cocktail decay, the time dilation of the moving ρ ’s generates a hardening of its q_t spectrum by a factor $\gamma_t=M_t/M$ ($M_t^2=M^2+q_t^2$). The resulting spectrum recovers the standard Cooper-Frye [132] description for freezeout at a fixed time in the laboratory frame (cf. also Refs. [133, 134]). This, in turn, implies that the apparent temperature of the radiation formula (41) is smaller than the actual temperature figuring into the Boltzmann factor (independent of flow effects) by about $\sim 10\%$.¹⁰

In analogy to the pion- p_T spectra discussed above, the ρ spectra are expected to have a primordial component (emanating from hard N - N collisions) which does not equilibrate with the medium. Such a component has been introduced in Refs. [131, 106] including a schematic treatment for Cronin effect and jet-quenching as inferred from pion spectra in S-Au and Pb-Au collisions at SPS [135] (also note that, at high q_t , this component scales with N_{coll} , rather than N_{part} as for the (low- p_T) cocktail).

Another primordial dilepton source is the well-known Drell-Yan (DY) process, i.e., quark-antiquark annihilation in binary N - N collisions. To leading order $q\bar{q} \rightarrow e^+e^-$ is $\mathcal{O}(\alpha_s^0\alpha^2)$ and can be reliably calculated in perturbation theory at sufficiently large masses, $M \gtrsim 2$ GeV, utilizing parton distribution functions as input [136]. A finite pair momentum, $q_t > 0$, can be generated by intrinsic parton k_t and at next-to-leading order (NLO) (the latter is the dominant effect). The extrapolation of DY to small masses is problematic, but at a scale of $q_t \simeq 2$ GeV its contribution to dilepton spectra at SPS is potentially sizable. In Ref. [106] it has been suggested to estimate the spectrum of slightly virtual DY pairs, i.e., for $M^2 \ll q_t^2$, by an extrapolation of a finite- q_t DY expression to zero mass and constrain the resulting photon spectrum by measured photon spectra in p - A collisions.

¹⁰The time dilation factor for ρ decays in the thermal radiation formula is compensated by the same time dilation in ρ formation, as a consequence of detailed balance.

Semileptonic final-state decays of correlated D and \bar{D} mesons (i.e., corresponding to an associately produced $c\bar{c}$ pair) lead to an irreducible dilepton signal. The pertinent mass spectrum is, in fact, sensitive to reinteractions of the charm quarks and/or hadrons in the medium. At SPS energies, the relevance of this effect for correlated $D\bar{D}$ decays is currently an open question [137]. Theoretical calculations discussed in the following are employing N_{coll} -extrapolated spectra from p - p collisions (based on PYTHIA [139] simulations) as provided by the NA60 collaboration [35].

4.2.2 CERN-SPS I: NA60

In section we discuss several calculations of $\mu^+\mu^-$ spectra in semicentral In(158 AGeV)-In collisions as measured by NA60. The excellent mass resolution and statistics of the data allowed for a subtraction of the hadronic cocktail (excluding ρ and $D\bar{D}$ decays), resulting in the so-called “excess spectra” (in more recent, acceptance-corrected, NA60 spectra [138] correlated $D\bar{D}$ decays are also subtracted, with some caveat as to their medium modifications, as mentioned above).

Theoretical predictions [20] of the low-mass excess spectra utilizing the in-medium ρ spectral function of Ref. [30] (cf. Sec. 3.4.2) showed good agreement with the first data of NA60 [35]. More complete calculations including QGP radiation (as in Ref. [140] but with hard-thermal loop resummed rates [78]), in-medium ω and ϕ decays [105], 4π -like annihilation (relevant at intermediate mass) [36], as well as primordial ρ and Drell-Yan (DY) contributions (relevant at high q_t), are summarized in Fig. 17. In connection with a slight update of the fireball model (larger acceleration implying smaller lifetime), the resulting description of the NA60 invariant-mass spectra is quite satisfactory over the entire range, including projections onto low ($q_t < 0.5$ GeV) and high ($q_t > 1.0$ GeV). In-medium ω and ϕ contributions are rather localized in mass, while QGP and DY radiation are at the 10-15% level at masses below 1 GeV. The in-medium plus freezeout (FO) ρ contributions [20] remain the dominant source confirming the notion that the NA60 low-mass data probe the in-medium ρ spectral function. This is also borne out of the acceptance-corrected q_t -spectra where, for $M < 1$ GeV the ρ contribution prevails up to momenta of $q_t \simeq 1$ GeV.¹¹ At $q_t > 1$ GeV DY and primordial ρ -mesons become an increasingly important source, but the data for $M=0.4$ - 0.6 GeV and 0.6 - 0.9 GeV cannot be fully accounted for. These discrepancies are less pronounced for central In-In collisions, and may possibly be resolved by a stronger transverse expansion within the constraints of the hadronic spectra (we return to this question below). At masses $M=1$ - 1.4 GeV, the most significant sources are hadronic emission from multi-pion states (e.g., π - a_1 , ρ - ρ or π - ω annihilation), QGP and $D\bar{D}$ decays. The hadronic contribution is significantly enhanced (by maximally a factor of ~ 2 around $M \simeq 1$ GeV) due to the effects of chiral mixing [36] (recall Sec. 3.2.1), which currently cannot be discriminated by the data. The q_t spectra for $M=1$ - 1.4 GeV are well described over the entire momentum range.

Fig. 18 summarizes the results of hydrodynamic calculations [117, 118] based on hadronic emission rates within the chiral-reduction approach [74, 75, 76] (cf. Sec. 3.2.1), freezeout ρ mesons (including the proper γ factor relative to thermal radiation) and perturbative $q\bar{q}$ annihilation in the QGP (pQGP). The overall structure of the NA60 mass spectrum is roughly reproduced (cf. upper left panel of Fig. 18), but the ρ resonance figur-

¹¹The experimental q_t -spectra in Figs. 17, 18, 19 are not absolutely normalized; the theoretical q_t -spectra in Fig. 17 are normalized using the M -spectra at low q_t ; however, whereas the experimental M -spectra for $q_t > 1$ GeV are reasonably reproduced, the q_t -spectra for $M=0.4$ - 0.6 GeV are underestimated for $q_t > 1$ GeV.

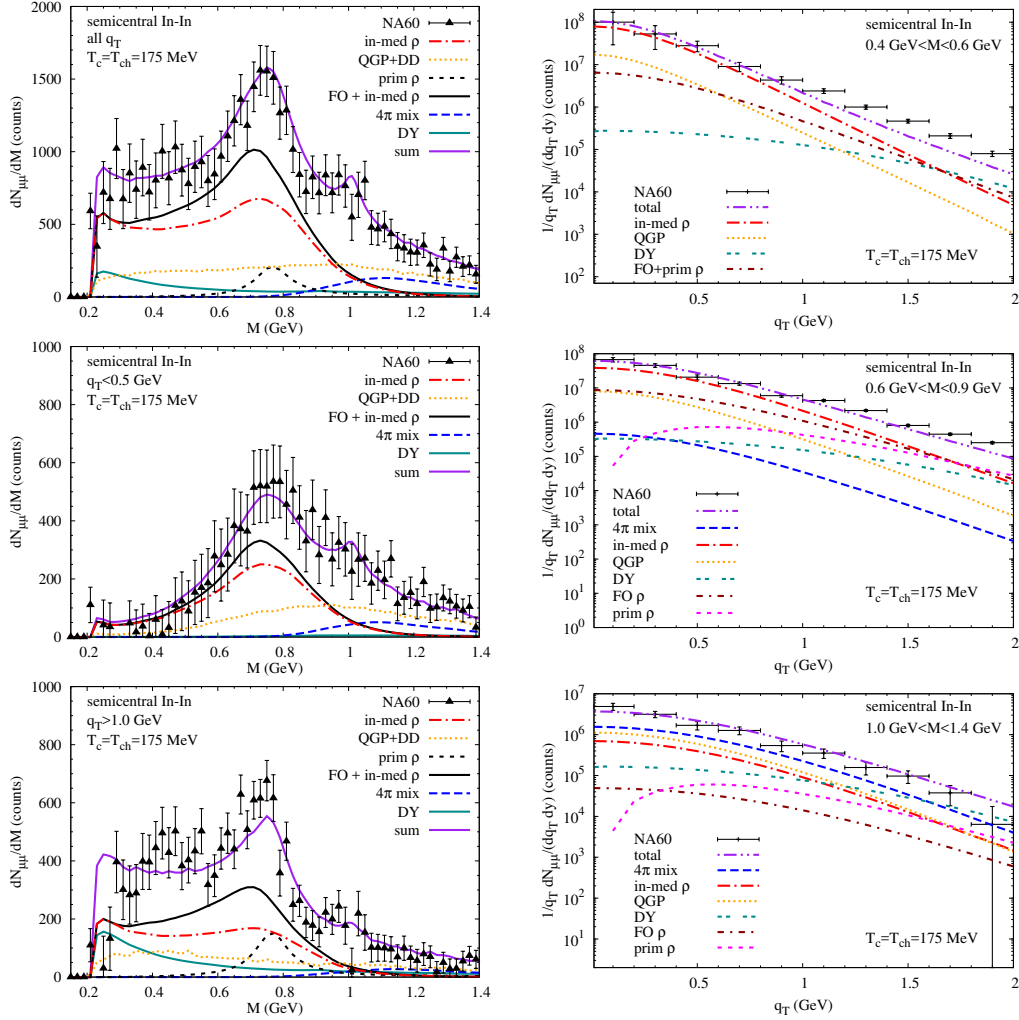


Figure 17: *Dimuon invariant-mass (left panels) and acceptance-corrected transverse-momentum (right panels) spectra in semi-central In(158 AGeV)-In collisions. Calculations [106] for thermal emission utilizing in-medium ρ , ω and ϕ spectral functions based on hadronic-many body theory [30, 105], 4π annihilation including chiral mixing [36] and QGP emission, supplemented by non-thermal sources (Drell-Yan annihilation, primordial and freeze-out ρ -meson, open-charm decays), are compared to NA60 data [35, 141, 142].*

ing into the EM correlator lacks significant in-medium broadening, despite the reduction in peak strength due to the mixing effect (the agreement improves for semiperipheral and peripheral collisions [117]). The freezeout- ρ contribution compares quite well with the one in the upper left panel of Fig. 17 which includes a broadening but also occurs at higher pion density (recall the discussion in Sec. 4.2.1). The level of the pQGP contribution is very similar to the fireball model of Refs. [36, 106] in Fig. 17. As in Refs. [36, 106] the hadronic contribution at $M > 1$ GeV is based on a fit to the EM correlator in vacuum, but the mixing effect is less pronounced in the virial scheme, leading to a slightly smaller

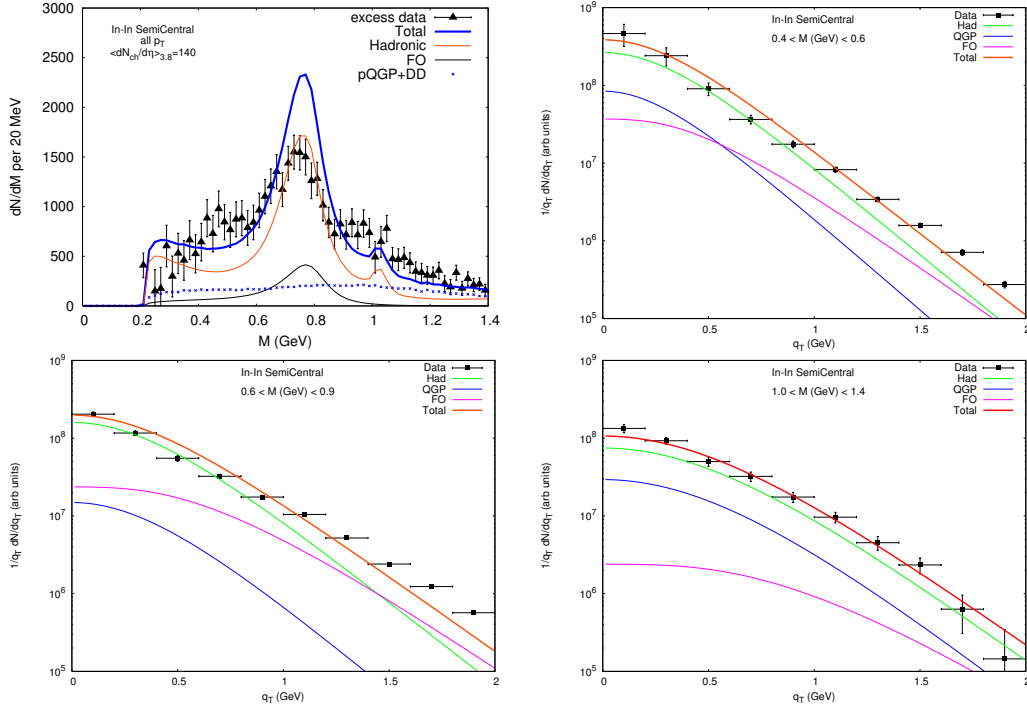


Figure 18: NA60 dimuon spectra [35, 141, 142] compared to calculations [117, 118] employing thermal rates from the chiral reduction approach [75] and perturbative $q\bar{q}$ annihilation, folded over a hydrodynamic expansion for semicentral In(158 AGeV)-In collisions, supplemented with free ρ -meson decays after thermal freezeout. Upper left: M -spectra; other panels: q_t spectra in three mass bins.

contribution in the dilepton spectrum (possibly also due to the absence of pion chemical potentials). The shapes of the q_t spectra (local slopes) of all 3 contributions displayed in Fig. 18 (in-medium hadronic, freezeout ρ and QGP) agree well with the fireball calculations of Refs. [36, 106] as demonstrated in a direct comparison in Ref. [141]. This suggests good consistency of the fireball and hydrodynamic evolution.

In Ref. [120] a thermal fireball expansion (cf. Tab. 1, middle column) has been applied to compute dimuon spectra utilizing in-medium ρ and ω spectral functions (based on empirical scattering amplitudes on pions and nucleons, recall solid lines in Fig. 12) [99], vacuum 4π annihilation (with both charged [144] and neutral pions), as well as QGP rates based on the quasiparticle model of Ref. [143], cf. Fig. 19. The overall shape and magnitude of the mass spectra is rather well reproduced, except close to the dimuon threshold where the importance of baryon effects is apparently underestimated (the underlying ρ spectral function at $T=150$ MeV shows little variation between baryon densities of $\varrho_B=0.5\varrho_0$ and ϱ_0 [120]). The q_t spectra can be reasonably well described without contributions from DY or primordial ρ 's, which differs from the hydrodynamic (DZ) [117, 118] and HR-fireball [36, 106] results, cf. Ref. [141] (recall that the RR fireball model describes NA60 pion spectra over the entire p_T range by thermal emission); part of this discrepancy is due to the slightly larger expansion velocity and the square-root radial profile of the transverse rapidity, cf. Tab. 1. Another significant difference concerns the magnitude of the QGP

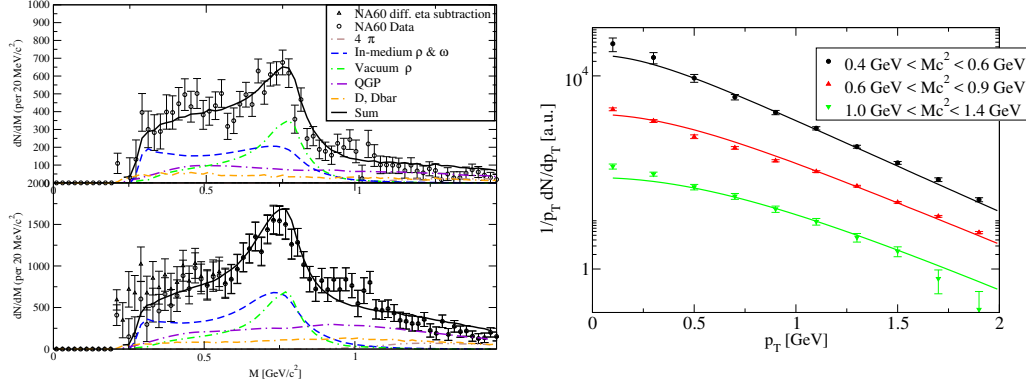


Figure 19: NA60 dimuon spectra [35, 141, 142] compared to calculations [120] employing thermal rates with in-medium ρ and ω spectral functions [99] and free 4π annihilation in hadronic matter, as well as $q\bar{q}$ annihilation in the QGP [143], folded over a thermal fireball expansion for semicentral In(158 AGeV)-In collisions, supplemented with free ρ -meson decays after thermal freezeout. Left panel: M -spectra for all q_t (bottom) and for $q_t > 1$ GeV (top); right panel: q_t spectra in three mass bins.

contribution, which is by a factor of ≥ 2 larger in Ref. [120] than in Refs. [36, 117]. Part of this discrepancy is due to the quasiparticle QGP EoS employed in Ref. [120], which entails larger temperatures (including T_0) at given fireball volume. It is also related to the prevailing role of QGP radiation for $M \geq 1$ GeV.

The sensitivity of the NA60 data to the critical and chemical freezeout temperatures has been elaborated in Ref. [106], by varying T_c from 160-190 MeV and T_{ch} from 160-175 MeV (keeping the fireball expansion parameters fixed), representing current uncertainties in lattice QCD [4, 5] and thermal model fits [8, 9]. With “quark-hadron” duality

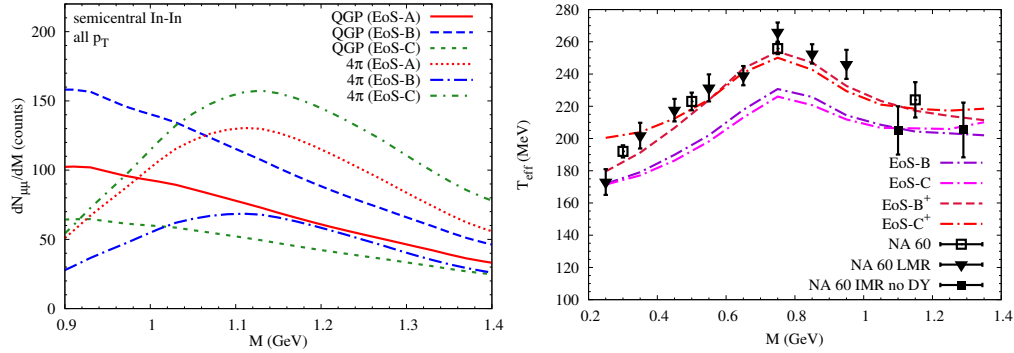


Figure 20: Sensitivity of dilepton spectra to critical and chemical-freezeout temperature [106]. Left panel: QGP and hadronic (4π) radiation at intermediate mass for $T_c = T_{ch} = 175$ MeV (EoS-A), $T_c = T_{ch} = 160$ MeV (EoS-B) and $(T_c, T_{ch}) = (190, 160)$ MeV (EoS-C); right panel: slope parameters in q_t -spectra for EoS-B and EoS-C (lower curves) and for 15% increased fireball expansion (EoS-B⁺ and EoS-C⁺, where the latter additionally includes ω t -channel exchange in $\pi\rho \rightarrow \pi e^+e^-$ reactions; all without Drell-Yan contribution); data are from Refs. [141, 142].

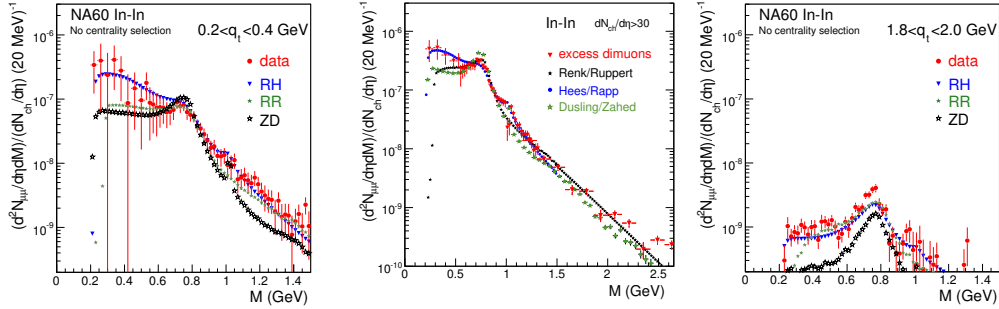


Figure 21: Comparison of acceptance-corrected excess dimuon mass spectra (for $0.2 < q_t / \text{GeV} < 0.4$ (left), $q_t > 0.2 \text{ GeV}$ (middle) and $1.8 < q_t / \text{GeV} < 2.0$ (right)) in minimum-bias In(158 AGeV)-In collisions [145, 137, 138] to model predictions for semicentral In-In of RH (EoS-A) [106], RR [120] and ZD [118], normalized to the average N_{ch} of the data.

in the thermal dilepton rates [30] in this temperature regime (at *all* masses, cf. Fig. 14), the invariant-mass spectra turn out to be remarkably *insensitive* to these variations [106] (duality of the QGP and hadronic emission for $M \lesssim 1.5 \text{ GeV}$ close to T_c is not realized in the rates underlying the calculations of Refs. [117, 120]). However, the partition of QGP and hadronic (4π) emission at intermediate masses changes appreciably from hadron-gas dominated spectra for $T_c \geq 175 \text{ MeV}$ to QGP dominated ones for $T_c = 160 \text{ MeV}$, cf. left panel of Fig. 20. In the latter case, the smaller value for $T_{\text{ch}} = 160 \text{ MeV}$ implies smaller chemical potentials in the hadronic phase. This is part of the reason for the reduction in hadronic emission, but also leads to a larger freezeout temperature by about 15 MeV (recall the discussion in Sec. 4.2.1 and right column in Tab. 1). This, in turn, helps in the description of the transverse-momentum spectra at $q_t > 1 \text{ GeV}$. However, an additional increase in the transverse fireball acceleration by 15% seems to be required to achieve quantitative agreement with the effective slope parameters as displayed in the right panel of Fig. 20. It remains to be checked whether this can be consistent with a more complete set of hadronic spectra in In(158 AGeV)-In collisions.

A comparison the three model calculations discussed above to acceptance-corrected mass spectra in minimum-bias In(158 AGeV)-In [145] in Fig. 21 reiterates the importance of baryon-driven medium effects [106] at low M and low q_t , as well as the lack of high- q_t yield in the ρ -mass region and below for Refs. [118] and [106] with EoS-A. The latter improves when increasing the fireball expansion as in the right panel of Fig. 20. Also note that comparing minimum-bias data to calculations at an average N_{ch} underestimates the theoretical contributions which scale with N_{coll} (DY and primordial ρ 's).

4.2.3 CERN-SPS II: CERES/NA45 and WA98

The refinements in the analysis of the NA60 dimuon spectra (fireball evolution and additional sources) have been rechecked against existing and updated EM data at the SPS.

The updated calculations of Ref. [106] agree well with the combined '95/'96 CERES dielectron data (left panel of Fig. 22). For the 2000 data (right panel of Fig. 22), the cocktail-subtracted excess spectra in central Pb-Au corroborate the main findings of the NA60 data, i.e., a quantitative agreement with the in-medium ρ of Ref. [30] and the predominance of baryon effects. The longer lifetime of the fireball in central Pb-Au (factor

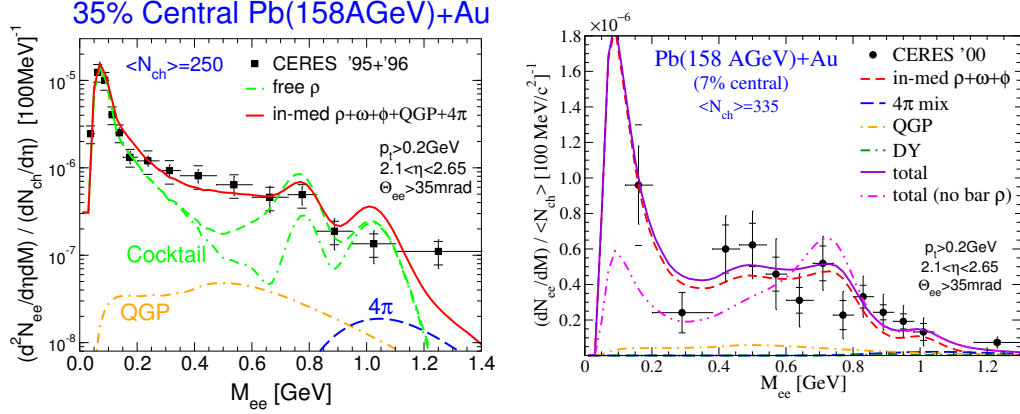


Figure 22: *CERES/NA45* data for e^+e^- invariant-mass spectra in Pb(158 AGeV)-Au collisions at the SPS [32, 37]. The left panel corresponds to semicentral collisions including the contribution from long-lived hadron decays after freeze-out (“cocktail”, dash-dotted line), while the right panel shows “excess” spectra for central collisions. The theoretical predictions are based on in-medium ρ spectral functions [30] supplemented by ω and ϕ decays, as well as Drell-Yan and 4π annihilation [106] (as for the NA60 data, see Fig. 17).

~ 2 relative to In-In) reduces the uncertainties due to ρ -meson cocktail contributions. In addition, dielectrons enable access to very low masses, where the '00 CERES data may bear a first hint of a large enhancement as predicted by hadronic many-body theory.

As emphasized in Sec. 3.5, (very) low-mass dilepton rates are intimately related to thermal photon spectra. In Ref. [108] the in-medium ρ spectral function of Ref. [30] has been carried to the photon point and convoluted over the same fireball expansion as before; when supplemented with t -channel exchange reactions, QGP emission and primordial (hard) photons constrained by p -A data, the resulting q_t spectra are consistent with WA98 photon spectra, see lower right panel of Fig. 23; the updated fireball evolution barely affects the total spectra. The contributions from the lightlike ρ are prevalent up to $q_t \simeq 1$ GeV (cf. Fig. 15), after which t -channel processes takes over. Primordial photons outshine the combined thermal yield (hadronic+QGP) for $q_t \gtrsim 2$ GeV. This is nicely consistent with the calculations of Ref. [149], see lower left panel in Fig. 23. In earlier calculations of Refs. [148, 126] the thermal yield is significantly larger, due to an increased QGP contribution caused by a short formation time of $\tau_0 = 0.2$ - 0.33 fm/ c with associated peak temperatures of up to $T_0 = 335$ MeV (for $\tau_0 = 1$ fm/ c [108, 149] average initial temperatures are slightly above $\bar{T}_0 = 200$ MeV). Even for this upper estimate of QGP emission¹², the latter is smaller than the hadronic one for momenta $q_t \leq 1.5$ - 2 GeV, and the pQCD photons are at the $\sim 40\%$ level of the combined thermal contribution at $q_t \simeq 2$ GeV.

Similar conclusions arise from theoretical analyses [140, 150, 151] of intermediate-mass dimuon spectra ($1.5 \leq M_{\mu\mu}/\text{GeV} < 3$) in Pb-Pb collisions at SPS [152]: unless the initial temperature significantly exceeds $T_0 = 250$ MeV, the thermal contribution falls below primordial sources (DY) at masses and transverse momenta beyond $M, q_t \simeq 1.5$ - 2 GeV. This is fully confirmed by the recent NA60 intermediate-mass dilepton spectra [137].

¹²At SPS energy, with a Lorentz contraction of $\gamma \simeq 9$ for the incoming nuclei, the time for full nuclear overlap is ca. 0.8 fm/ c .

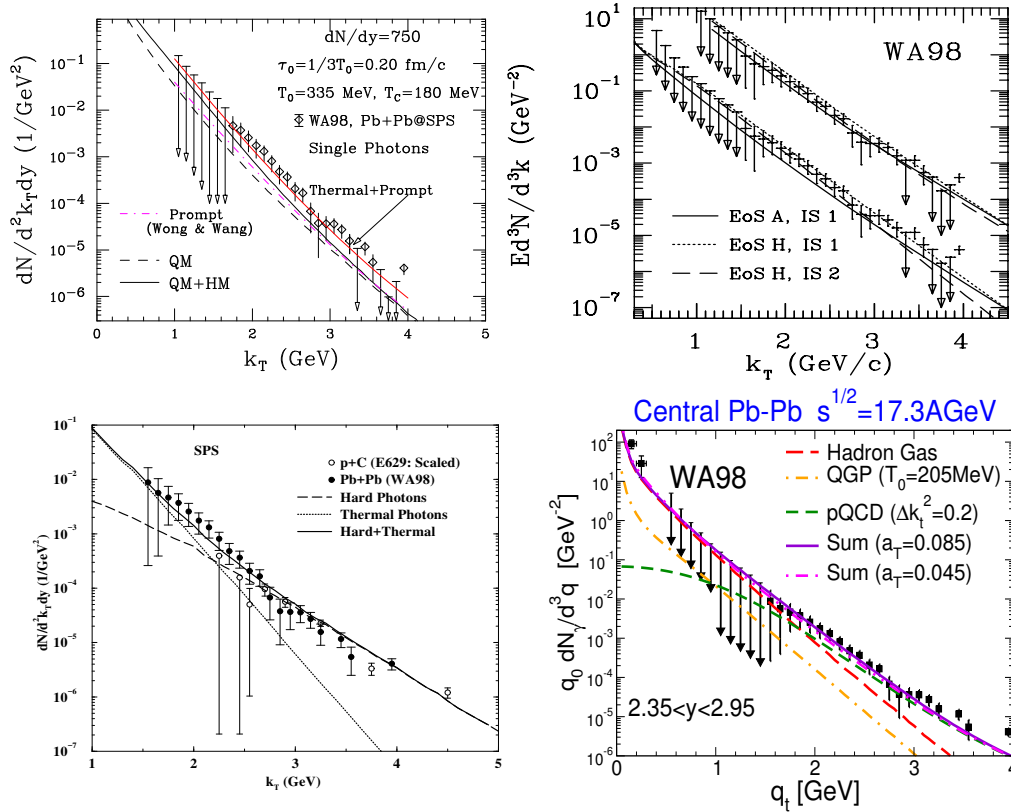


Figure 23: *Direct photon spectra in central Pb(158 AGeV)-Pb collisions at the SPS as measured by the WA98 collaboration [146, 147]. The upper panels contain theoretical calculations [148, 126] with a moderate primordial pQCD component and a hot initial state ($\tau_0=0.2-0.33$ fm/c; in the upper left panel the lower curves are without primordial emission), while the calculations in the lower panels [149, 108] contain primordial emission with Cronin effect and a larger thermalization time ($\tau_0 \simeq 1$ fm/c).*

4.2.4 Future Dilepton Measurements

Dilepton programs will be pursued with high priority over a wide range of collision energies. The large enhancement observed in a low-energy (40 AGeV) run at SPS [38] is in line with the prediction of hadronic-many body theory that medium effects caused by baryons play a leading role [70]. This trend continues down to much lower bombarding energies of 1-2 AGeV. However, at these energies recent transport calculations suggest that the low-mass enhancement, which could not be explained by hadronic in-medium effects [27], is related to primordial N - N Bremsstrahlung [153], as well as $\Delta \rightarrow Ne^+e^-$ and η Dalitz decays [154, 155]. A better sensitivity to medium effects appears to be in the ρ - ω mass region, where the (lack of) yield indicates a strong broadening of the vector resonances [156, 154, 157].

At the high-energy frontier, first RHIC data [42] find a large e^+e^- signal especially in the mass region around $M \simeq 0.3$ GeV. The excess is concentrated at low q_t and in central collisions, and cannot be explained by current in-medium spectral functions. It is tempting to speculate that the excess is caused by the formation of a disoriented chiral condensate

(DCC), as pion-DCC annihilation shares the above features [158]. However, the magnitude of this dilepton source cannot easily compete with hadronic medium effects, unless the DCC domains are rather large and abundant. In this case, footprints of the DCC should be visible in other observables (e.g., π^0 and p_T fluctuations). Precision measurements within the RHIC-II program will be of crucial importance here [43].

Finally, dilepton data will play a critical role in the CBM experiment at the future GSI facility (FAIR). In the planned energy regime, $E_{\text{lab}}=10\text{-}40$ AGeV, one envisages the largest nuclear compression and thus maximal baryon density, ideally suited to scrutinize the current understanding of medium effects. An extra benefit could be the occurrence of a critical point or a true mixed phase at a first-order transition, with extended fireball lifetimes further enhancing the dilepton signal.

4.3 Critical Appraisal

In this section we evaluate the current status of determining the in-medium vector spectral functions (focusing on the ρ meson) and the implications for chiral restoration.

Calculations of ρ -meson spectral functions based on effective chiral Lagrangians coupled with many-body techniques agree on a strong broadening with small (positive) mass shifts. At normal nuclear matter density, one finds an increase in width of $\Delta\Gamma_\rho \simeq 250$ MeV with an estimated error of $\sim 30\%$, i.e., the vacuum width almost triples. The question whether the parameters in the effective Lagrangian are subject to in-medium changes requires further input. In the vector-manifestation scenario, reduced bare masses and coupling constants are inferred from a matching of the correlators to an operator product expansion (OPE) at spacelike momenta governed by the in-medium reduction of the condensates. However, it turns out that, within current uncertainties, the softening of the ρ spectral function as imposed by the OPE at nuclear matter density is fully accounted for by the broadening due to hadronic many-body effects. More accurate tests of this assertion, especially at higher densities/temperatures, will require a more precise determination of the in-medium condensates on the OPE side of the QCD sum rule. The predicted broadening is supported by several recent experiments where dilepton spectra have been measured with impressive precision: at JLAB, photoproduction data off mid-size nuclei find a ρ broadening of $\Delta\Gamma_\rho^{\text{NUC}} \simeq 70\text{-}100$ MeV without significant mass shift, consistent with many-body effects at about half nuclear density and 3-momenta of $\sim 1\text{-}2$ GeV. The NA60 dilepton spectra in central In-In collisions exhibit an *average* ρ width of $\bar{\Gamma}_\rho^{\text{HIC}} \simeq 400$ MeV i.e., an additional broadening of $\Delta\bar{\Gamma}_\rho^{\text{HIC}} \simeq 250$ MeV. Typical kinetic freeze-out conditions at SPS energies are $(\rho_B^{\text{fo}}, T_{\text{fo}}) \simeq (0.3\rho_0, 120\text{MeV})$. With initial temperatures of $T_0 \simeq 200$ MeV (as suggested by “effective” slope parameters in the q_T spectra for $M > 1$ GeV, as well as direct photon spectra in Pb-Pb), the average ρ width thus reflects the medium at an average temperature of $\bar{T} \simeq 150$ MeV (the growing fireball 3-volume “biases” low-mass dilepton radiation to more dilute stages). This implies that the ρ width approaches its mass when the system moves toward the (pseudo) critical temperature, $\Gamma_\rho(T \rightarrow T_c) \rightarrow m_\rho$, i.e., the resonance “melts” (see also Ref. [159]). Inspection of the theoretical predictions for the width of the ρ as extracted from the vector spectral function corroborates this conclusion, cf. Fig. 24. The circumstantial “duality” of hadronic and partonic EM emission rates close to T_c lends robustness to the pertinent predictions for dilepton spectra in heavy-ion collisions as they become independent on details of the evolution model, in particular of the treatment of the phase transition region. The excess radiation at intermediate mass, with its rather soft emission characteristics in q_t , as well as direct photon spectra, further

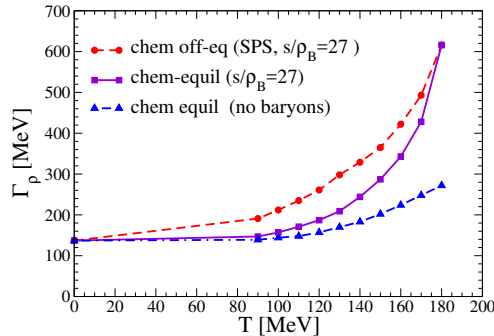


Figure 24: Temperature dependence of the ρ width as evaluated in hadronic many-body theory [30] at fixed entropy per baryon representative for heavy-ion collisions at full SPS energy (dashed and solid line: with and without meson chemical potentials). For the dash-dotted line, medium effects due to baryons are switched off.

consolidate the origin of thermal radiation from around T_c .

A no less challenging task is to connect the above findings to the chiral transition. It has recently been argued that the statistical operator consisting of a (free) hadron resonance gas (HRG) is capable of reproducing several features of lattice QCD computations of the equation of state (EoS) until rather close to the (pseudo-) critical temperature [160, 161]. Beyond T_c the lattice EoS levels off, reflecting quark-gluon degrees of freedom, while the HRG EoS diverges (Hagedorn catastrophe). The ρ melting offers a microscopic explanation for this transition: under moderate conditions, the *interacting* HRG physics drives the ρ broadening to an extent which justifies the use of well-defined quasi-particle states in the statistical operator. With further increasing temperature and density, resonance overlap in the ρ spectral function drives it to a continuum shape *with a strength resembling a weakly interacting $q\bar{q}$ pair*, i.e., the resonance strength in the statistical operator converts into partonic strength. The phenomenon of overlapping resonances merging into a perturbative $q\bar{q}$ continuum is, of course, well known from the e^+e^- annihilation cross section into hadrons above $M \simeq 1.5$ GeV. It is suggestive that the thermal medium provides the necessary phase space for low-mass resonances which, via their mutual “mixing” in different hadronic correlators, “restore” quark-hadron duality down to $M \rightarrow 0$, implying chiral restoration. To quantify this picture the evaluation of chiral order parameters is mandatory. It is tempting to speculate that the rather sharp increase of the ρ width close to the expected critical temperature (especially in chemical equilibrium as realized in lattice QCD, represented by the solid line in Fig. 24) is signaling the chiral transition. QCD sum rules remain a valuable tool if the T (and μ_B) dependence of the quark and gluon condensates can be made more precise. Ideally, the latter are determined from first-principle lattice QCD calculations. Possibly the most promising approach, which has been little exploited thus far, are chiral (or Weinberg) sum rules. Their use hinges on the in-medium axialvector spectral function. The latter is much more difficult to constrain due to a principal lack of experimental information, encoded in either 3-pion or $\pi\text{-}\gamma$ final states. This stipulates the importance of calculating the axialvector correlator in chiral models. In connection with a realistic vector correlator and lattice-QCD input on the in-medium condensates, the explicit realization of chiral restoration can be investigated. First efforts in this direction have been undertaken [162, 163, 164, 165], but a full treatment including quantitative V and A spectral functions, even in the vacuum, is currently lacking.

5 Conclusions

Medium modifications of hadronic spectral functions play a key role in the diagnosis of hot/dense strongly interacting matter and its condensate structure. Experimentally, the most promising approach is dilepton spectroscopy which directly probes the vector spectral function of the hadronic medium. For the ρ -meson, which dominates the low-mass vector channel, effective hadronic theories largely agree on a strong broadening of the resonance, with little mass shift. Baryon effects prevail over those induced by mesons, and the predicted modifications in cold nuclear matter are compatible with QCD sum rules at finite density. Intense experimental efforts over the last ~ 15 years have culminated to a new level of precision which broadly confirms the theoretical expectations: production experiments off ground-state nuclei find an increase of the ρ width by ~ 80 MeV, while the effect in heavy-ion collisions at the SPS is by a factor of ~ 3 larger. Part of this difference is due to the access to the low-momentum regime in the heavy-ion measurements. It is therefore highly desirable to push the sensitivity of the nuclear experiments to low 3-momenta where significantly larger medium effects are predicted. The average ρ width extracted in heavy-ion collisions suggests that the ρ resonance “melts” close to the expected phase boundary, in agreement with extrapolations of hadronic models. This is a first explicit evidence that melting resonances are involved in the transition from hadronic to quark degrees of freedom. Modern quark-model calculations could provide complementary insights when approaching T_c from above. Unquenched lattice QCD computations of the vector correlator would undoubtedly set valuable benchmarks and possibly shed light on the conjecture that the width is connected to order parameters of chiral symmetry restoration. In addition, information on quark condensates and pion decay constant(s) below T_c can be connected to hadronic vector and axialvector spectral functions utilizing Weinberg sum rules. The synergy of hadronic and quark models with first-principle lattice QCD computations, augmented by quantitative applications to experiment at current and future facilities, opens exciting perspectives to improve our knowledge about the chiral transition in hot/dense QCD matter and the generation of luminous mass in the Universe.

Acknowledgments

We thank H.J. Specht and S. Damjanovic for valuable discussions and suggestions. RR has been supported by a U.S. National Science Foundation CAREER Award under grant PHY-0449489, and by the A. v. Humboldt-Foundation through a Bessel Research Award.

References

- [1] E.V. Shuryak, *The QCD Vacuum, Hadrons and Superdense Matter*, 2. edition, World Scientific Lecture Notes in Physics, Vol. **71** (2004).
- [2] P. Braun-Munzinger and J. Wambach, [arXiv:0801.4256\[hep-ph\]](#).
- [3] L. Y. Glozman, *Phys. Rept.* **444**, 1 (2007).
- [4] M. Cheng *et al.*, *Phys. Rev. D* **74**, 054507 (2006).
- [5] Y. Aoki, Z. Fodor, S. D. Katz, and K. K. Szabo, *Phys. Lett. B* **643**, 46 (2006).

- [6] U. W. Heinz and M. Jacob (2000), [arXiv:nucl-th/0002042](#).
- [7] I. Arsene *et al.* (BRAHMS Collaboration), Nucl. Phys. A **757**, 1 (2005);
B.B. Back *et al.* (PHOBOS Collaboration), *ibid.* 28 (2005);
J. Adams *et al.* (STAR Collaboration), *ibid.* 102 (2005);
K. Adcox *et al.* (PHENIX Collaboration), *ibid.* 184 (2005).
- [8] P. Braun-Munzinger, K. Redlich and J. Stachel (2003), in R.C. Hwa, X.N. Wang (editors), *Quark-gluon plasma* vol. 3 (World Scientific, 2004) p491, [arXiv:nucl-th/0304013](#).
- [9] F. Becattini, M. Gazdzicki, A. Keranen, J. Manninen and R. Stock, Phys. Rev. C **69**, 024905 (2004); F. Becattini, J. Manninen, and M. Gazdzicki, Phys. Rev. C **73**, 044905 (2006).
- [10] D. Teaney, J. Lauret, and E. V. Shuryak (2001), [arXiv:nucl-th/0110037](#).
- [11] T. Hirano and K. Tsuda, Phys. Rev. C **66**, 054905 (2002).
- [12] P. F. Kolb and U. W. Heinz (2003), published in R.C. Hwa, X.N. Wang (editors), *Quark-gluon plasma* vol. 3 (World Scientific, 2004) p634, [arXiv:nucl-th/0305084](#).
- [13] C. Nonaka and S. A. Bass, Phys. Rev. C **75**, 014902 (2007).
- [14] A. Adare *et al.* (PHENIX Collaboration), Phys. Rev. Lett. **98**, 162301 (2007).
- [15] B. I. Abelev *et al.* (STAR Collaboration), Phys. Rev. C **75**, 054906 (2007).
- [16] E. L. Feinberg, Nuovo Cim. A **34**, 391 (1976).
- [17] E. V. Shuryak, Phys. Lett. B **78**, 150 (1978).
- [18] L. D. McLerran and T. Toimela, Phys. Rev. D **31**, 545 (1985).
- [19] J. J. Sakurai, *Currents and Mesons* (University of Chicago Press, Chicago, 1969).
- [20] R. Rapp, J. Phys. G **31**, S217 (2005).
- [21] G.E. Brown and M. Rho, Phys. Rev. Lett. **66**, 2720 (1991); Phys. Rept. **269**, 333 (1996).
- [22] G. Agakishiev *et al.* (CERES/NA45 Collaboration), Phys. Rev. Lett. **75**, 1272 (1995).
- [23] G.-Q. Li, C. M. Ko, and G. E. Brown, Phys. Rev. Lett. **75**, 4007 (1995).
- [24] W. Cassing, W. Ehehalt, and C. M. Ko, Phys. Lett. B **363**, 35 (1995).
- [25] R. Rapp and J. Wambach, Adv. Nucl. Phys. **25**, 1 (2000).
- [26] J. Alam, S. Sarkar, P. Roy, T. Hatsuda, and B. Sinha, Annals Phys. **286**, 159 (2001).
- [27] W. Cassing and E. L. Bratkovskaya, Phys. Rept. **308**, 65 (1999).
- [28] C. Gale and K. L. Haglin (2003), in R. C. Hwa, X. N. Wang (editors), *Quark-gluon plasma* vol. 3 (World Scientific, 2004) p364, [arXiv:hep-ph/0306098](#).

- [29] R. Rapp, G. Chanfray, and J. Wambach, Nucl. Phys. A **617**, 472 (1997).
- [30] R. Rapp and J. Wambach, Eur. Phys. J. A **6**, 415 (1999).
- [31] G. Agakishiev *et al.* (CERES/NA45 Collaboration), Phys. Lett. B **422**, 405 (1998).
- [32] G. Agakishiev *et al.* (CERES/NA45 Collaboration), Eur. Phys. J. C **41**, 475 (2005).
- [33] S. Bethke, Prog. Part. Nucl. Phys. **58**, 351 (2007).
- [34] R. Rapp, Nucl. Phys. A **661**, 33 (1999).
- [35] R. Arnaldi *et al.* (NA60 Collaboration), Phys. Rev. Lett. **96**, 162302 (2006).
- [36] H. van Hees and R. Rapp, Phys. Rev. Lett. **97**, 102301 (2006).
- [37] D. Adamova *et al.* (CERES/NA45 Collaboration), Phys. Lett. B **666**, 425 (2008).
- [38] D. Adamova *et al.* (CERES/NA45 Collaboration), Phys. Rev. Lett. **91**, 042301 (2003).
- [39] R. J. Porter *et al.* (DLS Collaboration), Phys. Rev. Lett. **79**, 1229 (1997).
- [40] G. Agakishiev *et al.* (HADES Collaboration), Phys. Rev. Lett. **98**, 052302 (2007).
- [41] G. Agakishiev *et al.* (HADES Collaboration), Phys. Lett. B **663**, 43 (2008).
- [42] S. Afanasiev *et al.* (PHENIX Collaboration) (2007), [arXiv:0706.3034\[nucl-ex\]](https://arxiv.org/abs/0706.3034).
- [43] G. David, R. Rapp, and Z. Xu, Phys. Rept. **462**, 176 (2008).
- [44] D. Trnka *et al.* (CBELSA/TAPS Collaboration), Phys. Rev. Lett. **94**, 192303 (2005).
- [45] R. Nasseripour *et al.* (CLAS Collaboration), Phys. Rev. Lett. **99**, 262302 (2007).
- [46] M. Naruki *et al.* (E325 Collaboration), Phys. Rev. Lett. **96**, 092301 (2006).
- [47] H. Fritzsche, M. Gell-Mann and H. Leutwyler, Phys. Lett. B **47**, 365 (1973).
- [48] D. J. Gross and F. Wilczek, Phys. Rev. Lett. **30**, 1343 (1973).
- [49] H. D. Politzer, Phys. Rev. Lett. **30**, 1346 (1973).
- [50] R. Barate *et al.* (ALEPH Collaboration), Eur. Phys. J. C **4**, 409 (1998).
- [51] K. Ackerstaff *et al.* (OPAL Collaboration), Eur. Phys. J. C **7**, 571 (1999).
- [52] S. Weinberg, Phys. Rev. Lett. **18**, 507 (1967).
- [53] T. Das, V. S. Mathur, and S. Okubo, Phys. Rev. Lett. **19**, 859 (1967).
- [54] H. Leutwyler, *Restoration of Chiral Symmetry*, In *Dobogokoe 1991, Proceedings, Effective field theories of the standard model* 193-224.
- [55] E. G. Drukarev and E. M. Levin, Prog. Part. Nucl. Phys. **27**, 77 (1991).
- [56] T. D. Cohen, R. J. Furnstahl, and D. K. Griegel, Phys. Rev. C **45**, 1881 (1992).

- [57] S. Zschocke, B. Kämpfer, O. P. Pavlenko, and G. Wolf (2002), [arXiv:nucl-th/0202066](#).
- [58] M. Cheng *et al.*, Phys. Rev. D **77**, 014511 (2008).
- [59] D. E. Miller, Phys. Rept. **443**, 55 (2007).
- [60] T. Hatsuda and T. Kunihiro, Phys. Rev. Lett. **55**, 158 (1985).
- [61] G. E. Brown, C.-H. Lee, M. Rho, and E. Shuryak, Nucl. Phys. A **740**, 171 (2004).
- [62] M. Mannarelli and R. Rapp, Phys. Rev. C **72**, 064905 (2005).
- [63] A. Starostin *et al.* (Crystal Ball Collaboration), Phys. Rev. Lett. **85**, 5539 (2000).
- [64] N. Grion *et al.* (CHAOS Collaboration), Nucl. Phys. A **763**, 80 (2005).
- [65] F. Bloch *et al.*, Eur. Phys. J. A **32**, 219 (2007).
- [66] T. Hatsuda, T. Kunihiro, and H. Shimizu, Phys. Rev. Lett. **82**, 2840 (1999).
- [67] R. Rapp *et al.*, Phys. Rev. C **59**, 1237 (1999).
- [68] M. J. Vicente Vacas and E. Oset, Phys. Rev. C **60**, 064621 (1999).
- [69] O. Buss, L. Alvarez-Ruso, A.B. Larionov, and U. Mosel, Phys. Rev. C **74**, 044610 (2006).
- [70] R. Rapp, Pramana **60**, 675 (2003).
- [71] M. Dey, V. L. Eletsky, and B. L. Ioffe, Phys. Lett. B **252**, 620 (1990).
- [72] B. Krippa, Phys. Lett. B **427**, 13 (1998).
- [73] G. Chanfray, J. Delorme, M. Ericson and M. Rosa-Clot, Phys. Lett. B **455**, 39 (1999).
- [74] J. V. Steele, H. Yamagishi, and I. Zahed, Phys. Lett. B **384**, 255 (1996).
- [75] J. V. Steele, H. Yamagishi, and I. Zahed, Phys. Rev. D **56**, 5605 (1997).
- [76] J. V. Steele and I. Zahed, Phys. Rev. D **60**, 037502 (1999).
- [77] F. Karsch, E. Laermann, P. Petreczky, S. Stickan, and I. Wetzorke, Phys. Lett. B **530**, 147 (2002).
- [78] E. Braaten, R. D. Pisarski, and T.-C. Yuan, Phys. Rev. Lett. **64**, 2242 (1990).
- [79] M. Asakawa, T. Hatsuda, and Y. Nakahara, Prog. Part. Nucl. Phys. **46**, 459 (2001).
- [80] G. D. Moore and J.-M. Robert (2006), [arXiv:hep-ph/0607172](#).
- [81] C. R. Allton *et al.*, Phys. Rev. D **71**, 054508 (2005).
- [82] J.I. Kapusta and E.V. Shuryak, Phys. Rev. D **49**, 4694 (1994).
- [83] M. A. Shifman, A. I. Vainshtein, and V. I. Zakharov, Nucl. Phys. B **147**, 385 (1979).

- [84] T. Hatsuda and S. H. Lee, Phys. Rev. C **46**, 34 (1992).
- [85] M. Asakawa and C. M. Ko, Nucl. Phys. A **560**, 399 (1993).
- [86] F. Klingl, N. Kaiser and W. Weise, Nucl. Phys. A **624**, 527 (1997).
- [87] S. Leupold, W. Peters and U. Mosel, Nucl. Phys. A **628**, 311 (1998).
- [88] J. Ruppert, T. Renk and B. Müller, Phys. Rev. C **73**, 034907 (2006).
- [89] Y. Kwon, M. Procura and W. Weise, [arXiv:0803.3262\[nucl-th\]](https://arxiv.org/abs/0803.3262).
- [90] M. Bando, T. Kugo, S. Uehara, K. Yamawaki, and T. Yanagida, Phys. Rev. Lett. **54**, 1215 (1985).
- [91] H. Gomm, O. Kaymakcalan, and J. Schechter, Phys. Rev. D **30**, 2345 (1984).
- [92] M. Harada and K. Yamawaki, Phys. Rept. **381**, 1 (2003).
- [93] M. Harada and C. Sasaki, Phys. Rev. D **74**, 114006 (2006)
- [94] M. Urban, M. Buballa, R. Rapp, and J. Wambach, Nucl. Phys. A **673**, 357 (2000).
- [95] C. Song, Phys. Rev. D **53**, 3962 (1996).
- [96] R. Rapp and C. Gale, Phys. Rev. C **60**, 024903 (1999).
- [97] A. Dobado, A. Gomez Nicola, F. J. Llanes-Estrada and J. R. Pelaez, Phys. Rev. C **66**, 055201 (2002)
- [98] K. Haglin, Nucl. Phys. A **584**, 719 (1995)
- [99] V.L. Eletsky, M. Belkacem, P.J. Ellis and J.I. Kapusta, Phys. Rev. C **64**, 035202 (2001).
- [100] M. Post, S. Leupold, and U. Mosel, Nucl. Phys. A **741**, 81 (2004).
- [101] D.M. Manley, R.A. Arndt, Y. Goradia and V.L. Teplitz, Phys. Rev. D **30**, 904 (1984).
- [102] T.P. Vrana, S.A. Dytman, and T.S.H. Lee, Phys. Rept. **328**, 181 (2000).
- [103] R. Rapp, M. Urban, M. Buballa, and J. Wambach, Phys. Lett. B **417**, 1 (1998).
- [104] M. F. M. Lutz, G. Wolf, and B. Friman, Nucl. Phys. A **706**, 431 (2002).
- [105] R. Rapp, Phys. Rev. C **63**, 054907 (2001).
- [106] H. van Hees and R. Rapp, Nucl. Phys. A **806**, 339 (2008).
- [107] R. Rapp (2002), [arXiv:nuc1-th/0204003](https://arxiv.org/abs/nuc1-th/0204003).
- [108] S. Turbide, R. Rapp, and C. Gale, Phys. Rev. C **69**, 014903 (2004).
- [109] J. I. Kapusta, P. Lichard and D. Seibert, Phys. Rev. D **44**, 2774 (1991) [Erratum-
ibid. D **47**, 4171 (1993)].

- [110] P. Arnold, G. D. Moore, and L. G. Yaffe, JHEP **0112**, 009 (2001).
- [111] M. H. Wood *et al.* [CLAS Collaboration], Phys. Rev. C **78**, 015201 (2008).
- [112] F. Riek, R. Rapp, T. S. Lee and Y. Oh, [arXiv:0812.0987\[nucl-th\]](#).
- [113] G. M. Huber *et al.* (TAGX Collaboration), Phys. Rev. C **68**, 065202 (2003).
- [114] W. Cassing, E. L. Bratkovskaya, R. Rapp and J. Wambach, Phys. Rev. C **57**, 916 (1998).
- [115] P. Huovinen, M. Belkacem, P. J. Ellis and J. I. Kapusta, Phys. Rev. C **66**, 014903 (2002).
- [116] E. L. Bratkovskaya, W. Cassing and O. Linnyk, [arXiv:0805.3177\[nucl-th\]](#).
- [117] K. Dusling, D. Teaney, and I. Zahed, Phys. Rev. C **75**, 024908 (2007).
- [118] K. Dusling and I. Zahed (2007), [arXiv:hep-ph/0701253](#).
- [119] T. Renk and J. Ruppert, Phys. Rev. C **77**, 024907 (2008).
- [120] J. Ruppert, C. Gale, T. Renk, P. Lichard, and J. I. Kapusta, Phys. Rev. Lett. **100**, 162301 (2008).
- [121] I. G. Bearden *et al.* (NA44 Collaboration), Phys. Rev. Lett. **78**, 2080 (1997).
- [122] H. Appelshäuser *et al.* (NA49 Collaboration), Eur. Phys. J. C **2**, 661 (1998).
- [123] F. Antinori *et al.* (WA97 Collaboration), J. Phys. G **27**, 2325 (2001); J. Phys. G **33**, 403 (2007).
- [124] D. Adamova *et al.* (CERES Collaboration), Nucl. Phys. A **714**, 124 (2003).
- [125] V.V. Skokov and V.D. Toneev, Phys. Rev. C **73**, 021902 (2006).
- [126] P. Huovinen, P. V. Ruuskanen and S. S. Räsänen, Phys. Lett. B **535**, 109 (2002).
- [127] C. Alt *et al.* [NA49 Collaboration], Phys. Rev. C **68**, 034903 (2003).
- [128] J.P. Wurm, J. Bielcikova [CERES/NA45 Collaboration], [arXiv:nucl-ex/0407019](#).
- [129] R. Rapp, Phys. Rev. C **66**, 017901 (2002).
- [130] D. Teaney, [arXiv:nucl-th/0204023](#).
- [131] R. Rapp, H. van Hees and T. Strong, Braz. J. Phys. **37**, 779 (2007).
- [132] F. Cooper and G. Frye, Phys. Rev. D **10**, 186 (1974).
- [133] J. Knoll (2008), [arXiv:0803.2343\[nucl-th\]](#).
- [134] W. Cassing and E. L. Bratkovskaya (2008), [arXiv:0808.0022\[hep-ph\]](#).
- [135] D. d'Enterria, Eur. Phys. J. C **43**, 295 (2005).
- [136] F. Halzen and D. M. Scott, Phys. Rev. D **18**, 3378 (1978).

- [137] R. Arnaldi *et al.* [NA60 Collaboration], [arXiv:0810.3204\[nucl-ex\]](#).
- [138] R. Arnaldi *et al.* [NA60 Collaboration], [arXiv:0812.3053\[nucl-ex\]](#).
- [139] T. Sjostrand, P. Eden, C. Friberg, L. Lonnblad, G. Miu, S. Mrenna and E. Norrbin, *Comput. Phys. Commun.* **135**, 238 (2001).
- [140] R. Rapp and E. V. Shuryak, *Phys. Lett. B* **473**, 13 (2000).
- [141] S. Damjanovic *et al.* (NA60 Collaboration), *Nucl. Phys. A* **783**, 327 (2007).
- [142] R. Arnaldi *et al.* (NA60 Collaboration), *Phys. Rev. Lett.* **100**, 022302 (2008).
- [143] T. Renk, R. A. Schneider and W. Weise, *Phys. Rev. C* **66**, 014902 (2002).
- [144] P. Lichard and J. Juran, *Phys. Rev. D* **76**, 094030 (2007).
- [145] S. Damjanovic *et al.* [NA60 Collaboration], *J. Phys. G* **35**, 104036 (2008).
- [146] M. M. Aggarwal *et al.* (WA98 Collaboration), *Phys. Rev. Lett.* **85**, 3595 (2000).
- [147] M.M. Aggarwal *et al.* (WA98 Collaboration), *Phys. Rev. Lett.* **93**, 022301 (2004).
- [148] D.K. Srivastava and B. Sinha, *Phys. Rev. C* **64**, 034902 (2001).
- [149] J. Alam, B. Mohanty, P. Roy, S. Sarkar, and B. Sinha, *Phys. Rev. C* **67**, 054902 (2003).
- [150] K. Gallmeister, B. Kampfer and O. P. Pavlenko, *Phys. Lett. B* **473**, 20 (2000).
- [151] I. Kvasnikova, C. Gale and D. K. Srivastava, *Phys. Rev. C* **65**, 064903 (2002).
- [152] M. C. Abreu *et al.* (NA38 Collaboration), *Eur. Phys. J. C* **14**, 443 (2000).
- [153] F. de Jong and U. Mosel, *Phys. Lett. B* **392**, 273 (1997).
- [154] E.L. Bratkovskaya and W. Cassing, *Nucl. Phys. A* **807**, 214 (2008).
- [155] D. Schumacher, S. Vogel and M. Bleicher, *Acta Phys. Hung. A* **27**, 451 (2006).
- [156] K. Shekhter, C. Fuchs, A. Faessler, M. Krivoruchenko and B. Martemyanov, *Phys. Rev. C* **68**, 014904 (2003).
- [157] E. Santini *et al.*, *Phys. Rev. C* **78**, 034910 (2008).
- [158] Y. Kluger, V. Koch, J. Randrup and X.N. Wang, *Phys. Rev. C* **57**, 280 (1998).
- [159] C. A. Dominguez and M. Loewe, *Z. Phys. C* **49**, 423 (1991).
- [160] F. Karsch, K. Redlich and A. Tawfik, *Phys. Lett. B* **571**, 67 (2003).
- [161] S. Ejiri, F. Karsch and K. Redlich, *Phys. Lett. B* **633**, 275 (2006).
- [162] R. Rapp, *Eur. Phys. J. A* **18**, 459 (2003).
- [163] M. Harada and C. Sasaki, *Phys. Rev. D* **73**, 036001 (2006).
- [164] S. Strüber and D. H. Rischke, *Phys. Rev. D* **77**, 085004 (2008).
- [165] M. Harada, C. Sasaki and W. Weise, [arXiv:0807.1417\[hep-ph\]](#).

Thermal Photons and Collective Flow at the Relativistic Heavy-Ion Collider

Hendrik van Hees

*Institut für Theoretische Physik, Goethe-Universität Frankfurt, Germany,
Frankfurt Institute for Advanced Studies (FIAS),
Ruth-Moufang-Str. 1, D-60438 Frankfurt, Germany*

Charles Gale

Department of Physics, McGill University, 3600 University Street, Montreal, Canada H3A 2T8

Ralf Rapp

*Cyclotron Institute and Department of Physics & Astronomy,
Texas A&M University, College Station, Texas 77843-3366, USA*

(Dated: August 11, 2011)

We update our calculations of thermal-photon production in nuclear collisions at the Relativistic Heavy-Ion Collider (RHIC). Specifically, we address the recent experimental observation of an elliptic flow of direct photons comparable in magnitude to that of pions, which is at variance with expectations based on quark-gluon plasma (QGP) dominated photon radiation. Our thermal emission rate is based on previous work, i.e., resummed leading-order QGP emission and in-medium hadronic rates in the confined phase. These rates are nearly degenerate at temperatures close to the expected QCD-phase change. The rates are convoluted over an improved elliptic-fireball expansion with transverse- and elliptic-flow fields quantitatively constrained by empirical light- and strange-hadron spectra. The resulting direct-photon spectra in central Au-Au collisions are characterized by hadron-dominated emission up to transverse momenta of ~ 2 -3 GeV. The associated large elliptic flow in the hadronic phase mitigates the discrepancy with the measured photon- v_2 compared to scenarios with QGP-dominated emission.

I. INTRODUCTION

Dileptons and photons are the only particles which escape the interior of the fireball created in ultrarelativistic heavy-ion collisions (URHICs) unaffected. Their production, on the other hand, is rooted in the strongly interacting medium and thus illuminates the latter's properties, see Refs. [1–3] for reviews. Recent highlights of electromagnetic observables in URHICs include “measurements” of the in-medium vector-spectral function via dilepton *invariant*-mass spectra at the SPS [4–6] and of the medium temperature via direct photons at RHIC [7].

It is well known that the thermal component in the observed electromagnetic spectra results from a convolution of the temperature- and density-dependent emission rate over the entire space-time history of the expanding fireball in URHICs. From the interplay of decreasing temperature and increasing three-volume in the course of the fireball expansion, it can be fairly well established that photon and dilepton emission in the low-energy regime, $q_0 \lesssim 1 \text{ GeV}^1$, are dominated by the hadronic phase. At energies beyond $\sim 1 \text{ GeV}$, the situation is less clear, since the competition between hadronic and QGP sources will be sensitive to additional ingredients [10], *e.g.*, the relative strength of hadronic and QGP emission rates,

the phase-transition temperature (which formally demarcates the space-time dependence of the two sources) and the transverse flow (inducing a blue shift to higher q_t which is more pronounced in the later hadronic phase)².

In this context, recent measurements of the elliptic flow of direct photons (i.e., after the subtraction of long-lived hadron decays, mostly $\pi^0, \eta \rightarrow \gamma\gamma$) in semicentral Au-Au collisions [11] have revealed remarkable results. It has been found that the pertinent flow coefficient, $v_2^\gamma(q_t)$, is as large as that of charged pions up to momenta of $q_t \simeq 3 \text{ GeV}$ (albeit the photon data carry somewhat larger error bars). This result is difficult to reconcile with a dominant QGP emission source. Primordial photons from binary N - N collisions, whose emission is expected to be isotropic, will further reduce the total direct-photon v_2 . Current model calculations [12–14] using a hydrodynamically expanding medium with QGP and hadronic radiation, as well as primordial photons, underpredict the experimentally measured v_2 by a factor of ~ 5 (~ 3 when accounting for the maximal systematic error in the measurement). The question thus arises what could be missing in these calculations.

In the present paper we re-examine several aspects related to thermal photon emission from the hadronic medium. Since the v_2 in the hadronic phase of URHICs is large, an augmented hadronic component is a natural

¹ The energy variable, q_0 , encompasses both mass (M) and transverse-momentum (q_t) dependencies, *e.g.*, $q_0 = (M^2 + q_t^2)^{1/2}$ for $q_z = 0$.

² Note that the blue-shift distortion does not apply to dilepton *invariant*-mass spectra if a finite detector acceptance can be fully corrected for.

candidate to improve the description of thermal-photon emission at RHIC and thus reduce the discrepancy with the v_2 data. First, we note that typical hydrodynamical evolutions with first-order phase transitions tend to underestimate the radial (and possibly elliptic) flow built up in the fireball at the end of the QGP phase. This was borne out of a recent phenomenological analysis of light- and strange-hadron spectra using blast-wave parameterizations of the respective sources at thermal and chemical and freezeout (with $T_{\text{ch}} \simeq 100$ MeV and $T_{\text{fo}} \simeq 180$ MeV, respectively) [15]. In particular, the observed universality in kinetic-energy scaling of the v_2 of light and strange hadrons, together with an earlier decoupling of multi-strange hadrons (as inferred from their p_t spectra), suggests that most of the hadronic v_2 is indeed of partonic origin [16]. Second, for the thermal emission rates from hadronic matter we use our previous results of Ref. [9], which, in particular, include contributions from baryons which are known to be important from dilepton calculations [10], even at RHIC [17]. Finally, we take into account chemical off-equilibrium effects in the hadronic phase, i.e., effective chemical potentials for pions, kaons, etc., which can further augment the hadronic component in thermal-photon spectra (*e.g.*, typical processes like $\pi\rho \rightarrow \pi\gamma$ are enhanced by a pion fugacity to the third power).

Our paper is organized as follows. In Sec. II we briefly recall our input for the thermal-photon rates as taken from Ref. [9], as well as for the primordial contribution, which we check against pp data. In Sec. III we update our description of the thermal fireball evolution by constructing (a time evolution of) flow fields which is consistent with the empirical extraction at chemical and thermal freezeout. In Sec. IV we evolve the rates over the fireball evolution and discuss the resulting photon- q_t spectra, in particular the composition of the thermal yields. In Sec. V we present our results for the direct-photon v_2 in comparison to the recent PHENIX data [11] and in light of other model results. Finally, Sec. VI contains our conclusions.

II. PHOTON SOURCES

The photon spectrum resulting from a heavy-ion (or pp) reaction is usually referred to as inclusive photons. The subtraction of long-lived final-state decays leads to the notion of direct photons, which are the ones of interest in the present context. For direct photons, we further distinguish the radiation of thermal photons (Sec. II A), characterized by an equilibrium-emission rate to be integrated over the space-time evolution of the medium, and a non-thermal component emanating from primordial interactions prior to thermalization (Sec. II B).

A. Thermal Emission

In the present work we adopt the thermal emission rates of photons as developed and compiled in Ref. [9].

For QGP radiation we use the numerical parameterization of the complete leading-order in α_s rate as given in Ref. [18]. The main input for the QGP rate is the strong coupling “constant” for which we take an expression with temperature-dependent one-loop running at the scale $\sim 2\pi T$, $\alpha_s(T) = 6\pi/27 \ln(T[\text{GeV}]/0.022)$. This amounts to values of around 0.3 in the relevant temperature regime, $T = 1-2T_c$, which turns out to be consistent with recent estimates from the (perturbative) Coulomb term in in-medium heavy-quark free energies [22].

The basis of the thermal emission rate in hadronic matter forms the electromagnetic correlation function computed in Refs. [9, 23] using hadronic many-body theory with effective Lagrangians. It has been successfully used [1] in the interpretation of dilepton data at the SPS [4, 5] and has been carried to the photon point in Ref. [9]. It includes a rather extensive set of meson and baryon resonances in the interaction of the isovector current with a thermal heat bath of hadrons. It has been augmented by additional meson-exchange reactions in a meson gas which become important at photon momenta $q \gtrsim 1$ GeV, *e.g.*, π , ω , and a_1 exchange in $\pi + \rho \rightarrow \pi + \gamma$ as well as strangeness-bearing reactions (*e.g.*, $\pi + K^* \rightarrow K + \gamma$) [9]. An important element in constraining the hadronic vertices to empirical information, such as hadronic and radiative decay branchings, is the (gauge-invariant) introduction of vertex form factors. The latter lead to a substantial reduction of the hadronic emission rate with increasing photon momentum, which is essential for quantitative descriptions of hadronic emission rates at the momenta of experimental interest ($q_t \lesssim 3.5$ GeV for thermal radiation). Without vertex form factors, hadronic photon rates should not be considered reliable for momenta $q \geq 1$ GeV. We do not include here additional $\pi\pi$ Bremsstrahlung contributions ($\pi\pi \rightarrow \pi\pi\gamma$) as evaluated in Refs. [24, 25]. This source is important at low momenta, $q_t \lesssim 0.5$ GeV, but plays no role in the region of interest of the present investigation ($q_t \geq 1$ GeV).

The resulting total hadronic and QGP emission rates were found to be remarkably close to each other for temperatures around the putative transition temperature, $T_c \simeq 180$ MeV. This is appealing from a conceptual point of view in terms of a possibly continuous matching of the bottom-up and top-down extrapolated hadronic and QGP rates, respectively. It is also welcome from a practical point of view, since it much reduces the uncertainties associated with identifying the medium in the fireball as hadronic or partonic, which, in the case of a cross-over, may not even be well defined. If QGP and hadronic rates are significantly different across T_c , appreciable uncertainties in the calculated photon spectra have been found as a result of this ambiguity [14].

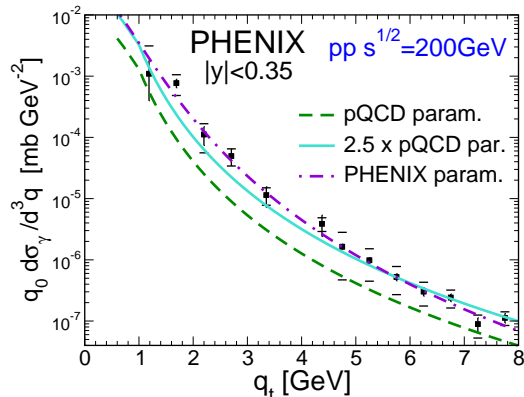


FIG. 1: (Color online) Empirical fits to the direct-photon spectrum measured by PHENIX [28] in p - p collisions at $\sqrt{s} = 200$ GeV; dash-dotted line: power-law fit [28], solid and dashed line: x_t -scaling ansatz [29] with and without K factor, respectively.

B. Non-Thermal Sources

After subtraction of final-state decays, the main source other than “thermal” radiation from the interacting medium is associated with “primordial” photons produced upon first impact of the nuclei via binary NN collisions. Primordial photon spectra are usually estimated from the direct contribution in pp collisions, where no significant reinteractions are expected. This is supported by the generally good agreement of the measured photon spectra with next-to-leading order (NLO) perturbative QCD (pQCD) calculations [26] for primordial production. In the following we will adopt a simple power-law fit performed by the PHENIX collaboration [7, 27] to their pp data [7, 28], cf. Fig. 1. Figure 4 in Ref. [7] reveals that the NLO pQCD calculations are slightly below the PHENIX parameterization in the relevant q_t range of ~ 1 -7 GeV. Therefore, we will alternatively estimate the primordial contribution via a x_t -scaling motivated parameterization [29], upscaled by a K -factor of 2.5 to best match the PHENIX pp data for $q_t = 5$ -8 GeV. This fit produces a slightly smaller yield of photons with momenta $q_t = 1$ -5 GeV compared to the PHENIX fit and is thus very similar to the NLO pQCD calculations.

In principle, photons can also be radiated off fast-moving partons (jets) interacting with the medium. The combined elliptic flow of this source is expected to be close to zero [19]. We therefore subsume this source in our primordial contribution (whose fragmentation part, *e.g.*, is expected to be reduced in the medium), which is a posteriori justified by an adequate description of the spectral yields in Au-Au collisions once thermal radiation is implemented.

III. FIREBALL AND TRANSVERSE-FLOW FIELD

The continuous emission of photons throughout the evolution of a heavy-ion reaction causes their elliptic-flow signal to be more sensitive to its time evolution than that of hadronic final states. Therefore, a calculation of the photon- v_2 requires special care in constructing a realistic time evolution of both radial and elliptic flow (the former affects the spectral weight of photon emission at a given time snapshot). In principle, hydrodynamic models are believed to be able to accomplish such a task; however, current uncertainties including initial conditions (*e.g.*, fluctuations and initial flow fields), viscosity corrections and the coupling to hadronic cascades in the dilute stages render this a challenging task, which has not been completed (yet). In the present paper we take a more pragmatic (and simple) approach which nevertheless accurately captures two experimentally established snapshots of the fireball evolution, namely the flow fields at chemical freezeout at $T_{\text{ch}} \simeq 170$ MeV and kinetic freezeout at $T_{\text{fo}} \simeq 100$ MeV. The latter is well determined by the transverse-momentum (p_t) spectra and elliptic flow of light hadrons (π , K , p) [30–32], while the former can be extracted from spectra and flow of multi-strange hadrons [16, 31, 33]. A detailed fit of these snapshots using an elliptic blast-wave source has been performed in Ref. [15], which was also shown to be compatible with the empirical constituent-quark number and transverse kinetic-energy (KE_T) scaling of the elliptic flow of light and strange hadrons. We use these results to improve a previously constructed expanding elliptic fireball [34] so that its evolution passes through these benchmarks at the end of the mixed phase and at thermal freezeout. Representative examples of the resulting multi-strange (ϕ mesons) and light-hadron (π , p) spectra and v_2 at chemical and thermal freezeout, respectively, are illustrated in Fig. 2.

Concerning initial conditions, we assume an initial longitudinal fireball size of $z_0 = 0.6$ fm corresponding to $c\tau_0 \simeq z_0/\Delta y \simeq 0.33$ fm ($\Delta y \simeq 1.8$) as our default value for both 0-20% and 20-40% centrality classes. With total entropies of $S = 7900$ and 3600 (assumed to be conserved), this translates into (average) initial temperatures of $T_0 \simeq 355$ MeV and 325 MeV, and charged-hadron multiplicities of $dN_{\text{ch}}/dy \simeq 610$ and 280, respectively, adjusted to recent STAR data [32].

The time evolution of the inclusive elliptic flow is shown in Fig. 3. The observed KE_T scaling of light and multi-strange hadrons is the main constraint which requires a rather rapid increase of the bulk v_2 , and a subsequent leveling off shortly after chemical freezeout. The final values of $\sim 2.5\%$ and $\sim 5\%$ for the pion- v_2 are adjusted to experimental data [31].

Another important aspect in our medium evolution is the implementation of chemical freezeout, *i.e.*, the use of effective meson (and baryon) chemical potentials to preserve the observed hadron ratios in the fireball expan-

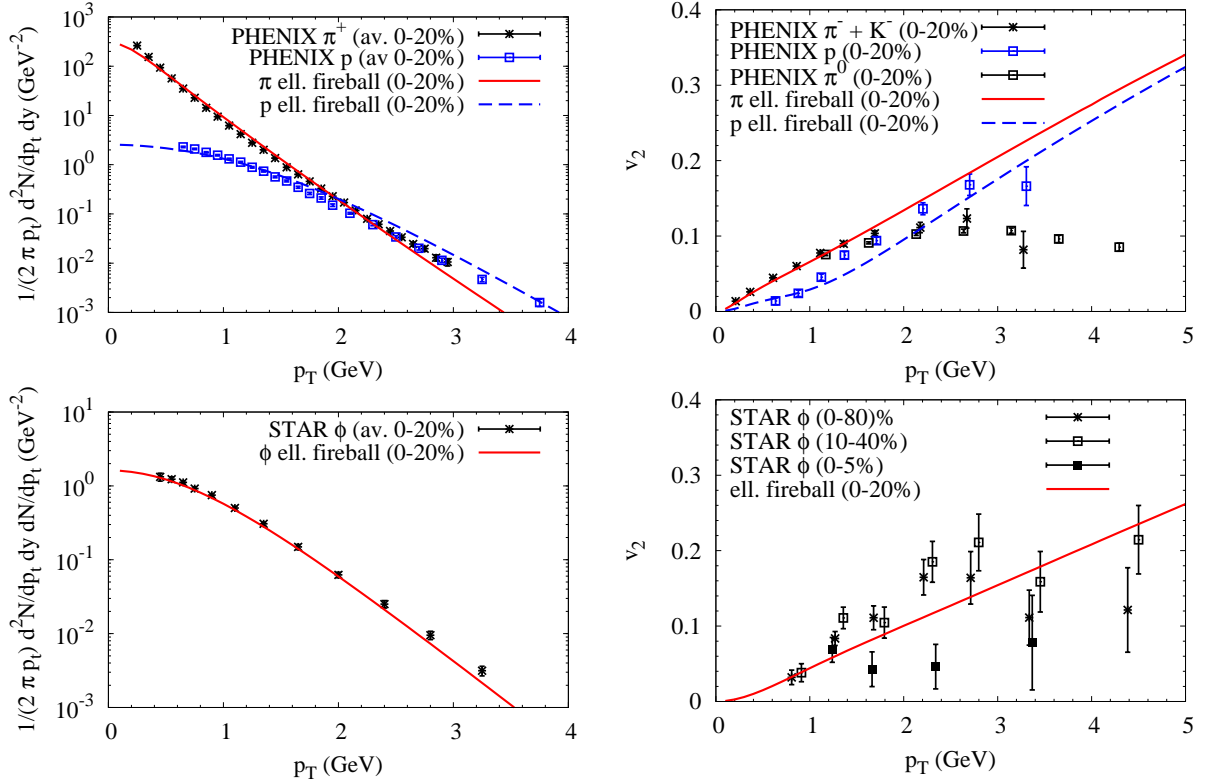


FIG. 2: (Color online) Snapshots of p_t spectra and v_2 for pions and protons (upper panels), as well as ϕ mesons (lower panels), following from our fireball evolution in 0-20% Au-Au($\sqrt{s} = 200$ AGeV) collisions at thermal and chemical freezeout, respectively. The π and p curves are for direct emission only (no resonance feeddown) with absolute normalization while the ϕ yield is (re-) normalized to the data. Data are from Refs. [16, 43, 44].

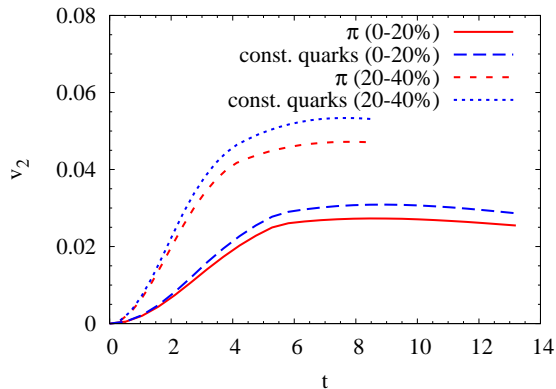


FIG. 3: (Color online) Time evolution of the inclusive elliptic flow for 0-20% and 20-40% Au-Au($\sqrt{s}=200$ AGeV) collisions within our fireball model, evaluated with either constituent-quark or pion content of the medium.

sion at temperatures between T_{ch} and T_{fo} . We do this as described in Ref. [35], which was adopted in our previous work [9]. Most of the hydrodynamic evolutions used for photon calculations at RHIC to date assume chemical equilibrium throughout the hadronic phase. This assumption likely leads to an appreciable underestimate of the thermal hadronic component in the observed photon spectra, and thus of its contribution to the direct-photon elliptic flow. For example, typical meson annihilation processes such as $\pi + \rho \rightarrow \pi + \gamma$ (proceeding through t - and s -channel π , ω and a_1 exchanges), are augmented by an initial pion fugacity, $z_\pi^3 = \exp(3\mu_\pi/T)$ (in Boltzmann approximation), where $\mu_\pi \simeq 100$ MeV in the vicinity of thermal freezeout, $T_{fo} \simeq 100$ MeV. This implies a significantly larger enhancement in photon production in the later hadronic stages relative to the conservation of the hadron ratios for which the chemical potentials are introduced. In other words, the faster cooling of the fireball in chemical off-equilibrium relative to the equilibrium evolution is overcompensated in the leading photon-production channels due to a “high” power of pion densities.

IV. DIRECT-PHOTON SPECTRA

We start the comparison of our theoretical calculations of direct photons to data at RHIC with the absolute yields in the transverse-momentum (q_t spectra). Let us first illustrate the quantitative effect of updating the radial expansion starting from our original predictions in Ref. [9].³ In the latter, a transverse acceleration of the fireball surface of $a_T = 0.053c^2/\text{fm}$ had been assumed, which, together with a fireball lifetime of $15 \text{ fm}/c$, leads to a surface velocity of $\beta_s \simeq 0.62$ and a freezeout temperature of $T_{fo} = 108 \text{ MeV}$ for Au-Au collisions in the 0-20% centrality bin ($N_{\text{part}} = 280$ and $N_{\text{coll}} = 765$). The pertinent photon spectra, displayed in the upper panel of Fig. 4, closely resemble the results of Fig. 12 in Ref. [9].⁴ A window of QGP-radiation dominance is present for $q_t \simeq 1.5\text{-}3 \text{ GeV}$.

The situation changes somewhat with an update performed in 2007 triggered by the analysis of NA60 dileptons at the SPS, specifically in the context of their q_t -spectra. The fireball acceleration was increased to $a_T = 0.08\text{-}0.1c^2/\text{fm}$ to better reproduce hadron spectra, which also allowed for a significantly improved description of the slope parameters in the dilepton q_t spectra [10]. It was also checked that the agreement with the WA98 direct-photon spectra at SPS [36], as found in Ref. [9], was not distorted (see, *e.g.*, Fig. 23 in Ref. [1]). At RHIC, the pertinent fireball of lifetime $\tau \simeq 15 \text{ fm}/c$ results in a freezeout temperature of $T_{fo} = 98 \text{ MeV}$ with a surface transverse flow of $\beta_s = 0.77$. The consequences for the direct-photon spectra, using the same thermal emission rates and fireball chemistry as before, are illustrated in the middle panel of Fig. 4: while the spectral distribution of the QGP radiation is barely affected, the hadronic radiation spectrum becomes noticeably harder, thus shifting the crossing with the QGP part up to $q_t \simeq 1.8 \text{ GeV}$. In combination with an improved estimate of the primordial emission, adjusted to then available PHENIX pp data, the QGP window shrinks appreciably, with a maximum fraction of ca. 42% of the total at $q_t \simeq 2.1 \text{ GeV}$.

Finally, recent systematic analyses of light-hadron

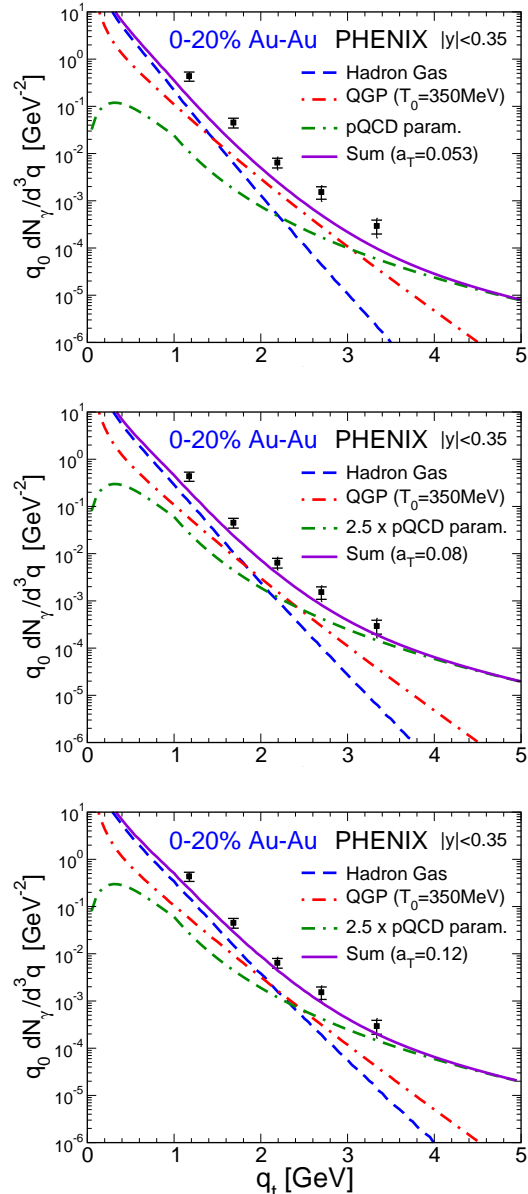


FIG. 4: (Color online) The impact of an increasingly strong radial flow in an expanding fireball model on direct-photon spectra in 0-20% central Au-Au collisions at RHIC. The transverse fireball acceleration increases from $0.053/\text{fm}$ (upper panel, corresponding to Ref. [9]) via 0.08 (middle panel; see Refs. [1, 10]) to $0.12/\text{fm}$ (lower panel). The same QGP and hadronic emission rates have been used in all cases, while the primordial contribution has been upscaled in the middle and lower panel. As a benchmark, we also show the pertinent PHENIX data [7].

spectra by the STAR collaboration [32] requires an even

³ For simplicity we will use for this purpose a cylindrically symmetric fireball (no v_2) and apply an average boost of 70% of the fireball surface flow to the photon spectra in the rest frame, $\langle\beta\rangle = 0.7\beta_s$.

⁴ We note that in Figs. 12 and 13 of Ref. [9] the contribution labeled “Hadron Gas” only includes the in-medium ρ spectral function part, not the meson-gas contributions also calculated in there. Unfortunately, we recently realized that the spectral function part in the photon spectra at RHIC and LHC (Figs. 12 and 13 in Ref. [9]) was computed with the spin-averaged ρ propagator, $D_\rho = (2D_\rho^T + D_\rho^L)/3$, which, at the photon point (where the transverse part, D_ρ^T , should be used), is by a factor of $2/3$ too small. It was done correctly in the rate plots and for the SPS calculations shown in Ref. [9]. In the present work we refer to the “Hadron Gas” emission as the sum of spectral-function and meson-gas contributions.

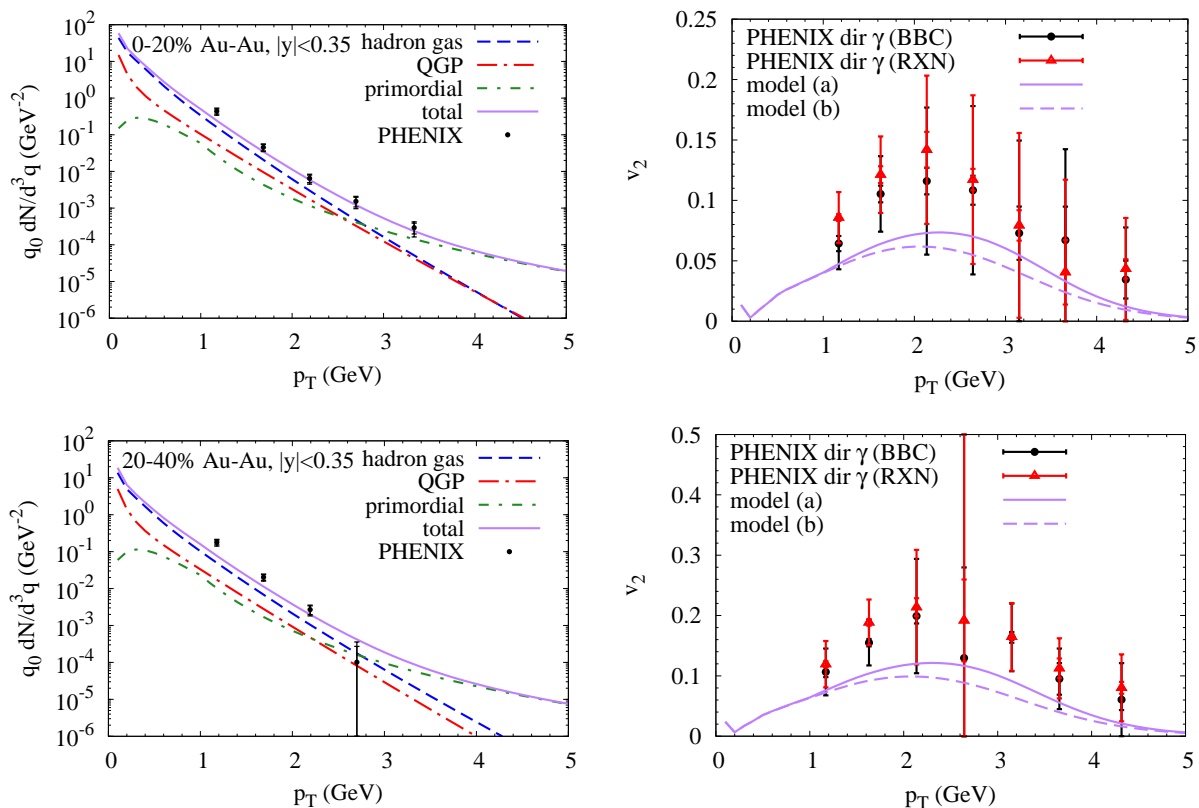


FIG. 5: (Color online) Comparison of our calculated direct-photon spectra (left panels) and their elliptic-flow coefficient (right panels) from an elliptically expanding fireball model with QGP and hadronic radiation, supplemented with primordial emission, to PHENIX data [7, 11] in 0-20% (upper panels) and 20-40% (lower panels) central Au-Au($\sqrt{s} = 200$ AGeV) collisions. Models (a) and (b) in the right panels refer to the use of the pQCD parameterization and the PHENIX fit for primordial production, respectively (in the left panels, only model (a) is displayed).

harder expansion, to reach a thermal freezeout configuration at $T_{fo} \simeq 90$ -95 MeV and $\langle\beta\rangle \simeq 0.59$ for central Au-Au collisions. This can be achieved in the fireball model by a further increase of the acceleration to $a_T = 0.12$ c^2 /fm at a slightly reduced lifetime of $\tau \simeq 14$ fm/ c . As expected, for the direct-photon spectra this implies a further hardening of the hadronic emission and thus an additional squeezing of the QGP window to a small region around $q_t \simeq 2.4$ GeV, cf. lower panel of Fig. 4. The increasing transverse flow of the three fireballs also seems to improve the description of the PHENIX direct-photon spectra, although that was not the objective of this exercise.

The final (third) fireball setup has been refined by implementing realistic ellipticities and an explicit linearly increasing flow profile in the transverse boost of the photon emission rate. The corresponding comparisons to hadronic data have been discussed in the previous section. The resulting direct-photon q_t spectra from thermal

QGP and hadronic sources, supplemented with an N_{coll} -scaled primordial contribution, are compared to PHENIX data in the 0-20% and 20-40% centrality classes of Au-Au($\sqrt{s} = 200$ AGeV) in the two left panels of Fig. 5. The more central data set is fairly well reproduced, even though there appears to be a slight underestimation of the datum at the lowest $q_t \simeq 1.2$ GeV. The inclusion of the full transverse-flow profile leads to a further hardening of the hadronic component relative to the lower panel in Fig. 4, while the QGP component is essentially unaffected, even at the highest q_t (continuing the constant trend of the three panels in Fig. 4). This means that the high- q_t QGP radiation is entirely determined by the earliest radiation, where no flow has built up yet; the subsequent QGP flow cannot overcome the softening due to the decreasing temperature. This further implies a significant dependence of the high- q_t QGP yield on the thermalization time (a quantitative example will be discussed at the end of Sec. V). On the other hand, hadronic

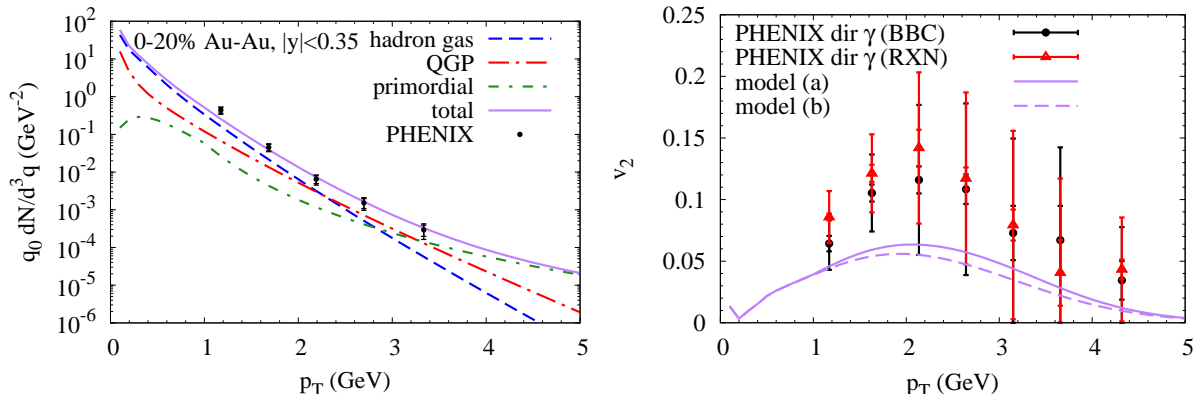


FIG. 6: (Color online) Same as Fig. 5 for 0-20% Au-Au collisions, but with a QGP contribution evaluated for a reduced thermalization time of $\tau_0 \simeq 0.17$ fm/c translating into an average initial temperature of $T_0 \simeq 445$ MeV.

emission only sets in at T_c when there is already substantial flow in the system, and thus even at high momenta the hadronic spectra are sensitive to the fireball flow field.

In the 20-40% centrality bin, the discrepancy between the theoretical yields and the data becomes somewhat more severe, hinting at a missing relatively soft source (and therefore suggestive for the later hadronic phase). One speculation at this point could be related to $\omega \rightarrow \pi^0\gamma$ decays. These have been subtracted by the PHENIX collaboration employing m_t scaling of the ω spectra with π^0 's [27], assuming $\omega/\pi^0 = 1$, as found in pp measurements [37], as well as in 0-92% Au-Au collisions for $p_t > 4$ GeV. If, however, ω mesons at lower p_t become part of the chemically equilibrated medium in heavy-ion collisions, one expects their multiplicity at given m_t to be up to 3 times larger, due their spin degeneracy. In this case there might be a direct-photon component in the Au-Au data at low $q_t \leq 2$ GeV due to some fraction of final-state $\omega \rightarrow \pi^0\gamma$ decays which have not been subtracted (and which would carry large v_2). This possibility may be worth further experimental and theoretical study.

It is quite remarkable that the hadronic yield dominates over the QGP one over the entire plotted range. This will have obvious ramifications for the v_2 of the direct photons, which is larger in the hadronic phase. The sub-leading role of the (early) QGP component further implies that the effects of initial-state fluctuations on thermal-photon production [20, 21] are diminished.

To examine the dependence of the QGP yield on the thermalization time, we have conducted calculations with a factor-2 reduced initial longitudinal size, $z_0 = 0.3$ fm, corresponding to $\tau_0 \simeq 0.17$ fm/c as used, *e.g.*, in Ref. [14], cf. Fig. 6. The QGP spectra in 0-20% Au-Au collisions increase over the $z_0 = 0.6$ fm calculation by a factor of 1.6, 2.7 and 4.8 at $q_t = 2, 3$ and 4 GeV, respectively, and turn out to be in fair agreement (within ca. 30%) with the hydrodynamic calculations reported in Ref. [14] (us-

ing smooth initial conditions). The significance of this increase mostly pertains to momenta, $q_t > 2$ GeV, where a small “QGP window” reopens, but it does not significantly affect the description of the experimental yields.

To further characterize the nature of the direct-photon excess (i.e., beyond the pp -scaled primordial emission), we evaluate the effective slope parameters, T_{eff} , of our thermal spectra. We recall that PHENIX extracted the effective slope of the excess radiation in their data as $T_{\text{eff}} = 221 \pm 19^{\text{stat}} \pm 19^{\text{syst}}$ MeV [7]. In Fig. 7 we compare this range with the temperature evolution, $T(\tau)$, of our fireball; they only overlap inside the QGP phase. However, when accounting for the flow-induced blue shift, as estimated by the schematic expression for a massless particle,

$$T_{\text{eff}} \simeq T \sqrt{\frac{1 + \langle \beta \rangle}{1 - \langle \beta \rangle}}, \quad (1)$$

the overlap with the experimental window is shifted to significantly later in the evolution, mostly for a flowing hadronic source with a restframe temperature of $T \simeq 100$ -150 MeV. This suggests a reinterpretation of the experimental slope as mainly hadronic in origin, which, as we will see in Sec. V below, is further supported by the v_2 data. An explicit fit of the slope to our total thermal spectrum from the elliptic fireball (with $T_0 = 355$ MeV) in the range $q_t \simeq 1 - 3$ GeV yields $T_{\text{eff}} \simeq 240$ -250 MeV, which is at the upper end of the data (consistent with the slight underestimate of the lowest- q_t datum; also note that the use of the average, $\langle \beta \rangle = 0.7\beta_s$ in Eq. (1), tends to underestimate the actual slopes, especially at high q_t and β_s ; we noted that already when going from the spectra in the lower panel of Fig. 4 to the full results in the upper left panel of Fig. 5). Higher initial temperatures are less favorable, since they result in a further increase of the slope, *e.g.*, by 10-15 MeV for $T_0 = 445$ MeV.

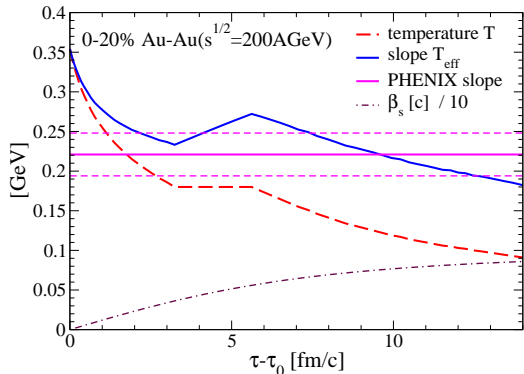


FIG. 7: (Color online) Time dependence of the effective slope parameter of thermal-photon radiation emitted from our fireball for 0-20% Au-Au collisions ($s^{1/2} = 200$ GeV) for QGP and hadronic sources for $\tau - \tau_0 \lesssim 3$ fm/c and $\gtrsim 6$ fm/c, respectively), using Eq. (1) with $\langle\beta\rangle = 0.7\beta_s$. For comparison, we plot the effective slope extracted by PHENIX from their data (horizontal line with dashed lines indicating the experimental error) [7], and the “true” temperature in the thermal restframe (long-dashed line). Also shown is the surface flow velocity of the fireball (dash-dotted line).

V. DIRECT-PHOTON ELLIPTIC FLOW

With a fair description of the photon q_t spectra at hand, we proceed to the calculation of the direct-photon elliptic flow as a function of transverse momentum, $v_2(q_t)$. The results for the 0-20% and 20-40% centrality classes of Au-Au collisions at RHIC are again compared to PHENIX data, see upper- and lower-right panel of Fig. 5, respectively. The shape of our calculated $v_2(q_t)$ matches the measurements rather well, but our maximum value of ca. 7.5% (12%) is below the central values of the 0-20% (20-40%) data. Our results are a factor of 3-4 larger than existing calculations using hydrodynamic expansions, and reach into the lower end of the (mostly systematic) experimental uncertainties. The main differences compared to the hydro calculations are the following: our equilibrium hadronic rates [9] are significantly larger than in previous studies, our hadronic phase includes meson-chemical potentials and lasts longer (both due to a smaller T_{fo} as dictated by data and a slightly larger T_{ch} as used in our previous calculations [9, 17, 35]), and our bulk elliptic flow is built up faster than in standard (ideal) hydro calculations (recall that only a small increase of the v_2 during the hadronic phase facilitates its KE_T -scaling properties of multi-strange and light hadrons [15]; also note that a more rapid expansion in the QGP and transition region has been identified as an important ingredient to solve the “HBT puzzle” [39]). The combined effect of these four points is a thermal source which is dominated by hadronic emission carrying most of the finally observed elliptic flow from its beginning on, i.e., for $T \leq T_c$. For the reduced thermalization

time of $\tau_0 = 0.17$ fm/c the maximal v_2 drops by ca. 15% to $v_2^{\max} \simeq 6.3\%$, cf. right panel in Fig. 6.

In the present work, we have assumed a critical temperature of $T_c \simeq 180$ MeV, which is in line with $N_f = 2 + 1$ flavor lattice calculations reported, *e.g.*, in Ref. [40]. However, very recent lattice data [41] (as well as earlier ones [42]) indicate that T_c could be as low as 155-160 MeV and therefore one should ask what impact this could have on our results. A pertinent study has been done in the context of dilepton production at SPS energies [10]. When varying the critical temperature by ± 15 MeV around the default value of $T_c = 175$ MeV, the QGP emission spectra in the intermediate-mass region ($M \gtrsim 1$ GeV) vary by up to $\pm 50\%$ (less at higher masses where the contribution from earlier phases increases). At the same time, the hadronic emission part varies by approximately the same amount in the opposite direction, so that the total yield roughly stays the same while the relative QGP and hadronic partition varies appreciably. We expect similar effects for the photon q_t spectra. If one still requires the multi-strange hadron spectra to freeze out at T_c , we expect that the v_2 in the hadronic phase does not significantly change with T_c . However, since for smaller T_c the hadronic contribution to the direct photon yields is reduced, so should be the total (weighted) v_2 . For example, if for the 0-20% centrality class the QGP-hadronic partition of $1/3-2/3$ at $q_t \simeq 2$ GeV changes to $1/2-1/2$, we estimate that $v_2(q_t)$ is lowered from 7% to 6%.

VI. CONCLUSIONS

We have updated and extended our calculations of thermal-photon spectra at RHIC by constructing an improved elliptic fireball expansion which is quantitatively constrained by bulk-hadron data. In particular, we have implemented the notion of sequential freezeout by reproducing an empirical extraction of radial and elliptic flow from multi-strange and light-hadron data at chemical and kinetic decoupling, respectively. The fireball evolution has been combined with existing photon emission rates in the hadronic and QGP phases to obtain thermal-photon spectra in Au-Au collisions at RHIC. Supplemented with a primordial component estimated from pp collisions, we have compared our calculations to spectra and v_2 of direct photons as recently measured by the PHENIX collaboration. Due to a large medium flow (as required by hadron data), relatively large hadronic photon rates (approximately degenerate with QGP rates around T_c), and effective chemical potentials to conserve the observed hadron ratios, we have found that the hadronic medium outshines the QGP for most of the momenta where thermal radiation is relevant. This, in turn, leads to a maximal elliptic flow coefficient of $v_2 \simeq 10\%$ in semicentral Au-Au, which is a factor of ~ 3 increased over previous estimates based on QGP-dominated emission. Consequently, the discrepancy with the PHENIX v_2 data is

reduced appreciably. Our results are corroborated by evaluating the effective slope parameters of the radiation from the thermal source, which have the largest overlap with the experimental value of $T_{\text{eff}} \simeq 220$ MeV in the (flowing) hadronic phase. Initial QGP temperatures of above $T_0 \simeq 400$ MeV are increasingly disfavored by both the slope and v_2 data. Further scrutiny is needed whether these results can be confirmed in dynamical space-time models, i.e., in hydrodynamical and transport simulations, and what the quantitative impact of the transition temperature is (using, *e.g.*, the (3+1)D viscous hydrodynamics of Ref. [45]). The prevalence of the hadronic emission in our calculations reiterates the necessity of a good understanding of the strongly coupled hadronic phase in heavy-ion collisions. With these considerations, a satisfactory explanation of the (surprisingly?) strong direct-photon v_2 signal at RHIC might be possible. The

extension of the v_2 studies to virtual photons (aka dileptons) would also be illuminating. First phenomenological studies of this observable have been initiated [46, 47] and are also planned within our framework.

Acknowledgments

We thank G. David and M. He for valuable discussions. The work of RR is supported by the US National Science Foundation under grant no. PHY-0969394 and by the A.-v.-Humboldt foundation. The work of HvH is supported by the Hessian LOEWE initiative through the Helmholtz International Center for FAIR. CG is funded by the Natural Sciences and Engineering Research Council of Canada.

-
- [1] R. Rapp, J. Wambach and H. van Hees, in *Relativistic Heavy-Ion Physics*, edited by R. Stock and Landolt Börnstein (Springer), New Series **I/23A**, 4-1 (2010); [arXiv:0901.3289 [hep-ph]].
- [2] C. Gale, in *Relativistic Heavy-Ion Physics*, edited by R. Stock and Landolt Börnstein (Springer), New Series **I/23A**, 6-3 (2010); arXiv:0904.2184 [hep-ph].
- [3] J. Alam, S. Sarkar, P. Roy, T. Hatsuda and B. Sinha, *Annals Phys.* **286**, 159 (2001).
- [4] R. Arnaldi *et al.* [NA60 Collaboration], *Phys. Rev. Lett.* **96**, 162302 (2006).
- [5] D. Adamova *et al.* [CERES/NA45 Collaboration], *Phys. Lett. B* **666**, 425 (2008).
- [6] R. Arnaldi *et al.* [NA60 Collaboration], *Eur. Phys. J. C* **61**, 711 (2009); H.J. Specht *et al.* [NA60 Collaboration], *AIP Conf. Proc.* **1322**, 1 (2010).
- [7] A. Adare *et al.* [PHENIX Collaboration], *Phys. Rev. Lett.* **104**, 132301 (2010).
- [8] S. Turbide, C. Gale, E. Frodermann and U. Heinz, *Phys. Rev. C* **77**, 024909 (2008).
- [9] S. Turbide, R. Rapp and C. Gale, *Phys. Rev. C* **69**, 014903 (2004).
- [10] H. van Hees and R. Rapp, *Nucl. Phys. A* **806**, 339 (2008).
- [11] A. Adare *et al.* [PHENIX Collaboration], arXiv:1105.4126 [nucl-ex].
- [12] R. Chatterjee, E.S. Frodermann, U.W. Heinz and D.K. Srivastava, *Phys. Rev. Lett.* **96**, 202302 (2006).
- [13] F.M. Liu, T. Hirano, K. Werner and Y. Zhu, *Phys. Rev. C* **80**, 034905 (2009).
- [14] H. Holopainen, S. Räsänen and K.J. Eskola, arXiv:1104.5371 [hep-ph].
- [15] M. He, R.J. Fries and R. Rapp, *Phys. Rev. C* **82**, 034907 (2010).
- [16] B.I. Abelev *et al.* [STAR Collaboration], *Phys. Rev. Lett.* **99**, 112301 (2007).
- [17] R. Rapp, *Phys. Rev. C* **63**, 054907 (2001).
- [18] P.B. Arnold, G.D. Moore and L.G. Yaffe, *JHEP* **0112**, 009 (2001).
- [19] S. Turbide, C. Gale and R. J. Fries, *Phys. Rev. Lett.* **96**, 032303 (2006).
- [20] M. Dion, C. Gale, S. Jeon, J. F. Paquet, B. Schenke and C. Young, arXiv:1107.0889 [hep-ph].
- [21] R. Chatterjee, H. Holopainen, T. Renk and K. J. Eskola, arXiv:1106.3884 [hep-ph].
- [22] F. Riek and R. Rapp, *Phys. Rev. C* **82**, 035201 (2010).
- [23] R. Rapp and J. Wambach, *Eur. Phys. J. A* **6**, 415 (1999).
- [24] D.K. Srivastava, *Phys. Rev. C* **71**, 034905 (2005).
- [25] W. Liu and R. Rapp, *Nucl. Phys. A* **796**, 101 (2007).
- [26] L.E. Gordon and W. Vogelsang, *Phys. Rev. D* **48**, 3136 (1993).
- [27] G. David, private communication.
- [28] S.S. Adler *et al.* [PHENIX Collaboration], *Phys. Rev. Lett.* **98**, 012002 (2007).
- [29] D.K. Srivastava, *Eur. Phys. J. C* **22**, 129 (2001).
- [30] A. Adare *et al.* [PHENIX Collaboration], *Phys. Rev. Lett.* **98**, 162301 (2007).
- [31] B.I. Abelev *et al.* [STAR Collaboration], *Phys. Rev. C* **77**, 054901 (2008).
- [32] B.I. Abelev *et al.* [STAR Collaboration], *Phys. Rev. C* **79**, 034909 (2009).
- [33] S. Afanasiev *et al.* [PHENIX Collaboration], *Phys. Rev. Lett.* **99**, 052301 (2007).
- [34] H. van Hees, V. Greco and R. Rapp, *Phys. Rev. C* **73**, 034913 (2006).
- [35] R. Rapp, *Phys. Rev. C* **66**, 017901 (2002).
- [36] M.M. Aggarwal *et al.* [WA98 Collaboration], *Phys. Rev. Lett.* **85**, 3595 (2000).
- [37] S.S. Adler *et al.* [PHENIX Collaboration], *Phys. Rev. C* **75**, 051902 (2007).
- [38] A. Adare *et al.*, arXiv:1105.3467 [nucl-ex].
- [39] S. Pratt, *Phys. Rev. Lett.* **102**, 232301 (2009).
- [40] M. Cheng *et al.*, *Phys. Rev. D* **81**, 054504 (2010).
- [41] A. Bazavov and P. Petreczky, arXiv:1107.5027 [hep-lat].
- [42] S. Borsanyi, Z. Fodor, C. Hoelbling, S.D. Katz, S. Krieg, C. Ratti and K. K. Szabo [Wuppertal-Budapest Collaboration], *JHEP* **1009**, 073 (2010).
- [43] S. S. Adler *et al.* [PHENIX Collaboration], *Phys. Rev. Lett.* **91**, 182301 (2003).
- [44] S. S. Adler *et al.* [PHENIX Collaboration], *Phys. Rev. C* **69**, 034909 (2004).

- [45] B. Schenke, S. Jeon and C. Gale, Phys. Rev. C **82**, 014903 (2010).
- [46] R. Chatterjee, D. K. Srivastava, U. W. Heinz and C. Gale, Phys. Rev. C **75**, 054909 (2007).
- [47] J. Deng, Q. Wang, N. Xu and P. Zhuang, arXiv:1009.3091 [nucl-th].

Dilepton production in proton-induced reactions at SIS energies with the GiBUU transport model

Janus Weil^{1a}, Hendrik van Hees², Ulrich Mosel¹

¹ Institut für Theoretische Physik, Universität Giessen, D-35392 Giessen, Germany

² Institut für Theoretische Physik, Goethe-Universität Frankfurt, D-60438 Frankfurt am Main, Germany

Received: date / Revised version: date

Abstract. We present dilepton spectra from p+p, d+p and p+Pb reactions at SIS energies, which were simulated with the GiBUU transport model in a resonance model approach. These spectra are compared to the data published by the HADES and DLS collaborations. It is shown that the ρ spectral function includes non-trivial effects already in elementary reactions, due to production via baryon resonances, which can yield large contributions to the dilepton spectrum. Dilepton spectra from nuclear reactions in the energy range of the HADES experiment are thus found to be sensitive also to properties of nucleon resonances in the nuclear medium.

PACS. PACS-key describing text of that key – PACS-key describing text of that key

1 Introduction

While the vacuum properties of most hadrons are known to reasonable accuracy nowadays, it is a heavily debated question how these properties change inside nuclear matter. In particular, various theoretical predictions regarding the in-medium properties of the light vector mesons have been suggested. For recent reviews on in-medium effects, see [1,2,3].

Among these expected in-medium effects, a so-called “collisional broadening” of the meson spectral function, due to collisions with the hadronic medium, is expected. A second class of predictions claims that the vector-meson masses are shifted in the medium due to the partial restoration of chiral symmetry [4]. QCD sum rules can constrain these effects, but do not provide definitive predictions [5].

The more prominent hadronic decay modes of the vector mesons are unfavorable for studying in-medium effects, since they are affected by strong final-state interactions with the hadronic medium – in contrast to the rare dilepton decay modes. As the leptons only interact electromagnetically, they are ideally suited to carry the in-medium information outside to the detector, nearly undisturbed by the hadronic medium.

Dilepton spectra from nuclear reactions with elementary projectiles have been studied for example with the CLAS detector at JLAB, where photons with energies of a few GeV interact with nuclei [6], or by the E325 experiment at KEK, where 12 GeV protons were used as projectiles [7]. On the side of the hadronic decays, most notably $\omega \rightarrow$

$\pi^0\gamma$ is being investigated by the CBELSA/TAPS group in photon-induced reactions [8,9].

Early measurements of dilepton spectra from heavy-ion collisions in the low-energy regime were conducted by the DLS collaboration [10], showing an excess over the expected yield. A similar excess was also observed in experiments at higher energies [11,12], where it could be attributed to an in-medium broadening of spectral functions [13,14,15]. For the DLS data such in-medium effects never provided a convincing explanation – a problem that was soon known as the “DLS puzzle” [16,17,18,19].

More recently, the HADES collaboration at GSI has set up an ambitious program for measuring dilepton spectra from p+p, p+A and A+A reactions [20,21,22,23,24,25], in order to systematically check the old DLS data with improved statistics and to finally resolve the DLS puzzle. Up to now this endeavor has fully confirmed the validity of the DLS data and shifted the puzzle into the theory sector. It is clear that a detailed understanding of the elementary reactions is the most important prerequisite for explaining the heavy-ion data.

In this paper, we apply the Gießen Boltzmann-Uehling-Uhlenbeck transport model (GiBUU) [26] to the elementary reactions (nucleon-nucleon and proton-nucleus) studied by the HADES collaboration. We use GiBUU to generate dilepton events and pass them through the HADES acceptance filter, in order to compare our calculations directly to the experimental data measured by HADES.

^a Email: janus.weil@theo.physik.uni-giessen.de

2 The GiBUU transport model

Our tool for the numerical simulation of dilepton spectra is the GiBUU hadronic transport model, which provides a unified framework for various types of elementary reactions on nuclei as well as heavy-ion collisions [26,27]. This model takes care of the correct transport-theoretical description of the hadronic degrees of freedom in nuclear reactions, including the propagation, elastic and inelastic collisions and decays of particles.

In GiBUU the spectral one-particle phase-space distributions, $F(x, p)$, of all particles are obtained by solving the coupled Kadanoff-Baym equations [28] for each particle species in their gradient-expanded form [29]

$$\mathcal{D}F(x, p) - \text{tr} \{ \Gamma f \text{Re} S^{\text{ret}}(x, p) \}_{\text{pb}} = C(x, p), \quad (1)$$

with

$$\mathcal{D}F = \{ p_0 - H, F \}_{\text{pb}}. \quad (2)$$

Here $\{ \dots \}_{\text{pb}}$ denotes a Poisson bracket. In the so-called backflow term (second term on the left-hand side in (1)), that is essential for off-shell transport, $f(x, p)$ is the phase-space density related to F by

$$F(x, p) = 2\pi g f(x, p) \mathcal{A}(x, p), \quad (3)$$

where $\mathcal{A}(x, p)$ is the spectral function of the particle¹ and g is the spin-degeneracy factor. The quantity Γ in the backflow term is the width of the spectral function, and $S^{\text{ret}}(x, p)$ denotes the retarded Green's function. Off-shell transport is thus included and leads to the correct asymptotic spectral functions of particles when they leave the nucleus. The expression $C(x, p)$ on the right-hand side of (1) denotes the collision term that couples all particle species; it contains both a gain and a loss term. For a short derivation of this transport equation and further details we refer the reader to [26]. In order to solve the BUU equation numerically, we rely on the test-particle ansatz. Here the phase-space densities are approximated by a large number of test particles, each represented by a δ -distribution in coordinate and momentum space.

The collision term contains all sorts of scattering and decay processes: elastic and inelastic two-body collisions, decays of unstable resonances and even three-body collisions. The two-body part of the collision term is separated into two different regimes in terms of the available energy, \sqrt{s} : a resonance model description at low energies and the PYTHIA string model at high energies.

For baryon-baryon collisions, the transition between the two is usually performed at $\sqrt{s} = 2.6$ GeV. There is a small window around this border (± 0.2 GeV), where both models are merged linearly into each other in order to ensure a smooth transition. For meson-baryon collisions, the transition region lies at $\sqrt{s} = 2.2 \pm 0.2$ GeV.

Unfortunately, the transition region in this default GiBUU prescription lies right inside the range of energies used for

the HADES experiment. However, we think that it is important to describe all HADES spectra with one consistent model. In this paper we therefore explore the possibility of pushing the transition region up to higher energies and using an extended resonance model for all reactions measured by HADES.

In the high-energy regime the GiBUU collision term relies on the Monte Carlo event generator PYTHIA (v6.4) [30, 31], which is based on the Lund string model. Although PYTHIA clearly has its strengths at higher energies (tens to hundreds of GeV), it is used in GiBUU down to energies of a few GeV. This works surprisingly well, as has recently been demonstrated for example by GiBUU's successful description of pion data measured by the HARP collaboration [32].

Despite this good description of pion observables in the few-GeV energy regime, it turned out that the HADES dilepton data for p+p collisions at 3.5 GeV pose a somewhat greater challenge for PYTHIA [33]. Most prominently, the vector-meson production is strongly overestimated by the default PYTHIA parameters, and also the intrinsic p_T distribution needs to be adjusted slightly to reproduce the HADES p_T spectra.

Since a resonance description should in principle be applicable in the energy regime probed by the HADES experiment ($\sqrt{s} < 3.5$ GeV), we try in the following to set up such a description as an alternative to the string model approach.

3 The resonance-model approach

The low-energy part of the nucleon-nucleon collision term is given by a resonance model based on the Teis analysis [34], in which all collision cross sections are assumed to be dominated by the excitation of baryon resonances. The GiBUU model currently contains around 30 nucleon resonances, for a complete list see [26]. However, only the subset used in the Teis analysis is actually being populated in NN collisions, see table 1. The properties (masses, widths and branching ratios) of all the resonances are taken from the partial-wave analysis of Manley [35]. All of these states, except for the $P_{33}(1600)$, are not only found in the Manley analysis, but have been confirmed, e.g., by the more recent analysis of Arndt et al. [36] and received a four-star rating from the PDG [37]. We note already here that some of the branching ratios which are important for the present study, in particular those for decay into ρN and ωN are not very well known and still under experimental investigation [38,39].

We use all the resonance parameters and branching ratios exactly as given by Manley, with one exception: The $\rho\Delta$ decay channels are introduced by Manley only in order to account for missing inelasticities, which are not covered by one- and two-pion final states. In that sense, Manley has no real evidence for the $\rho\Delta$ final state in particular, but just uses this decay channel to account for the left-over strength. Therefore we take the freedom to replace the $\rho\Delta$ decays by $\sigma\Delta$, in order to avoid an overestimation of the ρ -meson production. The influence of Manley's $\rho\Delta$

¹ \mathcal{A} is normalized as $\int_0^\infty \mathcal{A}(x, p) dp_0 = 1$.

	rating	M_0 [MeV]	Γ_0 [MeV]	$ \mathcal{M}^2 /16\pi$ [mb GeV ²]		branching ratio in %						
				NR	ΔR	πN	ηN	$\pi\Delta$	ρN	σN	$\pi N^*(1440)$	$\sigma\Delta$
P ₁₁ (1440)	****	1462	391	70	—	69	—	22 _P	—	9	—	—
S ₁₁ (1535)	***	1534	151	8	60	51	43	—	2 _S + 1 _D	1	2	—
S ₁₁ (1650)	****	1659	173	4	12	89	3	2 _D	3 _D	2	1	—
D ₁₃ (1520)	****	1524	124	4	12	59	—	5 _S + 15 _D	21 _S	—	—	—
D ₁₅ (1675)	****	1676	159	17	—	47	—	53 _D	—	—	—	—
P ₁₃ (1720)	*	1717	383	4	12	13	—	—	87 _P	—	—	—
F ₁₅ (1680)	****	1684	139	4	12	70	—	10 _P + 1 _F	5 _P + 2 _F	12	—	—
P ₃₃ (1232)	****	1232	118	OBE	210	100	—	—	—	—	—	—
S ₃₁ (1620)	**	1672	154	7	21	9	—	62 _D	25 _S + 4 _D	—	—	—
D ₃₃ (1700)	*	1762	599	7	21	14	—	74 _S + 4 _D	8 _S	—	—	—
P ₃₁ (1910)	****	1882	239	14	—	23	—	—	—	—	67	10 _P
P ₃₃ (1600)	***	1706	430	14	—	12	—	68 _P	—	—	20	—
F ₃₅ (1905)	**	1881	327	7	21	12	—	1 _P	87 _P	—	—	—
F ₃₇ (1950)	****	1945	300	14	—	38	—	18 _F	—	—	—	44 _F

Table 1. Resonance parameters according to Manley [35] (columns 2-4), together with matrix elements for production in pp collisions (columns 5 and 6) and branching ratios of the resonance decay modes (columns 7-13). Subscripts indicate the relative angular momentum of the outgoing particles in the respective decay channel.

decay channels on dilepton spectra was already discussed in [40] for the case of pion-induced reactions. The dilepton spectra actually give a hint that the needed 3π inelasticity might not be in the $\rho\Delta$, but instead in some other channel, as e.g. $\sigma\Delta$.

Also the width parametrizations are taken from the Manley analysis, where the partial widths for, e.g., $\Delta \rightarrow \pi N$ and $\rho \rightarrow \pi\pi$ are parametrized according to

$$\Gamma(m) = \Gamma_0 \frac{m_0}{m} \left(\frac{q}{q_0} \right)^3 \frac{q_0^2 + \Lambda^2}{q^2 + \Lambda^2}. \quad (4)$$

Here m_0 is the mother particle's pole mass, m is its off-shell mass, Γ_0 is the on-shell width (at $m = m_0$); q denotes the final-state center-of-mass momentum for mass m , while q_0 is the same quantity for mass m_0 , and $\Lambda = 1/R = 1 \text{ fm}^{-1}$ can be viewed as a cutoff-parameter. It has been shown in [41], that eq. (4) gives a good description of the experimental phase shifts in $\pi\pi$ and πN scattering. For the detailed treatment of the other decay channels, we refer to chapter 3.3.1 of [26].

The resonance model used in this work is based on the Teis model, but modifies and extends it in several aspects. We take into account the following nucleon-nucleon scattering channels:

1. $NN \rightarrow NN$
2. $NN \rightarrow N\Delta$,
3. $NN \rightarrow NN^*$, $N\Delta^*$,
4. $NN \rightarrow \Delta\Delta$,
5. $NN \rightarrow \Delta N^*$, $\Delta\Delta^*$,
6. $NN \rightarrow NN\pi$ (non-res. BG)
7. $NN \rightarrow NN\omega$, $NN\pi\omega$, $NN\phi$ (non-res.),
8. $NN \rightarrow BYK$ (with $B = N, \Delta$; $Y = A, \Sigma$).

For the elastic cross sections (first item), we rely on the parametrizations by Cugnon et al. [42] (for beam momenta below $p_{\text{lab}} \approx 2.776 \text{ GeV}$) and the PDG [43] (above). For details see also [26].

The single-resonance excitation channels (items 2 and 3) were already included in the Teis analysis. While the $N\Delta$ channel is treated by an OBE model according to Dmitriev et al. [44], the higher resonances are produced in a pure phase-space approach with constant matrix elements,

$$\sigma_{NN \rightarrow NR} = \frac{C_I}{p_i s} \frac{|\mathcal{M}_{NR}|^2}{16\pi} \int d\mu \mathcal{A}_R(\mu) p_F(\mu). \quad (5)$$

Here, p_i and p_F denote the center-of-mass momenta in the initial and final state, respectively. The matrix elements, \mathcal{M}_{NR} , have previously been fitted by Teis to exclusive meson production (π , 2π , η and ρ). Our values are listed in tab. 1. \mathcal{A}_R denotes the resonance spectral function,

$$\mathcal{A}_R(\mu) = \frac{2}{\pi} \frac{\mu^2 \Gamma_R(\mu)}{(\mu^2 - M_R^2)^2 + \mu^2 \Gamma_R^2(\mu)}. \quad (6)$$

In principle all production channels are assumed to be isospin-symmetric, with the Clebsch-Gordan factors, C_I , resulting from this symmetry. The only exception from this isospin symmetry is the $S_{11}(1535)$ resonance: The exclusive η production, which is assumed to proceed exclusively via this resonance, is known to be significantly larger for pn than for pp [45], therefore we use

$$|\mathcal{M}_{pn \rightarrow NN^*(1535)}|^2 = 6.5 \cdot |\mathcal{M}_{pp \rightarrow NN^*(1535)}|^2. \quad (7)$$

Note that while the $S_{11}(1535)$ is known to dominate the η production in pp at low energies, there may of course be other contributions [46].

The single-pion production cross section can not be described satisfactorily by resonance contributions alone, and one has to add a non-resonant background term [26,34] (slightly refitted here), whose largest contributions appear on the left-hand shoulder of the $N\Delta$ peak.

Most of the resonance-production matrix elements are adopted from Teis. However, we make a few modifications. In particular we reduce the contributions of the $D_{15}(1675)$, $P_{31}(1910)$ and $P_{33}(1600)$, which were extremely large in

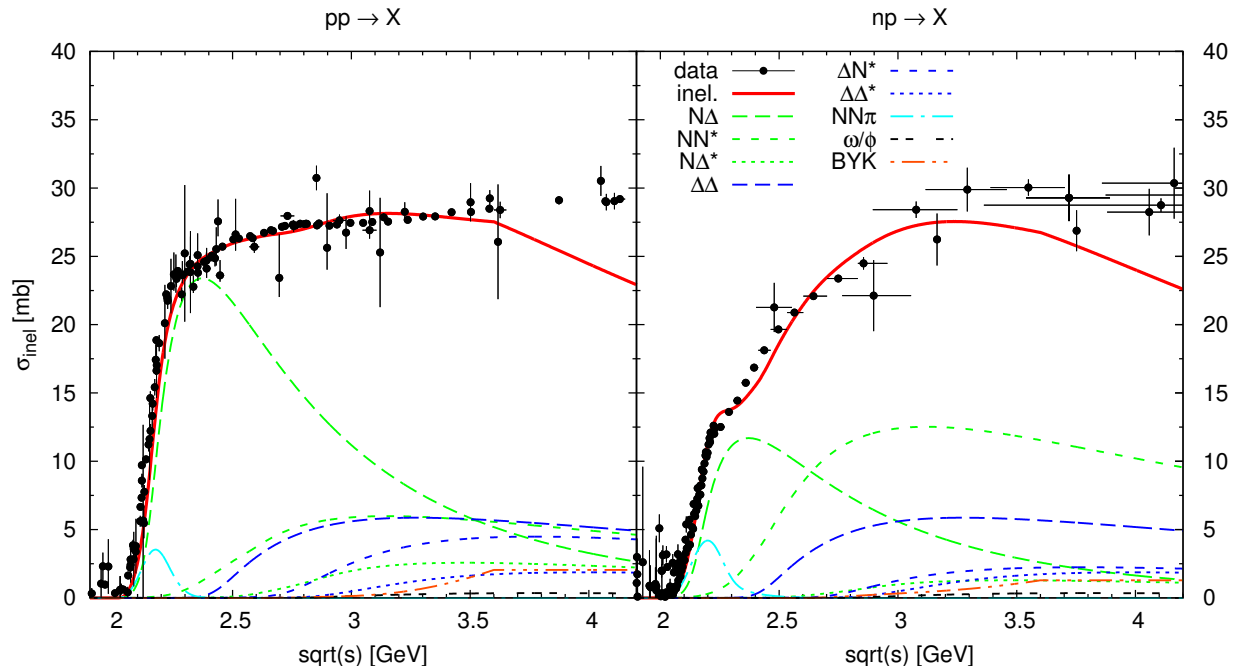


Fig. 1. (Color online) Inelastic pp and pn cross sections in the resonance model. The data points shown here have been obtained by subtracting the parametrized elastic cross section from the total cross section data [37].

the Teis analysis, in favor of the $P_{11}(1440)$ and double- Δ contributions. This gives an improved threshold behavior of the 2π production channels (in line with the analysis of Cao et al. [47]), as well as a better agreement with the inelastic nucleon-nucleon cross sections, cf. fig. 1.

Furthermore, we add another isospin-asymmetry factor for the $P_{11}(1440)$ state:

$$|\mathcal{M}_{pn \rightarrow NN^*(1440)}|^2 = 2 \cdot |\mathcal{M}_{pp \rightarrow NN^*(1440)}|^2. \quad (8)$$

This is done in order to improve the agreement with the np inelastic cross section data, which would otherwise be underestimated significantly.

Also the double-resonance production (items 4 and 5), which in the Teis model was limited to $\Delta\Delta$, is performed in a phase-space approach, analogous to the single-resonance excitation:

$$\sigma_{NN \rightarrow \Delta R} = \frac{C_I}{p_i s} \frac{|\mathcal{M}_{\Delta R}|^2}{16\pi} \times \int d\mu_1 d\mu_2 \mathcal{A}_\Delta(\mu_1) \mathcal{A}_R(\mu_2) p_F(\mu_1, \mu_2). \quad (9)$$

Here one integrates over the spectral functions of both resonances ($\mu_{1,2}$ being their masses).

In the Teis analysis, the production mechanisms were restricted to $NN \rightarrow NR$ and $NN \rightarrow \Delta\Delta$, so the obvious extension candidate would be general double-resonance excitation channels ($NN \rightarrow R_1 R_2$). The channels taken

into account by Teis were fitted to single- and double-pion production data. Therefore his model is only guaranteed to work in the low-energy region. At higher energies, the model starts to fail, since the more inclusive multi-meson final states are not included. If we want to describe NN collisions in the HADES energy regime of $\sqrt{s} \approx 2.4 - 3.2$ GeV with a resonance model, we clearly need to extend the Teis approach. We do this by restricting ourselves to the same set of resonances (cf. tab. 1), but extending the production mechanisms.

Since Teis already describes the exclusive π , 2π , ρ and η production, what is missing are channels like e.g. $\pi\eta$, $\pi\rho$, 3π , 2η , 2ρ , etc. Unfortunately there are almost no experimental data available for these channels. We thus have to rely on the cross sections obtained from PYTHIA as an estimate to fix these channels. According to PYTHIA, the inclusive ρ and η production is in fact dominated by the channels $\pi\rho$ and $\pi\eta$, respectively, at the highest HADES energy of $\sqrt{s} \approx 3.2$ GeV. Therefore we concentrate on these two for now, and neglect all others. Our strategy to satisfy these channels relies on double-resonance excitation, $NN \rightarrow \Delta R$, where the Δ decays into πN , while the other resonance R will be one with an ηN or ρN decay channel, so that we end up with a $\pi\eta$ or $\pi\rho$ final state (note that we do not include cascade decays of single resonances into $\pi\eta N$, as treated for example in [48], since our model misses the corresponding decays modes, such as $\eta\Delta$). We add three new classes of production channels:

- i) $NN \rightarrow \Delta S_{11}(1535) (\rightarrow NN\pi\eta)$,

- ii) $NN \rightarrow \Delta N^* (\rightarrow NN\pi\rho)$,
 $N^* = D_{13}(1520), S_{11}(1650), F_{15}(1680), P_{13}(1720)$,
- iii) $NN \rightarrow \Delta\Delta^* (\rightarrow NN\pi\rho)$,
 $\Delta^* = S_{31}(1620), D_{33}(1700), F_{35}(1905)$.

For each of these we need one new parameter, namely the matrix elements, $|\mathcal{M}_1|^2/16\pi = 60 \text{ mb GeV}^2$, $|\mathcal{M}_2|^2/16\pi = 12 \text{ mb GeV}^2$ and $|\mathcal{M}_3|^2/16\pi = 21 \text{ mb GeV}^2$, as listed in tab. 1. As noted before, we fix the matrix elements to roughly fit the PYTHIA cross sections for $\pi\eta$ and $\pi\rho$ production (with further constraints from the total pp cross section as well as the HADES dilepton data). As for the exclusive production, we assume that the η meson is produced exclusively via the $S_{11}(1535)$, while the ρ production proceeds via a number of N^* and Δ^* resonances. It should be noted that the new channels will not affect the exclusive meson production fitted by Teis, except for the 2π channel, which gets minor contributions from these channels.

The production of ω and ϕ mesons is not carried out via baryonic resonances in our model (although a coupling of the ω to nucleon resonances has been reported for example in [49,50,51,38]). Instead, their production cross sections are parametrized in a phenomenological manner [52]:

$$\sigma(pp \rightarrow ppV) = a(1-x)^b x^c, \quad \text{with } x = s_0/s. \quad (10)$$

Here $s_0 = (2m_N + m_V)^2$ is the threshold energy, and the parameters a , b and c are listed in table 2. We use this parametrization not only for exclusive ω and ϕ production, but also for $NN \rightarrow NN\pi\omega$. Since there are no data available for this channel, we fitted its parameters to the PYTHIA results.

	$\sqrt{s_0}$ [GeV]	a [mb]	b	c	Ref.
ω	2.658	5.3	2.3	2.4	[53]
$\pi\omega$	2.796	1.0	1.5	1.1	-
ϕ	2.895	0.01	1.26	1.66	[54]

Table 2. Parameters for vector-meson production.

As seen in fig. 1, we achieve a good agreement with data for the inelastic pp cross section up to about $\sqrt{s} = 3.5 \text{ GeV}$. At higher energies 3π and 4π production becomes important, which is underestimated by our model (and other channels which we miss completely). In the np cross section there are minor deviations, and unfortunately also the quality of the data is not quite as good as for pp .

4 Dilepton decays and form factors

In the GiBUU model the following dilepton decay modes are taken into account:

- direct decays, as $V \rightarrow e^+e^-$,
with $V = \rho^0, \omega, \phi$ or $\eta \rightarrow e^+e^-$,

- Dalitz decays, as $P \rightarrow e^+e^-\gamma$ with $P = \pi^0, \eta$
or $\omega \rightarrow \pi^0 e^+e^-$ or $\Delta \rightarrow N e^+e^-$.

Most of them are treated similarly as in [41]. The leptonic decay widths of the vector mesons are taken under the assumption of strict vector-meson dominance (VMD),

$$\Gamma_{V \rightarrow e^+e^-}(\mu) = C_V \frac{m_V^4}{\mu^3}, \quad (11)$$

where μ is the meson's off-shell mass, m_V is the pole mass, and the constants C_V are listed in table 3 (taken from [37]). Although the physical threshold of the dileptonic decay channels of course lies at $2m_e$, contributions of ρ mesons below $m = 2m_\pi$ are frequently neglected in transport simulations. The reason for this artificial threshold is purely numerical: The ρ spectral function has a sharp drop at the 2π threshold, and it is numerically very difficult to populate the spectral function below this threshold, where it is almost vanishing. Here we make additional numerical efforts to include the contribution of ρ mesons below the 2π threshold, since it can give significant contributions to the total dilepton spectrum for certain reactions.

V	m_V (MeV)	Γ_{ee} (keV)	$C_V = \Gamma_{ee}/m_V$
ρ	775.49	7.04	$9.078 \cdot 10^{-6}$
ω	782.65	0.60	$7.666 \cdot 10^{-7}$
ϕ	1019.455	1.27	$1.246 \cdot 10^{-6}$

Table 3. Dilepton-decay constants for $V \rightarrow e^+e^-$.

While the direct decay of the η meson into a $\mu^+\mu^-$ pair has been observed, for the corresponding e^+e^- decay only an upper limit of $\text{BR}(\eta \rightarrow e^+e^-) < 2.7 \cdot 10^{-5}$ is known [55]. In fact this limit has been pushed down to $4.9 \cdot 10^{-6}$ lately using HADES dilepton data [24]. However, the theoretical expectation from helicity suppression is still four orders of magnitude lower [56]. The absence of any η peak in the measured spectra allows us to conclude that the true branching ratio must be significantly lower than the upper limit just mentioned [57]. Therefore we do not include the $\eta \rightarrow e^+e^-$ decay in our analysis.

The Dalitz decays of the pseudoscalar mesons, $P = \pi^0, \eta$, are treated via the parametrization [58],

$$\frac{d\Gamma_{P \rightarrow \gamma e^+e^-}}{d\mu} = \frac{4\alpha}{3\pi} \frac{\Gamma_{P \rightarrow \gamma\gamma}}{\mu} \left(1 - \frac{\mu^2}{m_P^2}\right)^3 |F_P(\mu)|^2, \quad (12)$$

with $\Gamma_{\pi^0 \rightarrow \gamma\gamma} = 7.8 \cdot 10^{-6} \text{ MeV}$, $\Gamma_{\eta \rightarrow \gamma\gamma} = 4.6 \cdot 10^{-4} \text{ MeV}$ and the form factors,

$$F_{\pi^0}(\mu) = 1 + b_{\pi^0} \mu^2, \quad b_{\pi^0} = 5.5 \text{ GeV}^{-2}, \quad (13)$$

$$F_{\eta}(\mu) = \left(1 - \frac{\mu^2}{\Lambda_{\eta}^2}\right)^{-1}, \quad \Lambda_{\eta} = 0.676 \text{ GeV}. \quad (14)$$

The above value of Λ_{η} has been recently determined from the HADES data at 2.2 GeV beam energy [59] and agrees reasonably well with the values found by NA60 [60] and

CB/TAPS [61]. As shown in [62], the dilepton decays of the pseudoscalar mesons is expected to follow an anisotropic angular distribution,

$$\frac{d\Gamma_{P \rightarrow \gamma e^+ e^-}}{d \cos \theta} \propto 1 + \cos^2(\theta), \quad (15)$$

where θ is the angle of the electron momentum with respect to the dilepton momentum. This has been confirmed recently by HADES data [63]. All other decays are treated isotropically in our model.

The parametrization of the ω Dalitz decay,

$$\begin{aligned} \frac{d\Gamma_{\omega \rightarrow \pi^0 e^+ e^-}}{d\mu} &= \frac{2\alpha}{3\pi} \frac{\Gamma_{\omega \rightarrow \pi^0 \gamma}}{\mu} \\ &\times \left[\left(1 + \frac{\mu^2}{\mu_\omega^2 - m_\pi^2} \right)^2 - \frac{4\mu_\omega^2 \mu^2}{(\mu_\omega^2 - m_\pi^2)^2} \right]^{3/2} \\ &\times |F_\omega(\mu)|^2, \end{aligned} \quad (16)$$

$$|F_\omega(\mu)|^2 = \frac{A_\omega^4}{(\Lambda_\omega^2 - \mu^2)^2 + A_\omega^2 \Gamma_\omega^2}, \quad (17)$$

is adopted from [64, 41] with $\Gamma_{\omega \rightarrow \pi^0 \gamma} = 0.703$ MeV, $A_\omega = 0.65$ GeV and $\Gamma_\omega = 75$ MeV. Here we note that the form factor of the ω Dalitz decay is also well-constrained by data [60].

For the Δ -Dalitz decay, we use the parametrization from [65],

$$\begin{aligned} \frac{d\Gamma_{\Delta \rightarrow N e^+ e^-}}{d\mu} &= \frac{2\alpha}{3\pi\mu} \Gamma_{\Delta \rightarrow N \gamma^*}, \quad (18) \\ \Gamma_{\Delta \rightarrow N \gamma^*} &= \frac{\alpha}{16} \frac{(m_\Delta + m_N)^2}{m_\Delta^3 m_N^2} [(m_\Delta + m_N)^2 - \mu^2]^{1/2} \\ &\times [(m_\Delta - m_N)^2 - \mu^2]^{3/2} |F_\Delta(\mu)|^2, \end{aligned} \quad (19)$$

where we neglect the electron mass. The electromagnetic N- Δ transition form factor $F_\Delta(\mu)$ is an issue of ongoing debate. Unlike the other semileptonic Dalitz decays, it is poorly constrained by data. At least at the real-photon point ($\mu = 0$) it is fixed by the decay width $\Gamma_{\Delta \rightarrow N \gamma} \approx 0.66$ MeV [37] to $|F_\Delta(0)| = 3.03$, and also in the space-like region this form factor is well-constrained by electron-scattering data on the nucleon. However, it is basically unknown in the time-like regime, which is being probed by the Δ Dalitz decay.

Theoretical models for the N- Δ transition form factor usually assume one or more VMD-inspired peaks in the time-like region [66, 67, 68, 69]. However, the data in the space-like region does not provide sufficient constraints to fix the behavior in the time-like region.

Moreover, a VMD-like Δ form factor would imply a coupling of the Δ to the ρ meson, which has never been observed directly and could only play a role far off the Δ pole, where its strength is completely unknown [70].

In order to demonstrate the uncertainty connected to this form factor, we will in the following use as an example the

model of [68]. However, we note that recently a new form-factor calculation has appeared [69], whose results differ significantly from the ones given in [68].

For the other baryonic resonances we don't explicitly include a Dalitz decay, but evaluate their contributions to the dilepton spectrum through the two-step process $R \rightarrow N \rho \rightarrow N e^+ e^-$. In the transport-typical manner we cut the corresponding diagrams, separating the production and decay vertices of the resonance and neglecting any phases and interferences. Below the 2π threshold, the ρ meson width becomes very small because here only the electromagnetic decay width is active. This smallness of the width, however, is counteracted to some degree by the propagator of the virtual photon that enhances small dilepton masses, see eq. (11). In an alternative treatment, in which the N^* resonances undergo direct Dalitz decay, an electromagnetic form factor at the $NN^*\gamma^*$ vertex would mimic the ρ propagator. These two methods are fully equivalent if the phase relations between the decaying resonance and the dileptons can be neglected and a corresponding form factor is used (our model relies on the assumption of strict VMD). Any interaction of the ρ meson between its production and decay, leading to a broadening of the ρ spectral function, could be absorbed into a medium dependence of the form factor.

Further we include pn-Bremsstrahlung in phase-space corrected soft-photon approximation [71, 72], which can be written as

$$\frac{d\sigma_{pn \rightarrow p n e^+ e^-}}{dM dE d\Omega} = \frac{\alpha^2}{6\pi^3} \frac{q}{ME^2} \bar{\sigma}(s) \frac{R_2(s_2)}{R_2(s)}, \quad (20)$$

$$\bar{\sigma}(s) = \frac{s - (m_1 + m_2)^2}{2m_1^2} \sigma_{el}^{pn}(s), \quad (21)$$

$$R_2(s) = \sqrt{1 - (m_1 + m_2)^2/s}, \quad (22)$$

$$s_2 = s + M^2 - 2E\sqrt{s}, \quad (23)$$

where M is the mass of the dilepton pair, q , E and Ω are its momentum, energy and solid angle in the pn center-of-mass frame and s is the Mandelstam's variable. Further, m_1 is the mass of the charged particle (proton), m_2 is the mass of the neutral particle (neutron) and σ_{el}^{pn} is the elastic pn cross section.

pp-Bremsstrahlung can not be treated in this simple approximation, since it involves a destructive interference between the graphs involved. Due to this interference it is much smaller than the pn-Bremsstrahlung and therefore is being neglected here.

Further we note that also the Bremsstrahlung contribution involves a form factor, i.e. the time-like nucleon form factor. Just as the Δ transition form factor, it is not well-constrained in the time-like region and is usually neglected, also in recent OBE models [73, 74, 75].

5 Dilepton spectra from elementary N+N collisions

After describing the basic ingredients of the model, we will now present simulated dilepton spectra for various elementary reactions (p+p and d+p). The HADES collaboration has performed measurements of dilepton spectra from elementary p+p reactions at the beam energies listed in table 4.

E_{kin}	\sqrt{s}	p_{lab}	$p_{\text{lep}}^{\text{min}}$	$p_{\text{lep}}^{\text{max}}$
1.25	2.42	1.98	0.05	1.8
2.20	2.76	2.99	0.10	2.0
3.50	3.17	4.34	0.08	2.0

Table 4. Kinematic conditions of the elementary collisions measured by HADES and corresponding cuts on the single lepton momenta (all numbers in GeV).

For the beam energy of 1.25 AGeV, also dp collisions have been measured. All simulated spectra have been filtered with the HADES acceptance filter (HAFT, version 2.0) [76,77], in order to take care of the geometrical acceptance and resolution of the detector. In addition, a dilepton opening angle cut of $\theta_{ee} > 9^\circ$ is applied in all cases, as well as the single-lepton momentum cuts listed in table 4, matching the experimental analysis procedure.

5.1 p + p at 1.25 GeV

The lowest HADES energy, $E_{\text{kin}} = 1.25$ GeV, corresponding to $\sqrt{s} \approx 2.4$ GeV, is just below the η production threshold, and also for ρ mesons there is only a small sub-threshold contribution from the low-mass tail of the ρ spectral function.

This means that the dilepton spectrum is dominated by the π^0 and Δ Dalitz decays. One should note that at this energy, almost all pions are produced via excitation and decay of the Δ resonance.

Both of these Dalitz decays involve a transition form factor. But while the form factor of the π^0 Dalitz channel has been determined experimentally to a reasonable precision [58], the electromagnetic transition form factor of the Δ Dalitz decay is basically unknown in the time-like region (cf. previous sect.).

However, the dilepton spectrum at $E_{\text{kin}} = 1.25$ GeV is only mildly sensitive to this form factor, since the energy is not large enough to reach the VM pole-mass region. As fig. 2 shows, the simulation profits from including a form factor (shaded band) which exhibits a moderate rise in the time-like region of small q^2 , but it is not sensitive to the actual VMD peak of such a form factor. Here we have used the form factor from [68], but we have also verified that using a standard VMD form factor yields virtually the same results for this energy.

It is interesting to note that other calculations achieve a good agreement with the HADES data for pp collisions

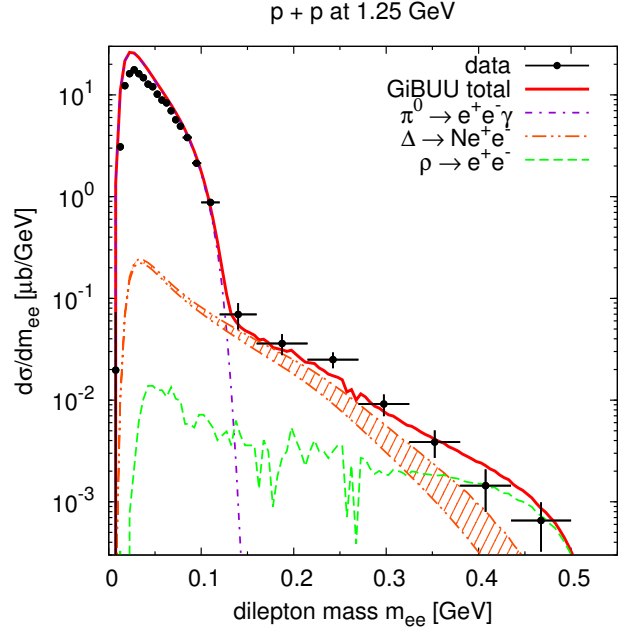


Fig. 2. (Color online) Dilepton mass spectrum for pp at 1.25 GeV, in comparison to the data from [22]. The different contributions are indicated in the figure. The hatched area indicates the effect of the Δ form factor.

at 1.25 GeV without including any form factor for the Δ Dalitz channel [75] (which might be partly due to the different width parametrization used).

Furthermore we note that the slight overshooting in the pion channel is apparently due to the higher resonances, which are produced only in phase-space approximation. The missing treatment of proper angular momentum distributions seems to interfere with the HADES acceptance here, however it does not seem to be a problem at higher energies. We have verified that the discrepancy disappears if all pions are produced exclusively via Δ excitation, neglecting contributions from higher resonances.

5.2 d + p at 1.25 GeV

In addition to the proton beam, also a deuteron beam with a kinetic energy of 1.25 AGeV has been used by HADES. Here, a trigger on forward-going protons has been set up in order to select the (quasi-free) np collisions, which are only accessible in this way.

Due to the motion of the bound nucleons in the deuteron, the energy of the NN collisions is smeared out here, compared to the proton-beam case, with a tail reaching above the η -production threshold. The momentum distribution of the nucleons is determined by the deuteron potential, which in our simulations is given by the Argonne V18 potential [78].

Fig. 3 shows the dilepton invariant mass spectrum for this reaction. While the π^0 -Dalitz channel in the low-mass re-

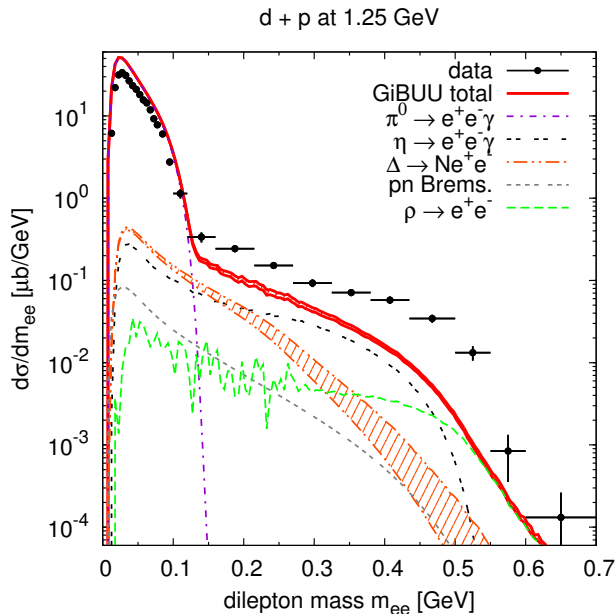


Fig. 3. (Color online) Dilepton mass spectrum for d+p at 1.25 GeV, in comparison to the data from [22].

gion shows a similarly good agreement as in the pp case, the data points at larger invariant masses are underestimated by a factor of two or more.

A stronger Δ channel can apparently not explain the shoulder in the data around 500 MeV, since it falls off too steeply, even when including a form factor. In addition to the enhanced η production in $np \rightarrow np\eta$, as described earlier, we have included a $np \rightarrow d\eta$ channel, which dominates the η production from np at threshold [45].

Unfortunately, the strong $pn \rightarrow pn\rho^0$ channel is experimentally not so well known. In our model, the ρ^0 production in d+p at 1.25 GeV is dominated by the $D_{13}(1520)$ and $S_{11}(1535)$ resonances. The latter is enhanced in np (because of its dominant role in η production). The former is assumed to be isospin-symmetric, which may not be the case.

In an OBE-model study [75] it has been found that the radiation from internal pion lines (with the appropriate VMD form factor) gives a sizable contribution at large invariant masses. Such a diagram implicitly contains a ρ^0 propagator (through the form factor), and gives additional ρ -like contributions on top of the resonance contributions included in our model.

Moreover, we might underestimate the ‘pure’ Bremsstrahlung contributions, which do not involve resonance excitations, due to the soft-photon approximation. However, it is not expected that these terms would yield any dominant contributions [79, 80, 75].

As recently argued in [81], the inclusion of a ‘radiative capture’ channel $np \rightarrow de^+e^-$, fixed via deuteron photodisintegration, might give further contributions in the high-mass region.

According to our analysis, the most probable candidate to fill the missing yield are indeed ρ -like contributions. The radiation from internal pion lines is one such graph which we miss; this channel mainly contributes at large masses [75]. Furthermore, the subthreshold ρ production via resonances could be underestimated on the neutron by our model. Analogous to the η case, it might be enhanced over $pp \rightarrow \rho^0 X$. And finally, channels like $np \rightarrow d\rho^0$ (related to the radiative capture) could contribute, which are completely unknown.

The discrepancy of data and theory for the d+p reaction is specific for this reaction at this particular energy; the results for nuclear collisions to be discussed later do not show such a disagreement. We note that the observed cross section represents only about 15 - 20% of the actual cross section; the rest is being cut away by the acceptance filter. Thus, any deficiencies, for example, in the angular distribution of our dileptons could show up in rather large errors of the spectra after the acceptance cuts have been performed.

5.3 p + p at 3.5 GeV

Fig. 4 shows a comparison plot of a GiBUU simulation to HADES data [24] for a proton beam of 3.5 GeV kinetic energy impinging on a fixed proton target. This is the

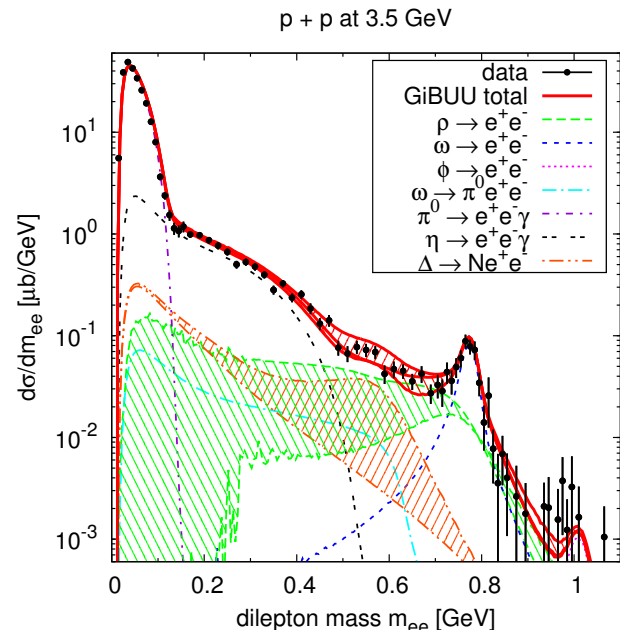


Fig. 4. (Color online) Dilepton mass spectrum for pp collisions at 3.5 GeV. Data from [24]. The hatched areas indicate the effects of the Δ form factor [68] and baryon-resonance contributions to the ρ production, respectively. The total is shown (from bottom to top) with Δ form factor (left-hatched), ρ resonance contributions (right-hatched) and with both of these effects together.

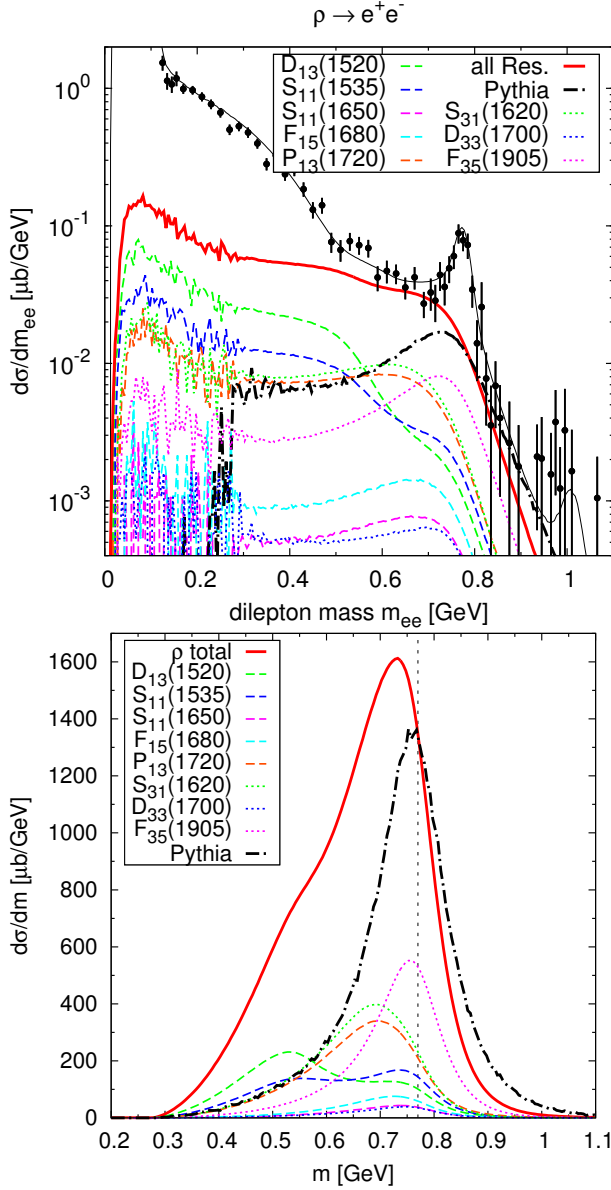


Fig. 5. (Color online) Top: Resonance contributions to the ρ channel in the dilepton mass spectrum. Bottom: Resonance contributions to the ρ mass distribution. The dashed line indicates the vacuum pole mass of the ρ meson. For comparison we also show the ρ meson contribution from our earlier Pythia simulations [33].

highest beam energy (per nucleon) used by the HADES experiment and corresponds to a center-of-mass energy of $\sqrt{s} = 3.18$ GeV.

At this energy, the η , ω and ρ production channels are fully open, and even the ϕ production becomes energetically possible. The data only show a hint of a ϕ peak with very

poor statistics, but it seems to be slightly underestimated by our simulation.

The η and ρ production is dominated by the channels $NN \rightarrow NN\pi\eta$ and $NN \rightarrow NN\pi\rho$, respectively. In our model these are saturated by double-resonance excitation, cf. sec. 3. The ω meson is presently produced in a non-resonant phase-space prescription through the exclusive and the $\pi\omega$ channel.

Under these assumptions, we get a very good agreement with the data over the whole mass range, as shown in fig. 4.

It is interesting to note that the shape of the ρ channel shown here differs significantly from the one obtained in our previous string-model investigations via PYTHIA [33], which has been adopted for the PLUTO simulations in [24]. The latter is given by the lower dashed (green) line in Fig. 4, whereas the new resonance-model based treatment yields the upper dashed line. The ρ -shape effect is due to the production of ρ mesons via nucleon resonances, i.e. $NN \rightarrow NR \rightarrow NN\rho$ and $NN \rightarrow \Delta R \rightarrow NN\pi\rho$, where the lighter resonances like e.g. $D_{13}(1520)$ will preferentially contribute to the low-mass part of the ρ spectral function. Together with the $1/m^3$ factor of the dilepton decay width, this results in a very flat distribution, which lacks a clear peak at the nominal mass, and dominates the dilepton spectrum in the intermediate mass region around 500 - 700 MeV.

The ρ spectral function is thus ‘modified’ already in the vacuum, simply due to the production mechanism via nucleon resonances. As seen in fig. 5, the ρ mass distribution in pp at 3.5 GeV peaks around 730 MeV, with an additional shoulder around 500 MeV (due to low-mass resonances, mainly the $D_{13}(1520)$). This spectral shape is due to phase-space limitations and special resonance properties. It differs significantly from the mass distribution resulting from a PYTHIA simulation [33], which lacks any resonance contributions. Similar effects were already ob-

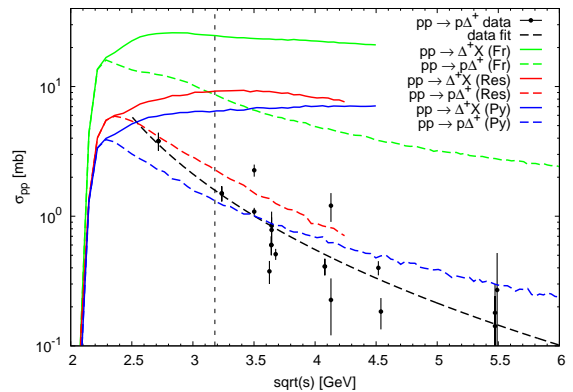


Fig. 6. (Color online) Inclusive and exclusive Δ^+ production cross sections in different models (FRITIOF 7.02, PYTHIA 6.4 and the GIBUU resonance model), compared to data from [82].

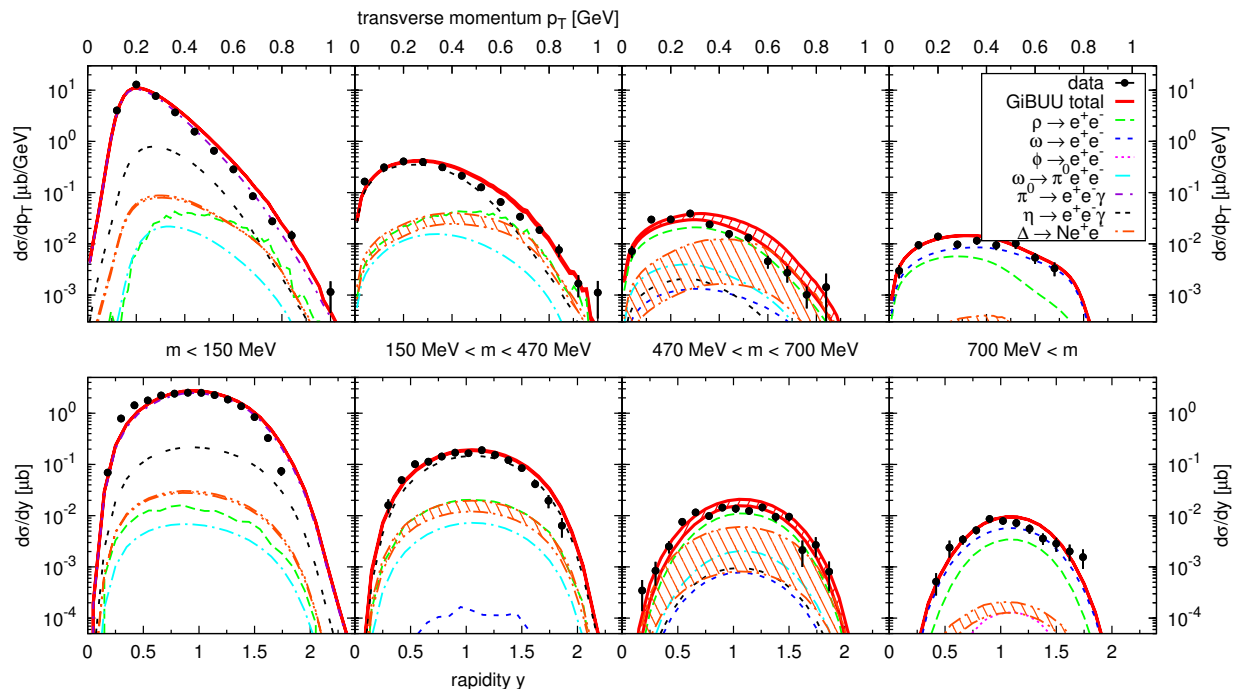


Fig. 7. (Color online) Transverse momentum and rapidity spectra of dilepton pairs from pp at 3.5 GeV in four mass bins. The hatched area indicates the effect of the Δ form factor. Data from [24].

served, e.g., in C+C reactions [83]. We stress here that this is not an ‘in-medium’ effect at all: It is solely caused by the production mechanism and occurs already in elementary p+p collisions in the vacuum. This effect is crucial for understanding the intermediate mass region of the dilepton spectrum in pp collisions at 3.5 GeV (as seen in fig. 4) and might also play an important role at 2.2 GeV (see next section).

The particular influence of the $N^*(1520)$ resonance on dilepton spectra from NN collisions have already been investigated in [84], where it was concluded that the $N^*(1520)$ can indeed give sizable contributions to the DLS and HADES spectra, but is subject to moderate uncertainties.

It should be noted that the exact composition of the resonance contributions to the ρ channel, and therefore also its exact shape, are not fixed by data so far, but rather represent an ‘educated guess’. The resonance composition can be checked via πN invariant mass spectra.

Moreover, possible $\rho\Delta$ decay modes of certain resonances could give further contributions to the dilepton cocktail, as mentioned earlier.

Comparing our cocktail to other transport models like HSD [85] or UrQMD [86], one of the most significant discrepancies shows up in the size of the Δ channel. While in our model the Δ does not give any significant contribution to the total dilepton yield at $E_{\text{kin}} = 3.5$ GeV (without a form factor), this is not so for the two other models. Both of them have a much stronger Δ channel, which even dominates the dilepton spectrum in the intermediate mass region around 600 MeV. We stress here that

there are several factors of uncertainty in the Δ channel, for example the inclusive production cross section, but also the parametrization of the Δ decay width (hadronic as well as leptonic) and the completely unsettled question of the electromagnetic $N\text{-}\Delta$ transition form factor.

Although the inclusive Δ production cross section is not that well known at $E_{\text{kin}} = 3.5$ GeV, one can get constraints from the exclusive cross section, cf. fig. 6, as well as the inclusive one at lower energies (where it is fixed via pion production). Both constraints are respected in our resonance model, while e.g. the FRITIOF model clearly overestimates the exclusive Δ^+ production, and in particular does not seem to respect the correct isospin relations.

On the question of the electromagnetic $N\text{-}\Delta$ transition form factor, it should be noted that in our simulations the Iachello model [68] agrees reasonably well with the data (depending on the contributions of other baryonic resonances), while a naive VMD form factor, as used e.g. in [87], would clearly overshoot the data.

In order to understand the underlying processes, it is not sufficient to consider only the mass spectrum. Other observables can give further insight into the reaction dynamics and can serve as a cross check for the validation of theoretical models. In order to compare to the data from [24], we examine the transverse momentum and rapidity distributions in four different mass bins (see fig. 7):

- $m < 150$ MeV, dominated by the π^0 Dalitz channel,
- $150 \text{ MeV} < m < 470$ MeV, dominated by the η Dalitz decay,

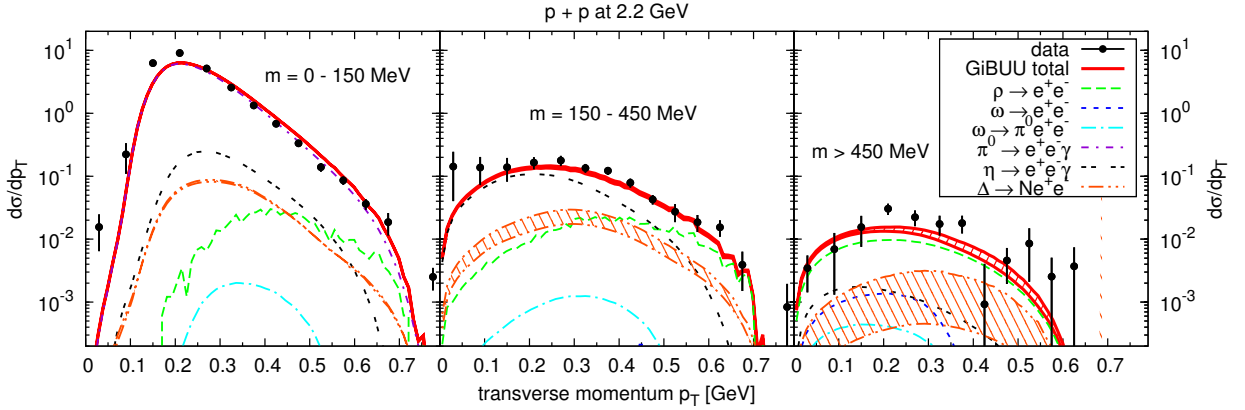


Fig. 9. (Color online) Transverse momentum spectra of dilepton pairs from pp at 2.2 GeV in three mass bins. The hatched area indicates the effect of the Δ form factor. Data from [25].

- $470 \text{ MeV} < m < 700 \text{ MeV}$, dominated by the direct ρ decay (possibly with contributions from the Δ Dalitz),
- $700 \text{ MeV} < m$, dominated by the ω and ρ .

Distinguishing several mass bins is useful in order to separate the contributions of different channels. In all four mass bins, we achieve an excellent agreement with the HADES data [24]. In particular it should be noted that a stronger Δ channel would apparently destroy the very good agreement in the p_T spectra, since it would yield too large high- p_T contributions in the two mass bins of 150-470 and 470-700 MeV.

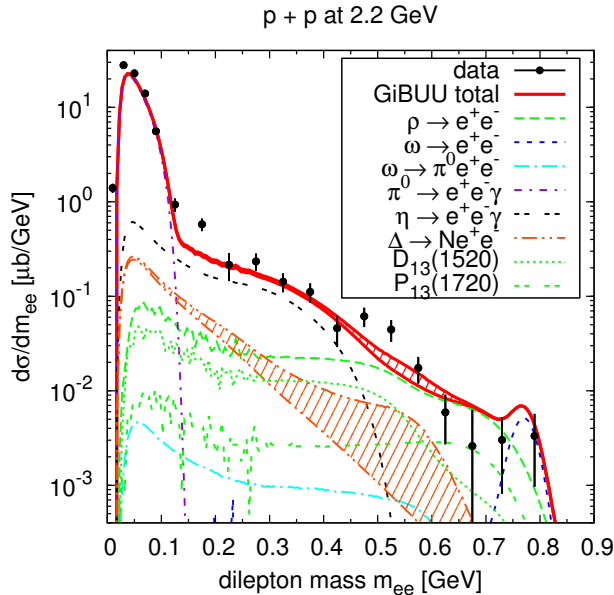


Fig. 8. (Color online) Dilepton mass spectrum for pp at 2.2 GeV. The hatched area indicates the effect of the Δ form factor. Data from [25].

5.4 p + p at 2.2 GeV

A third, intermediate, beam energy of 2.2 GeV has been used for the HADES experiment. This energy is well above the η production threshold and is just high enough to reach the pole mass of the light vector mesons, ρ and ω , which dominate the high-mass part of the dilepton spectrum (as seen in fig. 8). The Δ channel plays a less important role here, since it is buried underneath the strong η and ρ channels. The ω only gives a small contribution, since the energy is only just at the threshold of ω production.

The ρ channel exhibits slightly more structure here than at 3.5 GeV, showing a moderate step around 550 MeV. This step marks the border between a low-mass part, which is dominated by the $D_{13}(1520)$ resonance, and a high-mass part dominated by the $P_{13}(1720)$. In fig. 8 we show the contributions of these two resonances to the ρ channel, but omit the subdominant contributions of other resonances (for the sake of readability). The resonance contributions indeed improve the agreement with the data, compared to the PLUTO cocktail, which only includes phase-space population of the ρ [25]. However, there are still minor deviations, which seem to suggest an underestimation of the $D_{13}(1520)$ and an overestimation of the $P_{13}(1720)$ in our resonance cocktail at this energy.

In fig. 9 we show the p_T spectra for three different mass bins in comparison to the data from [25]. Our simulations give a better agreement with the data than the PLUTO cocktail shown in [25] in all three mass bins. Most notably, we get an improvement from the larger ρ contribution in the highest mass bin.

5.5 Comparison to elementary DLS data

In addition to the recently measured HADES data, also the elementary data measured previously by the DLS collaboration are available for comparison with our model [88]. Unfortunately they are of inferior quality in terms

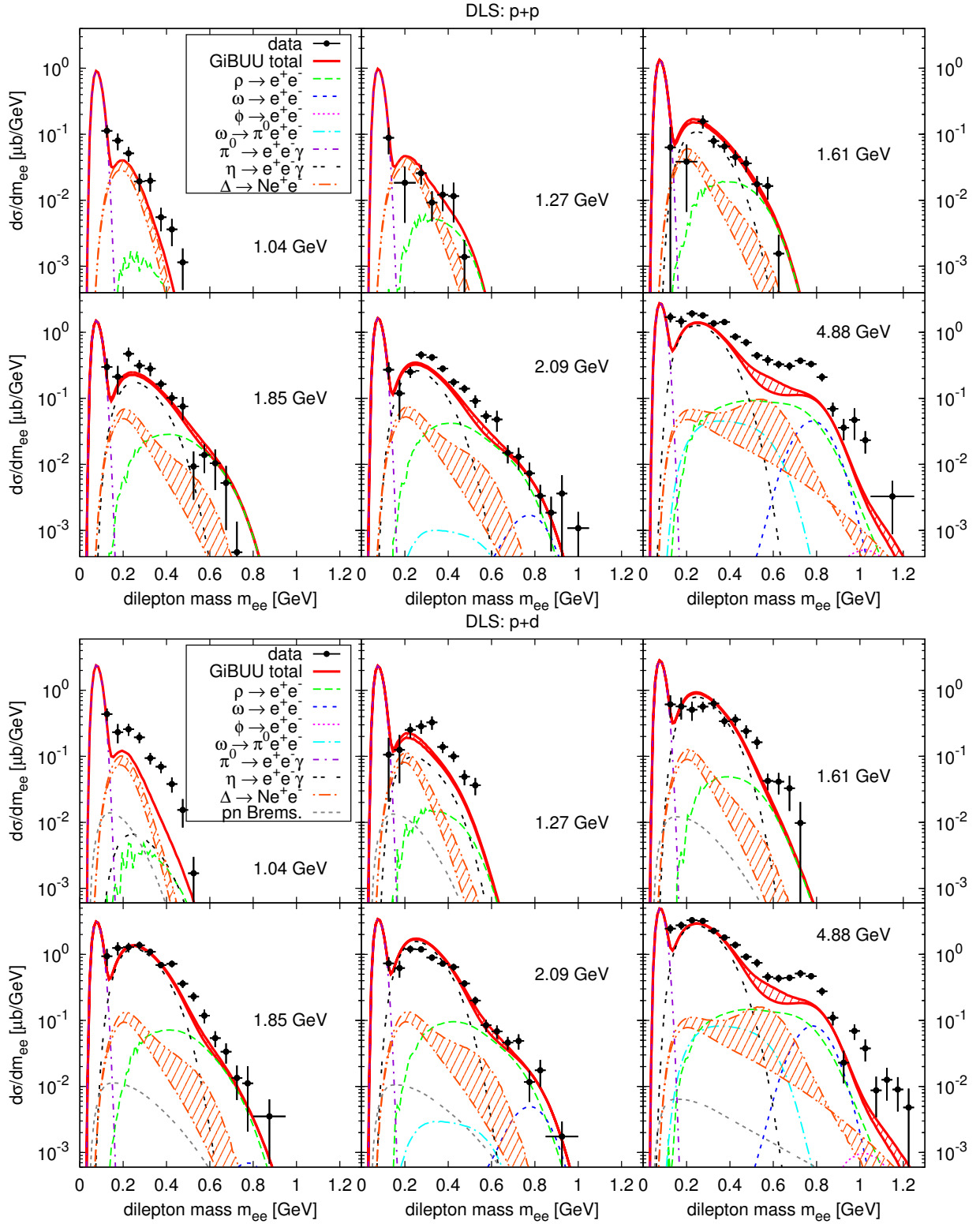


Fig. 10. (Color online) Dilepton mass spectra in comparison to DLS data [88]. Top: p+p, bottom: p+d.

of statistics and acceptance. However, more beam energies have been measured than in the case of HADES, so that they can still provide additional constraints, which are useful for understanding the elementary cocktail.

In order to compare to the DLS data, the GiBUU dilepton events have been filtered through the DLS acceptance filter, version 4.1, as available from [89]. In addition to the acceptance filtering, the events have been smeared with a Gaussian of width $\sigma = 0.1m_{ee}$, in order to account for the mass resolution of the detector. No further cuts have been applied. The kinematics of the reactions measured by DLS are summarized in table 5. At each of the given energies, a p+p and p+d reaction was measured.

E_{kin}	\sqrt{s}	p_{lab}
1.04	2.34	1.74
1.27	2.43	2.00
1.61	2.56	2.37
1.85	2.64	2.63
2.09	2.73	2.88
4.88	3.56	5.74

Table 5. Kinematic conditions of the elementary collisions measured by DLS (in GeV).

The comparison of the GiBUU model results to the DLS data is shown in Fig. 10. As before, we show the effect of the Δ transition form factor as a hatched band and note that it slightly improves the agreement with the data in almost all cases.

It is apparent that at the medium beam energies there is a reasonable agreement, both in p+p and p+d. The largest deviations are visible at the highest beam energy of 4.88 GeV, which is already at the border of validity of our resonance model. Apparently the inclusive production of ρ and ω mesons is underestimated there.

The underestimation at the lowest energy of 1.04 GeV is similar to that seen in the HADES experiment at a comparable energy (see Fig. 3). Since at this somewhat lower energy the η production plays no role, the discrepancy seems to indicate a problem with the Δ or Bremsstrahlung contributions. However, we note again that the population of the Δ resonance is constrained rather well by the pion and total cross sections, which we describe rather well (see Fig. 1). On the other hand, the decay of the resonance is fixed by the electromagnetic coupling at the photon point, so that there is no ambiguity there. Further, form factors have only little influence at such low energies. We thus have to conclude that we have no explanation for the discrepancy yet and note that related, earlier calculations similarly underestimated the DLS dilepton yield at this lowest energy [19].

6 Dilepton spectra from p+Nb collisions

Fig. 11 shows simulated dilepton spectra for p+Nb collisions at 3.5 GeV using vacuum spectral functions, compared to preliminary data from [90]. As for p+p at 3.5

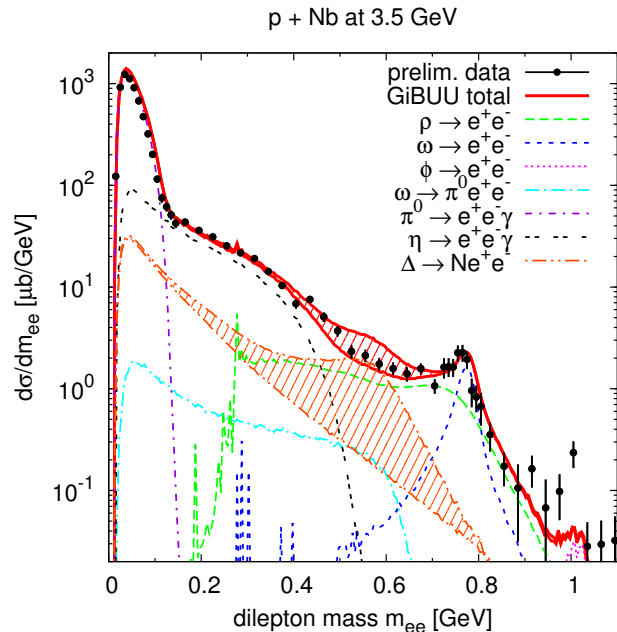


Fig. 11. (Color online) Dilepton mass spectrum for p+Nb at 3.5 GeV, showing all contributing channels with vacuum spectral functions. The hatched area indicates the effect of the Δ form factor. Preliminary data taken from [90], scaled to fit the π^0 and η yield.

GeV, we filter our dilepton events through the HADES acceptance filter and cut on $0.08 \text{ GeV} < p_{\text{lep}} < 2.0 \text{ GeV}$ and $\theta_{ee} > 9^\circ$. The level of agreement is similar to the p+p reaction at the same energy. Note, however, that the data are not absolutely normalized in terms of a cross section yet. Therefore we have scaled the data points to match the simulation in the low-mass region, which is dominated by the π^0 and η Dalitz channels. Moreover, the data have not been fully corrected for all detector effects yet, which is the reason for a slight shift of the mass scale (on the order of 1%), which is visible at the ω peak [91]. It is evident that the data can be quite well described if the electromagnetic Δ decay width does not contain the form factor of ref. [68] which would create a hump in the spectrum around 0.6 GeV.

In contrast to the NN collisions in the preceding chapter, here we neglect the ρ -meson contributions below the 2π threshold (due to numerical reasons). As seen in fig. 11, they do not contribute significantly to the total dilepton yield.

6.1 In-medium effects

In p+Nb reactions there are additional effects, compared to the elementary p+p reactions. First of all, the primary p+N collisions will be nearly identical, apart from binding effects and some Fermi smearing and Pauli blocking, but besides p+p also p+n collisions play a role. Further-

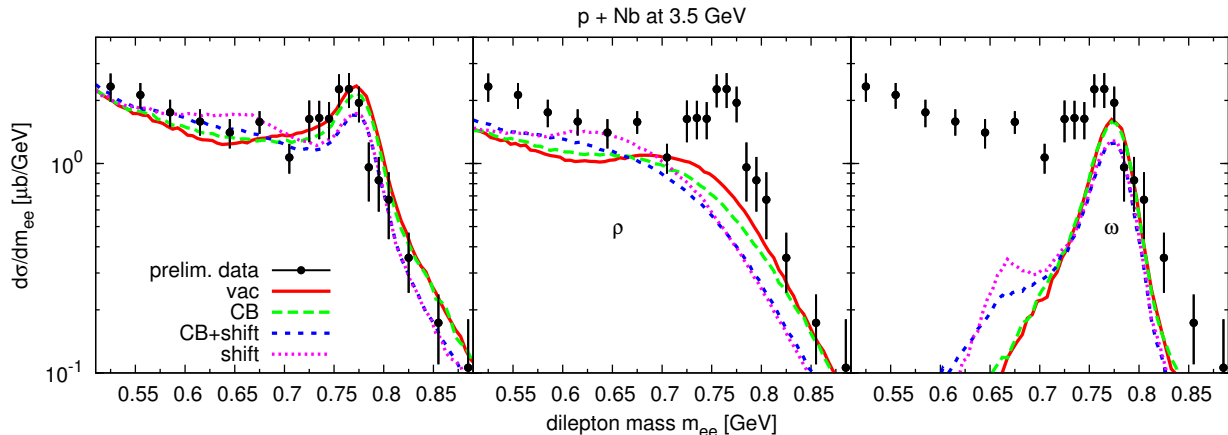


Fig. 12. (Color online) Dilepton mass spectra for p+Nb at 3.5 GeV. Comparison of different in-medium scenarios (vacuum spectral functions for the vector mesons, collisional broadening, 16% mass shift, collisional broadening plus mass shift). Left: Total spectrum, center: ρ contribution, right: ω contribution. Preliminary data taken from [90], scaled to fit the π^0 and η yield.

more, the produced particles undergo final-state interactions within the Nb nucleus, and processes like meson absorption and regeneration may become important. The secondary collisions will on average have lower energies than the primary N+N collisions. Finally also the vector-meson spectral functions may be modified in the nuclear medium.

The propagation of particles with density-dependent spectral functions (usually referred to as “off-shell propagation”) poses a particular challenge. Our approach to this problem is based on the off-shell equations of motion of test particles, as given in [92] and [93]. Such an off-shell treatment is necessary for including in-medium modifications of the spectral functions (e.g. collisional broadening of the vector mesons). The collisional width inside a nuclear medium of density, ρ , can be related to the collision cross section, σ_{NX} , in low-density approximation as

$$\Gamma_{\text{coll}} = \rho \langle v_{\text{rel}} \sigma_{NX} \rangle, \quad (24)$$

where v_{rel} is the relative velocity and the brackets indicate an integration over the Fermi momentum of the nucleons. This collisional width will in general depend on the momentum of the involved particle, X . In order to avoid numerical difficulties connected with the appearance of superluminal test particles, we neglect the momentum dependence and use the simplified form,

$$\Gamma_{\text{coll}} = \Gamma_0 \frac{\rho}{\rho_0}, \quad (25)$$

where $\rho_0 = 0.168 \text{ fm}^{-3}$ is the normal nuclear matter density. The value of Γ_0 should on average match the momentum-dependent width as obtained from the collision term. We typically use $\Gamma_0 = 150 \text{ MeV}$ for the ρ and $\Gamma_0 = 80 \text{ MeV}$ for the ω meson. More details on off-shell propagation in the GiBUU model in general can be found in [26].

The mass spectrum above 500 MeV can receive modifications from the inclusion of in-medium effects in the vector-meson spectral functions. Fig. 12 shows the typical

in-medium scenarios: The first one includes a collisionally broadened in-medium width, while the second one assumes a pole-mass shift according to

$$m^*(\rho) = m_0 \left(1 - \alpha \frac{\rho}{\rho_0} \right), \quad (26)$$

with a scaling parameter, $\alpha = 16\%$. The third scenario combines both of these effects. The modifications introduced by these scenarios are roughly on the same order of magnitude as the systematic errors of the data, and so far there is no clear evidence for medium modifications of the vector-meson properties in cold nuclear matter from the HADES data. However, it looks as if a mass shift tends to deteriorate the agreement with the data.

Regarding the ω absorption, it should be noted that the GiBUU implementation yields an average collisional width of roughly $\Gamma_0 = 80 \text{ MeV}$. This appeared too low to explain the transparency-ratio measurement of [94], which seemed to demand values of 130 to 150 MeV. For the HADES dilepton data, such a discrepancy currently does not seem to exist.

However, one should keep in mind that a statement about ω absorption depends on a number of prerequisites. For example, one needs to have the ρ contribution well under control, since it represents a large background under the ω peak. Given the discussion about resonance contributions to the elementary ρ production, this is already not a trivial task, even more complicated by possible in-medium modifications of the ρ meson. Furthermore, the size of the ω peak in pNb crucially depends not only on the production cross section in pp collisions (which is well determined via the elementary pp data at 3.5 GeV), but also in pn, which is unknown. We assume ω production cross sections which are isospin-independent, i.e. equal in pp and pn.

In addition to the in-medium modifications of the vector mesons, also the baryonic resonances can receive similar modifications in the medium. Since the production via baryon resonances is particularly important for the ρ

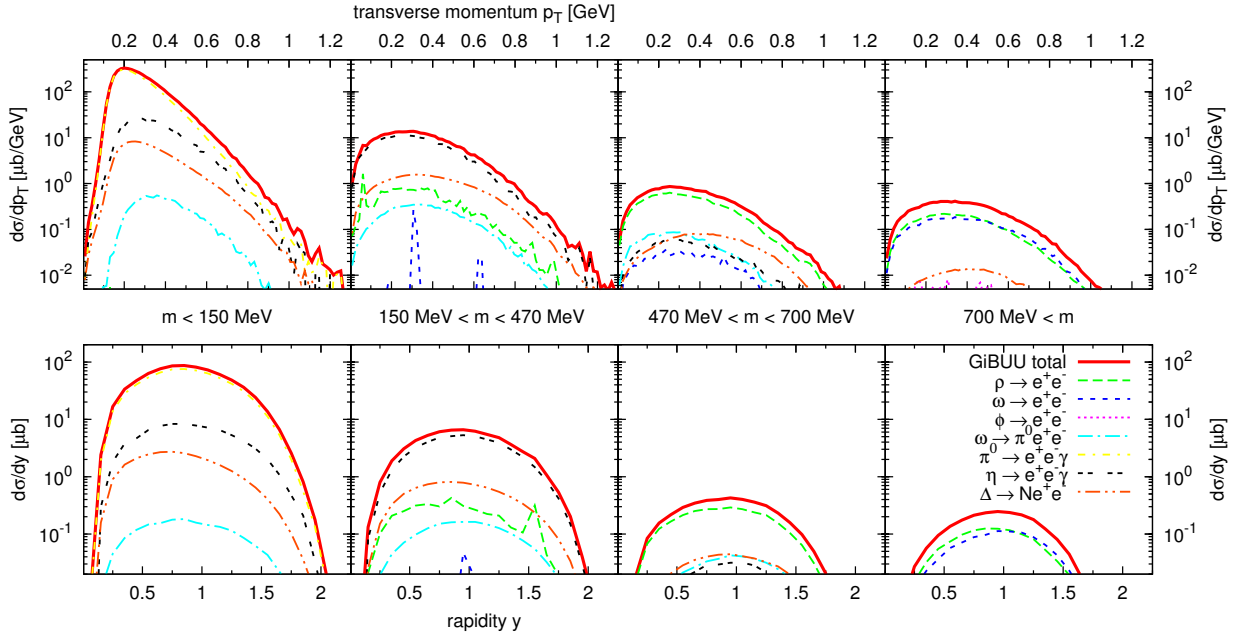


Fig. 13. (Color online) p_T and rapidity spectra of dileptons from p+Nb reactions in four mass bins.

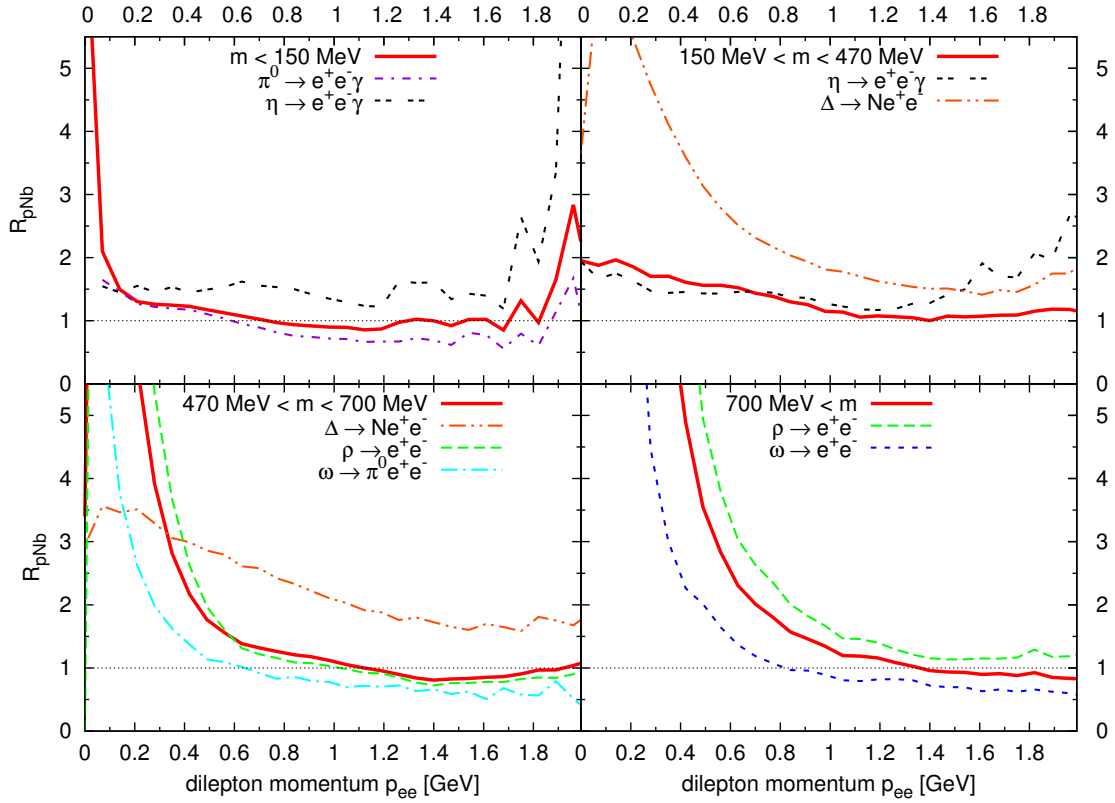


Fig. 14. (Color online) Ratio of dilepton yield from p+Nb and p+p collisions at 3.5 GeV as a function of momentum, in four mass bins.

meson, in-medium modifications of these resonances can lead to further modifications of the ρ contribution to the dilepton spectrum, which should be considered in future investigations.

The p_T and rapidity spectra for p+Nb are depicted in fig. 13 with the same mass binning as in the p+p case. The shown p_T and rapidity spectra do not include any in-medium effects for the vector mesons and are not significantly sensitive to such modifications.

For a further discussion of the nuclear effects, it is useful to consider the quantity

$$R_{\text{pNb}} = \frac{\sigma_{\text{pNb} \rightarrow e^+e^-X}}{\sigma_{\text{pp} \rightarrow e^+e^-X}} \cdot \frac{\sigma_{\text{pp} \rightarrow X}}{\sigma_{\text{pNb} \rightarrow X}}, \quad (27)$$

i.e., the ratio of dilepton yields in pNb vs. pp, normalized to the total cross section for these reactions (whose ratio is roughly $\sigma_{\text{pNb} \rightarrow X} / \sigma_{\text{pp} \rightarrow X} \approx 25.0$ in our simulations). If medium effects are negligible, this quantity will be unity. Therefore, any deviation from unity indicates medium effects such as, e.g., absorption ($R < 1$) or secondary production ($R > 1$). Fig. 14 shows R_{pNb} as a function of the dilepton momentum in four different invariant-mass bins, with the contributions from the different source channels. While R_{pNb} is relatively flat in the π^0 region, the higher mass bins show a strong enhancement at low momenta, which can be understood as secondary particle production and/or elastic rescattering. The high momentum region in all mass bins tends to show a slight depletion, connected to absorption.

The observable R_{pNb} could also help to pin down the relative contribution of the Δ Dalitz channel to the dilepton spectrum. As can be seen in Fig. 14, the Δ 's ratio is rather large, due to the enhanced production of the $\Delta^{+,0}$ charge states in pn collisions, relative to pp. The isospin factors for $NN \rightarrow N\Delta^{+,0}$ are a factor of two larger in pn than in pp.

This isospin dependence could provide additional constraints for distinguishing the ρ and Δ contributions in the intermediate mass range of 470 - 700 MeV. Since the ρ channel dominates our simulated cocktail in this mass range (without a Δ form factor), the total value of R_{pNb} roughly follows the R -value of the ρ channel. If the spectrum would be dominated by the Δ Dalitz channel in this mass range, then the total value of R_{pNb} would be more similar to the Δ 's R -value.

7 Conclusions

We have shown that the HADES data from elementary N+N collisions can be described consistently by an extended resonance model over the whole range of beam energies. We have set up such a model based on the earlier resonance model approach by Teis et al.

For describing the dilepton mass spectrum at the highest beam energy of 3.5 GeV, an essential ingredient is a ρ spectral function, which is modified through the production via nucleon resonances, with an enhanced low-mass contribution from low-lying resonances like the $D_{13}(1520)$.

After fixing the model with the constraints given by the elementary N+N collisions, the p+Nb reaction at 3.5 GeV is reasonably well described by the GiBUU transport model, using the same input and without requiring any in-medium mass shifts. According to our model, the p+Nb data show only a limited sensitivity to collisional broadening of the ρ meson.

These results also provide the basis for a further investigation of the heavy-ion collisions at SIS energies measured by the HADES collaboration [20, 21, 23].

Acknowledgments

We thank the HADES collaboration for providing us with the data and the HADES acceptance filter and for many fruitful discussions. Special thanks go to Tetyana Galatyuk, Anar Rustamov, Manuel Lorenz and Malgorzata Gumberidze. Moreover we are grateful to Kai Gallmeister and Volker Metag for many stimulating discussions of the topics presented here. This work was supported by HIC4FAIR, HGS-HIRE and BMBF.

References

1. S. Leupold, V. Metag, U. Mosel, *Int. J. Mod. Phys. E* **19**, 147 (2010), [arXiv: 0907.2388 \[nucl-th\]](#)
2. R.S. Hayano, T. Hatsuda, *Rev. Mod. Phys.* **82**, 2949 (2010), [arXiv: 0812.1702 \[nucl-ex\]](#)
3. R. Rapp, J. Wambach, H. van Hees, *Landolt-Börnstein* **I/23**, 4 (2010), [arXiv: 0901.3289 \[hep-ph\]](#)
4. T. Hatsuda, S.H. Lee, *Phys. Rev. C* **46**, 34 (1992)
5. S. Leupold, W. Peters, U. Mosel, *Nucl. Phys. A* **628**, 311 (1998), [arXiv: 9708016 \[nucl-th\]](#)
6. M. Wood et al. (CLAS), *Phys. Rev. C* **78**, 015201 (2008), [arXiv: 0803.0492 \[nucl-ex\]](#)
7. M. Naruki, H. Funahashi, Y. Fukao, M. Kitaguchi, M. Ishino et al., *Phys. Rev. Lett.* **96**, 092301 (2006), [arXiv: 0504016 \[nucl-ex\]](#)
8. M. Nanova et al. (CBELSA/TAPS Collaboration), *Phys. Rev. C* **82**, 035209 (2010), [arXiv: 1005.5694 \[nucl-ex\]](#)
9. M. Nanova et al. (CBELSA/TAPS), *Eur. Phys. J. A* **47**, 16 (2011), [arXiv: 1008.4520 \[nucl-ex\]](#)
10. R. Porter et al. (DLS Collaboration), *Phys. Rev. Lett.* **79**, 1229 (1997), [arXiv: 9703001 \[nucl-ex\]](#)
11. D. Adamova et al. (CERES/NA45 Collaboration), *Phys. Rev. Lett.* **91**, 042301 (2003), [arXiv: 0209024 \[nucl-ex\]](#)
12. R. Arnaldi et al. (NA60 Collaboration), *Phys. Rev. Lett.* **96**, 162302 (2006), [arXiv: 0605007 \[nucl-ex\]](#)
13. H. van Hees, R. Rapp, *Phys. Rev. Lett.* **97**, 102301 (2006), [arXiv: 0603084 \[hep-ph\]](#)
14. J. Ruppert, C. Gale, T. Renk, P. Lichard, J.I. Kapusta, *Phys. Rev. Lett.* **100**, 162301 (2008), [arXiv: 0706.1934 \[hep-ph\]](#)
15. H. van Hees, R. Rapp, *Nucl. Phys. A* **806**, 339 (2008), [arXiv: 0711.3444 \[hep-ph\]](#)
16. E. Bratkovskaya, W. Cassing, R. Rapp, J. Wambach, *Nucl. Phys. A* **634**, 168 (1998), [arXiv: 9710043 \[nucl-th\]](#)
17. C. Ernst, S. Bass, M. Belkacem, H. Stoecker, W. Greiner, *Phys. Rev. C* **58**, 447 (1998), [arXiv: 9712069 \[nucl-th\]](#)

18. E. Bratkovskaya, C. Ko, Phys. Lett. B **445**, 265 (1999), [arXiv: 9809056 \[nucl-th\]](#)
19. K. Shekhter, C. Fuchs, A. Faessler, M. Krivoruchenko, B. Martemyanov, Phys. Rev. C **68**, 014904 (2003), [arXiv: 0305015 \[nucl-th\]](#)
20. G. Agakishiev et al. (HADES Collaboration), Phys. Rev. Lett. **98**, 052302 (2007), [arXiv: 0608031 \[nucl-ex\]](#)
21. G. Agakishiev et al. (HADES Collaboration), Phys. Lett. B **663**, 43 (2008), [arXiv: 0711.4281 \[nucl-ex\]](#)
22. G. Agakishiev et al. (HADES Collaboration), Phys. Lett. B **690**, 118 (2010), [arXiv: 0910.5875 \[nucl-ex\]](#)
23. G. Agakishiev et al. (HADES Collaboration), Phys. Rev. C **84**, 014902 (2011), [arXiv: 1103.0876 \[nucl-ex\]](#)
24. G. Agakishiev et al. (HADES Collaboration), Eur. Phys. J. A **48**, 64 (2012), [arXiv: 1112.3607 \[nucl-ex\]](#)
25. G. Agakishiev et al. (HADES Collaboration), Phys. Rev. C **85**, 054005 (2012), [arXiv: 1203.2549 \[nucl-ex\]](#)
26. O. Buss, T. Gaitanos, K. Gallmeister, H. van Hees, M. Kaskulov et al., Phys. Rep. **512**, 1 (2012), [arXiv: 1106.1344 \[hep-ph\]](#)
27. *GiBUU website*, <http://gibuu.physik.uni-giessen.de>
28. L. Kadanoff, G. Baym, *Quantum Statistical Mechanics* (Addison Wesley Publishing Company, 1994)
29. W. Botermans, R. Malfliet, Phys. Rep. **198**, 115 (1990)
30. *Pythia website*, <http://projects.hepforge.org/pythia6>
31. T. Sjostrand, S. Mrenna, P. Skands, JHEP **05**, 026 (2006), [arXiv: 0603175 \[hep-ph\]](#)
32. K. Gallmeister, U. Mosel, Nucl. Phys. A **826**, 151 (2009), [arXiv: 0901.1770 \[hep-ex\]](#)
33. J. Weil, K. Gallmeister, U. Mosel, PoS **BORMIO2011**, 053 (2011), [arXiv: 1105.0314 \[nucl-th\]](#)
34. S. Teis, W. Cassing, M. Effenberger, A. Hombach, U. Mosel et al., Z. Phys. A **356**, 421 (1997), [arXiv: 9609009 \[nucl-th\]](#)
35. D. Manley, E. Saleski, Phys. Rev. D **45**, 4002 (1992)
36. R. Arndt, W. Briscoe, I. Strakovsky, R. Workman, Phys. Rev. C **74**, 045205 (2006), [arXiv: 0605082 \[nucl-th\]](#)
37. K. Nakamura et al. (Particle Data Group), J. Phys. G **37**, 075021 (2010)
38. V. Shklyar, H. Lenske, U. Mosel, G. Penner, Phys. Rev. C **71**, 055206 (2005), [arXiv: 0412029 \[nucl-th\]](#)
39. A. Anisovich, R. Beck, E. Klempt, V. Nikonov, A. Sarantsev et al., Eur. Phys. J. A **48**, 15 (2012), [arXiv: 1112.4937 \[hep-ph\]](#)
40. M. Effenberger, E.L. Bratkovskaya, W. Cassing, U. Mosel, Phys. Rev. C **60**, 027601 (1999), [arXiv: 9901039 \[nucl-th\]](#)
41. M. Effenberger, Ph.D. thesis, Justus-Liebig-Universität Gießen (1999), available online at <http://theorie.physik.uni-giessen.de/>
42. J. Cugnon, J. Vandermeulen, D. L'Hote, Nucl. Instrum. Meth. B **111**, 215 (1996)
43. L. Montanet et al. (Particle Data Group), Phys. Rev. D **50**, 1173 (1994)
44. V. Dmitriev, O. Sushkov, C. Gaarde, Nucl. Phys. A **459**, 503 (1986)
45. H. Calen, J. Dyring, K. Fransson, L. Gustafsson, S. Haegstroem et al., Phys. Rev. C **58**, 2667 (1998)
46. F. Balestra, Y. Bedfer, R. Bertini, L. Bland, A. Brenschede et al., Phys. Rev. C **69**, 064003 (2004)
47. X. Cao, B.S. Zou, H.S. Xu, Phys. Rev. C **81**, 065201 (2010), [arXiv: 1004.0140 \[nucl-th\]](#)
48. V. Kashevarov et al. (Crystal Ball at MAMI Collaboration, TAPS Collaboration, A2 Collaboration), Eur.Phys.J. **A42**, 141 (2009), [0901.3888](#)
49. U. Mosel, M. Post (2001), [arXiv: 0103059 \[nucl-th\]](#)
50. M. Post, U. Mosel, Nucl. Phys. A **699**, 169 (2002), [arXiv: 0108017 \[nucl-th\]](#)
51. G. Penner, U. Mosel, Phys. Rev. C **66**, 055212 (2002), [arXiv: 0207069 \[nucl-th\]](#)
52. A. Sibirtsev, Nucl. Phys. A **604**, 455 (1996)
53. M. Abdel-Bary et al. (COSY-TOF Collaboration), Phys. Lett. B **647**, 351 (2007), [arXiv: 0702059 \[nucl-ex\]](#)
54. E. Paryev, J. Phys. G **36**, 015103 (2009), [arXiv: 0810.1124 \[nucl-th\]](#)
55. M. Berlowski, C. Bargholtz, M. Bashkanov, D. Bogoslowsky, A. Bondar et al., Phys. Rev. D **77**, 032004 (2008)
56. T. Browder et al. (CLEO), Phys. Rev. D **56**, 5359 (1997), [arXiv: 9706005 \[hep-ex\]](#)
57. P. Mühlich, Ph.D. thesis, Justus-Liebig-Universität Gießen (2007), available online at <http://theorie.physik.uni-giessen.de/>
58. L.G. Landsberg, Phys. Rep. **128**, 301 (1985)
59. B. Spruck, Ph.D. thesis, Justus-Liebig-Universität Gießen (2008), <http://geb.uni-giessen.de/geb/volltexte/2008/6667/>
60. R. Arnaldi et al. (NA60), Phys. Lett. B **677**, 260 (2009), [arXiv: 0902.2547 \[hep-ph\]](#)
61. H. Berghäuser, V. Metag, A. Starostin, P. Aguar-Bartolome, L. Akasoy et al., Phys. Lett. B **701**, 562 (2011)
62. E. Bratkovskaya, O. Teryaev, V. Toneev, Phys. Lett. B **348**, 283 (1995)
63. G. Agakishiev et al. (HADES Collaboration), Eur.Phys.J. **A48**, 74 (2012), [arXiv: 1203.1333 \[nucl-ex\]](#)
64. E.L. Bratkovskaya, W. Cassing, Nucl. Phys. A **619**, 413 (1997), [arXiv: 9611042 \[nucl-th\]](#)
65. M.I. Krivoruchenko, A. Faessler, Phys. Rev. D **65**, 017502 (2002), [arXiv: 0104045 \[nucl-th\]](#)
66. M. Krivoruchenko, B. Martemyanov, A. Faessler, C. Fuchs, Annals Phys. **296**, 299 (2002), [arXiv: 0110066 \[nucl-th\]](#)
67. G. Caia, V. Pascalutsa, J. Tjon, L. Wright, Phys. Rev. C **70**, 032201 (2004), [arXiv: 0407069 \[nucl-th\]](#)
68. Q. Wan, F. Iachello, Int. J. Mod. Phys. A **20**, 1846 (2005)
69. G. Ramalho, M. Pena, Phys. Rev. D **85**, 113014 (2012), [arXiv: 1205.2575 \[hep-ph\]](#)
70. M. Post, S. Leupold, U. Mosel, Nucl. Phys. A **689**, 753 (2001), [arXiv: 0008027 \[nucl-th\]](#)
71. C. Gale, J.I. Kapusta, Phys. Rev. C **40**, 2397 (1989)
72. G. Wolf, G. Batko, W. Cassing, U. Mosel, K. Niita et al., Nucl. Phys. A **517**, 615 (1990)
73. R. Shyam, U. Mosel, Phys. Rev. C **67**, 065202 (2003), [arXiv: 0303035 \[hep-ph\]](#)
74. L. Kaptari, B. Kampfer, Nucl. Phys. A **764**, 338 (2006), [arXiv: 0504072 \[nucl-th\]](#)
75. R. Shyam, U. Mosel, Phys. Rev. C **82**, 062201 (2010), [arXiv: 1006.3873 \[hep-ph\]](#)
76. *HADES website*, <http://www-hades.gsi.de>
77. T. Galatyuk, *private communications*
78. R.B. Wiringa, V. Stoks, R. Schiavilla, Phys. Rev. C **51**, 38 (1995), [arXiv: 9408016 \[nucl-th\]](#)
79. M. Schäfer, H. Donges, A. Engel, U. Mosel, Nucl. Phys. A **575**, 429 (1994), [arXiv: 9401006 \[nucl-th\]](#)

80. F. de Jong, U. Mosel, Phys. Lett. B **379**, 45 (1996), [arXiv: 9602016 \[nucl-th\]](#)
81. B. Martemyanov, M. Krivoruchenko, A. Faessler, Phys. Rev. C **84**, 047601 (2011), [arXiv: 1108.4265 \[nucl-th\]](#)
82. A. Baldini, V. Flaminio, W. Moorhead, D. Morrison, H. Schopper, Landolt-Börnstein. New Series, 1/12B (1988)
83. D. Schumacher, S. Vogel, M. Bleicher, Acta Phys. Hung. A **27**, 451 (2006), [arXiv: 0608041 \[nucl-th\]](#)
84. E. Bratkovskaya, W. Cassing, M. Effenberger, U. Mosel, Nucl. Phys. A **653**, 301 (1999), [arXiv: 9903009 \[nucl-th\]](#)
85. E. Bratkovskaya, W. Cassing, Nucl. Phys. A **807**, 214 (2008), [arXiv: 0712.0635 \[nucl-th\]](#)
86. K. Schmidt, E. Santini, S. Vogel, C. Sturm, M. Bleicher et al., Phys. Rev. C **79**, 064908 (2009), [arXiv: 0811.4073 \[nucl-th\]](#)
87. A. Titov, B. Kämpfer, E. Bratkovskaya, Phys. Rev. C **51**, 227 (1995)
88. W. Wilson et al. (DLS Collaboration), Phys. Rev. C **57**, 1865 (1998), [arXiv: 9708002 \[nucl-ex\]](#)
89. *DLS website*, <http://macdls.lbl.gov/DLS.WWW.Files>
90. M. Weber (HADES Collaboration), Int. J. Mod. Phys. A **26**, 737 (2011)
91. M. Lorenz, *private communications*
92. W. Cassing, S. Juchem, Nucl. Phys. A **665**, 377 (2000), [arXiv: 9903070 \[nucl-th\]](#)
93. S. Leupold, Nucl. Phys. A **672**, 475 (2000), [arXiv: 9909080 \[nucl-th\]](#)
94. M. Kotulla et al. (CBELSA/TAPS Collaboration), Phys. Rev. Lett. **100**, 192302 (2008), [arXiv: 0802.0989 \[nucl-ex\]](#)

Pseudo-Critical Enhancement of Thermal Photons in Relativistic Heavy-Ion Collisions?

Hendrik van Hees^{a,b}, Min He^c, Ralf Rapp^d

^aFrankfurt Institute for Advanced Studies, Ruth-Moufang-Straße 1, D-60438 Frankfurt, Germany

^bInstitute for Theoretical Physics, Max-von-Laue-Straße 1, D-60438 Frankfurt, Germany

^cDepartment of Applied Physics, Nanjing University of Science and Technology, Nanjing 210094, China

^dCyclotron Institute and Department of Physics&Astronomy, Texas A&M University, College Station, TX 77843-3366, U.S.A.

Abstract

We compute the spectra and elliptic flow of thermal photons emitted in ultrarelativistic heavy-ion collisions (URHICs) at RHIC and LHC. The thermal emission rates are taken from complete leading-order rates for the QGP and hadronic many-body calculations including baryons and antibaryons, as well as meson-exchange reactions (including Bremsstrahlung). We first update previous thermal fireball calculations by implementing a lattice-QCD based equation of state and extend them to compare to recent LHC data. We then scrutinize the space-time evolution of Au-Au collisions at RHIC by employing an ideal hydrodynamic model constrained by bulk- and multistrange-hadron spectra and elliptic flow, including a non-vanishing initial flow. We systematically compare the evolutions of temperature, radial flow, azimuthal anisotropy and four-volume, and exhibit the temperature profile of thermal photon radiation. Based on these insights, we put forward a scenario with a “pseudo-critical enhancement” of thermal emission rates, and investigate its impact on RHIC and LHC direct photon data.

Keywords: heavy-ion collisions, QCD phase diagram, direct photons

PACS: 25.75.-q, 25.75.Dw, 25.75.Nq

1. Introduction

The thermal emission rate of photons from strongly interacting matter encodes several interesting properties of the radiating medium (see, *e.g.*, Refs. [1, 2, 3, 4, 5] for reviews). Its spectral slope reflects the temperature of the system while its magnitude is related to the interaction strength of the charge carriers. In ultrarelativistic heavy-ion collisions (URHICs), the size of the interacting fireball is much smaller than the mean-free path of photons. Thus, the latter can probe the hot and dense interior of the medium. However, the observed photon spectra receive contributions from all reaction stages, *i.e.*, primordial NN collisions, pre-equilibrium, quark-gluon plasma (QGP) and hadronic phases, plus final-state decays of short-lived resonances (these so-called “direct” photons exclude decays of long-lived hadrons, *e.g.*, π and η). Calculations of direct-photon spectra require good control over both the microscopic emission rates and the space-time evolution of the medium. The latter not only determines the local emission temperature, but also

Preprint submitted to Elsevier

September 12, 2014

the collective-flow field which generally imparts a net blue-shift on the radiated photons. In addition, the azimuthal asymmetry of the thermal photon spectra, v_2^γ , is of interest [6, 7, 8, 9, 10, 11, 12, 13]: since the bulk v_2 requires several fm/c to build up, the observed value for photons helps to further constrain their emission history.

Direct-photon spectra in URHICs have been extracted in Pb-Pb($\sqrt{s} = 0.017$ ATeV) collisions at the Super Proton Synchrotron (SPS) [14], in Au-Au($\sqrt{s} = 0.2$ ATeV) at the Relativistic Heavy-Ion Collider (RHIC) [15], and in Pb-Pb($\sqrt{s} = 2.76$ ATeV) at the Large Hadron Collider (LHC) [16]. At SPS, various theoretical models could approximately reproduce the measured spectra by adding thermal radiation from an equilibrated expanding fireball to a primordial component estimated from pp data [17, 18, 19, 20, 21]. The thermal yield prevailed over the primordial one up to transverse momenta of $q_T \approx 2$ -4 GeV. However, a decomposition into contributions from QGP and hadronic radiation, which would allow for a better characterization of the origin of the signal, remains ambiguous. By subtracting the primordial component from their data, the PHENIX collaboration extracted the “excess radiation” and determined its inverse-slope parameter (“effective temperature”) in Au-Au collisions at RHIC as $T_{\text{eff}} = 221 \pm 19^{\text{stat}} \pm 19^{\text{syst}}$ MeV. Accounting for the aforementioned blue-shift effect, this result indicates that most of the radiation emanates from matter temperatures $T < 200$ MeV, challenging the notion of early QGP radiation [9]. A subsequent first measurement of the direct-photon v_2 supports this finding [22]: in the regime where thermal radiation is expected to be large, $q_T \lesssim 3$ GeV, $v_2^\gamma(q_T)$ turns out to be comparable to that of pions, which are only emitted at the end of the fireball evolution, *i.e.*, at thermal freezeout, $T_{\text{fo}} \simeq 100$ MeV. The large v_2^γ , also found at LHC [23], thus puts rather stringent constraints on the origin of the excess photons.

In previous work [9] we have calculated thermal photon spectra at RHIC, differing from existing calculations in mainly two aspects. First, a more extensive set of hadronic thermal photon rates has been employed [19], which, in particular, includes the contributions from baryons and antibaryons (known to be important in the dilepton context [24, 25]). These rates approximately match complete leading-order (LO) QGP rates around the pseudo-critical temperature, $T_{\text{pc}} \simeq 170$ MeV [26], thus rendering a near continuous emissivity across the transition region. Second, a schematic medium evolution was constructed utilizing a blast-wave type elliptic-fireball model, quantitatively fit to spectra and v_2 of bulk hadrons (π , K, p) at $T_{\text{fo}} \simeq 100$ MeV and multistrange hadrons (e.g., ϕ and Ω^-) at $T_{\text{ch}} = 170$ MeV. The implementation of this “sequential freezeout” is phenomenologically motivated [27], and, in particular, leads to a saturation of the bulk-medium v_2 close to the transition regime, after about 4-6 fm/c for central and semi-central Au-Au collisions at RHIC. As a result, the direct-photon v_2 increased by a factor of ~ 3 over existing calculations, reaching into the error bars of the PHENIX data.

In the present paper we expand on and scrutinize these findings by extending the calculations to LHC energy and then employing a previously constructed ideal hydrodynamic bulk-evolution [28] to conduct a detailed comparison to the emission characteristics of the fireball. Much like the latter, this hydro evolution has been quantitatively constrained by bulk-hadron spectra and v_2 , utilizing the concept of sequential freezeout. Both evolutions will be based on a lattice-QCD equation of state (EoS) for the QGP, matched to a hadron resonance gas (HRG) with chemical freezeout. The comparisons will encompass the time evolution of radial and elliptic flow, temperature, four volume and photon emission profile. Motivated by these comparisons, which identify the transition

region as a key contributor to thermal photon spectra, we conjecture an enhancement of the currently available photon emission rates around T_{pc} and explore in how far this could help to resolve the discrepancies with the data.

Our article is organized as follows. In Sec. 2 we recall basic ingredients and features of the fireball (Sec. 2.1) and hydrodynamic (Sec. 2.2) bulk evolutions, including analyses of their time and temperature profiles of collective flow and four volume (Sec. 2.3). In Sec. 3 we investigate the spectra and elliptic flow of thermal photons emitted from the fireball (Sec. 3.1) and hydro (Sec. 3.2), and (after adding primordial production) compare to recent RHIC and LHC data. In Sec. 4 we analyze the differences in the fireball and hydro photon results in view of the insights from Sec. 2 and discuss possible origins of current discrepancies with data. We conclude and outline future investigations in Sec. 5.

2. Bulk Evolution Models

The calculation of thermal-photon spectra in URHICs is based on the differential emission rate per unit phase space from a strongly interacting medium of temperature T and baryon-chemical potential μ_B ,

$$q_0 \frac{dN_\gamma}{d^4x d^3q} = - \frac{\alpha_{EM}}{\pi^2} f^B(q_0; T) \times \text{Im} \Pi_{EM}^T(q_0 = q; \mu_B, T) . \quad (1)$$

Here, the rate is written in terms of the 3-D transverse part of the electromagnetic current correlator, Π_{EM}^T , and the thermal Bose distribution function, f^B , where $q_0 = q$ denote the energy and three-momentum of the photon in the local rest frame of the medium. This expression is leading order in the electromagnetic (EM) coupling α_{EM} , required to produce the photon without further EM interaction when traversing the fireball. Alternatively, one may express the rate in terms of photon-production scattering matrix elements, appropriately convoluted over the thermal distribution functions of the incoming particles. This approach is usually more convenient when evaluating tree-level diagrams (*e.g.*, t -channel meson exchanges) which are expected to prevail at high photon energies [19].

The calculation of a thermal photon spectrum in URHICs requires to integrate the above rate over the entire four-volume of the reaction, $V_4 = \int d^4x$, accounting for the local temperature and collective expansion velocity of the emission point. In the following, we will briefly recall how this four-volume integration is done in two different models, *i.e.*, a schematic blast-wave type fireball (Sec. 2.1) and ideal hydrodynamics (Sec. 2.2); both are based on the same equation of state and fits to the same set of bulk-hadron observables. This will be followed by a detailed comparison of the flow, temperature and four-volume profiles (Sec. 2.3).

2.1. Thermal Fireball

The thermal fireball model is based on an isotropically expanding cylinder with volume

$$V_{FB}(t) = \pi a(t)b(t)(z_0 + ct), \quad (2)$$

where the elliptic transverse area is characterized by semi-major and -minor axes, $a(t)$ and $b(t)$, respectively. Their initial values are estimated from the nuclear overlap at

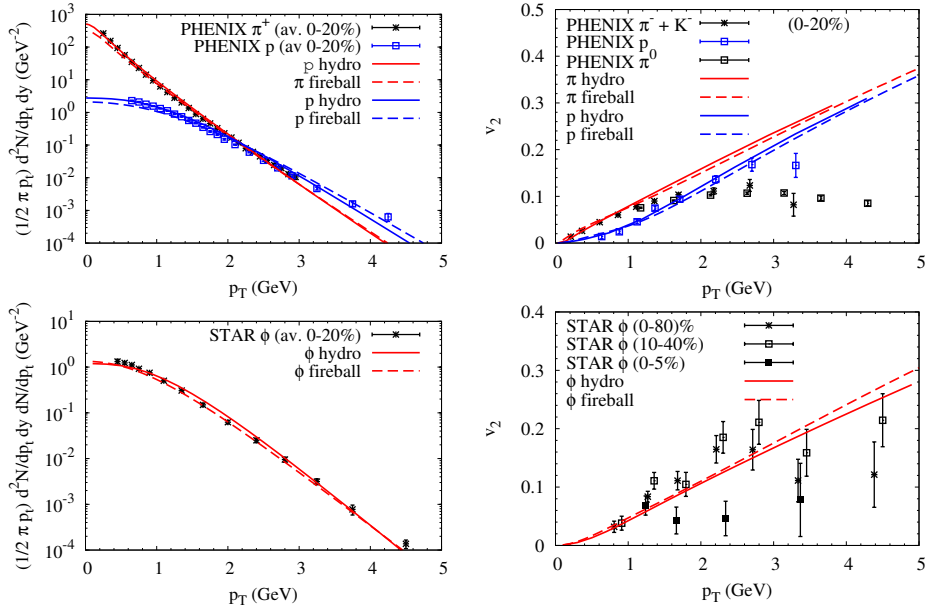


Figure 1: (Color online) Fits to the spectra and elliptic flow of light hadrons ($T_{fo} \simeq 110$ MeV, upper two panels) and ϕ mesons ($T_{fo} = 160$ MeV, lower two panels) in Au-Au($\sqrt{s} = 200$ AGeV) collisions, using EoS *latPHG* within either the fireball (dashed lines) or ideal hydrodynamic model (solid lines). The data are taken from Refs. [33, 34, 35, 36].

given impact parameter, while the initial longitudinal size, z_0 , controls the formation time of the thermal medium. Assuming a constant total entropy, S_{tot} , of the fireball at given collision centrality (fixed by the observed number of charged particles), the time evolution of the entropy density follows as $s(t) = S_{tot}/V_{FB}(t)$. Once the EoS is specified, i.e., the temperature dependence of s , one can convert $s(t)$ into $T(t)$. In our previous calculations of thermal-photon spectra [9] we used a quasi-particle QGP EoS with a first-order transition into a HRG and chemical freezeout at $T_c = T_{ch} = 180$ MeV [24]. Here, we update the EoS with a fit to lattice-QCD data for the QGP part [28], smoothly matched to a HRG at $T_{pc} = 170$ MeV and chemical freezeout at $T_{ch} = 160$ MeV, at both RHIC and LHC energies [29, 30]. For $T < T_{ch}$, effective chemical potentials for pions, kaons, antibaryons etc., are introduced [31] to preserve the finally observed hadron ratios extracted from the chemical-freezeout fits, while strong processes (*e.g.*, $\pi\pi \leftrightarrow \rho$) are assumed to maintain chemical equilibrium (so-called *partial* chemical equilibrium). Following Ref. [28] we refer to this EoS as “*latPHG*”.

With this set-up, the time dependence of the elliptic radii, $a(t)$ and $b(t)$, can be constructed with guidance from hydrodynamic models [32] to approximately reproduce their time evolution of the radial and elliptic flow, as well as momentum-space anisotropy [9]. In addition, the idea of sequential freeze-out has been implemented, *i.e.*, a kinetic decoupling of multistrange hadrons (*e.g.*, ϕ and Ω^-) at chemical freezeout. This requires a somewhat faster transverse expansion than in the original hydro models [32], but is

consistent with the observed phenomenon of constituent-quark number scaling of elliptic flow. Importantly, it implies that the bulk- v_2 essentially saturates close to $T_c \simeq T_{\text{ch}}$. With a suitable choice in initial conditions this can be recovered in hydrodynamic simulations [28], as we will see below. For a more accurate reproduction of the final-state hadron multiplicities compared to our previous work [9] (accounting for the modified EoS, feeddown and a narrowing of the fireball rapidity distributions due to the large transverse flow), we have reduced the total entropy in our fireball by ca. 20%. With a freeze-out temperature of $T_{\text{fo}} \simeq 100(160)$ MeV, the measured p_T spectra and elliptic flow of light (multistrange) hadrons can be reasonably well described, cf. dashed lines in Fig. 1¹. One might be concerned that the calculated $v_2(p_T)$ for thermal pions and protons exceeds the data toward higher p_T , in a regime which is still relevant for thermal photon production. However, the thermal p_T spectra start to underpredict the experimental yields data in this regime. For example, for pions with $p_T \simeq 3$ GeV, the thermal spectrum accounts for ca. 65% of the experimental yield; weighting the thermal pion- v_2 of $\sim 22\%$ with this fraction gives $\sim 14\%$, which is not far from the data, $v_2(p_T = 3\text{GeV}) \simeq 11\%$. While these estimates pertain to kinetic freezeout, the calculations for the ϕ meson represent a snapshot at $T_{\text{ch}} = 160$ MeV; they approximately follow the measured spectra and v_2 out to higher p_T .

2.2. Ideal Hydrodynamics

The hydrodynamic model used in the present study has been described in detail in Ref. [28]. It is based on the 2+1-dimensional ideal hydro code of Ref. [32] (AZHYDRO), augmented with the updated EoS described above (*latPHG*) and initial conditions tuned to reproduce bulk and multistrange hadron yields, spectra and v_2 in central and semicentral Au-Au collisions at full RHIC energy. Specifically, a rather compact initial-entropy density profile was adopted, proportional to the binary-collision density in the optical Glauber model (this is not unlike what has been obtained in gluon saturation models); with a thermalization time of $\tau_0 = 0.6$ fm/ c , the central initial temperature amounts to $T_0 = 398$ MeV in 0-20% Au-Au($\sqrt{s_{NN}} = 200$ GeV). Furthermore, a sizable initial radial flow with a surface value of around $0.13c$ has been introduced (and a very small positive v_2 to optimize the hadron fits). All of these features (lattice EoS, compact initial profile and initial radial flow) lead to a more violent radial expansion, which enables an improved description of the bulk-hadron v_2 at kinetic freezeout even within ideal hydrodynamics. At the same time, it generates an earlier saturation of the bulk-medium v_2 , which, in particular, requires multistrange hadrons to freeze out at the chemical freezeout temperature T_{ch} to reproduce their p_T spectra and v_2 (this is not unwelcome as their hadronic cross sections might be too small to maintain kinetic equilibrium at lower temperatures). A more violent expansion has also been identified as a key to the solution of the ‘‘HBT puzzle’’ [37]. As emphasized in Ref. [28], the ideal-hydro tunes are not meant to supplant principally more realistic viscous evolutions, but rather to explore limitations and flexibilities in the (ideal-) hydro description, within ‘‘reasonable’’ variations of the input. In Fig. 1, the solid lines show some of the hydro results for bulk spectra and elliptic flow in comparison to RHIC data, which turn out to be very similar to the schematic fireball.

¹We have not removed the entropy lost to multistrange hadrons (which amounts to $\sim 2\%$) from the fireball; we neglect this correction in both fireball and hydro evolution.

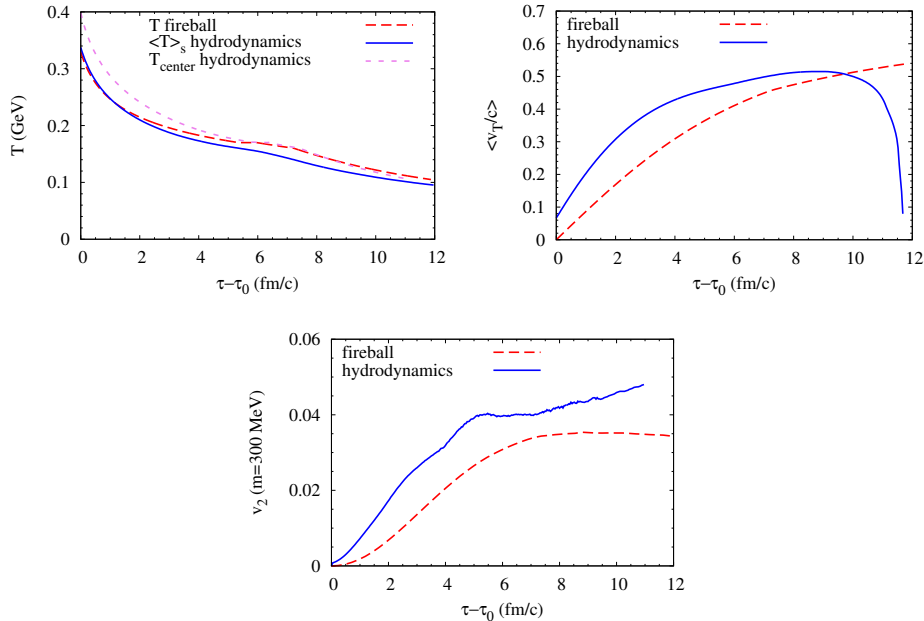


Figure 2: (Color online) Time evolution of average temperature (upper left panel), average transverse flow velocity (upper right panel) and elliptic flow (lower panel, using a particle mass of $m = 300$ MeV) in the expanding fireball (dashed lines) and hydrodynamic evolution (solid lines). In addition, the upper left panel contains the temperature evolution of the central hydro cell (short-dashed line).

2.3. Comparison of Space-Time Properties

We are now in position to systematically compare the space-time evolutions of the schematic fireball and the ideal hydro solution. We focus on 0-20% central Au-Au collisions at RHIC energy ($\sqrt{s} = 200$ AGeV), where both models describe the bulk spectra and v_2 fairly well, based on the same EoS (*latPHG*). Since the isotropic nature of the fireball is rather schematic compared to the more elaborate profiles in the hydro evolution, we investigate in this Section how this difference manifests itself in suitably averaged bulk quantities, which are expected to play an important role in the photon emission observables discussed in the next Section.

Let us first investigate the time evolution of (average) temperature, radial and elliptic flow, see Fig. 2. The temperature of the fireball is generally rather close to the average one from the hydro model, but exhibits systematically slightly higher values in the late states of the evolution (see upper left panel). This goes along with a 10-15% longer lifetime of the fireball evolution, indicating a somewhat slower cooling in the later stages. The radial flow (upper right panel of Fig. 2) starts out higher in the hydro (due to finite initial flow), but then levels off more quickly than in the fireball, eventually dropping below the latter's. For the elliptic flow comparison, we evaluate the v_2 coefficient of the momentum spectra of particles with an average mass of 300 MeV at fixed proper time (lower panel

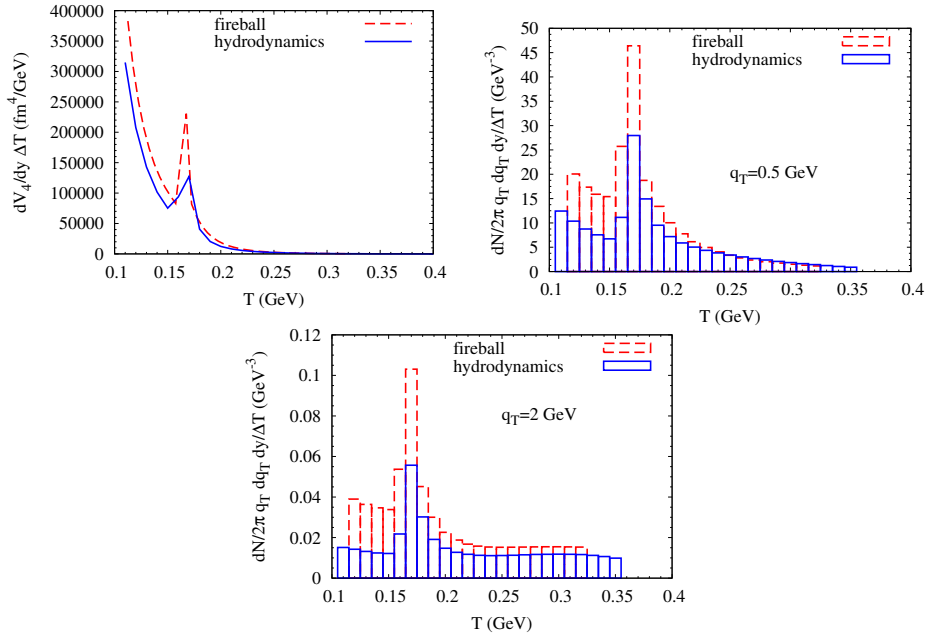


Figure 3: (Color online) Temperature evolution of the differential emission four-volume (upper left panel) and the double-differential photon emission rate (QGP for $T > T_{pc}$ and hadronic for $T < T_{pc}$) for two transverse momenta ($q_T = 0.5$ GeV and $q_T = 2$ GeV in the upper right and lower panel, respectively), in the expanding fireball (dashed lines) and hydrodynamic evolution (solid lines).

of Fig. 2). For the hydrodynamic evolution this involves a varying temperature while the fireball is spatially homogeneous at each time.

To properly interpret the observed photon spectra it is important to understand how the different emission stages contribute to the total. From the rate expression, Eq. (1), one sees that the weighting is governed by three ingredients: the (differential) four-volume, the thermal weight (Bose factor) and the EM spectral function (at the photon point). The former two are governed by the bulk-medium evolution. To make a closer connection to the underlying matter properties, we now plot pertinent quantities as a function of temperature, rather than time. The upper left panel in Fig. 3 shows the T dependence of the differential four-volume, $\Delta V_4/\Delta T$, over temperature intervals of $\Delta T = 10$ MeV (and per unit rapidity). For both fireball and hydro evolution this quantity shows a distinct maximum structure around the pseudocritical temperature of $T_{pc} \simeq 170$ MeV, as a consequence of the rapid change in the entropy density in the EoS (a remnant of the latent heat). One also finds a pronounced increase in the differential four-volume in the late(r) hadronic stages of the collision (stipulating the importance of a realistic hadronic photon emission rate). Again we find that the ideal hydro evolution seems to cool somewhat faster than the fireball (this might slightly change in a viscous

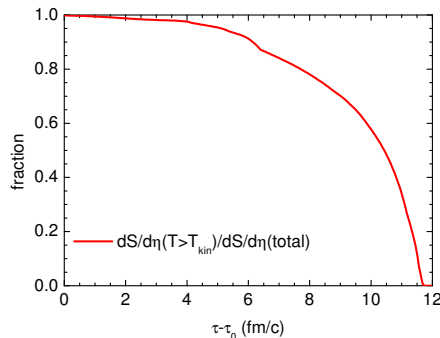


Figure 4: (Color online) Time evolution of the entropy fraction (relative to the total) which is in fluid cells at temperatures above the kinetic freezeout temperature in the hydrodynamic model.

evolution where some of the expansion work is dissipated into heat). Whereas hadron emission at kinetic freezeout in the hydro evolution is a continuous process, the fireball freezeout of the entire three-volume occurs at the end of the evolution. This difference is illustrated in Fig. 4, where we plot the *time* dependence of the fraction of the total entropy that is above the kinetic-freezeout temperature in the hydro evolution. This fraction shows a marked departure from one at times already well before the total lifetime; in contrast, this fraction is equal to one throughout the fireball evolution. Recall, however, that the three-volume at small temperatures must be very similar in both evolutions, since the total three-volume at freeze-out figures into the calculation of hadron multiplicities (and spectra), which agree rather well. Our hydro evolution, on the other hand, does not allow for the possibility that the freeze-out front “re-swallows” previously frozen-out matter cells. This effect has been studied, *e.g.*, in Ref. [38], where it was found to be significant even in the context of hadron observables. It would be interesting to investigate its impact on thermal-photon spectra.

The increase in emission four-volume is counteracted by the drop in temperature, suppressing the thermal distribution function in the rate. This renders the energy argument in the Bose function as an important scale. As is well known (see, *e.g.*, Ref. [39] for an analogous study in the dilepton context), larger energies increase the sensitivity of the exponential to temperature variations and thus will lead to a stronger weighting of earlier phases. To exhibit this interplay in a more realistic way, we include the weights from the QGP and hadronic spectral functions, $\text{Im}\Pi_{EM}$, in plotting the temperature-differential photon spectra for two representative transverse energies (see upper right and lower panel of Fig. 3); in other words, we use the full rate expression - the same for both evolution models - figuring in our comparisons to data in the following sections (recall that the AMY QGP rates (full LO result) [26] and the TRG hadronic rates [19] are nearly degenerate around T_{pc} , thus avoiding a “bias” for either phase). For low photon momenta (energies), $q_T = 0.5 \text{ GeV}$, the “phase transition” peak observed in the four-volume is remarkably enhanced, but also the high-temperature part now exhibits significant emission strength. As expected, the high-temperature component increases further at larger momentum ($q_T = 2 \text{ GeV}$), albeit not dramatically. A pronounced peak

around T_{pc} persists also for these kinematics.

This analysis clearly identifies the importance of the “pseudo-critical” regime, around T_{pc} , for thermal photon radiation, as found in Ref. [9]. The macrophysics encoded in the underlying EoS plays an important role through a rapid change in entropy density over a rather small temperature window, possibly augmented by a reduction in the velocity of sound, c_s^2 , figuring into the hydro evolution (a pertinent slowing down has not been implemented into the fireball evolution). An equally important role is plaid by the microphysics, *i.e.*, relatively large hadronic emission rates, comparable to the QGP ones, in the transition region. Together with substantial flow-induced blue shifts, this led to generating a sizable photon v_2 in our previous fireball calculations [9]. These features can be recovered within hydrodynamic evolutions, *if* the collective flow is built up sufficiently fast, which can be realized via a modest initial radial-flow field and a compact initial-density profile. However, quantitative differences remain, which we further analyze in the following two sections by comparing the photon spectra from both approaches with each other and to direct photon data at RHIC and LHC.

3. Direct Photon Spectra at RHIC and LHC

All thermal photon spectra presented in this Section are based on the same emission rates, from a complete LO calculation in a perturbative QGP [26] and hadronic many-body calculations supplemented with t -channel meson exchange reactions [19] as well as $\pi\pi$ and πK Bremsstrahlung [40]. We also note that short-lived (strong) resonance decays are usually not subtracted from the experimental spectra. To account for these “strong feeddown” photons (*e.g.*, $\Delta \rightarrow N\gamma$, etc.), we follow Refs. [41, 9] by running our evolution for an extra 1 fm/c after kinetic freezeout. Strictly speaking, as elaborated in Ref. [42], these final-state decays would have to be calculated with slightly modified kinematics compared to thermal processes (with an extra Lorentz- γ factor), but we neglect this difference in the present study. Ultimately, their contribution to the total direct- γ v_2 turns out to be rather modest (*e.g.*, increasing it by typically 5-10% around $q_T = 2$ GeV), and even less for the spectra.

3.1. Thermal Fireball

We start by updating the fireball calculations at RHIC, which in Ref. [9] were conducted with a first-order EoS (and a by now outdated chemical-freezeout temperature of $T_{ch} = 180$ MeV), by implementing the *latPHG* EoS of Ref. [28] with chemical freezeout at $T_{ch} = 160$ MeV. The resulting thermal spectra are compared to the results of Ref. [9] in Fig. 5 using the same total entropy. Since the partitioning of hadronic and QGP emission in the mixed phase of the first-order transition is now entirely assigned to the nonperturbative QGP phase, and due to a lower critical temperature in the *latPHG*, the QGP contribution significantly increases while the hadronic part decreases compared to the first-order scenario. This “reshuffling” by itself corroborates that the major portion of the thermal emission originates from around the phase transition region, independent of the details of the EoS. While the total (integrated) photon yield is not changed much (analogous to what has been found for low-mass dileptons [25]), the high- q_T part of the spectrum benefits from the increased temperature in the QGP close to T_{pc} and from the later chemical freezeout in the hadronic phase, which slows down the drop in temperature

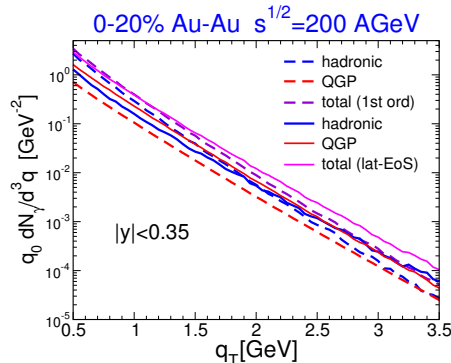


Figure 5: (Color online) Comparison of thermal photon spectra in Au+Au($\sqrt{s} = 0.2A$ TeV) collisions from an expanding fireball using either a first-order quasiparticle-QGP + HRG EoS with $T_c = T_{cm} = 180$ MeV [9] (dashed lines) or a cross-over IQCD + HRG EoS with $T_{pc} = 170$ MeV and $T_{ch} = 160$ MeV; red, blue and purple/pink lines represent QGP, hadronic and total contributions, respectively.

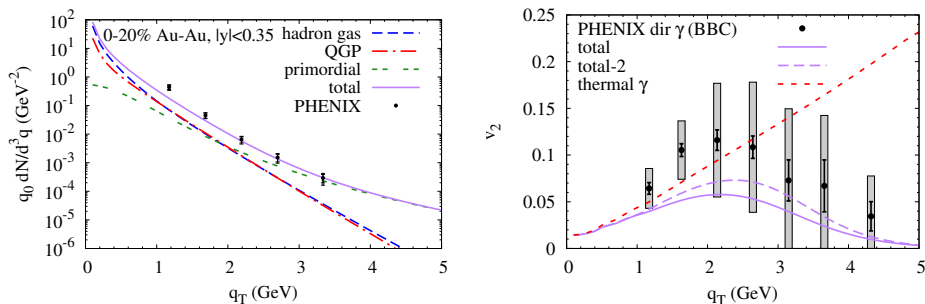


Figure 6: (Color online) Direct photon spectra (left panel) and elliptic flow (right panel) from the expanding fireball in 0-20% Au+Au($\sqrt{s} = 0.2A$ TeV) collisions with updated total entropy using the *latPHG* EoS, compared to PHENIX data [15, 22]. In the left panel, blue dashed, red dashed-dotted, green short-dashed-dotted and purple solid lines correspond to hadronic, QGP and primordial contributions, and their sum (“total”), respectively. The primordial contribution is based on the PHENIX pp parameterization. In the right panel, the red short-dashed line is the combined thermal v_2 ; the purple solid and long-dashed lines are the total direct-photon v_2 using two different primordial contributions, either the PHENIX pp parameterization (as in the left panel) or an x_t -scaling ansatz (labeled “total-2”). Both primordial contributions are assumed to carry vanishing v_2 .

that arises in the presence of pion (and other effective) chemical potentials (for the inclusive yields, and at low q_T , the faster temperature drop is (over-) compensated by the fugacity factors).

As mentioned above, we have further updated our fireball calculations by a careful readjustment of the entropy when using *latPHG*, leading to a 20% decrease compared to Ref. [9]. With our nonlinear dependence of thermal photon production on the charged-particle multiplicity, $\propto N_{ch}^x$ with $x \simeq 1.5$ [19, 25] (larger at higher q_T), the thermal yields are somewhat reduced compared to our earlier results. The comparison to the PHENIX data for direct photons in Fig. 6 shows discrepancies at low q_T for both spectral yields and

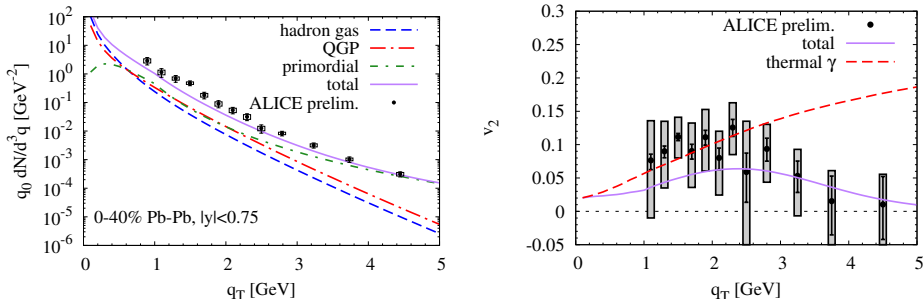


Figure 7: (Color online) Direct photon spectra (left panel) and elliptic flow (right panel) from the expanding fireball in 0-40% Pb+Pb($\sqrt{s} = 2.76$ ATeV) collisions using *latPHG* EoS, compared to preliminary ALICE data [16, 23]. In the left panel, red, blue, green and purple lines represent QGP, hadronic and primordial contributions, as well as the total, respectively. In the right panel we show the combined thermal v_2 (red dashed line) and the total v_2 (purple solid line).

v_2 , while for $q_T \geq 2$ GeV the calculations are within the experimental errors. We illustrate uncertainties in the determination of the primordial photon component due to initial hard NN scatterings: on the one hand, we used a phenomenological parameterization by the PHENIX collaboration of their pp data [15]; on the other hand, we used the x_t -scaling ansatz of Ref. [43], fitted to the high- q_T part of the PHENIX pp data with a K -factor of 2.5. The latter spectrum turns out to be somewhat smaller than the PHENIX parameterization at small q_T . This has rather little impact on the total q_T spectrum, but it affects the v_2 more significantly, inducing an increase of the total direct-photon v_2 of up to $\sim 25\%$ around $q_T \simeq 2.5$ GeV. Further theoretical studies of the hard component are needed to better quantify this effect, *e.g.*, via a suppression of fragmentation photons or nuclear effects on the initial parton distribution functions.

Finally, we turn to LHC energies, where preliminary direct-photon data are available from ALICE for 0-40% central Pb+Pb($\sqrt{s} = 2.76$ ATeV) collisions [16, 23]. We model these reactions with an average charged-particle multiplicity of $dN_{\text{ch}}/dy = 1040$ over a rapidity interval of $|y| < 0.75$. For primordial photon production from binary NN collisions, we employ the x_t -scaling ansatz [43], fitted to the high- q_T ALICE photon spectra with a K -factor of 2. The description of the spectra and v_2 is at a comparable level as at RHIC, with indications for an underestimate in both observables in the regime where thermal radiation is most significant, cf. Fig. 7.

3.2. Ideal Hydrodynamics

The direct-photon results from the ideal-hydro tune with *latPHG* EoS and default emission rates at RHIC are displayed in Fig. 8. The QGP contribution to the q_T spectra agrees within ca. 30% with the fireball results, but the hadronic portion falls short by a larger margin, especially toward higher q_T . This is not unexpected as the lifetime of the hydro evolution in the hadronic phase is noticeably smaller, due to a faster cooling in the local rest frame of the ideal hydro cells (leading to smaller four-volumes, recall Fig. 3). In addition, the average temperature in the late stages is smaller in hydrodynamics than in the fireball (cf. upper left panel of Fig. 2), which leads to a reduction especially in the high- q_T region of the hadronic emission. Consequently, the hydro spectra and

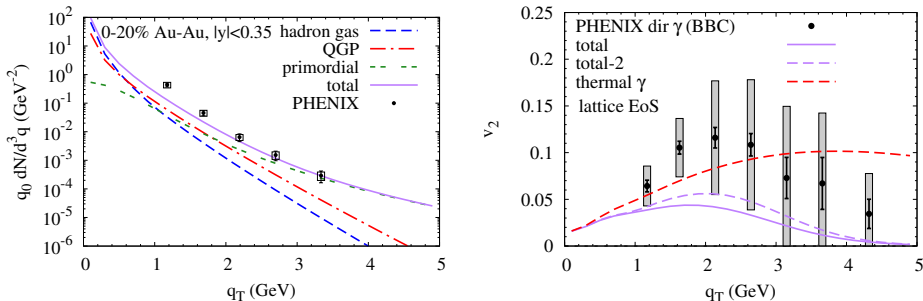


Figure 8: (Color online) Direct photon spectra (left panel) and v_2 (right panel) in Au+Au($\sqrt{s} = 0.2$ ATeV) using ideal hydrodynamics, compared to PHENIX data [15, 22]; line identifications as Fig. 6.

v_2 come out lower than for the fireball evolution; this increases the discrepancy with the PHENIX data for both observables, although not by much. Both evolution models result in an underestimate of the first two data points of the PHENIX spectra, and barely reach into the lower portions of the error bars of the v_2 data: the maximal v_2 reaches $\sim 4.4\%$ for the hydrodynamic evolution, compared to $\sim 5.7\%$ for the fireball, both when using the PHENIX pp baseline spectra (larger for the x_t scaling ansatz). However, our hydro results are well above other hydrodynamic calculations reported in the literature [8, 10, 44]. One difference lies in a faster build-up of the v_2 , which essentially saturates when the system reaches the pseudo-critical region in the cooling process, for both fireball and hydro (cf. lower panel of Fig. 2). As mentioned above, this feature is essential in describing the spectra and v_2 of multistrange hadrons with an early kinetic freezeout close to the chemical freezeout temperature, and thus rather well motivated by hadron phenomenology (including the constituent-quark number scaling of v_2). In the hydrodynamic modeling this can be realized by initial conditions including a finite transverse flow at thermalization, together with a compact energy-density profile. Both features increase the transverse flow early on, which ultimately leads to an earlier saturation of v_2 (since the initial spatial anisotropy is converted faster into momentum space); it also increases the blue shift of the photons emitted from around T_{pc} , which helps to build up the photon yield with large v_2 in the $q_T = 2-3$ GeV region. Another difference to existing hydro calculations is the larger rate in the hadronic phase, in particular the contributions associated with the photon point of the in-medium ρ spectral function, which includes sources from interactions involving baryons and antibaryons [41] and higher excited meson resonances [45].

Next, we turn to our hydro results at LHC, adopting a similar ansatz for the initial conditions as at RHIC, *i.e.*, with a finite transverse flow and compact entropy density profile. A factor of ~ 2 underestimate of the preliminary photon spectra measured by ALICE in 0-40% Pb-Pb($\sqrt{s} = 2.76$ ATeV) is found for momenta below $q_T \simeq 2$ GeV, see left panel of Fig. 9. The calculated v_2 is not inconsistent with these data within the current experimental uncertainties, see right panel of Fig. 9. Although the hadronic component in the thermal spectra is again considerably smaller than in the fireball spectra, the relatively stronger QGP component in both calculations compared to RHIC renders the overall impact of the hadronic emission less relevant. The QGP component from the

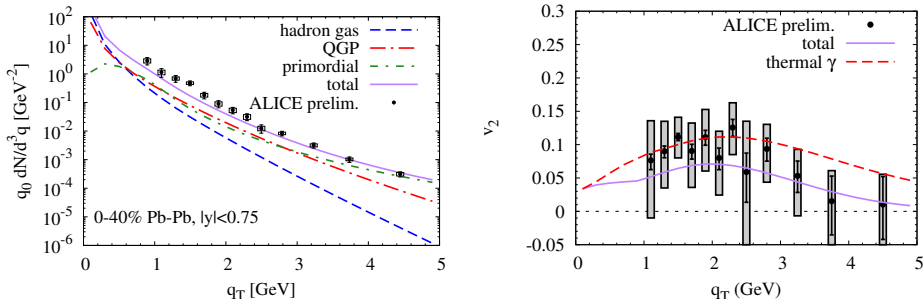


Figure 9: (Color online) Direct photon spectra (left panel) and v_2 (right panel) in 0-40% Pb+Pb($\sqrt{s} = 2.76$ ATeV) using ideal hydrodynamics, compared to preliminary ALICE data [16, 23]; line identifications as in Fig. 8.

hydro is now somewhat stronger than from the fireball (especially at high q_T), leading to closer agreement in the total photon spectra and v_2 , and also with the data. Note that the v_2 of the thermal component at $q_T \gtrsim 3$ GeV is significantly larger for the fireball than for the hydro (cf. dashed lines in the right panels of Figs. 7 and 9, respectively), due to the larger hadronic component in the former.

4. Discussion

The general trend of our results reported above for both fireball and hydrodynamic evolutions is an underestimate of both spectra and v_2 for both PHENIX and preliminary ALICE data for photon momenta $q_T \leq 3$ GeV, which is the region where the thermal radiation is expected to be most relevant. In the following, we will investigate possibilities how these deficits may be overcome. For simplicity, we concentrate on the hydrodynamic space-time evolution for these studies.

One option to increase thermal radiation in URHICs is a decrease of the thermalization time, τ_0 , of the medium, as investigated, *e.g.*, in Refs. [46, 9, 47]. While the total yield generally increases above $q_T > 1$ GeV, its slope becomes harder and the total v_2 becomes smaller, both not favored by the data. This reiterates the need for a softer radiation source with larger v_2 . In the following, we will stick to our default value of $\tau_0 = 0.6$ fm/ c .

In Refs. [9, 48, 44] an enhancement of the photon emission rates in the pseudo-critical region, beyond the default rates used above, has been conjectured. This may not be unexpected, from a theoretical point of view. On the QGP side, the AMY rates are based on perturbative parton rescattering, which in other contexts tends to fall short in producing sufficient interaction strength, *e.g.*, in both phenomenology and lattice calculations of η/s or the heavy-quark diffusion coefficient [49, 50]. Especially close to the hadronization transition, confining interactions are expected to play an important role (as, *e.g.*, borne out of lattice calculations for the heavy-quark free energies [51]). An increase in partonic scattering rates is a natural mechanism to also increase photon radiation (see, *e.g.*, Ref. [52]), which is quite different from a perturbative scenario with weakly interacting quasi-particles. On the hadronic side, an enhancement of the current

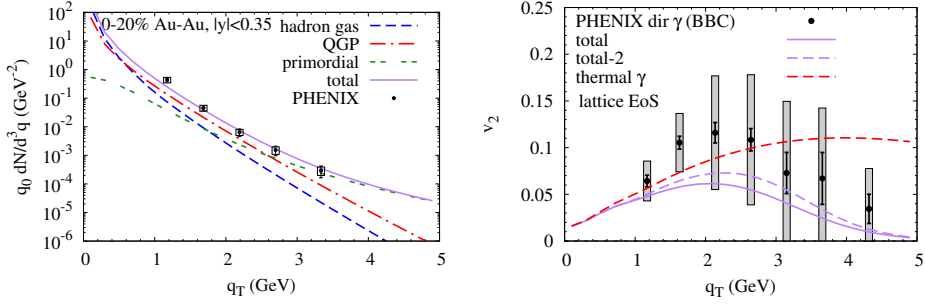


Figure 10: (Color online) Direct photon spectra (left panel) and v_2 (right panel) from hydrodynamics at RHIC when introducing a “pseudo-critical” enhancement of QGP and hadronic rates around T_{pc} , compared to PHENIX data [15, 22]; line identifications as Fig. 6.

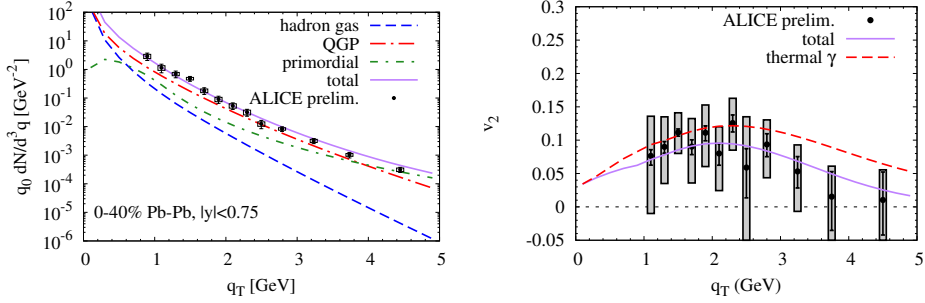


Figure 11: (Color online) Direct photon spectra (left panel) and v_2 (right panel) at LHC with enhanced photon rates around T_{pc} , compared to preliminary ALICE data [16, 23].

rates is conceivable as well, since the TRG rates (including contributions from the in-medium ρ spectral function) may not exhaust all relevant reaction channels in hadronic resonance matter; investigations to identify and calculate possibly important channels not considered thus far are in progress [53] (we note in passing that hadronic Bremsstrahlung is an unlikely candidate since its spectrum tends to be too soft [40]). To mimic a “pseudo-critical” enhancement of our default rates, we increase the latter by a baseline factor of 2, further amplified up to a maximum factor of 3 at $T_{pc} = 170$ MeV, linearly ramped up from $T = 140$ MeV and down until $T = 200$ MeV again. The results are encouraging (cf. Figs. 10 and 11): the description of both PHENIX and preliminary ALICE spectra and v_2 improves significantly. The calculated v_2 at RHIC still tends to only reach into the lower portions of the experimental errors, but we recall that larger hadronic contributions, as suggested by the fireball calculations, would help to increase it further.

Let us briefly expand on a speculation raised in Ref. [9], that there might be an hitherto undetermined uncertainty in the subtraction of the radiative $\omega \rightarrow \pi^0\gamma$ decays, since the latter have not been explicitly measured in the low- q_T region in the Au-Au environment. For this purpose, and to obtain an absolute upper estimate, we simply add to our thermal spectra (calculated with the amplified rates) the photon contribution from final-state ω decays based on our hydro ω spectra at thermal freezeout (as a three-pion

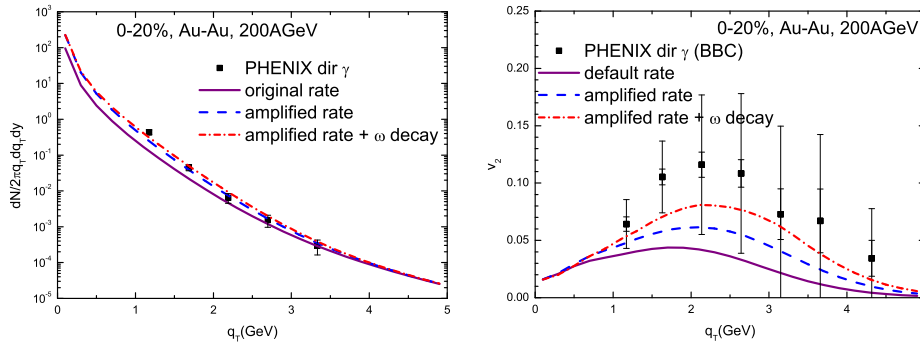


Figure 12: (Color online) Direct photon spectra (left panel) and v_2 (right panel) from hydrodynamics at RHIC when adding $\omega \rightarrow \pi^0 + \gamma$ decays at thermal freezeout to the scenario with enhanced rates (dash-dotted line), compared to the enhanced-rate (dashed line) and default-rate (solid line) scenarios, as well as the PHENIX data [15, 22]; all calculations use the PHENIX pp baseline for the primordial component.

or $\rho\pi$ resonance, the ω receives a pion fugacity factor to the third power). The result of this exercise is shown in Fig. 12, illustrating an appreciable effect on both spectra and v_2 which would still be significant if reduced by a factor of 2.

Finally, we conduct a schematic study of the effect of quark undersaturation in the early (Q)GP phases, as expected from gluon saturation models [54]. Similar to earlier calculations for thermal EM emission [55, 56, 24], we find the gluon Compton process, $gq \rightarrow q\gamma$, to still contribute appreciably (and with a harder slope than in a chemically equilibrated QGP at the same total entropy), unless the $q\bar{q}$ undersaturation is strong enough to largely suppress the early thermal yield altogether. This suppression would have to be made up by an even larger enhancement in the later phases compared to what we assumed above.

5. Summary and Conclusions

In this paper we have studied the properties of thermal photon radiation at collider energies, in an attempt to better understand recent measurements of direct photon spectra and their elliptic flow. Using QGP and hadronic thermal emission rates as available from the literature, we first focused on a detailed comparison of the space-time evolution as given by a blast-wave type fireball and ideal hydrodynamics. Both were based on the same equation of state and fits to the same set of hadron data using the concept of sequential freeze-out for multistrange and light hadrons. The relevance of this concept for photon radiation lies in a rather early saturation of v_2 and larger blue shifts by the time the expanding system reaches the phase transition region (in the hydro model, this can be realized by compact initial conditions with non-zero radial flow). We have found that the emission characteristics of the QGP part agree rather well between hydro and fireball, while the latter leads to significantly larger photon radiation in the hadronic phase, especially toward higher q_T . We traced this back to a slower cooling with larger average temperatures and radial flow in the fireball, which, at least in part, is due to a

continuous freezeout in hydrodynamics leading to an appreciable reduction of the “active” matter cells in the later stages of the evolution. Both evolution models clearly identify the transition region around $T_{pc} \simeq 170$ MeV as a key source of thermal photon emission. After the addition of primordial photons extrapolated from pp collisions, both hydro and fireball results tend to be somewhat (although not dramatically) below the measured spectra and v_2 in Au-Au and Pb-Pb collisions at RHIC and LHC, with a preference for the fireball due to its larger hadronic contribution. We then shifted our focus to the microscopic emission rates. We argued that an enhancement of the currently employed emission rates is plausible, especially in the pseudo-critical region where the medium is expected to be most strongly coupled. Upon amplifying our default rates by a baseline factor of 2, reaching up to 3 around $T_{pc} \pm 30$ MeV, we found that the photon results from the hydro model come rather close to the experimental spectra and v_2 within current uncertainties. The additional hadronic contributions suggested by the fireball model would further improve the situation. Microscopic calculations of photon rates to search for additional sources not considered thus far are underway.

Acknowledgments.— We thank C. Gale and R.J. Fries for discussions, and gratefully acknowledge fruitful exchanges at the EMMI RRTF workshop on “Direct-photon flow puzzle” organized by K. Reygers and J. Stachel. This work has been supported by the U.S. National Science Foundation through grants PHY-0969394 and PHY-1306359, by the A.-v.-Humboldt Foundation, by NSFC grant 11305089, by the German Federal Ministry of Education and Research (BMBF Förderkennzeichen 05P12RFFTS), and by the Hessian initiative for excellence (LOEWE) through the Helmholtz International Center for FAIR (HIC for FAIR).

References

- [1] J. Alam, S. Sarkar, P. Roy, T. Hatsuda and B. Sinha, *Annals Phys.* **286**, 159 (2001).
- [2] T. Peitzmann and M.H. Thoma, *Phys. Rep.* **364**, 175 (2002).
- [3] F. Arleo *et al.*, arXiv:hep-ph/0311131.
- [4] R. Rapp, J. Wambach and H. van Hees, in *Relativistic Heavy-Ion Physics*, edited by R. Stock and Landolt Börnstein (Springer), New Series **I/23A**, 4-1 (2010); [arXiv:0901.3289 [hep-ph]].
- [5] C. Gale, in *Relativistic Heavy-Ion Physics*, edited by R. Stock and Landolt Börnstein (Springer), New Series **I/23A**, 6-3 (2010); arXiv:0904.2184 [hep-ph].
- [6] R. Chatterjee, E.S. Frodermann, U.W. Heinz and D.K. Srivastava, *Phys. Rev. Lett.* **96**, 202302 (2006).
- [7] F.-M. Liu, T. Hirano, K. Werner and Y. Zhu, *Phys. Rev. C* **80**, 034905 (2009).
- [8] H. Holopainen, S. Räsänen and K.J. Eskola, *Phys. Rev. C* **84**, 064903 (2011).
- [9] H. van Hees, C. Gale and R. Rapp, *Phys. Rev. C* **84**, 054906 (2011).
- [10] M. Dion, J.-F. Paquet, B. Schenke, C. Young, S. Jeon and C. Gale, *Phys. Rev. C* **84**, 064901 (2011).
- [11] P. Mohanty, V. Roy, S. Ghosh, S.K. Das, B. Mohanty, S. Sarkar, J.-e Alam and A.K. Chaudhuri, *Phys. Rev. C* **85**, 031903 (2012).
- [12] C. Shen, U.W. Heinz, J.-F. Paquet, I. Kozlov and C. Gale, arXiv:1308.2111 [nucl-th].
- [13] O. Linnyk, W. Cassing and E. Bratkovskaya, *Phys. Rev. C* **89**, 034908 (2014).
- [14] M.M. Aggarwal *et al.* [WA98 Collaboration], *Phys. Rev. Lett.* **85**, 3595 (2000).
- [15] A. Adare *et al.* [PHENIX Collaboration], *Phys. Rev. Lett.* **104**, 132301 (2010).
- [16] M. Wilde [ALICE Collaboration], *Nucl. Phys. A* **904-905**, 573c (2013).
- [17] D.K. Srivastava and B. Sinha, *Phys. Rev. C* **64**, 034902 (2001).
- [18] P. Huovinen, P.V. Ruuskanen and S.S. Räsänen, *Phys. Lett. B* **535**, 109 (2002).
- [19] S. Turbide, R. Rapp and C. Gale, *Phys. Rev. C* **69**, 014903 (2004).
- [20] P. Mohanty, J.K. Nayak, J.-e Alam and S.K. Das, *Phys. Rev. C* **82**, 034901 (2010).
- [21] B. Bauchle and M. Bleicher, *PoS BORMIO 2010*, 062 (2010).
- [22] A. Adare *et al.* [PHENIX Collaboration], *Phys. Rev. Lett.* **109**, 122302 (2012).

- [23] D. Lohner *et al.* [ALICE Collaboration], J. Phys. Conf. Ser. **446**, 012028 (2013).
- [24] R. Rapp, Phys. Rev. C **63**, 054907 (2001).
- [25] R. Rapp, Adv. High Energy Phys. **2013**, 148253 (2013).
- [26] P.B. Arnold, G.D. Moore and L.G. Yaffe, JHEP **0112**, 009 (2001).
- [27] M. He, R.J. Fries and R. Rapp, Phys. Rev. C **82**, 034907 (2010).
- [28] M. He, R.J. Fries and R. Rapp, Phys. Rev. C **85**, 044911 (2012).
- [29] A. Andronic, P. Braun-Munzinger and J. Stachel, Nucl. Phys. A **772**, 167 (2006).
- [30] J. Stachel, A. Andronic, P. Braun-Munzinger and K. Redlich, arXiv:1311.4662 [nucl-th].
- [31] R. Rapp, Phys. Rev. C **66**, 017901 (2002).
- [32] P.F. Kolb and U.W. Heinz, In R. C. Hwa (ed.) et al.: Quark gluon plasma, 634, [nucl-th/0305084].
- [33] B.I. Abelev *et al.* [STAR Collaboration], Phys. Rev. Lett. **99**, 112301 (2007).
- [34] S.S. Adler *et al.* [PHENIX Collaboration], Phys. Rev. Lett. **91**, 182301 (2003).
- [35] S.S. Adler *et al.* [PHENIX Collaboration], Phys. Rev. C **69**, 034909 (2004).
- [36] J. Adams *et al.* [STAR Collaboration], Phys. Rev. Lett. **92**, 112301 (2004).
- [37] S. Pratt, Phys. Rev. Lett. **102** (2009) 232301.
- [38] F. Grassi, Braz. J. Phys. **35**, 52 (2005).
- [39] R. Rapp, Acta Phys. Polon. B **42**, 2823 (2011).
- [40] W. Liu and R. Rapp, Nucl. Phys. A **796**, 101 (2007).
- [41] R. Rapp and J. Wambach, Eur. Phys. J. **A6**, 415 (1999).
- [42] H. van Hees and R. Rapp, Nucl. Phys. A **806**, 339 (2008).
- [43] D.K. Srivastava, Eur. Phys. J. C **22**, 129 (2001).
- [44] C. Shen, U.W. Heinz, J.-F. Paquet and C. Gale, arXiv:1308.2440 [nucl-th].
- [45] R. Rapp and C. Gale, Phys. Rev. C **60**, 024903 (1999).
- [46] R. Chatterjee and D.K. Srivastava, Phys. Rev. C **79**, 021901 (2009).
- [47] R. Chatterjee, H. Holopainen, T. Renk and K.J. Eskola, Phys. Rev. C **85**, 064910 (2012).
- [48] R. Rapp, PoS CPOD **2013**, 008 (2013).
- [49] T. Schäfer and D. Teaney, Rept. Prog. Phys. **72**, 126001 (2009).
- [50] R. Rapp and H. van Hees, R. C. Hwa, X.-N. Wang (Ed.) Quark Gluon Plasma 4, World Scientific, 111 (2010).
- [51] O. Kaczmarek and F. Zantow, Phys. Rev. D **71**, 114510 (2005).
- [52] V.V. Goloviznin, A.M. Snigirev and G.M. Zinovjev, JETP Lett. **98** (2013) 61.
- [53] N. Holt, P. Hohler and R. Rapp, work in progress.
- [54] L. McLerran and B. Schenke, arXiv:1403.7462 [hep-ph].
- [55] M. Strickland, Phys. Lett. B **331**, 245 (1994).
- [56] D.K. Srivastava, M.G. Mustafa and B. Müller, Phys. Rev. C **56**, 1064 (1997).

Thermal Dileptons as Fireball Thermometer and Chronometer

Ralf Rapp¹ and Hendrik van Hees^{2,3}

¹*Cyclotron Institute and Physics Department, Texas A&M University, College Station, Texas 77843-3366, USA*

²*Institut für Theoretische Physik, Johann-Wolfgang-Goethe-Universität Frankfurt, Max-von-Laue-Str. 1, D-60438 Frankfurt, Germany*

³*Frankfurt Institute for Advanced Studies, Ruth-Moufang-Str. 1, D-60438 Frankfurt, Germany*

(Dated: November 18, 2014)

Thermal dilepton radiation from the hot fireballs created in high-energy heavy-ion collisions provides unique insights into the properties of the produced medium. We first show how the predictions of hadronic many-body theory for a melting ρ meson, coupled with QGP emission utilizing a modern lattice-QCD based equation of state, yield a quantitative description of dilepton spectra in heavy-ion collisions at the SPS and the RHIC beam energy scan program. We utilize these results to systematically extract the excess yields and their invariant-mass spectral slopes to predict the excitation function of fireball lifetimes and (early) temperatures, respectively. We thereby demonstrate that future measurements of these quantities can yield unprecedented information on basic fireball properties. Specifically, our predictions quantify the relation between the measured and maximal fireball temperatures, and the proportionality of excess yields and total lifetime. This information can serve as a “caloric” curve to search for a first-order QCD phase transition, and to detect non-monotonous lifetime variations possibly related to critical phenomena.

PACS numbers:

Collisions of heavy nuclei at high energies enable the creation of hot and dense strongly interacting matter, not unlike the one that filled the Universe during its first few microseconds. While the primordial medium was characterized by a nearly vanishing net baryon density (at baryon chemical potential $\mu_B \simeq 0$), heavy-ion collisions can effectively vary the chemical potential by changing the beam energies, thus facilitating systematic investigations of large parts of the phase diagram of Quantum Chromodynamics (QCD). The yields and transverse-momentum (p_T) spectra of produced hadrons have been widely used to determine the conditions of the fireball at chemical and kinetic freezeout, to infer its properties when the hadrons decouple. Electromagnetic radiation (photons and dileptons), on the other hand, is emitted throughout the evolution of the expanding fireball with negligible final-state interactions and thus, in principle, probes the earlier hotter phases of the medium [1]. In particular, dilepton invariant-mass spectra have long been recognized as the only observable which gives direct access to an in-medium spectral function of the QCD medium, most notably of the ρ meson [2–5]. They also allow for a temperature measurement which is neither distorted by blue-shift effects due to collective expansion (as is the case for p_T spectra of hadrons and photons), nor limited by the hadron formation temperature [6].

Significant excess radiation of dileptons in ultrarelativistic heavy-ion collisions (URHICs), beyond final-state hadron decays, was established at the CERN-SPS program, at collision energies of $\sqrt{s_{NN}} \simeq 20$ GeV [7, 8]. The excess was found to be consistent with thermal radiation from a locally equilibrated fireball [9, 10], with the low-mass spectra requiring substantial medium effects on the ρ line shape. The SPS dilepton program culminated in the high-precision NA60 data, which quantitatively con-

firmed the melting of the ρ resonance and realized the long-sought thermometer at masses $M > 1$ GeV, with $T = 205 \pm 12$ MeV, exceeding the pseudo-critical temperature computed in thermal lattice-QCD (lQCD), $T_{pc} = 150$ –170 MeV [11]. With the spectral shape under control, the magnitude of low-mass excess enabled an unprecedented extraction of the fireball lifetime, $\tau_{FB} = 7 \pm 1$ fm/c.

In the present letter, based on a good description of existing dilepton data from CERES, NA60 and STAR, we show that temperature and lifetime measurements through intermediate- and low-mass dileptons are a quantitative tool to characterize the fireballs formed in heavy-ion collisions. We predict pertinent excitation functions over a large range in center-of-mass energy, $\sqrt{s_{NN}} \simeq 6$ –200 GeV. The motivation for this study is strengthened by several recent developments. First, we show that the implementation of a modern lQCD equation of state (EoS) into the fireball evolution of In-In collisions at SPS recovers an accurate description of the NA60 excess data over the entire mass range, thus superseding earlier results with a first-order transition [12]. Second, the predictions of this framework turn out to agree well with the low-mass dilepton data from the STAR beam-energy scan-I (BES-I) campaign [13, 14], in Au-Au collisions from SPS to top RHIC energies, $\sqrt{s_{NN}} = 19.6, 27, 39, 62.4$ and 200 GeV [15]. Third, a very recent implementation of the in-medium ρ spectral function into coarse-grained UrQMD transport calculations yields excellent agreement with both NA60 and HADES data in Ar-KCl ($\sqrt{s_{NN}} = 2.6$ GeV) reactions [16]; and fourth, several future experiments (CBM, NA60+, NICA, STAR BES-II) plan precision measurements of dilepton spectra in the energy regime of $\sqrt{s_{NN}} \simeq 5$ –20 GeV [17], where the fireball medium is expected to reach maximal baryon density and possibly come close to a critical point in the

QCD phase diagram [18]. Our predictions thus provide a baseline for fundamental, but hitherto undetermined properties of the fireball, allowing for accurate tests of our understanding of these. In turn, marked deviations of upcoming data from the theoretical predictions will help discover new phenomena that induce unexpected structures in the lifetime and/or temperature excitation functions.

Let us recall the basic elements figuring into our calculation of dilepton excess spectra in URHICs. We assume local thermal equilibrium of the fluid elements in an expanding fireball, after a (short) initial equilibration period. The thermal radiation of dileptons is obtained from the differential production rate per unit four-volume and four-momentum [19–21],

$$\frac{dN_{ll}}{d^4x d^4q} = -\frac{\alpha^2}{3\pi^3} \frac{L(M)}{M^2} \text{Im} \Pi_{\text{EM},\mu}^\mu(M, q) f_B(q_0; T), \quad (1)$$

with $f_B(q_0; T)$: thermal Bose function, $\alpha = \frac{e^2}{4\pi} \simeq \frac{1}{137}$: electromagnetic (EM) coupling constant, $L(M)$: final-state lepton phase space factor, and $M = \sqrt{q_0^2 - q^2}$: dilepton invariant mass (q_0 : energy, q : three-momentum in the local rest frame of the medium). The EM spectral function, $\text{Im} \Pi_{\text{EM},\mu}^\mu$, is well known in the vacuum, being proportional to the cross section for $e^+e^- \rightarrow$ hadrons. In the low-mass region (LMR), $M \leq 1$ GeV, it is saturated by the light vector mesons ρ , ω and ϕ , while the intermediate-mass region (IMR), $M \geq 1.5$ GeV, is characterized by a continuum of multi-meson states.

Medium effects on the EM spectral function are calculated as follows. In hadronic matter the vector-meson propagators are computed using many-body theory based on effective Lagrangians with parameters constrained by vacuum scattering and resonance decay data [9, 22, 23]. The resulting ρ spectral function strongly broadens and melts in the phase transition region (similar for the ω , which, however, contributes less than 10%; the ϕ is assumed to decouple near T_{pc} and does not produce thermal hadronic emission). For masses $M \geq 1$ GeV, we include emission due to multi-pion annihilation using a continuum extracted from vacuum τ -decay data, augmented with medium effects due to chiral mixing [24, 25] in the LMR-IMR transition region ($1 \text{ GeV} \leq M \leq 1.5 \text{ GeV}$) [12]. For QGP emission, we employ an IQCD-motivated emission rate [15] fitted to M -dependent spectral functions above T_{pc} [26, 27] and supplemented by a finite- q dependence taken from perturbative photon rates [28]. The resulting QGP rates are quite similar to the hard-thermal-loop results [29], but with improved low-mass behavior and nontrivial three-momentum dependence. The QGP and in-medium hadronic rates are nearly degenerate at temperatures around ~ 170 MeV.

To obtain dilepton spectra in URHICs, the rates are integrated over the space-time evolution of the collision. As in our previous work [12, 15, 30, 31], we employ a simplified model in terms of an isentropically

\sqrt{s} (GeV)	6.3	8.8	19.6	62.4	200
z_0 (fm/c)	2.1	1.87	1.41	0.94	0.63
T_{pc} (MeV)	161	163	170	170	170
T_{ch} (MeV)	134	148	160	160	160
μ_B^{ch} (MeV)	460	390	197	62	22
T_{kin} (MeV)	113	113	111	108	104

TABLE I: Excitation function of fireball parameters for the equation of state (T_{pc}), initial (z_0) and chemical/kinetic freezeout (T_{ch} , μ_B^{ch} , T_{kin}) conditions.

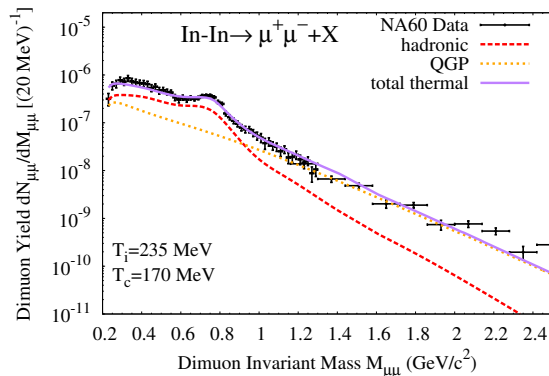


FIG. 1: (Color online) Excess dimuon invariant-mass spectra in In-In ($\sqrt{s_{NN}} = 17.3$ GeV) collisions at the SPS. Theoretical calculations (solid line), composed of hadronic radiation (using in-medium ρ and ω spectral functions and multi-pion annihilation with chiral mixing, dashed line) and QGP radiation (using a lattice-QCD inspired rate, dotted line) are compared to NA60 data [8, 41].

expanding thermal fireball. Its radial and elliptic flow are parameterized akin to hydrodynamic models and fitted to observed bulk-particle spectra and elliptic flow (π , K , p) at kinetic freezeout, $T_{\text{kin}} \simeq 100$ -120 MeV, and to multistrange hadron observables (e.g., ϕ) at chemical freezeout, $T_{\text{ch}} \simeq 160$ MeV. The kinetic freezeout temperatures and radial flow velocities are in accordance with systematic blast-wave analyses of bulk-hadron spectra from SPS, RHIC and LHC [32]. The key link of the fireball expansion to dilepton emission is the underlying EoS, which converts the time-dependent entropy density, $s(\tau) = S/V_{\text{FB}}(\tau) \equiv s(T(\tau), \mu_B(\tau))$ (V_{FB} : fireball volume), into temperature and chemical potential. We employ the EoS constructed in Ref. [33], where a parameterization of the $\mu_B=0$ IQCD results for the QGP [34, 35] has been matched to a hadron resonance gas (HRG) at $T_{\text{pc}}=170$ MeV, with subsequent hadrochemical freezeout at $T_{\text{ch}}=160$ MeV. We here extend this construction to finite $\mu_B=3\mu_q$ with guidance from IQCD: The pseudo-critical temperature is reduced as $T_{\text{pc}}(\mu_q) = T_{\text{pc}}[1 - 0.08(\mu_q/T_{\text{pc}})^2]$ [36, 37], and the QGP EoS is modified as $s(\mu_q, T) = s(T)[1 + c(\mu_q/\pi T)^2]$ with

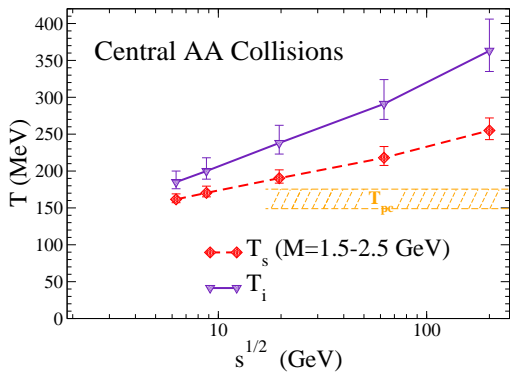


FIG. 2: (Color online) Excitation function of the inverse-slope parameter, T_s , from intermediate-mass dilepton spectra ($M=1.5\text{-}2.5$ GeV, diamonds connected with dashed line) and initial temperature (triangles connected with solid line) in central heavy-ion collisions ($A \simeq 200$). The hatched area schematically indicates the pseudo-critical temperature regime at vanishing (and small) chemical potential as extracted from various quantities computed in lattice QCD [11].

$c \simeq 3$ [38, 39]. For the HRG, we adopt the chemical freeze-out parameters of Ref. [40], cf. Tab. I.

We first test our updated approach with the most precise dilepton data available, the acceptance-corrected NA60 excess dimuons in In-In ($\sqrt{s_{NN}}=17.3$ GeV) [8, 41], cf. Fig. 1. Good agreement with the invariant-mass spectrum is found, which also holds for the q_t dependence, as well as for CERES data [42] (not shown). This confirms our earlier conclusions that the ρ -meson melts around T_{pc} [12], while the IMR is dominated by radiation from above T_{pc} [43–46], mostly as a consequence of a non-perturbative EoS [47]. Furthermore, our predictions for low-mass and q_t spectra of the RHIC BES-I program [15] agree well with STAR dielectron data [13, 14]. Given this robust framework for thermal dilepton radiation in URHICs, we extract in the following the excitation function of two key fireball properties, namely its total lifetime and an average temperature, directly from dilepton observables.

For the temperature determination we utilize the IMR, where medium effects on the EM spectral function are parametrically small, of order T^2/M^2 , providing a stable thermometer: With $\text{Im} \Pi_{EM} \propto M^2$, and in nonrelativistic approximation, one obtains $dR_{ll}/dM \propto (MT)^{3/2} \exp(-M/T)$, which is *independent* of the medium’s collective flow, *i.e.*, there are no blue-shift effects. The observed spectra necessarily involve an average over the fireball evolution, but the choice of mass window, $1.5 \text{ GeV} \leq M \leq 2.5 \text{ GeV}$, implies $T \ll M$ and thus enhances the sensitivity to the early high- T phases of the evolution. Since primordial (and pre-equilibrium) contributions are not expected to be of exponential shape (e.g., power law for Drell-Yan), their “contamination” may be

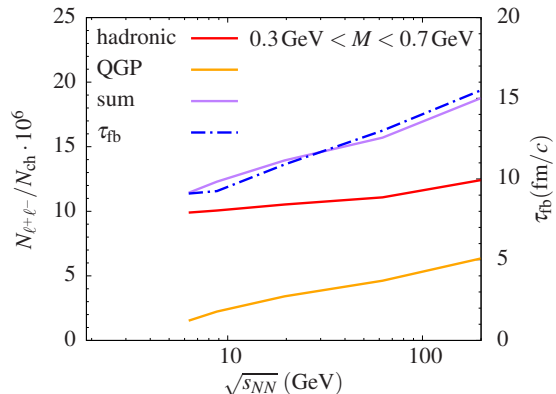


FIG. 3: (Color online) Excitation function of low-mass thermal radiation (“excess spectra”) integrated over the mass range $M=0.3\text{-}0.7$ GeV, as given by QGP (orange line) and in-medium hadronic (red line) contributions and their sum (purple line). The underlying fireball lifetime (dot-dashed line) is given by the right vertical scale.

judged by the fit quality of the exponential ansatz. The inverse slopes, T_s , extracted from the thermal radiation as computed above are displayed in Fig. 2 for collision energies of $\sqrt{s_{NN}}=6\text{-}200$ GeV. We find a smooth dependence ranging from $T \simeq 160$ MeV to 260 MeV. The latter unambiguously demonstrates that a thermalized QGP with temperatures well above the pseudo-critical one has been produced. Our results furthermore quantify that the “measured” average temperature is about 30% below the corresponding initial one (T_i). This gap significantly decreases when lowering the collision energy, to less than 15% at $\sqrt{s_{NN}}=6$ GeV. This is in large part a consequence of the (pseudo-) latent heat in the transition which needs to be burned off in the expansion/cooling. The collision energy range below $\sqrt{s_{NN}}=10$ GeV thus appears to be well suited to map out this transition regime and possibly discover a plateau in the IMR dilepton slopes akin to a “caloric curve”. Another benefit at these energies is the smallness of the open-charm contribution (not included here), so that its subtraction does not create a large systematic error in the thermal-slope measurement. The main theoretical uncertainty in our calculations is associated with the assumed initial longitudinal fireball size, z_0 (which is proportional to the thermalization time): varying the default values quoted in Table I by $\pm 30\%$ induces a $\sim 5\text{-}7\%$ change in the extracted slopes, and a somewhat larger change for the initial temperatures. At given \sqrt{s} , the ratio T_s/T_i is stable within less than 10%.

We finally investigate the relation between the fireball lifetime and the thermal dilepton yields, integrated over a suitable mass window. In Fig. 3 we display the results for a window below the free ρ/ω mass, which is often used to characterize the low-mass excess radiation. It turns out that the integrated thermal excess radiation tracks the total fireball lifetime remarkably well, within

less than 10%. An important reason for this is that, despite the dominantly hadronic contribution, the QGP one is still significant. The latter would be relatively more suppressed when including the ρ/ω peak region. Likewise, the hadronic medium effects are essential to provide sufficient yield in the low-mass region. We have explicitly checked that when hadronic medium effects are neglected, or when the mass window is extended, the proportionality of the excess yield to the lifetime is compromised. With such an accuracy, low-mass dileptons are an excellent tool to detect any “anomalous” variations in the fireball lifetime. A good control over the in-medium spectral shape is essential here, at the level established in the comparison to the NA60 data in Fig. 1.

In summary, we have computed thermal dilepton spectra in heavy-ion collisions over a wide range of collision energies, utilizing in-medium QGP and hadronic emission rates in connection with a lattice-QCD equation of state extrapolated to finite chemical potential. Our description satisfies the benchmark of the high-precision NA60 data at the SPS and is compatible with the recent

results from the RHIC beam-energy scan. Within this framework, we have extracted the excitation function of the low-mass excess radiation and the Lorentz-invariant slope of intermediate-mass spectra. The former turns out to accurately reflect the average fireball lifetime. The latter signals QGP radiation well above the critical one at top RHIC energy, but closely probes the transition region for center-of-mass energies below 10 GeV. Dilepton radiation is thus well suited to provide direct information on the QCD phase boundary in a region where a critical point and an onset of a first-order transition are conjectured.

Acknowledgments

This work was supported in part by a U.S. National Science Foundation under grant PHY-1306359, by the Humboldt foundation (Germany), by BMBF and LOEWE.

-
- [1] E.V. Shuryak, Phys. Lett. B **78**, 150 (1978).
 - [2] G.E. Brown and M. Rho, Phys. Rev. Lett. **66**, 2720 (1991).
 - [3] R.D. Pisarski, Phys. Rev. D **52**, 3773 (1995).
 - [4] R. Rapp and J. Wambach, Adv. Nucl. Phys. **25**, 1 (2000).
 - [5] M. Harada and K. Yamawaki, Phys. Rept. **381**, 1 (2003).
 - [6] P. Braun-Munzinger, J. Stachel and C. Wetterich, Phys. Lett. B **596**, 61 (2004).
 - [7] I. Tserruya, in *Relativistic Heavy-Ion Physics*, edited by R. Stock and Landolt Börnstein (Springer), New Series **I/23A** (2010) 4-2 [arXiv:0903.0415[nucl-ex]].
 - [8] H.J. Specht [NA60 Collaboration], AIP Conf. Proc. **1322**, 1 (2010).
 - [9] R. Rapp and J. Wambach, Eur. Phys. J. A **6**, 415 (1999).
 - [10] R. Rapp and E. V. Shuryak, Phys. Lett. B **473**, 13 (2000).
 - [11] S. Borsanyi *et al.*, JHEP **1009**, 073 (2010).
 - [12] H. van Hees and R. Rapp, Nucl. Phys. A **806**, 339 (2008).
 - [13] F. Geurts [STAR Collaboration], Nucl. Phys. A **904-905**, 217c (2013).
 - [14] P. Huck [STAR Collaboration], arXiv:1409.5675[nucl-ex].
 - [15] R. Rapp, Adv. High Energy Phys. **2013**, 148253 (2013).
 - [16] S. Endres, H. van Hees and M. Bleicher, in prep. (2014).
 - [17] B. Friman *et al.*, Lect. Notes Phys. **814**, 1 (2011).
 - [18] M. A. Stephanov, PoS LAT **2006**, 024 (2006).
 - [19] L. D. McLerran and T. Toimela, Phys. Rev. D **31**, 545 (1985).
 - [20] H. A. Weldon, Phys. Rev. D **42**, 2384 (1990).
 - [21] C. Gale and J. I. Kapusta, Nucl. Phys. B **357**, 65 (1991).
 - [22] M. Urban, M. Buballa, R. Rapp and J. Wambach, Nucl. Phys. A **641**, 433 (1998).
 - [23] R. Rapp, Phys. Rev. C **63**, 054907 (2001).
 - [24] M. Dey, V. L. Eletsky and B. L. Ioffe, Phys. Lett. B **252**, 620 (1990).
 - [25] J.V. Steele, H. Yamagishi, and I. Zahed, Phys. Lett. B **384**, 255 (1996).
 - [26] H.-T. Ding *et al.*, Phys. Rev. D **83**, 034504 (2011).
 - [27] B.B. Brandt, A. Francis, H.B. Meyer and H. Wittig, JHEP **1303**, 100 (2013).
 - [28] J.I. Kapusta, P. Lichard and D. Seibert, Phys. Rev. D **44**, 2774 (1991) [Erratum-ibid. D **47**, 4171 (1993)].
 - [29] E. Braaten, R.D. Pisarski and T.-C. Yuan, Phys. Rev. Lett. **64**, 2242 (1990).
 - [30] H. van Hees, C. Gale and R. Rapp, Phys. Rev. C **84**, 054906 (2011).
 - [31] H. van Hees, M. He and R. Rapp, arXiv:1404.2846 [nucl-th].
 - [32] L. Kumar [STAR Collaboration], arXiv:1408.4209[nucl-ex].
 - [33] M. He, R.J. Fries and R. Rapp, Phys. Rev. C **85**, 044911 (2012).
 - [34] S. Borsanyi *et al.*, JHEP **1011**, 077 (2010).
 - [35] M. Cheng *et al.*, Phys. Rev. D **81**, 054504 (2010).
 - [36] G. Endrodi, Z. Fodor, S. D. Katz and K. K. Szabo, JHEP **1104**, 001 (2011).
 - [37] O. Kaczmarek *et al.*, Phys. Rev. D **83**, 014504 (2011).
 - [38] S. Borsanyi *et al.*, JHEP **1208**, 053 (2012).
 - [39] P. Hegde *et al.*, arXiv:1408.6305 [hep-lat].
 - [40] P. Braun-Munzinger and J. Stachel, arXiv:1101.3167 [nucl-th].
 - [41] R. Arnaldi *et al.* [NA60 Collaboration], Eur. Phys. J. C **61**, 711 (2009).
 - [42] G. Agakichiev *et al.* [CERES Collaboration], Eur. Phys. J. C **41**, 475 (2005).
 - [43] T. Renk and J. Ruppert, Phys. Rev. C **77**, 024907 (2008).
 - [44] K. Dusling, D. Teaney and I. Zahed, Phys. Rev. C **75**, 024908 (2007).
 - [45] J. K. Nayak, J. e. Alam, T. Hirano, S. Sarkar and B. Sinha, Phys. Rev. C **85**, 064906 (2012).
 - [46] O. Linnyk, E. L. Bratkovskaya, V. Ozvenchuk, W. Cassing and C. M. Ko, Phys. Rev. C **84**, 054917 (2011).
 - [47] R. Rapp, PoS CPOD **2013**, 008 (2013).

A coarse-graining approach for dilepton production at SPS energies

Stephan Endres,* Hendrik van Hees, Janus Weil, and Marcus Bleicher
*Frankfurt Institute for Advanced Studies, Ruth-Moufang-Strasse 1, D-60438 Frankfurt, Germany and
 Institut für Theoretische Physik, Universität Frankfurt,
 Max-von-Laue-Strasse 1, D-60438 Frankfurt, Germany*
 (Dated: April 24, 2015)

Coarse-grained output from transport calculations is used to determine thermal dilepton emission rates by applying medium-modified spectral functions from thermal quantum field theoretical models. By averaging over an ensemble of events generated with the UrQMD transport model, we extract the local thermodynamic properties at each time step of the calculation. With an equation of state the temperature T and chemical potential μ_B can be determined. The approach goes beyond simplified fireball models of the bulk-medium evolution by treating the full (3+1)-dimensional expansion of the system with realistic time and density profiles. For the calculation of thermal dilepton rates we use the in-medium spectral function of the ρ meson developed by Rapp and Wambach and consider thermal QGP and multi-pion contributions as well. The approach is applied to the evaluation of dimuon production in In+In collisions at top SPS energy. Comparison to the experimental results of the NA60 experiment shows good agreement of this ansatz. We find that the experimentally observed low-mass dilepton excess in the mass region from 0.2 to 0.6 GeV can be explained by a broadening of the ρ spectral function with a small mass shift. In contrast, the intermediate mass region ($M > 1.5$ GeV) is dominated by a contribution from the quark-gluon plasma. These findings agree with previous calculations with fireball parametrizations. This agreement in spite of differences in the reaction dynamics between both approaches indicates that the time-integrated dilepton spectra are not very sensitive to details of the space-time evolution of the collision.

PACS numbers: 24.10.Lx, 25.75.-q, 25.75.Dw, 25.75.Cj

Keywords: Monte Carlo simulations, Relativistic heavy-ion collisions, Particle and resonance production, Dilepton production

I. INTRODUCTION

The in-medium properties of hadrons have been a field of intense studies in theory and experiment over the last years [1–6]. One aims to learn more about the phase diagram of QCD and especially to find hints for a possible restoration of chiral symmetry. For such studies of hot and dense nuclear matter, dileptons are a unique tool. As they do not interact strongly, they suffer only negligible final-state interactions with the medium and thus provide insight into the spectral properties of their source, i.e., dileptons provide a direct view on the in-medium electromagnetic current-current correlation function of QCD matter during the entire history of the collision, from first nucleon-nucleon reactions to final freeze-out [2, 7, 8]. However, this advantage also comes with a drawback. As we only get time-integrated spectra over the whole space-time evolution of a nuclear reaction, it is difficult to disentangle the various contributing processes which requires a realistic description of all collision stages.

Considering the different experimental efforts to investigate dilepton production in heavy-ion collisions, the NA60 experiment plays a prominent role. It measured dimuons in heavy-ion collisions at top SPS energies with an unprecedented precision. The high accuracy of the measurement enabled the subtraction of the background contributions (long-lived mesons as η , η' , ω , ϕ) from the

dilepton spectra. Consequently, the NA60 results deliver direct insight into the in-medium effects on the ρ spectral function in the low-mass region up to 1 GeV [9–11] and the thermal dimuon emission in the intermediate mass region [12]. A main finding was a large excess of lepton pairs in the mass region 0.2-0.4 GeV, which confirmed the previous results by CERES [13]. Theoretical studies showed that this excess can be explained by a strong broadening of the ρ spectral function with small mass shifts [14–17].

In general there exist two different types of approaches to describe heavy-ion collisions, microscopic and macroscopic ones. The microscopic models, e.g., transport models as UrQMD [18, 19], HSD [20] or GiBUU [21], focus on the description of all the subsequent hadron-hadron collisions (respectively interactions of partons), according to the Boltzmann equation. The difficulty here is to implement in-medium effects in such a microscopic non-equilibrium approach which is highly non-trivial, but nevertheless some investigations on that issue have been conducted successfully [22–31]. On the other hand, in macroscopic models such as thermal fireball models [32] or hydrodynamics [16, 33–37], the application of in-medium hadronic spectral functions from thermal quantum-field theory is straightforward. However, due to their plainness the fireball parametrizations might oversimplify the real dynamics of a nuclear reaction, and hydrodynamical simulations may not be applicable to the less hot and dense medium created at lower collision energies. Furthermore, the creation of

* endres@th.physik.uni-frankfurt.de

an equilibrium state of hot and dense matter after quite short formation times is usually assumed in these models whereas the results from microscopic investigations indicate the importance of non-equilibrium effects during the evolution of a heavy-ion collision [38].

Combining a realistic (3+1)-dimensional expansion of the system with full in-medium spectral functions for the thermal emission of dileptons is yet an important challenge for theory. One approach that has proven successful in explaining the NA60 results is the investigation of dilepton production with a hybrid model [39]. It combines a cascade calculation of the reaction dynamics with thermal emission from an intermediate hydrodynamic stage. However, as all hydro-approaches it is only working properly for sufficiently large collision energies. Furthermore, the hybrid-approach falls into three different stages, a pre-hydro phase, the hydrodynamic stage and the transport phase after particlization. An application of in-medium spectral functions hereby only applies for the rather short hydro stage.

For the study presented in this paper we follow an approach which uses a microscopic description for the whole evolution of the collision and enables the use of in-medium spectral functions from thermal quantum-field theoretical models at all stages. Taking a large number of events generated with the Ultra-relativistic Quantum Molecular Dynamics (UrQMD) model, we place the output on a space-time grid and extract the local temperature and baryon chemical potential by averaging energy and baryon density over the events (i.e., we “coarse-grain” the microscopic results) which allows for the calculation of local thermal dilepton emission. This ansatz was previously proposed and used to calculate hadron, dilepton and photon spectra [40]. For the present work we modify the approach to include also the very initial stage of the reaction (which was separately treated in the cited work) and account for non-equilibrium effects with respect to the pion dynamics. Additionally we include non-thermal contributions to really cover the whole evolution of the nucleus-nucleus reaction.

This paper is structured as follows. In Section II the coarse-graining approach is described in detail and the different contributions to the dilepton emission included in the model are introduced. Subsequently we present the results for the space-time evolution of the nuclear reaction in Section III A followed by the dilepton invariant-mass and transverse-momentum spectra, which we compare to the experimental results in III B. Finally, in Section IV a summary and an outlook on further studies is given.

II. THE MODEL

A. The coarse-graining approach

The underlying input for our calculations stems from the Ultra-relativistic Quantum Molecular Dynamics Ap-

proach (UrQMD) [18, 19, 41, 42]. It is a non-equilibrium transport approach that includes all hadronic resonance states up to a mass of 2.2 GeV and constitutes an effective solution of the relativistic Boltzmann equation. A heavy-ion collision is simulated such that all hadrons are propagated on classical trajectories in combination with elastic and inelastic binary scatterings and resonance decays. At higher energies, string excitation is possible as well. The model has been checked to describe hadronic observables up to RHIC energies with good accuracy [41]. For the further investigations we use the UrQMD output in time steps. This provides positions, momenta, and energies of all particles and resonances at that specific moment in time. The size of each time step for the present calculations is chosen as $\Delta t = 0.2 \text{ fm}/c$.

In the UrQMD model, the particle distribution function of all hadrons is given by an ensemble of point particles, which at time t are defined by their positions \vec{x}_h and momenta \vec{p}_h . Each particle’s contribution to the phase-space density is then defined as

$$\delta^{(3)}(\vec{x} - \vec{x}_h(t))\delta^{(3)}(\vec{p} - \vec{p}_h(t)). \quad (1)$$

With a sufficiently large number of events the distribution function $f(\vec{x}, \vec{p}, t)$ takes a smooth form

$$f(\vec{x}, \vec{p}, t) = \left\langle \sum_h \delta^{(3)}(\vec{x} - \vec{x}_h(t))\delta^{(3)}(\vec{p} - \vec{p}_h(t)) \right\rangle. \quad (2)$$

Hereby, the ensemble average $\langle \cdot \rangle$ is taken over simulated events. As the UrQMD model constitutes a non-equilibrium approach, the equilibrium quantities have to be extracted locally at each space-time point. In consequence we set up a grid of small space-time cells with a spatial extension Δx of 0.8 fm and average the UrQMD output for each cell on that grid. One can then determine the energy-momentum tensor $T^{\mu\nu}$ and the baryon four-flow according to the following expressions:

$$\begin{aligned} T^{\mu\nu} &= \int d^3p \frac{p^\mu p^\nu}{p_0} f(\vec{x}, \vec{p}, t) \\ &= \frac{1}{\Delta V} \left\langle \sum_{i=1}^{N_h \in \Delta V} \frac{p_\mu^i \cdot p_\nu^i}{p_0^i} \right\rangle, \end{aligned} \quad (3)$$

$$\begin{aligned} j_\mu^B &= \int d^3p \frac{p^\mu}{p_0} f^B(\vec{x}, \vec{p}, t) \\ &= \frac{1}{\Delta V} \left\langle \sum_{i=1}^{N_{B/\bar{B}} \in \Delta V} \pm \frac{p_\mu^i}{p_0^i} \right\rangle. \end{aligned} \quad (4)$$

For the net-baryon flow in (4) only the distribution function of baryons and anti-baryons $f^B(\vec{x}, \vec{p}, t)$ is considered, excluding all mesons. Each anti-baryon hereby gives a negative contribution to j_μ^B . On the contrary, the distribution function for all hadrons in the cell enters in $T^{\mu\nu}$.

According to Eckart’s definition [43] the local rest-frame (LRF) is tied to conserved charges, in our case the net-baryon number. Consequently one has to perform a

Lorentz transformation into the frame, where $\vec{j}^B = 0$. The unit vector in direction of the baryon flow takes the form

$$u^\mu = \frac{j^\mu}{(j^\nu j_\nu)^{1/2}} = (\gamma, \gamma \vec{v}), \quad (5)$$

where $u_\mu u^\mu = 1$. With this, the rest-frame values for the baryon and energy density are obtained by

$$\rho_B = j_\mu u^\mu = j_{\text{LRF}}^0, \quad (6)$$

$$\varepsilon = u_\mu T^{\mu\nu} u_\nu = T_{\text{LRF}}^{00}. \quad (7)$$

B. Equilibration and thermal properties of the cells

For the case of a fully equilibrated ideal fluid the energy-momentum tensor would be completely diagonal in the local rest-frame. An important question is to which extent equilibrium is obtained in the present approach and how one can deal with deviations from it.

In macroscopic descriptions of nuclear reaction dynamics local equilibrium is usually introduced as an ad-hoc assumption. (In fireball models, one even assumes a globally equilibrated system). The equilibration of the system is generally assumed to be very fast (on the scale of 1-2 fm/c), after an initial phase. In contrast, no such hypothesis is made within transport approaches, where only the microscopic interactions between the constituent particles of the medium are described. Furthermore, these approaches implicitly include effects as e.g. viscosities or heat conduction and do not fully account for detailed balance. Consequently, non-equilibrium is the normal case at any stage of the collision. On the other hand, to calculate thermal emission rates for dileptons from many-body quantum-field theoretical models, it is necessary know the temperature and baryochemical potential which are by definition equilibrium properties. But when extracting thermodynamic properties from a transport model one has to deal with the problem that many cells are not found in equilibrium. As the coarse-graining approach aims to treat the entire space-time evolution of the collision, this case has to be handled with special care.

Ideally, if complete local equilibrium is achieved, then in each cell the momentum spectrum and the particle abundances should follow a Maxwell-Jüttner-distribution

$$f_{\text{eq}}(p, m_i) = \exp\left(-\frac{\sqrt{p^2 + m_i^2} - \mu}{T}\right), \quad (8)$$

with μ being the chemical potentials for the conserved quantities and T being the temperature. Unfortunately, most of the time this ideal case is not realized during the evolution in the present classical transport simulation. For the present investigation however, the following criteria are more relevant, because they allow to include the deviations from equilibrium.

Using the momentum-space anisotropy to characterize the local kinetic equilibrium, one observes from Fig.

2 that kinetic equilibrium may only be reached after 10 fm/c (see also section III A). The question arises, whether the larger anisotropies of the momentum distribution before 10 fm/c affect the extracted energy densities that are of relevance for our studies. We overcome this problem by employing an anisotropic energy-momentum tensor for the extraction of the energy density, as detailed below. The approach to local chemical equilibrium is more difficult to quantify. Approximate chemical equilibrium may also only be reached towards the end of the reaction. Here we take the chemical off-equilibrium situation into account by extracting a pion chemical potential and employing corresponding fugacity factors.

The findings of the present work are in line with previous detailed studies comparing the particle yields and spectra of the UrQMD transport approach at different times with those of the statistical model [44–46] which showed that it takes roughly 10 fm/c until local kinetic and chemical equilibrium is approximately reached for nucleus-nucleus collisions at SPS energies [38, 47, 48].

In summary, to account for the non-equilibrium effects in the present study, which obviously dominate large parts of the evolution, we will use the following scheme: One (i) considers the pressure (respectively momentum) anisotropies in each cell and applies an approach developed for anisotropic hydrodynamics to extract the effective energy density which is used for all further considerations, (ii) introduces an EoS assuming thermal and chemical equilibrium and (iii) finally extracts a pion chemical potential μ_π which is the non-equilibrium effect with the largest impact on the thermal dilepton rates. These aspects will be considered in detail in the following. However, note that step (i) only accounts for deviations from the purely kinetic condition of isotropic momentum distributions and (iii) accounts for the chemical off-equilibrium of the pions only. Besides, when applying the EoS, kinetic and chemical equilibrium in the end remain an assumption here as in any macroscopic approach.

1. Kinetic anisotropies

When considering the kinetic properties of the system, one finds that the underlying transport approach in parts depicts large deviations from pressure isotropy. This is especially important for the early stages of the reaction due to the large initial longitudinal momenta carried by the nucleons of the two nuclei traversing each other. In consequence, the longitudinal pressure is much higher than the transverse pressure. To handle this kinetic off-equilibrium situation, a description developed for anisotropic hydrodynamics is employed [49] which allows for differing longitudinal and transverse pressures. In this case the energy-momentum tensor takes the form

$$T^{\mu\nu} = (\varepsilon + P_\perp) u^\mu u^\nu - P_\perp g^{\mu\nu} - (P_\perp - P_\parallel) v^\mu v^\nu. \quad (9)$$

Here ε is the energy density, P_{\perp} and P_{\parallel} are the pressures perpendicular and in direction of the beam, respectively; u^{μ} is the fluid four-velocity and v^{μ} the four-vector of the beam direction. To define realistic values for energy density ε and pressure P in the energy-momentum tensor we introduce an anisotropy parameter

$$x = (P_{\parallel}/P_{\perp})^{3/4} \quad (10)$$

and apply a generalized equation of state [50] according to the following relations

$$\varepsilon_{\text{real}} = \varepsilon/r(x), \quad (11)$$

$$P_{\text{real}} = P_{\perp}/[r(x) + 3xr'(x)], \quad (12)$$

$$P_{\text{real}} = P_{\parallel}/[r(x) - 6xr'(x)]. \quad (13)$$

The relaxation function $r(x)$, with its derivative $r'(x)$, characterizes the properties of a system which exhibits a Boltzmann-like pressure anisotropy. It is given by

$$r(x) = \begin{cases} \frac{x^{-1/3}}{2} \left(1 + \frac{x \operatorname{artanh} \sqrt{1-x}}{\sqrt{1-x}} \right) & \text{for } x \leq 1 \\ \frac{x^{-1/3}}{2} \left(1 + \frac{x \operatorname{arctan} \sqrt{x-1}}{\sqrt{x-1}} \right) & \text{for } x \geq 1 \end{cases}. \quad (14)$$

With this procedure one can translate the anisotropic momentum distribution into a local-equilibrium description that gives a realistic value of ε for our further calculations. This effective model to account for the anisotropic pressure of the cell properties allows to treat the early stage of the reaction in the same way as at later times, when a local kinetic equilibration of the system has set in. However, large differences between the “regular” energy density $\varepsilon = T^{00}$ and the effective density $\varepsilon_{\text{real}}$ only show up for the first few fm/c of the evolution of the nuclear reaction. After that time we find the longitudinal and perpendicular pressures being of at least the same order of magnitude and $\varepsilon_{\text{real}} \approx \varepsilon$, i.e., no significant deviations from the assumption of isotropic momentum distributions (for details see Section III A and [38]). For all further studies we assume that $\varepsilon_{\text{real}}$ represents the energy density of the cell.

2. Equation of state

Having determined the rest-frame energy and baryon density, an equation of state (EoS) is needed as additional input to calculate the temperature T and baryochemical potential μ_B for each cell. As the actual EoS for QCD matter is still not completely determined, this is an uncertainty within the calculation. For the present study we use a hadron-gas EoS with vacuum masses and without mean-field potentials (HG-EoS) [51, 52] following from hadronic chiral model calculations [53, 54]. The included hadrons agree with the degrees of freedom in UrQMD. However, this approach does not account for a phase transition to a deconfined phase as it is neither implemented in UrQMD nor in the hadron gas EoS. For

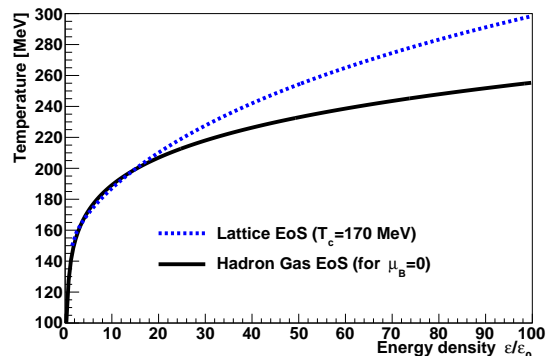


FIG. 1. (Color online) Comparison of the two equations of state used in our model, the hadron gas EoS [51] with UrQMD-like degrees of freedom (black line) and the Lattice EoS [55] to model the deconfined phase (blue line). We show the temperature dependence on the energy density (in units of normal nuclear-matter density, ε_0). While for the Lattice EoS $\mu_B = 0$ intrinsically, we set the chemical potential to zero as well for the hadron gas EoS for reasons of comparison.

heavy-ion collisions at SPS energies, where we find initial temperatures significantly above the expected critical temperature T_c , it will be also important to consider dilepton emission from cells with such high temperatures during the evolution of the medium. Therefore, we supplement the hadron-gas EoS with a partonic equation of state [55] which is obtained from a fit to lattice-QCD data of the form

$$\varepsilon/T^4 = \frac{c \cdot (1 + e^{-a/b})}{1 + e^{(T_c/T - a)/b}} \cdot e^{\lambda T_c/T}, \quad (15)$$

with fit parameters $a = 0.9979$, $b = 0.1163$, $c = 16.04157$ and $\lambda = 0.1773$ and critical temperature $T_c = 170$ MeV. To ensure a smooth transition between the two EoS without any jumps in temperature (i.e., to avoid discontinuities in the evolution), the values of T from the lattice EoS are matched with the HG-EoS in the temperature range from 150-170 MeV and exclusively used above T_c .

In Figure 1 a comparison of the relation between temperature and energy density is shown for the two equations of state used in the model. The hadron-gas EoS is represented by the black line and the lattice EoS by the blue dashed line. While for the lattice EoS $\mu_B = 0$ is valid intrinsically, the baryon density and in consequence the chemical potential are set to zero in this plot for the hadron gas EoS for reasons of comparison. However, the rather moderate baryon chemical potential found at top SPS energy does not have a large impact on the relation between energy density and temperature and gives rise to a deviation from the curve for $\rho_B = \mu_B = 0$ of at maximum a few MeV. As observed from Fig. 1, both equations of state agree very well up to an energy density of roughly $15\varepsilon_0$, which corresponds to a temperature of

200 MeV. This implies that both EoS are dual in the region around the phase transition, guaranteeing a smooth cross-over transition when changing from the QGP EoS to the hadron-gas EoS across the phase transition.

The parametrization of the Rapp-Wambach spectral function [56], which will be used in this study for convenient and reliable application, is constructed such that the presence of baryonic matter enters via a dependence on an effective baryon density

$$\rho_{\text{eff}} = \rho_N + \rho_{\bar{N}} + 0.5(\rho_{B^*} + \rho_{\bar{B}^*}). \quad (16)$$

It includes nucleons and excited baryons as well as their anti-particles. The reason not to take μ_B is that the interaction between the ρ and a baryon is the same as with an anti-baryon, i.e., it is not the net-baryon number that affects the electromagnetic current-current correlation function but the sum of baryons and anti-baryons. In our approach, we calculate the value of ρ_{eff} not via the EoS but directly from the cell's rest-frame.

3. Pion chemical potential

In full chemical equilibrium all meson chemical potentials are zero since the meson number is not a conserved quantity. When applying the EoS as described above, the explicit assumption is that in each cell we find a thermally and chemically equilibrated system. However, it has been shown that in transport models during the initial non-equilibrium stage – which is dominated by high energy densities – an over-dense pionic system is created and remains for significant time-scales due to the long relaxation time of pions [57, 58]. This is mainly caused by initial string fragmentation and resonances decaying into more than two final particles (e.g. $\omega \rightarrow 3\pi$) for which the back-reaction channel is not implemented. Also macroscopic approaches find non-zero μ_π after the number of pions is fixed at the chemical freeze-out but the system further cools down and expands [59]. The appearance of a finite μ_π has a large effect on the creation of ρ mesons and therefore on the thermal dilepton emission (see section II C). Therefore, though in general assuming chemical equilibrium, we exclude the pions from this assumption and extract a pion chemical potential in each cell via a Boltzmann approximation. The according relation for a relativistic gas is given by [60]

$$\mu_\pi = T \cdot \ln \left(\frac{2\pi^2 n_\pi}{g_\pi T m^2 K_2 \left(\frac{m}{T} \right)} \right), \quad (17)$$

with the pion density n_π in the cell, the pion degeneracy $g_\pi = 3$, and the Bessel function of the second kind, K_2 . Other meson chemical potentials as, e.g., a kaon chemical potential are not considered in the present study, as the dependence of the ρ spectral function with regard to μ_K is negligible.

C. Dilepton emission rates

By assuming that the cells in our (3+1)-dimensional space-time grid are in local equilibrium (except for the finite μ_π) we can calculate the thermal emission from these cells. The dilepton emission is related to the imaginary part of the electromagnetic current-current correlation function [61, 62], $\text{Im} \Pi_{\text{em}}^{(\text{ret})}$. The full expression for the dilepton emission rate per four-volume and four-momentum from a heat bath at temperature T and chemical potential μ_B takes the form [32]

$$\frac{dN_{ll}}{d^4x d^4q} = - \frac{\alpha_{\text{em}}^2 L(M)}{\pi^3 M^2} f^B(q \cdot U; T) \times \text{Im} \Pi_{\text{em}}^{(\text{ret})}(M, \vec{q}; \mu_B, T), \quad (18)$$

where f^B denotes the Bose-distribution function and L the lepton phase-space factor,

$$L(M) = \sqrt{1 - \frac{4m_\mu^2}{M^2}} \left(1 + \frac{2m_\mu^2}{M^2} \right), \quad (19)$$

which reaches 1 rapidly above the threshold, given by twice the lepton mass.

To calculate invariant-mass spectra from equation (18) we integrate over four-volume and three-momentum

$$\frac{dN_{ll}}{dM} = \int d^4x \frac{M d^3\vec{p}}{p_0} \frac{dN_{ll}}{d^4x d^4p} \quad (20)$$

In our case the integration over the four-volume simply reduces to a multiplication of the cell's four-volume.

1. Thermal ρ emission

There exist several approaches to calculate the in-medium spectral functions, e.g., by using empirical scattering amplitudes [63]. Here the ρ spectral function from hadronic many-body calculations by Rapp and Wambach [64] is used, which has proven a good agreement with experimental results at CERN-SPS and RHIC energies in previous studies [14, 15, 32]. In this approach, the hadronic part of the electromagnetic current-current correlator is saturated by light vector mesons according to the Vector Dominance Model (VDM). The correlator is hereby related to the ρ spectral function, respectively the propagator, as

$$\text{Im} \Pi_{\text{em}}^{(\text{ret})} = \frac{(m_\rho^{(0)})^4}{g_\rho^2} \text{Im} D_\rho^{(\text{ret})}. \quad (21)$$

To determine the propagator, several contributions to the self-energy have to be considered, i.e., in this case the meson gas ($\Sigma_{\rho M}$) and nuclear matter effects ($\Sigma_{\rho B}$) as well as the in-medium $\rho\pi\pi$ width ($\Sigma_{\rho\pi\pi}$). This results in

$$D_\rho = \frac{1}{M^2 - (m_\rho^{(0)})^2 - \Sigma_{\rho\pi\pi} - \Sigma_{\rho M} - \Sigma_{\rho B}}. \quad (22)$$

For the present study we use a parametrization of the Rapp-Wambach spectral function [56] that has been checked against the full spectral function and proven to agree well, with a maximal deviation of up to 15% in the mass region around 0.4 GeV.

To arrive at the final yield $N_{\rho \rightarrow ll}$ we have to generalize (18) for a chemical off-equilibrium state with finite pion chemical potential. It is necessary to include an additional (squared) fugacity factor, which is in Boltzmann approximation

$$z_\pi^2 = \exp\left(\frac{2\mu_\pi}{T}\right). \quad (23)$$

The reason for this is that the above expression for the dilepton emission rate (18) is independent of the hadronic initial and final states as only chemical potentials of conserved charges are considered (for which $Q_i = Q_f$). However, since the pion number N_π is not a conserved quantity this assumption is no longer correct for $\mu_\pi \neq 0$ which means that generally $N_{\pi,i} - N_{\pi,f} \neq 0$.

2. Multi pion emission

While the ρ meson is expected to dominate the dilepton emission in the low invariant mass range up to $M = 1$ GeV, a continuum starts to develop above, and multi-pion interactions will contribute at higher masses.

As detailed in [65], the vector correlator at finite temperature takes the form

$$\Pi_{\mu\nu}^V(p, T) = (1 - \varepsilon)\Pi_{\mu\nu}^V(p, 0) + \varepsilon\Pi_{\mu\nu}^A(p, 0) \quad (24)$$

with the mixing parameter $\varepsilon = T^2/(6F_\pi^2)$ (F_π : pion-decay constant). In this paper, we follow the same approach as presented in [14, 15], using

$$\begin{aligned} \Pi_V(p) = & (1 - \varepsilon)z_\pi^4\Pi_{V,4\pi}^{\text{vac}} + \frac{\varepsilon}{2}z_\pi^3\Pi_{A,3\pi}^{\text{vac}} \\ & + \frac{\varepsilon}{2}(z_\pi^4 + z_\pi^5)\Pi_{A,5\pi}^{\text{vac}} \end{aligned} \quad (25)$$

according to vector/axial-vector correlators from tau-decay data provided by ALEPH [66]. The pion chemical potentials are implemented via the fugacity factor z_π . The two-pion piece, as well as the three-pion piece corresponding to the a_1 decay, $a_1 \rightarrow \pi + \rho$, have been excluded as they are already included via the ρ spectral function.

3. Quark-gluon plasma emission

The dilepton emission from the quark-gluon plasma has been considered to be one of the most promising probes for the formation of a deconfined phase. In such a QGP phase, a quark can annihilate with an anti-quark into a dilepton pair (via a virtual photon).

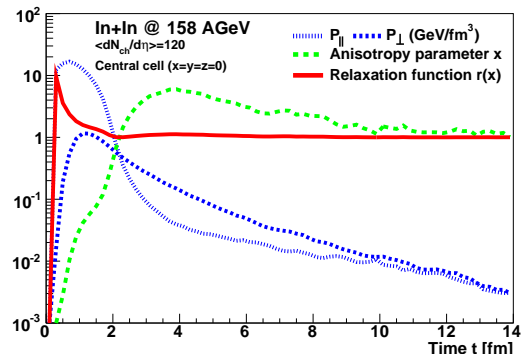


FIG. 2. (Color online) Longitudinal and transverse pressure for the central cell, as well as the anisotropy parameter $x = (P_{\parallel}/P_{\perp})^{3/4}$ and the relaxation function $r(x)$ as defined in equation (14).

Here we use a corresponding spectral function extrapolated from lattice QCD correlators for three-momentum $\vec{q} = 0$ [67] and with a light-like limit, consistent with the leading order α_s photon production rate [32]. The emission rate per four-volume and four-momentum takes the form

$$\frac{dN_{ll}}{d^4x d^4p} = \frac{\alpha_{em}^2}{6\pi^3} \sum_q e_q^2 \frac{\rho_V(p_0, \vec{p}, T)}{(p_0^2 - \vec{p}^2)(e^{p_0/T} - 1)}, \quad (26)$$

where ρ_V denotes the vector spectral function. The current calculation assumes that the chemical potential is zero in the deconfined phase, i.e., that the quark and anti-quark distributions are equal.

For comparison also the pure perturbative quark-gluon plasma contribution is calculated. The rate has been evaluated for lowest order $q\bar{q}$ annihilation [68] as

$$\begin{aligned} \frac{dN_{ll}}{d^4x d^4p} = & \frac{\alpha_{em}^2 T}{4\pi^4 p} f^B(p_0; T) \sum_q e_q^2 \\ & \times \ln \frac{(x_- + y)(x_+ + \exp[-\mu_q/T])}{(x_+ + y)(x_- + \exp[-\mu_q/T])} \end{aligned} \quad (27)$$

with the expressions $x_{\pm} = \exp[-(p_0 \pm p)/2T]$ and $y = \exp[-(p_0 + \mu_q)/T]$. Again, the quark chemical potential μ_q is zero for our considerations.

4. Non-thermal ρ emission

In addition to the thermal contribution, we also have to handle those cells where (i) the temperature is lower than 50 MeV (late stage), i.e., where it is not reasonable to assume a thermal emission and (ii) with no baryon but only meson content (in these cells the density is usually also quite low) which inhibits a determination of a local rest frame according to the Eckart description and

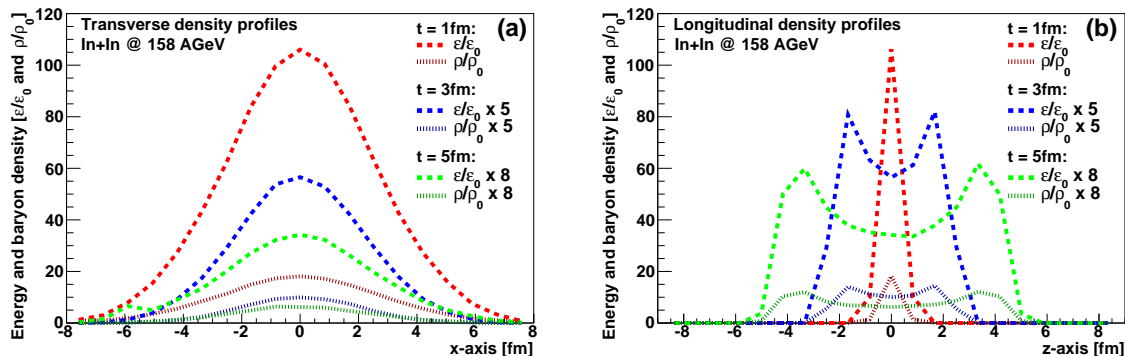


FIG. 3. (Color online) Transverse (a) and longitudinal (b) profiles of the energy density ε and the baryon density ρ_B . The left plot shows the dependence of ε and ρ_B on the position along the x -axis, with y and z coordinates fixed to 0. The right plot shows the dependence along the z -axis (i.e., along the beam axis) with $x = y = 0$. The results are presented in units of the normal nuclear-matter densities, ε_0 and ρ_0 .

in consequence one can not determine T and μ_B in this way. In these cases we directly take the ρ^0 mesons from the UrQMD calculations. Within the transport approach they are mainly produced either via decay of heavy resonances (e.g. $N_{1520}^* \rightarrow \rho N$) or the reaction $\pi\pi \rightarrow \rho$. Production via strings is possible as well. For these ρ^0 mesons we apply a shining procedure that is conventionally used to calculate dilepton emission from a transport approach [69].

The mass-dependent width for the direct decay of a ρ^0 meson to a dilepton pair is expressed according to [70]

$$\Gamma_{V \rightarrow ll}(M) = \frac{\Gamma_{V \rightarrow ll}(m_\rho)}{m_\rho} \frac{m_\rho^4}{M^3} \cdot L(M), \quad (28)$$

with the partial decay width at the ρ -pole mass $\Gamma_{\rho \rightarrow ll}(m_\rho)$; $L(M)$ denotes the lepton phase-space factor (19).

The according dilepton yield is then obtained by summing over all ρ^0 mesons from the low temperature cells,

$$\frac{dN_{ll}}{dM} = \frac{\Delta N_{ll}}{\Delta M} = \sum_{i=1}^{N_{\Delta M}} \sum_{j=1}^{N_\rho} \frac{\Delta t}{\gamma_\rho} \frac{\Gamma_{\rho \rightarrow ll}(M)}{\Delta M}. \quad (29)$$

Here $\Gamma_{\rho \rightarrow ll}(M)$ is the electromagnetic decay width of the considered resonance defined in (28) and Δt is the length of a time step within our calculation. The factor γ_ρ^{-1} is introduced to account for the fact that the ρ meson lives longer in the center of mass system of the UrQMD calculation than in its rest frame in which the shining is applied (relativistic time dilation).

Note that we use the shining procedure only for cells for which we do *not* calculate the thermal emission, in consequence we avoid any form of double-counting.

III. RESULTS

The following calculations were performed with the coarse-graining approach as described above. To compare our results with the data recorded by the NA60 Collaboration, an input of 1000 UrQMD events with a random impact-parameter distribution restricted to $b < 8.5$ fm has been used, which corresponds to a value of $\langle dN_{ch}/d\eta \rangle \approx 119$ in one unit of rapidity around mid-rapidity in the center-of-mass frame. This is very close to the value of $\langle dN_{ch}/d\eta \rangle_{\text{exp}} = 120$ which NA60 measured within their acceptance.

Note that several coarse-graining runs with different UrQMD events as input had to be performed to obtain enough statistics, especially for the non-thermal ρ contribution.

A. Space-time evolution

As dileptons are radiated over the whole space-time evolution of the nuclear reaction, it is important to model the dynamics as realistically as possible. When studying the electromagnetic radiation from the hot and dense phase of heavy-ion collisions, the thermodynamic properties of the fireball are the main input for the calculations.

We first investigate the anisotropic situation at the beginning of the collision. Figure 2 shows – for the central cell at the origin of our grid – the time evolution of the longitudinal and transverse pressure, P_{\parallel} and P_{\perp} , together with the anisotropy parameter, x , and the relaxation function, $r(x)$, as defined in Eqs. (10) and (14). As one expects, the first time steps are characterized by high values of P_{\parallel} while P_{\perp} is rather negligible first but increases significantly later. Both quantities initially differ by three orders of magnitude. In the course of the evolution the values are approaching each other and become

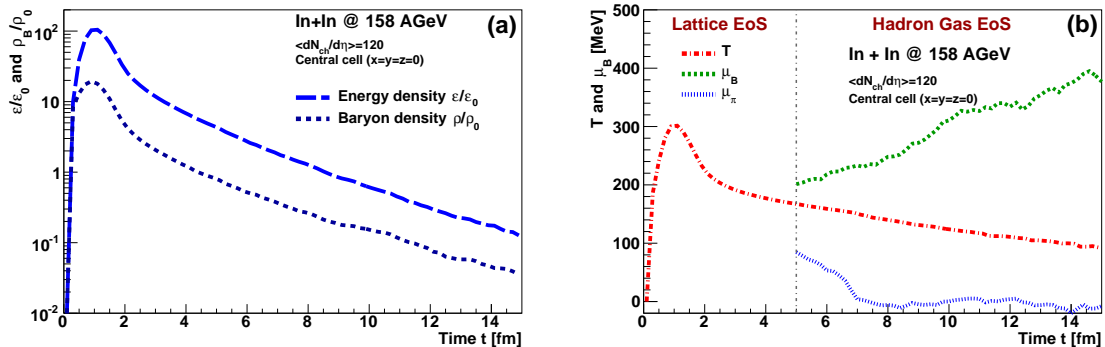


FIG. 4. (Color online) Left panel (a): Time evolution of the baryon density ρ_B (short dashed) and energy density ε (long dashed) for the cell at the center of the coarse-graining grid ($x = y = z = 0$). The results are given in units of the ground-state densities ε_0 and ρ_0 . Right panel (b): Time evolution of the temperature T (red dash-dotted), baryon chemical potential μ_B (green short dashed) and the pion chemical potential μ_π (blue dotted) in the central cell. The thin grey line indicates the transition from the Lattice EoS to the Hadron Gas EoS at the transition temperature of $T = 170$ MeV.

equal around $t = 2$ fm/c. But they do not remain equal at later times but the perpendicular pressure then exceeds the longitudinal one by a factor 3-5 in the further development until they finally equalize around $t = 10$ fm/c. This finding agrees with previous studies of the kinetic equilibration within the UrQMD model [38]. When considering the influence of the pressure anisotropy on the local thermodynamic properties one has to bear in mind that according to (11) the realistic energy density in the cell is determined by the relaxation function $r(x)$. Its value drops rapidly from an initial value of 10 (i.e. the realistic isotropized energy density is here only 10% of the actual energy density in the cell) to 1 at $t = 2$ fm/c and remains on that level. In consequence, the anisotropy does not significantly influence the thermodynamic properties in the cell after 2 fm/c.

The transverse and the longitudinal profiles of the energy density ε and the baryon density ρ_B are presented in Figure 3. The left plot (a) shows the distribution of ρ and ε in dependence on the position along the x -axis whereas $y = z = 0$ and the right plot (b) shows the dependence on the z -position (i.e. along the beam axis) with $x = y = 0$. The results are plotted for three different time steps, at 1, 3 and 5 fm/c after the beginning of the collision. (Note that the results for $t = 3$ fm/c and 5 fm/c are scaled up for better comparability.) The shape of the transverse profile looks almost identical at all times with a clear peak at $x = 0$, which is falling off smoothly on both sides at the more peripheral and less dense regions where consequently also less energy is deposited. However, both energy and baryon density decrease clearly in the course of time due to the expansion of the system. This expansion can directly be seen in the longitudinal profile on the right side. On the one hand, we see one clear peak structure at $t = 1$ fm/c when the two nuclei still mostly overlap. However, at $t = 3$ fm/c

and 5 fm/c we observe a double-peak structure with maxima that shear off from each other. A region of high ε and ρ_B is created in between when the two nuclei have traversed each other. Stopping effects have produced this hot and dense zone, whereas some remnants of the nuclei still fly apart with high velocity. As we can see from these profiles, the highest initial baryon and energy densities should be expected at the origin of our grid in the center of the collision. Indeed the time evolution of ε and ρ in Figure 4 (a) shows a rapid rise up to baryon and energy densities of 20 times respectively 100 times the ground state densities. The maxima are reached at a time of about 1.2 fm/c after the beginning of the collision and in the following the densities decrease again – first rapidly, then slower again. After application of the equation of state we observe a similar behavior for the time dependence of the temperature, with values of up to 300 MeV. It is important to bear in mind that we apply two different EoS here, a lattice EoS for temperatures above 170 MeV to mimic a Quark-Gluon-Plasma phase and a Hadron-Gas EoS for lower temperatures. As we see, a smooth transition in temperature between the two EoS is obtained around $t = 5$ fm/c, which one would have already expected from the fact that the EoS agree quite well for $T < 200$ MeV. The baryo-chemical potential from the hadron gas EoS slowly rises from a value of 200 MeV at the transition time up to a maximum of 400 MeV in the course of the evolution. This increase is similar to the findings of [40] and caused by the stronger relative decline of the energy density compared to the baryon density. A different behavior can be observed for the pion chemical potential μ_π , which is around 100 MeV first and then drops to values around 0. This is unlike the findings of fireball approaches, where particle numbers are fixed at a freeze-out and the subsequent cooling of the system leads to a build-up of a finite pion chemical

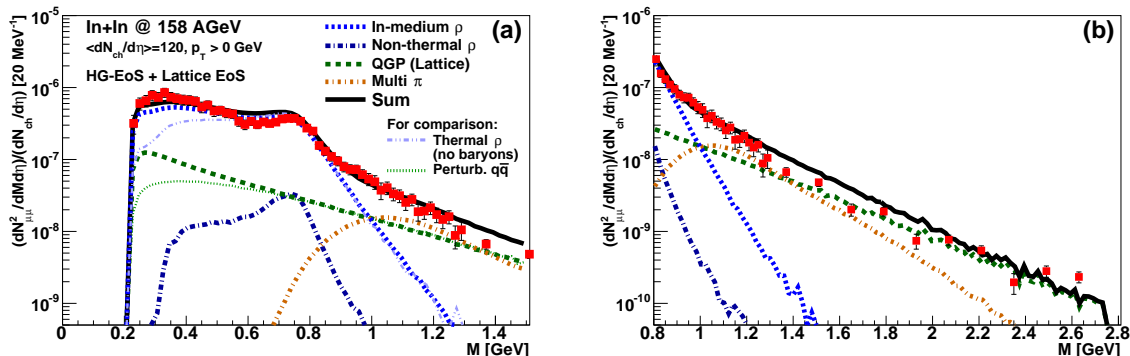


FIG. 5. (Color online) Invariant mass spectra of the dimuon excess yield in In+In collisions at a beam energy of 158 AGeV, for the low-mass region up to 1.5 GeV (a) and the intermediate-mass regime up to 2.8 GeV (b). We show the contributions of the in-medium ρ emission according to the Rapp-Wambach spectral function [56] (blue short dashed), the contribution from the Quark-Gluon Plasma, i.e., $q\bar{q}$ -annihilation, according to lattice rates [32, 67] (green dashed) and the emission from multi-pion reactions, taking vector-axial-vector mixing into account [15] (orange dash-dotted). Additionally a non-thermal transport contribution for the ρ is included in the yield (dark blue dash-dotted). Only left plot: For comparison the thermal ρ without any baryonic effects, i.e. for $\rho_{\text{eff}} = 0$, is shown (violet dash-double-dotted) together with the yield from pure perturbative $q\bar{q}$ -annihilation rates (green dotted). The results are compared to the experimental data from the NA60 Collaboration [11, 12, 71]

potential. The picture in our transport approach is completely different, as pions can be produced and absorbed over the whole evolution in the system.

As we see from the time evolution of the central cell, the temperature reaches values of 100 MeV even after a time of 15 fm/c. However, this is a special case and for most cells the temperature has already dropped beyond significance before. But in contrast to many approaches with a fixed lifetime of the fireball, here an underlying microscopic transport description is applied which takes into account that some singular cells still reach quite high temperatures and densities even after the usually assumed fireball lifetimes. The contribution to the dilepton yield from these few cells is, however, quite negligible.

B. Dilepton spectra

The next step is to investigate how the space-time evolution obtained by coarse-graining the transport simulations is reflected within the resulting dilepton spectra. It is hereby of particular interest whether and how the differences in the reaction dynamics as compared to the fireball parametrizations will be reflected in the $\mu^+\mu^-$ -distributions as measurable in experiment (and whether one by this can discriminate between different scenarios of the fireball evolution).

In Figure 5 the resulting dimuon invariant-mass spectra from the coarse-graining calculations are compared to data from the NA60 Collaboration. There the dimuon excess yield in In+In collisions at a beam energy of $E_{\text{lab}} = 158 \text{ AGeV}$ with $\langle dN_{\text{ch}}/d\eta \rangle = 120$ is shown, for the low-mass region up to $M = 1.5 \text{ GeV}$ (a) and the

intermediate-mass regime up to 2.8 GeV (b). We show the contributions of the in-medium ρ emission, from the quark-gluon plasma, i.e., $q\bar{q}$ -annihilation, and the emission from multi-pion reactions, taking vector-axial-vector mixing into account. The dilepton emission due to decays of ρ mesons from the low-temperature cells is included as well, but in the full p_t -integrated spectrum it is rather negligible compared to the other contributions. Comparison with the experimental data from the NA60 Collaboration [11, 71] shows a very good agreement of our theoretical result with their measurement. Only a slight tendency to underestimate the data in the invariant mass region from 0.2 to 0.4 GeV and a minor excess above the data in the pole region is observed. As the low-mass enhancement and the melting of the peak at the pole mass are mainly caused by the baryonic effects on the ρ meson spectral function and very sensitive to the presence of baryons and anti-baryons, this might be due to the fact that the baryon densities (respectively the baryon chemical potential) are still slightly too low in our approach. An additional modification of the spectral shape not considered here may also be caused by the ω - t -channel exchange. It has been found, however, to give only a small contribution to the total yield and is significant only for high transverse momenta [15]. Furthermore, one has to bear in mind as well that there is an uncertainty of up to 15% around $M \approx 0.4 \text{ GeV}$ between the parametrized spectral function and its full evaluation from thermal field theory which has been found in a full comparison between both approaches [56], as mentioned above. Taking this and the systematic uncertainties of the experimental data and of the model calculations into account, we conclude that the approach is fully able to

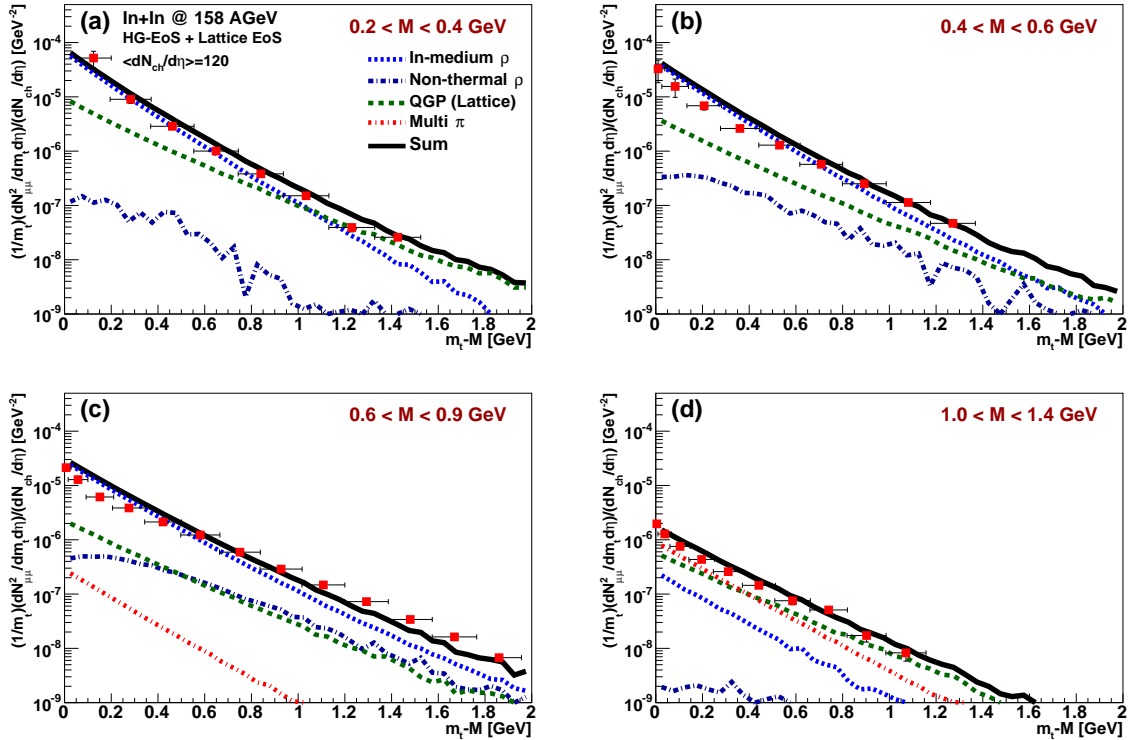


FIG. 6. (Color online) Transverse-mass ($m_t - M$) spectra in four different mass bins of the dimuon-excess yield in In+In collisions at a beam energy of 158 AGeV. We have the mass ranges $0.2 \text{ GeV} < M < 0.4 \text{ GeV}$ (a), $0.4 \text{ GeV} < M < 0.6 \text{ GeV}$ (b), $0.6 \text{ GeV} < M < 0.9 \text{ GeV}$ (c) and the highest mass bin with $1.0 \text{ GeV} < M < 1.4 \text{ GeV}$ (d). The different contributions are the same as in Figure 5. The results are compared to the experimental data from the NA60 Collaboration [72].

describe the total NA60 invariant mass spectrum with excellent accuracy.

To get an impression of the dominant role of baryon-induced medium modifications, the thermal ρ contribution assuming the absence of all baryons and anti-baryons (i.e., for $\rho_{\text{eff}} = 0$) is also shown in Figure 5. In this case only meson-gas effects have an influence on the spectral function. Compared to the full in-medium ρ , it exhibits slightly more strength at the ρ meson's pole mass but is significantly below the experimental yield for $M < 0.6 \text{ GeV}$ by a factor of 2-5. Clearly, only the inclusion of interactions with baryonic matter can explain the low-mass dilepton excess, as has been noticed in previous studies [15].

Comparing the dilepton emission rates obtained from the lattice and from perturbative $q\bar{q}$ -annihilation, both rates are identical for masses larger than 0.8 MeV, while the non-perturbative effects included in the lattice calculations give rise to a strong increase (up to a factor 3) of the yield at lower invariant masses. It is notable that the shape of the slope in the region $M > 1.5 \text{ GeV}$ is described with very good accuracy. This is important, as the

hadronic contribution which dominates at lower masses becomes negligible here, and the yield is dominated by emission from the QGP phase. The intermediate-mass region is therefore a good benchmark for a correct description of the $q\bar{q}$ emission and allows for a reliable determination of the space-time averaged temperature without distortion from blue-shift effects due to flow (as is the case for effective slopes of p_t spectra) [73]. Note, however, that in contrast to the results from a fireball approach we here get a slightly larger contribution from the hadronic domain (ρ and multi- π), whereas in the fireball approach a more dominant QGP contribution is found, especially at low masses [15, 73]. This finding strengthens the hypothesis of duality between the hadronic and partonic dilepton emission in the transition temperature region between both phases [2].

In Figure 6 we present the transverse-mass ($m_t - M$) spectra in four different mass bins of the dimuon-excess yield in In+In collisions. The results are shown for mass bins of $0.2 \text{ GeV} < M < 0.4 \text{ GeV}$ (a), $0.4 \text{ GeV} < M < 0.6 \text{ GeV}$ (b), $0.6 \text{ GeV} < M < 0.9 \text{ GeV}$ (c), and $1.0 \text{ GeV} < M < 1.4 \text{ GeV}$ (d). The different contributions

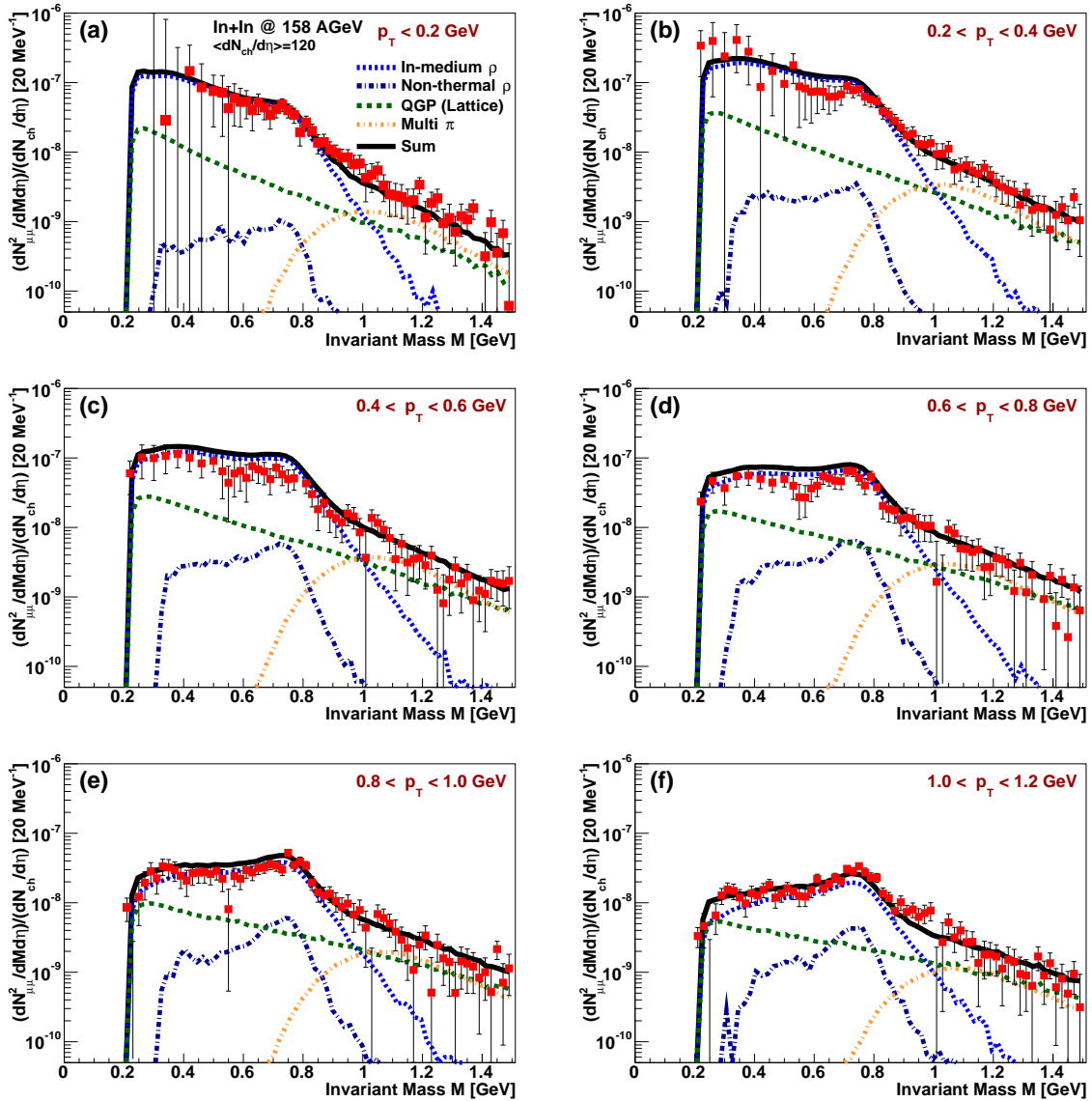


FIG. 7. The invariant mass spectra of the dimuon excess yield in In+In collisions at a beam energy of 158 AGeV, for the low-mass region as in the left plot of Figure 5, but for 6 different p_t -bins ranging from $p_t = 0$ to 1.2 GeV. The different contributions are the same as in Figures 5 and 6. The results are compared to the experimental data from the NA60 Collaboration [11].

are the same as in Figure 5. Comparison to the NA60 results [72] shows again a very good agreement. The calculations are in almost all cases within the error bars of the experimental data. Interesting is the dominance of the different contributions in certain transverse-mass respectively -momentum ranges. While the in-medium ρ dominates the spectra at low m_t for all but the highest mass bin, the QGP and the non-thermal ρ do not significantly contribute at low m_t but their relative strength

increases when going to higher transverse mass.

Besides the invariant-mass and the transverse-mass spectra, we also studied the former as resolved in different p_t -slices. This analysis is of special interest as theoretical studies show that the medium modifications of the ρ spectral function depend strongly on the momentum. While a significant change of the spectral shape is predicted based on constraints from vacuum scattering and decay data at low momenta, this effect should

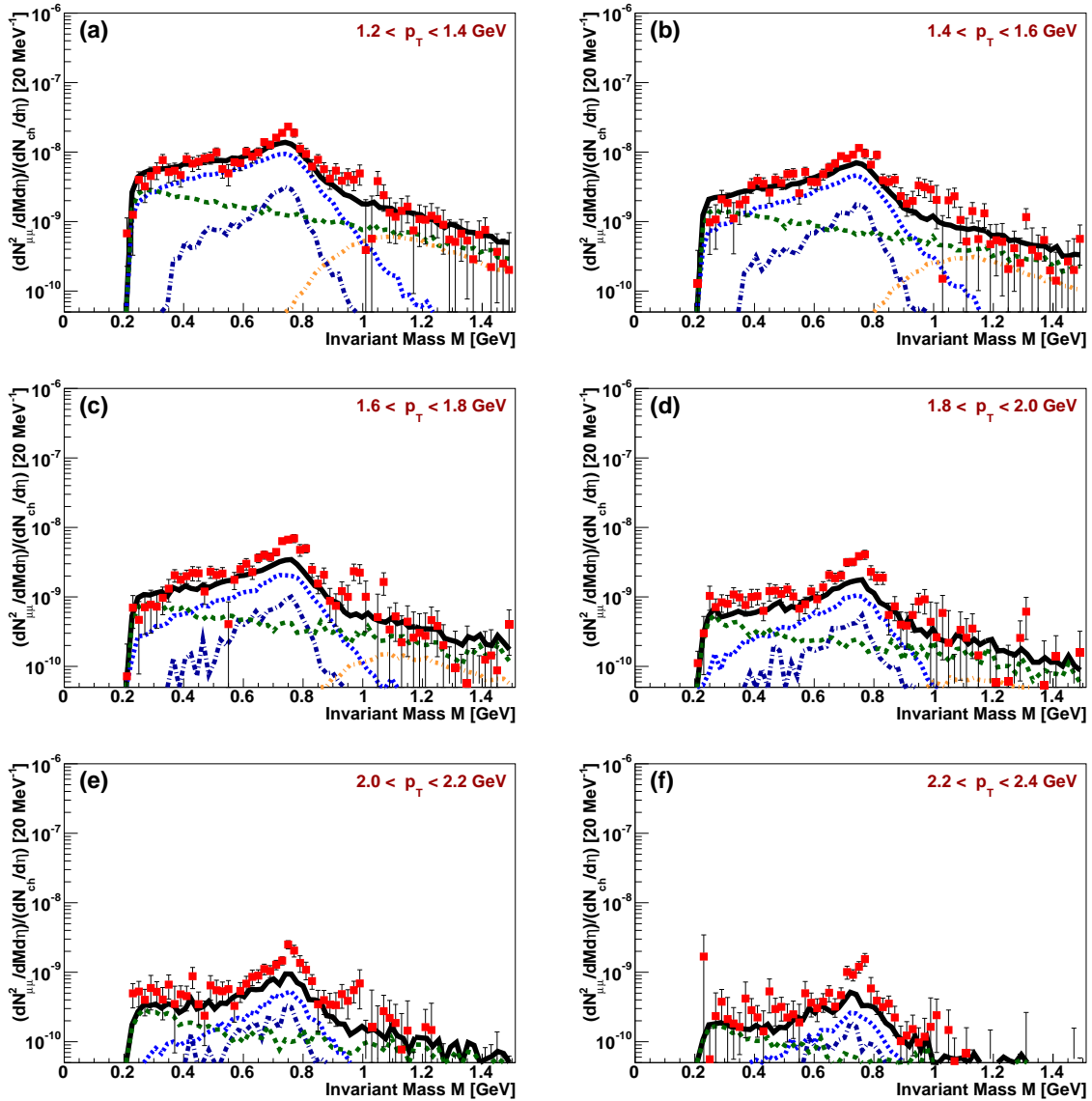


FIG. 8. Same as in Figure 7, but for higher p_t -bins ranging from $p_t = 1.2$ to 2.4 GeV. The different contributions are the same as in Figures 5 and 6. The results are compared to the experimental data from the NA60 Collaboration [11].

become less and less significant for higher momenta [6]. The resulting invariant mass spectra are shown in Figures 7 and 8, with 12 different plots representing the different p_t -bins with a width of $\Delta p_t = 200$ MeV, ranging from the lowest values $0.0 \leq p_t \leq 0.2$ GeV up to the highest transverse momentum bin with $2.2 \text{ GeV} \leq p_t \leq 2.4$ GeV. Our calculations once again agree with the data and especially show the clear momentum dependence of the ρ contribution in the region below the meson's pole mass. While for the lowest p_t -bin the yield in the mass range

from 0.2 GeV to 0.4 GeV exceeds even the yield at the pole mass, this excess becomes increasingly smaller when we go to higher transverse momenta. For the highest p_t -bin the shape of the ρ in the invariant mass spectrum looks almost as in the vacuum. Besides, the relative contribution from the non-thermal transport ρ is increasing when going to higher transverse momentum. It is in addition noteworthy that also the non-thermal ρ , for which no explicit in-medium modifications are implemented in UrQMD, shows dynamically some p_t -dependence of the

spectral shape. However, this is not surprising since the transport model includes effects like resonance excitation, rescattering or reabsorption that can cause such a momentum dependent mass distribution, i.e., the spectral properties of the transport ρ include some medium effects and thus differ from those in the vacuum. The very same microscopic mechanisms, of course, also cause the medium modifications of the spectral functions within the thermal quantum-field theoretical models.

Yet, for p_t greater than 1.2 GeV the yield in the pole mass region of the ρ meson, i.e. at $M \approx 770$ MeV, is still not described fully. The experimental data show a more prominent and sharper peak structure than we find within our approach. Some of the "freeze-out" respectively "vacuum" ρ contribution might be missing in spite of including the non-thermal transport ρ .

In general it is interesting to see how the correct description of all the three different thermal contributions is necessary to achieve agreement with the data over the whole transverse momentum range. For example, at the lowest masses (below 0.4 GeV) the broadened ρ delivers the significant contribution for low p_t , while at higher p_t the emission from the deconfined phase dominates at these masses. This is another good benchmark that shows that we obviously describe the thermal emission quite realistically. Nevertheless, one also has to stress that the results for the total dilepton spectra obtained in the present study agree with the studies performed with fireball parametrizations, though the space-time evolution shows significant differences between the two models. This indicates that the time-integral nature of dilepton spectra to a large extent disguises the details of the reaction dynamics by averaging over volume and lifetime.

IV. CONCLUSIONS & OUTLOOK

In this paper we have presented a coarse-graining approach to the calculation of dilepton production in heavy-ion collisions. Using an ensemble of several events from transport calculations with the UrQMD model, we put the output on a space-time grid of small cells. By averaging the particle distribution in each cell over a large number of events and going into the local rest frame we can calculate the energy and baryon density and consequently temperature and chemical potential by introducing an equation of state. When the thermodynamic properties of the cell are known the corresponding thermal dilepton emission rates can be determined. With this procedure it is aimed to achieve a more realistic description of dilepton production in heavy-ion collisions. Since a complete non-equilibrium treatment of medium modifications is an extremely difficult task, the coarse-graining approach is intended as a compromise to apply in-medium spectral functions in combination with a microscopic description of the bulk evolution of a heavy-ion collision.

The agreement between our results for thermal dilep-

ton invariant- and transverse-mass spectra and the experimental findings of the NA60 collaboration is very good. The coarse-graining study also confirms previous calculations with the same spectral function within a fireball approach [14, 15, 73]. However, it is remarkable that in spite of differences in the dynamics of the reaction, the final results are so similar in both approaches. The main distinctions are, in summary:

- (i) The rise of large chemical potentials in the earlier stages of the reaction within the coarse-graining approach, while in the fireball model a finite μ_π shows up after the freeze-out.
- (ii) A larger fraction of QGP dilepton contribution is found in the fireball model while we get less QGP and more hadronic emission when coarse-graining the microscopic dynamics.
- (iii) The lifetime of the hot and dense system is about 7 fm/c in the fireball parametrization while we still find thermal emission even after much longer time of 15 fm/c in the present study. Note hereby that for the latter case T , μ_B (respectively ρ_{eff}) and μ_π are determined locally whereas the fireball model assumes global thermal equilibrium.

The obvious explanation for the agreement is that the dilepton spectra are only time-integrated results and therefore less significant with regard to the very details of the reaction evolution but rather the global scale of the dynamics, i.e., one is mainly sensitive to the average thermal properties of the system. The high-mass tail of the invariant mass spectrum, which is clearly dominated by the QGP emission (i.e. for $M > 1.5$ GeV) is a good example for this. It reflects the true average temperature of the source (without blue shifts as in the photon case) and was found to be roughly 205 MeV in fireball models. Looking at the details, one finds however that the QGP yield for very high masses over 2.5 MeV is larger in the coarse-graining, but the overall slope of the partonic emission is flatter so that the differences between the two approaches show up especially at lower masses. This can be explained by the fact that we have some very hot cells with temperatures above 300 MeV populating the yield at very high masses, while the initial temperature in the fireball is only 245 MeV. In contrast, the overall QGP emitting volume is larger in the fireball model due to the assumption of global equilibrium, while only a limited number of cells reaches above T_c in the coarse-graining approach. For lower masses, less QGP yield is counter-balanced by a larger hadronic contribution. This is not surprising, because the lower number of high-temperature cells corresponds to a larger fraction of low-temperature emission. A more detailed comparison beyond this will be addressed in a future work. However, it becomes already clear that there are several aspects which only show up in their combined effect in the dilepton spectra, so e.g. a smaller volume can be compensated by a longer lifetime of the fireball.

Nevertheless, in spite of the insensitivity with regard to the detailed reaction dynamics, we can also draw some conclusions by the agreement of the results from the fireball and coarse-graining model:

1. The large influence of baryons on the spectral shape of the ρ which is clearly responsible for the enhancement of the dilepton yield in the mass range $0.2 \text{ GeV} < M_{\mu\mu} < 0.6 \text{ GeV}$. The most significant modifications of the spectral function of the ρ are found at low momenta, in line with previous experimental and theoretical investigations.
2. Thermal emission from the QGP, at least in parts for temperatures significantly above the critical temperature T_c . Without this both models fail to fully explain the invariant mass spectrum at higher invariant masses.
3. Especially for the mass region above the ρ meson, i.e. for $1 \text{ GeV} < M_{\mu\mu} < 2 \text{ GeV}$ the results also strengthen the hypothesis of quark-hadron duality, i.e., that the thermal emission rates are dual in the temperature range around the transition temperature between the partonic and the hadronic phase.

For the future the latter two points deserve further investigation, especially with regard to the transition from the hadronic to the partonic phase. The present results show that it will be hard to definitely determine details of the evolution of the reaction by means of dilepton spectra. But the question whether electromagnetic probes can give hints for the creation of a QGP phase or whether

duality prohibits to discriminate between hadronic and partonic emission in the transition region might be clarified in theoretical studies at lower collision energies as, e.g., covered by the Beam-Energy Scan program at the Relativistic Heavy Ion Collider (RHIC) and the future FAIR facility (with $E_{\text{lab}} = 8 - 35 \text{ AGeV}$). But also a full understanding of the medium modifications of hadron properties and the possible restoration of chiral symmetry has not yet been obtained and further theoretical and experimental studies are desirable, especially exploring the high- μ_B region of the QCD phase diagram.

Considering the aspects mentioned above, the fundamental applicability of the coarse-graining approach for all kinds of collision energies opens the possibility for a broad variety of future investigations. For low-energy heavy-ion collisions as investigated at the GSI SIS (HADES) it offers a unique option, since an application of conventional hydrodynamic or fireball models seems not reasonable here and microscopic transport models failed to give an unambiguous explanation of the observed dilepton spectra at low bombarding energies. The expected high baryon densities in these cases make a detailed study of the thermodynamic properties interesting.

ACKNOWLEDGMENTS

The authors especially thank Ralf Rapp for providing his spectral function and for many fruitful discussions. This work was supported by the Hessian Initiative for Excellence (LOEWE) through the Helmholtz International Center for FAIR (HIC for FAIR), the Federal Ministry of Education and Research (BMBF) and the Helmholtz Research School for Quark-Matter Studies (H-QM).

-
- [1] T. Hatsuda and S. H. Lee, *Phys. Rev. C* **46**, 34 (1992).
 - [2] R. Rapp and J. Wambach, *Adv. Nucl. Phys.* **25**, 1 (2000).
 - [3] G. Brown and M. Rho, *Phys. Rept.* **363**, 85 (2002).
 - [4] R. S. Hayano and T. Hatsuda, *Rev. Mod. Phys.* **82**, 2949 (2010).
 - [5] R. Rapp, J. Wambach, and H. van Hees, in R. Stock (ed.), *Relativistic Heavy Ion Physics*, vol. 23 of *Landolt-Börnstein - Group I Elementary Particles, Nuclei and Atoms*, 134–175 (Springer, Berlin, 2010).
 - [6] S. Leupold, V. Metag, and U. Mosel, *Int. J. Mod. Phys. E* **19**, 147 (2010).
 - [7] L. H. Xia, C. M. Ko, L. Xiong, and J. Q. Wu, *Nucl. Phys. A* **485**, 721 (1988).
 - [8] C. Gale and K. L. Haglin, in R. C. Hwa and X.-N. Wang (eds.), *Quark-Gluon Plasma 3* (World Scientific, Singapore, 2004), arXiv: hep-ph/0306098.
 - [9] R. Arnaldi et al. (NA60 Collaboration), *Phys. Rev. Lett.* **96**, 162302 (2006).
 - [10] R. Arnaldi et al. (NA60 Collaboration), *Phys. Rev. Lett.* **100**, 022302 (2008).
 - [11] R. Arnaldi et al. (NA60 Collaboration), *Eur. Phys. J. C* **61**, 711 (2009).
 - [12] R. Arnaldi et al. (NA60 Collaboration), *Eur. Phys. J. C* **59**, 607 (2009).
 - [13] G. Agakichiev et al. (CERES Collaboration), *Phys. Rev. Lett.* **75**, 1272 (1995).
 - [14] H. van Hees and R. Rapp, *Phys. Rev. Lett.* **97**, 102301 (2006).
 - [15] H. van Hees and R. Rapp, *Nucl. Phys. A* **806**, 339 (2008).
 - [16] K. Dusling, D. Teaney, and I. Zahed, *Phys. Rev. C* **75**, 024908 (2007).
 - [17] J. Ruppert, C. Gale, T. Renk, P. Lichard, and J. I. Kapusta, *Phys. Rev. Lett.* **100**, 162301 (2008).
 - [18] S. A. Bass, M. Belkacem, M. Bleicher, M. Brandstetter, L. Bravina, et al., *Prog. Part. Nucl. Phys.* **41**, 255 (1998).
 - [19] M. Bleicher, E. Zabrodin, C. Spieles, S. A. Bass, C. Ernst, et al., *J. Phys. G* **25**, 1859 (1999).
 - [20] W. Ehehalt and W. Cassing, *Nucl. Phys. A* **602**, 449 (1996).
 - [21] O. Buss, T. Gaitanos, K. Gallmeister, H. van Hees, M. Kaskulov, et al., *Phys. Rept.* **512**, 1 (2012).
 - [22] W. Cassing, E. Bratkovskaya, R. Rapp, and J. Wambach, *Phys. Rev. C* **57**, 916 (1998).
 - [23] B. Schenke and C. Greiner, *Phys. Rev. C* **73**, 034909 (2006).
 - [24] B. Schenke and C. Greiner, *Phys. Rev. Lett.* **98**, 022301 (2007).
 - [25] B. Schenke and C. Greiner, *Nucl. Phys. A* **785**, 170

- (2007).
- [26] E. Bratkovskaya, W. Cassing, and O. Linnyk, Phys. Lett. B **670**, 428 (2009).
- [27] W. Cassing and E. Bratkovskaya, Nucl. Phys. A **831**, 215 (2009).
- [28] H. Barz, B. Kampfer, G. Wolf, and M. Zetenyi, Open Nucl. Part. Phys. J. **3**, 1 (2010).
- [29] O. Linnyk, E. Bratkovskaya, V. Ozvenchuk, W. Cassing, and C. Ko, Phys. Rev. C **84**, 054917 (2011).
- [30] J. Weil, H. van Hees, and U. Mosel, Eur. Phys. J. A **48**, 111 (2012).
- [31] J. Weil, U. Mosel, and V. Metag, Phys. Lett. B **723**, 120 (2013), 1210.3074.
- [32] R. Rapp, Adv. High Energy Phys. **2013**, 148253 (2013).
- [33] D. Teaney, J. Lauret, and E. Shuryak (2001), arXiv: nucl-th/0110037.
- [34] T. Hirano and K. Tsuda, Phys. Rev. C **66**, 054905 (2002).
- [35] P. F. Kolb and U. Heinz, in R. C. Hwa and X.-N. Wang (eds.), *Quark-Gluon Plasma 3* (World Scientific, Singapore, 2004).
- [36] C. Nonaka and S. A. Bass, Phys. Rev. C **75**, 014902 (2007).
- [37] G. Vujanovic, C. Young, B. Schenke, R. Rapp, S. Jeon, et al., Phys. Rev. C **89**, 034904 (2014).
- [38] L. Bravina, E. Zabrodin, M. I. Gorenstein, S. Bass, M. Belkacem, et al., Phys. Rev. C **60**, 024904 (1999).
- [39] E. Santini, J. Steinheimer, M. Bleicher, and S. Schramm, Phys. Rev. C **84**, 014901 (2011).
- [40] P. Huovinen, M. Belkacem, P. J. Ellis, and J. I. Kapusta, Phys. Rev. C **66**, 014903 (2002).
- [41] H. Petersen, M. Bleicher, S. A. Bass, and H. Stöcker (2008), 0805.0567.
- [42] <http://www.urqmd.org>.
- [43] C. Eckart, Phys. Rev. **58**, 919 (1940).
- [44] P. Braun-Munzinger, J. Stachel, J. Wessels, and N. Xu, Phys. Lett. B **365**, 1 (1996).
- [45] J. Cleymans, D. Elliott, H. Satz, and R. Thews, Z. Phys. C **74**, 319 (1997).
- [46] A. Andronic, P. Braun-Munzinger, and J. Stachel, Nucl. Phys. A **772**, 167 (2006).
- [47] L. Bravina, M. I. Gorenstein, M. Belkacem, S. Bass, M. Bleicher, et al., Phys. Lett. B **434**, 379 (1998).
- [48] L. Bravina, M. Brandstetter, M. I. Gorenstein, E. Zabrodin, M. Belkacem, et al., J. Phys. G **25**, 351 (1999).
- [49] W. Florkowski and R. Ryblewski, Phys. Rev. C **83**, 034907 (2011).
- [50] W. Florkowski, M. Martinez, R. Ryblewski, and M. Strickland, Nucl. Phys. A **904-905**, 803c (2013).
- [51] D. Zschesche, S. Schramm, J. Schaffner-Bielich, H. Stöcker, and W. Greiner, Phys. Lett. B **547**, 7 (2002).
- [52] H. Petersen, J. Steinheimer, G. Burau, M. Bleicher, and H. Stöcker, Phys. Rev. C **78**, 044901 (2008).
- [53] P. Papazoglou, D. Zschesche, S. Schramm, J. Schaffner-Bielich, H. Stöcker, et al., Phys. Rev. C **59**, 411 (1999).
- [54] D. Zschesche, G. Zeeb, and S. Schramm, J. Phys. G **34**, 1665 (2007).
- [55] M. He, R. J. Fries, and R. Rapp, Phys. Rev. C **85**, 044911 (2012).
- [56] R. Rapp (2014), private communication.
- [57] M. Kataja and P. Ruuskanen, Phys. Lett. B **243**, 181 (1990).
- [58] H. Bebie, P. Gerber, J. Goity, and H. Leutwyler, Nucl. Phys. B **378**, 95 (1992).
- [59] P. F. Kolb and R. Rapp, Phys. Rev. C **67**, 044903 (2003).
- [60] J. Sollfrank, P. Koch, and U. W. Heinz, Z. Phys. C **52**, 593 (1991).
- [61] E. L. Feinberg, Nuovo Cim. A **34**, 391 (1976).
- [62] L. D. McLerran and T. Toimela, Phys. Rev. D **31**, 545 (1985).
- [63] V. L. Eletsky, M. Belkacem, P. Ellis, and J. I. Kapusta, Phys. Rev. C **64**, 035202 (2001).
- [64] R. Rapp and J. Wambach, Eur. Phys. J. A **6**, 415 (1999).
- [65] M. Dey, V. Eletsky, and B. L. Ioffe, Phys. Lett. B **252**, 620 (1990).
- [66] R. Barate et al. (ALEPH Collaboration), Eur. Phys. J. C **4**, 409 (1998).
- [67] H.-T. Ding, A. Francis, O. Kaczmarek, F. Karsch, E. Laermann, et al., Phys. Rev. D **83**, 034504 (2011).
- [68] J. Cleymans, J. Fingberg, and K. Redlich, Phys. Rev. D **35**, 2153 (1987).
- [69] K. Schmidt, E. Santini, S. Vogel, C. Sturm, M. Bleicher, et al., Phys. Rev. C **79**, 064908 (2009).
- [70] G.-Q. Li, C. M. Ko, G. E. Brown, and H. Sorge, Nucl. Phys. A **611**, 539 (1996).
- [71] H. J. Specht (NA60 Collaboration), AIP Conf. Proc. **1322**, 1 (2010).
- [72] S. Damjanovic et al. (NA60 Collaboration), Nucl. Phys. A **783**, 327 (2007).
- [73] R. Rapp and H. van Hees (2014), arXiv: 1411.4612 [hep-ph].

Dilepton production and reaction dynamics in heavy-ion collisions at SIS energies from coarse-grained transport simulations

Stephan Endres,* Hendrik van Hees, Janus Weil, and Marcus Bleicher
*Frankfurt Institute for Advanced Studies, Ruth-Moufang-Straße 1, D-60438 Frankfurt, Germany and
 Institut für Theoretische Physik, Universität Frankfurt,
 Max-von-Laue-Straße 1, D-60438 Frankfurt, Germany*
 (Dated: July 6, 2015)

Dilepton invariant-mass spectra for heavy-ion collisions at SIS 18 and BEVALAC energies are calculated using a coarse-grained time evolution from the Ultra-relativistic Quantum Molecular Dynamics (UrQMD) model. The coarse-graining of the microscopic simulations enables to calculate thermal dilepton emission rates by application of in-medium spectral functions from equilibrium quantum-field theoretical calculations. The results show that extremely high baryon chemical potentials dominate the evolution of the created hot and dense fireball. Consequently, a significant modification of the ρ spectral shape becomes visible in the dilepton invariant-mass spectrum, resulting in an enhancement in the low-mass region $M_{ee} = 200$ to 600 MeV/ c^2 . This enhancement, mainly caused by baryonic effects on the ρ spectral shape, can fully describe the experimentally observed excess above the hadronic cocktail contributions in Ar+KCl ($E_{\text{lab}} = 1.76$ AGeV) reactions as measured by the HADES collaboration and also gives a good explanation of the older DLS Ca+Ca ($E_{\text{lab}} = 1.04$ AGeV) data. For the larger Au+Au ($E_{\text{lab}} = 1.23$ AGeV) system, we predict an even stronger excess from our calculations. A systematic comparison of the results for different system sizes from C+C to Au+Au shows that the thermal dilepton yield increases stronger ($\propto A^{4/3}$) than the hadronic background contributions, which scale with A , due to its sensitivity on the time evolution of the reaction. We stress that the findings of the present work are consistent with our previous coarse-graining results for the NA60 measurements at top SPS energy. We argue that it is possible to describe the dilepton results from SIS 18 up to SPS energies by considering the modifications of the ρ spectral function inside a hot and dense medium within the same model.

PACS numbers: 24.10.Lx, 25.75.Cj
 Keywords: Monte Carlo simulations, Dilepton production

I. INTRODUCTION

The study of dilepton production has for long been proposed as a good method to probe the change of hadronic properties in the hot and dense matter created in heavy-ion collisions and also as a possible observable for the creation of a deconfined phase at sufficiently high collision energies [1–4]. In contrast to the vacuum situation, a hadron can not only decay in a hot and dense medium but also interact with the constituents of the medium in scattering processes and resonance excitation. Many theoretical efforts have been undertaken over the last years to gain a better understanding of the in-medium properties of vector mesons [5–8]. The behavior of hadrons is of immanent interest for a full understanding of the phase structure given by Quantum Chromodynamics (QCD). One much-discussed aspect here is the change of the symmetries of QCD which is expected when going from the vacuum to finite temperature and finite baryochemical potential, especially the predicted restoration of chiral symmetry [9, 10]. Unlike all hadronic observables, which only provide information on the final freeze-out stage of the system, dileptons are not subject to strong interactions and consequently escape the fireball unscathed.

However, this also means that lepton pairs from all stages of the reaction will reach the detector. Especially for a theoretical description this is a big challenge, as it demands a realistic description of the whole space-time evolution of the heavy-ion reaction and taking the various dilepton sources into account.

On the experimental side several groups have undertaken the challenging task to measure dilepton spectra in heavy-ion collisions and thereby constrain the theoretical predictions. At SPS energies the NA60 Collaboration was able to measure the ρ in-medium spectral function for the first time, thanks to the high precision of the measurement [11]. The results were in line with previous CERES results [12] and found an excess in the invariant mass range from 0.2 to 0.6 GeV/ c^2 . This excess can be explained by a broadening of the ρ meson inside the hot and dense medium with small mass shifts [13–16]. At RHIC, these investigations were extended to even higher collision energies with basically the same results except for less dominant baryonic effects and a larger fraction of dileptons stemming from the QGP [17, 18].

Still more challenging is the interpretation of the dilepton measurements, which were performed in the low-energy regime at SIS 18 and BEVALAC. For collision energies around $E_{\text{lab}} \approx 1 - 2$ AGeV, which will be in the focus of the present study, the DLS Collaboration measured a large excess beyond the results of theoretical microscopic calculations several years ago [19]. This

* endres@th.physik.uni-frankfurt.de

disagreement between experiment and theory was called the ‘‘DLS puzzle’’. In consequence, it triggered further experimental and theoretical investigations. Recently, the HADES experiment confirmed the former DLS results with a higher precision [20–23]. Although the theoretical microscopic models have been largely improved and extended since this time [24–29], a full and unambiguous description of the data has not yet been found. A satisfying answer is complicated by the fact that at such low energies a large number of processes contributes to the dilepton production, for which many parameters (like cross-sections, branching ratios, etc.) are not well-known. In addition interference effects are posing serious problems for transport Monte-Carlo simulations based on the evolution of phase-space densities. Here future measurements, for example in pion induced reactions as conducted by HADES, could give better constraints for the various parameters and reduce the uncertainty of the different contributions [30]. In any case, a full description of in-medium effects via off-shell dynamics or multi-particle interactions at high densities remains a difficult task, although some investigations on these issues have been conducted successfully [25, 31–37].

Besides the microscopic transport models, there exist also macroscopic approaches describing the evolution of the heavy-ion collision in terms of its thermodynamic properties. At high collision energies, i.e. at SPS or RHIC, a thermal calculation of dilepton emission is often applied, where a fireball expansion or a hydrodynamic calculation is used to model the bulk evolution of the system, while the dilepton emission is calculated using spectral functions at a given T and μ_B [13, 15, 38–40]. But this approach works only if the collision energy is high enough. The application at $E_{\text{lab}} \approx 1\text{--}2\text{ AGeV}$ is hardly reliable.

However, there are no reasons why a macroscopic description of the reaction dynamics should not be possible at SIS18 and BEVALAC energies, provided one can extract realistic values of energy and baryon density and, in consequence, temperature and baryochemical potential. On the contrary, due to the expected high values of the baryon chemical potential, a study of the thermal properties of the system and the influence on the spectral shape of vector mesons might be very instructive. In the present work we argue that it is possible to obtain realistic values of T and μ_B from microscopic calculations, provided one uses a large ensemble of events and averages over them (i.e. one ‘‘coarse-grains’’ the results) to obtain a locally smooth phase-space distribution. This ansatz, which was first presented and applied for the calculation of dilepton and photon spectra in [41], constitutes a compromise between (non-equilibrium) microscopic transport simulations and the calculation of dilepton emission with (equilibrium) spectral functions.

The same model was described in detail in [16] and already successfully applied to investigate dilepton production at SPS energies [42, 43]. The ansatz is used basically unchanged for the present low-energy study. The

only important extension is the implementation of the in-medium spectral function for the ω meson. While for the NA60 results the cocktail contribution of the ω was already subtracted from the thermal dilepton spectra, for comparing our calculations to the experimental HADES and DLS results a full description of the ω contribution is required. Furthermore, the high baryon densities and slow evolution of the system increase the significance of its medium modifications at the energies considered here.

Note that we focus the present investigation on the larger systems Ar+KCl and Au+Au, where local thermalization can be assumed due to the size of the hot and dense fireball. For the smaller C+C system, which was also studied by HADES and DLS (in nearly minimum bias reactions), one finds that the average number of NN-collisions is so small that the assumption of a local thermalization is questionable. Furthermore, the experimental results indicate that the C+C dilepton spectra can be interpreted as the superposition of the underlying p+p and p+n collisions without any significant in-medium effects [22]. (However, when studying the effect of the system size on the dilepton production we will also consider central C+C collisions later on for completeness.)

This paper is organized as follows. Section II gives an introduction to the model and an overview of the different contributions considered for the calculation. Section III then presents the results for the thermodynamic evolution of the reaction (Sec. III A) and the resulting dilepton spectra (Sec. III B), furthermore the effect of the system size and fireball lifetime on the thermal dilepton yield is studied (Sec. III C). Finally, conclusions are drawn and an outlook to future studies is given in section IV.

II. THE MODEL

The full theoretical description of the dilepton spectra requires to consider a large number of different production processes. At SIS energies, all dileptons stem from hadronic sources, in contrast to the situation at SPS, RHIC or LHC energies, where a significant contribution is assumed to come from $q\bar{q}$ -annihilation in the quark-gluon plasma [44]. In general one can distinguish between two different hadronic contributions, such from long-lived particles (especially π and η mesons) and those from the short-lived light vector mesons (mainly ρ , but also ω and ϕ). The former have a life time which is significantly larger than the duration of the hot and dense stage in a heavy-ion collision. Consequently, almost all of the decays of the long-lived mesons into lepton pairs will happen in the vacuum, i.e., no modification of the spectral shape is expected for those contributions. In contrast the latter mesons have a short life time and will therefore decay to a significant amount inside the fireball and their spectral properties are altered by the medium.

These differences are also significant for our approach. For the π and η meson contribution it is neither nec-

essary nor adequate to calculate thermal dilepton emission. The yields of these hadrons are determined directly from calculations with the UrQMD transport approach. For the ρ and the ω , however, we calculate the thermal emission from coarse-grained transport simulations by application of in-medium spectral functions. Here the influence of the space-time evolution of the fireball is immanent, as the spectral shape will largely depend on the values of temperature T and baryon chemical potential μ_B . Although for the ϕ some medium-modifications of the spectral shape are predicted as well, we here skip a full thermal calculation for the present investigation. On the one hand, ϕ production is strongly suppressed at the low energies considered here and will therefore hardly give any significant contribution to the invariant mass spectrum, on the other hand the predicted medium effects are rather small. Consequently, the ϕ contribution is directly extracted from the UrQMD calculations, as applied for the π and η . At higher invariant dilepton masses, i.e. mainly above $1 \text{ GeV}/c^2$, also multi-pion states in form of broad resonances influence the dilepton production. This contribution is also calculated as thermal emission.

The underlying model for all our considerations is the Ultra-relativistic Quantum Molecular Dynamics approach (UrQMD), which is a non-equilibrium cascade model [45–48]. It includes all relevant hadronic resonances up to a mass of $2.2 \text{ GeV}/c^2$. The model gives an effective solution to the Boltzmann equation. The hadrons are propagated on classical trajectories and can interact in form of elastic and inelastic scatterings. Production of new particles via resonance formation (e.g., $\pi + \pi \rightarrow \rho$) or the decay of resonances in form of $\Delta \rightarrow N + \pi$. String excitation is possible for hadron-hadron collisions with $\sqrt{s} > 3 \text{ GeV}$ but is negligible in the SIS energy regime considered here.

A. Coarse-Grained Contributions

For the calculation of thermal emission rates by applying in-medium spectral functions, one needs to extract the local thermodynamic properties from the UrQMD simulations. To obtain a phase-space distribution that is sufficiently smooth in a small volume ΔV around each point in space-time, we simulate a large ensemble of events. A grid of space-time cells with $\Delta x = \Delta y = \Delta z = 0.7 - 0.8 \text{ fm}$ and $\Delta t = 0.6 \text{ fm}/c$ is set up and the energy-momentum tensor $T_{\mu\nu}$ as well as the net-baryon four-flow j_μ^B are determined in each of these cells as

$$\begin{aligned} T^{\mu\nu} &= \int d^3p \frac{p^\mu p^\nu}{p^0} f(\vec{x}, \vec{p}, t) = \frac{1}{\Delta V} \left\langle \sum_{i=1}^{N_h \in \Delta V} \frac{p_i^\mu \cdot p_i^\nu}{p_i^0} \right\rangle, \\ j_B^\mu &= \int d^3p \frac{p^\mu}{p^0} f_B(\vec{x}, \vec{p}, t) = \frac{1}{\Delta V} \left\langle \sum_{i=1}^{N_{B/\bar{B}} \in \Delta V} \pm \frac{p_i^\mu}{p_i^0} \right\rangle. \end{aligned} \quad (1)$$

The rest frame according to Eckart [49] can be found by performing a Lorentz boost such that the baryon flow vanishes in the cell, i.e. $\vec{j}_B = 0$. In the Eckart frame we extract the energy density ϵ and baryon density ρ_B as an input to obtain the temperature T and baryon chemical potential μ_B by applying an equation of state. At SIS energies it is sufficient to use a hadron-resonance gas (HG-EoS) [50]. This HG-EoS includes the same degrees of freedom as the UrQMD model.

It is important to bear in mind that the procedure as described above assumes local (isotropic) equilibrium in the cell. In macroscopic descriptions of heavy-ion collisions kinetic and chemical equilibrium is usually introduced as an ad-hoc assumption. However, we extract the thermal properties from a transport (i.e. non-equilibrium) approach which has effects as viscosity and heat conduction. Although the creation of an approximately equilibrated stage is usually considered to happen on extremely short time scales after the beginning of the collision, it is difficult to prove the creation of thermal and chemical equilibrium explicitly. Previous studies comparing UrQMD calculations with the results from the statistical thermal model showed that it might take up to 8-10 fm/c before one can assume the system to be in approximate kinetic and chemical equilibrium on a global scale [51, 52]. For practical reasons we use the momentum-space anisotropy to characterize to which degree the local kinetic equilibrium is constituted in the present study. Here, the coarse-grained microscopic transport calculations show a significant deviation from equilibrium in form of large pressure differences between the longitudinal and transverse components of the energy momentum tensor at the beginning of the reaction: During the first few fm/c the longitudinal pressure is significantly larger than the transverse pressures, which is mainly due to the deposition of high longitudinal momenta from the colliding nuclei. It has been suggested that in this case one can determine realistic values for the energy density by using a generalized equation of state [53, 54] where

$$\epsilon_{\text{real}} = \frac{\epsilon}{r(x)}. \quad (2)$$

For a system with Boltzmann-type pressure anisotropies the relaxation function $r(x)$ takes the form

$$r(x) = \begin{cases} \frac{x^{-1/3}}{2} \left(1 + \frac{x \operatorname{artanh} \sqrt{1-x}}{\sqrt{1-x}} \right) & \text{for } x \leq 1 \\ \frac{x^{-1/3}}{2} \left(1 + \frac{x \operatorname{arctan} \sqrt{x-1}}{\sqrt{x-1}} \right) & \text{for } x \geq 1 \end{cases}, \quad (3)$$

where $x = (P_{\parallel}/P_{\perp})^{3/4}$ denotes the pressure anisotropy. With this result we can extract meaningful energy densities from the coarse-grained distributions also in the very early stage of the reaction, as has already been shown in [16].

With the values of T and μ_B known for all cells, the calculation of the thermal dilepton emission is straight-

forward [7, 55] and takes the form

$$\frac{dN_{ll}}{d^4x d^4q} = -\frac{\alpha_{\text{em}}^2 L(M)}{\pi^3 M^2} f^{\text{B}}(q \cdot U; T) \times \text{Im} \Pi_{\text{em}}^{(\text{ret})}(M, \vec{q}; \mu_B, T) \quad (4)$$

with the Bose distribution function f^{B} and the lepton phase-space $L(M)$, while M and q denote the invariant mass and the momentum of the lepton pair, respectively, and α_{em} is the electromagnetic coupling constant. The relevant physical quantity is the retarded electromagnetic current-current correlator $\Pi_{\text{em}}^{(\text{ret})}$ which contains all the information on the medium effects of the spectral function.

Note that equation (4) is derived for the case of full chemical equilibrium, which requires all chemical potentials of non-conserved charges to be zero. Similar to the kinetic anisotropies at the beginning of the reaction, also deviations from the chemical equilibrium composition of the system appear at the early stages of transport simulations. Especially an overpopulation of pions is observed here, which dominates the evolution for a significant period of time [56]. The appearance of a finite pion chemical potential μ_π was explained by the large initial production of pions and their long relaxation time [57, 58]. This is of particular importance for the present study since a finite chemical potential μ_π was considered to have a significant influence on the thermal dilepton emission rates by its influence on the π - ρ interactions [59, 60]. For the present calculations, we extract the pion chemical potential in Boltzmann approximation for each cell and consider its effect on the thermal dilepton emission (i) in form of its direct influence on the spectral functions and (ii) as additional fugacity factor, which will show up in equation (4) for the chemical non-equilibrium case.

In the following the different thermal contributions which are considered for the present study are discussed.

1. Thermal ρ and ω Emission

Several approaches for the description of in-medium effects on vector mesons exist. However, a full description of the different effects that influence the spectral shape in a hot and dense medium are highly non-trivial, and there are only a few calculations that include both the effects of finite temperature and density. E.g. in Ref. [61] the in-medium spectral functions were determined using empirical scattering amplitudes. However, this spectral function is calculated in low-density approximation for a weakly interacting pion-nucleon gas and tested only up to densities of $2\rho_0$. The application of this approach is therefore questionable for the situation at SIS energies where very high net baryon densities are reached.

In the present work a calculation from hadronic many-body theory [62–65] is applied, which has proven to successfully describe the dilepton spectra at SPS and RHIC energies [14, 66]. In the medium, three different contri-

butions to the self-energy of the ρ are taken into account here. These are

- (a) the modification of the pion cloud of the ρ meson by particle-hole and Δ -hole excitations in the medium,
- (b) scattering with mesons ($M = \pi, K, \bar{K}, \rho$) and
- (c) scattering with the most abundant baryon resonances ($B = N, \Delta_{1232}, N_{1440}^*, \dots$).

The in-medium propagator consequently takes the form

$$D_\rho = \frac{1}{M^2 - m_\rho^2 - \Sigma_{\rho\pi\pi} - \Sigma_{\rho M} - \Sigma_{\rho B}}. \quad (5)$$

The ω spectral function [66] is similarly constructed. However, here the situation is more complicated as the ω is basically a three-pion state, and the vacuum self-energy is given by decays into $\rho\pi$ or 3π . The full in-medium propagator reads

$$D_\omega = [M^2 - m_\omega^2 + i m_\omega (\Gamma_{3\pi} + \Gamma_{\rho\pi} + \Gamma_{\omega\pi \rightarrow \pi\pi}) - \Sigma_{\omega b_1} - \Sigma_{\omega B}]^{-1}. \quad (6)$$

It includes the following contributions:

- (a) $\omega \rightarrow \rho\pi$ decays including the corrections from the medium-modified ρ spectral function,
- (b) the direct $\omega \rightarrow 3\pi$ decays,
- (c) $\omega\pi \rightarrow \pi\pi$ inelastic scattering,
- (d) $\omega\pi \rightarrow b_1$ resonance scattering and
- (e) $\omega N \rightarrow N_{(1520)}, N_{(1650)}$ resonance scattering at an effective nucleon density ρ_{eff} .

To take into account the off-equilibrium of the pions an additional fugacity factor is introduced in equation (4), as already explained above. In one-loop approximation, for the thermal ρ and ω emission one obtains an additional overall fugacity factor [7]

$$z_\pi^n = e^{n\mu_\pi/T}. \quad (7)$$

The exponent n hereby takes the value 2 in case of the ρ emission and 3 for the ω contribution [13]. The final yield is then calculated according to

$$\frac{dN_{e^+e^-}}{dM} = \Delta x^4 \int \frac{d^3p}{p_0} \frac{dN_{e^+e^-}}{d^4x d^4p} z_\pi^n. \quad (8)$$

Note that the four-volume $\Delta x^4 = \Delta t \Delta V$ of the cell is an invariant quantity and therefore the same in all reference frames.

As it is not reasonable or possible to calculate thermal dilepton emission for all cells (e.g., due to low temperature) we also include a non-thermal (“freeze-out”) contribution for the ρ and ω meson. Those dileptons are directly extracted from the UrQMD calculations (for details see section II B 3).

2. Multi- π Contribution

Although it is known from previous theoretical investigations at higher collision energies that the multi-pion contribution plays a significant role only for masses greater than $1 \text{ GeV}/c^2$, which is mostly beyond the kinematic limit of dilepton production at SIS energies, we include this contribution for completeness. Here the same description as developed in [13, 14] is applied which uses chiral reduction techniques for the case of the chiral limit [67]. This leads to a chiral mixing of the isovector part of the vector and axial-vector correlators. The isovector-current correlation function takes the form

$$\begin{aligned} \Pi_V(p) = & (1 - \varepsilon) z_\pi^4 \Pi_{V,4\pi}^{\text{vac}} + \frac{\varepsilon}{2} z_\pi^3 \Pi_{A,3\pi}^{\text{vac}} \\ & + \frac{\hat{\varepsilon}}{2} (z_\pi^4 + z_\pi^5) \Pi_{A,5\pi}^{\text{vac}}, \end{aligned} \quad (9)$$

where $\hat{\varepsilon}$ denotes the mixing parameter which depends on temperature, critical temperature and the pion chemical potential. The result is an admixture of three-pion and five-pion axial-vector pieces on the vector four-pion part. Once again, as in case of the ρ and ω spectral functions, the effect of a finite pion chemical potential also enters in form of a fugacity factor z_π^n with $n = 3, 4, 5$ denoting the pion multiplicity of the corresponding state. Note that the two-pion and the three-pion piece corresponding to the decay $a_1 \rightarrow \rho + \pi$ are already included in the ρ spectral function and are therefore not considered for the multi-pion contribution.

B. Transport Contributions

1. π and η Dalitz Decay

The π^0 and the η pseudo-scalar mesons can both decay into a lepton pair via the Dalitz decays

$$\pi^0 \rightarrow \gamma l^+ l^-, \quad \eta \rightarrow \gamma l^+ l^-. \quad (10)$$

Following the scheme presented in [27], we treat this decay as a two-step process: First the decay of the pseudo-scalar meson into a photon γ and a virtual photon γ^* and the following electromagnetic conversion of the γ^* into a lepton pair [68]. The width of the meson decaying into a photon and a virtual photon can be related to the radiative decay width. The full expression then takes the form

$$\begin{aligned} \frac{d\Gamma_{M \rightarrow \gamma l^+ l^-}}{dM^2} = & 2\Gamma_{M \rightarrow 2\gamma} \left(1 - \frac{M^2}{m_M^2}\right)^3 \\ & \times |F_{M\gamma\gamma^*}(M^2)|^2 \frac{\alpha_{em}}{3\pi M^2} L(M). \end{aligned} \quad (11)$$

With the lepton phase space $L(M)$ and the form factor $F_{P\gamma\gamma^*}(M^2)$. Here we use the form factors as obtained from fits to experimental data, which are in very good

agreement with the values as predicted by the Vector Dominance Model [68]:

$$\begin{aligned} F_{\pi^0\gamma\gamma^*}(M^2) &= 1 + b_{\pi^0} M^2, \\ F_{\eta\gamma\gamma^*}(M^2) &= \left(1 - \frac{M^2}{\Lambda_\eta^2}\right)^{-2}, \end{aligned} \quad (12)$$

with $b_{\pi^0} = 5.5 \text{ GeV}^{-2}$ and $\Lambda_\eta = 0.72 \text{ GeV}$. Note that for this contribution, we only consider those particles from the final freeze-out of the calculation, neglecting all π and η which are reabsorbed during the evolution of the collision.

2. ϕ Direct Decay

The width for the direct decays of the vector mesons can be determined via [69]

$$\Gamma_{V \rightarrow ll}(M) = \frac{\Gamma_{V \rightarrow ll}(m_V)}{m_V} \frac{m_V^4}{M^3} L(M). \quad (13)$$

For the branching ratio at the meson pole mass m_V we use the value from the particle data group, $\Gamma_{\phi \rightarrow ee}(m_V)/\Gamma_{\text{tot}} = 2.95 \cdot 10^{-4}$ [70].

An important difference compared to the procedure for the long-lived pseudo-scalar mesons is the assumption that the ϕ mesons continuously emit dileptons over their lifetime [71]. That means, we track the time of production and the decay (or absorption) of the ϕ and integrate over the corresponding lifetime in the particle's rest frame.

$$\frac{dN_{ll}}{dM} = \frac{\Delta N_{ll}}{\Delta M} = \sum_{i=1}^{N_{\Delta M}} \sum_{j=1}^{N_p} \int_{t_i}^{t_f} dt \frac{\Gamma_{V \rightarrow ll}(M)}{\gamma_V \Delta M}. \quad (14)$$

The factor γ_V is here introduced to account for the relativistic time dilation in the computational frame compared to the vector mesons rest frame.

This ‘‘shining approach’’ is identical with the assumption of simply having one additional dilepton from each ϕ (weighted with the according branching ratio) if there is no absorption. But inside a dense medium, there is a significant chance that the particle will not decay but suffer an inelastic collision. Therefore the probability for the decay into a dilepton is reduced, and the shining as described above accounts for this effect [72].

3. Non-thermal ρ and ω

There are two situations, where a thermal calculation of the dilepton emission from spectral functions becomes difficult or even unreasonable. Firstly, for cells with no baryon content, where the Eckart definition of the rest-frame does not apply (those cells are found in the late stage of the reaction in very peripheral cells) and secondly for cells where the temperature is found to be below 50 MeV . In the latter case, when going to such usually

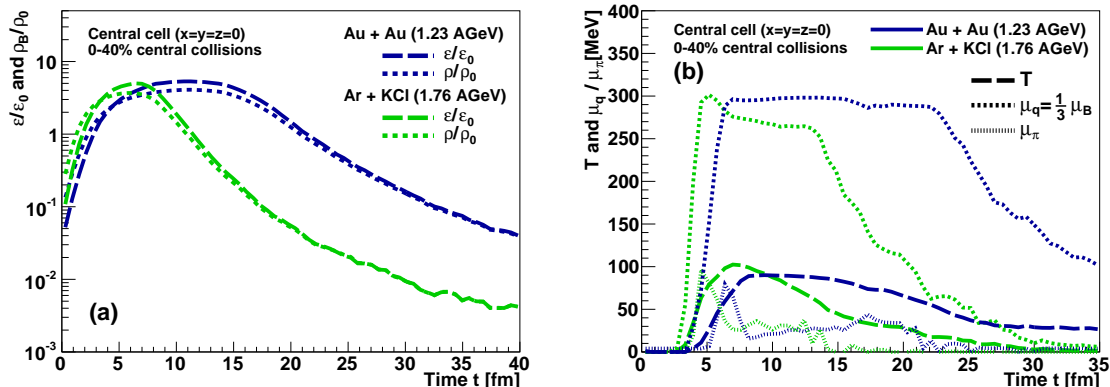


Figure 1. (Color online) Time evolution of the energy and baryon densities ε and ρ in units of the according ground-state densities (a) and for temperature T as well as the baryon and pion chemical potential, μ_B respectively μ_π (b) for the central cell (i.e., at $x = y = z = 0$). The results as obtained via coarse-graining of microscopic transport calculations are shown for Ar+KCl collisions at $E_{\text{lab}} = 1.76$ AGeV and for Au+Au reactions at 1.23 AGeV.

low-density cells, the determination of T and μ_B becomes less accurate and one will necessarily come to the point where the assumption of a thermalized system in the cell becomes unreliable. Consequently, we do not assume any thermal dilepton emission here. This procedure is in line with the findings of thermal-model studies [73], where it was shown that the freeze-out temperature in heavy-ion collisions at $E_{\text{lab}} = 1 - 2$ AGeV is around 50 MeV. This also indicates that it is neither necessary nor suggestive to assume thermalization of the system at lower temperatures.

However, one has to consider that dilepton emission from ρ and ω mesons is of course also possible in the cells for which one of the conditions mentioned above pertains. As the macroscopic picture is questionable here, we apply a similar procedure as for the ϕ (described in section II B 2) to extract the dilepton emission from the microscopic simulation. The width for the direct decays of the vector mesons can likewise be determined via equation (13). For the branching ratio at the meson-pole mass we use the values from the particle data group, i.e. $\Gamma_{\rho \rightarrow ee}/\Gamma_{\text{tot}} = 4.72 \cdot 10^{-5}$ and $\Gamma_{\omega \rightarrow ee}/\Gamma_{\text{tot}} = 7.28 \cdot 10^{-5}$ [70]. However, the ω can not only decay into a lepton pair directly, but also via Dalitz conversion into a pseudoscalar meson and a dilepton. As in the case of the π and the η equation (11) applies here. Only the form factor is different and takes the form

$$|F_\omega(M^2)|^2 = \frac{\Lambda_\omega^2 (\Lambda_\omega^2 + \gamma_\omega^2)}{(\Lambda_\omega^2 - M^2) + \Lambda_\omega^2 \gamma_\omega^2} \quad (15)$$

with the parameters $\Lambda_\omega = 0.65$ GeV and $\gamma_\omega = 0.04$ GeV [27, 74].

Similarly to the procedure for the ϕ meson, a continuous emission of dileptons from the ρ and ω is assumed in these special cases. However, as we consider space-time

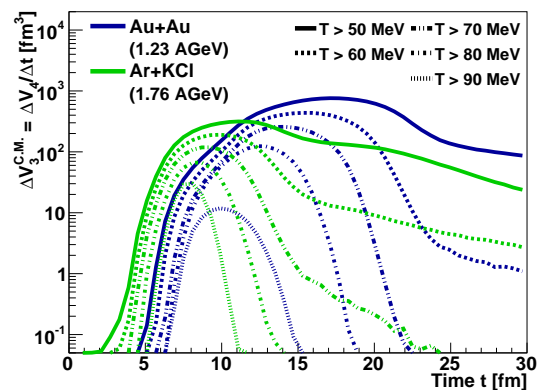


Figure 2. (Color online) Time evolution of the thermal volume $V_3^{\text{C.M.}}$ as seen from the center-of-momentum frame of the collision. This is equal to the thermal four-volume V_4 for each timestep divided by the length of Δt , which is $0.6 \text{ fm}/c$ here. The results are shown for Ar+KCl collisions at $E_{\text{lab}} = 1.76$ AGeV and for Au+Au reactions at 1.23 AGeV as obtained via coarse-graining of microscopic transport calculations. The results are plotted for different temperatures.

cells with a definite length of the time-steps Δt , the dilepton rate is multiplied with this time instead of the actual particle's lifetime within the cascade simulation. This is done to guarantee consistency, avoid double counting and strictly distinguish between cells with thermal and non-thermal emission. Consequently, here equation (14)

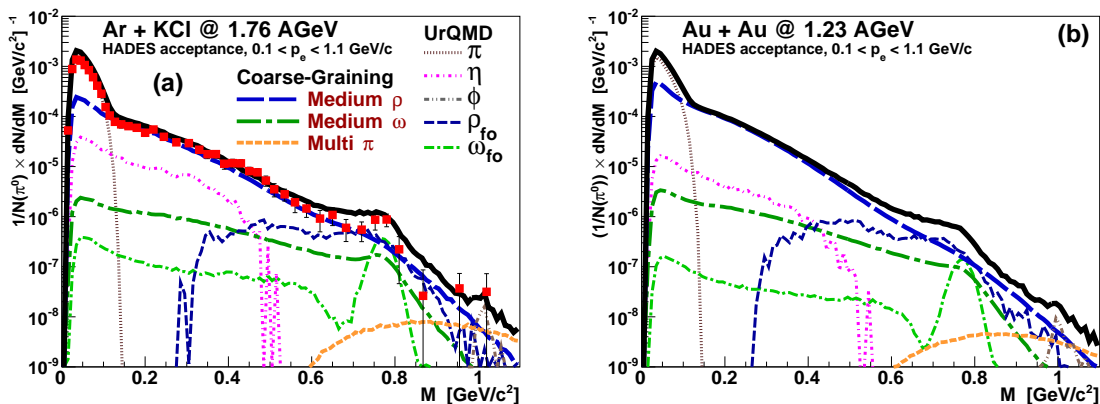


Figure 3. (Color online) Invariant mass spectra of the dielectron yield for Ar+KCl collisions at $E_{\text{lab}} = 1.76$ AGeV (a) and for Au+Au at $E_{\text{lab}} = 1.23$ AGeV (b). The results are normalized to the average total number of π^0 per event and shown within the HADES acceptance. The results for Ar+KCl are compared to the experimental data from the HADES Collaboration [23].

takes the form

$$\frac{dN_{ll}}{dM} = \frac{\Delta N_{ll}}{\Delta M} = \sum_{i=1}^{N_{\Delta M}} \sum_{j=1}^{N_V} \frac{\Delta t}{\gamma_V} \frac{\Gamma_{V \rightarrow ll}(M)}{\Delta M}, \quad (16)$$

and is applied for each time step Δt .

III. RESULTS

For the results presented here we used calculations with an ensemble of 1000 UrQMD events. However, several runs using different UrQMD events as input had to be performed to obtain enough statistics especially for the non-thermal ρ and ω contributions. Note that in case of the experimental Ar+KCl reaction we simulated the collision of two calcium ions instead, as this makes the calculation easier for symmetry reasons. Effectively it is the same as the Ar+K or Ar+Cl reactions that were measured in the experiment and the size of the system remains identical. To simulate the correct impact parameter distribution, we made a Woods-Saxon type fit to the HADES trigger conditions for Ar+KCl [75] and Au+Au [76]. In both cases this approximately corresponds to a selection of the 0-40% most central collisions. The number of π^0 per event, which will be important for the normalization of the dilepton spectra, are found to agree well with the HADES measurement for Ar+KCl reactions. Here the HADES collaboration measured $N_{\pi^0}^{\text{exp}} = 3.5$ where we find $N_{\pi^0}^{\text{sim}} \approx 3.9$, i.e. the deviation is only 12%. For the larger Au+Au system a number $N_{\pi^0}^{\text{sim}} \approx 8.0$ results from the events generated with the UrQMD model. Note that for reasons of self-consistency we normalize the dilepton spectra with the UrQMD π^0 yield, not the experimental one.

The final dilepton results were filtered with the HADES acceptance filter [77], and momentum cuts were applied to compare the simulations with the experimental results. As only very preliminary results and no filters are available for the Au+Au reactions at 1.23 AGeV, we used the same filter as for p+p and p+n reactions at 1.25 AGeV which should be quite close to the final acceptance [76].

In case of the DLS Ca+Ca spectrum, version 4.1 of the DLS acceptance filter [78] is used. Furthermore, an RMS smearing of 10% is applied to account for the detector resolution. For this reaction we used a minimum-bias simulation of Ca+Ca events, because impact-parameter distributions are not available for DLS. Here the final invariant-mass spectrum is normalized to the total cross-section of a Ca+Ca reaction.

A. Reaction Dynamics

The main difference between the two heavy-ion reactions considered here (as measured by the HADES Collaboration) is the size of the colliding nuclei. Therefore, it is interesting to first have a look at the evolution of the reaction for both systems. In Fig. 1 the evolution of the baryon and energy density (a) as well as the evolution of temperature and the chemical potentials (b) are shown. The maximum density values in the central cell of the grid, i.e., in the center of the collision, reach similar values up to roughly 3-6 times ground-state baryon density ρ_0 and energy density ε_0 for both reactions. In case of the larger system (Au+Au) a plateau develops for a duration of more than 10 fm/c, while for Ar+KCl (respectively Ca+Ca in our simulations) the densities drop off rather quickly after reaching the maximum. Note that the values for the energy density ε shown in Fig. 1 (a) are

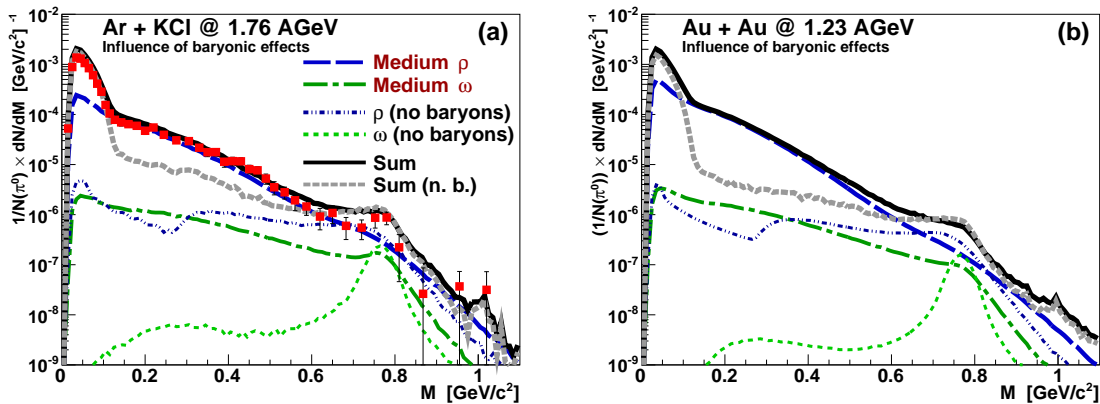


Figure 4. (Color online) Comparison of invariant mass spectra with the full spectral function and for the case of no baryonic effects (i.e. for $\rho_{\text{eff}} = 0$). As in Fig. 3, the dielectron yields for Ar+KCl collisions at $E_{\text{lab}} = 1.76$ AGeV (a) and for Au+Au at $E_{\text{lab}} = 1.23$ AGeV (b) are shown within HADES acceptance and normalized to the average number of produced π^0 . Note that the UrQMD contributions are included in the sum, but the different single yields are not shown explicitly for reasons of lucidity.

corrected for the pressure anisotropy at the beginning of the collision.

With regard to the evolution of temperature and baryochemical potential in Fig. 1 (b), we find that again similar top values are obtained. In both reactions, Ar+KCl and Au+Au, we get peak values of $T \approx 100$ MeV and $\mu_B \approx 900$ MeV. (Note that the quark chemical potential $\mu_q = \frac{1}{3}\mu_B$ is shown instead of the baryon chemical potential.) Especially for the Au+Au reaction the baryon chemical potential shows a more prominent plateau than the baryon density. However, note that T and μ_B depend on ε and ρ_B non-linearly via the EoS. For the collisions at SIS energies studied here, μ_B rapidly rises to values very close to the nucleon mass - but once it reaches such a high level it exhibits a much less significant rise in spite of a further increase of ρ_B . This is a consequence of the Fermi statistics which takes effect in this case. Furthermore, it is clear that the values of μ_B are much higher here and show a different evolution than in our recent study for top SPS energy [16]. In case of Au+Au collisions the central cell stays for approximately 20 fm/c in a stage with extremely high baryochemical potential, so that any baryon-driven effect on the dilepton spectra should be clearly visible for this system. Similar findings are also true for Ar+KCl reactions, but with significantly shorter lifetime. The maximum temperature is approximately 10 MeV higher in the latter reaction due to the slightly higher collision energy.

The pion chemical potential rises up to values of around 100 MeV and then equally quickly drops to values around 20-50 MeV for the rest of the reaction. The peak at the beginning can be explained with the non-equilibrium nature of the cascade, where a large number of pions is produced rapidly at the very beginning before

the system has time to equilibrate.

The corresponding evolution of the thermal four-volume at each time step, divided by its duration Δt , as obtained for both systems from the coarse-grained microscopic transport calculations is shown in Fig. 2. This quantity is the spatial volume for the different temperature ranges as seen from the center-of-momentum frame of the collision. One observes that the hotter cells created during the evolution of the system (for temperatures above 80 respectively 90 MeV) are present only for comparatively short time spans, and their number is significantly smaller than the volume of cells with lower temperatures. While we only show the evolution of the first 30 fm/c in Fig. 2 for the sake of clarity, we mention that even at the end of the simulation after 70 fm/c one still finds a few cells at temperatures above 50 MeV. Note, however, that the dilepton emission from these late stage cells is marginal and insignificant with respect to the overall time-integrated dilepton spectra.

B. Dilepton Spectra

1. HADES Results

The resulting dielectron invariant-mass spectra for the two heavy-ion reactions measured by the HADES Collaboration are presented in Fig. 3. The left figure (a) shows the Ar+KCl results at 1.76 AGeV compared to the experimental data and the right figure (b) shows our prediction for the larger Au+Au system at 1.23 AGeV (no dilepton data are published for the Au+Au measurement yet). The coarse-graining results for the Ar+KCl case show good agreement with the experimental data,

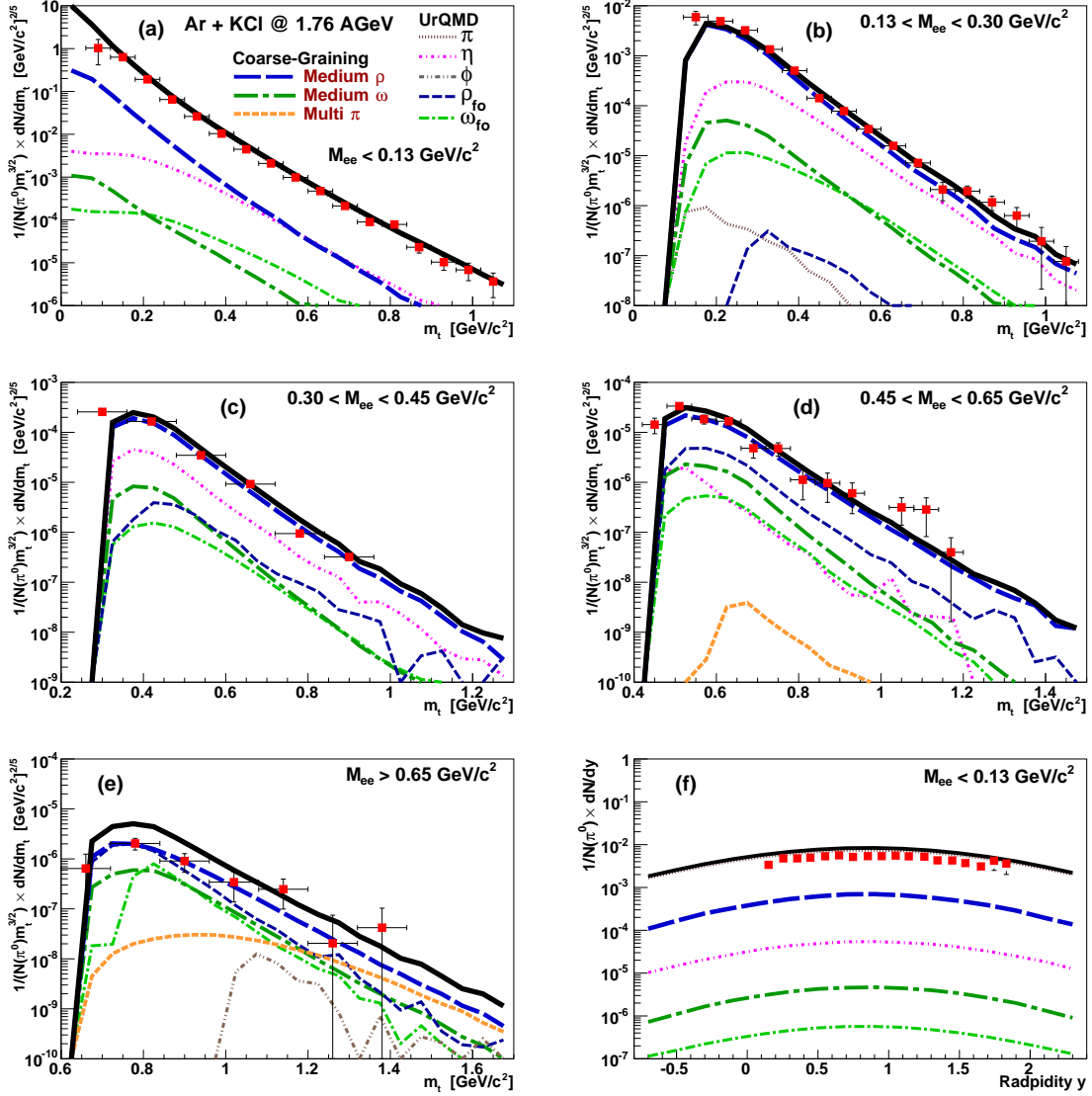


Figure 5. (Color online) Transverse-mass spectra of the dielectron yield in different mass bins (a)-(e) and the dielectron rapidity spectrum of pairs with invariant mass $M_{ee} < 0.13$ GeV/c² (f) for Ar+KCl collisions at $E_{\text{lab}} = 1.76$ AGeV. The results are compared to the experimental data from the HADES Collaboration [23]. In contrast to Figures 3 and 4 the theoretical results here are not shown within the HADES acceptance, as these data are already fully corrected for acceptance and efficiency.

especially the mass range between 0.2 and 0.6 GeV/c² can be well described within this approach. This is different from previous simulations which have indicated an excess of the experimental outcome above the cocktail respectively the transport calculations [23, 79, 80]. The dominant contribution stems from a broadened ρ . It is further noteworthy that also the ω shows a non-negligible broadening in our model results. A slight overestimation of the experimental dilepton yield shows up for the low-

mass region (below 150 MeV/c²) which is dominated by π Dalitz decays, an effect that also has been found in other transport calculations [79]. However, it remains unclear where this pion excess stems from. As the dielectron yield is normalized to the total π^0 number, theory and experiment should agree in the pion-dominated mass-region. Therefore the deviation may be due to a phase-space effect, connected to the geometrical detector acceptance. Another slight excess of the model results is manifest

around the pole mass of the ρ . A significant part of the dileptons here stems from non-thermal ρ mesons, which directly come from the UrQMD calculations using the shining method. As for UrQMD the ρ -production cross sections in the threshold region are known to be slightly too large [80], this overestimation is probably due to the non-thermal contribution.

The medium effects become even stronger in the larger Au+Au system, as can be seen in the right part (b) of Fig. 3. The yield from the thermal ρ is higher at low masses compared to the Ar+KCl reaction and also the thermal ω is slightly stronger here. This is in line with the findings of the previous section III A, where it was pointed out that the hot and dense stage lives substantially longer in the Au+Au reaction. Consequently, the ρ contribution is larger for the Au+Au system as compared to the Ar+KCl reaction, especially at the low masses where the in-medium broadening comes into account.

The dramatic effect of the presence of baryonic matter on the dilepton spectra can be seen in Fig. 4. Here the thermal contributions to the e^+e^- invariant mass spectrum of the ρ and the ω for the case that no baryons and anti-baryons are present (i.e. the effective baryon density ρ_{eff} is put to zero) are compared to the results with the full medium effects. The baryon-driven effects are significant, with the broadening around the pole masses of the ρ and ω meson and the strong increase in the low-mass dilepton yield, which is again more distinct for the larger Au+Au system as compared to Ar+KCl. Additionally the total sum for the two cases with and without baryonic effects is shown, including also all the UrQMD contributions (details are omitted for clarity). Here we find stronger differences between Ar+KCl and Au+Au, mainly due to the relatively smaller contribution from the η for Au+Au reactions, compared to the stronger broadening of the ρ .

Looking not only at the invariant-mass spectra but also at the transverse-mass distributions in different mass bins in Fig. 5 (a)-(e), one finds again a good agreement of our model calculations with the HADES data for Ar+KCl. While for the lowest mass bin ($M_{ee} < 0.13 \text{ GeV}/c^2$) the pion contribution dominates, the thermal ρ is the most significant contribution to the dileptons in all other bins. For the highest mass bin ($M_{ee} > 0.65 \text{ GeV}/c^2$), which includes the pole mass region of the ρ , one can observe a slight overestimation of the total yield, similar to the one observed in the invariant mass spectrum in this mass region (see Fig. 3 (a)). Once again, we argue that this is due to the high ρ -production cross section in the threshold region and therefore stems from the non-thermal transport ρ . As one can see, the thermal ρ alone would describe the data very well.

Note that in some kinematic regions statistical fluctuations are seen in the transverse mass spectra. However, naturally this mainly affects subleading contributions and the very high transverse masses. As the production of certain particles is highly suppressed at SIS energies (e.g., in case of the ϕ meson) it would need ex-

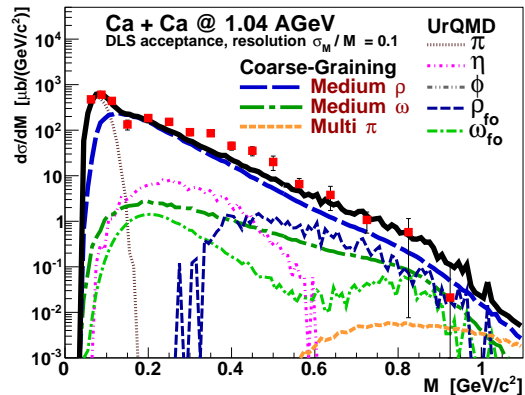


Figure 6. (Color online) Invariant-mass spectrum of the dilepton yield for Ca+Ca collisions at $E_{\text{lab}} = 1.04 \text{ AGeV}$ within the experimental acceptance. The result is compared to the data from the DLS Collaboration [19].

cessive computing resources to remove these statistical fluctuations completely. Nevertheless, the effect on the total yield is usually rather small - especially compared to the uncertainty of the experimental measurement. In general, an estimate of the global (statistical and systematic) error of our dilepton calculations is extremely difficult due to the many different parameters (cross-sections, branching ratios, spectral functions, etc.) which enter the calculation and because for other sources (e.g., the filtering) the error can hardly be quantified. At least for the long-lived contributions (mainly π and η) a comparison between different transport models indicates that their contribution to the dilepton spectra is quite well determined and does not differ much between the models [26–29]. For the thermal contributions (ρ and ω) the two main error sources are the uncertainties of the spectral function and of the description of the reaction dynamics, i.e., the time-evolution of temperature and chemical potential.

For the lowest mass bin, the HADES collaboration has also measured the rapidity distribution of dielectrons. The results from the coarse-grained simulations as well as the data points are shown in Fig. 5 (f). The shape of the spectrum is reproduced well, but with some 20% excess above the data points which was already visible in the invariant mass spectrum. Note that the rapidity values are for the laboratory frame, i.e. for $E_{\text{lab}} = 1.76 \text{ AGeV}$ mid-rapidity corresponds to a value of $y_0 = 0.86$.

2. DLS Results

Although the DLS measurement was done with a smaller acceptance and lower resolution than in the more recent analyses by the HADES Collaboration, it is nev-

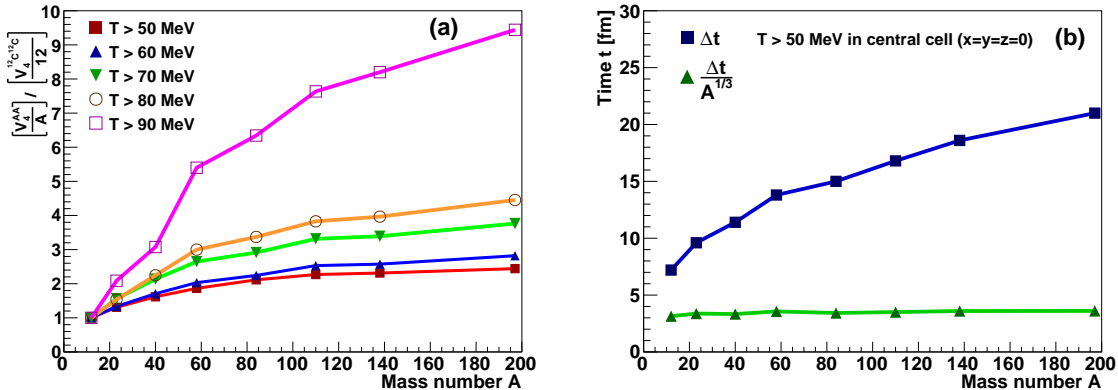


Figure 7. (Color online) (a) Ratio of the thermal four-volume V_4 for different temperatures to the mass number A of the colliding nuclei. The results are normalized to the ratio obtained with $^{12}\text{C} + ^{12}\text{C}$ collisions. (b) Time duration over which the central cell of the coarse-graining grid (for $x = y = z = 0$) emits thermal dileptons, i.e., for this period of time the central cell has a temperature which is above 50 MeV (blue squares) and the same scaled by $A^{1/3}$ (green triangles). Both plots (a) and (b) show the results in dependence on mass number A for central collisions and a collision energy $E_{\text{lab}} = 1.76 \text{ A GeV}$.

ertheless interesting to compare our results also with these heavy-ion data. The system Ca+Ca which was measured by DLS is comparable to the Ar+KCl reaction, as mentioned above. However, the DLS Collaboration performed the measurement at a lower energy of $E_{\text{lab}} = 1.04 \text{ A GeV}$. In Fig. 6 the coarse-grained UrQMD results for the according invariant-mass spectrum is shown within the DLS acceptance, together with the experimental data points [19]. In general the spectrum does not differ strongly from the simulations for HADES, but the peaks – especially in case of the ω – are more smeared out here, which is due to the low mass resolution of only $\sigma_M/M = 10\%$ of the detector, and the acceptance at low masses is suppressed compared to the HADES measurements. (For comparison, the mass resolution of the HADES experiment is roughly 2% in the region of the ρ and ω pole masses [30].) While the overall description of the experimental spectrum with the present model is relatively good, a slight excess of the data above our model curve is present in the mass range from 0.2 up to 0.6 GeV/c^2 . This is in contrast to the findings for the HADES case, where we could describe this mass region quite accurately.

What might be the reasons for this deviation? It is possible that at this very low energy other processes presently not considered in our model might become more dominant here, e.g., an explicit bremsstrahlung contribution (note, however, that some bremsstrahlung effects are already considered within the in-medium spectral functions). As it has been shown that the importance of bremsstrahlung contributions increases with decreasing collision energy, these effects might be more significant than in Ar+KCl reactions at the slightly higher energies used for the HADES experiment. Nevertheless, there are still uncertainties within the different model

calculations for the bremsstrahlung contribution, differing by a factor 2–4 [81, 82]. A main problem here is the correct determination of the overall effect of the different interfering processes, which is highly non-trivial. Another issue is that the lower collision energy also results in slightly lower temperatures peaking around 80 MeV, which is indicating less thermalization of the colliding system. Besides, one has to take into account that the DLS experiment with its two-arm set-up had a more limited acceptance as compared to the HADES detector. This makes it difficult to draw clear quantitative conclusions from the comparison to the data. Additionally, the lack of a measured impact-parameter distribution hampers precise calculations within the coarse-graining approach, as the medium effects can be quite sensitive to the centrality of the collision.

However, it was shown (at least for C+C reactions) that the HADES results agree very well with those measured by the DLS collaboration if the HADES data are filtered with the DLS acceptance [21]. So these data should provide a good additional check for theoretical models in spite of their lower accuracy. Overall, the agreement of our results with the data is quite good, especially considering that previous pure transport calculations with the UrQMD model (without bremsstrahlung) clearly underestimated the Ca+Ca data from DLS by a factor of 5-10 in the mass range from 0.2 to 0.6 GeV/c^2 [72].

C. System size and lifetime effects on thermal dilepton emission

The results of the previous section indicate that the size of the colliding nuclei (and in consequence also the size and duration of the hot and dense fireball created

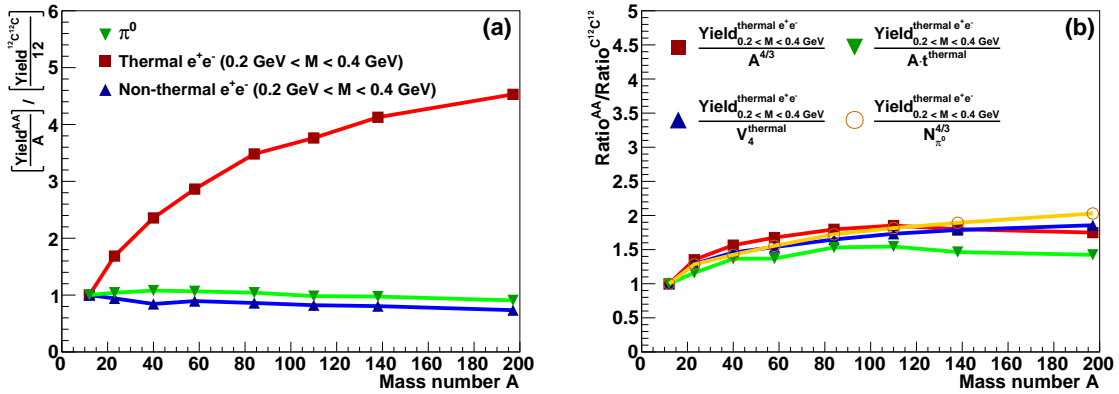


Figure 8. (Color online) (a) Ratio of the thermal (red squares) and non-thermal dilepton yield (blue triangles) in the invariant mass range from 0.2 to 0.4 GeV/c² to the mass number A of the colliding nuclei; the same ratio is plotted for the total number of π^0 (green triangles). The results are normalized to the ratio obtained with $^{12}\text{C} + ^{12}\text{C}$ collisions. (b) Ratio of the thermal dilepton yield in the invariant mass range from 0.2 to 0.4 GeV/c² to $A^{4/3}$ (red squares), to the thermal four-volume (blue triangles), to the product of A and the time t^{thermal} in which the central cell (for $x = y = z = 0$) emits thermal dileptons, i.e., is at $T > 50$ MeV (green triangles), and to the number of π^0 produced in the reaction scaled with an exponent 4/3 (orange circles). All ratios are normalized to the result obtained for $^{12}\text{C} + ^{12}\text{C}$. Both plots (a) and (b) show the results for central collisions and a collision energy $E_{\text{lab}} = 1.76$ AGeV.

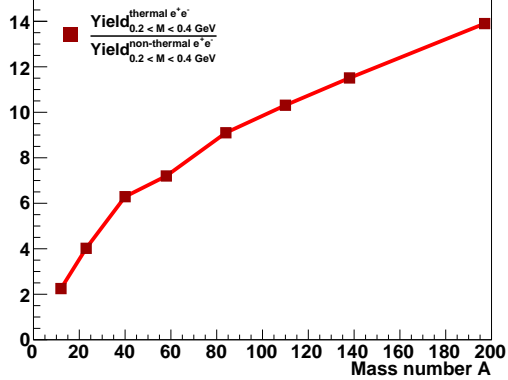


Figure 9. (Color online) Ratio of the thermal to the non-thermal dilepton yield in the mass range $0.2 \text{ GeV}/c^2 < M_{ee} < 0.4 \text{ GeV}/c^2$ for A+A collisions at $E_{\text{lab}} = 1.76$ AGeV. This ratio depicts the ‘‘excess’’ of the thermal dilepton yield with regard to the cocktail contributions. The results are shown in dependence on the mass number A of the colliding nuclei.

thereby) largely influence the thermal dilepton yield. This encourages a systematic study of the system size dependence for thermal and non-thermal contributions and also raises the question, up to which point the assumption of a thermalized system seems reasonable. For this purpose we compare different systems from C+C to Au+Au in central collisions at an energy of $E_{\text{lab}} = 1.76$ AGeV.

Fig. 7 (a) shows the ratio of the thermal four-volume V_4 for different temperatures to the mass number A of the colliding nuclei. The results are normalized to the ratio obtained with $^{12}\text{C} + ^{12}\text{C}$ collisions. It is noteworthy here that the four-volume of the hottest cells ($T > 90$ MeV) shows a much stronger increase than the overall thermal volume (i.e., for $T > 50$ MeV). However, only the relative increase is shown in this plot. In direct comparison the number of cells with highest temperatures is very small compared to the total volume (approximately 1/30 for C+C). It is furthermore striking that the increase of the thermal four-volume is not proportional to A , but it shows a stronger increase for larger systems. This is not surprising, as A is only a measure for the volume of the colliding nuclei. In studies with the statistical model it was shown that at SIS energies the thermal freeze-out volume is closely related to the initial overlap volume of the system created in $A - A$ collisions [73, 83]. However, the thermal four-volume is also determined by the lifetime of the fireball. As it is difficult to determine some kind of an average lifetime within the coarse-graining approach, we concentrate on the central cell of the grid and assume that the time for which it remains at an temperature greater than 50 MeV should be to first order a good approximation of the overall thermal lifetime. Fig. 7 (b) shows the mentioned time duration over which the central cell emits thermal dileptons in dependence on A . Note that this duration approximately scales with $A^{1/3}$, i.e. with the diameter of the nuclei. Obviously the main influence on the lifetime at those low energies seems to be the time the two nuclei need to traverse each other.

The question now is which influence the evolution of

the four-volume has on the production of lepton pairs. In Fig. 8 (a) the ratio of thermal and non-thermal dilepton yield as well as the total π^0 yield in the invariant mass range from 0.2 to 0.4 GeV/ c^2 in relation to the mass number A of the colliding nuclei is shown. The results are – again – normalized to the ratio obtained with C+C collisions. While the ratio of the π^0 number as well as the non-thermal dileptons to the mass number remains roughly 1 for all system sizes (i.e. the non-thermal dilepton and π^0 yield increases linearly with A), the thermal yield shows a significantly stronger rise. This finding is in line with the larger thermal excess found in our calculations in Au+Au compared to Ar+KCl reactions.

If one now compares the thermal yield with the corresponding total thermal four-volume (which is all cells with $T > 50$ MeV), as shown in Fig. 8 (b), the finding indicates that the ratio between both shows only a very slight increase and remains almost constant, independent of the system size. The same is found if one calculates the relation between the thermal yield and the product of A with the thermal lifetime of the central cell (compare Fig. 7 (b)) or directly looks at the ratio between the thermal dilepton yield and mass number A respectively the number of produced neutral pions N_{π^0} scaled by an exponent $\alpha = 4/3$. All those quantities give an approximate measure of the thermal four-volume at the low energies considered here. At higher collision energies as, e.g., obtained at the CERN SPS or at RHIC (where the whole fireball is more pion-dominated rather than baryon-dominated) one would still expect an increase with $N_{\pi^0}^\alpha$, but not any longer with A^α . However, note that in these cases the nuclei will traverse each other much faster and one will also find a significant transverse expansion of the fireball, so that the diameter of the nuclei can no longer be considered as a rough measure of the lifetime; consequently the parameter α might be different here. Nevertheless, in a different model calculation [44] it was found that the thermal dilepton yield at top RHIC energy scales with the number of charged particles as N_{ch}^α , where α is found to take a value of approximately 1.45. This result is not so far from the value obtained within our simple picture – at a completely different energy regime.

In consequence, we learn from these results that the non-thermal dilepton contributions (from long-lived mesons as the π^0 and the η , respectively from the freeze-out ρ and ω) increase with A and therefore directly with the volume of the colliding system. This is due to the fact that these contributions reflect the final hadronic composition, after the whole reaction dynamics has ended. Therefore the time-evolution of the system is irrelevant here. In contrast, the thermal dilepton emission does not only increase with the volume, but also with the time in which the colliding system remains in a hot and dense stage. This is obvious, as the thermally emitted dileptons will escape the fireball unscathed, while all hadronic particles undergo processes as rescattering and reabsorption. In consequence, the thermal yield increases roughly

proportional to $V \cdot \Delta t \sim A \cdot A^{1/3} = A^{4/3}$. Exactly due to the different mechanisms contributing to thermal and non-thermal dilepton yields, one observes a significant increase of their ratio when going to larger system sizes. This ratio is shown (for the invariant mass range from 0.2 to 0.4 GeV/ c^2) in Fig. 9 with its value increasing from slightly over two for C+C up to 14 for Au+Au.

The present results qualitatively agree with a recent study on the same issue performed within different microscopic transport models, where the total dilepton yield was found not to scale with A or the number of neutral pions, but showing a stronger increase due to the complicated dynamics of the reaction [26]. There, from a microscopic point of view, it was also argued that the time evolution of the reaction is the main reason for the increasing dilepton yield in larger systems. If the dense phase with many binary scatterings lasts longer, according to this picture, a larger bremsstrahlung contribution (which is proportional to the number of collisions) and the repeated regeneration of Δ resonances raises the dilepton yield. However, the contribution of other baryonic resonances was not explicitly considered there.

IV. CONCLUSIONS & OUTLOOK

We have presented results on dilepton production in Ar+KCl and Au+Au collisions at GSI SIS18 and in Ca+Ca collisions at BEVALAC energies. The results are obtained using a coarse-grained microscopic transport approach and employing state-of-the-art spectral functions. With this approach the experimental dilepton spectra in heavy-ion collisions at $E_{\text{lab}} = 1\text{-}2$ AGeV can be successfully described. The model represents a third way to explore the dynamics of heavy-ion reactions. In contrast to hydrodynamic/thermal fireball calculations or microscopic transport simulations it allows for a consistent treatment of both, high-energy and low-energy collisions.

Our results show that the dominant in-medium effect, which is also visible in the dilepton spectra, stems from a strong broadening of the spectral shape of the ρ meson due to the high baryon density in the fireball. This causes a melting of the ρ peak and results in an enormous increase of the dilepton production below the pole mass. The reason for this is mainly the interaction with the baryonic resonances, especially the Δ and N_{1520}^* , which are included in the spectral function and give significant additional strength to the ρ contribution at these low masses. The effect is much stronger at SIS energies than for RHIC or SPS. Here, the baryon-chemical potential remains very high for a significant time. This is visible in the dilepton spectra which always represent a four-volume integral over the whole space-time evolution. In the present study we also find a significant broadening of the ω meson at SIS energies.

Furthermore, the influence of the size of the colliding system on the thermal dilepton yield was studied. While

we find the non-thermal contribution in the mass range from 0.2 to 0.4 GeV/ c^2 (which stems mainly from the long-lived η -meson but also from the “freeze-out” ρ and ω) to scale linearly with the mass number A , a stronger increase of the thermal ρ and ω yield is observed. Their contribution to the dilepton yield scales with At^{thermal} , i.e., the system’s volume multiplied with the lifetime of the thermal stage. Since t^{thermal} increases with the diameter of the nuclei which is proportional to $A^{1/3}$, we argue that the thermal dilepton emission should scale with $A^{4/3}$. As the number of neutral pions directly scales with A , we find the thermal dilepton yield also increasing with $N_{\pi^0}^{4/3}$. For future studies it might be quite instructive to check whether this proportionality still holds for higher collision energies.

It is interesting to compare our findings with the results of pure transport calculations. There, in recent calculations the dilepton excess in the invariant-mass spectra above the cocktail were mainly explained by two different effects: (i) Bremsstrahlung contributions and (ii) Dalitz decays of baryonic resonances [26, 29]. It is important to understand that both effects are also included in the spectral functions applied here. These processes, as implemented in the transport models, correspond to cuts of the in-medium self-energy diagrams of the ρ meson. For example, a contribution to the self-energy from a Δ -hole excitation would be represented in the transport model by the process $\Delta \rightarrow \rho N \rightarrow \gamma^* N$, assuming strict vector meson dominance. However, due to the completely different character of the approaches it is difficult to compare the single contributions quantitatively. Also note that the self-energies in hadronic many-body quantum-field theory approach correspond to a *coherent* superposition of the various scattering processes, while in transport approaches naturally the various processes are summed *incoherently*. A future detailed analysis of the self-energy contributions and their relative strengths might be fruitful to better understand how far the both approaches, i.e., the transport (kinetic) and the equilibrium thermal

quantum-field theory description of the dilepton-emission rates at such low energies agree. One should keep in mind that the same microscopic scattering and decay processes are underlying both approaches.

Apart from this, the main outcome of the present investigation is the possibility of a consistent description of dilepton production from SPS down to SIS energies within the same model. In both energy regimes the spectra can be described reasonably well by the assumption of medium modifications of the vector mesons’ spectral properties, whereby the ρ plays the most significant role.

In the future, the CBM experiment at FAIR will offer the possibility to study medium effects in a collision-energy range, where this kind of study has not been carried out yet. With high (net-)baryon densities but also temperatures reaching up to or above the critical temperature T_c , this will be a further test for the spectral functions and theoretical models. Besides, the high luminosities expected at FAIR might enable to perform more detailed and systematic studies, as, e.g., the effect of various different system sizes on the dilepton yield or a study for different centralities, to obtain more information on the evolution of the reaction dynamics.

ACKNOWLEDGEMENTS

The authors thank the HADES Collaboration and especially Tetyana Galatyuk for providing the acceptance filters and experimental data. Furthermore, we acknowledge Ralf Rapp for providing the parametrization of the spectral functions and many fruitful discussions. This work was supported by the Bundesministerium für Bildung und Forschung, Germany (BMBF), the Hessian Initiative for Excellence (LOEWE) through the Helmholtz International Center for FAIR (HIC for FAIR) and the Helmholtz Association through the Helmholtz Research School for Quark-Matter Studies (H-QM).

-
- [1] E. L. Feinberg, Nuovo Cim. A **34**, 391 (1976).
 - [2] E. V. Shuryak, Phys. Lett. B **78**, 150 (1978).
 - [3] C. Gale and J. I. Kapusta, Phys. Rev. C **35**, 2107 (1987).
 - [4] C. Gale and J. I. Kapusta, Nucl. Phys. A **495**, 423C (1989).
 - [5] T. Hatsuda and S. H. Lee, Phys. Rev. C **46**, 34 (1992).
 - [6] F. Klingl, N. Kaiser, and W. Weise, Nucl. Phys. A **624**, 527 (1997).
 - [7] R. Rapp and J. Wambach, Adv. Nucl. Phys. **25**, 1 (2000).
 - [8] S. Leupold, V. Metag, and U. Mosel, Int. J. Mod. Phys. E **19**, 147 (2010).
 - [9] R. D. Pisarski, Phys. Lett. B **110**, 155 (1982).
 - [10] G. Brown and M. Rho, Phys. Rept. **363**, 85 (2002).
 - [11] R. Arnaldi et al. (NA60 Collaboration), Phys. Rev. Lett. **96**, 162302 (2006).
 - [12] G. Agakichiev et al. (CERES Collaboration), Phys. Rev. Lett. **75**, 1272 (1995).
 - [13] H. van Hees and R. Rapp, Phys. Rev. Lett. **97**, 102301 (2006).
 - [14] H. van Hees and R. Rapp, Nucl. Phys. A **806**, 339 (2008).
 - [15] K. Dusling, D. Teaney, and I. Zahed, Phys. Rev. C **75**, 024908 (2007).
 - [16] S. Endres, H. van Hees, J. Weil, and M. Bleicher, Phys. Rev. C **91**, 054911 (2015).
 - [17] L. Adamczyk et al. (STAR Collaboration), Phys. Rev. Lett. **113**, 022301 (2014).
 - [18] F. Geurts (STAR Collaboration), J. Phys. Conf. Ser. **458**, 012016 (2013).
 - [19] R. Porter et al. (DLS Collaboration), Phys. Rev. Lett. **79**, 1229 (1997).

- [20] G. Agakichiev et al. (HADES Collaboration), Phys. Rev. Lett. **98**, 052302 (2007).
- [21] G. Agakishiev et al. (HADES Collaboration), Phys. Lett. B **663**, 43 (2008).
- [22] G. Agakishiev et al. (HADES Collaboration), Phys. Lett. B **690**, 118 (2010).
- [23] G. Agakishiev et al. (HADES Collaboration), Phys. Rev. C **84**, 014902 (2011).
- [24] E. Bratkovskaya and W. Cassing, Nucl. Phys. A **807**, 214 (2008).
- [25] E. Bratkovskaya, W. Cassing, and O. Linyk, Phys. Lett. B **670**, 428 (2009).
- [26] E. Bratkovskaya, J. Aichelin, M. Thomere, S. Vogel, and M. Bleicher, Phys. Rev. C **87**, 064907 (2013).
- [27] K. Schmidt, E. Santini, S. Vogel, C. Sturm, M. Bleicher, et al., Phys. Rev. C **79**, 064908 (2009).
- [28] J. Weil, H. van Hees, and U. Mosel, Eur. Phys. J. A **48**, 111 (2012).
- [29] J. Weil, S. Endres, H. van Hees, M. Bleicher, and U. Mosel (2014), arXiv: 1412.3733 [nucl-th].
- [30] T. Galatyuk (HADES Collaboration), Int. J. Mod. Phys. Conf. Ser. **26**, 1460052 (2014).
- [31] B. Schenke and C. Greiner, Phys. Rev. C **73**, 034909 (2006).
- [32] B. Schenke and C. Greiner, Phys. Rev. Lett. **98**, 022301 (2007).
- [33] B. Schenke and C. Greiner, Nucl. Phys. A **785**, 170 (2007).
- [34] E. L. Bratkovskaya, W. Cassing, R. Rapp, and J. Wambach, Nucl. Phys. A **634**, 168 (1998).
- [35] W. Cassing and E. Bratkovskaya, Nucl. Phys. A **831**, 215 (2009).
- [36] H. Barz, B. Kämpfer, G. Wolf, and M. Zetenyi, Open Nucl. Part. Phys. J. **3**, 1 (2010).
- [37] J. Weil, U. Mosel, and V. Metag, Phys. Lett. B **723**, 120 (2013).
- [38] J. Ruppert, C. Gale, T. Renk, P. Lichard, and J. I. Kapusta, Phys. Rev. Lett. **100**, 162301 (2008).
- [39] E. Santini, J. Steinheimer, M. Bleicher, and S. Schramm, Phys. Rev. C **84**, 014901 (2011).
- [40] G. Vujanovic, C. Young, B. Schenke, R. Rapp, S. Jeon, et al., Phys. Rev. C **89**, 034904 (2014).
- [41] P. Huovinen, M. Belkacem, P. J. Ellis, and J. I. Kapusta, Phys. Rev. C **66**, 014903 (2002).
- [42] S. Endres, H. van Hees, J. Weil, and M. Bleicher, J. Phys. Conf. Ser. **599**, 012020 (2015).
- [43] S. Endres, H. van Hees, J. Weil, and M. Bleicher, EPJ Web Conf. **97**, 00014 (2015).
- [44] R. Rapp, Adv. High Energy Phys. **2013**, 148253 (2013).
- [45] S. A. Bass, M. Belkacem, M. Bleicher, M. Brandstetter, L. Bravina, et al., Prog. Part. Nucl. Phys. **41**, 255 (1998).
- [46] M. Bleicher, E. Zabrodin, C. Spieles, S. A. Bass, C. Ernst, et al., J. Phys. G **25**, 1859 (1999).
- [47] H. Petersen, J. Steinheimer, G. Burau, M. Bleicher, and H. Stöcker, Phys. Rev. C **78**, 044901 (2008).
- [48] <http://www.urqmd.org>.
- [49] C. Eckart, Phys. Rev. **58**, 919 (1940).
- [50] D. Zschesche, G. Zeeb, and S. Schramm, J. Phys. G **34**, 1665 (2007).
- [51] L. Bravina, E. Zabrodin, M. I. Gorenstein, S. Bass, M. Belkacem, et al., Phys. Rev. C **60**, 024904 (1999).
- [52] L. Bravina, E. Zabrodin, M. I. Gorenstein, S. Bass, M. Belkacem, et al., Nucl. Phys. A **661**, 600 (1999).
- [53] W. Florkowski and R. Ryblewski, Phys. Rev. C **83**, 034907 (2011).
- [54] W. Florkowski, M. Martinez, R. Ryblewski, and M. Strickland, Nucl. Phys. A **904-905**, 803c (2013).
- [55] L. D. McLerran and T. Toimela, Phys. Rev. D **31**, 545 (1985).
- [56] D. Bandyopadhyay, M. Gorenstein, H. Stöcker, W. Greiner, and H. Sorge, Z. Phys. C **58**, 461 (1993).
- [57] H. Bebie, P. Gerber, J. Goity, and H. Leutwyler, Nucl. Phys. B **378**, 95 (1992).
- [58] M. Kataja and P. Ruuskanen, Phys. Lett. B **243**, 181 (1990).
- [59] R. Baier, M. Dirks, K. Redlich, and D. Schiff, Phys. Rev. D **56**, 2548 (1997).
- [60] R. Baier, M. Dirks, and K. Redlich, Acta Phys. Polon. B **28**, 2873 (1997).
- [61] V. L. Eletsky, M. Belkacem, P. Ellis, and J. I. Kapusta, Phys. Rev. C **64**, 035202 (2001).
- [62] R. Rapp, G. Chanfray, and J. Wambach, Nucl. Phys. A **617**, 472 (1997).
- [63] M. Urban, M. Buballa, R. Rapp, and J. Wambach, Nucl. Phys. A **641**, 433 (1998).
- [64] R. Rapp and J. Wambach, Eur. Phys. J. A **6**, 415 (1999).
- [65] R. Rapp and C. Gale, Phys. Rev. C **60**, 024903 (1999).
- [66] R. Rapp, Phys. Rev. C **63**, 054907 (2001).
- [67] M. Dey, V. Eletsky, and B. L. Ioffe, Phys. Lett. B **252**, 620 (1990).
- [68] L. G. Landsberg, Phys. Rept. **128**, 301 (1985).
- [69] G.-Q. Li, C. M. Ko, G. E. Brown, and H. Sorge, Nucl. Phys. A **611**, 539 (1996).
- [70] K. Olive et al. (Particle Data Group), Chin. Phys. C **38**, 090001 (2014).
- [71] U. W. Heinz and K. S. Lee, Nucl. Phys. A **544**, 503 (1992).
- [72] C. Ernst, S. Bass, M. Belkacem, H. Stöcker, and W. Greiner, Phys. Rev. C **58**, 447 (1998).
- [73] J. Cleymans, H. Oeschler, and K. Redlich, Phys. Rev. C **59**, 1663 (1999).
- [74] E. Bratkovskaya, W. Cassing, M. Effenberger, and U. Mosel, Nucl. Phys. A **653**, 301 (1999).
- [75] G. Agakishiev et al. (HADES Collaboration), Eur. Phys. J. A **47**, 21 (2011).
- [76] T. Galatyuk (2014), private communication.
- [77] <http://www-hades.gsi.de>.
- [78] http://macdls.lbl.gov/DLS_WWW_Files/Filter_4.1/.
- [79] J. Weil and U. Mosel, J. Phys. Conf. Ser. **426**, 012035 (2013).
- [80] S. Endres and M. Bleicher, J. Phys. Conf. Ser. **426**, 012033 (2013).
- [81] L. Kaptari and B. Kämpfer, Nucl. Phys. A **764**, 338 (2006).
- [82] R. Shyam and U. Mosel, Phys. Rev. C **82**, 062201 (2010).
- [83] P. Braun-Munzinger, K. Redlich, and J. Stachel, in R. C. Hwa and X.-N. Wang (eds.), *Quark-Gluon Plasma 3* (World Scientific, Singapore, 2004), arXiv: nucl-th/0304013.

Rôle of the pion electromagnetic form factor in the $\Delta(1232) \rightarrow \gamma^*N$ timelike transition

G. Ramalho¹, M. T. Peña², J. Weil³, H. van Hees^{3,4} and U. Mosel⁵

¹*International Institute of Physics, Federal University of Rio Grande do Norte, Avenida Odilon Gomes de Lima 1722, Capim Macio, Natal-RN 59078-400, Brazil*

²*Centro de Física Teórica e de Partículas (CFTP), Instituto Superior Técnico (IST), Universidade de Lisboa, Avenida Rovisco Pais, 1049-001 Lisboa, Portugal*

³*Frankfurt Institute for Advanced Studies, Ruth-Moufang-Straße 1, D-60438 Frankfurt, Germany*

⁴*Institut für Theoretische Physik, Universität Frankfurt, Max-von-Laue-Straße 1, D-60438 Frankfurt, Germany and*

⁵*Institut für Theoretische Physik, Universität Giessen, D35392- Giessen, Germany*

(Dated: December 14, 2015)

The $\Delta(1232) \rightarrow \gamma^*N$ magnetic dipole form factor (G_M^*) is described here within a new covariant model that combines the valence quark core together with the pion cloud contributions. The pion cloud term is parameterized by two terms: one connected to the pion electromagnetic form factor, the other to the photon interaction with intermediate baryon states. The model can be used in studies of pp and heavy ion collisions. In the timelike region this new model improves the results obtained with a constant form factor model fixed at its value at zero momentum transfer. At the same time, and in contrast to the Iachello model, this new model predicts a peak for the transition form factor at the expected position, i.e. at the ρ mass pole. We calculate the decay of the $\Delta \rightarrow \gamma N$ transition, the Dalitz decay ($\Delta \rightarrow e^+e^-N$), and the Δ mass distribution function. The impact of the model on dilepton spectra in pp collisions is also discussed.

I. INTRODUCTION

To understand the structure of hadrons, baryons in particular, in terms of quarks and gluons at low energies, is theoretically challenging due to the intricate combination of confinement and spontaneous chiral symmetry breaking, and the non-perturbative character of QCD in that energy regime. Fortunately, experimentally electromagnetic and hadron beams in accelerator facilities are decisive tools to reveal that structure, and seem to indicate a picture where effective degrees of freedom as baryon quark cores dressed by clouds of mesons play an important role. For a review on these issues see [1]. Although different, experiments with electromagnetic and strong probes complement each other. In electron scattering, virtual photons disclose the region of momentum transfer $q^2 < 0$, and spacelike form factors are obtained [1–3]. Scattering experiments of pions or nucleons with nucleon targets involving Dalitz decays of baryon resonances [2–5] provide information on timelike form factors, defined in the $q^2 > 0$ region where the meson spectrum arises. The results of all these different measurements have to match at the photon point ($q^2 = 0$).

Among the several baryon resonances the Δ excitation and decays have a special role and are not yet fully understood. The electromagnetic transition between the nucleon and the $\Delta(1232)$, and in particular its dominant magnetic dipole form factor $G_M^*(q^2)$, as function of q^2 , is a prime example that discloses the complexity of the elec-

tromagnetic structure of the excited states of the nucleon and illustrates the limitations of taking into account only valence quark degrees of freedom for the description of the transition.

In the region of small momentum transfer $G_M^*(q^2)$ is usually underestimated by valence quark contributions alone. Several models have been proposed in order to interpret this finding. Most of them are based on the interplay between valence quark degrees of freedom and the so-called meson cloud effects, in particular, the dominant pion cloud contribution [1, 6–11]. Other recent works on the $\Delta \rightarrow \gamma^*N$ transition can be found in Refs. [12–15].

In this work we propose a hybrid model which combines the valence quark component, determined by a constituent quark model, constrained by lattice QCD and indirectly by experimental data, with a pion cloud component. The pion cloud component is written in terms of the pion electromagnetic form factor and therefore constrained by data.

The $\Delta \rightarrow \gamma^*N$ transition in the timelike region was studied using vector meson dominance (VMD) models [16–19], the constant form factor model [5, 20], a two component model (model with valence quark and meson cloud decomposition), hereafter called the Iachello model [5, 21, 22], and the covariant spectator quark model [4] (which incidentally also assumes VMD for the quark electromagnetic current).

The Iachello model pioneered the timelike region studies of the $\Delta \rightarrow \gamma^*N$ transition. The model was successful in the description of the nucleon form factors [21]

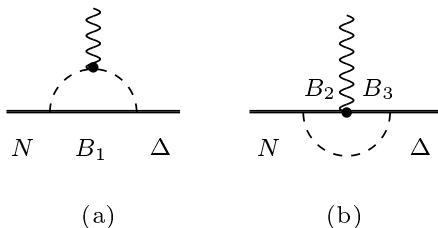


FIG. 1: Pion cloud contributions for the $\Delta \rightarrow \gamma^* N$ electromagnetic transition form factors. Between the initial and final state there are several possible intermediate octet baryon and/or decuplet baryon states: B_1 in diagram (a); B_2 and B_3 in diagram (b).

but has been criticized for generating the pole associated with the ρ -meson pole near $q^2 \simeq 0.3 \text{ GeV}^2$, below $q^2 = m_\rho^2 \simeq 0.6 \text{ GeV}^2$ [5] as it should. The constant form factor model is a good starting point very close to $q^2 = 0$ but, on the other hand, does not satisfactorily take into account the finite size of the baryons and their structure of non-pointlike particles.

In the covariant spectator quark model the contributions for the transition form factors can be separated into valence quark and meson cloud effects (dominated by the pion). The valence quark component is directly constrained by lattice QCD data, and has been seen to coincide with the valence quark core contributions obtained from an extensive data analysis of pion photoproduction [8, 23, 24]. Its comparison to experimental data enables the extraction of information on the complementary meson cloud component in the spacelike region [4, 6]. However the extension to the timelike region of the meson cloud is problematic given the difficulty of a calculation that comprises also in a consistent way the whole meson spectrum. In Ref. [4] the meson cloud was parameterized by a function F_ρ , taken from the Iachello model where it describes the dressing of the ρ -propagator by intermediate $\pi\pi$ states. As noted before, unfortunately, the function F_ρ has a peak that is displaced relatively to the ρ -meson pole mass. Here, by directly using the pion form factor data we corrected for this deficiency.

Moreover, in previous works [4, 6–9] we have assumed that the pion cloud contributions for the magnetic dipole form factor could be represented by a simple parameterization of one term only. But in the present work we introduce an alternative parameterization of the pion cloud which contains two terms. These two leading order contributions for the pion cloud correspond to the two diagrams of Fig. 1. We use then a parameterization of the pion cloud contributions for G_M^* where diagram (a) is related to the pion electromagnetic form factor $F_\pi(q^2)$, and is separated from diagram (b). Diagram (a), where the photon couples directly to the pion, is dominant according to chiral perturbation theory, which is valid in

the limit of massless and structureless quarks. But the other contribution, from diagram (b), where the photon couples to intermediate (octet or decuplet) baryon states while the pion is exchanged between those states, becomes relevant in models with constituent quarks with dressed masses and non-zero anomalous magnetic moments. This was shown in Ref. [10] on the study of the meson cloud contributions to the magnetic dipole moments of the octet to decuplet transitions. The results obtained for the $\Delta \rightarrow \gamma^* N$ transition in particular, suggests that both diagrams contribute with almost an equal weight.

II. IACHELLO MODEL

In the Iachello model the dominant contribution to the $\Delta \rightarrow \gamma^* N$ magnetic dipole form factor is the meson cloud component (99.7%) [5]. The meson cloud contributions is estimated by VMD in terms of a function F_ρ from the dressed ρ propagator, which in the limit $q^2 \gg 4m_\pi^2$, reads [4]

$$F_\rho(q^2) = \frac{m_\rho^2}{m_\rho^2 - q^2 - \frac{1}{\pi} \frac{\Gamma_\rho^0}{m_\pi} q^2 \log \frac{q^2}{m_\pi^2} + i \frac{\Gamma_\rho^0}{m_\pi} q^2}, \quad (2.1)$$

$$= \frac{m_\rho^2}{m_\rho^2 + Q^2 + \frac{1}{\pi} \frac{\Gamma_\rho^0}{m_\pi} Q^2 \log \frac{Q^2}{m_\pi^2}}.$$

In the previous equation $Q^2 = -q^2$, m_π is the pion mass, and Γ_ρ^0 is a parameter that can be fixed by the experimental ρ decay width into 2π , $\Gamma_\rho^0 = 0.149 \text{ GeV}$ or $\Gamma_\rho^0 = 0.112 \text{ GeV}$ depending on the specific model [4, 22].

III. COVARIANT SPECTATOR QUARK MODEL

Within the covariant spectator quark model framework the nucleon and the Δ are dominated by the S -wave components of the quark-diquark configuration [6, 25, 26]. In this case the only non-vanishing form factor of the $\Delta \rightarrow \gamma^* N$ transition is the magnetic dipole form factor, which anyway dominates in all circumstances.

One can then write [6–8]

$$G_M^*(q^2, W) = G_M^B(q^2, W) + G_M^\pi(q^2), \quad (3.1)$$

where G_M^B is the contribution from the bare core and G_M^π the contribution of the pion cloud. Here W generalizes the Δ mass M_Δ to an arbitrary invariant mass W in the intermediate states [4]. We omitted the argument W on G_M^π since we take that function to be independent of W .

Following Refs. [4, 6–8] we can write

$$G_M^B(q^2, W) = \frac{8}{3\sqrt{3}} \frac{M}{M+W} f_v(q^2) \mathcal{I}(q^2, W), \quad (3.2)$$

where

$$\mathcal{I}(q^2, W) = \int_k \psi_\Delta(P_+, k) \psi_N(P_-, k), \quad (3.3)$$

is the overlap integral of the nucleon and the Δ radial wave functions which depend on the nucleon (P_-), the Delta (P_+) and the intermediate diquark (k) momenta. The integration symbol indicates the covariant integration over the diquark on-shell momentum. For details see Refs. [4, 6].

As for $f_v(q^2)$ it is given by

$$f_v(q^2) = f_{1-}(q^2) + \frac{W+M}{2M} f_{2-}(q^2) \quad (3.4)$$

where f_{i-} ($i = 1, 2$) are the quark isovector form factors that parameterize the electromagnetic photon-quark coupling. The form of this parameterization assumes VMD mechanism [6, 25, 27]. See details in Appendix A.

In this work we write the pion cloud contribution as

$$G_M^\pi(q^2) = 3 \frac{\lambda_\pi}{2} \left[F_\pi(q^2) \left(\frac{\Lambda_\pi^2}{\Lambda_\pi^2 - q^2} \right)^2 + \tilde{G}_D^2(q^2) \right], \quad (3.5)$$

where λ_π is a parameter that define the strength of the pion cloud contributions, $F_\pi(q^2)$ is a parameterization of the pion electromagnetic form factor and Λ_π is the cutoff of the pion cloud component from diagram (a). The function \tilde{G}_D^2 on Eq. (3.5) simulates the contributions from the diagram (b), and therefore includes the contributions from several intermediate electromagnetic transitions between octet and/or decuplet baryon states.

From perturbative QCD arguments it is expected that the latter effects fall off with $1/Q^8$ [28]. At high Q^2 a baryon-meson system can be interpreted as a system with $N = 5$ constituents, which produces transition form factors dominated by the contributions of the order $1/(Q^2)^{(N-1)} = 1/Q^8$. This falloff power law motivates our choice for the form of \tilde{G}_D^2 : the timelike generalization of a dipole form factor $G_D = \left(\frac{\Lambda_D^2}{\Lambda_D^2 - q^2} \right)^2$, where Λ_D is a cutoff parameter defining the mass scale of the intermediate baryons.

The equal relative weight of the two terms of Eq. (3.5), given by the factor $\frac{1}{2}\lambda_\pi$, was motivated by the results from Ref. [10], where it was shown that the contribution from each diagram (a) and (b) for the total pion cloud in the $\Delta \rightarrow \gamma^* N$ transition is about 50%. The overall factor 3 was included for convenience, such that in the limit $q^2 = 0$ one has $G_M^\pi(0) = 3\lambda_\pi$. Since $G_M^*(0) \simeq 3$, λ_π represents the fraction of the pion cloud contribution to $G_M^*(0)$.

In the spacelike regime, in order to describe the valence quark behavior ($1/Q^4$) of the form factors associated with the nucleon and Δ baryons, the dipole form factor G_D with a cutoff squared value $\Lambda_D^2 = 0.71 \text{ GeV}^2$ had been used in previous works [6, 25]. As we will show, a model with $\Lambda_D^2 = 0.71 \text{ GeV}^2$ provides a very good description of the $\Delta \rightarrow \gamma^* N$ form factor data in the region

$-2 \text{ GeV}^2 < q^2 < 0$. However, since in the present work we are focused on the timelike region, we investigate the possibility of using a larger value for Λ_D^2 , such that the effects of heavier resonances ($\Lambda_D^2 \approx 1 \text{ GeV}^2$) can also be taken into account.

To generalize G_D to the timelike region we define $\tilde{G}_D(q^2)$

$$\tilde{G}_D(q^2) = \frac{\Lambda_D^4}{(\Lambda_D^2 - q^2)^2 + \Lambda_D^2 \Gamma_D^2}, \quad (3.6)$$

where $\Gamma_D(q^2)$ is an effective width discussed in Appendix B, introduced to avoid the pole $q^2 = \Lambda_D^2$. Since $\Gamma_D(0) = 0$, in the limit $q^2 = 0$, we recover the spacelike limit $\tilde{G}_D(0) = G_D(0) = 1$. We note that differently from the previous work [4] \tilde{G}_D is the absolute value of G_D , and not its real and imaginary parts together.

To summarize this Section: Eq. (3.5) modifies the expression of the pion cloud contribution from our previous works, by including an explicit term for diagram (b) of Fig. 1. Diagram (a) is calculated from the pion form factor experimental data. Diagram (b) concerns less known phenomenological input. The q^2 dependence of that component is modeled by a dipole function squared. Since λ_π was fixed already by the low q^2 data, in the spacelike region, the pion cloud contribution is defined only by the two cutoff parameters Λ_π and Λ_D .

Next we discuss the parameterization of the pion electromagnetic form factor $F_\pi(q^2)$, which fixes the term for diagram (a) and is known experimentally.

IV. PARAMETERIZATION OF $F_\pi(q^2)$

The data associated with the pion electromagnetic form factor $F_\pi(q^2)$ is taken from the $e^+e^- \rightarrow \pi^+\pi^-$ cross-section (the sign of $F_\pi(q^2)$ is not determined).

The function $F_\pi(q^2)$ is well described by a simple monopole form as $F_\pi(q^2) = \frac{\alpha}{\alpha - q^2 - i\beta}$, where α is a cutoff squared and β is proportional to a constant width. An alternative expression for $F_\pi(q^2)$, that replaces the Iachello form F_ρ is,

$$F_\pi(q^2) = \frac{\alpha}{\alpha - q^2 - \frac{1}{\pi} \beta q^2 \log \frac{q^2}{m_\pi^2} + i\beta q^2}. \quad (4.1)$$

Eq. (4.1) simulates the effect of the ρ pole with an effective width regulated by the parameter β . Note that also Eq. (4.1) has a form similar to the function F_ρ of the Iachello model given by Eq. (2.1). In particular, when $\alpha \rightarrow m_\rho^2$ and $\beta \rightarrow \frac{\Gamma_\rho^0}{m_\pi}$, we recover Eq. (2.1). The advantage of Eq. (4.1) over Eq. (2.1) is that α and β can be adjusted independently to the $|F_\pi|^2$ data. The result for those parameters from the fit in both time- and spacelike regions gives

$$\alpha = 0.696 \text{ GeV}^2, \quad \beta = 0.178. \quad (4.2)$$

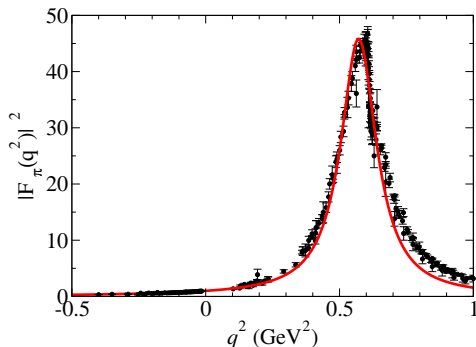


FIG. 2: Fit to $|F_\pi(q^2)|^2$ data using Eq. (4.1). The data are from Refs. [29, 30].

In the Iachello model (2.1) one has $\beta \simeq 1.1$, a very different value. The fit is illustrated in Fig 2. The best fit selects $\alpha \simeq 0.7 \text{ GeV}^2$, which is larger than $m_\rho^2 \simeq 0.6 \text{ GeV}^2$. However, in the best fit to the data, the value of α is *corrected* by the logarithmic counterterm in the denominator of Eq. (4.1), that pushes the maximum of $|F_\pi(q^2)|^2$ to the correct position, $q^2 \simeq 0.6 \text{ GeV}^2$. In the Iachello model, since $\beta \simeq 1.1$, the correction is too strong, and the maximum moves to $q^2 \simeq 0.3 \text{ GeV}^2$, differing significantly from the $|F_\pi(q^2)|^2$ data.

To describe the physics associated with the ρ -meson, we restricted the fit to $q^2 < 0.6 \text{ GeV}^2$, which causes a less perfect description of F_π at the right side of the peak. However increasing q^2 beyond that point slightly worsens the fit. This probably indicates that although the ω width is small, there may be some interference from the ω mass pole, and that the parameters α and β account for these interference effects. Although the spacelike data was also included in the fit, the final result is insensitive to the spacelike constraints. We obtain also a good description of the spacelike region (examine the region $q^2 < 0 \text{ GeV}^2$ in Fig 2). The full extension of the region where a good description is achieved is $-1 \text{ GeV}^2 < q^2 < 1 \text{ GeV}^2$.

A similar quality of the fit is obtained with both a constant width or a q^2 -dependent ρ -width. However a better fit can be obtained with a more complex q^2 -dependence, which accounts better for the ω -meson pole effect, as shown in previous works [32, 33]. Since this work is meant to probe the quality of the results that one can obtain for the transitions form factors, the simple analytic form of Eq. (4.1) suffices for $F_\pi(q^2)$.

In addition, the covariant spectator quark model built from this function describes well the $\Delta \rightarrow \gamma^* N$ form factor in the spacelike region as shown in Fig. 3. Using the best fit of F_π given by the parameters (4.2) we can calculate the pion cloud contribution $G_M^*(q^2)$ through Eq. (3.5), and consequently the result for $G_M^*(q^2, M_\Delta)$. For the parameters λ_π and Λ_π^2 we use the results of the previous works $\lambda_\pi = 0.441$ and $\Lambda_\pi^2 = 1.53 \text{ GeV}^2$,

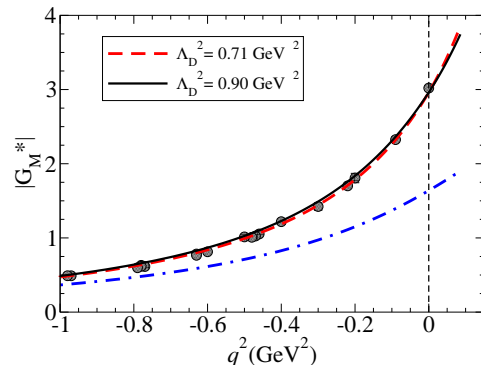


FIG. 3: Results for $|G_M^*(q^2)|$ for the covariant spectator quark model combined with the pion cloud contribution from Eq. (3.5). The data are from Refs. [31]. The dashed-dotted-line is the contribution from the core [4].

obtained from the comparison of the constituent quark model to the lattice QCD data and experimental data [4, 7, 8].

In Fig. 3 we present the result of our model for $|G_M^*(q^2, W)|$ for the case $W = M_\Delta$. In that case the imaginary contribution (when $q^2 > 0$) is very small and the results can be compared with the spacelike data ($q^2 < 0$). In the figure the dashed-dotted-line indicate the result for $G_M^B(q^2, M_\Delta)$ discussed in a previous work [4].

In the same figure we show the sensitivity to the cutoff Λ_D of the pion cloud model, by taking the cases $\Lambda_D^2 = 0.71 \text{ GeV}^2$ and $\Lambda_D^2 = 0.90 \text{ GeV}^2$. They are consistent with the data, although the model with $\Lambda_D^2 = 0.71 \text{ GeV}^2$ gives a slightly better description of the data. The two models are also numerically very similar to the results of Ref. [4] for $W = M_\Delta$. For higher values of W the results of the present model and the ones from Ref. [4] will differ.

Although the model with $\Lambda_D^2 = 0.71 \text{ GeV}^2$ gives a (slightly) better description of the spacelike data, for the generalization to the timelike region it is better to have a model with large effective cutoffs when compared with the scale of the ρ meson pole (the ρ mass m_ρ). This is important to separate the effects of the physical scales from the effective scales (adjusted cutoffs).

V. RESULTS

The results for $|G_M^*(q^2)|$ from the covariant spectator quark model for the cases $W = 1.232 \text{ GeV}$, $W = 1.6 \text{ GeV}$, $W = 1.8 \text{ GeV}$, and $W = 2.2 \text{ GeV}$ are presented in Fig. 4. The thin lines represent the contribution from the bare quark core component of the model, and the thick line the sum of bare quark and pion cloud contributions.

In the figure the results for each value W are restricted by the timelike kinematics through the condition $q^2 \leq$

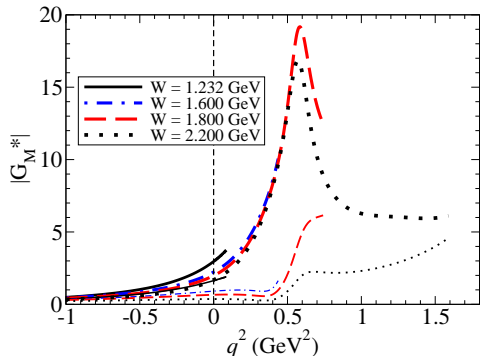


FIG. 4: Results for $|G_M^*(Q^2)|$ for $W = 1.232$ GeV, $W = 1.6$ GeV, $W = 1.8$ GeV and $W = 2.2$ GeV. The thick lines indicate the final result. The thin lines indicate the contribution of the core.

$(W - M)^2$, since the nucleon and the resonance (with mass W) are treated both as being on their mass shells. Therefore the form factor covers an increasingly larger region on the q^2 axis, as W increases. See Ref. [4] for a complete discussion.

The figure illustrates well the interplay between the pion cloud and the bare quark core components. The pion cloud component is dominating in the region near the ρ peak. Away from that peak it is the bare quark contribution that dominates. The flatness of the $W = 2.2$ GeV curve for $q^2 > 1$ GeV² is the net result of the falloff of the pion cloud and the rise of the quark core terms. In addition, the figure shows that dependence on W yields different magnitudes at the peak, and we recall that this dependence originates from the bare quark core contribution alone. This bare quark core contribution is mainly the consequence of the VMD parameterization of the quark current where there is an interplay between the effect of the ρ pole and a term that behaves as a constant for intermediate values of q^2 (see Appendix A).

We will discuss now the results for the widths $\Gamma_{\gamma^*N}(q, W)$ of the Δ Dalitz decay, and for the Δ mass distribution $g_\Delta(W)$.

A. Δ Dalitz decay

The width associated with the Δ decay into γ^*N can be determined from the $\Delta \rightarrow \gamma^*N$ form factors for the Δ mass W . Assuming the dominance of the magnetic dipole form factors over the other two transition form factors, we can write [4, 5, 38]

$$\Gamma_{\gamma^*N}(q, W) = \frac{\alpha}{16} \frac{(W + M)^2}{M^2 W^3} \times \sqrt{y_+ y_-} |G_M^*(q^2, W)|, \quad (5.1)$$

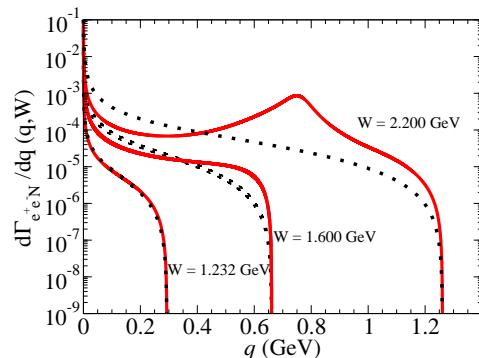


FIG. 5: Results for $\frac{d\Gamma_{e^+e^-N}}{dq}(q, W)$ for three different values of energies W . The solid line is the result of our model. The dotted line is the result of the constant form factor model.

where $q = \sqrt{q^2}$, $\alpha \simeq 1/137$ is the fine-structure constant and $y_\pm = (W \pm M)^2 - q^2$.

At the photon point ($q^2 = 0$), in particular, we obtain the $\Gamma_{\gamma N}$ in the limit $q^2 = 0$ from Eq. (5.1) [5, 18, 37]

$$\Gamma_{\gamma N}(W) = \Gamma_{\gamma^*N}(0, W). \quad (5.2)$$

We can also calculate the derivative of the Dalitz decay width $\Gamma_{e^+e^-N}(q, W)$ from the function $\Gamma_{\gamma^*N}(q, W)$ using the relation [5, 18, 37, 38]

$$\begin{aligned} \Gamma'_{e^+e^-N}(q, W) &\equiv \frac{d\Gamma_{e^+e^-N}}{dq}(q, W) \\ &= \frac{2\alpha}{3\pi q} \Gamma_{\gamma^*N}(q, W). \end{aligned} \quad (5.3)$$

The Dalitz decay width $\Gamma_{e^+e^-N}(q, W)$ is given by

$$\Gamma_{e^+e^-N}(W) = \int_{2m_e}^{W-M} \Gamma'_{e^+e^-N}(q, W) dq, \quad (5.4)$$

where m_e is the electron mass. Note that the integration holds for the interval $4m_e^2 \leq q^2 \leq (W - M)^2$, where the lower limit is the minimum value necessary to produce an e^+e^- pair, and $(W - M)^2$ is the maximum value available in the $\Delta \rightarrow \gamma^*N$ decay for a given W value.

The results for $\frac{d\Gamma_{e^+e^-N}}{dq}(q, W)$ for several mass values W (1.232, 1.6 and 2.2 GeV) are presented in Fig. 5. These results are also compared to the calculation given by the constant form factor model, from which they deviate considerably.

Also, the Δ decay width can be decomposed at tree level into three independent channels

$$\Gamma_{\text{tot}}(W) = \Gamma_{\pi N}(W) + \Gamma_{\gamma N}(W) + \Gamma_{e^+e^-N}(W), \quad (5.5)$$

given by the decays $\Delta \rightarrow \pi N$, $\Delta \rightarrow \gamma N$ and $\Delta \rightarrow e^+e^-N$. The two last terms are described respectively

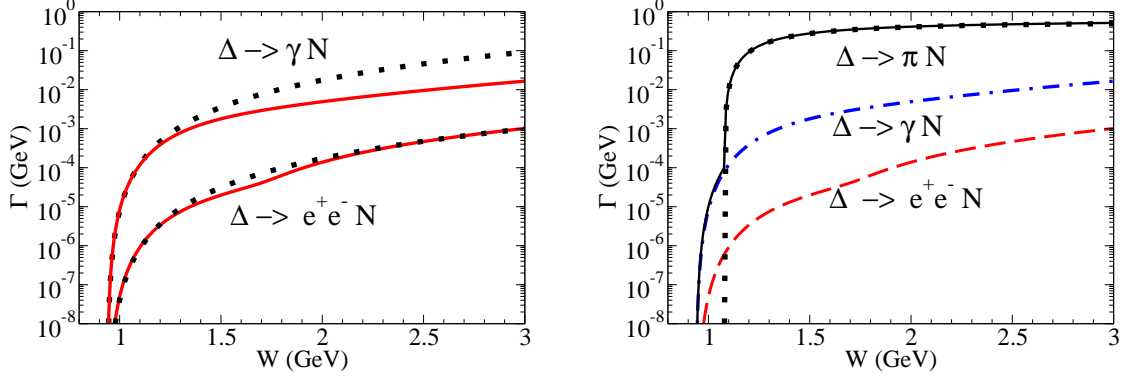


FIG. 6: Results for the partial widths as function of W . At left: partial widths (solid line) for $\Delta \rightarrow \gamma N$ and $\Delta \rightarrow e^+e^-N$, compared with the constant form factor model (dotted line). At right: the partial widths are compared with the $\Delta \rightarrow \pi N$ width (dotted line) and with the sum of all widths (thin solid line).

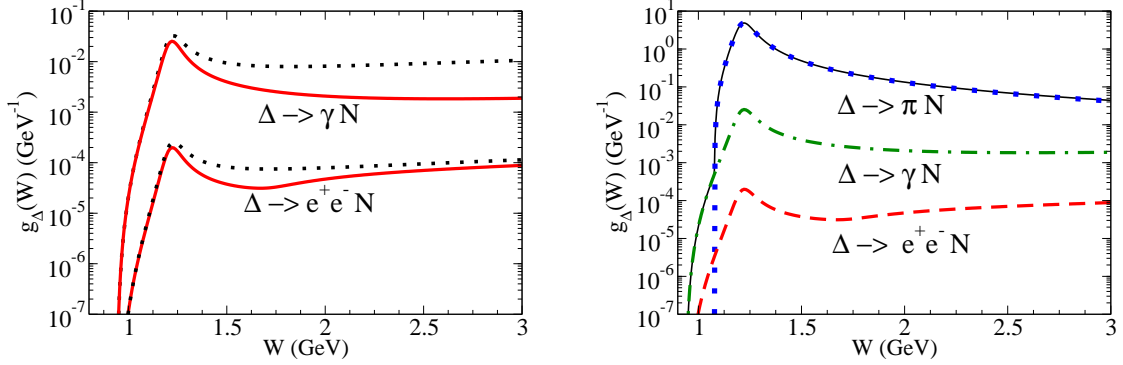


FIG. 7: Results for $g_\Delta(W)$ and the partial contributions $g_{\Delta \rightarrow \pi N}(W)$, $g_{\Delta \rightarrow \gamma N}(W)$ and $g_{\Delta \rightarrow e^+e^-N}(W)$. At left: $g_{\Delta \rightarrow \gamma N}(W)$ and $g_{\Delta \rightarrow e^+e^-N}(W)$ in comparison with constant form factor model (dotted line). At right: all contributions compared with the total $g_\Delta(W)$ (thin solid line).

by Eqs. (5.2) and (5.4). The $\Gamma_{\pi N}$ term can be parameterized as in [36, 39]

$$\Gamma_{\pi N}(W) = \frac{M_\Delta}{W} \left(\frac{q_\pi(W)}{q_\pi(M_\Delta)} \right)^3 \frac{\kappa^2 + q_\pi^2(M_\Delta)}{\kappa^2 + q_\pi^2(W)} \Gamma_{\pi N}^0, \quad (5.6)$$

where $\Gamma_{\pi N}^0$ is the $\Delta \rightarrow \pi N$ partial width for the physical Δ , $q_\pi(W)$ is the pion momentum for a Δ decay with mass W , and κ a cutoff parameter. Following Refs. [34, 35] we took $\kappa = 0.197$ GeV. The present parameterization differs from other forms used in the literature [5, 37] and from our previous work [4].

The results for the partial widths as functions of the mass W are presented in Fig. 6. On the left panel we compare $\Gamma_{\gamma N}$ and $\Gamma_{e^+e^-N}$ with the result of the constant form factor model. On the right panel we present the total width $\Gamma_{\text{tot}}(W)$ as the sum of the three partial widths.

B. Δ mass distribution

To study the impact of the Δ resonance propagation in nuclear reactions like the NN reaction, it is necessary to know the Δ mass distribution function $g_\Delta(W)$. As discussed before, W is an arbitrary resonance mass that may differ from the resonance pole mass (M_Δ). The usual ansatz for g_Δ is the relativistic Breit-Wigner distribution- [4, 5]

$$g_\Delta(W) = A \frac{W^2 \Gamma_{\text{tot}}(W)}{(W^2 - M_\Delta^2)^2 + W^2 [\Gamma_{\text{tot}}(W)]^2}, \quad (5.7)$$

where A is a normalization constant determined by $\int g_\Delta(W) dW = 1$ and the total width $\Gamma_{\text{tot}}(W)$ (5.6).

The results for $g_\Delta(W)$ and the partial contributions

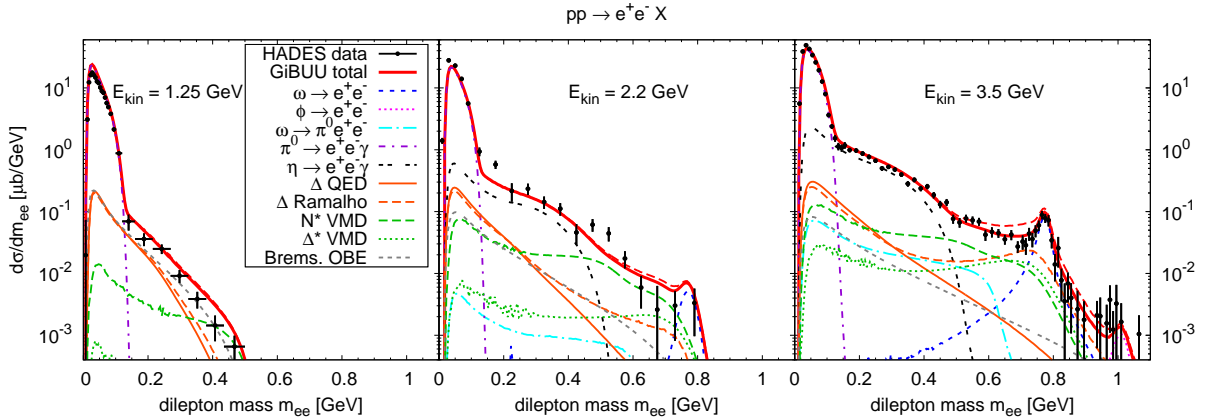


FIG. 8: Transport-model calculations of dilepton mass spectra $d\sigma/dm_{ee}$ from proton-proton collisions ($pp \rightarrow e^+e^-X$) at three different beam energies, with and without a $\Delta \rightarrow \gamma^*N$ form factor, compared to experimental data measured with the HADES detector [40–42].

$$g_{\Delta \rightarrow \gamma N}(W) = \frac{\Gamma_{\gamma N}(W)}{\Gamma_{\text{tot}}(W)} g_{\Delta}(W), \quad (5.8)$$

$$g_{\Delta \rightarrow e^+e^-N}(W) = \frac{\Gamma_{e^+e^-N}(W)}{\Gamma_{\text{tot}}(W)} g_{\Delta}(W), \quad (5.9)$$

$$g_{\Delta \rightarrow \pi N}(W) = \frac{\Gamma_{\pi N}(W)}{\Gamma_{\text{tot}}(W)} g_{\Delta}(W), \quad (5.10)$$

are presented in Fig. 7. The results are also compared with the constant form factor model.

C. Dilepton production from NN collisions

The $\Delta \rightarrow \gamma^*N$ magnetic dipole form factor in the timelike region is known to have a significant influence on dilepton spectra. Therefore we show in Fig. 8 a transport-model calculation of the inclusive dielectron production cross section $d\sigma/dm_{ee}$ for proton-proton collisions ($pp \rightarrow e^+e^-X$), where $m_{ee} = q$. These results have been obtained with the GiBUU model [34, 39] for three different proton beam energies and are compared to experimental data measured with the HADES detector [40–42]. Except for the contribution of the Δ Dalitz decay, the calculations are identical to those presented in an earlier publication [35]. The Δ Dalitz decay is shown in two variants, once with a constant form factor fixed at the photon point (i.e., in 'QED' approximation) and once using the form-factor model described in the preceding sections.

At the lowest beam energy of 1.25 GeV, the produced Δ baryons are close to the pole mass and therefore the results with and without the form factor are very similar. At higher beam energies, however, the model for the $\Delta \rightarrow \gamma^*N$ form factor has a much larger impact, because higher values of W are reached, where the form factor deviates strongly from the photon point value. In Fig. 9 we illustrate the influence of W by showing

the W distribution of produced $\Delta^{+,0}$ baryons in the GiBUU simulations. We note that several different processes contribute to the inclusive $\Delta^{+,0}$ production, such as $NN \rightarrow N\Delta$, $\Delta\Delta$, ΔN^* etc., each of which will produce a different W distribution due to different kinematics and phase space. Furthermore it should be remarked that the tails of this distribution, just as the Δ spectral function in Eq. (5.7), depend significantly on the specific parameterization of the hadronic width for $\Delta \rightarrow \pi N$. However, for electromagnetic observables as shown in Fig. 8, the dependence on the hadronic width is very weak, since in Eq. (5.9) the total width cancels out in the numerator and only stays in the denominator.

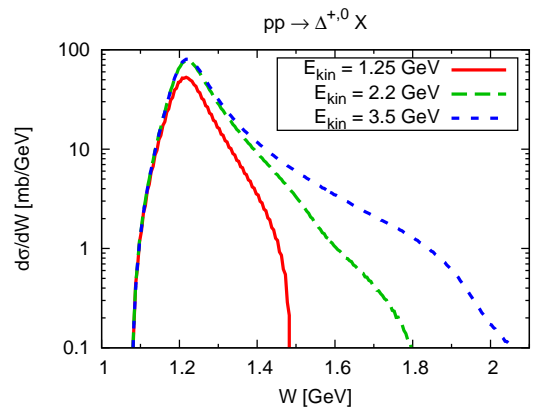


FIG. 9: Mass distribution of produced $\Delta^{+,0}$ baryons in GiBUU simulations, for pp collisions at three different beam energies.

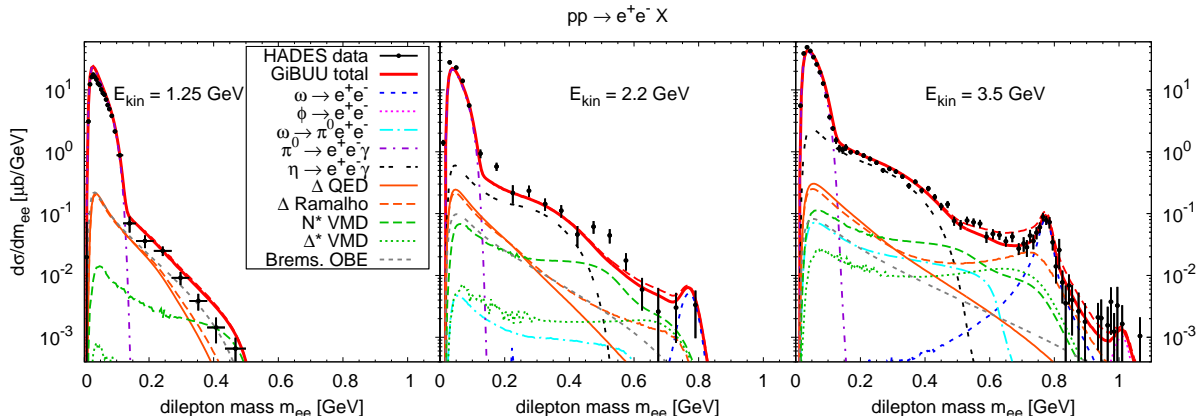


FIG. 10: Modified calculations of dilepton mass spectra $d\sigma/dm_{ee}$ from proton-proton collisions ($pp \rightarrow e^+e^-X$), using reduced $R \rightarrow \rho N$ branching ratios for two resonances (see text).

Coming back to Fig. 8, it should be noted that the choice of the form factor has little influence on the overall agreement of the total dilepton spectrum with the experimental data at the two lowest beam energies, because the influence of the form factor is weak or the Δ contribution is small compared to other channels. At the highest beam energy of 3.5 GeV, however, the choice of the form factor does have an impact on the total spectrum for masses above 600 MeV. While the constant-form-factor result combined with the other channels from GiBUU shows a good agreement with the data, using the q^2 dependent form factor results in a slight overestimation of the data, which is most severe for masses of around 700 MeV. However, we note that the Δ contribution by itself does not overshoot the data. Only in combination with the other channels (in particular the heavier baryons, such as N^* and Δ^*) the overestimation is seen.

There could be various reasons for this enhancement over the data, but we want to mention here only the two most likely ones. One could lie in the form factor itself, more precisely in the omission of an W dependence of the overall weight λ_π for the pion cloud. This parameter for the weight of the pion cloud should probably depend on W . If the two diagrams (a) and (b) of the pion cloud contribution would decrease simultaneously with W , as we can expect from the drop of the m_π/W ratio, this could potentially cure the observed overestimation.

On the other hand, the reason for the disagreement could also be found in the other channels that are part of the transport calculation. In particular the contributions of the higher baryonic resonances (N^* and Δ^*) are subject to some uncertainties. These resonance contributions were recently investigated via exclusive pion production at 3.5 GeV with the HADES detector [43], which showed that the GiBUU model does a rather good job in describing the resonance cocktail for the exclusive channels (with some minor deviations). However, there are also significant non-exclusive channels for pion and dilepton

production at this energy. Moreover, the form factors of the higher resonances are a matter of debate (they are treated in a strict-VMD assumption in the calculation).

It was remarked in [43] that some of the branching ratios for $R \rightarrow \rho N$, which directly influence the dilepton yield via the VMD assumption, might be overestimated in GiBUU, in particular for the $N^*(1720)$ and the $\Delta^*(1905)$. Both have a very large ρN branching ratio of 87% in GiBUU [34] (as adopted from [36]) and also in the current PDG database these branching ratios are listed with rather large values [44], which are essentially compatible with the GiBUU values. However, some recent partial-wave analyses [45, 46] claim much smaller values for these branching ratios, showing some tension with the PDG and GiBUU values. We show in Fig. 10 the effect of using smaller values for these branching ratios on the dilepton spectra, adopting the upper limits from the Bonn-Gatchina analysis [45] (as given in [43]), namely 10% for $N^*(1720) \rightarrow \rho N$ and 42% for $\Delta^*(1905) \rightarrow \rho N$. We note that the values in [46] are even smaller. As seen in Fig. 10, this change indeed reduces the contributions from the N^* and Δ^* resonances by a fair amount, in particular in the high-mass region ($m_{ee} > 600$ MeV). This improves the agreement with the highest data points at 2.2 GeV, and it also mitigates the overshooting over the data at 3.5 GeV when the $\Delta \rightarrow \gamma^* N$ form factor is used, but it does not fully cure it.

Thus it is quite likely that the remaining excess is caused by the negligence of the W dependence in the pion cloud contribution of the form factor. A more detailed investigation of the W dependence of the pion cloud is planned in a further study that will analyze all these aspects.

VI. SUMMARY AND CONCLUSIONS

In this work we present a new covariant model for the $\Delta \rightarrow \gamma^* N$ transition in the timelike region. The model is based on the combination of valence quark and meson cloud degrees of freedom. The bare quark contribution was calibrated previously to lattice QCD data. One of the pion cloud components is fitted to the pion electromagnetic form factor F_π (with the fit being almost insensitive to the spacelike data and strongly dependent on the timelike data) and the other, associated with intermediate octet/decuplet baryon states, parameterized by an effective cutoff Λ_D .

Our model induces a strong effect on the $\Delta \rightarrow \gamma^* N$ magnetic dipole form factor in the region around the ρ -meson pole (where the magnitude is about four times larger than at $q^2 = 0$). This effect was missing in the frequently used Iachello model. The pion cloud effects dominate in the region $q^2 \leq 1.5 \text{ GeV}^2$. For larger q^2 the effects of the valence quark became dominant, and the q^2 -dependence is smoother. At low energies, the new form factor has little influence on the overall agreement of the total dilepton spectrum in NN collisions with the experimental data, and no large difference between our new model and the VMD model is seen. However at the highest beam energy of 3.5 GeV, the choice of the form factor does affect the total spectrum for masses above 600 MeV.

Measurements of independent channels, for instance exclusive pion induced Δ production data, can help to better constrain the pion cloud contribution. The methods presented in this work can in principle be extended to higher mass resonances as $N^*(1440)$, $N^*(1520)$, $N^*(1535)$, $N^*(1710)$ and $\Delta^*(1600)$, for which there are already predictions of the covariant spectator quark model [47, 48] in the spacelike region. The calculation of the $N^*(1520)$ form factors in the timelike region [49], extending the results from Ref. [47] is already under way.

Acknowledgments

The authors thank Marcin Stolarski and Elmar Biermat for the information about the pion electromagnetic form factors. G.R. was supported by the Brazilian Ministry of Science, Technology and Innovation (MCTI-Brazil). M.T.P. received financial support from Fundação para a Ciência e a Tecnologia (FCT) under Grants Nos. PTDC/FIS/113940/2009, CFTP-FCT (PEst-OE/FIS/U/0777/2013) and POCTI/ISFL/2/275. This work was also partially supported by the European Union under the HadronPhysics3 Grant No. 283286. J.W. acknowledges funding of a Helmholtz Young Investigator Group VH-NG-822 from the Helmholtz Association and GSI.

Appendix A: Quark form factors

We use a parameterization of the quark isovector form factors motivated by VMD [8, 23, 25]

$$\begin{aligned} f_{1-}(q^2) &= \lambda_q + (1 - \lambda_q) \frac{m_\rho^2}{m_\rho^2 - q^2} - c_- \frac{M_h^2 q^2}{(M_h^2 - q^2)^2} \\ f_{2-}(q^2) &= \kappa_- \left\{ d_- \frac{m_\rho^2}{m_\rho^2 - q^2} + (1 - d_-) \frac{M_h^2}{M_h^2 - q^2} \right\}, \end{aligned} \quad (\text{A1})$$

where $m_\rho = 775$ MeV is the ρ -meson mass, M_h is the mass of an effective heavy vector meson, κ_- is the quark isovector anomalous magnetic moment, c_- , d_- are mixture coefficients, and λ_q is a parameter related with the quark density number in the deep inelastic limit [25]. The term in M_h , where $M_h = 2M$, simulates the effects of the heavier mesons (short range physics) [25], and behaves as a constant for values of q^2 much smaller than $4M^2$. The width associated with the pole $q^2 = M_h^2$ is discussed in the Appendix B.

The ρ pole appears when one assumes a stable ρ with zero decay width $\Gamma_\rho = 0$. For the extension of the quark form factors to the timelike regime we consider therefore the replacement

$$\frac{m_\rho^2}{m_\rho^2 - q^2} \rightarrow \frac{m_\rho^2}{m_\rho^2 - q^2 - i m_\rho \Gamma_\rho(q^2)}. \quad (\text{A2})$$

On the r.h.s. we introduce Γ_ρ the ρ decay width as a function of q^2 .

The function $\Gamma_\rho(q^2)$ represents the $\rho \rightarrow 2\pi$ decay width for a virtual ρ with momentum q^2 [32, 50]

$$\Gamma_\rho(q^2) = \Gamma_\rho^0 \frac{m_\rho^2}{q^2} \left(\frac{q^2 - 4m_\pi^2}{m_\rho^2 - 4m_\pi^2} \right)^{\frac{3}{2}} \theta(q^2 - 4m_\pi^2), \quad (\text{A3})$$

where $\Gamma_\rho^0 = 0.149$ GeV.

Appendix B: Regularization of high momentum poles

For a given W the squared momentum q^2 is limited by the kinematic condition $q^2 \leq (W - M)^2$. Then, if one has a singularity at $q^2 = \Lambda^2$, that singularity will appear for values of W such that $\Lambda^2 \leq (W - M)^2$, or $W \geq M + \Lambda$.

To avoid a singularity at $q^2 = \Lambda^2$, where Λ^2 is any of the cutoffs introduced in our pion cloud parameterizations, and quark current (pole M_h) we implemented a simple procedure. We start with

$$\frac{\Lambda^2}{\Lambda^2 - q^2} \rightarrow \frac{\Lambda^2}{\Lambda^2 - q^2 - i\Lambda\Gamma_X(q^2)}, \quad (\text{B1})$$

where

$$\Gamma_X(q^2) = 4\Gamma_X^0 \left(\frac{q^2}{q^2 + \Lambda^2} \right)^2 \theta(q^2), \quad (\text{B2})$$

In the last equation Γ_X^0 is a constant given by $\Gamma_X^0 = 4\Gamma_\rho^0 \simeq 0.6$ GeV.

In Eq. (B2) the function $\Gamma_X(q^2)$ is defined such that $\Gamma_X(q^2) = 0$ when $q^2 < 0$. Therefore the results in the spacelike region are kept unchanged. For $q^2 = \Lambda^2$ we obtain $\Gamma_X = \Gamma_X^0$, and for very large q^2 it follows $\Gamma_X \simeq 4\Gamma_X^0$. Finally the value of Γ_X^0 was chosen to avoid very narrow peaks around Λ^2 .

While the width $\Gamma_\rho(q^2)$ associated with the ρ -meson pole in the quark current is nonzero only when $q^2 > 4m_\pi^2$, one has for $\Gamma_X(q^2)$ nonzero values also in the interval $4m_\pi^2 > q^2 > 0$. However, the function $\Gamma_X(q^2)$ changes

smoothly in that interval and its values are negligible.

This procedure was used in Ref. [4, 34] for the calculation of the $\Delta \rightarrow \gamma^* N$ form factors in the timelike regime. In the present case the emerging singularities for $W > M + \Lambda_D \simeq 1.84$ GeV are avoided, and for $W < 1.84$ GeV, the results are almost identical to the ones without regularization. The suggested procedure avoids the singularities at high momentum and at the same time preserves the results for low momentum. In the cases considered the high q^2 contributions are suppressed and the details of regularization procedure are not important.

-
- [1] I. G. Aznauryan, A. Bashir, V. Braun, S. J. Brodsky, V. D. Burkert, L. Chang, C. Chen and B. El-Bennich *et al.*, *Int. J. Mod. Phys. E* **22**, 1330015 (2013) [arXiv:1212.4891 [nucl-th]].
- [2] W. J. Briscoe, M. Döring, H. Haberzettl, D. M. Manley, M. Naruki, I. I. Strakovsky and E. S. Swanson, *Eur. Phys. J. A* **51**, 129 (2015) [arXiv:1503.07763 [hep-ph]].
- [3] G. Agakishiev *et al.*, *Eur. Phys. J. A* **50**, 82 (2014) [arXiv:1403.3054 [nucl-ex]].
- [4] G. Ramalho and M. T. Peña, *Phys. Rev. D* **85**, 113014 (2012) [arXiv:1205.2575 [hep-ph]].
- [5] F. Dohrmann *et al.*, *Eur. Phys. J. A* **45**, 401 (2010) [arXiv:0909.5373 [nucl-ex]].
- [6] G. Ramalho, M. T. Peña and F. Gross, *Eur. Phys. J. A* **36**, 329 (2008) [arXiv:0803.3034 [hep-ph]].
- [7] G. Ramalho, M. T. Peña and F. Gross, *Phys. Rev. D* **78**, 114017 (2008) [arXiv:0810.4126 [hep-ph]].
- [8] G. Ramalho and M. T. Peña, *Phys. Rev. D* **80**, 013008 (2009) [arXiv:0901.4310 [hep-ph]].
- [9] G. Ramalho and K. Tsushima, *Phys. Rev. D* **87**, 093011 (2013) [arXiv:1302.6889 [hep-ph]].
- [10] G. Ramalho and K. Tsushima, *Phys. Rev. D* **88**, 053002 (2013) [arXiv:1307.6840 [hep-ph]].
- [11] S. S. Kamalov, S. N. Yang, D. Drechsel, O. Hanstein and L. Tiator, *Phys. Rev. C* **64**, 032201 (2001) [arXiv:nucl-th/0006068]; T. Sato and T. S. H. Lee, *Phys. Rev. C* **63**, 055201 (2001) [arXiv:nucl-th/0010025].
- [12] V. M. Braun, A. Lenz, G. Peters and A. V. Radyushkin, *Phys. Rev. D* **73**, 034020 (2006) [hep-ph/0510237].
- [13] C. Alexandrou, G. Koutsou, J. W. Negele, Y. Proestos and A. Tsapalis, *Phys. Rev. D* **83**, 014501 (2011) [arXiv:1011.3233 [hep-lat]].
- [14] G. Eichmann and D. Nicmorus, *Phys. Rev. D* **85**, 093004 (2012) [arXiv:1112.2232 [hep-ph]].
- [15] J. Segovia, C. Chen, I. C. Clot, C. D. Roberts, S. M. Schmidt and S. Wan, *Few Body Syst.* **55**, 1 (2014) [arXiv:1308.5225 [nucl-th]].
- [16] M. Schafer, H. C. Donges, A. Engel and U. Mosel, *Nucl. Phys. A* **575**, 429 (1994) [nucl-th/9401006].
- [17] F. de Jong and U. Mosel, *Phys. Lett. B* **392**, 273 (1997) [nucl-th/9611051].
- [18] M. I. Krivoruchenko, B. V. Martemyanov, A. Faessler and C. Fuchs, *Annals Phys.* **296**, 299 (2002) [arXiv:nucl-th/0110066].
- [19] A. Faessler, C. Fuchs, M. I. Krivoruchenko and B. V. Martemyanov, *J. Phys. G* **29**, 603 (2003) [nucl-th/0010056].
- [20] M. Zetenyi and G. Wolf, *Phys. Rev. C* **67**, 044002 (2003) [arXiv:nucl-th/0103062].
- [21] F. Iachello, A. D. Jackson and A. Lande, *Phys. Lett. B* **43**, 191 (1973).
- [22] F. Iachello and Q. Wan, *Phys. Rev. C* **69**, 055204 (2004); R. Bijker and F. Iachello, *Phys. Rev. C* **69**, 068201 (2004) [arXiv:nucl-th/0405028].
- [23] G. Ramalho and M. T. Peña, *J. Phys. G* **36**, 115011 (2009) [arXiv:0812.0187 [hep-ph]].
- [24] B. Julia-Diaz, H. Kamano, T. S. Lee, A. Matsuyama, T. Sato and N. Suzuki, *Phys. Rev. C* **80**, 025207 (2009).
- [25] F. Gross, G. Ramalho and M. T. Peña, *Phys. Rev. C* **77**, 015202 (2008) [nucl-th/0606029].
- [26] F. Gross, G. Ramalho and M. T. Peña, *Phys. Rev. D* **85**, 093005 (2012) [arXiv:1201.6336 [hep-ph]].
- [27] G. Ramalho, K. Tsushima and F. Gross, *Phys. Rev. D* **80**, 033004 (2009) [arXiv:0907.1060 [hep-ph]].
- [28] C. E. Carlson and J. L. Poor, *Phys. Rev. D* **38**, 2758 (1988); C. E. Carlson, *Few Body Syst. Suppl.* **11**, 10 (1999) [arXiv:hep-ph/9809595].
- [29] A. D. Bukin *et al.*, *Phys. Lett. B* **73**, 226 (1978); A. Quenzer *et al.*, *Phys. Lett. B* **76**, 512 (1978); L. M. Barkov *et al.*, *Nucl. Phys. B* **256**, 365 (1985); R. R. Akhmetshin *et al.* [CMD-2 Collaboration], *Phys. Lett. B* **527**, 161 (2002) [hep-ex/0112031]; R. R. Akhmetshin *et al.* [CMD-2 Collaboration], *Phys. Lett. B* **648**, 28 (2007) [hep-ex/0610021].
- [30] S. R. Amendolia *et al.* [NA7 Collaboration], *Nucl. Phys. B* **277**, 168 (1986); C. N. Brown *et al.*, *Phys. Rev. D* **8**, 92 (1973); C. J. Bebek *et al.*, *Phys. Rev. D* **9**, 1229 (1974); C. J. Bebek, C. N. Brown, M. Herzlinger, S. D. Holmes, C. A. Lichtenstein, F. M. Pipkin, S. Raither and L. K. Sisterson, *Phys. Rev. D* **13**, 25 (1976); C. J. Bebek *et al.*, *Phys. Rev. D* **17**, 1693 (1978); G. M. Huber *et al.* [Jefferson Lab Collaboration], *Phys. Rev. C* **78**, 045203 (2008) [arXiv:0809.3052 [nucl-ex]].
- [31] W. Bartel, B. Dudelzak, H. Krehbiel, J. McElroy, U. Meyer-Berkhout, W. Schmidt, V. Walther and G. Weber, *Phys. Lett. B* **28**, 148 (1968); S. Stein *et al.*, *Phys. Rev. D* **12**, 1884 (1975); K. Nakamura *et al.* [Particle Data Group Collaboration], *J. Phys. G* **37**, 075021 (2010).
- [32] H. B. O'Connell, B. C. Pearce, A. W. Thomas and A. G. Williams, *Prog. Part. Nucl. Phys.* **39**, 201 (1997) [hep-ph/9501251].

- [33] H. C. Donges, M. Schafer and U. Mosel, Phys. Rev. C **51**, 950 (1995) [nucl-th/9407012].
- [34] J. Weil, H. van Hees, and U. Mosel, Eur. Phys. J. A **48**, 111 (2012) [Erratum-ibid. A **48**, 150 (2012)] [arXiv:1203.3557 [nucl-th]].
- [35] J. Weil, S. Endres, H. van Hees, M. Bleicher and U. Mosel, arXiv:1410.4206 [nucl-th].
- [36] D. M. Manley and E. M. Saleski, Phys. Rev. D **45** 4002 (1992).
- [37] G. Wolf, G. Batko, W. Cassing, U. Mosel, K. Niita and M. Schaefer, Nucl. Phys. A **517**, 615 (1990).
- [38] M. I. Krivoruchenko and A. Faessler, Phys. Rev. D **65**, 017502 (2001) [arXiv:nucl-th/0104045].
- [39] O. Buss *et al.*, Phys. Rept. **512**, 1 (2012) [arXiv:1106.1344 [hep-ph]].
- [40] G. Agakishiev *et al.* [HADES Collaboration], Phys. Lett. B **690**, 118 (2010) [arXiv:0910.5875 [nucl-ex]].
- [41] G. Agakishiev *et al.* [HADES Collaboration], Phys. Rev. C **85**, 054005 (2012) [arXiv:1203.2549 [nucl-ex]].
- [42] G. Agakishiev *et al.* [HADES Collaboration], Eur. Phys. J. A **48**, 64 (2012) [arXiv:1112.3607 [nucl-ex]].
- [43] G. Agakishiev *et al.*, Eur. Phys. J. A **50**, 82 (2014). [arXiv:1403.3054 [nucl-ex]].
- [44] K. A. Olive *et al.* [Particle Data Group Collaboration], Chin. Phys. C **38** (2014) 090001.
- [45] A. V. Anisovich, R. Beck, E. Klempt, V. A. Nikonov, A. V. Sarantsev and U. Thoma, Eur. Phys. J. A **48** (2012) 15 [arXiv:1112.4937 [hep-ph]].
- [46] M. Shrestha and D. M. Manley, Phys. Rev. C **86** (2012) 055203 [arXiv:1208.2710 [hep-ph]].
- [47] G. Ramalho and M. T. Peña, Phys. Rev. D **89**, 094016 (2014) [arXiv:1309.0730 [hep-ph]].
- [48] G. Ramalho and K. Tsushima, Phys. Rev. D **81**, 074020 (2010) [arXiv:1002.3386 [hep-ph]]; G. Ramalho and K. Tsushima, Phys. Rev. D **82**, 073007 (2010) [arXiv:1008.3822 [hep-ph]]; G. Ramalho and M. T. Peña, Phys. Rev. D **84**, 033007 (2011) [arXiv:1105.2223 [hep-ph]]; G. Ramalho and K. Tsushima, Phys. Rev. D **89**, 073010 (2014) [arXiv:1402.3234 [hep-ph]].
- [49] G. Ramalho and M. T. Peña, work in progress.
- [50] G. J. Gounaris and J. J. Sakurai, Phys. Rev. Lett. **21**, 244 (1968).

Photon and dilepton production at the Facility for Antiproton and Ion Research and the beam energy scan program at the Relativistic Heavy-Ion Collider using coarse-grained microscopic transport simulations

Stephan Endres,* Hendrik van Hees, and Marcus Bleicher

*Frankfurt Institute for Advanced Studies, Ruth-Moufang-Straße 1, D-60438 Frankfurt, Germany and
Institut für Theoretische Physik, Universität Frankfurt,
Max-von-Laue-Straße 1, D-60438 Frankfurt, Germany*

(Dated: May 2, 2016)

We present calculations of dilepton and photon spectra for the energy range $E_{\text{lab}} = 2 - 35$ AGeV which will be available for the Compressed Baryonic Matter (CBM) experiment at the future Facility for Anti-Proton and Ion Research (FAIR). The same energy regime will also be covered by phase II of the Beam Energy Scan at the Relativistic Heavy-Ion Collider (RHIC-BES). Coarse-grained dynamics from microscopic transport calculations of the Ultra-relativistic Quantum Molecular Dynamics (UrQMD) model is used to determine temperature and chemical potentials, which allows for the use of dilepton and photon-emission rates from equilibrium quantum-field theory calculations. The results indicate that non-equilibrium effects, the presence of baryonic matter and the creation of a deconfined phase might show up in specific manners in the measurable dilepton invariant mass spectra and in the photon transverse momentum spectra. However, as the many influences are difficult to disentangle, we argue that the challenge for future measurements of electromagnetic probes will be to provide a high precision with uncertainties much lower than in previous experiments. Furthermore, a systematic study of the whole energy range covered by CBM at FAIR and RHIC-BES is necessary to discriminate between different effects, which influence the spectra, and to identify possible signatures of a phase transition.

PACS numbers: 25.75.Cj, 24.10.Lx

Keywords: Dilepton & photon production, Monte Carlo simulations

I. INTRODUCTION

A major goal of the study of heavy-ion collisions at relativistic and ultra-relativistic collision energies is to explore the properties of strongly interacting matter at finite temperatures and densities [1, 2]. When two colliding nuclei hit each other, the nuclear matter is compressed, and a large amount of energy is deposited in a small spatial volume. This results in the creation of a fireball of hot and dense matter [3, 4]. The fireball lives for a time span of the order of several fm/c until the collective expansion of the matter has driven the strongly interacting system to a final state of freely streaming particles.

Today, almost the entire phase diagram governed by Quantum Chromodynamics (QCD) is accessible for experimental exploration at various accelerator facilities. The temperature T and baryochemical potential μ_B inside the fireball are mainly determined by the energy which is deposited in the nuclear collision; more precisely, the collision energy determines the trajectory of the system in the $T - \mu_B$ plane of the QCD phase diagram. At the highest currently available energies at RHIC and LHC the reaction is dominated by high temperatures, significantly above the critical temperature T_c , for which the creation of a deconfined state of quarks and gluons is assumed. At the same time the baryochemical po-

tential is low or close to zero for the largest part of the fireball evolution. This situation is similar to the conditions which prevailed in the universe a short time after the big bang. On the other side, one finds a complementary situation if considering heavy-ion collisions at laboratory frame energies of the order of 1 AGeV. Here only moderate temperatures are obtained, insufficient to create a Quark-Gluon Plasma. However, the very high net baryon densities or baryochemical potentials reached in this case might provide valuable information about those effects which are not mainly driven by temperature but by the presence of compressed baryonic matter. This situation resembles the environments in (super)nova explosions and neutron stars.

To learn about the different regions of the phase diagram one needs observables which do not only reflect the diluted final state after the freeze-out of the system but rather convey information about the entire fireball evolution. For this purpose electromagnetic probes, i.e., photons and dileptons have been for long suggested as ideal probes [5, 6]: Once produced, photons and dileptons only participate in electromagnetic and weak interactions for which the mean free paths are much longer than the size and the lifetime of the fireball. Consequently, they can leave the zone of hot and dense matter undisturbed. Since electromagnetic probes are emitted in a large variety of processes over the whole lifetime of the fireball, the measured spectra reflect the time-integrated evolution of the thermodynamic properties of the system. While this allows to obtain convoluted information about

* endres@th.physik.uni-frankfurt.de

the properties of matter it also poses a serious challenge for the theoretical description. On the one hand, one needs to identify the relevant microscopic processes that contribute to dilepton and photon emission and to determine the corresponding production rates. On the other hand it is important to give a realistic description of the complete reaction dynamics.

The intense experimental study of photon and dilepton production in the high-energy regime (at SPS [7–9], RHIC [10–13], and LHC [14] energies), but also for very low collision energies as measured at SIS 18 and BEVALAC [15–18] in comparison to theoretical model calculations has significantly enhanced our knowledge of the reaction dynamics and the properties of matter in the hot and dense medium created in a heavy-ion reaction. The importance of partonic emission for the correct theoretical description of the high-mass region of dilepton invariant mass spectra and the high- p_t photon spectra has been pointed out [19–21] and the various different hadronic contributions (especially for the photon production channels) could be identified [22–24]. Nevertheless, the most important finding was the large influence of the baryonic matter on the vector mesons' spectral shape. Especially in the case of the ρ meson this causes a strong broadening of the spectral function with small mass shifts [25–28]. This effect has been observed as an enhancement in the low-mass region of the dilepton invariant mass spectra and also shows up as a stronger low-momentum thermal photon yield. Note that the ρ broadening is most dominant at low collision energies, where one obtains the largest baryochemical potentials, but even at RHIC energies baryonic effects are by far not negligible.

However, there still remains an up to now unexplored energy window between the $E_{\text{lab}} = 1 - 2 A \text{ GeV}$ dilepton measurements by the DLS and HADES Collaborations and the CERES results for $E_{\text{lab}} = 40 A \text{ GeV}$. The future Compressed Baryonic Matter (CBM) experiment at the Facility for Anti-Proton and Ion Research (FAIR) with the SIS 100/300 accelerator provides the unique possibility to study heavy-ion collisions with beam energies from 2 up to 35 A GeV and will therefore enable us to get an insight into exactly that regime of the phase diagram of highest baryon densities where no dilepton or photon measurements have been performed till now [29, 30]. In addition, also phase II of the Beam Energy Scan (BES) program at RHIC will allow to perform measurements in fixed-target mode at lab-frame energies of 7.7, 9.1, 11.5, 14.5 and 19.6 A GeV, i.e., in the same collision energy range as FAIR [31]. Further complementary investigations are also planned for the NICA in Dubna [32].

From a theoretical point of view, the handling of this energy range is quite challenging, as the transition from a purely hadronic fireball at low collision energies to the creation of a partonic phase is expected here. Furthermore, at the high baryochemical potentials which still dominate the fireball at these energies, a first order phase transition from a hadron gas to the QGP is assumed, in

contrast to the situation at RHIC or the LHC where a cross-over is predicted by Lattice QCD calculations [33].

Although transport models were applied successfully to describe electromagnetic observables in heavy-ion collisions [34–36], they generally have some shortcomings when describing very hot and dense systems. In detail, problems include the following aspects: Firstly, while the Boltzmann approach works quite well for quasi-particles of infinite lifetime, for broad resonances as the ρ meson a correct description is challenging. Furthermore, in dense matter the intervals between scatterings become extremely short and will consequently modify the spectral characteristics of the single particles (collisional broadening). To describe the off-shell dynamics correctly a transport description with dynamical spectral functions following the description of Kadanoff and Baym [37] is required. However, a practical implementation of this is currently not possible. Secondly, in a dense medium not only binary scatterings will occur but also multi-particle interactions play a role, which is beyond the capabilities of the common transport models. And finally, the microscopic models usually concentrate on either the transport of hadrons or partons. However, modelling a transition from an initially up-heating hadron gas to a deconfined phase and the later particlization when the system cools down is extremely difficult to realize within a transport approach.

There have been several investigations over the last years on these aspects (see, e.g., Refs. [38–44]), but a full treatment of all these issues is still beyond the scope of present investigations.

On the other side, the short mean free paths of particles in a medium might suggest to treat the reactions from a macroscopic point-of-view. However, approaches as simple fireball expansion models [45] or hydrodynamics [46], which have been successfully applied for SPS, RHIC and LHC energies, also have their shortcomings in the FAIR energy regime for three main reasons: Firstly, the separation of the fireball expansion from dynamics of the initial projectile-target dynamics is not applicable; secondly, the often applied simplification to assume a 2+1-dimensional boost invariant geometry is not possible; and finally, the time scale necessary for an approximate thermal equilibration of the fireball will be longer due to the slower overall evolution of the reaction and the lower temperatures reached.

To avoid the disadvantages of both pictures the coarse-graining method has been developed, based on previous studies [47], and was successfully applied to describe dilepton production at SPS and SIS 18 energies [27, 28, 48]. The approach represents a combination of the microscopic picture from the underlying transport simulations with the resulting description of the dynamics in terms of the macroscopic quantities temperature and chemical potential. By averaging over many events one can extract the local energy and baryon densities at each space-time point from the transport simulations and use an equation of state to determine the corresponding

temperature and baryochemical potential. With this the calculation method of thermal dilepton and photon emission by application of full in-medium spectral functions is straightforward, employing the rates available from equilibrium quantum field theory.

In the present work the coarse-graining approach is used to calculate photon and dilepton spectra with focus the FAIR energy regime, but naturally the results also serve as a theoretical prediction for the fixed-target measurements of the RHIC-BES since the prospected collision energies of both experimental programs overlap. Although the details of the future experimental set-ups are not yet determined, the results shall provide a general baseline calculation for the interpretation of the measurements to be conducted. Furthermore, it shall be investigated if and how one can obtain valuable information on the properties of matter from the measured spectra and discriminate between several effects that might influence the dilepton and photon results. In detail, we will concentrate on the following three aspects: The modification of the thermal emission pattern by high baryochemical potentials, signals for a phase transition or the creation of a deconfined phase and possible non-equilibrium effects on the thermal rates.

This paper is structured as follows. In Section II the coarse-graining approach will be presented. Thereafter, in Section III we will introduce the various microscopic sources for thermal emission of photons and dileptons and in short discuss the non-thermal cocktail contributions. In Section IV the results for the fireball evolution and the photon and dilepton spectra at FAIR energies are shown. The results are used to systematically analyse in which way it might be possible to discriminate between different scenarios for the fireball evolution in Section V. We conclude the present work with a summary and an outlook to subsequent investigations.

II. THE MODEL

While microscopic transport models describe the reaction dynamics of a heavy-ion collision in terms of many different degrees of freedom, the general idea of the coarse-graining approach is that in principle only a very reduced amount of the provided information is necessary to account for the thermal production of electromagnetic probes. The microscopic information about all individual particles and their specific properties – such as mass, charge and momentum – are ignored and the whole dynamics is reduced to macroscopic quantities which are assumed to fully determine the local thermodynamic properties: The energy and particle densities.

The coarse-graining method combines two advantages: On the one hand the collision dynamics is still based on the microscopic transport evolution and thereby gives a very nuanced picture of the entire collision evolution, on the other hand the reduction to macroscopic state variables enables an easy application of in-medium spectral

functions from equilibrium quantum field theory calculations.

In the following the ingredients of the approach are presented in detail.

A. Ultrarelativistic Quantum Molecular Dynamics

The underlying microscopic input for the present calculations stems from the Ultra-relativistic Quantum Molecular Dynamics (UrQMD) approach [49–51]. It is a non-equilibrium microscopic transport model based on the principles of molecular dynamics [52, 53]. It constitutes an effective Monte Carlo solution to the relativistic Boltzmann equation and connects the propagation of hadrons on covariant trajectories with a probabilistic description of the hadron-hadron scattering processes. To account for the quantum nature of the particles, each hadron is represented by a Gaussian density distribution, and quantum statistical effects such as Pauli blocking are considered [54].

The model includes all relevant mesonic and baryonic resonances up to a mass of $2.2 \text{ GeV}/c^2$. Production of particles occurs via resonant scattering of particles (e.g., $NN \rightarrow N\Delta$ or $\pi\pi \rightarrow \rho$) or the decay of higher resonances, e.g., the process $\Delta \rightarrow \pi N$. The individual interaction and decay processes are described in terms of measured and extrapolated hadronic cross-sections and branching ratios. For collision energies above $\sqrt{s_{NN}} = 3 \text{ GeV}$ also the excitation of strings is possible.

B. Coarse-graining of microscopic dynamics

Within the UrQMD model the particle distribution function $f(\vec{x}, \vec{p}, t)$ is determined by the space and momentum coordinates of all the different particles in the system at a certain time. However, due to the finite number h of hadronic particles involved and produced in a heavy-ion collision, one needs to take the average over a large ensemble of events to obtain a smooth phase-space distribution of the form

$$f(\vec{x}, \vec{p}, t) = \left\langle \sum_h \delta^{(3)}(\vec{x} - \vec{x}_h(t)) \delta^{(3)}(\vec{p} - \vec{p}_h(t)) \right\rangle. \quad (1)$$

Note that this distribution is Lorentz invariant if all particles are on the mass-shell, as provided in our case. Due to the non-equilibrium nature of the model, one will of course have to extract the particle distribution function locally. In the present approach, this is done by the use of a grid of small space-time cells where for each of these cells we determine the (net-)baryon four-flow and the

energy-momentum tensor according to the relations

$$j_B^\mu = \int d^3p \frac{p^\mu}{p^0} f^B(\vec{x}, \vec{p}, t), \quad (2)$$

$$T^{\mu\nu} = \int d^3p \frac{p^\mu p^\nu}{p^0} f(\vec{x}, \vec{p}, t). \quad (3)$$

In practice, the integration is done by summing over the δ functions. As we use cells of finite size, we have

$$\delta^{(3)}(\vec{x} - \vec{x}_h(t)) = \begin{cases} \frac{1}{\Delta V} & \text{if } \vec{x}_h(t) \in \Delta V, \\ 0 & \text{otherwise} \end{cases} \quad (4)$$

and in the limit for small volumes the density of some observable \hat{O} then becomes

$$\int d^3p \hat{O}(\vec{x}, \vec{p}, t) f(\vec{x}, \vec{p}, t) = \frac{1}{\Delta V} \left\langle \sum_h^{\vec{x}_h \in \Delta V} \hat{O}(\vec{x}, \vec{p}, t) \right\rangle. \quad (5)$$

Consequently, Eqns. (2) and (3) take the form

$$T^{\mu\nu} = \frac{1}{\Delta V} \left\langle \sum_{i=1}^{N_h \in \Delta V} \frac{p_i^\mu \cdot p_i^\nu}{p_i^0} \right\rangle, \quad (6)$$

$$j_B^\mu = \frac{1}{\Delta V} \left\langle \sum_{i=1}^{N_{B/B} \in \Delta V} \pm \frac{p_i^\mu}{p_i^0} \right\rangle.$$

Having obtained the baryon flow, we can boost each cell into the rest frame as defined by Eckart [55], where j_μ^B is $(\rho_B, \vec{0})$. The according transformation of the energy-momentum tensor provides the rest frame energy density.

C. Non-equilibrium dynamics

While macroscopic models usually introduce thermal and chemical equilibrium as an ad-hoc assumption, microscopic simulations – in the present case the UrQMD simulations – are based on the description of single particle-particle interactions and non-equilibrium will be the normal case. Consequently, we have to account for these deviations from equilibrium in such a manner that we can reliably apply equilibrium spectral functions to calculate the emission of photons and dileptons.

In general it is difficult to really determine to which degree a system has reached equilibrium. Basically there are two dominant effects, which may serve as indicators for thermal and chemical equilibration: The momentum-space anisotropies and the appearance of meson-chemical potentials.

1. Thermal non-equilibrium

Regarding thermal equilibration, it was found in microscopic simulations that independent of the collision energy the system needs a time of roughly 10 fm/c after the

beginning of the heavy-ion collision until the transverse and longitudinal pressures are approximately equal [56]. The pressure anisotropy stems from the initial strong compression along the beam axis when the two nuclei first hit and traverse each other. As thermal equilibrium requires isotropy, one will obtain too high values for the energy density in highly anisotropic cells. To obtain effective quantities that account for the thermal properties in the system we apply a description that explicitly includes the momentum-space anisotropies and in which the energy momentum-tensor is assumed to take the form [57, 58]

$$T^{\mu\nu} = (\varepsilon + P_\perp) u^\mu u^\nu - P_\perp g^{\mu\nu} - (P_\perp - P_\parallel) v^\mu v^\nu. \quad (7)$$

where P_\perp and P_\parallel denote transverse or parallel pressure components, respectively; u^μ and v^μ are the cell's four-velocity and the four-vector of the beam direction. The effective energy density ε_{eff} is obtained via the generalized equation of state for a Boltzmann-like system of the form

$$\varepsilon_{\text{eff}} = \frac{\varepsilon}{r(x)}, \quad (8)$$

where the relaxation function $r(x)$ and its derivative $r'(x)$ are defined by

$$r(x) = \begin{cases} \frac{x^{-1/3}}{2} \left(1 + \frac{x \operatorname{artanh} \sqrt{1-x}}{\sqrt{1-x}} \right) & \text{for } x \leq 1 \\ \frac{x^{-1/3}}{2} \left(1 + \frac{x \operatorname{arctan} \sqrt{x-1}}{\sqrt{x-1}} \right) & \text{for } x \geq 1 \end{cases}, \quad (9)$$

and $x = (P_\parallel/P_\perp)^{3/4}$ denotes the pressure anisotropy.

As we have shown in our previous investigation at SPS energies [27], with this description the effective energy density deviates from the nominal one only for the very initial stage of the reaction, where the pressure components differ by orders of magnitude. Nevertheless, the effective energy density ε_{eff} allows to calculate meaningful T and μ_B values for these cells. After the very initial collision phase the differences still exist, but have hardly any influence on the energy density, so that we can assume that these cells are in approximate local equilibrium.

2. Chemical non-equilibrium

Chemical equilibration is a more difficult problem, but one obvious deviation in microscopic models is the appearance of meson chemical potentials, especially for the case of pions as these are the most abundantly produced particles. As the meson number is not a conserved quantity in strong interactions (in contrast to, e.g., the baryon number) meson chemical potentials can only show up if the system is out of chemical equilibrium. While pion chemical potentials are introduced in fireball models for the stage after the chemical freeze-out to obtain the correct final pion yields, in non-equilibrium transport models they intrinsically appear in the early stages of the reaction when a large number of pions is produced in

many initial scattering processes [59]. At higher collision energies this mainly happens via string excitation. The pion (and kaon) chemical potentials have a large influence on the photon and dilepton production rates as an overpopulation of pions increases the reactions in many important channels, for example $\pi\pi \rightarrow \rho \rightarrow \gamma/\gamma^*$ [60].

To implement the non-equilibrium effects in the calculations, we extract the pion and kaon chemical potentials in Boltzmann approximation as [61]

$$\mu_{\pi/K} = T \ln \left(\frac{2\pi^2 n}{gTm^2 K_2 \left(\frac{m}{T}\right)} \right), \quad (10)$$

where n denotes the cell's pion or kaon density and K_2 the Bessel function of the second kind. The degeneracy factor g is 3 in the case of pions and 2 for kaons. Note that the Boltzmann approximation is in order here, as the mesons in the transport model also account for Boltzmann statistics and no Bose effects are implemented. However, while for a Bose gas the chemical potential is limited to the meson's mass, in principle one can get higher values for μ_π or μ_K here in rare cases. As such values are non-physical, we assume that the maximum values to be reached are 140 MeV for μ_π and 450 MeV for μ_K .

D. Equation of state

Once the rest-frame properties of each cell are determined, an equation of state (EoS) is necessary to describe the thermodynamic system of the hot and dense matter in the cell under the given set of state variables, i.e., the (effective) local energy density and the local net densities of conserved charges (for the strong interactions considered here the baryon number is the relevant quantity). For the present calculations we apply a hadron gas equation of state (HG-EoS) that includes the same hadronic degrees of freedom as the underlying transport model [62]. The EoS allows us to extract the temperature and baryochemical potential for an equilibrated hadron gas at a given energy and baryon density. It is similar to the result obtained for UrQMD calculations in a box in the infinite time limit, when the system has settled to an equilibrated state.

However, in the FAIR energy regime a purely hadronic description of the evolving hot and dense fireball will not be sufficient. As the temperatures will exceed the critical temperature T_c , a transition from hadronic to partonic matter has to be implemented, and the dynamic evolution of the created Quark-Gluon Plasma has to be considered. On the other hand, it is necessary to keep the EoS consistent with the underlying dynamics which is purely hadronic. In our previous study at SPS energies [27], we supplemented the HG-EoS with a Lattice equation of state [63] for temperatures above $T_c \approx 170$ MeV, in line with the lattice results. In the range around the critical temperature the results of the HG-EoS and the Lattice EoS match very well for $\mu_B \approx 0$, while signifi-

cantly higher temperatures are obtained with the latter if one reaches temperatures significantly above T_c .

However, this procedure is problematic for the present study, as the transition from a hadronic to a partonic phase and back is assumed to take place at finite values of μ_B at FAIR energies, whereas the Lattice EoS is restricted to vanishing chemical potential. To avoid discontinuities in the evolution, we confine ourselves to the application of the HG-EoS, but with the assumption that the thermal emission from cells with a temperature above 170 MeV stems from the QGP (i.e., we employ partonic emission rates). This should be in order, as the temperatures will not lie too much above the critical temperature at the energies considered in the present work, where the deviations from a full QCD-EoS explicitly including a phase transition are expected to be rather moderate.

Nevertheless, we once again remind the reader that the underlying microscopic description is purely hadronic and it remains to be studied which consequences a phase transition has at the microscopic level of the reaction dynamics.

III. PHOTON & DILEPTON RATES

The mechanisms which contribute to the thermal emission of photons and dileptons are the same. Any process that can produce a real photon γ can also produce a virtual (massive) photon γ^* , decaying into a lepton pair. However, due to the different kinematic regimes probed by photons and dileptons, the importance of the single processes varies. In the following the various sources of thermal radiation considered in this work are presented.

Determining quantity for the thermal emission of real photons as well as virtual photons (i.e., dileptons) is the imaginary part of the retarded electromagnetic current-current correlation function $\Pi_{em}^{(ret)}$, to which the rates are directly proportional. It represents a coherent summation of the cuts of those Feynman diagrams which are describing the different processes contributing to thermal γ and γ^* emission, and therefore accounts for the photon or dilepton self-energy. In the rest frame, the thermal emission can be calculated according to [25]

$$\frac{dN_{ll}}{d^4x d^4q} = - \frac{\alpha_{em}^2 L(M)}{\pi^3 M^2} f_B(q; T) \times \text{Im} \Pi_{em}^{(ret)}(M, \vec{q}; \mu_B, T), \quad (11)$$

$$q_0 \frac{dN_\gamma}{d^4x d^3q} = - \frac{\alpha_{em}}{\pi^2} f_B(q; T) \times \text{Im} \Pi_{em}^{T, (ret)}(q_0 = |\vec{q}|; \mu_B, T). \quad (12)$$

Here $L(M^2)$ is the lepton phase-space factor (which plays a significant role only for masses close to the threshold $2m_l$ and is approximately one otherwise), f_B the Bose distribution function, and M the invariant mass of a lepton pair. Note that only the transverse polarization of the

current-current correlator enters for the photon rate, as the longitudinal projection vanishes at the photon point, i.e., for $M = 0$.

A. Thermal rates from hadronic matter

1. Vector meson spectral functions

In hadronic matter, all the spectral information of a hadron with certain quantum numbers is specified in $\text{Im} \Pi_{\text{em}}^{(\text{ret})}$ [64]. Assuming that Vector Meson Dominance (VMD) [65] is valid, the correlator can be directly related to the spectral functions of vector mesons. The important challenge for theoretical models is to consider the modifications of the particle's self-energy inside a hot and dense medium. Different calculations of in-medium spectral functions exist [66–70], however not many of them fully consider the effects of temperature and finite chemical potential. We here apply a hadronic many-body calculation from thermal field theory for the spectral functions of the ρ and ω mesons [71–73], which has proven to successfully describe photon and dilepton spectra from SIS 18 to LHC energies [20, 22, 27, 28, 45, 74, 75]. The calculation of the different contributions to the ρ spectral function takes three different effects into account: The modification due to the pion cloud, the direct scattering of the ρ with baryons (nucleons as well as excited N^* and Δ^* resonances) and with mesons (π, K, ρ, \dots) [76]. While the pion cloud effects also contribute in the vacuum, the scattering processes only show up in the medium. For the ω , the situation is slightly more complex since this meson basically constitutes a three-pion state. The vacuum self-energy is represented by a combination of the decays into $\rho + \pi$ or three pions, respectively. Further the inelastic absorption $\omega\pi \rightarrow \pi\pi$ and the scattering processes with baryons as well as the pion (i.e. $\omega\pi \rightarrow b_1$) are implemented [77]. In the same manner as in our previous dilepton study at SIS 18 energy [28], we relinquish a treatment of thermal emission from the ϕ vector meson here, for reason of the minor in-medium broadening effects observed for this hadron and its still low multiplicities at least for lower FAIR energies. In the case of vanishing invariant mass, i.e., for real photons, only the ρ vector meson will give a significant contribution. For the present calculation, we used the parametrization of the photon rates from the ρ as given in Eqs. (2)-(7) in Ref. [78], while a more advanced parametrization is necessary for the dilepton rates from the ρ and ω , due to their dependence on invariant mass and momenta [79].

Note that presently the photon parametrization of the ρ contribution is limited to baryon chemical potentials lower than 400 MeV and momenta larger than 0.2 GeV/ c . While we can easily neglect the lowest momentum region in the present study, the restriction to low μ_B is a problem for the lowest collision energies considered here, where one expects values of μ_B which significantly exceed this range. The difference will be dominant at lower mo-

menta, where the influence of baryonic effects is known to be largest, while the effect of a finite chemical potential is rather small at higher momenta [78]. However, for the present work we can assume the photon contribution from the ρ meson as a lower limit with regard to the baryonic effects.

2. Meson gas contributions

The contribution from vector mesons is not the only hadronic source of thermal emission. The mass region above the ϕ meson, i.e., for $M > 1 \text{ GeV}/c^2$, is no longer dominated by well defined particles, but here one finds a large number of overlapping broad resonances constituting multi-meson (mainly four-pion) states, which have a significant impact on the dilepton yield. We here apply a description relying on model-independent predictions using a low-temperature expansion in the chiral-reduction approach [74].

While the multi-meson effects only show up for high invariant masses, i.e., in the time-like kinematic region probed by dileptons, when going to real photons with $M \rightarrow 0$ several scattering and bremsstrahlung processes become important, which can be mostly neglected at finite M . While baryonic bremsstrahlung processes such as $NN \rightarrow NN\gamma$ and $\pi N \rightarrow \pi N\gamma$ are included in the vector meson spectral functions, meson-meson bremsstrahlung has to be added in the case of photon emission. The most dominant part will here come from the meson-meson scatterings $\pi\pi \rightarrow \pi\pi\gamma$ and $\pi K \rightarrow \pi K\gamma$, for which we use the rates calculated within an effective hadronic model [23] in form of the parametrization given by Eqs. (8) and (9) in Ref. [78]. Note that these bremsstrahlung processes are mainly contributing at low momenta, whereas they are rather subleading for photons of higher energy.

Besides the $\pi\pi$ bremsstrahlung, also other mesonic reactions contribute to the thermal photon production, such as strangeness bearing reactions and meson-exchange processes. In detail, these are $\pi\rho \rightarrow \pi\gamma$, $\pi K^* \rightarrow K\gamma$, $\pi K \rightarrow K^*\gamma$, $\rho K \rightarrow K\gamma$ and $K^*K \rightarrow \pi\gamma$. The corresponding thermal rates were calculated for a hot meson gas in Ref. [22], which are applied here together with the respective form factors.

Since the ω - t -channel exchange was found to give a significant contribution to thermal photon spectra via the $\pi\rho \rightarrow \pi\gamma$ process, it has been recently argued that also other processes including a $\pi\rho\omega$ vertex should be considered in the calculations, namely the $\pi\rho \rightarrow \gamma\omega$, $\pi\omega \rightarrow \gamma\rho$ and $\rho\omega \rightarrow \gamma\pi$ reactions for which the rates (including the form factors) are parametrized in Appendix B of Ref. [24]. Consequently, we also add these processes when calculating thermal photon spectra.

3. Influence of meson chemical potentials

As was already mentioned, we do not restrict ourselves to the consideration of emission from thermally and chemically equilibrated matter, but also include non-equilibrium effects in form of finite pion and kaon chemical potentials μ_π and μ_K . It has been shown that the influence of a non-equilibrium distribution of the respective mesons can be accounted for by introducing an additional fugacity factor

$$z_{M=\pi,K}^n = \exp\left(\frac{n\mu_M}{T}\right) \quad (13)$$

in the thermal dilepton and photon rates in Eqs. (11) and (12). The exponent n depends on the difference in pion or kaon number $N_{\pi/K}$ between initial and final state of the process, i.e. $n = N_{\pi/K}^i - N_{\pi/K}^f$. Note that while the pion fugacity enters in most processes, the effects of a finite kaon chemical potential only play a role for the πK bremsstrahlung and $\pi + K^* \rightarrow \pi + \gamma$, $\pi + K \rightarrow K^* + \gamma$ and $K^* + K \rightarrow \pi + \gamma$ photon production channels. For the dilepton channels considered here, μ_K can be neglected.

While for the single mesonic channels the initial and final state are always well defined, several different types of processes are included in the ρ and ω spectral functions, especially processes with baryons. For the ρ not only processes with an initial two-pion state of the type $\pi\pi \rightarrow \rho \rightarrow \gamma/\gamma^*$ are accounted for, but also reactions including only one or no pion as ingoing particle (e.g., $\pi N \rightarrow \Delta \rightarrow \gamma N$ or $NN \rightarrow \gamma NN$). However, as the correct fugacity depends on the initial pion number, one would obtain different enhancements for each channel. But as the different processes interfere with each other it is difficult to determine the exact strength of each channel and consequently one might hardly be able to account for some average enhancement factor. Instead we here apply a fugacity factor z_π^2 which would be correct for pure $\pi\pi$ annihilation processes. This can be interpreted as an upper estimate of the influence which the meson chemical potential might have on the thermal ρ emission rates. The same procedure is applied for the ω meson, where we assume a fugacity of z_π^3 . Note that while the multi-pion contribution also accounts for different initial states, they are each treated separately so that one can apply the correct fugacity factors here.

A full list of all hadronic contributions considered for the present calculation of thermal dilepton and photon emission, including the corresponding fugacity factors which account for the enhancement of the specific channel due to the meson chemical potentials, is given in Table I.

B. Quark-Gluon Plasma

For the thermal emission of electromagnetic probes from the Quark-Gluon Plasma one is again confronted

Type	Rates	Fugacity	Ref.
Dilepton	ρ (incl. baryon effects)	z_π^2	[73, 79]
	ω (incl. baryon effects)	z_π^3	[73, 79]
	Multi-Pion	$z_\pi^3 / z_\pi^4 / z_\pi^5$	[45]
Photon	ρ (incl. baryon effects)	z_π^2	[73, 78]
	$\pi\pi$ and πK Bremsstr.	$z_\pi^2 + 0.2z_\pi z_K$	[22, 78]
	$\pi\rho \rightarrow \gamma\pi$	z_π^3	[22]
	$\pi K^* \rightarrow K\gamma$	$z_\pi z_K$	[22]
	$\pi K \rightarrow K^*\gamma$	$z_\pi^2 z_K$	[22]
	$\rho K \rightarrow K\gamma$	z_π	[22]
	$K^* K \rightarrow \pi\gamma$	z_K	[22]
	$\pi\omega \rightarrow \gamma\rho$	z_π^4	[24]
	$\rho\omega \rightarrow \gamma\pi$	z_π^5	[24]
	$\pi\rho \rightarrow \gamma\omega$	—	[24]

TABLE I. Summary of the different dilepton contributions considered in the present calculations.

with the problem that different processes govern the dilepton production on the one side and photon emission on the other. Consequently, one has to apply two different descriptions for thermal rates, which are presented in the following.

In case of photon emission from a partonic phase of quarks and gluons the two main contributions stem from quark-antiquark annihilation ($q\bar{q} \rightarrow g\gamma$) and Compton scattering processes ($qg \rightarrow q\gamma$ or $\bar{q}g \rightarrow \bar{q}\gamma$) [80]. However, it was shown that these processes are not sufficient to describe the production mechanism correctly and that it is necessary to (a) include Feynman diagrams accounting for bremsstrahlung and inelastic annihilation processes which are enhanced due to near-collinear singularities and (b) to implement the Landau-Pomeranchuk-Migdal effect [81, 82]. The results of a full calculation of the photon emission, to leading order in α_{em} and the QCD coupling $g(T)$, was evaluated by Arnold, Moore and Yaffe and takes the following form [83]:

$$q_0 \frac{dR_\gamma}{d^3q} = -\frac{\alpha_{\text{em}}\alpha_s}{\pi^2} T^2 \left(\frac{5}{9}\right) f_B(q; T) \times \left[\ln\left(\sqrt{\frac{3}{4\pi\alpha_s}}\right) + \frac{1}{2} \ln\left(\frac{2q}{T}\right) + C_{\text{tot}} \right] \quad (14)$$

with

$$C_{\text{tot}} = C_{2\leftrightarrow 2}\left(\frac{q}{T}\right) + C_{\text{annih}}\left(\frac{q}{T}\right) + C_{\text{brems}}\left(\frac{q}{T}\right), \quad (15)$$

$$\alpha_s \approx \frac{6\pi}{27 \ln(T/0.022)}. \quad (16)$$

The functions $C_{2\leftrightarrow 2}$, C_{annih} and C_{brems} are approximated by the phenomenological fits given in Eqs. (1.9) and (1.10) in Ref. [83]. Note that this calculation assumes the chemical potential to be vanishing. However, the overall effect of finite values of a quark chemical potential (i.e., non-equal numbers of quarks and anti-quarks in the QGP phase) is known to be rather small.

In case of the thermal dilepton emission from the QGP, the leading order contribution is the electromagnetic annihilation of a quark and an anti-quark into a virtual photon, $q\bar{q} \rightarrow \gamma^*$. This process is irrelevant in the light-cone limit for $M \rightarrow 0$, as the annihilation of two massive quarks into a massless photon is kinematically forbidden. The pure perturbative quark-gluon plasma rate was calculated for the mentioned leading order process [84] as

$$\frac{dR_{ll}}{d^4p} = \frac{\alpha_{em}^2 T}{4\pi^4 p} f^B(p_0; T) \sum_q e_q^2 \times \ln \frac{(x_- + y)(x_+ + \exp[-\mu_q/T])}{(x_+ + y)(x_- + \exp[-\mu_q/T])} \quad (17)$$

with $x_{\pm} = \exp[-(p_0 \pm p)/2T]$ and $y = \exp[-(p_0 + \mu_q)/T]$. The quark chemical potential μ_q which shows up here is equal to $\mu_B/3$. This calculation approximates the full QCD results quite well at high energies, but for soft processes of the order $g_s(T)$, i.e., for dileptons with low masses and momenta, the one-loop calculation is not sufficient and hard-thermal-loop (HTL) corrections to the result as given in Eq.(17) have to be considered [85]. It was found that the rate for soft dileptons is then by orders of magnitude larger than the simple leading order calculation [26].

Recent calculations from thermal lattice-QCD suggest an even stronger enhancement of the rates for low-mass dileptons [86]. These results, which are applied in the present work, have been extrapolated to finite three-momenta by a fit to the leading-order pQCD rates such that the correlation function takes the form [26]

$$-\text{Im} \Pi_{EM} = \frac{C_{EM}}{4\pi} M^2 \left(\hat{f}_2(q_0, q; T) + Q_{LAT}^{tot}(M, q) \right), \quad (18)$$

where

$$Q_{LAT}^{tot}(M, q) = \frac{2\pi\alpha_s}{3} \frac{T^2}{M^2} \left(2 + \frac{M^2}{q_0^2} \right) \times KF(M^2) \ln \left[1 + \frac{2.912 q_0}{4\pi\alpha_s T} \right] \quad (19)$$

with a form factor $F(M^2) = 4T^2/(4T^2 + M^2)$ and a factor $K = 2$ to better fit the full lQCD rates. Note that in contrast to the pQCD result the rate in Eqs. (18) and (19) is calculated for $\mu_q = 0$ only, as a calculation for finite chemical potential is still beyond the current lattice calculations.

C. Hadronic decay contributions

While we restrict the calculation of photon yields to the thermal contribution, since all decay photons from long-lived hadronic resonances are usually subtracted from the experimental results, a full description of the dilepton spectra requires to take also the non-thermal contributions from the decay of pseudo-scalar and vector mesons

into account. We here follow the same procedures as in our previous work for SIS 18 energies. In detail, we determine the following non-thermal dilepton contributions:

1. The Dalitz decays of the pseudo-scalar π^0 and η mesons. To determine their contribution, we assume that each final state particle contributes with a weight of $\Gamma_{M \rightarrow e^+e^-}/\Gamma_{tot}$.
2. The direct decay of the ϕ meson into a lepton pair. As the lifetime of the ϕ is relatively short, we apply a shining procedure which takes absorption and re-scattering processes inside the medium into account.
3. Finally, we restricted the calculation of thermal dileptons to those cells where the temperature is larger than 50 MeV, as otherwise a thermal description becomes questionable. However, in principle one will of course also find ρ and ω mesons at lower temperatures. To account for this, in the mentioned cases we calculate a ‘‘freeze-out’’ contribution from the ρ and ω decays using the UrQMD results for these mesons.

For a more detailed description of the non-thermal hadronic contributions the reader is referred to Ref. [28]. We refrain from an extensive reproduction of the procedure here, as the cocktail contributions will not play a significant role in the present investigations.

IV. RESULTS

In the following we present the results of calculations with the coarse-graining approach for Au+Au collisions in the energy range of $E_{lab} = 2 - 35$ AGeV. We restrict the analysis to the 10% most central reactions, as the medium effects will be largest here. In terms of the microscopic UrQMD results, this roughly corresponds to an impact parameter range of $b = 0 - 4.5$ fm. For the coarse-graining we use ensembles of 1000 microscopic events each. The length of the time-steps is chosen as $\Delta t = 0.6$ fm/c, and the size of the spatial grid is $\Delta x = \Delta y = \Delta z = 0.8$ fm. These grid parameters are similar to the ones used for the previous studies at SIS 18 and SPS energies and constitute a good compromise between resolution and a sufficiently large hadron number per cell. To obtain enough statistics, especially for the non-thermal contributions, several runs with different ensembles are necessary.

A. Reaction dynamics

As the dilepton and photon production is directly related to the space-time evolution of the thermodynamic properties of the system, it seems natural to start with a study of the reaction dynamics obtained with the coarse-graining of UrQMD input.

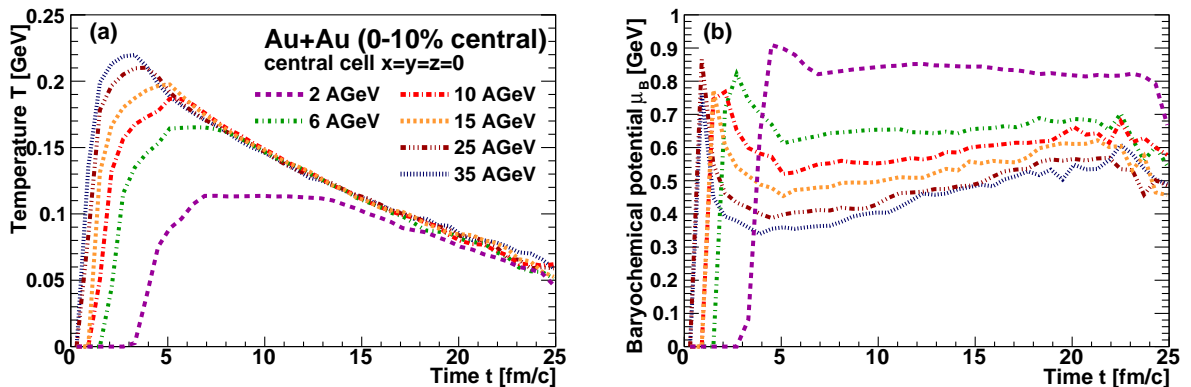


FIG. 1. (Color online) Time evolution of (a) temperature T and (b) baryochemical potential μ_B for the central cell of the coarse-graining grid for different beam energies $E_{\text{lab}} = 2 - 35$ AGeV. The results are obtained for the 0-10% most central collisions in Au+Au reactions.

In Fig. 1 the time evolution of temperature and baryochemical potential in the central cell of the grid is depicted for different beam energies. The evolution shows a significant increase of the temperature maxima from slightly above 100 MeV for 2 AGeV up to roughly 225 MeV for top SIS 300 energy. While the temperature is clearly below the critical temperature of 170 MeV for the lower energies, the highest energies covered by FAIR can probe also this deconfinement region of the phase diagram. The thermal lifetime of the central cell, i.e., the time for which it rests at temperatures above 50 MeV, increases slightly with increasing collision energy. This is mainly due to an earlier onset of thermalization after the first hadron-hadron collisions, which define the origin of the time axis. However, it is interesting that in the later phase of the collision the temperature curves for all energies show the same monotonous decrease and even lie on top of each other. A somewhat different behavior is observed for the evolution of the baryochemical potential μ_B . For all energies it shows a clear peak with values between 700 and 900 MeV at the beginning of the collision, which is due to the high baryon densities reached in the central cell when the two nuclei first come into contact. Afterwards μ_B decreases and then remains on a plateau level for a significant fraction of the reaction time for the lower energies, while one observes a slight increase for the higher beam energies towards later times. If we neglect the peak in the early reaction stage, the chemical potential shows a clear decrease with increasing collision energy. While for 2 AGeV the baryochemical potential remains around 900 MeV for the whole thermal lifetime, μ_B is only 350 MeV at $t = 5$ fm for 35 AGeV and slowly increases up to 600 MeV after $t = 20$ fm.

Note that the results shown in Fig. 1 are *only* for one single cell at the center of the collision. The evolution in other cells of the grid may differ largely in dependence on their location (e.g., one finds in general lower temper-

ature and chemical potential in more dilute peripheral cells). But yet it clearly depicts the influence of collision energy on T and μ_B . One finds two effects when going from the lowest to the highest FAIR energies: An *increasing* temperature combined with a *decreasing* baryochemical potential. This behavior is not specific for the central cell but reflected by the whole space-time evolution, as can be seen from Fig. 2. The two plots show the thermal four-volume in dependence of temperature T (X-axis) and baryochemical potential μ_B (Y-axis). Results are shown for $E_{\text{lab}} = 4$ AGeV (a) and 35 AGeV (b). We see that for the lower energy the largest part of the four volume is concentrated at values of the baryochemical potential between 500 and 800 MeV, while the temperature remains below 160 MeV for all cells. In contrast, for $E_{\text{lab}} = 35$ AGeV the four-volume distribution extends to higher temperatures up to $T = 240$ MeV while at the same time the distribution is shifted to lower baryochemical potentials especially for higher temperatures while the lower-temperature cells are mainly dominated by high values of μ_B . Interestingly, especially for the higher collision energy of 35 AGeV one finds some cells in a separate region with moderate to high temperature and very low baryochemical potential $\mu_B \approx 0$. These cells are mainly found in the more peripheral regions of the collision, where the baryon density (and particle density in general) is rather low and where nevertheless in some cases hadrons with large momenta are found, resulting in high energy density for these cells. However, compared to the large overall total thermal volume the relevance of these low- μ_B cells is negligible.

It is important to bear in mind that the dilepton and photon spectra will directly reflect the four-volume evolution in the $T - \mu_B$ plane, as presented here. The results show that at FAIR energies the region of the QCD phase diagram with temperatures above the critical temperature *and* large μ_B can be probed, in contrast to the situa-

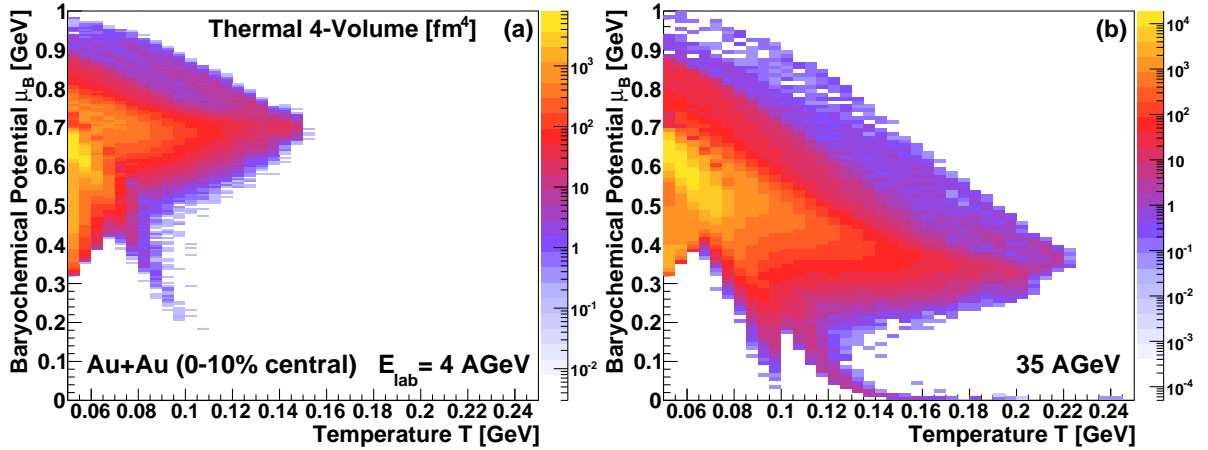


FIG. 2. (Color online) Thermal four-volume in units of fm^4 from the coarse-grained transport calculations in dependence of temperature T and baryochemical potential μ_B . Results are shown for $E_{\text{lab}} = 4$ AGeV (a) and 35 AGeV (b) in central Au+Au collisions.

tion at LHC or RHIC, where the transition from hadronic matter to a deconfined phase is assumed to happen at $\mu_B \approx 0$. However, note that the results presented here are obtained with a purely hadronic equation of state which does not include any effects of the phase transition itself. For an improvement the description one might need to implement the transition properly, to account, e.g., for the latent heat which would cause the cells to remain for a longer time at temperatures around T_c . Nevertheless the present results can serve as a lower limit baseline calculation, assuming that we have a smooth crossing from hadronic to QGP emission. Significant deviations from this assumption might then show up in the photon and

dilepton spectra. We will discuss this later.

As was pointed out before, the effects of chemical non-equilibrium show up in the form of finite meson chemical potentials for the π and K; and μ_π and μ_K can have a significant effect on the population of several photon and dilepton production channels. The mean values of the pion chemical potential μ_π and the kaon chemical potential μ_K in dependence on the cell's temperature for different collision energies are shown in Figure 3. Note that the results for the chemical potentials here are obtained by averaging the values of μ_π and μ_K over all space-time cells with a specific temperature. The study indeed indicates that regarding the pion density the system will be clearly out of equilibrium during the collision evolution. The value of μ_π increases with temperature, which is not surprising since a large part of the pion production in the microscopic simulation takes place in initial scatterings and via string formation at the beginning of the reaction, when the system still heats up. At all temperatures one finds that the μ_π decreases with increasing collision energy, which may indicate a faster and stronger equilibration of the system if more energy is deposited in the system. In addition, for top SIS 300 energies the initial emission is dominated by QGP radiation at temperatures above T_c and consequently a larger fraction of cells with $T < 170$ MeV is found later in the course of the fireball evolution, when the system is in a more equilibrated condition compared to the very beginning of the collision. For the higher collision energies we get average values up to $\mu_\pi = 100 - 120$ MeV around the critical temperature of 170 MeV. Note that for $E_{\text{lab}} = 4$ AGeV the maximum temperature found in the evolution is around 155 MeV, which explains the drop in the corresponding curve around this temperature.

In contrast to the large pion chemical potential, no

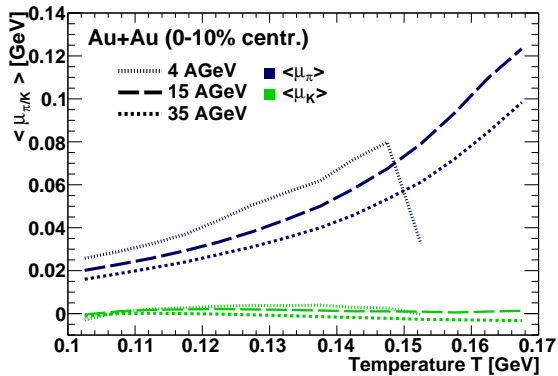


FIG. 3. (Color online) Average values of the pion chemical potential μ_π (blue lines) and the kaon chemical potential μ_K (green lines) in dependence on the cell temperature. Results are shown for central Au+Au collisions at three different collision energies, $E_{\text{lab}} = 4, 15$ and 35 AGeV.

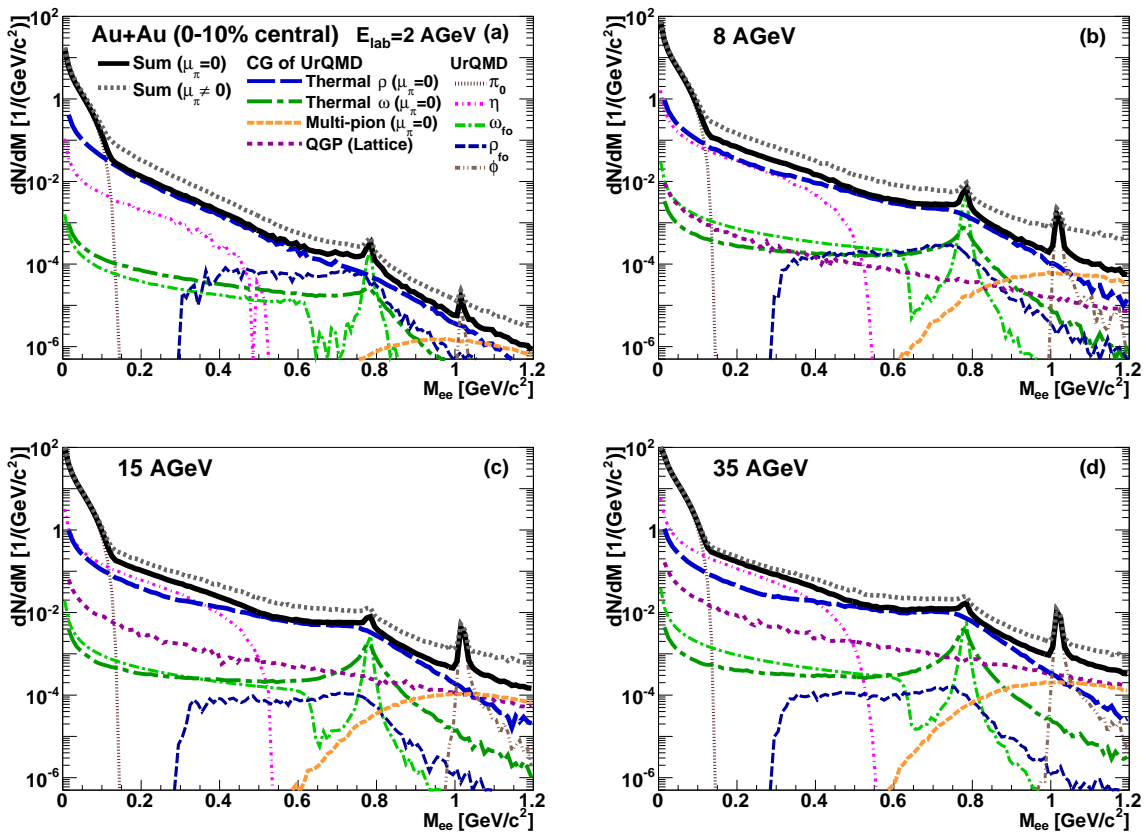


FIG. 4. (Color online) Dilepton invariant mass spectra for Au+Au reactions at different energies $E_{\text{lab}} = 2 - 35$ AGeV within the centrality class of 0-10% most central collisions. The resulting spectra include thermal contributions from the coarse-graining of the microscopic simulations (CG of UrQMD) and the non-thermal contributions directly extracted from the transport calculations (UrQMD). The hadronic thermal contributions are only shown for vanishing pion chemical potential, while the total yield is plotted for both cases, $\mu_\pi = 0$ and $\mu_\pi \neq 0$.

such dominant off-equilibrium effect is observed for the kaons, where $\mu_K \approx 0$ at all energies and temperatures. This is not surprising, as in the underlying microscopic simulations any inelastic reaction results in the creation of a π whereas the cross-section for kaon production is rather low in the cases considered here (and especially for the lower FAIR energies). Consequently, the kaon production is a slow process which seems to happen synchronously with the equilibration of the system while a large amount of pions is produced in the initial hard nucleon-nucleon scatterings before any equilibration could take place.

The present results for the pion chemical potential are quite different from other model descriptions. For example, in fireball parametrizations the particle numbers are fixed at the chemical freeze-out of the system and consequently meson chemical potentials develop when the system cools down. However, in the fireball model this is just an ad-hoc assumption, as such macroscopic models

are based on a presumed equilibrium within the system. In contrast, the overpopulation of pions is an intrinsic result stemming from the microscopic simulation in the case of the coarse-graining approach. Nevertheless, the very high pion chemical potentials in the temperature region close to the phase transition might be questionable, as one would assume that the transition from the Quark-Gluon Plasma to a hadronic phase should produce a system where the mesons are in an equilibrium state. A fully satisfying description of the chemical off-equilibrium evolution is not feasible within the present approach and would require a microscopic and dynamical description of the phase transition and its underlying dynamics.

B. Dilepton spectra

The dilepton invariant mass spectra in the low-mass range up to $M_{e^+e^-} = 1.2$ GeV/ c^2 for four different beam

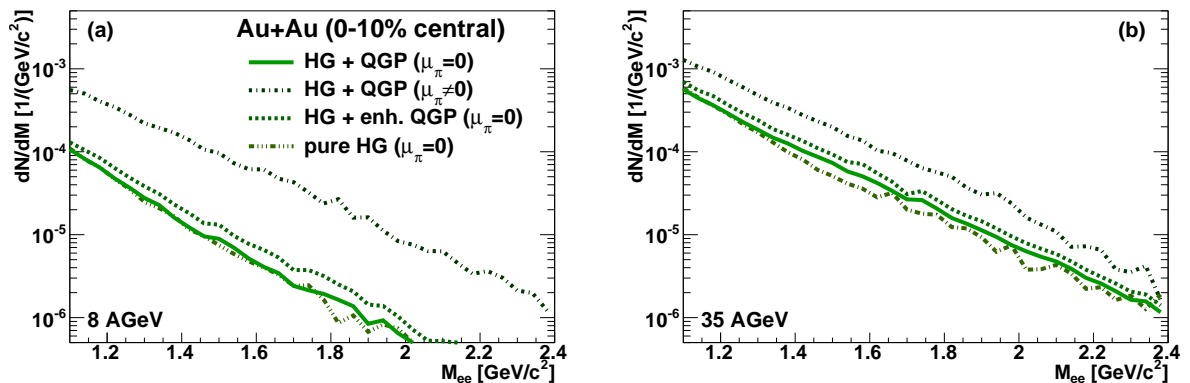


FIG. 5. (Color online) High-mass region of the dilepton $M_{e^+e^-}$ spectrum for central Au+Au collisions at $E_{\text{lab}} = 8$ AGeV (a) and 35 AGeV (b), assuming different emission scenarios. The the baseline calculation assumes hadronic emission up to 170 MeV with vanishing μ_π and partonic emission for higher temperatures (full line). Besides the results with a five times enhanced emission around the critical temperature (dashed line) and for a pure hadron gas scenario with emission at all temperatures from hadronic sources (dashed-triple-dotted line) are shown. Again, we also show the baseline result including finite pion chemical potential (dashed-dotted line).

energies ($E_{\text{lab}} = 2, 8, 15$ and 35 AGeV) are presented in Fig. 4. The comparison shows some interesting similarities and differences: While the very low masses up to $0.15 \text{ GeV}/c^2$ are generally dominated by the Dalitz decays of neutral pions, the region beyond the Dalitz peak up to the pole masses of the ρ and ω mesons (i.e., $\approx 770 \text{ MeV}/c^2$) is dominated by a strong thermal ρ contribution. The thermal yield shows an absolute increase with E_{lab} , but its importance decreases relative to the non-thermal η yield. This means that the thermal low-mass enhancement of the dilepton yield above a hadronic vacuum cocktail decreases with increasing collision energy. This observation is explained by the decrease of the baryon chemical potential at higher collision energies, as has been mentioned in the previous section. In contrast, the increasing temperature leads to a significantly flatter shape of especially the ρ distribution in the invariant mass spectrum. While for low energies the thermal yield decreases strongly when going to higher invariant masses, at the top FAIR energies this effect is less prominent and the population of high masses is enhanced. This is clearly seen by the fact that the multi-pion yield shows a strong rise.

While at the lowest of the four energies the whole system is well below the critical temperature T_c , we know from the temperature evolution in Fig. 1 (a) that the region around $T \approx 170 \text{ MeV}$ from is reached $E_{\text{lab}} = 6 - 8$ AGeV on. Consequently, in the dilepton invariant mass spectra of Fig. 4 the resulting QGP contribution is very small at 8 AGeV, but even at 35 AGeV the partonic yield is suppressed by roughly an order of magnitude compared to the leading contributions in the mass range up to $1 \text{ GeV}/c^2$.

The hadronic thermal yields in Fig. 4 are shown for the case of vanishing pion chemical potential. However, we

also compare the result for $\mu_\pi = 0$ with the total yield assuming finite values of μ_π . One can see that chemical non-equilibrium can increase the overall dilepton yield in the low-mass range up to a factor of two. For the region above $1 \text{ GeV}/c^2$ the effect can be even larger as the fugacity factor enters the thermal rate with a power of four for the multi-pion contribution. It is important to bear in mind that this result should rather be seen as an upper estimate, as the approximation $\mu_\rho = 2\mu_\pi$ is only correct for the rate $\pi\pi \rightarrow \rho$, which represents only one of the many processes included in the ρ spectral function. Furthermore, as UrQMD has no intrinsic description of the phase transition, the pion chemical potential might be overestimated in vicinity of the critical temperature. Nevertheless, the results show that a deviation from pion equilibrium has a huge impact on the thermal dilepton rates.

Considering possible signatures for a phase transition and the creation of a deconfined phase, the low-mass region is rather unsuited due to the dominance of the hadronic cocktail contributions and hadronic thermal emission from the vector mesons. Consequently, it might be more instructive to explore the mass range above the pole mass of the ϕ , where one has a continuum dominated by thermal radiation. In this region the hadronic cocktail contributions can be neglected and thermal sources will dominate the spectrum. In previous works [27, 45] it has been shown for SPS energies that the dilepton invariant mass spectrum at very high masses $M_{l+l^-} > 1.5 \text{ GeV}/c^2$ could only be explained by including thermal radiation from the Quark-Gluon Plasma. In Fig. 5 the higher invariant mass region for $M_{e^+e^-} > 1.1 \text{ GeV}/c^2$ is shown for the two collision energies $E_{\text{lab}} = 8$ and 35 AGeV. Here we compare four different scenarios to study whether the high-mass invariant mass spectrum might help to iden-

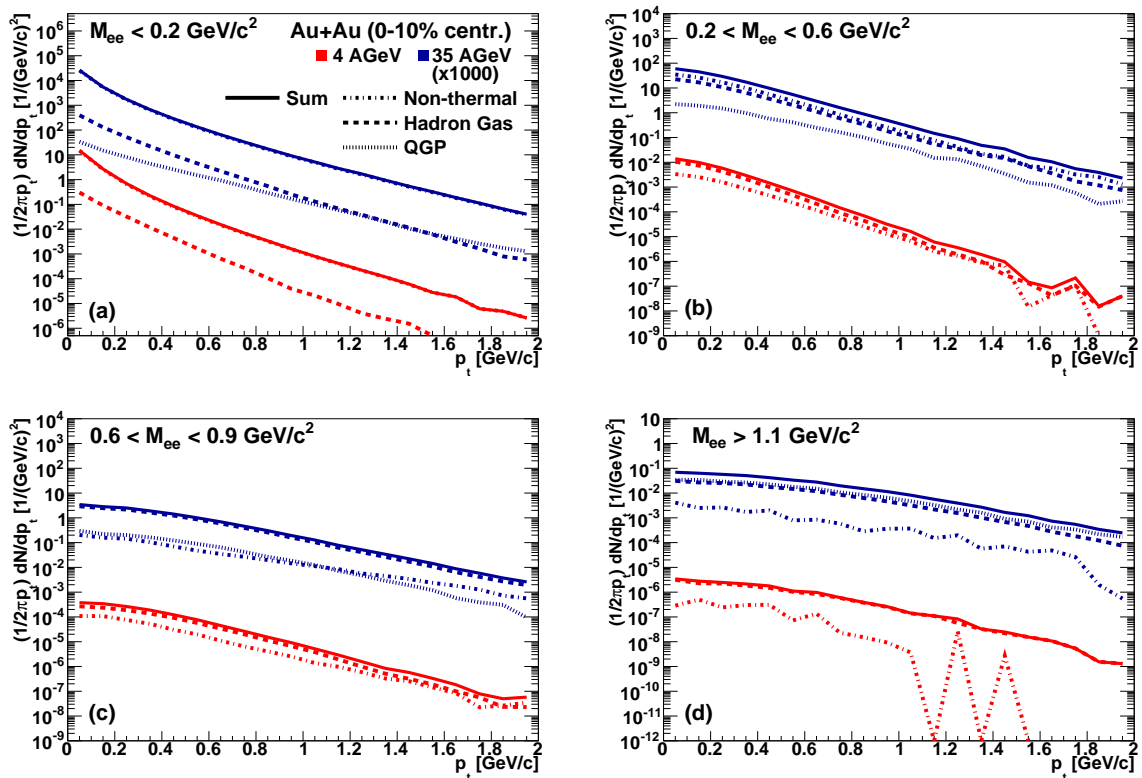


FIG. 6. (Color online) Transverse-momentum spectra of the dilepton yield in central Au+Au reactions $E_{\text{lab}} = 4 \text{ AGeV}$ (red) and 35 AGeV (blue). The results are shown for four different invariant mass bins: $M_{e^+e^-} < 0.2 \text{ GeV}/c^2$ (a), $0.2 < M_{e^+e^-} < 0.6 \text{ GeV}/c^2$ (b), $0.6 < M_{e^+e^-} < 0.9 \text{ GeV}/c^2$ (c) and $M_{e^+e^-} > 1.1 \text{ GeV}/c^2$ (d).

tify the creation of a Quark-Gluon Plasma. Besides the two standard scenarios (hadron gas + partonic emission above $T_c = 170 \text{ MeV}$) for (i) finite and (ii) vanishing μ_π , we include a scenario with (iii) a 5-times enhanced emission from the partonic phase around the transition temperature to simulate the effect of a critical slowdown of the system due to a first order phase transition and, finally, (iv) a pure hadron gas scenario, where we assume all thermal radiation (also for $T > 170 \text{ MeV}$) to stem from hadronic sources. For (iii) and (iv) $\mu_\pi = 0$ is assumed, too. The comparison shows that the spectral shape of the total yield is very similar for all scenarios, at both energies considered here. While the results for a purely hadronic scenario and including QGP emission from temperatures above T_c give quite the same results within 10% deviation, also the artificially enhanced QGP emission does not significantly increase the overall yield. In contrast, one observes a very strong enhancement due to a finite pion chemical potential, which shows up in our calculation by an overall increase by a factor of 5 at 4 AGeV and still a factor of 2 at 35 AGeV . The results indicate that it will be difficult to draw unambiguous conclusions from single measurements of the higher mass re-

gion at a specific energy, as according to our calculations a stronger QGP yield and less hadronic contribution can finally result in the same overall dilepton spectrum. Furthermore, the non-equilibrium effects may lead to much larger modifications of the spectrum than caused by the dynamics of the phase transition.

The transverse-momentum spectra, plotted for two different energies in different invariant mass bins in Fig. 6 underline the previous finding. Again the slopes of the curves for hadronic and partonic emission are very similar for high masses, especially for $M_{e^+e^-} > 1.1 \text{ GeV}$ they are virtually identical. On the contrary we find the partonic contribution to be harder (i.e., having a stronger relative yield at high transverse momenta) than the hadronic contribution at lower masses. Together with the very similar invariant-mass spectra at high masses obtained with and without a partonic phase in the reaction evolution, the result confirms previous studies which showed a duality of emission rates in the transition-temperature region [26]. However, note that this is no longer true if one goes to a temperature regime significantly above T_c . For this case clear differences between the hadronic and the partonic emission are observed. Unfortunately, even at the top

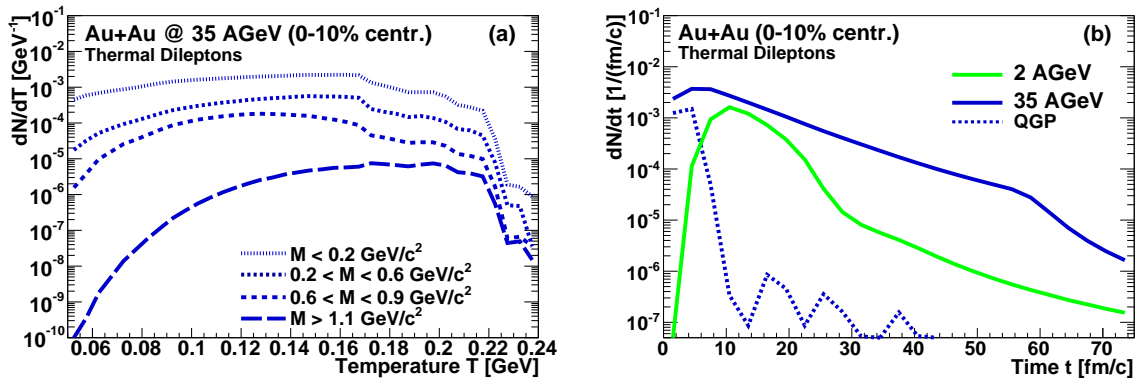


FIG. 7. (Color online) (a) Temperature dependence of dilepton emission dN/dT from thermal sources for central Au+Au at $E_{\text{lab}} = 35$ AGeV, i.e., the lepton pairs directly extracted from the hadronic cocktail as calculated with UrQMD are not included. The results are shown for four different invariant mass bins: $M_{e^+e^-} < 0.2$ GeV/ c^2 , $0.2 < M_{e^+e^-} < 0.6$ GeV/ c^2 , $0.6 < M_{e^+e^-} < 0.9$ GeV/ c^2 and $M_{e^+e^-} > 1.1$ GeV/ c^2 ; (b) Time evolution dN/dt of thermal dilepton emission for 2 (green) and 35 AGeV (blue). The dashed line shows the emission from the QGP for the top FAIR energy.

SIS 300 energy only few cells reach temperature maxima above 200 MeV and one will not see clear differences between the partonic and hadronic emission patterns even at high p_t and high $M_{e^+e^-}$.

The reason for the duality showing up only at high invariant masses (and momenta, respectively) is twofold: On the one hand, the low mass region is governed by the vector mesons with their specific spectral shapes and the baryonic effects on them. This effect has been called the “duality mismatch” [25] since the hadronic rates show an increase for finite baryochemical potentials, while the partonic emission rates are quite insensitive with regard to μ_q . On the other hand, while the spectra at low masses and momenta are populated by thermal emission at all temperatures, the production of dileptons for masses above 1 GeV/ c^2 and for higher values of p_t is strongly suppressed at low temperatures. This is visible from Fig. 7 (a), where the temperature dependent dilepton yield from thermal sources for Au+Au at $E_{\text{lab}} = 35$ AGeV is shown for different invariant-mass bins. (Note that the non-thermal lepton pairs directly extracted from the hadronic cocktail as calculated with UrQMD are not included here). The yields shown in this plot represent the sum of the contributions from all cells at a certain temperature. While for the lowest mass bin $M_{e^+e^-} < 0.2$ GeV/ c^2 the total thermal dilepton yield is built up by roughly equal fractions stemming from the whole temperature range, with slight suppression of emission from temperatures above T_c , one can see that the mass region above $M_{e^+e^-} = 1.1$ GeV/ c^2 is dominated by emission from temperatures between 140 to 220 MeV, which is exactly the assumed transition region between hadronic and partonic emission. Dilepton emission at lower temperatures is strongly suppressed in this mass range. Furthermore, one finds a smooth behavior of the thermal emission in the highest mass bin,

but at lower masses one observes a slight kink in the rates at $T_c = 170$ MeV. The finding indicates that for lower masses the partonic and hadronic rates do not perfectly match, as was discussed above. Another observation is the dominance of emission from the temperature range $T = 100 - 140$ MeV for the mass region from 0.6 to 0.9 GeV/ c^2 . This result is in contrast to the general trend of a shift of the emission to higher temperatures when going to higher masses. However, the very mass region covers the pole masses of the ρ and ω meson. As the peak structures show a melting especially for finite baryon densities, one will get the largest yields in this mass range from cells for which $\mu_B \approx 0$. A comparison with the T - μ_B distribution of the cells at this energy in Fig. 2 (b) shows that the largest fraction of cells for which the baryochemical potential is below 200 MeV lies exactly in the temperature range from 100 to 140 MeV.

Finally, it is instructing not only to look at the temperature but also at the time dependence of thermal dilepton emission as presented in Figure 7 (b). The total dilepton emission per timestep dN/dt as sum from all cells is shown for $E_{\text{lab}} = 2$ and 35 AGeV. In principle, the results reflect the findings from Fig. 1 and are similar to the temperature evolution depicted there. The system shows a faster heating for the top SIS 300 energy with higher temperatures, resulting in a larger number of emitted dileptons; partonic emission from cells with $T > T_c$ is found for the first 5 – 10 fm/c and only very sporadically thereafter. At lower energies the evolution is retarded and T remains below the critical temperature. However, in contrast to the slow heating of the system (which is simply due to the fact that the nuclei are moving slower) the thermal emission drops much earlier for 2 AGeV (compared to 35 AGeV) and only few cells with thermal emission are found for $t > 30$ fm/c. The higher energy deposited in the system with increasing E_{lab} ob-

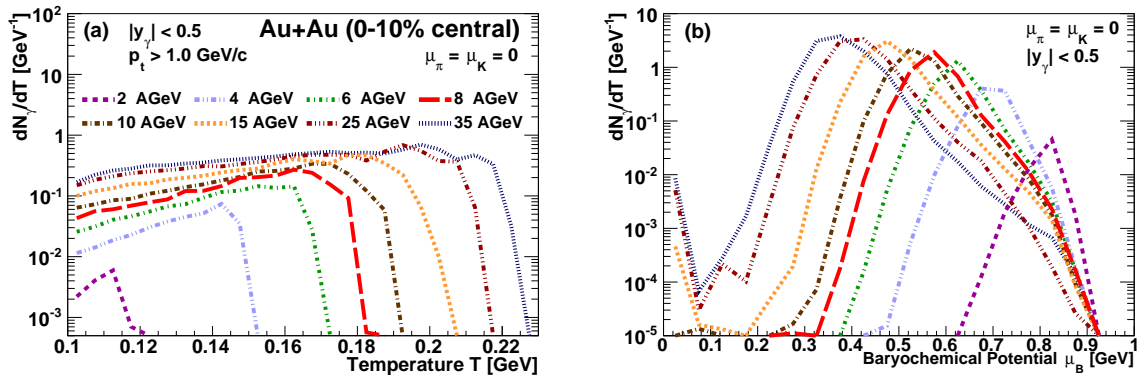


FIG. 8. (Color online) Thermal photon yield at mid-rapidity in dependence on (a) temperature, dN_γ/dT , and (b) baryochemical potential, $dN_\gamma/d\mu_B$, for central Au+Au collisions at different beam energies $E_{\text{lab}} = 2 - 35$ AGeV. The results are shown for the case of vanishing μ_π and μ_K .

viously results not only in higher initial temperatures, but also in an enhanced emission at later stages, as it takes the system longer to cool down. Interestingly, for both energies one finds some sparse cells with thermal emission even after 60-70 fm/c; however, their contribution to the overall result is suppressed by 3-4 orders of magnitude compared to the early reaction stages.

C. Photon spectra

While we have two kinematic variables (momentum and invariant mass) which can be probed for virtual photons, real (i.e., massless) photons only carry a specific energy. In this sense, dileptons are the more versatile probes of the hot and dense medium and carry additional information, especially regarding the spectral modifications of the vector mesons. Nevertheless, the correct description of the experimental photon spectra has been a major challenge for theory at SPS and RHIC energies. In the kinematic limit $M \rightarrow 0$ several processes become dominant which are negligible in the time-like region probed by dileptons, as was discussed in Sec. III. Consequently, the study of photon production can provide complementary information for the theoretical description of thermal emission rates and the reaction dynamics.

As the parametrized photon emission rates have some restrictions with regard to the μ_B range of their applicability, it will be instructive to find out at the beginning under which thermodynamic conditions the photons are emitted at FAIR. Fig. 8 shows the dependence of thermal photon emission (at mid-rapidity) on temperature in the left plot (a) and on baryochemical potential in the right plot (b). As in Fig. 7, the yields are the sum of the thermal contributions from all cells with a certain temperature or baryochemical potential, respectively. For both results we consider the case of vanishing meson chem-

ical potentials. Note that for the temperature dependence we consider only the thermal emission at higher transverse momentum values $p_t > 1$ GeV/c, as here the duality between hadronic and partonic rates should be approximately fulfilled, which is indeed visible from the continuous trend of the thermal photon emission around T_c . One can see that especially for lower collision energies the thermal emission is dominated by the cells which reach the maximum temperature, whereas the curves become flatter at higher energies. Even at the top energy of 35 AGeV with maximum temperatures above 220 MeV still a significant amount of emission also stems from the cells with temperatures around 100 MeV.

Regarding the photon emission related to baryochemical potential as presented in Fig. 8 (b), a clear energy dependent trend is visible: While at low energies the largest fraction of emission stems from cells with very high values of μ_B around 900 MeV, the emission weighted average chemical potential drops continuously to 300-400 MeV at 35 AGeV. However, the emission from cells with higher values of the baryochemical potential is by far not negligible. In consequence, the findings once again underline that the strongest baryonic modifications of the spectral functions will be present at low energies. The results also show that to fully account for the baryonic effects on the photon emission the spectral functions should be able to reliably cover the whole μ_B region from 0 to the nucleon mass (i.e. ≈ 900 MeV). The presently used parametrization will provide only a lower limit for the photon yield, especially for the lower collision energies.

In Fig. 9(a)-(d) the transverse momentum spectra of thermal photons for four different collision energies are presented. As for the dilepton invariant mass spectra, we show the results with (full black line) and without meson chemical potentials (dashed black); once again the two calculations provide a lower and upper boundary for the off-equilibrium influence on the thermal yields, respectively. Two observations can be made when com-

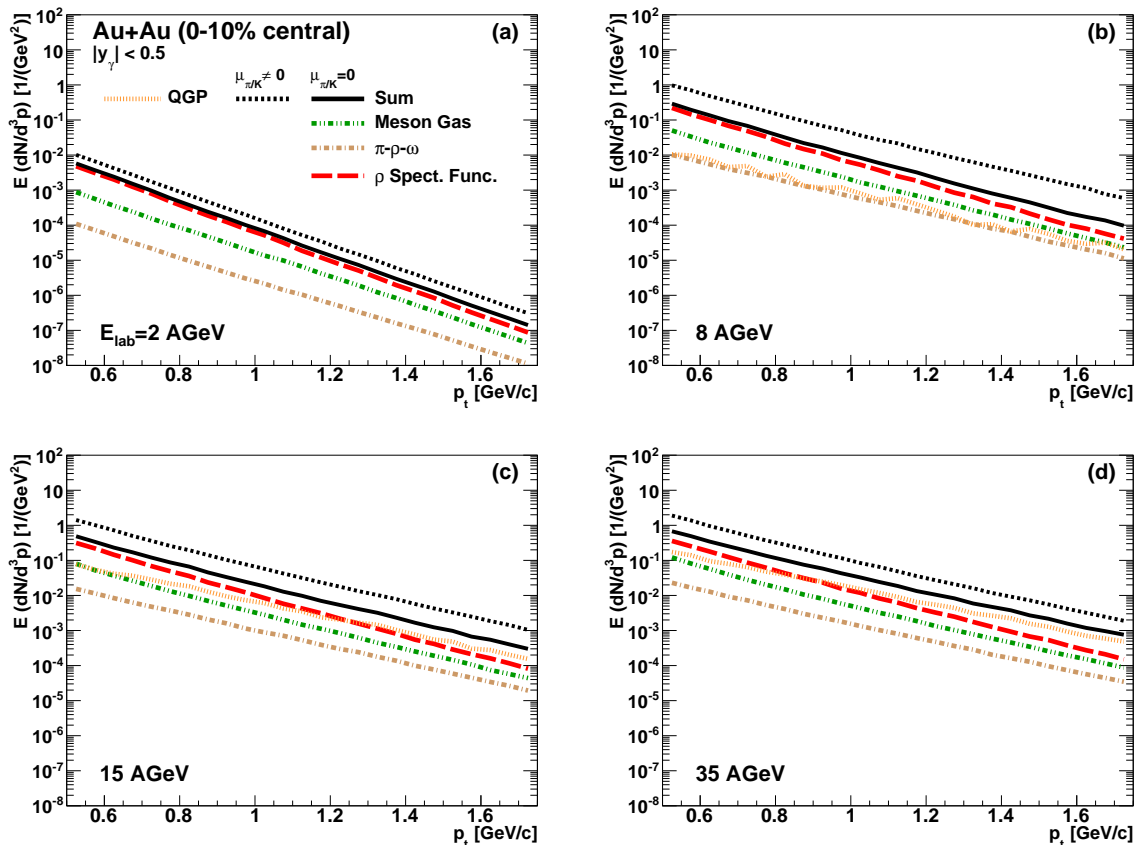


FIG. 9. (Color online) Transverse-momentum spectra at mid-rapidity ($|y_\gamma| < 0.5$) of the thermal photon yield for central Au+Au reactions at $E_{\text{lab}} = 2$ AGeV (a), 8 AGeV (b), 15 AGeV (c) and 35 AGeV (d). The total yields are plotted for both cases $\mu_\pi = 0$ (full black line) and $\mu_\pi \neq 0$ (dashed line). The single hadronic contributions from the ρ spectral function (red, long dashed), the meson gas (green, dashed-double-dotted) and the $\pi - \rho - \omega$ complex (beige, dashed-dotted) are only shown for vanishing pion chemical potential. The partonic contribution from the QGP is plotted as orange short-dashed line.

paring the results for the different energies: An overall increase of the photon p_t -yield with increasing energy and, secondly, a simultaneous hardening of the spectra, i.e., one gets a stronger relative contribution for higher momenta. This is similar to the dilepton invariant-mass spectra, where the yield in the higher mass region is suppressed for lower collision energies due to the lower overall temperatures in the fireball. (A more explicit comparison of the energy dependence of the results will be undertaken in Sec. IV D). Furthermore, one can see that at all energies the contribution from the ρ meson dominates above the other hadronic contributions especially for low p_t , while the relative dominance of the ρ decreases for higher momenta. The contribution from the Quark-Gluon Plasma is visible for $E_{\text{lab}} = 8$ AGeV and higher energies, giving an increasing fraction of the overall yield. Note the similarity between the low-mass dilepton and photon p_t spectra for 35 AGeV: In both cases the slope of the (virtual or real) photons emitted from the QGP

stage is significantly harder than the contribution from hadronic sources. Furthermore, looking only at the ρ and the partonic contribution, one finds that the first is stronger for $p_t < 1$ GeV/c, and the latter dominates for higher momenta - for both dileptons and photons. This behavior is expected as the real photon represents just the $M_{e^+e^-} \rightarrow 0$ limit of virtual photon production. This is another requirement of consistency for the thermal rates.

Although finite values of μ_π and μ_K have an even more pronounced effect on the photon rates than on the dilepton rates, as several processes to be considered are very sensitive to an overpopulation of pions, it is remarkable that the overall effect leaves the shape of the photon p_t spectra mostly unchanged: The yields are enhanced by the same factor at all transverse momenta. This is interesting as the effect of $\mu_{\pi/K} \neq 0$ on the different contributions is varying in strength. For example, the yield from the $\pi - \rho - \omega$ system shows a much stronger enhancement

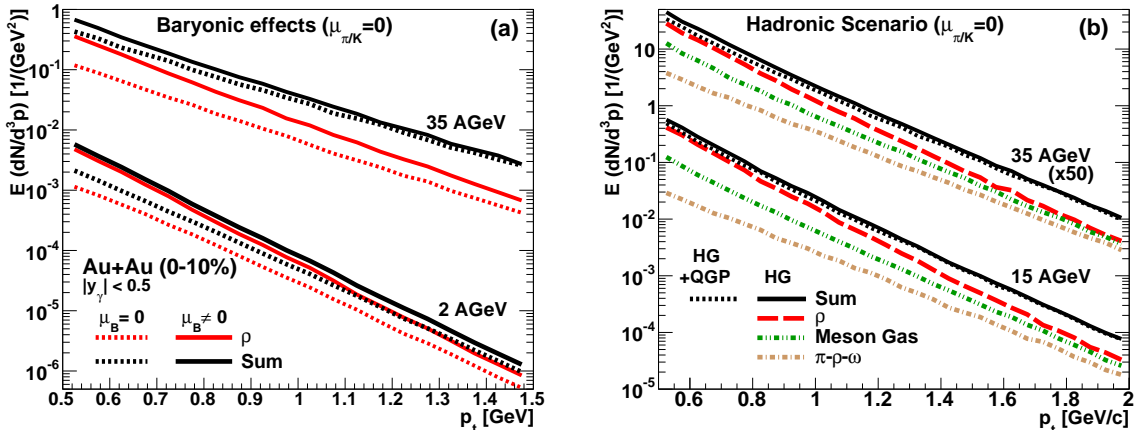


FIG. 10. (Color online) Comparison of the transverse-momentum spectra at mid-rapidity ($|y_\gamma| < 0.5$) of the thermal photon yield for central Au+Au reactions resulting from different emission scenarios. In (a) the effect of a finite baryon chemical potential μ_B on the transverse momentum spectrum for the ρ contribution and the total yield is shown for 2 AGeV (lower results) and 35 AGeV (upper results), comparing the standard scenario with $\mu_B \neq 0$ (full lines) with the results for $\mu_B = 0$ (dashed lines). Plot (b) shows the results for a purely hadronic scenario, i.e., for emission from the hadron gas also for $T > 170$ MeV and no partonic contribution. The single contributions are plotted as in Fig. 9; for comparison the total yield for the standard result including hadronic + partonic emission is shown (black dashed).

than the ρ contribution (compare Table I).

But not only meson chemical potentials influence the photon spectra, similar to the case of dileptons one expects also an enhancement of the ρ contribution in the presence of baryonic matter. In Fig. 10 (a) the effect of a finite baryon chemical potential μ_B on the transverse momentum spectrum for the ρ contribution and the total yield is shown for 2 AGeV and 35 AGeV, comparing the standard scenario with $\mu_B \neq 0$ (full lines) with the results for $\mu_B = 0$ (dashed lines). The comparison shows that especially at lower momenta the ρ contribution is significantly increased for finite baryochemical potential, while this effect is less dominant at larger p_t . Furthermore the effect is stronger for lower collision energies, where one obtains larger average values of μ_B . However, one should bear in mind that the parametrization for the photon emission rates is limited to chemical potentials below 400 MeV, so that one can not fully account for the very large chemical potentials in this case. In consequence, one can expect an even larger enhancement in the experimental measurements than in the present calculation.

To conclude the study of the different influences on the photon spectra, we also consider whether the possible creation of a deconfined phase has any effect on the thermal emission pattern. Plot (b) of Fig. 10 shows the results for a purely hadronic scenario, i.e., for emission from the hadron gas also for $T > 170$ MeV and no partonic contribution. For comparison also the total yield for the standard scenario including hadronic + partonic emission is shown. (For both cases the meson chemical potentials

are assumed to be zero.) Again, as for the high-mass dileptons (compare Fig. 5), the differences between the two scenarios are negligible, especially compared to the effect of the meson and baryochemical potentials. Only a very slight enhancement of the yield at low momenta is obtained for the pure hadron gas scenario, reflecting the different sensitivity of partonic and hadronic rates to finite μ_B .

D. Excitation function of photon and dilepton yields

In the previous sections several differences and similarities between dilepton and photon spectra have already been discussed. However, it is instructing to do this in more detail and to compare the energy dependence of the emission patterns for photons and dileptons. Considering experimental measurements, an advantage of studying the excitation function of thermal yields might be that the trends and results obtained hereby at different energies are more robust and less sensitive to errors of measurement. It reflects the results of several different measurements in contrast to single spectra at a specific energy. For reason of comparison and because the baryonic effects are strongest in this case, all results in the following will be considered for mid-rapidity $|y| < 0.5$.

In Fig. 11 the total thermal photon p_t and dilepton $M_{e^+e^-}$ spectra for eight different collision energies in the range $E_{\text{lab}} = 2-35$ AGeV are shown. It was already mentioned that—besides the hadronic structures due to the

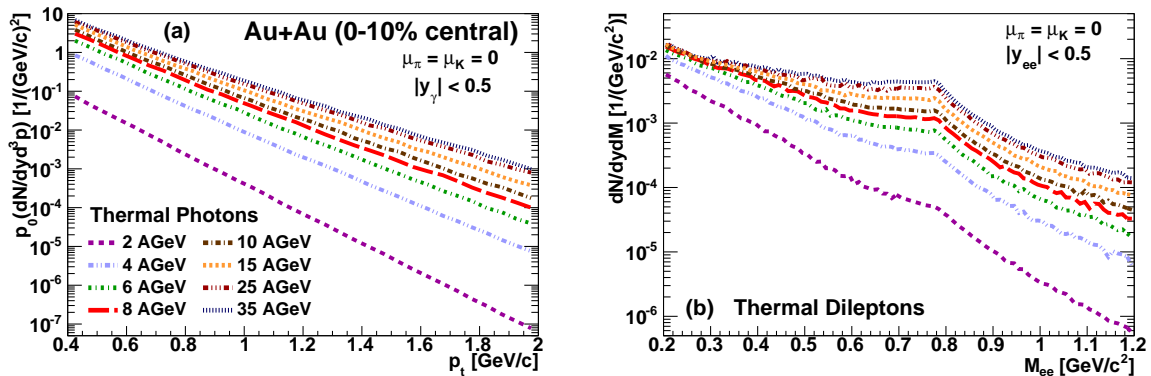


FIG. 11. (Color online) Comparison of the overall photon transverse momentum spectra (a) and the thermal dilepton invariant mass spectra (b) at mid-rapidity $|y| < 0.5$ for different energies in the range $E_{\text{lab}} = 2 - 35$ AGeV. The results are shown for vanishing meson chemical potentials $\mu_{\pi} = \mu_K = 0$.

direct connection of the dilepton spectrum with the spectral function of the light vector mesons—the two spectra are strikingly similar. And also the change of the spectra with increasing collision energy is alike. At high masses/momenta the yield shows a stronger increase with E_{lab} than in the low-mass/-momentum region. More quantitatively, this can be seen in Fig. 12 (a), where the relative increase of the thermal photon and dilepton yield for different transverse momentum or invariant mass regions, respectively, is shown. The results are normalized to 1 for $E_{\text{lab}} = 2$ AGeV. One observes that the relative increase is stronger for high momenta and masses than for the lower p_t or $M_{e^+e^-}$ bins. For example, the total dilepton yield for masses below $300 \text{ MeV}/c^2$ increases only by a factor of 2 from $E_{\text{lab}} = 2$ to 8 AGeV and remains nearly constant thereafter, whereas in the high mass region above $1 \text{ GeV}/c^2$ the yield increases by a factor 300 when going to the top SIS 300 energy of 35 AGeV. A similar behavior is found for the photons, where the yield shows a more pronounced rise at high momenta. As was pointed out already before, one reason for this is the fact that much energy is needed to produce a dilepton at high masses or a photon with high momentum. Their production is strongly suppressed at the rather moderate temperatures obtained at lower collision energies. Note that in general the overall increase in the photon spectra is slightly stronger than for the dilepton production. This might be due to the limitation of the photon parametrization to temperatures above 100 MeV and baryochemical potentials below 400 MeV, which might somewhat underestimate the photon yield at the lowest collision energies. Besides, one should keep in mind that in detail the processes contributing to the thermal emission rates for dileptons and photons differ, which may also explain some differences between the results.

In contrast, we find that the fraction of the QGP yield compared to the total thermal emission is larger for the high- $M_{e^+e^-}$ dileptons compared to the high- p_t pho-

tons. The first significant QGP contribution is found for $E_{\text{lab}} = 8$ AGeV, and the fraction continuously increases up to roughly 70% at 35 AGeV for dilepton masses above $1 \text{ GeV}/c^2$ and 50% for photon momenta over $1 \text{ GeV}/c$. At lower masses or momenta, respectively, the hadronic contribution becomes more dominant. This is not surprising, as one could already conclude that we probe lower temperatures at lower masses and momenta (compare Fig. 7). Furthermore the baryonic influence increases here. In the dilepton spectra the direct connection to the vector meson spectral functions makes a comparison between the photon and dilepton results for low momenta and masses difficult.

Finally, we consider also the thermal photon yield in relation to the number of (neutral) pions which are produced in the heavy-ion collision, as presented in Fig. 13. This ratio is of theoretical and experimental interest: For the experimental study of photons, decays of neutral pions are the major background in the analysis. On the theoretical side, the number of pions gives an estimate of the freeze-out volume and is not sensitive to the details of the reaction evolution. While the electromagnetic emission takes place over the whole lifetime of the fireball and therefore reflects the evolution of the system in the phase diagram, the pion yield allows to scale out trivial dependences. Previously, the thermal dilepton yield was found to scale with $N_{\pi}^{4/3}$ if one compares different system sizes at SIS 18 energies [28]. However, the situation is more complex here as we consider a large range of energies, which will be covered by FAIR. Several effects play a role, e.g., the lifetime of the fireball, the temperatures and baryochemical potentials which are reached and the different processes which contribute at different temperatures. While in our study at SIS 18 energies only the system size was modified (and all the other parameters could be assumed to remain quite constant, as one single energy was considered), in the present study *only* the size of the colliding nuclei is constant.

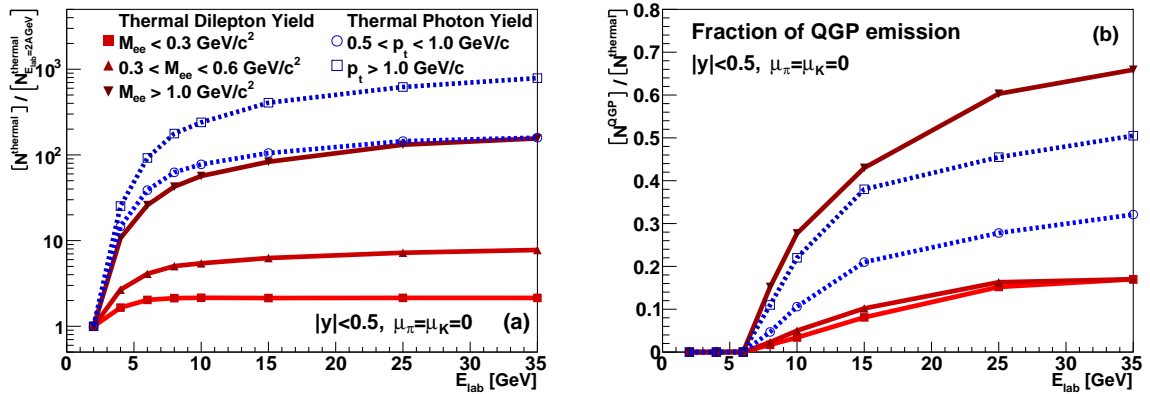


FIG. 12. (Color online) (a) Energy dependence of the thermal photon and dilepton yield in different invariant mass or transverse momentum bins, respectively. The yields are normalized to the result at $E_{\text{lab}} = 2 \text{ AGeV}$. (b) Fraction of thermal QGP emission in relation to the total thermal yield of photons or dileptons in different $M_{e^+e^-}$ and photon- p_t bins. All results in this figure are shown for mid-rapidity and vanishing meson chemical potentials.

The investigation of the N_γ/N_{π^0} ratio is here combined with a comparison of the different scenarios for the conditions of thermal emission, which were already studied in case of the photon and dilepton spectra (see Figs. 5 and 9). Varying E_{lab} (and, in consequence, T and μ_B) might result in distinct excitation functions of the ratio N_γ/N_{π^0} for the various scenarios, in contrast to the spectra for one specific energy where no unambiguous distinction was possible. In Fig. 13, one can see a strong increase of the photon to pion ratio for the lowest energies for both the lower p_t range from 0.5 to 1 GeV/c and the high transverse momentum region above 1 GeV/c in case of the baseline scenario with QGP emission for $T > 170 \text{ MeV}$ and $\mu_\pi = 0$. However, for higher collision energies above 10 AGeV we still observe a further increasing ratio for the higher momentum range, whereas at low p_t the ratio remains relatively constant and even decreases for the highest collision energy. One can understand the decreasing ratio for lower p_t reviewing again the energy dependence of T and μ_B as shown in Fig. 1. The rise of temperature becomes less intensive for higher collision energies, while the baryochemical potential decreases for higher collision energies, causing a less pronounced increase of the thermal yield (compare also Fig. 12). Besides, the effects due to finite μ_B are more pronounced at low momenta, explaining the different trends for the two p_t regions. Including the finite meson chemical potentials, we observe a strong increase of the ratio by factors 2-5 at all collision energies. The strongest effect in the present calculation is seen around 8 AGeV, so that a slight peak structure builds up. However, as mentioned already several times, this scenario can only be seen as an upper limit for the non-equilibrium effects, most probably the increase will be smaller.

When comparing the two scenarios including enhanced QGP emission around T_c on the one side and a pure

hadronic scenario on the other side it is interesting that both cases lead to a similar result, namely an increase of the N_γ/N_{π^0} ratio at higher collision energies. The effects show up more dominantly at high momenta, as this region is more sensitive with regard to emission from high temperatures. Note, however, that there are also significant differences between the two cases. The scenario with enhanced QGP emission around T_c shows the most prominent increase at $E_{\text{lab}} = 8 - 10 \text{ AGeV}$ whereas this enhancement becomes smaller again for higher energies. This can be explained by the fact that the relative fraction of emission from temperatures around 170-175 MeV is largest at those collision energies where the transition to a partonic phase is just reached. At higher E_{lab} the corresponding higher temperatures may outshine any effects from the transition region. On the contrary, the enhancement over the baseline scenario increases with energy for the case of a pure hadron gas. However, for highest collision energies the difference seems to remain stable or even to drop again.

We remind again that for the experimental measurement the ratio of thermal photons from Fig. 13 is of importance, as almost all of the π^0 mesons decay into a photon. Therefore the vast majority will be decay photons, not stemming from direct (thermal or prompt) emission processes. Their spectra have to be subtracted in experiment to draw conclusions about the direct photons from thermal sources. This might be relatively difficult for the lowest energies available at FAIR, as here the ratio is suppressed by up to an order of magnitude compared to the higher collision energies.

V. DISCRIMINATING DIFFERENT SCENARIOS

It has so far become clear that one can extract only limited information regarding the properties of the hot and dense fireball from single photon and dilepton spectra, as there are usually several different effects that might interfere and finally lead to the same invariant-mass or transverse-momentum yields. However, the picture might be quite different if—in addition—the results in distinct mass or momentum regions, respectively, are systematically compared for several collision energies. In this case one might be able to discriminate the hadronic and partonic effects from each other. The FAIR energy regime will be ideally suited for such a study, as the transition from pure hadronic fireballs to the creation of a deconfined phase will take place somewhere around $E_{\text{lab}} = 6 - 8 \text{ AGeV}$, as our results suggest. Nevertheless, there is no single observable that seems to allow for unambiguous conclusions on the details of the reaction evolution. On the contrary, it will still be necessary

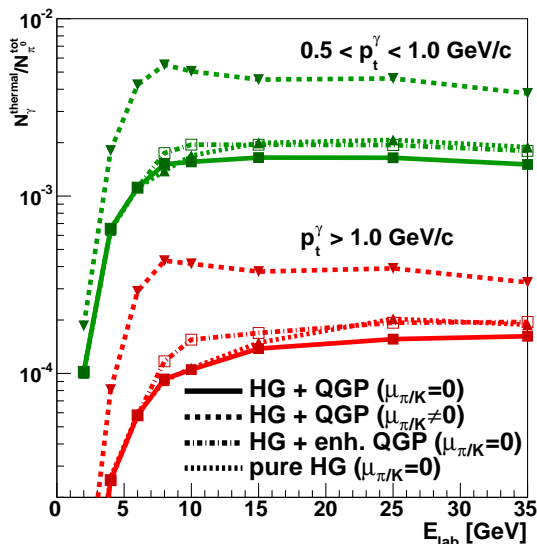


FIG. 13. (Color online) Energy dependence for the ratio of thermal photon yield $N_{\gamma}^{\text{thermal}}$ at mid-rapidity ($|y| < 0.5$) to the overall number of neutral pions N_{π^0} . The results are shown for two different regions of the photon transverse momenta, $0.5 < p_t < 1.0 \text{ GeV}/c$ (green) and $p_t > 1.0 \text{ GeV}/c$ (red). The baseline calculation assumes hadronic emission up to 170 MeV with vanishing $\mu_{\pi/K}$ and partonic emission for higher temperatures (full line). In addition, the results with a five times enhanced emission around the critical temperature (dashed-dotted line), for a pure hadron gas scenario with emission at all temperatures from hadronic sources (short dashed line) and including meson chemical potentials (dashed line) are shown.

to carefully compare theoretical calculations and experimental results.

Based on the findings of the present work, one may consider the following scheme which might help to determine the strength of the different effects on the thermal rates and discriminate between the contributions:

1. The influence of baryonic matter leads to an enhancement which is most dominant for low transverse momenta and low masses. In general, it steepens the p_t slope of the overall yield. A large advantage is that today the spectral function of the ρ meson is quite well known from previous experimental and theoretical studies. Detailed and precise photon (dilepton) measurements for low momenta (low masses) in the FAIR and RHIC-BES energy regime might give further constraints for the spectral function in the region of extremely high baryon densities and can, vice versa, help to see whether the models correctly describe the fireball evolution in terms of μ_B .
2. In contrast to the baryonic effects on the emission rates, non-equilibrium effects caused by finite pion (and kaon) chemical potentials will show up as enhancement in the dilepton and photon spectra at all masses and momenta, and will be visible at all collision energies. The effect should be slightly more dominant in the high invariant mass or high p_t region, as here the multi-meson contributions become more pronounced. Ideally, one can discriminate between the μ_B - and μ_{π} -driven effects by comparing the modification of the slope and the overall enhancement in relation to baseline calculations.
3. If the baryon and non-equilibrium effects are under control, one might be able to find signals from the partonic phase in the dilepton and photon spectra for high p_t and $M_{e^+e^-}$. In general, the dilepton and photon rates do not differ much from each other around T_c , but effects such as a critical slowdown of the evolution might lead to an increased yield from the Quark-Gluon Plasma. On the other hand the “duality mismatch” might lead to a relative decrease of the yield, as hadronic rates are sensitive to finite baryon and meson chemical potentials while the QGP rates show hardly any modification. However, any effects connected to a phase transition can only show up if the obtained temperatures are large enough. Consequently, we would observe subsequent modifications of the spectra only for energies larger than $E_{\text{lab}} = 6 - 8 \text{ AGeV}$, in contrast to non-equilibrium and baryonic effects which also appear at lower temperatures. Significant differences from calculations which *only* show up for the higher energies might then indicate the creation of a deconfined phase.
4. Furthermore, these effects should be dominant in the regions which are most sensitive to QGP forma-

tion: The region for $M_{e^+e^-} > 1$ GeV in the dilepton spectra, and for high- p_t in the photon respectively low-mass dilepton spectra (provided, it is possible to get control over the hadronic decay background). Another advantage in these regions is that they are relatively insensitive to the finite baryon chemical potential.

The different issues are not easy to disentangle and several interdependencies exist. Another aspect, which is not explicitly considered in our work but might further complicate the situation, is the influence of different EoS on the thermal yields. In the present work we use a Hadron-Gas EoS to provide consistency with the underlying microscopic model. However, previous investigations in a transport + hydrodynamics hybrid model showed that an MIT Bag Model EoS or a chiral EoS lead to different evolutions in the hydrodynamic phase compared to the HG-EoS, resulting in higher temperatures and, consequently, an increase of the emission rates.

VI. CONCLUSIONS & OUTLOOK

We have presented photon and dilepton spectra for the collision energy range $E_{\text{lab}} = 2 - 35$ AGeV, which will be covered by the future FAIR facility (and, in parts, by phase II of the BES at RHIC). The calculations were performed using a coarse-graining approach with transport simulations from the UrQMD model as input. In this approach local particle and energy densities are extracted from an ensemble average of the microscopic transport calculations, and an equation of state is used to calculate the corresponding values for temperature and chemical potential. The local thermodynamic properties are then used to determine the thermal emission rates.

The resulting spectra show a strong influence of finite baryochemical potentials and an enhancement due to non-equilibrium effects caused by finite meson chem-

ical potentials. Regarding the search for signals of the deconfinement phase transition, there is no clear signal from which the creation of a partonic phase can be unambiguously inferred. Similarly, the results suggest that it is also hard to identify the type of the transition, whether it is a cross-over or a first-order phase transition, as effects due to a critical slowing down might be small compared to other influences on the spectra. The main difficulty is the dual connection between hadronic and partonic emission rates in the transition region around the critical temperature T_c , resulting in very similar slopes in the invariant-mass and transverse-momentum spectra.

For a clarification of the open issues, experimental input is needed. Our results suggest that one needs very precise and detailed measurements, as different evolution scenarios for the nuclear collisions are modifying the dilepton and photon spectra in a quite subtle manner. Systematic studies of several collision energies in the future FAIR energy range from $E_{\text{lab}} = 2$ AGeV to 35 AGeV are required to get more insights into the structure of the phase diagram of QCD matter and especially to find clues for the creation of a deconfined phase. Besides the experimental efforts, it will be similarly important to intensify the theoretical studies.

ACKNOWLEDGMENTS

The authors especially thank Ralf Rapp for providing the parametrizations of the spectral functions and many fruitful discussions. This work was supported by the Hessian Initiative for Excellence (LOEWE) through the Helmholtz International Center for FAIR (HIC for FAIR), the Bundesministerium für Bildung und Forschung, Germany (BMBF) and the Helmholtz-Gemeinschaft through the Research School for Quark-Matter Studies (H-QM).

-
- [1] H. Stöcker and W. Greiner, *Phys. Rept.* **137**, 277 (1986).
 - [2] P. Danielewicz, R. Lacey, and W. G. Lynch, *Science* **298**, 1592 (2002).
 - [3] J. D. Bjorken, *Phys. Rev. D* **27**, 140 (1983).
 - [4] R. Stock, in H. Schopper (ed.), *Physics and Methods - Theory and Experiments*, vol. 21A of *Landolt-Börnstein - Group I Elementary Particles, Nuclei and Atoms* (Springer, Berlin, 2010).
 - [5] E. L. Feinberg, *Nuovo Cim. A* **34**, 391 (1976).
 - [6] E. V. Shuryak, *Phys. Lett. B* **78**, 150 (1978).
 - [7] D. Adamova et al. (CERES/NA45), *Phys. Rev. Lett.* **91**, 042301 (2003).
 - [8] M. M. Aggarwal et al. (WA98 Collaboration), *Phys. Rev. Lett.* **85**, 3595 (2000).
 - [9] R. Arnaldi et al. (NA60 Collaboration), *Phys. Rev. Lett.* **96**, 162302 (2006).
 - [10] L. Adamczyk et al. (STAR Collaboration), *Phys. Rev. Lett.* **113**, 022301 (2014), [Addendum: *Phys. Rev. Lett.* **113**, 049903 (2014)].
 - [11] S. S. Adler et al. (PHENIX Collaboration), *Phys. Rev. Lett.* **94**, 232301 (2005).
 - [12] A. Adare et al. (PHENIX Collaboration), *Phys. Rev. Lett.* **104**, 132301 (2010).
 - [13] A. Adare et al. (PHENIX), *Phys. Rev. C* **93**, 014904 (2016).
 - [14] M. K. Koehler (ALICE), *Nucl. Phys. A* **931**, 665 (2014).
 - [15] R. Porter et al. (DLS Collaboration), *Phys. Rev. Lett.* **79**, 1229 (1997).
 - [16] G. Agakichiev et al. (HADES Collaboration), *Phys. Rev. Lett.* **98**, 052302 (2007).
 - [17] G. Agakishiev et al. (HADES Collaboration), *Phys. Lett. B* **663**, 43 (2008).
 - [18] G. Agakishiev et al. (HADES Collaboration), *Phys. Rev. C* **84**, 014902 (2011).

- [19] B. Bauchle and M. Bleicher, Phys. Rev. C **82**, 064901 (2010).
- [20] H. van Hees, M. He, and R. Rapp, Nucl. Phys. A **933**, 256 (2015).
- [21] O. Linnyk, V. Konchakovski, T. Steinert, W. Cassing, and E. L. Bratkovskaya, Phys. Rev. C **92**, 054914 (2015).
- [22] S. Turbide, R. Rapp, and C. Gale, Phys. Rev. C **69**, 014903 (2004).
- [23] W. Liu and R. Rapp, Nucl. Phys. A **796**, 101 (2007).
- [24] N. P. M. Holt, P. M. Hohler, and R. Rapp, Nucl. Phys. A **945**, 1 (2015).
- [25] R. Rapp and J. Wambach, Adv. Nucl. Phys. **25**, 1 (2000).
- [26] R. Rapp, Adv. High Energy Phys. **2013**, 148253 (2013).
- [27] S. Endres, H. van Hees, J. Weil, and M. Bleicher, Phys. Rev. C **91**, 054911 (2015).
- [28] S. Endres, H. van Hees, J. Weil, and M. Bleicher, Phys. Rev. C **92**, 014911 (2015).
- [29] B. Friman, C. Hohne, J. Knoll, S. Leupold, J. Randrup, et al., Lect. Notes Phys. **814**, 1 (2011).
- [30] P. Senger, JPS Conf. Proc. **8**, 022001 (2015).
- [31] G. Odyniec, EPJ Web Conf. **95**, 03027 (2015).
- [32] A. N. Sissakian and A. S. Sorin (NICA Collaboration), J. Phys. G **36**, 064069 (2009).
- [33] C. S. Fischer, J. Luecker, and J. A. Mueller, Phys. Lett. **B702**, 438 (2011).
- [34] W. Cassing and E. L. Bratkovskaya, Phys. Rept. **308**, 65 (1999).
- [35] K. Schmidt, E. Santini, S. Vogel, C. Sturm, M. Bleicher, et al., Phys. Rev. C **79**, 064908 (2009).
- [36] J. Weil, H. van Hees, and U. Mosel, Eur. Phys. J. A **48**, 111 (2012).
- [37] L. P. Kadanoff and G. Baym, *Quantum Statistical Mechanics: Green's Function Methods in Equilibrium and Non-Equilibrium Problems* (W.A. Benjamin, New York, 1962).
- [38] E. L. Bratkovskaya, W. Cassing, R. Rapp, and J. Wambach, Nucl. Phys. A **634**, 168 (1998).
- [39] E. Bratkovskaya, W. Cassing, and O. Linnyk, Phys. Lett. B **670**, 428 (2009).
- [40] E. Bratkovskaya, J. Aichelin, M. Thomere, S. Vogel, and M. Bleicher, Phys. Rev. C **87**, 064907 (2013).
- [41] B. Schenke and C. Greiner, Phys. Rev. C **73**, 034909 (2006).
- [42] B. Schenke and C. Greiner, Phys. Rev. Lett. **98**, 022301 (2007).
- [43] J. Weil, U. Mosel, and V. Metag, Phys. Lett. B **723**, 120 (2013).
- [44] J. Berges, K. Boguslavski, S. Schlichting, and R. Venugopalan, Phys. Rev. D **92**, 096006 (2015).
- [45] H. van Hees and R. Rapp, Phys. Rev. Lett. **97**, 102301 (2006).
- [46] G. Vujanovic, C. Young, B. Schenke, R. Rapp, S. Jeon, et al., Phys. Rev. C **89**, 034904 (2014).
- [47] P. Huovinen, M. Belkacem, P. J. Ellis, and J. I. Kapusta, Phys. Rev. C **66**, 014903 (2002).
- [48] J. Steinheimer, M. Lorenz, F. Becattini, R. Stock, and M. Bleicher (2016), arXiv: 1603.02051 [nucl-th].
- [49] S. A. Bass, M. Belkacem, M. Bleicher, M. Brandstetter, L. Bravina, et al., Prog. Part. Nucl. Phys. **41**, 255 (1998).
- [50] M. Bleicher, E. Zabrodin, C. Spieles, S. A. Bass, C. Ernst, et al., J. Phys. G **25**, 1859 (1999).
- [51] H. Petersen, M. Bleicher, S. A. Bass, and H. Stocker (2008), arXiv: 0805.0567 [hep-ph].
- [52] A. R. Bodmer and C. N. Panos, Phys. Rev. C **15**, 1342 (1977).
- [53] J. J. Molitoris, J. B. Hoffer, H. Kruse, and H. Stoecker, Phys. Rev. Lett. **53**, 899 (1984).
- [54] J. Aichelin, Phys. Rept. **202**, 233 (1991).
- [55] C. Eckart, Phys. Rev. **58**, 919 (1940).
- [56] L. Bravina, E. Zabrodin, M. I. Gorenstein, S. Bass, M. Belkacem, et al., Nucl. Phys. A **661**, 600 (1999).
- [57] W. Florkowski and R. Ryblewski, Phys. Rev. C **83**, 034907 (2011).
- [58] W. Florkowski, M. Martinez, R. Ryblewski, and M. Strickland, Nucl. Phys. A **904-905**, 803c (2013).
- [59] D. Bandyopadhyay, M. Gorenstein, H. Stocker, W. Greiner, and H. Sorge, Z. Phys. C **58**, 461 (1993).
- [60] P. Koch, Phys. Lett. B **288**, 187 (1992).
- [61] J. Sollfrank, P. Koch, and U. W. Heinz, Z. Phys. C **52**, 593 (1991).
- [62] D. Zschesche, S. Schramm, J. Schaffner-Bielich, H. Stocker, and W. Greiner, Phys. Lett. B **547**, 7 (2002).
- [63] M. He, R. J. Fries, and R. Rapp, Phys. Rev. C **85**, 044911 (2012).
- [64] S. Leupold, V. Metag, and U. Mosel, Int. J. Mod. Phys. E **19**, 147 (2010).
- [65] J. J. Sakurai, *Currents and Mesons* (University of Chicago Press, Chicago, 1969).
- [66] F. Klingl, N. Kaiser, and W. Weise, Nucl. Phys. A **624**, 527 (1997).
- [67] M. Post, S. Leupold, and U. Mosel, Nucl. Phys. A **689**, 753 (2001).
- [68] D. Cabrera, E. Oset, and M. J. Vicente Vacas, Nucl. Phys. A **705**, 90 (2002).
- [69] F. Riek and J. Knoll, Nucl. Phys. A **740**, 287 (2004).
- [70] J. Ruppert and T. Renk, Phys. Rev. C **71**, 064903 (2005).
- [71] R. Rapp, G. Chanfray, and J. Wambach, Nucl. Phys. A **617**, 472 (1997).
- [72] R. Rapp and C. Gale, Phys. Rev. C **60**, 024903 (1999).
- [73] R. Rapp and J. Wambach, Eur. Phys. J. A **6**, 415 (1999).
- [74] H. van Hees and R. Rapp, Nucl. Phys. A **806**, 339 (2008).
- [75] H. van Hees, C. Gale, and R. Rapp, Phys. Rev. C **84**, 054906 (2011).
- [76] R. Rapp, J. Wambach, and H. van Hees, in R. Stock (ed.), *Relativistic Heavy Ion Physics*, vol. 23 of *Landolt-Bornstein - Group I Elementary Particles, Nuclei and Atoms*, 134–175 (Springer, Berlin, 2010).
- [77] R. Rapp, Phys. Rev. C **63**, 054907 (2001).
- [78] M. Heffernan, P. Hohler, and R. Rapp, Phys. Rev. C **91**, 027902 (2015).
- [79] R. Rapp (2014), private communication.
- [80] J. I. Kapusta, P. Lichard, and D. Seibert, Phys. Rev. **44**, 2774 (1991), [Erratum: Phys. Rev. D **47**, 4171 (1993)].
- [81] P. Aurenche, F. Gelis, R. Kobes, and H. Zaraket, Phys. Rev. D **58**, 085003 (1998).
- [82] P. Aurenche, F. Gelis, and H. Zaraket, Phys. Rev. D **61**, 116001 (2000).
- [83] P. B. Arnold, G. D. Moore, and L. G. Yaffe, JHEP **12**, 009 (2001).
- [84] J. Cleymans, J. Fingberg, and K. Redlich, Phys. Rev. D **35**, 2153 (1987).
- [85] E. Braaten, R. D. Pisarski, and T.-C. Yuan, Phys. Rev. Lett. **64**, 2242 (1990).
- [86] H.-T. Ding, A. Francis, O. Kaczmarek, F. Karsch, E. Laermann, et al., Phys. Rev. D **83**, 034504 (2011).

Energy, centrality and momentum dependence of dielectron production at collider energies in a coarse-grained transport approach

Stephan Endres,* Hendrik van Hees, and Marcus Bleicher

*Frankfurt Institute for Advanced Studies, Ruth-Moufang-Straße 1, D-60438 Frankfurt, Germany and
Institut für Theoretische Physik, Universität Frankfurt,
Max-von-Laue-Straße 1, D-60438 Frankfurt, Germany*

(Dated: June 23, 2016)

Dilepton production in heavy-ion collisions at collider energies—i.e., for the Relativistic Heavy-Ion Collider (RHIC) and the Large Hadron Collider (LHC)—is studied within an approach that uses coarse-grained transport simulations to calculate thermal dilepton emission applying in-medium spectral functions from hadronic many-body theory and partonic production rates based on lattice calculations. The microscopic output from the Ultra-relativistic Quantum Molecular Dynamics (UrQMD) model is hereby put on a grid of space-time cells which allows to extract the local temperature and chemical potential in each cell via an equation of state. The resulting dilepton spectra are in good agreement with the experimental results for the range of RHIC energies, $\sqrt{s_{NN}} = 19.6 - 200$ GeV. The comparison of data and model outcome shows that the newest measurements by the PHENIX and STAR Collaborations are consistent and that the low-mass spectra can be described by a cocktail of hadronic decay contributions together with thermal emission from broadened vector-meson spectral functions and from the Quark-Gluon Plasma phase. Predictions for dilepton results at LHC energies show no significant change of the spectra as compared to RHIC, but a higher fraction of thermal contribution and harder slopes of the transverse momentum distributions due to the higher temperatures and flow obtained.

PACS numbers: 25.75.Cj, 24.10.Lx

Keywords: Dilepton production, Monte Carlo simulations

I. INTRODUCTION

A better understanding of the phase structure of strongly interacting matter given by the fundamental theory of Quantum Chromodynamics (QCD) is one of the main goals of heavy-ion experiments at ultra-relativistic energies [1–5]. The collision of two nuclei produces a fireball of hot and dense matter, which typically lives for a time span of several fm/c until the system has cooled, due to collective expansion, to a point where the single particles do not further interact (freeze-out) [6]. The trajectory of the system within the QCD phase diagram is determined by the collision energy: While for lab-frame energies of few GeV one obtains rather low temperatures but finds high values of baryochemical potential, the situation becomes different when going to much higher collision energies; here the temperature increases while the baryochemical potential decreases.

As hadronic observables usually only reflect the properties of the system at the moment of freeze-out, electromagnetic probes are the appropriate tool to obtain information from the earlier stages of the reaction, when the system is at high temperatures and/or net-baryon densities [7, 8]. Since photons and dileptons do not interact strongly, they leave the fireball undisturbed once they are produced. However, in consequence the measurement of electromagnetic probes only gives a time integral over the various stages and sources during the evolution of

the reaction. From the theoretical viewpoint the understanding of the production of electromagnetic probes in a heavy-ion collision is complicated by the fact that the evolving fireball of hot and dense matter is not a static but a highly dynamical non-equilibrium system. However, no fully self-consistent approach to describe the in-medium dilepton production for the out-of-equilibrium case is available today. Consequently one has to apply model descriptions, which always means a reduction of the complexity of the problem to a level where it can be solved.

While hydrodynamic [9, 10] and fireball models [11, 12] are in general successful in describing the measured dilepton spectra by the STAR [13–15] and PHENIX [16] collaborations at RHIC, these models completely rely on a macroscopic description of the fireball. The application of thermal emission rates is usually straightforward in these models, but they require external assumptions such as an initial state and an additional description for the final-state interactions. Besides, their application at lower temperatures and densities is questionable. On the other hand, a full microscopic description of the electromagnetic emission—as it is realized in transport models [17–21] based on kinetic theory—is theoretically challenging, especially at very high collision energies. On the one hand, a fully coherent implementation of the different interfering processes and a correct off-shell treatment of the particles has not yet been obtained; on the other hand, it is also still unknown how the microscopic transition from the hadronic to the partonic phase (and vice versa) is actually realized in QCD. Nevertheless there exist several approaches which aim for such an advanced microscopic

* endres@th.physik.uni-frankfurt.de

description including off-shell and medium effects [22–28].

The coarse-graining approach, which is used in the present work for the theoretical calculation of dilepton production, is based on the concepts presented in Ref. [29] and has been successfully applied to describe spectra of electromagnetic probes at SIS 18, FAIR and SPS energies [30–33]. It offers a compromise between the microscopic and macroscopic description of the collision evolution. On the one hand the dynamics is here based on a purely microscopic description from the Ultrarelativistic Quantum Molecular dynamics (UrQMD) model [34, 35], on the other hand the “coarse-graining” (i.e., the reduction of the large amount of information regarding the phase-space coordinates of the single hadrons)—performed by averaging over a large ensemble events and extracting the local thermodynamic properties of the system—allows to describe the reaction dynamics in macroscopic terms of temperature and chemical potential. However, it has the advantage that it is in principle applicable to all phases of a heavy-ion collision and also works for lower collision energies where the use of other macroscopic models is questionable.

For the present paper previous studies are extended to energies available at the Relativistic Heavy-Ion Collider (RHIC) and the Large Hadron Collider (LHC), which covers the range of center-of-momentum energies from $\sqrt{s_{NN}} = 19.6$ GeV up to 5500 GeV. In this energy regime the net-baryon density is assumed to be close to zero for the greatest part of the fireball evolution, and a significant amount of the electromagnetic emission will stem from the Quark-Gluon Plasma (QGP). The specific conditions found at these collision energies offer the possibility to study—among others—the following issues:

- The experimental dilepton measurements will show whether the hadronic spectral functions, which have proven to successfully describe the low-mass dilepton excess, are also consistent with the conditions found in heavy-ion collisions at collider energies, where the baryochemical potential is significantly lower than the temperature for the greatest part of the reaction evolution. Previous work has shown that the in-medium effects on the spectral properties of baryon resonances should still play an important role since the modification of vector mesons is governed by the *sum* of the baryon and anti-baryon densities, not the net density [11].
- At higher invariant masses ($M_{e^+e^-} > 1 \text{ GeV}/c^2$) correlated open-charm decays give a significant contribution to the measured dilepton yield for RHIC and LHC energies [36]. Similar to the light vector mesons, whose spectral shape is modified in the medium, the charm contribution is known to be affected by the presence of a hot and dense medium [37–39]. However, it is unclear how strong these effects are. A direct measurement is difficult, as one also finds a strong thermal contribution from the

QGP in that mass region. It is therefore an important theoretical task to disentangle the different contributions and to provide a comprehensive description of the measured dilepton spectra. Although we do not consider charm contributions in the present study, the thermal results for the QGP contribution may serve as a baseline and help to limit the possible medium modifications for D and \bar{D} mesons.

- Due to the very high temperatures reached at the collider energies considered here, the partonic contribution to the overall dilepton yield will be much more dominant than at lower energies. This might facilitate to study the properties of the Quark-Gluon Plasma, e.g., its temperature [11, 40].
- Further, it will be interesting whether the reaction dynamics of the colliding system shows deviations as compared to the situation at lower energies. Large parts of the evolution are dominated by the Quark-Gluon Plasma, in contrast to the situation at SPS or even SIS 18 and FAIR. Experimental results for RHIC exhibited an unexpected large flow for direct photons, which is not fully explained by theory up to now [41, 42]. With regard to the coarse-graining approach it will be especially interesting to see in how far the underlying microscopic dynamics, which is completely hadronic, can account for the correct expansion of the system and the time-evolution of temperature and chemical potential.

The last aspect also points out a caveat. Whereas the creation of a deconfined phase with free quarks and gluons is assumed to take place in the early stages of heavy-ion collisions at RHIC and LHC energies, the microscopic dynamics from UrQMD does not include a description of this partonic phase. Nevertheless, we will argue that it is possible to extract a reasonable and realistic picture of the fireball evolution and thermal electromagnetic emission also at RHIC and LHC energies, including a description of emission from a QGP phase. While a lattice EoS and partonic rates can be applied to approximate the thermodynamic properties and emission patterns inside a partonic phase, it is on the other hand clear that the fireball evolution itself from the coarse-grained dynamics can not reflect any effects due to the creation of a Quark-Gluon Plasma on the microscopic level. Although it is assumed that the influences of a phase-transition or crossover on the gross microscopic evolution are not very significant, this is of course a limiting factor of the present model. Nevertheless, the results might help to understand if and how the phase structure of QCD is reflected in the microscopic dynamics, if the comparison of the model outcome to experimental data shows significant deviations.

This paper is structured as follows. In Sec. II the coarse-graining approach is introduced, and the various

dilepton-production mechanisms, which enter the calculations, are outlined. This is followed by a presentation of the results for the space-time evolution of the reaction (Sec. III A) and dilepton spectra for RHIC and LHC energies (in III B and III C). A comparison of the results for RHIC and LHC is given in Sec. III D. Finally, we conclude with a summary and an outlook to further studies in Sec. IV.

II. THE COARSE-GRAINING APPROACH

In the following, the basic features of the coarse-graining approach are outlined. This description is kept concise here, as the same model was in detail presented previously; for details we refer the reader to references [30, 31].

A. Microscopic simulations

As a first step, simulations for the different collision energies are conducted with the present version 3.4 of the Ultra-relativistic Quantum Molecular Dynamics (UrQMD) approach [34, 35, 43, 44], a semi-classical hadronic transport model based on the principles of kinetic theory, in which the evolution of a heavy-ion collision is described by the propagation of on-shell particles on classical trajectories in combination with a probabilistic treatment of the individual hadron-hadron scatterings. It constitutes an effective solution of the Boltzmann equation, where the collision term includes elastic and inelastic scatterings as well as resonance decays. To account for quantum effects, the particles are represented by Gaussian wave packets and effects such as Pauli blocking are included. For hadron-hadron collisions with energies above $\sqrt{s} = 3$ GeV the excitation of strings is possible. The model includes all relevant meson and baryon resonances up to a mass of $2.2 \text{ GeV}/c^2$. Resonance parameters and cross-sections are adapted and extrapolated to the values collected by the Particle Data Group [45].

For being able to deduce a realistic fireball evolution in terms of T and μ_B and—in consequence—meaningful dilepton spectra from the UrQMD simulation, one first has to check whether the model can describe the bulk results measured in experiment. In general, the UrQMD model has proven to describe the hadronic observables from heavy-ion reactions very well in a wide range of collision energies. Also up to RHIC and LHC energies the hadron production and the resulting yields, ratios, rapidity and transverse-momentum spectra are quite well described in the approach; for details we refer the reader to references [43, 46, 47]. However, looking at specific observables one also finds deviations of the model results from the experimental data. This is especially the case for the elliptic flow, v_2 : Whereas the elliptic flow is described quite well up to SPS energies, for higher collision energies the average elliptic flow $\langle v_2 \rangle$ under-

estimates the experimental results. At top RHIC energy of $\sqrt{s_{NN}} = 200$ GeV the transport model reaches only roughly 60% of the measured value [48]. Regarding the transverse-momentum dependence of v_2 , the under-prediction is most prominent for high p_t [49–51]. Nevertheless, the model reproduces the centrality dependence and the gross features of the v_2 particle-type dependence, such the mass-ordering for low p_t and the number-of-constituent-quark scaling for higher transverse momenta [52]. Since the build-up of v_2 in the model correlates to the rescattering rate, the low values of this observable in UrQMD can be interpreted as a hint that a strongly interacting phase of partons is created in the early reaction evolution [53–55] (see also Sec. II C).

However, the anisotropic flow effects are very small (at the order of few percent) and have only very little influence on the dilepton invariant-mass and transverse-momentum spectra. In consequence, the deviations from the experimental measurements will not play a significant role for our present study. This is of course different for studies of the anisotropic flow of electromagnetic probes, where the deviations from the measured bulk v_2 will be apparent. To reproduce these measurements, one will probably need an advanced description which includes the effects of the partonic phase on the fireball evolution.

B. Extracting thermodynamic properties

Note that within the UrQMD model one has a well determined phase-space distribution function $f(\vec{x}, \vec{p}, t)$, as the location and momenta of all particles are known. However, since the full microscopic treatment of the medium effects is quite complicated, the present approach aims to reduce (i.e., to coarse-grain) the amount of information given by $f(\vec{x}, \vec{p}, t)$, such that one can switch from a microscopic to a macroscopic description of the collision. Instead of the individual particle coordinates, the system is then defined by its thermodynamic properties. To do so, it is first necessary to obtain a smooth distribution function, which is realized by averaging over a large number of events:

$$f(\vec{x}, \vec{p}, t) = \left\langle \sum_h \delta^{(3)}(\vec{x} - \vec{x}_h(t)) \delta^{(3)}(\vec{p} - \vec{p}_h(t)) \right\rangle. \quad (1)$$

Here the angle brackets $\langle \cdot \rangle$ denote the ensemble average. It is important to bear in mind that the UrQMD model constitutes a non-equilibrium approach, whereas the thermodynamic properties are well defined only for equilibrated matter. Consequently, the approximate extraction of equilibrium quantities is consistent only locally. Thus a grid of small space-time cells is set-up where—following Eq. 1—for each of these cells the energy-momentum tensor and the baryon current are ex-

tracted as

$$\begin{aligned} T^{\mu\nu} &= \frac{1}{\Delta V} \left\langle \sum_{i=1}^{N_h \in \Delta p_i^V} p_i^0 \right\rangle, \\ j_B^\mu &= \frac{1}{\Delta V} \left\langle \sum_{i=1}^{N_{B/\bar{B}} \in \Delta V} \pm \frac{p_i^\mu}{p_i^0} \right\rangle. \end{aligned} \quad (2)$$

Here ΔV is the volume of the cell, and the sum is taken over all (anti-)baryons or hadrons in the cell, respectively. If one knows j_B^μ and $T^{\mu\nu}$, the local rest frame (LRF) can be determined by applying the definition of Eckart [56], which requires a vanishing baryon flow, $\vec{j}_B = 0$. The energy and net-baryon density of the cell are then defined as $\varepsilon = T_{\text{LRF}}^{00}$ and the baryon density is $\rho_B = j_{B,\text{LRF}}^0$.

To obtain temperature and baryochemical potential it is necessary to apply an equation of state (EoS) which translates the local energy and baryon densities into T and μ_B . For consistency with the underlying transport model, we apply a hadron gas EoS [57] for the lower temperature range up to $T = 170$ MeV. It includes the same hadronic degrees of freedom as the UrQMD approach. For higher temperatures a pure hadronic description is insufficient, as the phase transition to a Quark-Gluon Plasma also changes the degrees of freedom and consequently the equation of state. We therefore use an EoS from lattice calculations [58] (with a critical temperature $T_c = 170$ MeV) for cells with higher energy densities. While both EoS match in the temperature region from 150-170 MeV, the lattice EoS gives significantly higher temperatures for very hot cells. A comparison between both equations of state is given in Ref. [30].

It is important to bear in mind that the application of the lattice EoS for higher energy densities or temperatures, respectively, does not provide full consistency with the underlying hadronic dynamics in the transport model; in UrQMD only hadronic degrees of freedom are implemented, and no phase transition to a partonic phase is included. On the other hand, the very details of the microscopic dynamics are anyway “washed out” in the coarse-graining procedure by the reduction of the multitude of information and the averaging over the events. Since we only use the local energy density distribution from the microscopic simulations to calculate a temperature via the lattice EoS ($\mu_B = \mu_\pi = 0$ is always assumed for $T > 170$ MeV), a severe problem should only arise if the gross evolution of the density distribution would largely depend on the specific equation of state. This would imply differences in the measurable particle spectra. However, previous studies with a UrQMD+hydrodynamics hybrid model [59] have shown that the bulk evolution of the fireball is not significantly altered when using an EoS including a phase transition instead of a pure hadron gas EoS [60]. Taking this into account, the procedure as applied in the present approach seems justifiable. (The effect of the choice of EoS on the dilepton spectra is also studied in Sec. III B.)

C. Non-equilibrium effects

The approach as outlined above assumes a locally equilibrated system in each cell. However, it is clear that within a transport approach this condition is not always fulfilled in a satisfying manner. In contrast, due to the non-equilibrium nature of the model one finds significant deviations from kinetic and/or chemical equilibrium. For a correct description of the fireball evolution the consequences of these deviations need to be considered. Basically one finds two dominant effects which affect the thermodynamic properties and, consequently, the dilepton emission:

1. Pressure isotropy is necessary for a system to be in *kinetic equilibrium*. However, it is well known from previous studies [61, 62] that the initial stages of a heavy-ion collision are dominated by large differences between the longitudinal and transverse pressures. This is a consequence of the strong longitudinal compression of the nuclei at the beginning of the collision. In this case, the energy density is overestimated in the cell, as a large fraction of the energy is of no relevance with regard to the thermal properties of the system. To apply the coarse-graining approach also for the first few fm/c of the collision, it is therefore necessary to extract a realistic energy density ε_{eff} taking the limited degree of thermalization into account. This is achieved by the use of a generalized equation of state for a Boltzmann-like system [63, 64], that gives ε_{eff} in dependence on the “bare” energy density in the cell and the pressure anisotropy. The results for SPS energies showed that significant deviations of ε_{eff} are only found for the first 1-2 fm/c of the collision [30].
2. *Chemical non-equilibrium* shows up in the form of finite meson chemical potentials (in full equilibrium, all meson chemical potentials vanish as the meson number is not a conserved quantity, in contrast to, e.g., the net-baryon number) and most dominantly in form of a pion chemical potential μ_π , since the π mesons are the most abundantly produced particles. A finite μ_π is the consequence of an overpopulation of pion states. In a transport model, such an over-dense pion system is especially found at the very beginning of the reaction, when the fireball is still far from kinetic equilibrium and the first inelastic collisions produce a large number of pions [65]. The pion chemical potential is important for the population of ρ and ω vector mesons, as a high density of pions increases the probability for the production of these particles (besides, μ_π has also some moderate effects on the spectral shape) [66, 67]. To account for these effects we extract the pion chemical potential in each cell in Boltzmann approximation.

When the local energy and particle densities change in the course of the fireball evolution, the phase-space

distribution function, $f(\vec{x}, \vec{p}, t)$, is adjusted to the corresponding values of temperature and chemical potentials. If this adjustment is slower than the change of T and μ , one will find deviations from the local equilibrium distribution of the form [68]

$$f(\vec{x}, \vec{p}, t) = f_{\text{eq}}(\vec{x}, \vec{p}, t) + \delta f(\vec{x}, \vec{p}, t). \quad (3)$$

One consequence of this deviation from the equilibrium state is the appearance of finite transport coefficients, such as viscous stresses, heat flow, and diffusion [69]. Note that in the underlying transport dynamics used for the coarse-graining these effects are implicitly implemented due to the non-zero mean free path of the interacting hadrons. The resulting transport coefficients (e.g., viscosity and heat conductivity) from UrQMD have been in detail studied for the infinite-matter case in box calculations [70–73]. The results showed that for the shear viscosity to entropy ratio one obtains rather high values $\eta/s > 0.6$ within the model. This is in contrast to ideal hydrodynamic calculations which have been quite successful in describing the observables from heavy-ion collisions by neglecting the effect of those transport coefficients. The large elliptic flow measured in non-central heavy-ion reactions at RHIC energies suggests a very low value of the shear viscosity to entropy ratio η/s in the created hot and dense fireball. This was interpreted as a direct hint for the creation of a Quark-Gluon Plasma phase early during the fireball evolution [74, 75]. The high values of η/s from UrQMD can, in consequence, explain the underestimation of the resulting elliptic flow v_2 at RHIC in the model, as discussed in Sec. II A.

However, recently the role and importance of viscosity has come into theoretical focus and was studied intensively in hydrodynamical approaches [76–81], as it was found that pure ideal hydrodynamic calculations result in an overestimate of the elliptic flow for high transverse momenta and/or wrong slopes for the hadron- p_t spectra [68]. With regard to the dilepton emission, the appearance of a shear viscosity might show an effect in two ways: Firstly, by its influence on the bulk evolution—especially an increase of the directed flow and a reduction of the anisotropies—, and secondly by the direct modification of the emission rates due to modifications of the distribution functions [82].

Whereas the coarse-grained dynamics of the fireball naturally reflects the viscosities in the underlying microscopic simulations, as mentioned above, we do not consider the effects of the viscous corrections on the electromagnetic emission rates for two reasons: On the one hand it was shown that the influence of finite viscosity on the resulting invariant mass or transverse momentum spectra of dileptons and photons is rather small, especially for the low-mass region up to $2 \text{ GeV}/c^2$ [9, 10, 83]. (The case is somewhat different for the elliptic flow, where the modification of the emission rates might be more pronounced.) On the other hand there are presently no calculations available for the hadronic and partonic rates which are applied in our approach. The viscous correction for emis-

sion from the Quark-Gluon Plasma has so far only been calculated for the perturbative Born rate, i.e., for leading order $q\bar{q}$ annihilation [84]. However, this rate is known to significantly underestimate the thermal yield for lower masses, compared to more advanced hard-thermal loop or lattice rates [85, 86]. The situation is similar for the hadronic rates, where the effect of viscosity has been considered only for a low-density calculation [87] which cannot account for the full in-medium modifications of the vector mesons' spectral shape.

We will discuss the emission rates applied in the present approach in detail in the following section II D.

D. Thermal dilepton rates

The thermal emission of dileptons from an equilibrated system of hot and dense matter is determined by the imaginary part of the (retarded) electromagnetic current-current correlation function, $\text{Im} \Pi_{\text{em}}^{(\text{ret})}$, which is connected to the electromagnetic current j_μ [88]. The dilepton yield per four-volume and four-momentum can then be calculated according to the relation [67, 89]

$$\frac{dN_{ll}}{d^4x d^4q} = -\frac{\alpha_{\text{em}}^2 L(M)}{\pi^3 M^2} f_B(q; T) \text{Im} \Pi_{\text{em}}^{(\text{ret})}(M, \vec{q}; \mu_B, T), \quad (4)$$

where f_B is the Bose distribution function and $L(M)$ the lepton phase space.

In the hadronic low-mass regime (i.e., for $M_{e^+e^-} < 1 \text{ GeV}/c^2$) the electromagnetic current directly couples to the vector mesons and—assuming vector meson dominance (VMD)— Π_{em} is proportional to the vector-meson propagator

$$D_V = \frac{1}{q^2 - m_V^2 - \Sigma_V(q^2)} \quad (5)$$

where m_V is the bare mass of the meson and Σ_V the corresponding self-energy of the particle, related to its decay width. Whereas the self-energy in the vacuum can be deduced from experimental measurements of inelastic electron-positron scattering ($e^+e^- \rightarrow \text{hadrons}$), the situation for finite T and μ_B is more complicated and requires detailed model calculations. For the present work we apply the results from equilibrium quantum-field theory calculations with a hadronic many-body approach [90, 91]. They account for the interactions of the ρ and ω mesons with hadrons in a heat bath. For the ρ the pion cloud ($\Sigma_{\rho\pi\pi}$) as well as the direct contributions from ρ -hadron scatterings with baryons ($\Sigma_{\rho B}$) and mesons ($\Sigma_{\rho M}$) are included in the calculation of the in-medium self-energy. In this case Eq. 5 becomes

$$D_\rho = \frac{1}{M^2 - m_\rho^2 - \Sigma_{\rho\pi\pi} - \Sigma_{\rho B} - \Sigma_{\rho M}}. \quad (6)$$

The situation for the ω meson is more complex, as it constitutes a three-pion resonance. Here the self energy

includes $\omega \rightarrow \pi\rho$ and $\omega \rightarrow 3\pi$ decays as well as the inelastic $\omega\pi \rightarrow \pi\pi$, $\omega\pi \rightarrow b_1$ and $\omega N \rightarrow N^*$ scatterings. The resulting propagator reads

$$D_\omega = [M^2 - m_\omega^2 + im_\omega (\Gamma_{3\pi} + \Gamma_{\rho\pi} + \Gamma_{\omega\pi \rightarrow \pi\pi}) - \Sigma_{\omega\pi b_1} - \Sigma_{\omega B}]^{-1}. \quad (7)$$

To account for the symmetry of the interactions of ρ and ω mesons with baryons and anti-baryons, the spectral functions do not depend on the baryochemical potential μ_B but on an effective baryon density $\rho_B^{\text{eff}} = \rho_N + \rho_{\bar{N}} + 0.5(\rho_{B^*} + \rho_{\bar{B}^*})$ [92]. Here $\rho_{N/\bar{N}}$ denotes the nucleon / anti-nucleon density and ρ_{B^*/\bar{B}^*} is the density of excited baryon/anti-baryon resonances.

Note that in the case of a finite pion chemical potential an additional fugacity factor

$$z_\pi^n = \exp\left(\frac{n\mu_\pi}{T}\right) \quad (8)$$

enters in Eq. 4. The exponent n depends on the difference between initial and final pion number for the relevant channel [67, 93, 94]. For dilepton production from ρ mesons one has $n = 2$ whereas for the ω it is $n = 3$.

At the higher masses above $1 \text{ GeV}/c^2$ one no longer finds distinct resonances in the hadronic domain of the vector channel but a broad continuum of multi-pion states which couple to the electromagnetic current. In principle, also here the dilepton emission is related to the vector spectral function. However, the presence of pions at finite T causes a chiral mixing of the isovector part of the vector and axial-vector correlators [95]. The corresponding isovector-vector current correlation function takes the form [96]

$$\begin{aligned} \Pi_V(p) = & (1 - \varepsilon) z_\pi^4 \Pi_{V,4\pi}^{\text{vac}} + \frac{\varepsilon}{2} z_\pi^3 \Pi_{A,3\pi}^{\text{vac}} \\ & + \frac{\varepsilon}{2} (z_\pi^4 + z_\pi^5) \Pi_{A,5\pi}^{\text{vac}}, \end{aligned} \quad (9)$$

where the mixing coefficient ε is given by the thermal pion loop, and z_π again denotes the pion fugacity.

For temperatures above the critical temperature T_c the relevant degrees of freedom are no longer hadrons (vector mesons) but quarks and gluons. In this situation the strength of the electromagnetic current is accounted for by a partonic description and the thermal dilepton production occurs—to leading order—via the electromagnetic annihilation of quark-antiquark pairs, $q\bar{q} \rightarrow \gamma^*$. However, it has been shown that the pure pQCD result [84] underestimates the actual dilepton emission in the low energy regime (i.e., at low masses). Nonperturbative results indicate a strong enhancement due to α_s corrections and bremsstrahlung effects [85]. In the present work we apply a spectral function from lattice QCD calculations [86] which has been extrapolated for finite three-momenta by a fit to the according photon rate [11]. Note that these lattice rates are available only for vanishing quark chemical potential $\mu_q = 0$. However, the effects of a finite μ_q are quite small with regard to the dilepton emission rates and can be neglected here.

E. Non-thermal hadronic decay contributions

In addition to the thermal dilepton emission from the hot and dense fireball, there are also contributions from more long-lived mesons which mostly decay into lepton pairs after the freeze-out of the system, mainly the pseudoscalar π^0 and η mesons. Their Dalitz decays into a real and a virtual photon (which subsequently transforms in a lepton pair) dominate the very low invariant masses. The corresponding decay width is related to the probability for the decay into two photons and given by the Kroll-Wada formula [97]

$$\begin{aligned} \frac{d\Gamma_{P \rightarrow \gamma e^+ e^-}}{dM} = & \frac{2\alpha}{3\pi M} L(M) 2\Gamma_{P \rightarrow \gamma\gamma} \\ & \times \left(1 - \frac{M^2}{M_\rho^2}\right) |F_{P\gamma\gamma^*}(M^2)|, \end{aligned} \quad (10)$$

where the form factors $F_{P\gamma\gamma^*}$ are fitted to experimental data [98], consistent with the theoretical results assuming VMD.

Note that only the final state π and η mesons are considered for the procedure. Those mesons which are produced and absorbed again during the collision have a negligible probability for a dilepton decay due to their small decay width. The situation is somewhat different for the ϕ meson. In spite of the shorter lifetime we do not treat it as a thermal contribution (since the expected medium-effects are so small that they can be neglected) but consider the microscopic decays here as for the pseudoscalar mesons. However, in this case one assumes that the ϕ has an equal probability for the decay into a lepton pair at any time and therefore can continuously emit dileptons [99]. The total yield is then obtained as a time integral over the lifetime as

$$\frac{dN_{ll}}{dM} = \frac{\Delta N_{ll}}{\Delta M} = \sum_{i=1}^{N_{\Delta M}} \sum_{j=1}^{N_\phi} \int_{t_i}^{t_f} dt \frac{\Gamma_{\phi \rightarrow ll}(M)}{\gamma \Delta M}, \quad (11)$$

where the γ factor accounts for the relativistic time dilation in the computational frame compared to the mesons rest frame. This procedure explicitly takes absorption processes for the ϕ into account.

Besides, two more non-thermal contributions arise due to the fact that not for all cells it is possible to properly calculate the thermal contribution. This is mainly the case for the later stages of the reaction, for cells with (i) no baryon content, so that the LRF is not well-defined, or (ii) where the temperature is below 50 MeV, in which case the EoS and the emission rates no longer give reliable results. In these cases a “freeze-out” contribution for the ρ and ω meson is determined directly from the microscopic UrQMD results for those specific cells. The procedure is the same as for the ϕ given by Eq. 11, but the time-integration is performed only for the corresponding time-step size.

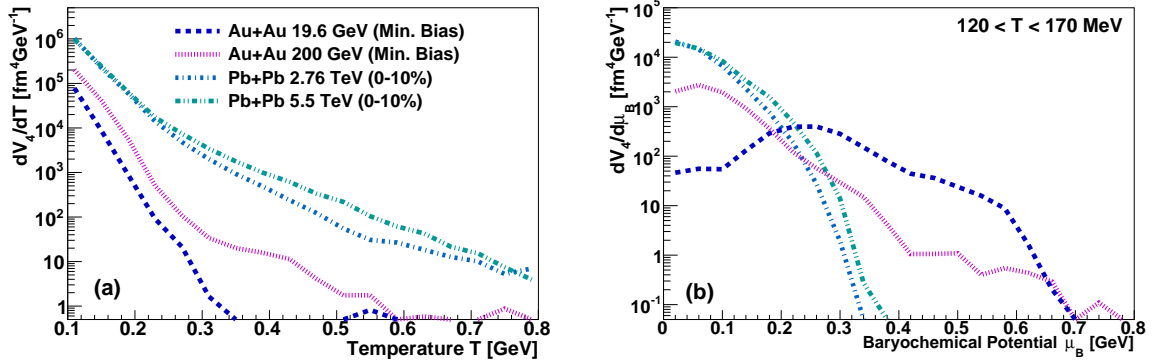


FIG. 1. (Color online) Thermal four-volume V_4 in dependence on temperature (a) and baryochemical potential (b) for Au+Au and Pb+Pb reactions at different collision energies.

III. RESULTS

For the present study the coarse-graining of the UrQMD transport output was performed with ensembles of 1000 UrQMD events for Au+Au collisions at RHIC and 500 events for Pb+Pb reactions at LHC energies. The time-step size was chosen as $\Delta t = 0.4 - 0.6$ fm/ c , and the spatial dimensions of the cell are defined as $\Delta x = \Delta y = \Delta z = 0.8 - 0.9$ fm, depending on the collision energy. The impact parameter distributions corresponding to different centrality classes were chosen using Glauber-Model fits to experimental data [14, 16]. Note that the minimum bias definitions slightly differ between the STAR and PHENIX collaborations; the former uses

0-80% most central collisions whereas the PHENIX trigger takes 0-92% central collisions into account.

A. Fireball evolution

The thermal dilepton emission from a hot and dense fireball created in a heavy-ion collision is determined by the trajectory of the system within the QCD phase diagram. More precisely, since for each space-time cell different values of temperature and baryochemical potential are obtained within the coarse-graining approach, the overall yield is directly related to the distribution of the thermal four-volume V_4 inside the fireball with regard to T and μ_B . Figure 1 (a) shows the total thermal four-volume summed over all cells in dependence on the respective temperature for Au+Au and Pb+Pb reactions at four different collision energies, from the lowest RHIC to top LHC energies. While for the low temperature range around 100 MeV the differences between the energies are not larger than one order of magnitude, the relative increase of the number of higher temperature cells is much stronger. For $\sqrt{s_{NN}} = 19.6$ GeV one hardly finds cells with temperature above 300 MeV, while at LHC energies there are some cells with up to 800 MeV (few rare cells even reach still higher temperatures up to 1000 MeV, which is not shown here).

When considering the μ_B dependence of the four-volume for the temperature range from 120 to 170 MeV in Figure 1 (b), one also finds that the average baryon chemical potential is decreasing when going to higher collision energies (note again, as outlined in Sec. II B, the lattice EoS for $T > 170$ MeV in general assumes vanishing baryochemical potential). At $\sqrt{s_{NN}} = 19.6$ GeV the most abundant μ_B -range lies between 200 and 300 MeV, whereas at LHC μ_B is close to zero for the overwhelming part of the thermal four-volume. Interesting is the fact that one gets a slightly stronger contribution from higher chemical potential when going from 2.76 to 5.5 GeV.

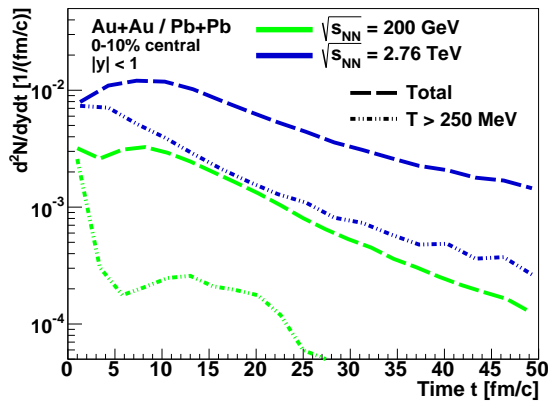


FIG. 2. (Color online) Time evolution of the thermal dilepton emission dN_{e+e-}/dt for central Au+Au collisions at $\sqrt{s_{NN}} = 200$ GeV (green) and Pb+Pb collisions at $\sqrt{s_{NN}} = 2.76$ TeV (blue). The total emission (long dashed) is shown as well as the resulting yield only from cells with a temperature above 250 MeV (dashed double-dotted).

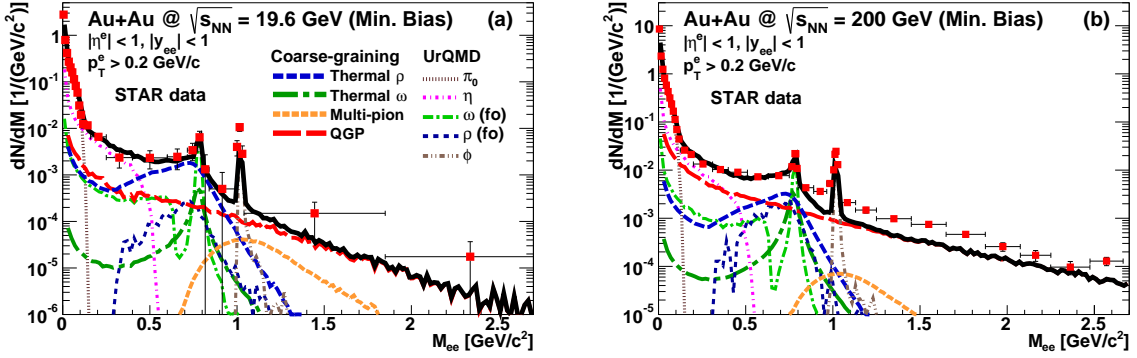


FIG. 3. (Color online) Dielectron invariant-mass spectra for minimum bias (i.e., 0-80% most central) Au+Au collisions at $\sqrt{s_{NN}} = 19.6$ GeV (a) and 200 GeV (b). The sum includes the thermal hadronic and partonic emission obtained with the coarse-graining, and also the hadronic π, η and ϕ decay contributions from UrQMD as well as the “freeze-out” contributions (from cold cells) of the ρ and ω mesons. The model results are compared to the experimental data obtained by the STAR Collaboration [14].

However, this might be an effect due to the limited temperature window considered here.

The resulting time evolution of the thermal dilepton emission dN/dt from all cells (and from those with temperature above 250 MeV only) is shown in Figure 2. The results for central (0-10%) Au+Au reactions at 200 GeV and Pb+Pb collisions at 2.76 TeV exemplarily expose the similarities and differences in the fireball dynamics for RHIC and LHC. In general, one observes that the evolution of the fireball for both energies is very similar, apart from the larger overall emission at 2.76 TeV compared to the 200 GeV case. This is a consequence of the larger thermal four-volume for all temperature regions, compare Fig. 1 (a). However, at the LHC the cooling of the system is slower, especially the emission from the very hot cells with $T > 250$ MeV shows a less significant drop than for the RHIC energy. In any case, the thermal emission from the later stages of the reaction—even 40-50 fm/c after the first initial nucleon-nucleon interactions—is remarkably large, although the influence on the total yield is very small, as dN/dt is suppressed by 1-2 orders of magnitude compared to the early maxima.

B. Relativistic Heavy-Ion Collider (RHIC)

The dilepton invariant-mass spectra for minimum bias Au+Au reactions at the two RHIC energies $\sqrt{s_{NN}} = 19.6$ and 200 GeV are presented in Figure 3. The results as obtained with the coarse-graining approach are compared to the experimental data from the STAR Collaboration [14]. The spectra are shown within the STAR acceptance, which means rapidity and pseudorapidity cuts ($|\eta^e| < 1$, $|y_{ee}| < 1$) were applied for single electrons and dileptons, respectively, together with an additional transverse momentum cut for electrons (i.e., here

$p_t^e > 0.2$ GeV). The comparison shows that in both cases the invariant-mass spectra for low masses below $1 \text{ GeV}/c^2$ are very well described within the model. While in comparison to pure hadronic decay cocktails an excess of the experimentally measured spectra was observed for the mass region $0.3 < M_{ee} < 0.7 \text{ GeV}/c^2$, our approach shows that this region is dominated by thermal emission from the ρ meson and from partonic emission. But there are also important differences visible when comparing the outcome for both energies: Due to the larger temperatures obtained for Au+Au reactions at 200 GeV, the low mass region is here dominated by QGP emission, only around the ρ pole mass the hadronic emission is dominant. In contrast, the thermal ρ contribution clearly outshines the partonic yield for the greatest part of the low mass region up to $1 \text{ GeV}/c^2$ at the lower collision energy of 19.6 GeV.

It is interesting that the spectral shape of the thermal ρ resembles its vacuum shape in both cases, compared to the very strong broadening and low-mass enhancement which is observed for SIS 18 and FAIR energies [31, 32]. However, this is not surprising since in the previous section it has already become clear that the baryochemical potential is rather low in most of the cells. And even if one considers that the baryonic modifications of the spectral shape for the ρ are governed by the effective baryon and anti-baryon density, the effects seem relatively small. One reason for this is that the initial heating is faster and stronger at RHIC energies and the early phase of the reaction is mostly dominated by partonic emission (which is quite insensitive with regard to finite quark chemical potential $\mu_q = 1/3\mu_B$), whereas the hadronic contributions are predominantly radiated at later stages when the baryon densities are lower. Consequently, the baryon-induced medium effects—which are the main cause of the ρ low-mass enhancement—are only very moderate

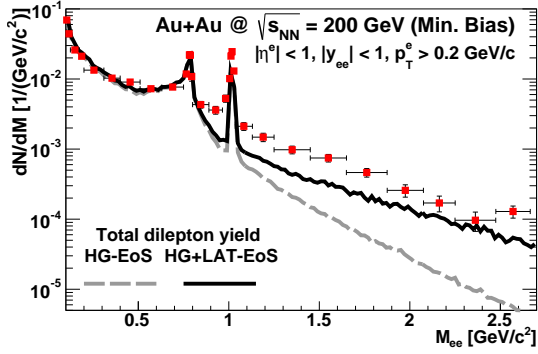


FIG. 4. (Color online) Comparison of the influence of different EoS on the dielectron invariant-mass spectrum for minimum bias Au+Au collisions at $\sqrt{s_{NN}} = 200$ GeV. We show the result obtained with a pure hadron gas equation of state (HG-EoS) and the combination of the hadron gas together with a lattice EoS at higher temperatures (HG+LAT-EoS). In both cases the hadronic rates are used up to $T = 170$ MeV and partonic rates for higher temperatures. The model results are compared to the experimental data obtained by the STAR Collaboration [14].

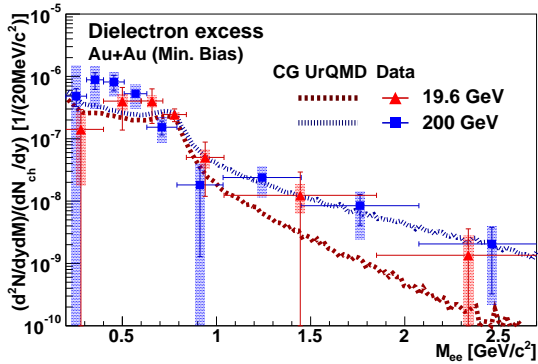


FIG. 5. (Color online) Dielectron excess spectrum for minimum bias (0-80% most central) Au+Au collision at $\sqrt{s_{NN}} = 19.6$ and 200 GeV as obtained with the coarse-graining of UrQMD simulations (CG UrQMD). The results include the thermal contributions from the ρ , multi-pion interactions and the QGP. Additionally the UrQMD freeze-out ρ is included for this calculation. The model results are compared to the results of experimental measurements by the STAR Collaboration [15].

here. Note that there is also a significant non-thermal ρ contribution from low-temperature and late-stage cells, which is more dominant for 200 GeV. This might be due to the longer lifetime of the system, with a significant number of those mesons in peripheral cells and late in the evolution. In contrast to the thermal ρ , the thermal ω contribution is rather negligible compared to the respective freeze-out contribution. This is mainly due to

the long lifetime of the ω , which is typically so long that this resonance mostly decays outside the hot and dense region.

In contrast to the low-mass region, for $M_{e^+e^-} > 1$ GeV/ c^2 the overall dilepton yield is no longer dominated by the peaks from various hadronic decays but one experimentally finds a structureless continuum. In our model the thermal emission from multi-pion interactions and from the partonic phase shine in this part of the spectrum. Note however that—as mentioned before—the present calculation does not include the Drell-Yan and, more important, the open-charm contributions to the spectrum. Nevertheless, as the strength of possible medium modification for D or \bar{D} mesons is yet unclear, our calculation can serve as a thermal baseline.

For $\sqrt{s_{NN}} = 19.6$ GeV the QGP emission is the dominant contribution in the mass region from 1 to 2.8 GeV/ c^2 with a significant contribution from the multi-pion part which is strongest around $M_{e^+e^-} = 1.1$ GeV/ c^2 . Here 20-30% of the thermal contribution are from the hadronic source, while for higher masses the multi-pion yield becomes rather insignificant. The comparison with experimental data allows no clear conclusions at this energy due to the limited statistics and rather large errors. The yield from the coarse-graining model is within the statistical error of the data but rather at the lower boundary. The situation is somewhat different for Au+Au collisions at 200 GeV. At this higher energy the QGP emission is now the dominant thermal contribution, whereas the hadronic contribution is suppressed by at least a factor of 10. Due to the significantly better statistics, one can observe that the model does not fully describe the STAR data, but the dilepton emission obtained within the model makes up for only roughly 50% of the measured yield in the region from 1 to 2 GeV/ c^2 . Interestingly, for even higher masses the agreement between model and data becomes better, the slope of the thermal emission seems to be slightly harder than the measured one. These results agree with previous studies indicating that the relative suppression of the charm contribution due to medium effects is more pronounced at higher masses, leaving it the dominant contribution only for lower masses around 1 GeV/ c^2 [39].

While by default we use a combination of a hadron gas and a lattice EoS (HG+Lat-EoS) for all calculations presented in this work, it was discussed in Sec. II B that this is not fully consistent with the underlying purely hadronic microscopic dynamics. In consequence, it is instructive to compare this standard scenario with the more consistent case where only the hadron gas equation of state (HG-EoS) is used for all temperature ranges to extract T and μ_B . Note that in both cases we use the hadronic rates up to $T = 170$ MeV and the partonic emission rates for higher temperatures for being able to directly compare the effect of the different EoS. The total invariant-mass spectra obtained with both EoS are put on top of each other for minimum bias Au+Au collisions at 200 GeV in Fig. 4. The results indicate that the dif-

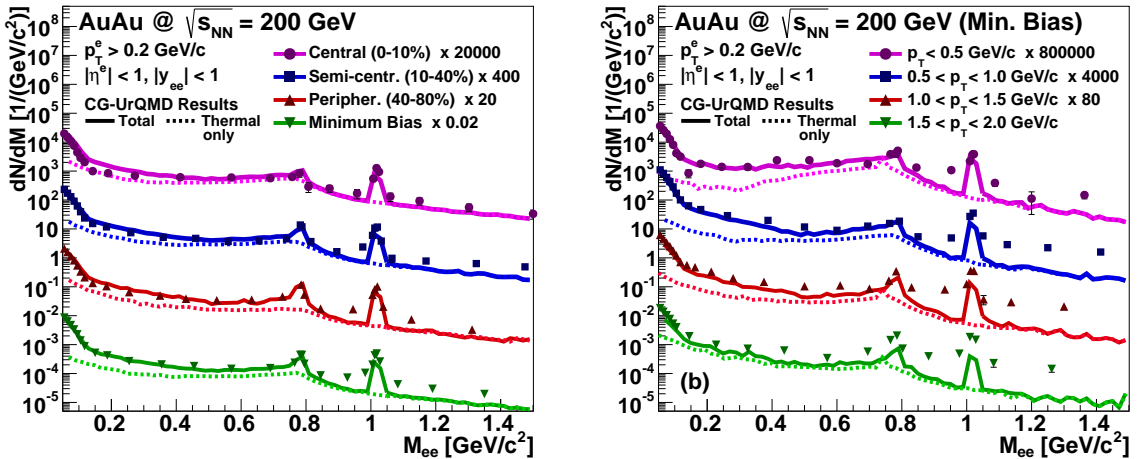


FIG. 6. (Color online) Dielectron invariant-mass spectra for Au+Au collisions at $\sqrt{s_{NN}} = 200$ GeV for different centralities (a) and transverse-momentum bins (b). Besides the total yields (full lines) we also show the thermal contribution separately (dashed lines). The results in (a) are shown for central (0-10%), semi-central (10-40%), peripheral (40-80%), and minimum bias (i.e., 0-80%) events. In (b) the spectra are shown for minimum bias collisions in four transverse-momentum bins covering the range from $p_t = 0$ to 2.0 GeV/c. The spectra are shown within the STAR acceptance and compared to the experimental data [14]. In addition, they are scaled for better comparability.

ferences with regard to the overall yield in the low mass region are rather small and result in no significant deviations in the thermal emission pattern for masses up to $M_{e^+e^-} = 1$ GeV/c². The slightly reduced QGP yield in this region due to the lower temperatures from the HG-EoS is mostly compensated by a larger hadronic contribution, especially around the ρ pole mass. However, the picture is quite different for masses above 1 GeV/c², dominated by the QGP emission: Here the use of the HG-EoS results in a significantly lower thermal yield and a softer slope. The yield is suppressed by almost an order of magnitude at $M_{e^+e^-} = 2.5$ GeV/c² compared to the HG+Lat-EoS scenario. This is not surprising, as these higher masses are dominated by emission from the very early hot stage of the fireball where the highest energy densities are reached. Here the differences between the two EoS are most dominant and the lattice equation of state results in significantly higher temperatures. On the one hand, this result indicates that the low-mass dilepton spectra are quite insensitive with regard to the EoS; on the other hand, it shows again that direct information regarding the phase structure of QCD might be deduced from the spectra at higher invariant masses, 1 GeV/c² $\lesssim M_{e^+e^-} \lesssim 2.5$ GeV/c². However, the experimental extraction of the thermal yield is difficult in this region as also a strong contribution from correlated charm decays is found here, see discussion above.

In addition to the full invariant-mass distributions, the STAR Collaboration also published dilepton excess spectra for minimum bias Au+Au collisions at 19.6 and 200 GeV [15]. Here the cocktail contributions (hadronic

decays, Drell-Yan and open charm) are subtracted such that the resulting spectra represent only the thermal dilepton emission. Furthermore the data are corrected for the experimental acceptance. In Figure 5 these results are compared to the thermal contribution from our model, including the non-thermal UrQMD “freeze-out” ρ and excluding the thermal ω contribution. (The ω is usually treated as part of the cocktail and was subtracted from the experimental spectrum.) We see that for the mass region $M_{e^+e^-} > 1$ GeV/c² in Au+Au collisions at $\sqrt{s_{NN}} = 200$ GeV the thermal result agrees very well with the data, indicating that the thermal part of this mass region seems to be accurately described with the coarse-graining approach. However, note that the subtracted cocktail contribution does not account for medium modifications of the charm contribution, so that the meaning of the high-mass excess spectrum is rather limited. At 19.6 GeV the thermal spectrum from the model seems to be slightly below the data for higher masses, but still within the large statistical and systematic errors. In the low-mass region the agreement between model and data is better for 19.6 GeV than for 200 GeV, but in both cases the experimental thermal excess seems to be slightly underestimated by the model. Nevertheless, considering the uncertainty of the data and the subtraction procedure the agreement is quite satisfactory.

So far we have considered dilepton spectra for minimum bias reactions and the full transverse-momentum range, but the thermal dilepton yield also largely depends on the centrality of the reaction and on the transverse-

momentum window in which the results are measured. Both dependencies were investigated by the STAR Collaboration for Au+Au collisions at 200 GeV [14], and the experimental data are presented together with the model results in Figure 6. The left plot (a) shows the invariant-mass spectra for central (0-10%), semi-central (10-40%) and peripheral (40-80%) collisions, together with the minimum bias result from Fig. 3 (b) for comparison. In all four centrality classes one observes quite a good description of the low invariant-mass data by the coarse-graining results. For higher masses larger than $1 \text{ GeV}/c^2$ the underestimation of the dilepton yield observed for minimum bias reactions is also found for other centrality classes. However, for the most central reactions the description seems to be slightly better. In this case the thermal emission alone can almost fully describe the dilepton data for higher masses. This would be in accordance with the assumption that the medium effects on the open charm production are most dominant for central collisions, leading to a suppression of the open-charm contribution to the dilepton spectra.

For the p_t dependence of e^+e^- production, the comparison between theory and data gives a more nuanced picture, as presented in Figure 6 (b). Here the scaled results for minimum bias Au+Au collisions in four different transverse momentum bins are shown. In the low invariant-mass region one finds a good description of the data for the lower transverse momentum bins up to $1 \text{ GeV}/c$, while especially for $p_t > 1.5 \text{ GeV}/c$ the measured results are underestimated by up to a factor 2. Interestingly, this does not only affect the thermal yield, but also the pure hadronic cocktail contributions, as can be seen from the underestimate for the π -dominated very low masses and the ω and ϕ peaks. The reason for this

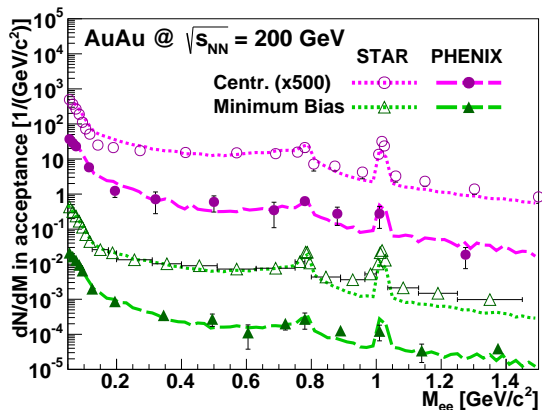


FIG. 7. (Color online) Comparison of the dielectron invariant-mass spectra for central (magenta) and minimum bias (green) Au+Au collisions at $\sqrt{s_{NN}} = 200 \text{ GeV}$ with the STAR and PHENIX data [14, 16] in the corresponding acceptances. The total sum of the model results for PHENIX is given by the long dashed lines, and for STAR by the short dashed lines.

might be the expansion dynamics from the underlying transport model, which is known to somewhat underestimate the collective flow of the fireball [48], resulting in too soft p_t spectra for the produced particles. However, the general trend when going from the low to the high transverse momentum region is the increasing importance of the thermal emission in the low-mass region and a flattening of the shape of the spectrum. This is due to two effects: On the one hand, the p_t^c cut for single electrons leads to a suppression of low masses ($M < 0.4 \text{ GeV}/c^2$) when the transverse momentum of the pair is close to zero. On the other hand, the emission of high- p_t dileptons occurs mostly at the higher temperatures which can be found in the early Quark-Gluon Plasma phase, whereas the hadronic emission is usually found to be softer.

Regarding the higher invariant-mass region for $M > 1 \text{ GeV}/c^2$, an underestimation of the thermal yield is visible, reaching from a factor 2 for low p_t up to a factor of 10 for the higher transverse momenta. This underprediction is not surprising, as it was already visible in the full p_t -integrated invariant-mass spectrum. As mentioned above, this is clearly due to the absence of the charm and Drell-Yan contributions in our calculation.

Although we have up to this point focused on the measurements by the STAR Collaboration, it is natural to compare the model results obtained from the coarse-graining approach also with the results of the PHENIX Collaboration. This is of importance, as the first results from PHENIX showed a strong enhancement of the dilepton invariant-mass spectrum for $0.3 < M_{ee} < 0.7 \text{ GeV}/c^2$ in central collisions, which was not compatible with the results from the STAR Collaboration [100]. In consequence, there has been much discussion about the different detector properties and corresponding acceptances, which made a direct comparison of the two results difficult. Also theoretical models failed to reproduce the PHENIX results [27, 101]. Recently, the PHENIX Collaboration published new results measured with an updated experimental set-up, including a hadron-blind detector (HBD) which could significantly improve the electron identification and the signal sensitivity [16]. In Figure 7 we show the model results for both central and minimum bias Au+Au collisions at $\sqrt{s_{NN}} = 200 \text{ GeV}$ within the PHENIX and STAR acceptances, together with the corresponding experimental data. The comparison clearly shows that the model not only describes the STAR data, but also the new PHENIX results for central as well as minimum bias collisions. However, note that the statistics obtained by PHENIX is significantly lower, leading to larger errors of the measurement. The main explanation for this is the two-arm set-up of the PHENIX detector so that many of produced electrons and positrons do not reach the detector; if only one particle of a pair reaches the detector, this further increases the background of the measurement. Nevertheless, within the errors of the measurement one can state that the PHENIX and STAR dilepton measurements now

fully agree with each other and that the low-mass excess above the hadronic cocktail can be explained by thermal hadronic and partonic emission from medium-modified spectral functions.

To conclude the study for RHIC energies, the model results are finally compared to the transverse momentum spectra from the PHENIX measurement in Figure 8. The (scaled) data and model results within experimental acceptance are presented for three different invariant-mass bins. The thermal contribution and the hadronic decay cocktail from UrQMD are shown separately, as well as the total yield. At very low masses ($M < 0.1 \text{ GeV}/c^2$) the hadronic cocktail contribution dominates the dilepton emission, mainly stemming from π^0 decays. Only for high p_t larger than $1.5 \text{ GeV}/c$ the thermal emission becomes significant. However, such high momenta are largely suppressed by a factor of 100 in that mass region. The model results agree quite well with the experimental measurements, only for lower p_t a slight overestimation of the yield is obtained. (Note that dilepton pairs with $p_t^{ee} < 0.4 \text{ GeV}/c$ are out of the PHENIX acceptance in this mass bin, as the single electron transverse momentum is required to be larger than $0.2 \text{ GeV}/c$.) In the mass region from 0.3 to $0.76 \text{ GeV}/c^2$ the thermal and nonthermal emission almost equally contribute for low p_t with a slight dominance of the hadronic cocktail for transverse momenta from 0.5 to $1.0 \text{ GeV}/c$. In contrast, the thermal dilepton emission clearly outshines the hadronic decays for higher p_t values above $1.5 \text{ GeV}/c$. Note that the present findings from the coarse-graining approach for this mass region roughly agree with the results from a fireball parametrization (using the same spectral functions as in our model) where the non-thermal emission dominates for lower momenta and the thermal contribution—mainly from the ρ —for higher momenta [16]. For the mass region $M_{e^+e^-} > 1.2 \text{ GeV}/c^2$ the thermal emission (i.e, here almost exclusively the partonic contribution from the QGP) is clearly the dominant source in the present calculations. However, the yield obtained with the coarse-graining approach is below the data about a factor 2-3 for low p_t and up to 10 for higher momenta, once again indicating the missing contributions from open-charm mesons. In spite of the significantly differing acceptances of the STAR and PHENIX experiments, the present results are consistent with the findings from the comparison of model results and data for the invariant-mass spectra in various p_t -bins (see Fig. 6 (b)).

C. Large Hadron Collider (LHC)

As became clear from the study of the reaction dynamics in Sec. III A, the fireball of hot and dense matter created in a heavy-ion collision reaches higher temperatures and cools down more slowly at the Large Hadron Collider in comparison to the reaction evolution for RHIC energies. However, there is no significant change with regard

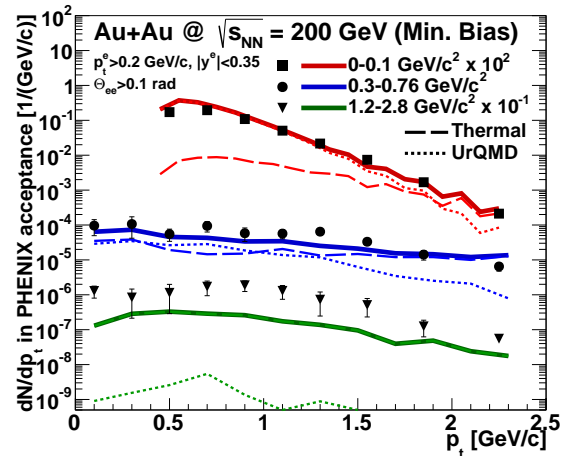


FIG. 8. (Color online) Dielectron transverse-momentum spectra for three mass bins (red: $M = 0 - 0.1 \text{ GeV}/c^2$, blue: $M = 0.3 - 0.76 \text{ GeV}/c^2$, green: $M = 1.2 - 2.8 \text{ GeV}/c^2$) within the PHENIX acceptance. The results here are for minimum bias Au+Au collisions at $\sqrt{s_{NN}} = 200 \text{ GeV}$. Besides the total yields from the model calculations (full lines) also the thermal (long dashed) and non-thermal hadronic decay contributions (short dashed) are presented. For comparison the experimental data from the PHENIX Collaboration [16] are shown as well.

to the baryon densities, the baryochemical potential was already close to zero for most cells at $\sqrt{s_{NN}} = 200 \text{ GeV}$. Consequently, the resulting invariant-mass spectra for central (0-10%) Pb+Pb collisions at center-of-mass energies of 2.76 and 5.5 TeV as shown in Figure 9 exhibit the same mostly vacuum-like spectral shape of the ρ meson contribution, together with an increased yield stemming from the Quark-Gluon Plasma. The partonic contribution is dominating the spectra for masses above $0.1 \text{ GeV}/c^2$, except for the pole-mass peaks of the three vector mesons ρ , ω and ϕ . However, the ρ contribution still plays a significant role as well, and its relative strength is not much smaller than at the top RHIC energy. In general, the increasing number of hot cells with temperature above T_c goes along with a longer lifetime of the fireball and a larger overall thermal four-volume also for temperatures below the critical temperature, which equally leads to a rise of the hadronic emission. In the same manner as there is no strong change of the spectra from RHIC to LHC, the situation does hardly change when going from 2.76 TeV to the maximum LHC energy of 5.5 TeV, except for an higher overall yield. We will study this energy dependence in more detail in Sec. III D.

The transverse momentum spectra for 2.76 TeV in Figure 10 are shown in two different mass bins, for the low-mass region ($0.2 < M_{ee} < 0.9 \text{ GeV}/c^2$) and for the intermediate masses above the ϕ pole mass ($1.05 < M_{ee} < 2.5 \text{ GeV}/c^2$). For the lower masses the finding is simi-

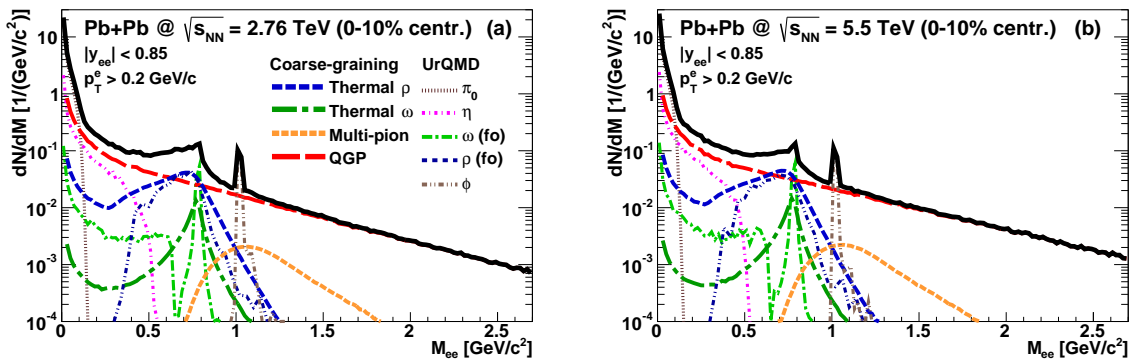


FIG. 9. (Color online) Dielectron invariant-mass spectra for 0-10% most central Pb+Pb collisions at $\sqrt{s_{NN}} = 2.76$ TeV (a) and 5.5 TeV (b). The sum includes the thermal hadronic and partonic emission obtained with the coarse-graining approach, and also the hadronic π , η , and ϕ decay contributions from UrQMD as well as the “freeze-out” contributions (from cold cells) of the ρ and ω mesons.

lar to those for Au+Au collisions at 200 GeV (compare Fig. 8): The hadronic sources are more dominant at low p_t , while the thermal emission is the major contribution for high momenta. In general the slope of the thermal emission is harder (i.e., flatter) than that of the hadronic decays. For the intermediate mass region above $1 \text{ GeV}/c^2$, the only dominant contribution stems from the Quark-Gluon Plasma, whereas the hadronic decays be-

come negligible. The overall slope of the higher masses is also harder, indicating emission from hotter cells on the one hand, but also the stronger flow which is proportional to the mass of the particles. As before one should, however, bear in mind that a full study for the high masses would need to include the missing charm and Drell-Yan contributions.

D. Comparison of RHIC and LHC results

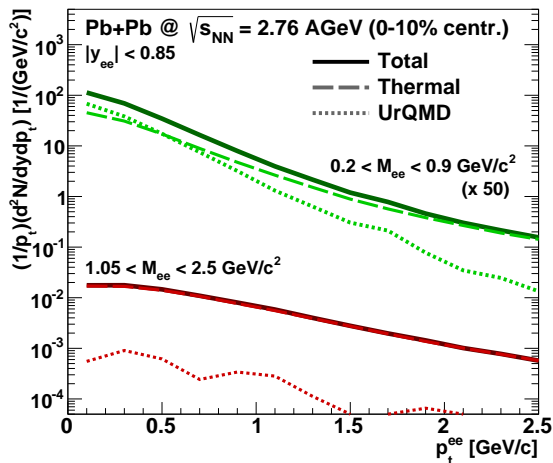


FIG. 10. (Color online) Dielectron transverse-momentum spectra for central Pb+Pb collisions at $\sqrt{s_{NN}} = 2.76$ TeV. The results are shown for the low-mass ($0.2 < M_{e^+e^-} < 0.9 \text{ GeV}/c^2$; green) and intermediate mass region ($1.05 < M_{e^+e^-} < 2.5 \text{ GeV}/c^2$; red). Besides the total yields from the model calculations (full lines) also the thermal (long dashed) and non-thermal UrQMD hadronic decay contributions (short dashed) are presented.

The previous results have already shown that the temperature and lifetime of the fireball increase when going from RHIC to LHC energies, which is connected with a larger yield from thermal dilepton production. In the following, these very qualitative findings shall be investigated in more detail.

In Figure 11 (a) the relative ratio of the thermal dilepton yield at mid-rapidity ($|y_{ee}| < 1$) for different mass regions is shown in relation to the yield which is obtained for Au+Au collisions at $\sqrt{s_{NN}} = 200$ GeV. In addition, the increase of the π^0 yield is shown, as comparison of the thermal results with the production of hadrons or dileptons from hadronic decays, respectively. The results depict that in general the thermal contributions exhibit a stronger increase than the π^0 yield. For the lower masses— 0.05 to 0.3 and 0.3 to $0.6 \text{ GeV}/c^2$ —the thermal yield scales with the number of neutral pions as $N_{\pi^0}^\alpha$, with α found to be approximately 1.9 here. For the mass region above the ϕ pole mass, where purely the QGP contributes to the thermal emission, the relative increase is even stronger with $\alpha \approx 2.4$. Note that the exponent α for the mass region where the excess above the cocktail is found (i.e., 0.3 - $0.6 \text{ GeV}/c^2$) is similar and only slightly larger compared to the one obtained using a fireball parametrization [11]; there the scaling with the total number of charged hadronic particles is found to be N_{ch}^α

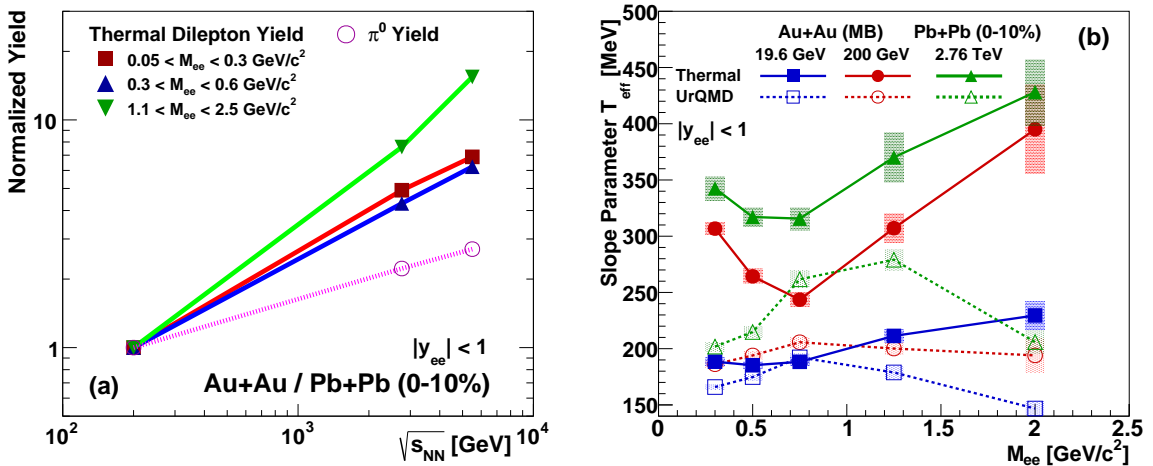


FIG. 11. (Color online) (a) Thermal dilepton yield for three different mass regions and the π^0 yield for central Au+Au/Pb+Pb collisions, normalized to the result for $\sqrt{s_{NN}} = 200$ GeV. (b) Mass dependent slope parameter T_{eff} for the thermal (full lines) and non-thermal (dashed lines) dilepton yields in minimum bias Au+Au collisions at 19.6 GeV (blue) and 200 GeV as well as for central Pb+Pb at 2.76 TeV (green). The error bands indicate the systematic error of the fit. All results are for mid-rapidity, i.e., for $|y_{ee}| < 1$.

and $\alpha = 1.8$. The somewhat stronger enhancement of the high-mass yield at LHC energies is explained by the fact that the number of QGP-emitting hot cells exhibits a larger increase than the lower temperature four-volume (compare Figs. 1 and 2).

Whereas the thermal yields alone allow for only rather qualitative conclusions regarding the underlying reaction dynamics, another observable that helps to determine the temperature and expansion dynamics of the created fireball is the slope of the transverse-mass spectra ($m_t = \sqrt{M_{ee}^2 + p_t^2}$). The effective slope parameter T_{eff} can be extracted using the fit function [102]

$$\frac{dN}{m_t dm_t} = C \cdot \exp\left(-\frac{m_t}{T_{\text{eff}}}\right). \quad (12)$$

Note that T_{eff} must not be confounded with the temperature of the medium, as the transverse momentum distribution from a thermal source is not only determined by the temperature: The radial flow of the system leads to a significant blue-shift of the m_t spectra as well [11]. The effective slope parameter for the thermal and hadronic cocktail (UrQMD) contributions at mid-rapidity for Au+Au and Pb+Pb collisions at three different energies ($\sqrt{s_{NN}} = 19.6, 200$ and 2760 GeV) is shown in Figure 11(b). The results are presented for different mass bins ranging from 0.2 to $2.5 \text{ GeV}/c^2$. To obtain T_{eff} the spectra were fitted in mass-dependent m_t -ranges corresponding to $0.5 < p_t < 1.8 \text{ GeV}/c$. Interestingly, the results exhibit completely different mass-dependencies for thermal and non-thermal contributions. T_{eff} of the non-thermal decay contributions reaches a maximum around the ρ and ω pole masses (for RHIC

energies) or around $1\text{-}1.5 \text{ GeV}/c^2$ (at LHC) and falls off when going to lower or higher energies. Conversely, the slope parameter of the thermal contributions drops with increasing mass or remains at the same level up to approximately $1 \text{ GeV}/c^2$ and then it shows a strong rise for higher masses.

The different mass-dependency of T_{eff} for the thermal and non-thermal decay contributions can be explained by the different conditions of emission: Where the thermal source is mainly of hadronic nature, i.e., especially around the ρ and ω pole masses, one finds a lower average emission temperature, compared to the mass ranges dominated by the partonic contribution. This effect is reflected in the thermal m_t -slopes. The increase of T_{eff} for masses above $1 \text{ GeV}/c^2$ is due to the fact that the thermal high mass emission is suppressed at lower temperatures. In contrast, the non-thermal hadronic decays mostly occur at a late stage of the fireball evolution, outside the hot and dense region. This leads to in general lower slope parameters obtained for the non-thermal contributions compared to the thermal ones. However, note that there is a difference between the contributions from the long-lived low-mass π^0 and η mesons, for which one finds the lowest T_{eff} , and especially the very short-lived freeze-out ρ contribution. In spite of the fact that here the ρ stems only from cells where no thermal emission is assumed, in its pole mass region one finds a harder slope than at the π^0 and η dominated low-masses. A reason might also be that these ρ mesons carry additional momentum due to their rather late and peripheral origin, compared to the other mesons. The decrease for higher masses above $1 \text{ GeV}/c^2$ —which are dominated by the ϕ

and still some ρ —might be explained by the kinematics of the microscopic decay processes, where high momenta are naturally suppressed if a particle with higher mass is produced, and the longer lifetime of the ϕ compared to the ρ meson.

The slope parameters for the thermal emission from the coarse-graining approach are similar to those from a fireball parametrization [11] for RHIC energies, but for the LHC they seem to be somewhat smaller. However, as already mentioned, it is known that the flow effects are underestimated within the UrQMD model at high collision energies [48], so that these differences should be mainly due to a less distinct expansion of the system and not due to differences in the average temperature. The same conclusion is suggested by the comparison of dilepton spectra with experimental data, where we saw an underestimation of the yield for high- p_t (see, e.g., Fig. 6 (b)).

IV. CONCLUSIONS & OUTLOOK

In this paper we have presented dilepton spectra for energies available at collider energies, obtained with an approach using coarse-grained UrQMD transport simulations to calculate the thermal dilepton emission. The results for RHIC energies are compared with the experimental data from the STAR and PHENIX Collaborations and show good agreement. Furthermore, we could depict that the newest PHENIX results collected with the HBD upgrade of the detector are now fully consistent with the STAR measurements and can both be reproduced within the coarse-graining approach. The excess above the hadronic cocktail in the region for $0.3 < M_{e^+e^-} < 0.7 \text{ GeV}/c^2$ is hereby explained by thermal emission from a broadened ρ and the Quark-Gluon Plasma.

For higher masses above the ϕ peak our results lie by tendency somewhat below the experimental data. This can be mainly ascribed to the missing implementation of the charm emission, which will be the dominant source for these high masses. However, our results show that also the partonic emission gives a significant contribution to the overall yield in this mass region. Furthermore, a comparison of different EoS indicates that the thermal dilepton spectrum for $M_{e^+e^-} > 1 \text{ GeV}/c^2$ might enable one to draw conclusions with regard to the QCD phase structure and the equation of state if the charm contribution can be reliably subtracted. The present results are consistent with the open-charm dilepton spectra obtained using a Langevin approach to simulate the in-medium effects on the invariant-mass spectra in a transport+hydro hybrid model. These simulations indicate a strong suppression of the open charm contribution in hot and dense matter compared to the vacuum case, making up only roughly 50% of the total high-mass yield [39]. In conse-

quence, a study of dilepton emission including the charm contribution in the coarse-graining approach would be very instructive for the full understanding of dilepton emission patterns for higher masses and is planned for future investigations.

While the energy and centrality dependence of the dilepton production are well reproduced within the model, the transverse-momentum dependence shows some deviations from the measurement for higher p_t , whereas the (dominant) low-momentum production is quite well described. This effect is probably connected to an underestimation of the collective flow in the underlying transport model. One should bear in mind that the model is purely hadronic and that it might therefore not be able to describe some dynamical effects adequately, which are due to the emergence of a partonic phase. However, considering the hadronic nature of the model, the agreement with experimental data as well as the spectra from fireball parametrizations is surprisingly good. In consequence, this substantiates the basic idea of the coarse-graining approach, namely that the only necessary information regarding the fireball evolution is the distribution of energy and particle densities (or T and μ , respectively), if one wants to determine the dilepton emission.

Together with the previous results for SIS 18, FAIR and CERN-SPS energies, the coarse-graining approach has proven a successful tool for the theoretical description of dilepton production in heavy-ion collisions over the whole domain of presently available energies, corresponding to a range of $\sqrt{s_{NN}}$ which spans over three orders of magnitude. It is, nevertheless, also apparent that the coarse-graining approach in its present form can not fully substitute a study of the QCD phase structure based on a microscopic picture of the fireball evolution including the effects from the creation of a deconfined phase of quasifree quarks and gluons. This will be important, e.g., for the study of the anisotropic flow of electromagnetic probes.

ACKNOWLEDGMENTS

The authors especially thank Ralf Rapp for providing the parametrizations of the spectral functions. S. E. acknowledges Jan Steinheimer for valuable and fruitful discussions. This work was supported by the Hessian Initiative for Excellence (LOEWE) through the Helmholtz International Center for FAIR (HIC for FAIR), the Bundesministerium für Bildung und Forschung, Germany (BMBF) and the Helmholtz-Gemeinschaft through the Research School for Quark-Matter Studies (H-QM). The computational resources for this work were provided by the LOEWE-CSC.

-
- [1] H. Stöcker and W. Greiner, *Phys. Rept.* **137**, 277 (1986).
- [2] P. Danielewicz, R. Lacey, and W. G. Lynch, *Science* **298**, 1592 (2002).
- [3] E. Shuryak, *Prog. Part. Nucl. Phys.* **62**, 48 (2009).
- [4] R. Rapp, J. Wambach, and H. van Hees, in R. Stock (ed.), *Relativistic Heavy Ion Physics*, vol. 23 of *Landolt-Börnstein - Group I Elementary Particles, Nuclei and Atoms*, 134–175 (Springer, Berlin, 2010).
- [5] J. Schukraft and R. Stock, in H. Schopper and L. Di Lella (eds.), *60 Years of CERN Experiments and Discoveries*, chap. 3, 61–87 (World Scientific, Singapore, 2015).
- [6] J. D. Bjorken, *Phys. Rev. D* **27**, 140 (1983).
- [7] E. L. Feinberg, *Nuovo Cim. A* **34**, 391 (1976).
- [8] E. V. Shuryak, *Phys. Lett. B* **78**, 150 (1978).
- [9] G. Vujanovic, C. Young, B. Schenke, R. Rapp, S. Jeon, et al., *Phys. Rev. C* **89**, 034904 (2014).
- [10] R. Ryblewski and M. Strickland, *Phys. Rev. D* **92**, 025026 (2015).
- [11] R. Rapp, *Adv. High Energy Phys.* **2013**, 148253 (2013).
- [12] R. Rapp and H. van Hees, *Phys. Lett. B* **753**, 586 (2016).
- [13] L. Adamczyk et al. (STAR Collaboration), *Phys. Rev. Lett.* **113**, 022301 (2014), [Addendum: *Phys. Rev. Lett.* **113**, 049903 (2014)].
- [14] L. Adamczyk et al. (STAR Collaboration), *Phys. Rev. C* **92**, 024912 (2015).
- [15] L. Adamczyk et al. (STAR Collaboration), *Phys. Lett. B* **750**, 64 (2015).
- [16] A. Adare et al. (PHENIX Collaboration), *Phys. Rev. C* **93**, 014904 (2016).
- [17] K. Schmidt, E. Santini, S. Vogel, C. Sturm, M. Bleicher, et al., *Phys. Rev. C* **79**, 064908 (2009).
- [18] J. Weil, H. van Hees, and U. Mosel, *Eur. Phys. J. A* **48**, 111 (2012).
- [19] J. Weil, S. Endres, H. van Hees, M. Bleicher, and U. Mosel, *J. Phys. Conf. Ser.* **612**, 012039 (2015).
- [20] S. Endres and M. Bleicher, *J. Phys. Conf. Ser.* **426**, 012033 (2013).
- [21] E. Bratkovskaya, J. Aichelin, M. Thomere, S. Vogel, and M. Bleicher, *Phys. Rev. C* **87**, 064907 (2013).
- [22] B. Schenke and C. Greiner, *Phys. Rev. C* **73**, 034909 (2006).
- [23] B. Schenke and C. Greiner, *Phys. Rev. Lett.* **98**, 022301 (2007).
- [24] J. Weil, U. Mosel, and V. Metag, *Phys. Lett. B* **723**, 120 (2013).
- [25] E. L. Bratkovskaya, W. Cassing, R. Rapp, and J. Wambach, *Nucl. Phys. A* **634**, 168 (1998).
- [26] E. Bratkovskaya and W. Cassing, *Nucl. Phys. A* **807**, 214 (2008).
- [27] O. Linnyk, W. Cassing, J. Manninen, E. L. Bratkovskaya, and C. M. Ko, *Phys. Rev. C* **85**, 024910 (2012).
- [28] O. Linnyk, E. L. Bratkovskaya, and W. Cassing, *Prog. Part. Nucl. Phys.* **87**, 50 (2016), 1512.08126.
- [29] P. Huovinen, M. Belkacem, P. J. Ellis, and J. I. Kapusta, *Phys. Rev. C* **66**, 014903 (2002).
- [30] S. Endres, H. van Hees, J. Weil, and M. Bleicher, *Phys. Rev. C* **91**, 054911 (2015).
- [31] S. Endres, H. van Hees, J. Weil, and M. Bleicher, *Phys. Rev. C* **92**, 014911 (2015).
- [32] S. Endres, H. van Hees, and M. Bleicher, *Phys. Rev. C* **93**, 054901 (2016).
- [33] J. Steinheimer, M. Lorenz, F. Becattini, R. Stock, and M. Bleicher (2016), arXiv:1603.02051 [nucl-th].
- [34] S. A. Bass, M. Belkacem, M. Bleicher, M. Brandstetter, L. Bravina, et al., *Prog. Part. Nucl. Phys.* **41**, 255 (1998).
- [35] M. Bleicher, E. Zabrodin, C. Spieles, S. A. Bass, C. Ernst, et al., *J. Phys. G* **25**, 1859 (1999).
- [36] A. Adare et al. (PHENIX Collaboration), *Phys. Lett. B* **670**, 313 (2009).
- [37] H. van Hees and R. Rapp, *Phys. Rev. C* **71**, 034907 (2005).
- [38] T. Lang, H. van Hees, J. Steinheimer, G. Inghirami, and M. Bleicher, *Phys. Rev. C* **93**, 014901 (2016).
- [39] T. Lang, H. van Hees, J. Steinheimer, and M. Bleicher (2013), arXiv:1305.7377 [hep-ph].
- [40] G. David, R. Rapp, and Z. Xu, *Phys. Rept.* **462**, 176 (2008).
- [41] A. Adare et al. (PHENIX Collaboration), *Phys. Rev. Lett.* **109**, 122302 (2012).
- [42] A. Adare et al. (PHENIX Collaboration) (2015), arXiv:1509.07758 [nucl-ex].
- [43] H. Petersen, M. Bleicher, S. A. Bass, and H. Stöcker (2008), arXiv:0805.0567 [hep-ph].
- [44] <http://www.urqmd.org>.
- [45] W. M. Yao et al. (Particle Data Group), *J. Phys. G* **33**, 1 (2006).
- [46] E. L. Bratkovskaya, M. Bleicher, M. Reiter, S. Soff, H. Stoecker, M. van Leeuwen, S. A. Bass, and W. Cassing, *Phys. Rev. C* **69**, 054907 (2004).
- [47] M. Mitrovski, T. Schuster, G. Graf, H. Petersen, and M. Bleicher, *Phys. Rev. C* **79**, 044901 (2009).
- [48] H. Petersen, Q. Li, X. Zhu, and M. Bleicher, *Phys. Rev. C* **74**, 064908 (2006).
- [49] M. Bleicher and H. Stoecker, *Phys. Lett. B* **526**, 309 (2002).
- [50] X.-l. Zhu, M. Bleicher, and H. Stoecker, *Phys. Rev. C* **72**, 064911 (2005).
- [51] X.-l. Zhu, M. Bleicher, and H. Stoecker, *J. Phys. G* **32**, 2181 (2006).
- [52] Y. Lu, M. Bleicher, F. Liu, Z. Liu, H. Petersen, P. Sorensen, H. Stoecker, N. Xu, and X. Zhu, *J. Phys. G* **32**, 1121 (2006).
- [53] P. F. Kolb, P. Huovinen, U. W. Heinz, and H. Heiselberg, *Phys. Lett. B* **B00**, 232 (2001).
- [54] V. P. Konchakovski, E. L. Bratkovskaya, W. Cassing, V. D. Toneev, S. A. Voloshin, and V. Voronyuk, *Phys. Rev. C* **85**, 044922 (2012).
- [55] J. Uphoff, F. Senzel, O. Fochler, C. Wesp, Z. Xu, and C. Greiner, *Phys. Rev. Lett.* **114**, 112301 (2015).
- [56] C. Eckart, *Phys. Rev.* **58**, 919 (1940).
- [57] D. Zschesche, S. Schramm, J. Schaffner-Bielich, H. Stöcker, and W. Greiner, *Phys. Lett. B* **547**, 7 (2002).
- [58] M. He, R. J. Fries, and R. Rapp, *Phys. Rev. C* **85**, 044911 (2012).
- [59] H. Petersen, J. Steinheimer, G. Burau, M. Bleicher, and H. Stöcker, *Phys. Rev. C* **78**, 044901 (2008).
- [60] J. Steinheimer, V. Dexheimer, H. Petersen, M. Bleicher,

- S. Schramm, and H. Stoecker, Phys. Rev. C **81**, 044913 (2010).
- [61] L. Bravina, E. Zabrodin, M. I. Gorenstein, S. Bass, M. Belkacem, et al., Nucl. Phys. A **661**, 600 (1999).
- [62] L. Bravina, E. Zabrodin, M. I. Gorenstein, S. Bass, M. Belkacem, et al., Phys. Rev. C **60**, 024904 (1999).
- [63] W. Florkowski and R. Ryblewski, Phys. Rev. C **83**, 034907 (2011).
- [64] W. Florkowski, M. Martinez, R. Ryblewski, and M. Strickland, Nucl. Phys. A **904-905**, 803c (2013).
- [65] D. Bandyopadhyay, M. Gorenstein, H. Stöcker, W. Greiner, and H. Sorge, Z. Phys. C **58**, 461 (1993).
- [66] P. Koch, Phys. Lett. B **288**, 187 (1992).
- [67] R. Rapp and J. Wambach, Adv. Nucl. Phys. **25**, 1 (2000).
- [68] U. Heinz, in R. Stock (ed.), *Relativistic Heavy Ion Physics*, vol. 23 of *Landolt-Börnstein - Group I Elementary Particles, Nuclei and Atoms*, 240–292 (Springer, Berlin, 2010).
- [69] A. Muronga, Phys. Rev. C **69**, 034903 (2004).
- [70] A. Muronga, Phys. Rev. C **69**, 044901 (2004).
- [71] N. Demir and S. A. Bass, Eur. Phys. J. C **62**, 63 (2009).
- [72] N. Demir and S. A. Bass, Phys. Rev. Lett. **102**, 172302 (2009).
- [73] T. E. Nemakhavhani and A. Muronga (2016), arXiv:1603.06347 [nucl-th].
- [74] U. W. Heinz and P. F. Kolb, Nucl. Phys. A **702**, 269 (2002).
- [75] M. Gyulassy and L. McLerran, Nucl. Phys. A **750**, 30 (2005).
- [76] D. Teaney, Phys. Rev. C **68**, 034913 (2003).
- [77] K. Dusling, Nucl. Phys. A **839**, 70 (2010).
- [78] M. Dion, J.-F. Paquet, B. Schenke, C. Young, S. Jeon, and C. Gale, Phys. Rev. C **84**, 064901 (2011).
- [79] B. Schenke and M. Strickland, Phys. Rev. D **76**, 025023 (2007).
- [80] S.-X. Liu, F.-M. Liu, K. Werner, and M. Yue (2015), arXiv:1508.05160 [hep-ph].
- [81] F.-M. Liu, S.-X. Liu, and K. Werner (2015), arXiv:1512.08833 [nucl-th].
- [82] C. Shen, U. W. Heinz, J.-F. Paquet, I. Kozlov, and C. Gale, Phys. Rev. C **91**, 024908 (2015).
- [83] C. Shen, J.-F. Paquet, U. Heinz, and C. Gale, Phys. Rev. C **91**, 014908 (2015).
- [84] J. Cleymans, J. Fingberg, and K. Redlich, Phys. Rev. D **35**, 2153 (1987).
- [85] E. Braaten, R. D. Pisarski, and T.-C. Yuan, Phys. Rev. Lett. **64**, 2242 (1990).
- [86] H.-T. Ding, A. Francis, O. Kaczmarek, F. Karsch, E. Laermann, et al., Phys. Rev. D **83**, 034504 (2011).
- [87] V. L. Eletsky, M. Belkacem, P. Ellis, and J. I. Kapusta, Phys. Rev. C **64**, 035202 (2001).
- [88] F. Klingl, N. Kaiser, and W. Weise, Nucl. Phys. A **624**, 527 (1997).
- [89] L. D. McLerran and T. Toimela, Phys. Rev. D **31**, 545 (1985).
- [90] R. Rapp and J. Wambach, Eur. Phys. J. A **6**, 415 (1999).
- [91] R. Rapp (2014), private communication.
- [92] H. van Hees and R. Rapp, Nucl. Phys. A **806**, 339 (2008).
- [93] R. Baier, M. Dirks, and K. Redlich, Acta Phys. Polon. B **28**, 2873 (1997).
- [94] R. Baier, M. Dirks, K. Redlich, and D. Schiff, Phys. Rev. D **56**, 2548 (1997).
- [95] M. Dey, V. Eletsky, and B. L. Ioffe, Phys. Lett. B **252**, 620 (1990).
- [96] H. van Hees and R. Rapp, Phys. Rev. Lett. **97**, 102301 (2006).
- [97] N. M. Kroll and W. Wada, Phys. Rev. **98**, 1355 (1955).
- [98] L. G. Landsberg, Phys. Rept. **128**, 301 (1985).
- [99] G.-Q. Li and C. M. Ko, Nucl. Phys. A **582**, 731 (1995).
- [100] A. Adare et al. (PHENIX Collaboration), Phys. Rev. C **81**, 034911 (2010).
- [101] R. Rapp, AIP Conf. Proc. **1322**, 55 (2010).
- [102] T. Renk and J. Ruppert, Phys. Rev. C **77**, 024907 (2008).